Disordered Block Polymers for Highly Selective Water Filtration Membranes

A DISSERTATION
SUBMITTED TO THE FACULTY OF
UNIVERSITY OF MINNESOTA
BY

Nicholas Edward Hampu

IN PARTIAL FULFILLMENT OF THE REQUIREMENTS
FOR THE DEGREE OF
DOCTOR OF PHILOSOPHY

Marc A. Hillmyer, Advisor

June 2020

Acknowledgements

Obtaining a PhD is never a solo endeavor, and my graduate career owes much to the help, support, and inspiration of a number of people. First, I would like to thank my high school chemistry teacher Michael Owen for demonstrating that chemistry can be fun and fostering an interest in the chemical sciences. As an undergraduate at Case Western Reserve University, I had the privilege of extensively participating in research and received ample encouragement to attend graduate school. Specifically, I would like to thank my undergraduate advisors Prof. Gary Wnek and Prof. Joao Maia for welcoming me into their labs, as well as Dr. Creusa Ferreira for serving as a valued mentor. Finally, I would like to thank Prof. David Schiraldi for convincing me to join the Polymer Science program and facilitating an environment that encouraged undergraduate participation in research.

At the University of Minnesota, I am privileged to have had an excellent advisor in Prof. Marc Hillmyer, who was always encouraging with positive feedback. When applying for graduate programs, I had two key requirements – joining a world-class research group in polymer science and not synthesizing a single polymer. At Minnesota, I met one of those criteria. I am incredibly grateful to Marc for welcoming into his group and convincing me that even I could make my own polymers. Marc has been an excellent mentor, helping me grow as a scientist and independent researcher. I am thankful that I have had the opportunity to pursue research topics that have aligned with my own scientific interests and have been allowed the flexibility to shape my own thesis research. Leaving his group at Minnesota, I can proudly say that I have grown as both a person and a scientist.

At Minnesota, I have had the great opportunity to work with excellent scientists both within the Hillmyer group and within the Polymer Group in general. I would like to especially thank my mentors Dr. Morgan Bates and Dr. Thomas Vidil for training me as both a polymer chemist and scientist during my early days in the lab. Later in my career, I have also greatly benefited from the mentorship of and collaboration with Dr. Jay Werber and Dr. Daphne Chan. One of the hardest, yet best, aspects of working in the Hillmyer group is the continuous stream of great researchers and great people both into and out of the lab. Throughout my time, I have had stimulating scientific discussion and fun times with many people, including Dr. Debbie Schneiderman, Dr. Alex Todd, Dr. Mike Larsen, Dr. Stacey Saba, Dr. Sujay Chopade, Dr. Angelika Neitzel, Dr. Guilhem De Hoe, Dr. Sebla Onbulak, Dr. Adrian Amador, Dr. Lucie Fournier, Dr. Eric Silver, Dr. Chris De Rosa, Dr. Esra Altay, Dr. Chip Resiman, Dr. Farihah Haque, Dr. Adam Feinberg, David Goldfeld, Claire Dingwell, and Colin Peterson. I would like to thank Christopher Rademacher who worked with me as an undergraduate researcher. I would also like to thank all the staff scientists who have assisted through the years with my research, including David Giles in the Polymer Characterization Facility, Chris Frethem and Hang-seung Lee in Charfac, and Steven Weigand at Argonne National Lab. Finally, I would like to thank everyone in the Polymer Group who has kept me awake and functioning during the late nights at APS: Aaron Lindsay, Claire Seitzinger, Cecilia Hall, Nick Van Zee, Bo Zhang, and Shuyi Xie.

During my graduate career, I have met a number of extraordinary people. I have enjoyed playing weekly pickup basketball games with Ashish Jayaraman, Dayne Plemmons, Greg Facas, Matt Palys, Spencer Reisbeck, Matt Hausladen, Kailong Jin, and Boran Zhao.

Additionally, I have appreciated the slow and steady growth of our softball team Sexy and Sustainable. Finally, I would like to thank all of my friends that I have made in both CEMS and the Chemistry Departments as well as my roommates over the years, Ryan Gnabasik, A. J. Hagen, Catherine Clark, and Remy Ford. All of the people here along with many others have greatly contributed to my success at the University of Minnesota.

Dedication

To my family.

Abstract

Reliable access to clean water is a major and growing societal challenge. Selective membrane technologies are expected to play a critical role in sustaining the water economy due to their energy efficient filtration of wastewater. High performing water filtration membranes require both high water permeability and high size-selectivity to ensure that purified water is produced in a cost-effective manner. Existing ultrafiltration membranes contain continuous and interconnected pores that allow for the rapid transport of water, satisfying the requirement of high water permeability. However, they typically exhibit broad pore size distributions that limit their size-selectivity and prohibit their application in highly precise separations. Block polymers represent a potentially powerful alternative class of materials for improved size-selectivity due to their self-assembly into well-defined domains of uniform size at the nanoscale. Removing one of the blocks generates the uniform pores required for precise separations. By coating a thin block polymer selective layer onto a commercially available ultrafiltration membrane, it may be possible to simultaneously obtain both high water permeability and high size-selectivity in a single membrane.

However, commercialization of block polymer membranes has been impeded by technological challenges associated with producing continuous pores in an industrially scalable fabrication process from the typically observed ordered block polymer morphologies. Rather than targeting these ordered morphologies, this thesis aims to utilize the disordered state of block polymers to produce higher performing and potentially more scalable membranes. By kinetically trapping disordered state composition fluctuations, a

disordered and co-continuous morphology can be obtained and subsequently converted into uniform and continuous pores without the need for challenging processing techniques. Chapter 1 introduces key concepts in block polymer self-assembly, including the order-disorder transition and composition fluctuations. Chapter 2 provides a summary of the technological requirements of an ideal water filtration membrane and discusses various strategies to integrate block polymers into these systems. Chapter 3 contains an overview of the various synthetic, processing, and characterization techniques employed throughout the thesis. Chapter 4 describes proof-of-concept results demonstrating that thermal cross-linking can be used to kinetically trap disordered state composition fluctuations. Chapter 5 details a strategy that introduces temporal control by using thermally stable photocuring strategies to arrest the disordered state. Chapter 6 describes a fundamental investigation into the temperature dependent morphological evolution of block polymers in the disordered state. Chapter 7 examines the use of large amplitude oscillatory shear to precisely control the domain structure of disordered block polymers. Chapter 8 integrates all these findings into the development of a novel co-casting technique to fabricate composite membranes with both high water permeability and high size-selectivity in a potentially scalable manner.

Table of Contents

List of Tables

List of Figures

List of Abbreviations

AIBN	azobisisobutyronitrile
BET	Brunauer-Emmett-Teller
BJH	Barret, Joyner, and Halenda
BPO	benzoyl peroxide
BTPH	benzyl triphenylphosphonium hexafluoroantimonate
$CDCl_3$	deuterated chloroform
CTA	chain-transfer agent
DBU	1,8-Diazabicyclo[5.4.0]undec-7-ene
DCM	dichloromethane
DCP	dicumyl peroxide
DMA	dynamic mechanical analysis
DSC	differential scanning calorimetry
FTIR	Fourier transform infrared
IST	4-iodophenyldiphenylsulfonium triflate
LAOS	large amplitude oscillatory shear
LS	light scattering
M_n	number-averaged molar mass
M_w	mass-averaged molar mass
NIPS	non-solvent induced phase separation
NMR	nuclear magnetic resonance
ODT	order-disorder transition
PDVB	poly(divinylbenzene)
PGMA	poly(glycidyl methacrylate)
PIMS	polymerization-induced microphase separation
PLA	poly(lactide)
PMMA	poly(methyl methacrylate)
PS	poly(styrene)
QSDFT	quenched solid density functional theory
RAFT	reversible addition-fragmentation chain transfer
RI	refractive index
S	styrene
SAXS	small-angle X-ray scattering
SEC	size exclusion chromatography
SEM	scanning electron microscopy
TEM	transmission electron microscopy
TGA	thermal gravimetric analysis
THF	tetrahydrofuran
T_g	glass transition temperature
T_{ODT}	order-disorder transition temperature
TRITC	tetramethylrhodamine isothiocyanate
UF	ultrafiltration

Chapter 1. Background: Block Polymer Self-assembly and the Order-Disorder Transition

1.1 Applications of Nanomaterials

Nanomaterials have the potential to revolutionize existing technologies and foster the development of completely new research areas. These materials are expected to have a high societal impact in a number of different areas, including energy storage and conversion,[1] drug delivery and medicine,[2] and water treatment.[3] Harnessing the arrangement of nanomaterials into well-defined and regular structures with nanoscale precision is crucial for capitalizing on their potential.[4] One of the most promising strategies to achieve this goal is bottom-up self-assembly.[5] Self-assembly describes the process of individual components organizing into a well-defined collective structure without external intervention due to specific and localized interactions.[4–6] In the case of nanomaterials, the individual components are molecules or macromolecules that form nanoscale patterns as a result of intermolecular interactions. Advances in nanotechnology require precise control of the symmetry and size of these nanoscale structures, and preferably, this would be achieved by modularly tuning the molecular design of the components.[4,6]

Block polymers, comprising two or more chemically distinct polymers covalently linked into a single chain, have received significant attention from the nanomaterials community due to their ability to self-assemble into regularly ordered nanostructures of tunable size and symmetry through careful design of the molar mass and composition.[7,8] Generally, higher molar masses correspond to larger self-assembled domains, typically ranging

between 10 – 50 nm in size.[9] Furthermore, a number of different nanostructured morphologies can be accessed by tuning the relative composition of the blocks (represented by the volume fraction, *f*). Traditionally, a transition from lamellae to three-dimensional network phases to cylinders to spherical packings is observed with increasing block length asymmetry (Figure 1.1).[7,8,10,11] The ability to control the size and structure of nanoscale features through the rational design of block polymer molecules can help harness nanomaterial self-assembly.This thesis will focus on the synthesis of self-assembled block polymers to serve as a template in the production of water filtration membranes with uniformly sized pores.

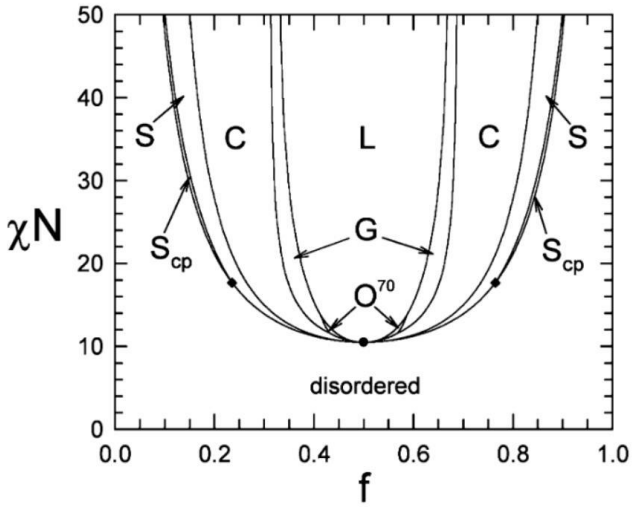

Figure 1.1. Phase diagram for melts of AB diblock copolymers, assuming monodisperse molar mass and conformational symmetry. At low temperatures or high degrees of polymerization, *N*, the block polymer microphase separates into various ordered morphologies with the symmetry depending upon the relative volume fraction, *f*. For this ideal case, there is a transition from lamellar (L) to gyroid (G) and Fddd (O^{70}) to cylindrical (C) to body centered cubic spherical (S) to face centered cubic spherical morphologies (S_{cp}) as *f* increase from 0.5 to 1.0. Reprinted with permission from Matsen, M. W. *Macromolecules* **2012**, *45*, 2161.[12] Copyright 2012 American Chemical Society.

1.2 Fundamentals of Block Polymer Self-assembly and Microphase Separation

Phase separation in multicomponent polymeric systems is governed by two competing effects – an enthalpic drive to minimize unfavorable interactions and an entropic drive to mix.[10] The tendency to phase separate can be represented by the free energy of mixing:

$$\frac{\Delta G_{mix}}{kT} = \frac{\phi_A}{N_A}\ln\phi_A + \frac{\phi_B}{N_B}\ln\phi_B + \chi\phi_A\phi_B \text{ (eq. 1)}$$

where ϕ is the volume fraction, N is the reference volume normalized degree of polymerization, and χ is an interaction parameter.[13,14] The first two terms represent entropic contributions to the free energy of mixing (by definition $\phi < 0$ and thus $\Delta S_{mix} < 0$), and the last term represents the enthalpic component of the free energy. At low temperatures, enthalpic contribution dominate and phase separation occurs.[10] In block polymers, the chemically distinct polymers are covalently linked into a single molecule, preventing macroscopic phase separation. These covalent linkages introduce an additional entropic penalty for separating the blocks, limiting phase separation to the molecular scale – a phenomenon termed microphase separation.[7,10] The driving force for microphase separation is captured by the segregation strength, χN. High values of χN drive the block polymer to self-assemble into an ordered, microphase separated morphology.

The interaction parameter, χ, represents the energy required to interchange two chemically distinct monomers, and it is classically described using Flory-Huggins lattice theory[13,14]

$$\chi = \frac{z}{kT}\left[\epsilon_{AB} - \frac{1}{2}(\epsilon_{AA} - \epsilon_{BB})\right] \text{ (eq. 2)}$$

Commonly, χ is calculated using the solubility parameters, δ, of the blocks and a reference volume, v_0, that represents the lattice size inherent to Flory-Huggins theory[14]

$$\chi = \frac{v_0(\delta_A - \delta_B)^2}{RT} \text{ (eq. 3)}$$

Equations 2 and 3 reveal that χ scales inversely with temperature, with lower temperatures corresponding to a larger chemical incompatibility and thus a stronger tendency to microphase separate. While equations 2 and 3 are useful as a conceptual framework, they only represent enthalpic contributions to the excess free energy of mixing. In reality, many systems also exhibit entropic contributions related to polymer conformation and packing frustration.[15] Therefore, a phenomenological approach is often taken to express χ in the form of

$$\chi = \frac{A}{T} + B = \chi_{enthalpic} + \chi_{entropic} \text{ (eq. 4)}$$

The interaction parameter represented by equation 4[14,15] can be obtained by fitting experimental data from dynamic mechanical analysis (DMA) and small angle X-ray scattering (SAXS) to models. Most block polymers exhibit A > 0 and B < 0, resulting in upper critical solution temperature behavior, i.e. increasing the temperature promotes block mixing.[13,15]

1.3 The Order-Disorder Transition

At low temperatures, χN is relatively large and enthalpic contributions to the free energy of mixing dominate, driving microphase separation into an ordered morphology.[10] The volume fraction, $f_A = N_A/(N_A + N_B)$, determines the geometry of the microphase separated domains.[7,8,10] This thesis will primarily focus on nearly symmetric diblock polymers with $f_A = 0.5$ that self-assemble into a lamellar morphology. For most block polymers, χ decreases with increasing temperature, resulting in a lower enthalpic contribution to the free energy. At high temperatures, entropic contributions will dominate, driving the domains to mix at the molecular scale. This results in a loss in long-range order, and this

transition from an ordered, microphase separated state to a disordered, phase-mixed state is termed an order-disorder transition (ODT). The temperature corresponding to the ODT is thus referred to as the order-disorder transition temperature, T_{ODT}.

The physics underlying the phase behavior of block polymers is commonly described using mean-field theories, particularly self-consistent field theory (SCFT).[11,16–19] Seminal work by Leibler used SCFT formalism to map the phase boundaries between various ordered morphologies as well as between the ordered and disordered states.[17] Further refinement of this classic work has transformed SCFT into a powerful tool for predicting the phase behavior of block polymers at high χN, i.e. for $\chi N >> (\chi N)_{ODT}$.[11,12,19,20] However, mean field theories, including SCFT, fail to accurately represent the phase behavior near the ODT for polymers of finite molar mass.[16] Notably, SCFT predicts the existence of a critical point at $f = 0.5$ and $\chi N = 10.5$ and a continuous, 2nd order transition from the ordered lamellar state to the disordered state, which are both inconsistent with experimental findings.[17] The failure of SCFT directly relates to its mean-field formalism, which neglects composition fluctuations and instead models the disordered state as a molecularly mixed, homogeneous state.[10,13,16] For real block polymers of finite molar mass, composition fluctuations destroy the critical point and 2nd order phase transition predicted by SCFT. Instead, fluctuations result in a weakly 1st order transition from an ordered morphology to a globally disordered state that remains locally microphase separated at the length scale of the block radius of gyration, R_g.[16,21–23] Composition fluctuations stabilize the disordered state and increase $(\chi N)_{ODT}$ relative to the mean-field prediction.[16,23] These disordered, yet microphase separated domains are thermodynamically stabilized by a topological entropy arising from

undulations about the average interfacial curvature.[24] The locally microphase separated domains form a transient pattern that has been hypothesized to resemble patterns observed during spinodal decomposition of immiscible liquids, comprising a disordered and co-continuous nanostructure (Figure 1.2).[21,25–28] Experimental evidence of composition fluctuations and the hypothesized nanostructure will be discussed throughout the duration of this chapter.

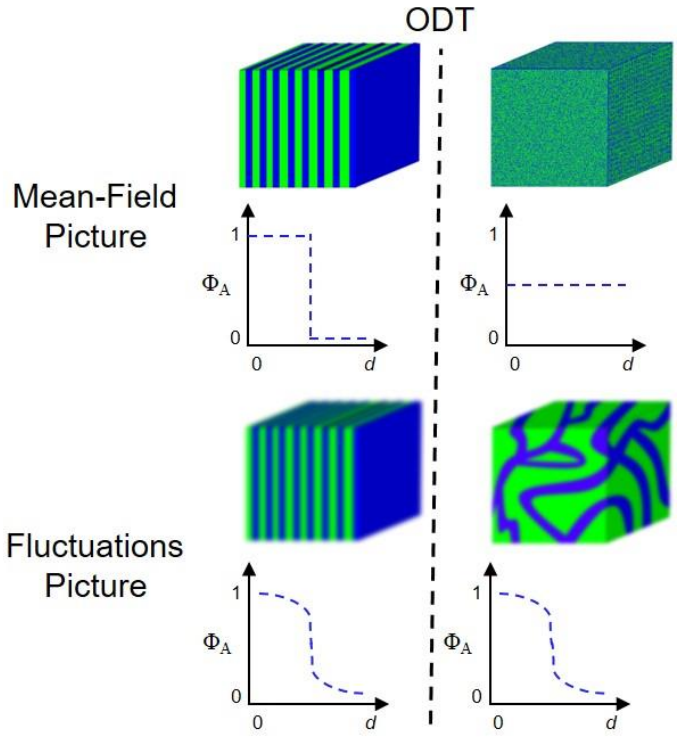

Figure 1.2. Cartoon representations of the domain structures across the T_{ODT} for both a mean-field system and a system with strong composition fluctuations. A sketch of the anticipated composition profile of the volume fraction of the A block (Φ_A) across one lamellar period (d) for varying χN is provided below the respective cartoon.

1.4 Experimental Evidence and Implications of Composition Fluctuations

1.4.1 Rheological Evidence

The existence of composition fluctuations near the ODT was first demonstrated experimentally by DMA, as described by Bates in 1984.[29] Time-temperature superposition

(TTS) was applied to rheological frequency sweeps acquired across a range of temperatures both below and above T_{ODT} (Figure 1.3). In the ordered state for $T < T_{ODT}$, the storage moduli, G', superimposed onto a single master curve. Conversely, in the disordered state for $T > T_{ODT}$, TTS failed in the low frequency regime.[29] The non-terminal frequency dependence of G' and the failure of TTS in the low frequency limit for $T > T_{ODT}$ were hypothesized to reflect nanostructural features that persisted even in the disordered state, resulting in a higher than expected elasticity.[29] Subsequent research has directly related this "rheological fingerprint" to the presence of composition fluctuations near the ODT, suggesting that it arises due to the hypothesized disordered and co-continuous nanostructure.[21,24,25,30–32]

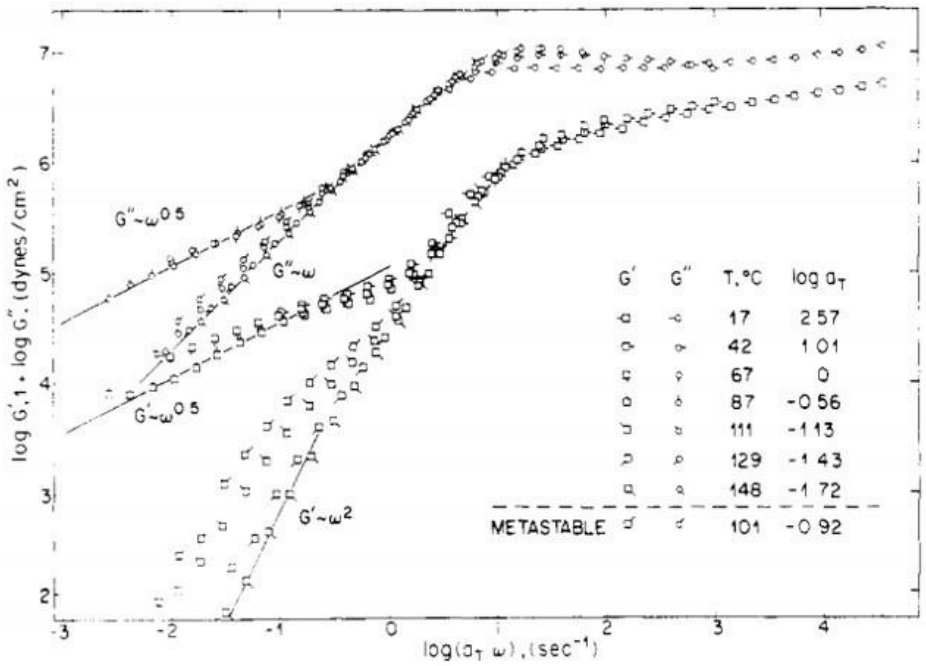

Figure 1.3. Dynamic frequency sweeps obtained for 1,4-polybutadiene-*block*-1,2-polybutadiene at temperatures below and above T_{ODT}. Time temperature superposition fails in the low frequency regime for $T > T_{ODT}$ due to composition fluctuations. Reproduced with permission from Bates, F. *Macromolecules* **1984**, *17*, 2607.[29] Copyright 1984 American Chemical Society.

1.4.2 Small Angle Scattering Evidence

Small angle neutron (SANS) and X-ray (SAXS) scattering experiments have also provided convincing evidence for the existence of composition fluctuations near the T_{ODT}.[21,25,26,30,31] Leibler used the random phase approximation (RPA) to calculate the structure factor, $S(q)$, and model the scattering behavior of the disordered state using SCFT.[17] The structure factor calculated by the RPA predicts a maximum in the scattered intensity above the T_{ODT} at a scattering vector, q, that corresponds to the block radius of gyration, $q \sim R_g^{-1/2}$. This maximum (often called the "correlation hole") does not reflect the presence of locally microphase separated domains. Instead, it is a consequence of chain incompressibility and block connectivity, i.e. chains of the "A" block are prohibited from occupying the same physical space as chains of the "B" block.[13,17]

Experimental SANS and SAXS data obtained from block polymers above T_{ODT} also exhibit a maximum in scattered intensity for intermediate values of q.[21,25] Plotting the inverse of the maximum scattered intensity, $I^{-1}(q^*)$, against the inverse of the experimental temperature, T^{-1}, has revealed a non-linear dependence of $I^{-1}(q^*)$ with T^{-1}.[21,25,26,31] These experimental observations contrast sharply with the RPA, which predicts a linear dependence of $I^{-1}(q^*)$ with T^{-1}.[17] Therefore, these scattering experiments demonstrate the persistence of local nanostructure in the disordered state, which was attributed to the presence of composition fluctuations.

While these rheological and scattering experiments clearly demonstrate that composition fluctuations result in locally microphase separated domains above T_{ODT}, they do not present a clear picture of the domain structure of the fluctuating disordered state. Superposition of the amplitudes associated with composition fluctuations in block polymer melts (as determined by theory) results in a pattern that resembles the pattern derived by Cahn to describe spinodal decomposition in immiscible liquids.[25,33] Spinodal decomposition is known to result in disordered and co-continuous domains; therefore, it has been speculated that the fluctuating disordered state of block polymers adopts a topologically similar pattern at the nanoscale.[26,31] Comparing SANS data obtained for a block polymer at $T > T_{ODT}$ with SANS data for an analogous polymer blend above the spinodal temperature corroborates this hypothesis (Figure 1.4).[25] After scaling the data to account for the different length scales associated with each system, the scattering patterns for the disordered block polymer and the phase separated polymer blend were remarkably similar for low to intermediate values of the normalized q, exhibiting similar peak breadths and shapes.[25] Knowing that the polymer blend exhibits a disordered and co-continuous morphology, it was hypothesized that the fluctuating disordered state forms a topologically similar pattern, consistent with theory.

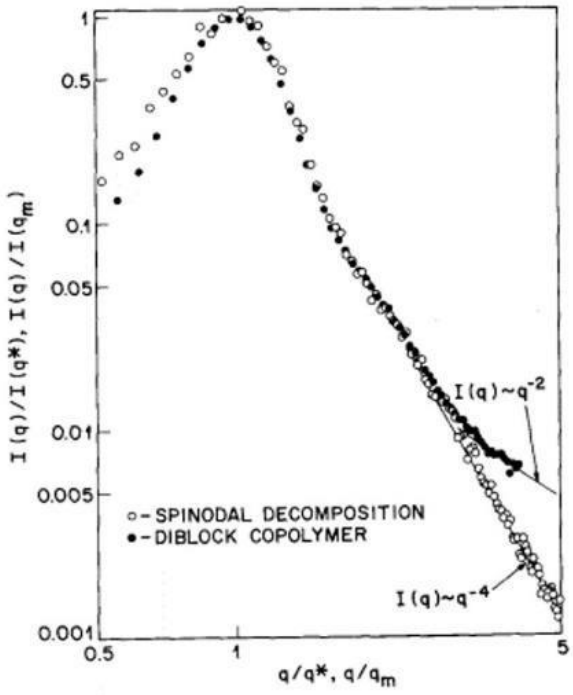

Figure 1.4. Small angle neutron scattering patterns for PEP-*b*-PEE (diblock copolymer) and for a PEP and PEE blend (spinodal decomposition). Scattered intensity $I(q)$ and scattering vector, q, were scaled by the intensity and scattering vector of the peak maximum, $I(q^*)$ and q^* respectively. The data for the polymer blend and the disordered block polymer superimpose for low to intermediate q, suggesting that they exhibit topologically similar structures. Reprinted with permission from Bates, F..; Rosedale, J.; Frederickson, G. *J. Chem. Phys.* **1990**, *92*, 6255.[25] Copyright 1990 American Institute of Physics.

1.4.3 Calorimetric Evidence

Composition fluctuations restore a weakly 1st order character to the ODT. Consequently, the ODT is expected to be accompanied by a latent heat associated with the transition from the ordered to the disordered state. Differential scanning calorimetry (DSC) is the prevailing technique for identifying the temperatures and enthalpies of phase transitions in crystalline homopolymers (typically melting and crystallization) and the glass transition temperature of amorphous homopolymers.[14] Although DSC has received comparatively less attention for characterizing the ODT in block polymers, recent experimental results

have demonstrated its relevance in elucidating the nature of composition fluctuations.[26,27,34] As an ordered, lamellar-forming block polymer was heated above its T_{ODT}, an endothermic transition was observed in a temperature range consistent with the T_{ODT} determined by SAXS and DMA, suggesting that this feature reflects the latent heat of the ODT.[26,27,34] The enthalpy of the ODT can be decomposed into two separate contributions.[26] First, there is a contribution related to the difference in the enthalpy between the homogeneously mixed and the microphase separated states. Additionally, there is a contribution stemming from interfacial contacts between the different domains, which is proportional to the interfacial tension and interfacial area. The experimental enthalpy of the ODT determined by DSC closely matches the enthalpy associated with interfacial contacts, and it is significantly lower than the enthalpy associated with complete domain mixing.[26] These results are consistent with simulations that revealed only a 7% change in domain composition across the ODT.[23] This suggests that the ODT is primarily characterized by a change in interfacial curvature rather than domain composition.[23,26] In effect, the ODT is a topological transition from a zero mean curvature and a zero Gaussian curvature lamellar state to a zero mean curvature and negative Gaussian curvature disordered state.[26] These conclusions generally support the existence of composition fluctuations, and they demonstrate the persistence of microphase separation above T_{ODT}.

1.4.4 Microscopic Evidence

All the experimental evidence discussed thus far represents indirect confirmation of disordered state composition fluctuations. Microscopic images would be powerful to provide direct visual evidence to corroborate these findings. However, the T_{ODT} typically

exists well above room temperature, while most electron micrographs of soft materials are obtained at room temperature or below. Therefore, the most convenient strategy to image the fluctuating disordered state is to first heat the block polymer above T_{ODT} and then kinetically trap this disordered state by either cross-linking or vitrification so that this morphology can be examined by SEM or TEM at room temperature.[35–38] This approach has been reported by Balsara et al for PS-*b*-PI-*b*-PS[35] and by Sakurai et al for PS-*b*-PB,[37] where the block polymers were radically cross-linked at temperatures both below and above T_{ODT}. These cross-linked polymers were then selectively stained and imaged by TEM. In both cases, a clear transition from a lamellar morphology for samples cross-linked below T_{ODT} to a disordered morphology for samples cross-linked above T_{ODT} was observed (Figure 1.5).[35,37] The clear visual evidence of distinct domains in the disordered state confirmed the existence of locally microphase separated domains. Furthermore, the disordered morphology generally resembled patterns observed during spinodal decomposition. Similar observations have been made for thin films[39] and for samples quenched from above T_{ODT}.[38] While each of these studies presents compelling evidence for a locally microphase separated disordered state, each of these micrographs only represents a two-dimensional projection of three-dimensional space. Consequently, they offer limited information regarding the proposed co-continuity of the fluctuating disordered domains. Chapters 4 – 8 of this thesis use similar cross-linking and quenching strategies to kinetically trap and subsequently visualize the disordered state. Additionally, the systems described in this thesis can be converted into porous materials, facilitating an examination of 3D domain continuity using nitrogen sorption analysis.

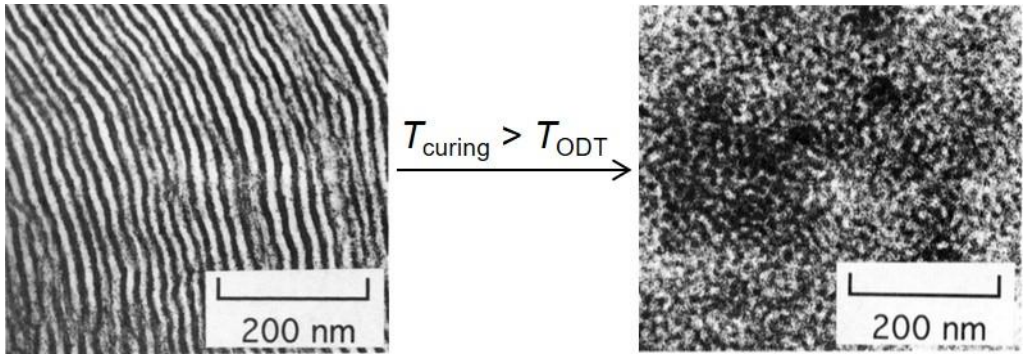

Figure 1.5. TEM micrographs of a PS-*b*-PI-*b*-PS triblock polymer radically cured in the ordered lamellar state below T_{ODT} (left image) and in the fluctuating disordered state above T_{ODT} (right image). Reproduced with permission from Sakurai, S.; Iwane, K.; Nomura, S. *Macromolecules.* **1993**, *26,* 5479.[37] Copyright 1993 American Chemical Society.

1.5 Relevance of the Disordered State to Potential Applications

The disordered and co-continuous domains resulting from composition fluctuations represent an intriguing structural motif that could aid in the development of advanced materials in a number of different applications.[40–43] In particular, the fluctuating disordered state may be particularly well-suited for the design of next generation membranes, particularly for water filtration. The well-defined and uniformly-sized domains can be converted into pores that precisely discriminate between species of nearly identical sizes by selectively removing one block.[3,44] Furthermore, these co-continuous pores are expected to result in uninterrupted channels that facilitate water transport.[43] The combination of these two features are expected to produce water filtration membranes with the highly desirable, yet elusive, properties of high water permeability and high size-selectivity.[3] Chapter 2 will discuss the desired characteristics of water filtration membranes and introduce commonly-used strategies to produce such membranes from block polymers. Chapters 4, 5, and 8 will then integrate fundamental knowledge of disordered state composition fluctuations into the design of water filtration membranes that exhibit the

desired properties outlined in Chapter 2, while Chapters 6 and 7 explore fundamental aspects of the ODT.

1.6 References

1) Wang, D.; Kou, R.; Choi, D.; Yang, Z.; Nie, Z.; Li, J.; Saraf, L. V.; Hu, D.; Zhang, J.; Graff, G. L.; Liu, J.; Pope, M. A.; Aksay, I. A. Ternary Self-Assembly of Ordered Metal Oxide−Graphene Nanocomposites for Electrochemical Energy Storage. *ACS Nano* **2010**, *4*, 1587–1595.

2) Peer, D.; Karp, J. M.; Hong, S.; Farokhzad, O. C.; Margalit, R.; Langer, R. Nanocarriers as an Emerging Platform for Cancer Therapy. *Nature Nanotechnology* **2007**, *2*, 751–760.

3) Werber, J. R.; Osuji, C. O.; Elimelech, M. Materials for next-Generation Desalination and Water Purification Membranes. *Nature Reviews Materials* **2016**, *1*, 16018.

4) Philp, D.; Stoddart, J. F. Self-Assembly in Natural and Unnatural Systems. *Angewandte Chemie International Edition* **1996**, *35*, 1154–1196.

5) Zhang, S. Fabrication of Novel Biomaterials through Molecular Self-Assembly. *Nature Biotechnology* **2003**, *21*, 1171–1178.

6) Whitesides, G. M.; Grzybowski, B. Self-Assembly at All Scales. *Science* **2002**, *295*, 2418.

7) Bates, F. S.; Frederickson, G. Block Copolymers - Designer Soft Materials. *Phys. Today* **1999**, *52*, 32–38.

8) Bates, C. M.; Bates, F. S. 50th Anniversary Perspective: Block Polymers—Pure Potential. *Macromolecules* **2017**, *50* (1), 3–22.

9) Sinturel, C.; Bates, F. S.; Hillmyer, M. A. High χ–Low N Block Polymers: How Far Can We Go? *ACS Macro Lett.* **2015**, *4*, 1044–1050.

10) Bates, F.; Frederickson, G. Block Copolymer Thermodynamics: Theory and Experiments. *Annu. Rev. Phys. Chem.* **1990**, *41*, 525–557.

11) Matsen, M. W. Fast and Accurate SCFT Calculations for Periodic Block-Copolymer Morphologies Using the Spectral Method with Anderson Mixing. *The European Physical Journal E* **2009**, *30*, 361.

12) Matsen, M. W. Effect of Architecture on the Phase Behavior of AB-Type Block Copolymer Melts. *Macromolecules* **2012**, *45*, 2161–2165.

13) Gillard, T. Phase Transitions and Fluctuations in Block Copolymer–Based Soft Materials, University of Minnesota, 2015.

14) Hiemenz, P.; Lodge, T. *Polymer Chemistry*, 2nd ed.; CRC Press.

15) Fredrickson, G. H.; Liu, A. J.; Bates, F. S. Entropic Corrections to the Flory-Huggins Theory of Polymer Blends: Architectural and Conformational Effects. *Macromolecules* **1994**, *27*, 2503–2511.

16) Frederickson, G.; Helfland, E. Fluctuation Effects in the Theory of Microphase Separation in Block Copolymers. *J. Chem. Phys* **1987**, *87*, 697–705.

17) Leibler, L. Theory of Microphase Separation in Block Copolymers. *Macromolecules* **1980**, *13*, 1602–1617.

18) Grzywacz, P.; Qin, J.; Morse, D. C. Renormalization of the One-Loop Theory of Fluctuations in Polymer Blends and Diblock Copolymer Melts. *Phys. Rev. E* **2007**, *76*, 61802.

19) Matsen, M. W.; Bates, F. Unifying Weak- and Strong-Segregation Block Copolymer Theories. *Macromolecules* **1996**, *29*, 1091–1098.

20) Matsen, M. W.; Schick, M. Stable and Unstable Phases of a Diblock Copolymer Melt. *Phys. Rev. Lett.* **1994**, *72*, 2660–2663.

21) Bates, F. S.; Rosedale, J. H.; Fredrickson, G. H.; Glinka, C. J. Fluctuation-Induced First-Order Transition of an Isotropic System to a Periodic State. *Phys. Rev. Lett.* **1988**, *61*, 2229–2232.

22) Grzywacz, P.; Qin, J.; Morse, D. C. Renormalization of the One-Loop Theory of Fluctuations in Polymer Blends and Diblock Copolymer Melts. *Phys. Rev. E* **2007**, *76*, 61802.

23) Medapuram, P.; Glaser, J.; Morse, D. Universal Phenomenology of Symmetric Diblock Copolymers near the Order−Disorder Transition. *Macromolecules* **2015**, *48*, 819–839.

24) Yadav, M.; Bates, F. S.; Morse, D. C. Network Model of the Disordered Phase in Symmetric Diblock Copolymer Melts. *Phys. Rev. Lett.* **2018**, *121*, 127802.

25) Rosedale, J. H.; Bates, F. S.; Almdal, K.; Mortensen, K.; Wignall, G. D. Order and Disorder in Symmetric Diblock Copolymer Melts. *Macromolecules* **1995**, *28*, 1429–1443.

26) Bates, F. S.; Rosedale, J. H.; Fredrickson, G. H. Fluctuation Effects in a Symmetric Diblock Copolymer near the Order–disorder Transition. *The Journal of Chemical Physics* **1990**, *92*, 6255–6270.

27) Lee, S.; Gillard, T.; Bates, F. Fluctuations, Order, and Disorder in Short Diblock Copolymers. *AIChE* **2013**, *59*, 3502–3513.

28) Gillard, T. M.; Medapuram, P.; Morse, D. C.; Bates, F. S. Fluctuations, Phase Transitions, and Latent Heat in Short Diblock Copolymers: Comparison of Experiment, Simulation, and Theory. *Macromolecules* **2015**, *48*, 2801–2811.

29) Bates, F. S. Block Copolymers near the Microphase Separation Transition. 2. Linear Dynamic Mechanical Properties. *Macromolecules* **1984**, *17*, 2607–2613.

30) Kennemur, J. G.; Hillmyer, M. A.; Bates, F. S. Rheological Evidence of Composition Fluctuations in an Unentangled Diblock Copolymer Melt near the Order–Disorder Transition. *ACS Macro Lett.* **2013**, *2*, 496–500.

31) Hickey, R.; Gillard, T.; Lodge, T.; Bates, F. Influence of Composition Fluctuations on the Linear Viscoelastic Properties of Symmetric Diblock Copolymers near the Order− Disorder Transition. *ACS Macro Letters* **2015**, *4*, 260–265.

32) Rosedale, J. H.; Bates, F. S. Rheology of Ordered and Disordered Symmetric Poly(ethylenepropylene)-Poly(ethylethylene) Diblock Copolymers. *Macromolecules* **1990**, *23*, 2329–2338.

33) Cahn, J. W. Phase Separation by Spinodal Decomposition in Isotropic Systems. *The Journal of Chemical Physics* **1965**, *42*, 93–99.

34) Gillard, T. M.; Phelan, D.; Leighton, C.; Bates, F. S. Determination of the Lamellae-to-Disorder Heat of Transition in a Short Diblock Copolymer by Relaxation Calorimetry. *Macromolecules* **2015**, *48*, 4733–4741.

35) Gomez, E. D.; Das, J.; Chakraborty, A. K.; Pople, J.; Balsara, N. Effect of Cross-Linking on the Thermodynamics of Lamellar Block Copolymers. *Macromolecules* **2006**, *39*, 4848–4859.

36) Hahn, H.; Chakraborty, A. K.; Das, J.; Pople, J.; Balsara, N. Order-Disorder Transitions in Cross-Linked Block Copolymer Solids. *Macromolecules* **2005**, *38*, 1277–1285.

37) Sakurai, S.; Iwane, K.; Nomura, S. Morphology of Poly(styrene-Block-Butadiene-Block-Styrene) Triblock Copolymers Cross-Linked in the Disordered State. *Macromolecules* **1993**, *26*, 5479–5486.

38) Sakamoto, N.; Hashimoto, T. Ordering Dynamics of a Symmetric Polystyrene-Block-Polyisoprene. 2. Real-Space Analysis on the Formation of Lamellar Microdomain. *Macromolecules* **1998**, *31*, 3815–3823.

39) Kim, S.; Nealey, P. F.; Bates, F. S. Directed Assembly of Lamellae Forming Block Copolymer Thin Films near the Order–Disorder Transition. *Nano Lett.* **2014**, *14*, 148–152.

40) Schulze, M. W.; McIntosh, L. D.; Hillmyer, M. A.; Lodge, T. P. High-Modulus, High-Conductivity Nanostructured Polymer Electrolyte Membranes via Polymerization-Induced Phase Separation. *Nano Lett.* **2014**, *14*, 122–126.

41) Saba, S. A.; Mousavi, M. P. S.; Bühlmann, P.; Hillmyer, M. A. Hierarchically Porous Polymer Monoliths by Combining Controlled Macro- and Microphase Separation. *J. Am. Chem. Soc.* **2015**, *137*, 8896–8899.

42) Portela, C. M.; Vidyasagar, A.; Krödel, S.; Weissenbach, T.; Yee, D. W.; Greer, J. R.; Kochmann, D. M. Extreme Mechanical Resilience of Self-Assembled Nanolabyrinthine Materials. *Proc Natl Acad Sci USA* **2020**, *117*, 5686.

43) Seo, M.; Hillmyer, M. A. Reticulated Nanoporous Polymers by Controlled Polymerization-Induced Microphase Separation. *Science* **2012**, *336*, 1422.

44) Jackson, E. A.; Hillmyer, M. A. Nanoporous Membranes Derived from Block Copolymers: From Drug Delivery to Water Filtration. *ACS Nano* **2010**, *4*, 3548–3553.

Chapter 2. Background: Ultrafiltration Membranes for Water Purification[1]

2.1 Introduction

Reliable access to clean water is essential to both human health and global stability. However, approximately 4 billion people experience water scarcity for at least one month of the year.[1] Global water demand is expected to expand 20 to 30% by 2050 due to population growth and industrialization, while global warming is expected to further disrupt the supply of clean water.[1,2] Therefore, equitable access to clean water will benefit from the utilization of all available water sources, including the energy-efficient treatment of municipal and industrial wastewater. Selective membrane technologies will play a critical role in developing a sustainable water economy.[3–7]

Membrane technologies are typically classified according to their effective pore size and separation mechanism. Ultrafiltration (UF) membranes, with pore sizes in the 1–100 nm range, are of particular interest for drinking water and wastewater treatment.[3,7,8] These nanoscale pores are ideal for rejecting wastewater contaminants, such as viruses, microbes, colloidal particles, and natural organic matter, according to their hydrodynamic size.[8] Consequently, UF membranes have found utility in decontamination of drinking water,

[1] This chapter was written as an unpublished perspective in collaboration with Drs. Jay Werber, Adam Feinberg, and Wui-Yarn Chan. The majority of the text was written by Nicholas Hampu with small excerpts on membrane applications written by the other authors.

wastewater treatment, and membrane bioreactors, providing higher quality filtered water than traditional treatment processes.[7] Additionally, UF membranes are critical tools in certain industrial processes (e.g. bioprocessing, dairy processing), enabling low cost and highly efficient separations.

Most commercial UF membranes are fabricated from homopolymer solutions using non-solvent induced phase separation (NIPS).[3,5,9] NIPS membranes exhibit continuous pores, thin selective layers, and high water permeability, but their broad pore size distribution can limit their size-selectivity and thus their utility for demanding and highly efficient separations.[3,5,10,11] Alternatively, track etched membranes display nearly uniform pore sizes and improved size-selectivity, but their low surface porosities and typically large thicknesses results in low water permeability. The ideal UF membrane would combine the high porosity and thin selective layers of NIPS membranes with the uniform pore sizes of track etched membranes. Block polymers, comprising two or more chemically distinct polymers covalently linked into a single chain, potentially provide a path to such a system due to their self-assembly into regular and periodic nanostructures of nearly uniform size.[7,12–14] By tuning the composition of the block polymer, a number of ordered morphologies (e.g. cylinders, gyroid, lamellae) with well-connected domains can be obtained and subsequently converted into continuous and uniform pores using various strategies.[6,7] Additionally, amphiphilic block polymers containing both hydrophobic and hydrophilic polymer blocks enhance the hydrophilicity and functionality of the membrane surface and pores as compared to homopolymer-derived NIPS membranes, increasing fouling resistance and operation lifetime.[15,16]

Solution processing techniques combined with amenable polymer chemistries are central to controlling the structure of block polymer membranes.[17–20] The primary objective is to ultimately produce pores of uniform size from the self-assembled block polymer domains. Achieving such a goal often requires careful design of the film casting process and, frequently, additional post-fabrication processes to produce homogeneous domains that span the entire thickness of the block polymer layer.[17,20–22] These processes must be carefully optimized to maximize the water permeability, size-selectivity, and process scalability. Membrane properties are highly dependent upon the polymer chemistry, processing conditions, and pore formation mechanism. Further developments in scalable and cost-effective methods to produce high-performing membranes are essential for block polymers to achieve commercial success, and positively impact water treatment processes.[17,22,23]

In this Perspective, we critically examine the state of the art in block polymer membrane fabrication, assess membrane performance to date, and identify areas, that in our view, require further improvement to produce commercially viable membranes. We first introduce several key applications of UF membranes in terms of their desired properties, and then discuss commonly employed strategies for block polymer UF membrane fabrication through the lens of materials needs, fundamental mechanistic principles, and processing requirements. Finally, we examine key structure-processing-performance relationships of these membranes in the context of their water permeability, size-selectivity, and fouling resistance. Through such relationships, we analyze how the

performance of block polymer UF membranes compares to existing commercial UF membranes and use these data to identify crucial aspects that merit further fundamental research and practical development. This work is intended to provide a critical overview of the existing block polymer membrane literature, while also stimulating thought on how to push these technologies towards pragmatic realization.

2.2 Membrane Properties and Important Applications

2.2.1 Principal Membrane Characteristics

For optimal performance in industrial applications, UF membranes must have sufficient water permeability, fouling resistance, size-selectivity, and mechanical robustness. flux (volume flow per time per membrane area) of pure water normalized to the applied hydraulic pressure (pressure applied to the fluid, water in this case) and is given typically in liters per meter squared per hour per bar ($Lm^{-2}h^{-1}bar^{-1}$). In the simplest model, the membrane is treated as a series of tortuous capillaries using the Hagen-Poiseuille equation[24]:

$$A = \frac{\varepsilon r_p^2}{8\tau^2 \mu \delta_m} \text{ (eq. 1)}$$

Here, ε is the surface porosity, r_p is the pore radius, τ is the pore tortuosity, μ is the viscosity of water, and δ_m is the membrane (active layer) thickness. Equation 1 often incorrectly shows A with a τ^{-1} dependence, only accounting for an increase in the effective path length for water permeation.[17,23,25] However, tortuosity increases both the effective path length of the capillaries and the capillary velocity and therefore results in a τ^{-2} dependence.[24]

Optimal membrane designs for permeability have thin active layers with high porosity and a macroporous substructure for mechanical support. High water permeabilities can allow for greater water fluxes or decreased applied pressure driving forces, thereby decreasing energy and equipment costs.[26] However, for many practical processes, hydraulic resistance from unstirred boundary layers in the feed channel (also called concentration polarization) and from fouling (build-up of organic matter on the surface of the membrane) can be substantial. Additionally, fouling is typically exacerbated at increased water flux.[27]

Fouling resistance and fouling mitigation are therefore critical considerations in membrane design.[3,28] Extensive fouling from the adhesion of biological, organic, and inorganic matter can result in pore blockage, decreased water permeability, and changes in the molecular weight cut-off (MWCO), which is conventionally defined as the lowest solute molecular weight (molar mass) where 90% solute rejection is observed.[26] The ideal UF membrane has a surface chemistry and topography engineered to prevent such adsorption, minimizing irreversible changes in the water permeability over the operation lifetime.[29,30] The charge of the membrane can also critically affect fouling resistance. For example, positively charged membranes are used to recover cationic latex paint in cathodic electrocoating processes, while negatively charged membranes lead to rapid fouling from the same particles.[31] Finally, many UF membranes are designed to allow for periodic backflushes or air scrubbing to sweep away foulant layers.[26,31] Hollow fiber geometries (capillaries with outer diameters of roughly 0.5–1 mm) are particularly advantageous in this regard. Facile backflushing and a high surface area/packing volume ratio make hollow fibers the main form factor used industrially.[26]

UF membranes mainly separate based on a molecular-sieve mechanism, where large solutes are excluded from entering the pore.[26] The primary selectivity metric is the MWCO. The selectivity of UF membranes is dictated by both the average pore size and the pore size distribution of the active layer, where the average pore size generally sets the MWCO and the pore size distribution governs the ability to discriminate between particles of similar size.[10,11] From a membrane selectivity perspective, an ideal membrane would be isoporous, having uniformly sized pores for precise separations. Selectivity for charged solutes is also affected by the charge (if any) of the membrane.[10] Tailored selectivities can also be engineered by pore wall functionalization, for example, to facilitate affinity-driven separations.[32,33]

Finally, all these considerations must be readily integrated into cost-effective manufacturing processes at industrially relevant size-scales to realize their full potential. This requires systems that are compatible with roll-to-roll coating processes and the existing membrane fabrication infrastructure. The relative importance of each of the above criteria is often highly dependent on the process in which they are employed. Several important applications of UF membranes are briefly examined in the following sections and summarized in Table 2.1.

Table 2.1. Common UF processes and important membrane properties

UF Process	Typical Materials	Typical Water Permeability ($Lm^{-2}h^{-1}bar^{-1}$)	Typical Pore Size	Targeted Contaminants	Operation Lifetime
Drinking Water Treatment[34–36]	PAN, PSF, PVDF	> 200	~20 nm	Viruses, Bacteria, Particulates	>5 y
Wastewater Treatment[26,34,35]	PAN, PSF, PVDF	> 200	~20 nm	Viruses, Bacteria, Pathogens	>5 y
RO Pre-treatment[26,31,34]	PAN, PSF, PVDF	> 200	~20 nm	Viruses, Bacteria, Organic Matter	>5 y
Membrane Bioreactors[37–40]	PE, PVDF, PTFE	> 500	30 nm to 1 μm	Bacteria, Organic Matter	8 to 10 y
RO Support Layer[3,34,41]	PSF, PES	200-400	20 nm	Ions, Salts	up to 7 y
Virus Filtration in Bioprocessing[42,43]	PES, PVDF	~500	15 nm	Viruses	Single Use

2.2.2 Water Treatment

Ultrafiltration plays a critical role in modern water treatment processes for drinking water, municipal wastewater, and pre-treatment for reverse osmosis.[34,44,45] In all of these processes, UF is used to remove suspended solids from water, yielding purified water as the desired product. Compared to conventional physical treatment steps (e.g., granular filtration), UF allows for smaller-footprint facilities, higher water quality (e.g., pathogen removal), and more robust water quality across varying feed water composition.[26,45] As mentioned above hollow fiber membranes are the dominant form factor, and the UF process is either operated in cross-flow, where the retentate is recycled, or in dead-end filtration mode, where the retentate accumulates on the membrane surface. In both modes, backflushing is periodically used to remove sediment build-up on the membrane surface. In these processes, water flux is frequently 50–100 L m^{-2} h^{-1}, although increased fluxes up

to 200 L m^{-2} h^{-1} are possible when the feed water is relatively non-fouling.[34,35] Organic matter (e.g., humic acid and carbohydrates) tends to be the main foulant.[46] UF membrane lifetimes in these plants are typically > 5 years.[34]

In municipal drinking water treatment processes, surface waters, such as lakes, reservoirs, and rivers, or groundwater are treated using a series of physicochemical treatment steps (e.g. flocculation, sedimentation, and granular filtration) designed to remove bacteria, viruses, and other suspended particles from solution.[26] Owing to its superior ability to remove pathogens, UF is commonly being adopted in modern industrial drinking water treatment facilities, either fully supplanting the physical separation steps or serving as a final polishing step.[45] As of 2009, UF and larger pore-size microfiltration (MF) processes had a total capacity of ~3 million m^3 d^{-1} in the United States, roughly equivalent to the household water use of ~8 million people.[36] However, the largest UF application in wastewater treatment is in membrane bioreactors (section 2.2.3).

Reverse osmosis (RO) is currently the most widespread and energy-efficient desalination technology and is also a central step in the potable reuse of municipal wastewater.[3,34] However, RO membranes are highly susceptible to fouling because of their surface chemistry and morphology. Furthermore, they are not easily backwashed and are typically not very stable to chemical cleaning, particularly with oxidizing chemicals such as chlorine. Therefore, UF is commonly used as pre-treatment to mitigate fouling of the RO membranes and to extend their lifetime.[34]

For each of the above water-treatment applications, key UF membrane characteristics include fouling resistance, the ability to be effectively cleaned, high water permeability, and relatively small pore sizes (i.e. < 20 nm in diameter) to allow for high rejection of viruses.[42] Variability in the membrane pore size is generally not deleterious for the overall performance, but it still has important ramifications on the permeability and selectivity. For example, a broader pore size distribution for a given water permeability will typically result in decreased retention of viruses and other pathogens. Water permeabilities > 200 L m^{-2} h^{-2} bar^{-1} are roughly required to allow for high water fluxes at low pressures (< 1 bar) and thus energy efficient separations. The uniform pore sizes of block polymer membranes should facilitate more efficient water treatment, provided that the water permeability is competitive with commercial NIPS membranes.

2.2.3 Membrane Bioreactors

Membrane bioreactors (MBRs) are a rapidly growing application that utilize UF membranes, with a current global treatment capacity estimated at 20 million m^3 d^{-1}.[47] There have been a number of thorough review articles on MBRs in recent years,[40,47] but it is useful to summarize the key points within this broader perspective. MBRs combine biodegradation and ultrafiltration in a single process, resulting in several advantages over either process in isolation. MBRs can operate at significantly higher biomass concentrations than traditional activated sludge bioreactors,[48] resulting in more efficient biodegradation of organics with a smaller reactor footprint. The addition of a UF membrane also results in an effluent that is effectively free of biological contaminants, without the need for gravitational settling.[49]

Typical MBRs are capable of removing > 99% of ammonium nitrogen, phosphorous, and oxidizable carbon. MBRs also remove > 99% of total suspended solids, versus ~60% for traditional activated sludge, owing to the selective membrane component.[49] Originally, MBRs consisted of an activated sludge bioreactor with a side-stream UF flat sheet membrane operating in crossflow.[50] Modern MBRs use submerged hollow fiber (HF) membranes packed into "cassettes".[51,52] The porous hollow fibers are generally made from polyethylene (PE),[37,53] polyvinylidene fluoride (PVDF)[38,54], or polytetrafluoroethylene (PTFE)[39,55] with pore diameters ranging from 30 nm to 1 μm. A typical HF cassette has a working lifetime of about 8 years, with the current generation expected to last a decade or more.[40] The dominant failure mode of HF membranes is irreversible fouling[40] which can be reduced by periodic backflushing or by air-scrubbing in aerobic MBRs.[56] As discussed in section 2.8.3, block polymer membranes present an opportunity to minimize irreversible fouling in next generation MBRs, improving reactor lifetime and lowering operation costs.

2.2.4 Support Layers for Reverse Osmosis Membranes

In RO membranes, a thin (< 200 nm), highly crosslinked polyamide selective layer allows for the separation of water and salt.[3,34] To withstand hydraulic pressures up to ~80 bar, the polyamide layer is supported by a UF-style membrane, typically comprising polysulfone (PSF) or polyethersulfone (PES). Water traversing the polyamide selective layer must therefore enter the pores of the UF support layer. Recent evidence suggests that the properties of the support layer (e.g., porosity, pore density, pore regularity) may substantially impact the overall water permeability of the composite membrane.[41] The

uniform pore sizes and tunable pore densities of block polymer membranes should allow for more fundamental studies and membrane optimization in this area.

2.2.5 Process Industry

UF is extensively used in process industries for both industrial wastewater treatment and the separation of target solutes from impurity solutes.[26,31] Consequently, monodisperse pore sizes may be highly advantageous, allowing for more selective processes with better yield of the desired product and removal of impurities. UF membranes find major applications in the food and beverage (e.g., dairy), metals and coatings, and bioprocessing industries.[26,31] For many of these processes, membranes with tailored chemistries and geometries for the target application are used. Specially designed membranes will be essential to enable new and emerging industrial applications.

The bioprocessing industry is a salient example of the need for specially designed membranes.[43] UF has two main applications in the production of protein therapeutics (e.g., monoclonal antibodies). The first is virus filtration to remove putative viruses.[42] Highly selective membranes are needed, allowing the target protein (e.g., monoclonal antibodies with diameters of ~10 nm) to permeate while reducing the putative virus concentration >10,000-fold. Viruses vary in size according to class, ranging from ~20 for parvoviruses to 300 nm for smallpox.[43] Therefore, pores would ideally be entirely between 10 and 20 nm in diameter to ensure complete removal of all viruses and permeation of the target protein. To enable straightforward processing, virus filtration is operated in dead-end filtration mode. The second UF process is the final purification step, where the protein is

concentrated and buffer exchanged into the final formulation buffer.[43] In this process, crossflow filtration with recirculation is performed using flat-sheet cassettes containing highly hydrophilic, fouling-resistant regenerated cellulose membranes with relatively small pore sizes to allow for high product retention. Water permeability is less important, as resistance from the protein gel layer dominates performance. A third potential application of UF is to replace the expensive affinity chromatography step, which uses protein-based ligands to separate the relatively large target antibody from other host cell proteins.[43] The monodisperse pore sizes of block polymer membranes could dramatically improve the performance of a UF-based process.

2.3 Current State and Limitations of Ultrafiltration Membranes

2.3.1 Homopolymer Non-solvent Induced Phase Separation

To better understand the potential application of block polymers in UF membrane processes, it is necessary to review the processing and properties of existing commercial homopolymer membranes. The current standard for commercial polymeric UF membrane fabrication is non-solvent induced phase separation (NIPS).[5] Ultrafiltration membranes produced using NIPS exhibit an integral and asymmetric structure, where a thin active layer with small pores that separate contaminants gradually transitions into a thicker substructure with large pores that provide a high water permeability and sufficient mechanical integrity.[3,5] The ubiquity of NIPS membranes is a function of the simple solution casting processes used in their fabrication, enabling the cost-effective and large-scale production of membranes with high water permeabilities.

In the NIPS process, a concentrated homopolymer solution is cast into a film. This solvent-swollen film is then immersed into a non-solvent (typically water). The influx of non-solvent causes the polymer and solvent to de-mix, and the system phase separates into polymer-rich and polymer-poor domains, which ultimately become the membrane matrix and pores, respectively.[5,9] The NIPS process is highly versatile and is amenable to a variety of polymer structures, such as polysulfone (PSF), polyethersulfone (PES), polyacrylonitrile (PAN), and poly(vinylidene fluoride) (PVDF), allowing the membrane properties to be tailored to the requirements of the targeted application.[5] Furthermore, the pore morphology and size can be rationally tuned through judicious selection of the polymer chemistry and concentration and through choice of solvent(s) and non-solvent(s) (Figure 2.1).[5,57]

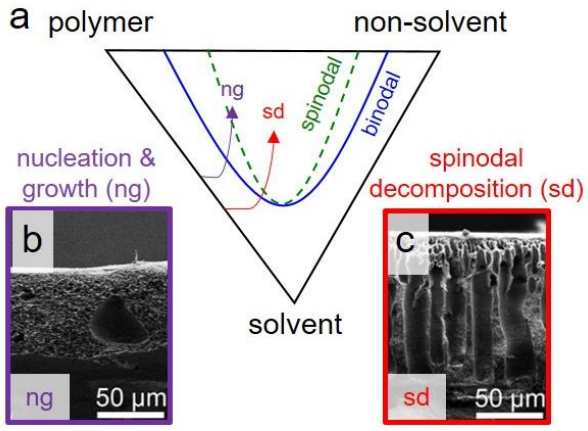

Figure 2.1. Sketch of a hypothetical phase diagram illustrating two different precipitation paths for homopolymer NIPS solutions (a). The purple curve denotes a solution with a higher polymer concentration that forms a spongey microstructure. A representative cross-sectional SEM image of such a system is presented in (b).[57] The red curve in (a) denotes a solution with a lower polymer concentration that forms a finger-like microstructure. A representative cross-sectional SEM image for such a system is presented in (c).[57]

The integrally structured and asymmetric architecture of NIPS membranes is highly desirable. Because the entire membrane is composed of a single material, the small surface pores that enable solute rejection are inherently connected to the larger pores in the

substructure. This results in high water permeability, minimizing the membrane areal footprint and energy consumption and maximizing water filtration. However, the broad pore size distribution of NIPS membranes limits their growth potential.[3,4] Low size-selectivity is undesirable for many high value applications that require near-perfect discrimination between solutes of similar sizes. Furthermore, these membranes are generally made from hydrophobic polymers which lack non-fouling surface functionalities.[59] The addition of hydrophilic homopolymers, such as poly(vinylpyrrolidone), into the NIPS casting solution can improve membrane hydrophilicity and increase fouling resistance.[5] However, homopolymer additives are bound to the membrane matrix through weak physical interactions and can leach out over time, resulting in performance deterioration. To expand the practical applications of UF membranes and facilitate next generation technologies, significant improvements to the size-selectivity and fouling resistance of UF membranes must be made without compromising their typically high water permeabilitieis and process scalability.

2.3.2 Homopolymer NIPS with surface segregating block polymer additives

To address limitations related to the surface chemistry of NIPS membranes, a variety of methods have been developed to coat or covalently graft hydrophilic polymers onto their surfaces. However, these approaches require additional processing steps, may constrict pores, and lack long term stability.[60] High density and stable functionalization of both the internal pores and external surface can be achieved without compromising the water permeability by adding amphiphilic block and comb polymers into the NIPS casting solution. During NIPS, the hydrophilic component segregates to the membrane surface and

pore walls, as confirmed by X-ray photoelectron spectroscopy (XPS), due to the lower chemical potential of the hydrophilic component in the aqueous coagulation bath.[61] The hydrophilic component prevents the irreversible adsorption of hydrophobic contaminants onto the membrane, while the hydrophobic component anchors the polymer to the membrane and helps mitigate leaching (Figure 2.2a). Additionally, heat treatments can be used to replace surface segregated block polymer molecules that are removed during membrane operation and cleaning with block polymer molecules that are trapped in the membrane interior, resulting in sustained fouling resistance.[61] The microstructure of these membranes can be tuned by varying the amphiphile concentration (typically 2-20 wt.%). Blends that contain a small amount of block polymer additive form dense skin layers with cellular substructures.[29,60] The porosity and density of macrovoids both increase with additive concentration due to compatibilization of the casting solution with the non-solvent, which facilitates instantaneous demixing.[61]

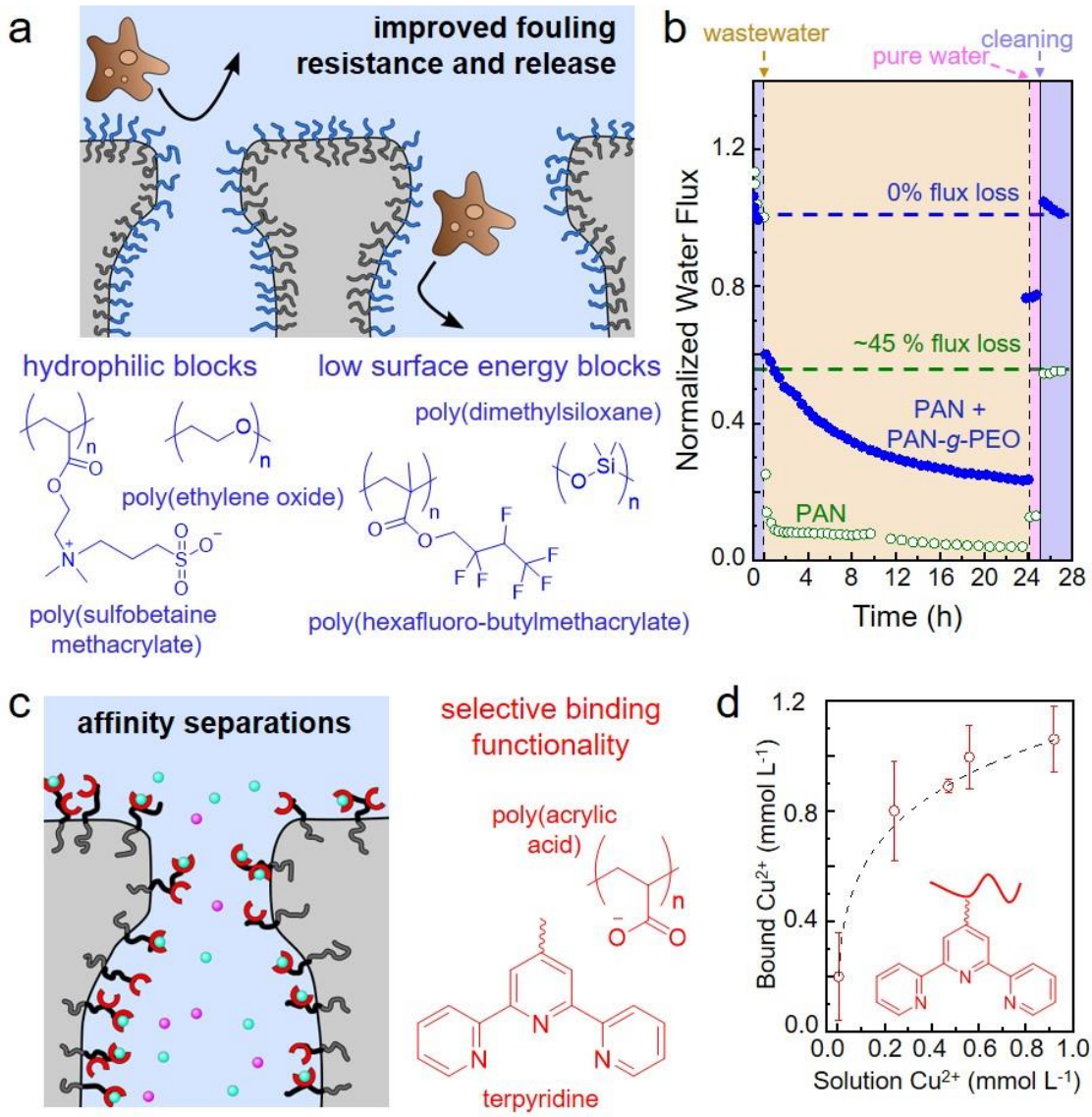

Figure 2.2. Incorporating a small amount of an amphiphilic block polymer into a homopolymer solution in NIPS results in the surface segregation of the block polymer molecules along the pore walls (a, c). The hydrophobic block (gray) anchors the molecule into the membrane matrix, while the hydrophilic block (blue) extends into water to improve the wettability of the pores. The chemical structures of representative hydrophilic and low surface energy polymers are presented in (a). The effectiveness of such chemistries in improving fouling resistance is demonstrated in (b). By incorporating a surface-segregating PAN-*g*-PEO polymer (closed blue circles) into a PAN membrane (open green circles), the water flux recovery ratio can be significantly improved following exposure to oil refinery wastewater and membrane cleaning.[62] Additionally, surface segregation can be used to promote affinity-driven separations by designing a hydrophilic block that also contains selective binding functionalities (c). This strategy was used to bind aqueous copper ions by functionalizing the PAA block of a surface segregating PS-*b*-PAA diblock with a terpyridine ligand (d).[32]

The surface segregation method can be applied to a wide range of polymer chemistries used in NIPS membrane fabrication. The hydrophobic segment of the block polymer or comb backbone may comprise the same polymer as the membrane bulk (PAN, PVDF),[29,60] or it may be a polymer that adsorbs to the matrix due to favorable van der Waals interactions (PMMA).[61] Common hydrophilic blocks and side chains include polyelectrolytes (PMAA, PAA),[60] anti-fouling segments (PEO),[29] and polyzwitterions (poly(sulfobetaine methacrylate))[64] (Figure 2.2a). These systems have been remarkably effective at reducing membrane fouling, where the incorporation of amphiphilic PAN-*g*-PEO comb polymers into PAN membranes resulted in near complete recovery of water flux after oil refinery wastewater filtration and membrane cleaning (Figure 2.2b).[63] Commercially available PEO-PPO-PEO triblock polymer surfactants (Pluronic or Poloxamer) have also been shown to effectively improve the fouling resistance.[65]

The surface segregation approach can also be extended to non-polar low surface energy segments, such as silicone and fluorinated polymeric materials, that impart foulant release functionalities. However, these polymer segments do not spontaneously migrate to the surface in aqueous coagulation baths due to their incompatibility with water (the most commonly used non-solvent). Therefore, they must be covalently bonded to hydrophilic polymer segments that promote their segregation to the membrane surface. Statistical copolymers containing fouling release segments, such as poly(hexafluorobutyl methacrylate) and polydimethylsiloxane (PDMS), with the previously discussed hydrophilic moieties induces segregation along the membrane surface and pore walls (Figure 2.2a).[66–69]

Beyond fouling resistance and release, surface segregation can also be used to impart new functionalities into NIPS membranes, facilitating affinity-driven separations (Figure 2.2c). For example, polyethylenimine and metal-binding terpyridine ligands attached to PAA-lined pores of PSF/PS-b-PAA blends were shown to effectively adsorb heavy metal contaminants (Figure 2.2d).[32] Continued development of functionalized surface segregated layers may further expand the scope of separations capabilities of UF membranes. However, despite the improved fouling resistance of NIPS membranes with surface-segregating block polymer additives, these membranes still exhibit broad pore size distributions and limited size-selectivity that is characteristic of NIPS membranes.

2.4 Selective Etching of Self-Assembled Ordered Block Polymers

Self-assembled block polymers are attractive targets for polymeric UF membranes, as their uniform domain sizes and tunable morphologies are expected to enable more precise separations than is currently possible with NIPS membranes.[3,6,7,14] A conceptually straightforward route to prepare block polymer-based UF membranes is to first cast a solid film and then use the inherent self-assembled nanostructure as a template for pore generation. These membranes can be either free-standing block polymer films or composite architectures, where a thin block polymer selective layer is cast atop a porous substrate (typically a NIPS membrane). Pores are generated by selectively removing (etching) one of the domains, and the pore size is directly related to the initial molar mass of the etchable block.[17,20,21]

Fabricating high performance UF membranes from solid block polymer thin films requires a basic understanding of the physics governing their self-assembly. Block polymers can exhibit a strong enthalpic drive to phase separate due to unfavorable interactions between chemically dissimilar blocks. However, the covalent linkages between these blocks limit this segregation to molecular length scales. Consequently, these materials microphase separate at the nanoscale into regularly ordered domains of nearly uniform size (Figure 2.3a).[12,13,69] The thermodynamic drive to microphase separate is described by the segregation strength, χN, where χ is an interaction parameter that scales inversely with temperature and N is the reference-volume-normalized degree of polymerization. At high values of χN (low temperatures or high molar masses), the enthalpic drive to phase separate dominates, and an ordered microphase separated morphology will be obtained. The symmetry of the morphology is governed by the volumetric ratio of the blocks, with a general transition from lamellae to network phases (gyroid) to cylinders to spheres as the block length asymmetry increases. At lower values of χN (higher temperatures and/or lower molar masses), the enthalpic drive to phase separate will decrease relative to the energetic considerations associated with the entropic drive to minimize chain stretching. Eventually, this results in a loss of long-range order at the order-disorder transition (ODT) temperature (T_{ODT}).[69,70] For a given block polymer chemistry (constant χ), this sets a lower practical limit on the attainable pore size, typically in the range of 5-10 nm.[71] Figure 2.3a presents illustrations of morphologies commonly found in the phase map for an idealized diblock polymer. Related diagrams for real polymers also include contributions from molar mass dispersity and conformational asymmetry (relative flexibilities of the polymer backbones) that will alter the behavior from this idealized state.[72–74] Furthermore, the introduction of

additional blocks and non-linear chain architectures can greatly enrich the complexity of the phase diagram, providing access to new equilibrium morphologies.[75–78]

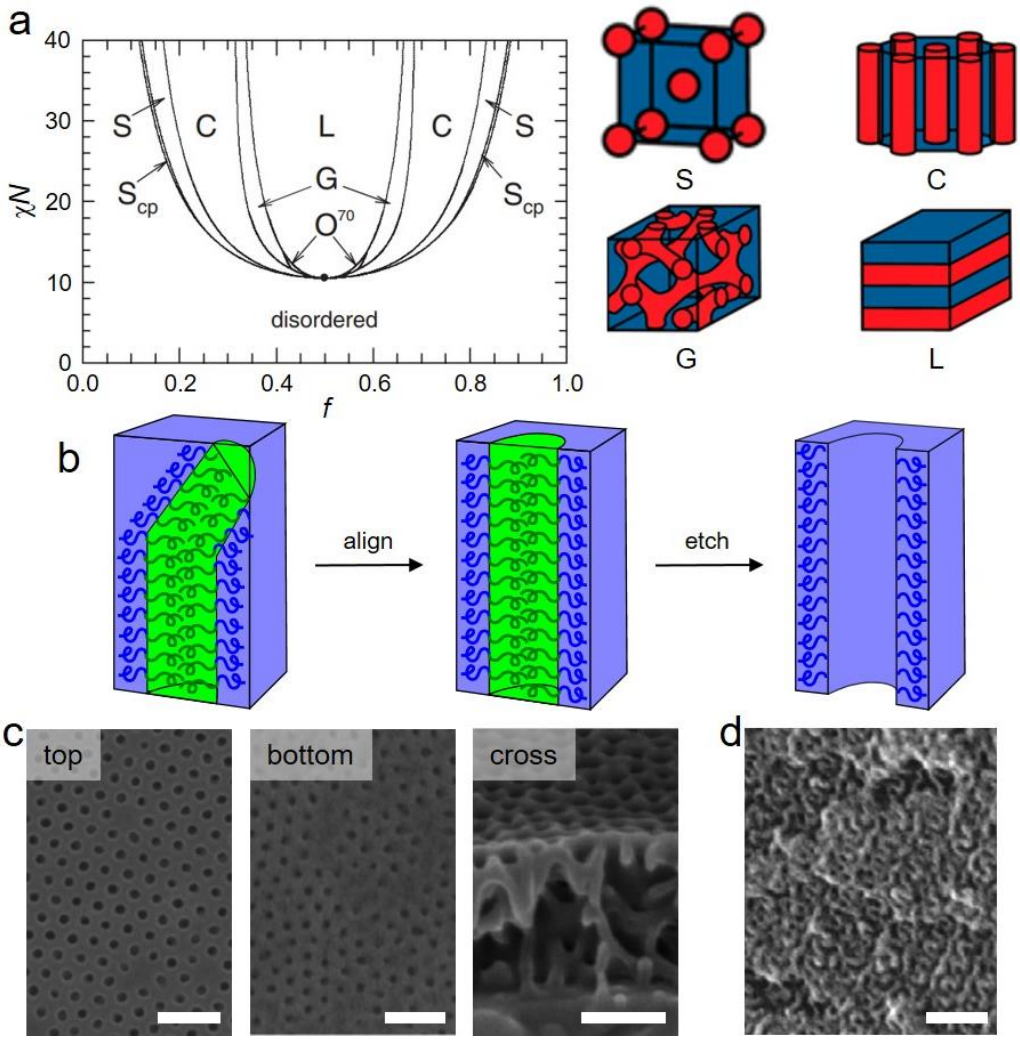

Figure 2.3. Illustration of block polymer self-assembly and the integration of these nanostructures into porous membranes. A representative phase diagram for diblock polymers is presented in (a) along with cartoon representations of the lamellar (L), double gyroid (G), hexagonally packed cylindrical (C), and spherical (S) morphologies.[79,80] For anisotropic morphologies, such as hexagonally packed cylinders, additional alignment steps are often required to obtain the continuous domains and pores that are required for water transport (b). This ensures that the pores span the length of the active layer, as demonstrated by SEM images of the top and bottom surfaces of a PS-*b*-PMMA selective layer following solvent vapor annealing and PMMA removal (c).[22] The scale bars correspond to 200 nm. Alternatively, a PB-*b*-PDMS block polymer with an isotropic and co-continuous double gyroid morphology eliminates the need for the alignment of anisotropic domains to produce continuous pores (d).[81] The scale bar corresponds to 100 nm.

2.4.1 Scope of Polymer Chemistries

Block polymers appropriate for use as self-assembled templates in UF membranes must incorporate one domain that can be selectively removed to generate pores without compromising the structure of the remaining matrix-forming block(s). The most commonly used sacrificial blocks are aliphatic polyesters, owing to their facile hydrolysis usually under mildly basic conditions. In particular, polylactide (PLA) has become ubiquitous in this regard due to its ease of synthesis, widespread availability, and innocuous degradation products.[17,20,21] Other than recent work on poly(propylene carbonate) (PPC),[82] research into the use of aliphatic polycarbonate, polyethers, and other aliphatic polyesters has been limited.

Other chemistries that are not susceptible to hydrolysis have also been used as the pore-forming block, although more involved degradation strategies are often needed. Early work focused on poly(methyl methacrylate) (PMMA) as the etchable block, where pores were generated by plasma etching or UV irradiation.[22,83] Alternatively, selective etching of poly(dimethylsiloxane) (PDMS) has been demonstrated in hydrofluoric acid and tetra-n-butylammonium fluoride (TBAF).[81,84,85] Rather than completely removing one block, pore generation can also be achieved by selective extraction of homopolymer diluents. For example, extraction of PEO homopolymer from the poly(4-vinylpyridine) (P4VP) domain of a PS-*b*-P4VP diblock and poly(acrylic acid) from the PEO phase of PS-*b*-PEO diblock generated narrow pore size distributions comparable to systems where one block was completely removed.[86–88] A summary of commonly used etchable blocks and their required etching conditions is provided in Table 2.2.

Table 2.2. Commonly used etchable blocks and their respective etching procedures

Etchable Polymer	Chemical Structure	Etching Mechanism	Etching Conditions for Thin Films
PLA	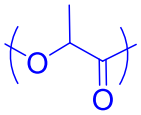	base-mediated hydrolysis	1 M NaOH 25 °C, 1-3 h[89,90]
PDMS	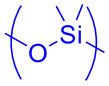	TBAF; HF	1 M TBAF, 25 °C;[85] 12 M HF, 0 °C, 2 h[81,84]
PMMA	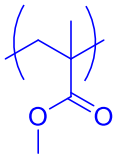	UV irradiation followed by acetic acid rinse; plasma etching	253 nm UV for 3 h acetic acid 1 h, 25 °C;[22] Ar/O_2 plasma, 1-5 min[83]
PEO	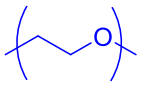	acid-catalyzed hydrolysis	14 M HI, 60 °C, 5 days[88]
PPC	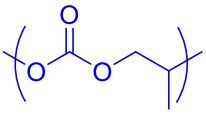	base-catalyzed hydrolysis	2 M NaOH 80 °C, 1 h[82]

Similar to NIPS, selectively etched membranes require a matrix-forming block with a sufficiently high elastic modulus to prevent pore collapse. Lower T_g polymers (such as polybutadiene) can be used, but their rubbery nature requires a high degree of cross-linking.[81,85,91] High T_g polymers, in contrast, are able to maintain pore integrity without the need for crosslinking; polystyrene (PS) has received significant attention for this reason.[17,20,22,86] A major disadvantage of a glassy and high T_g matrix, like PS, is a lack of toughness, especially when low molar mass blocks are used (e.g. in attempts to attain small pore sizes). Toughness can be improved by incorporating a low T_g polymer, such as polyisoprene or polybutadiene, into a multiblock architecture that combines the rubbery nature of the low T_g block with the rigid nature of the high T_g block. This strategy has resulted in an ~40-fold increase in strain at break for PS-*b*-PI-*b*-PS-*b*-PLA[21] compared to PS-*b*-PLA.[92]

2.4.2 Domain Alignment of Anisotropic Ordered Morphologies

An ideal block-polymer UF membrane has continuous and uninterrupted pores that span the entire length of the selective layer to achieve high water permeability. However, anisotropic cylindrical morphologies typically exhibit polycrystalline microstructures with domains that are misoriented at grain boundaries, disrupting pore continuity and inhibiting water transport (Figure 2.3b).[17,20,93] Therefore, careful design of the coating parameters or various alignment strategies are often required to obtain continuous pores.

In some cases, spontaneous orientation of cylindrical domains perpendicular to the film surface can be achieved through careful selection of the coating parameters.[17,20,93] Solvent evaporation effectively increases the segregation strength, creating a thermodynamic driving force for microphase separation.[93] Domains nucleate at the film-air interface and anisotropically grow across the film thickness along the concentration gradient. Rapidly drying a film increases the thermodynamic drive for domain growth more than it decreases the mobility of the polymer chains, resulting in the desired perpendicular orientation. Conversely, slower rates of solvent evaporation promote domain growth parallel to the film surface due to a driving force that increases slower than the decrease in chain mobility.[93] For the commonly used PS-*b*-PLA system, these parameters are well-documented and have been incorporated into UF membrane fabrication to varying degrees of success.[20,21,93] However, these parameters are highly system dependent, and identifying similar guidelines for different polymer chemistries requires extensive experimental screening.

If needed, the block polymer film can be thermally annealed above its highest T_g or T_m, where misoriented domains have sufficient mobility to rearrange into a more thermodynamically favorable orientation. Domain orientation is highly dependent upon the relative interfacial (polymer-substrate) and surface (polymer-air) energies of the blocks.[94–96] Perpendicular alignment occurs when the interfacial and surface energies of the constituent blocks are nearly identical or when the film thickness is smaller than the periodicity of the self-assembled domains.[94] However, block polymers with significantly different interfacial and surface energies orient parallel to the surfaces, resulting in an unsuitable morphology for UF membranes. The utility of thermal annealing can be limited by the long times (several hours) and high temperatures required, which can potentially degrade the block polymer or disrupt the pores in the support layer.

Instead of heating above T_g or T_m, exposure to solvent can lower the thermal transition below room temperature – a process termed solvent vapor annealing (SVA).[97] The polymer chains swell upon exposure to a non-preferential or slightly preferential solvent vapor, resulting in an increase in film thickness and chain mobility.[93,97,98] Solvent mediates the unfavorable enthalpic interactions between the different blocks, lowering χN. Additionally, solvents that are slightly preferential for one block effectively increase the relative volume occupied by that block, and thus the volume fraction, f. The increased mobility of the swollen chains facilitates re-organization into the thermodynamically favored (or potentially metastable) morphology corresponding to the decreased χN and the effective f.[97,98]

The morphology of the non-swollen state and the overall degree of swelling determine the swollen-state morphology. Rapid drying kinetically traps the morphology that can be achieved by traversing the lowest energy barrier, potentially enabling perpendicular orientation even when it would be otherwise energetically unfavorable.[97] In contrast, slow solvent removal results in the nucleation and growth of domains from the film surface, resulting in domains aligned along the most energetically favored orientation. [97]

The significant process dependence of SVA represents a major challenge. Expensive and time intensive optimization must be taken for each new configuration of solvent, polymer, and apparatus. Additionally, the need for specialized equipment limits the commercial production of large and cost-effective membranes. For composite block polymer membranes, the solvents may also plasticize the porous polymeric support layer and adversely affect its mechanical integrity and porosity. Support layer plasticization can be mitigated by transferring the block polymer selective layer from a solvent stable sacrificial substrate onto a porous support after SVA. This has been successfully demonstrated by using SVA to generate perpendicularly oriented cylinders in a PS-*b*-PMMA film on a solvent stable Si substrate and then transferring this film onto a porous PES substrate (Figure 2.3c) to produce a membrane with a high water permeability, 200 L m^{-2} h^{-1} bar^{-1}, and complete virus rejection.[22]

Magnetic fields offer a potentially powerful alternative to quickly align block polymer domains without the use of solvents.[99–102] The angular dependence of the free energy in the presence of the magnetic field drives domain alignment along the field direction. This

driving force is countered by a tendency to randomly orient domains to minimize their energy. Consequently, field-based alignment is only successful when the difference in the magnetic susceptibility between the blocks is high enough to make the angular dependent free energy significant compared to thermal energy. Identifying such a system is often challenging for traditional block polymers, so magnetic field alignment has found the most utility in systems that contain at least one liquid crystalline block.[101–103] Perpendicularly oriented cylindrical pores have been obtained in thin films of a brush block polymer composed of a selectively etchable polylactide block and a polynorbornene block with side chain liquid crystalline mesogens.[101,103] Non-liquid crystalline diblock polymers of PS-*b*-P4VP has also been successfully aligned due to an inherently high difference in magnetic susceptibilities between the PS and P4VP blocks.[104] However, films of both of these polymers were too thick to function as viable UF membranes.

Field-based alignment techniques are attractive for UF membrane fabrication, as they are fast and solvent-free processes suitable for composite membranes. However, successful incorporation of this approach has been limited by the technological challenge of overcoming surface interactions in films that are thin enough to serve as UF selective layers.[102] Furthermore, highly specialized equipment is required to achieve sufficiently strong magnetic fields, typically in the range of at several Tesla.

2.4.3 Utilization of Isotropic Ordered Morphologies

Morphologies that inherently possess co-continuous and interconnected domains eliminate the need for complicated alignment processes. The ordered network phases between the

lamellar and cylindrical regions of the phase diagram have received the most attention for this purpose, particularly the gyroid morphology.[81,84,85] However, applications of the gyroid morphology have been limited by the relatively narrow region of phase space (defined by χN and f) where this morphology is typically observed.[105] Targeting these domains often requires precision synthetic methods, such as anionic polymerization, which significantly increase the cost of polymer synthesis. Complex polymer architectures (multiblocks, miktoarm stars, etc.) and high dispersity blocks can slightly expand the thermodynamic stability of the gyroid phase but can also require complex synthetic methods.[73,106,107] Free-standing films of cross-linked PB-*b*-PDMS with a gyroid morphology have been used as UF membranes (Figure 2.3d), but these thick films (25 μm) displayed relatively low water permeabilities, ~10 L m^{-2} h^{-1} bar^{-1}.[81,84] To the best of our knowledge, composite membranes with a gyroid selective layer have not been reported, possibly due to difficulties in nucleating this morphology in very thin films (~100 nm).[108,109]

The inverse cylinder morphology (where the etchable block forms the matrix rather than the minority phase) is another potential option for continuous pores. Unlike the standard cylinder arrangement, placing the etchable block in the majority domain can result in continuous pores without the need to orient the minority cylindrical phase.[110] Based on the high volume fraction occupied by the etchable block ($f_{etchable}$ ~ 0.65–0.8), higher porosities than cylinders with an etchable minority phase ($f_{etchable}$ ~ 0.2-0.35) are attainable. However, upon etching, the matrix-forming domains are discontinuous, so inter-domain cross-linking is required to prevent pore collapse. Such a strategy has been employed in the fabrication

of NF membranes from polymerizable surfactants.[110] Similar approaches have yet to be investigated for block polymer systems for UF membranes, but it may be a promising area for future research.

2.4.4 Film Casting Strategies

A number of different strategies have been employed to fabricate block polymer UF membranes. The simplest method involves solvent casting free-standing films of block polymer from solution.[23,25,81,84] Upon solvent evaporation, a solid film comprising solely block polymer is obtained. While this strategy does not require any elaborate processing steps and is thus easy to scale, relatively thick films (on the order of hundreds of microns) are needed to provide the mechanical robustness necessary for hydraulic pressure-driven membrane operations. Due to their small pores, these thick films have low water permeabilities that are generally not competitive with existing NIPS membranes, despite their improved size-selectivity.[25,81]

Thinner (yet still mechanically robust) block polymer films would be highly advantageous for improving water permeability in a practical manner. One strategy is to fabricate composite membranes comprising a thin block polymer selective layer that imparts a high size-selectivity on top of a thicker macroporous support layer (often a NIPS membrane) that imparts high water permeability and mechanical robustness. The most direct route towards such a composite membrane is to directly coat a dilute block polymer solution atop a porous NIPS membrane.[17,20,21,82] The pores of the support layer are often filled with water (or another liquid that is immiscible with the casting solvent) prior to coating the block

polymer film to prevent infiltration into the support.[17,20] Additionally, the support layer must be resistant to the casting solvent used for the block polymer layer.

Blade coating techniques are particularly attractive for the block polymer solution due to the simplicity and scalability of these processes. However, the literature in this area has revealed challenges associated with fabricating block polymer layers that are thin enough (less than approximately 1 μm) to achieve a high water permeability.[17,82] Conversely, spin coating has resulted in the fabrication of sub-100 nm block polymer selective layers with significantly improved water permeability, but spin casting is difficult to implement at the scale of industrially relevant membrane modules.[20,21] Rather than directly coating onto an existing porous membrane, it is also possible to first coat a very thin (sub-100 nm) block polymer film on top of a non-porous sacrificial substrate and then transfer it onto a NIPS membrane.[21,22] Salt discs[21] and silicon wafers[22] are the most commonly used sacrificial substrates, as they are easily dissolved in water and hydrofluoric acid, respectively, to yield a thin and free-standing block polymer film. Sacrificial substrates often have high solvent and thermal stabilities as compared to NIPS membranes, enabling the use of annealing and post-functionalization processes that might compromise the integrity of a porous polymeric support.[22] However, the process of transferring a large film is extremely challenging, which limits the viability of this approach.

2.5 Selective Etching of Kinetically Trapped Disordered Block Polymers

Instead of equilibrium ordered morphologies, recent work in the field has focused on kinetically trapped disordered morphologies with co-continuous microphase separated

domains.[89,90,111–113] These systems generally exhibit advantages similar to those of the gyroid morphology (inherently continuous domains without the need for alignment), while being accessible across a wider range of block polymer compositions. Owing to their self-assembled domains, these disordered morphologies exhibit narrow pore size distributions comparable to equilibrium ordered morphologies. Consequently, both high size-selectivity and high water permeability are achievable in a single system. As these disordered morphologies are non-equilibrium states under typical UF use conditions, cross-linking reactions or thermal processing techniques are required to kinetically trap these states prior to use.[89,111]

2.5.1 Polymerization Induced Microphase Separation

One kinetic trapping strategy is polymerization induced microphase separation (PIMS).[111,114] In PIMS, a polymer end-functionalized with a chain transfer agent (CTA) appropriate for reversible addition fragmentation chain transfer (RAFT) polymerization is dissolved in a mixture of mono and difunctional monomers. A polylactide macro-chain transfer agent (PLA-CTA) dissolved in a monomeric mixture of styrene and divinyl benzene (DVB) has been used extensively in this approach.[111,114] Thermal[111,114,115] or UV initiation[116] results in the RAFT copolymerization of the monomers to form a cross-linked block polymer. As the block polymer grows (N increases), the segregation strength increases, inducing microphase separation. The cross-linking reaction kinetically traps the incipient microphase separated domains in a disordered and co-continuous state before the block polymer can order into its thermodynamic equilibrium morphology.[111,114] Following removal of the etchable domains, a continuous network of uniformly sized pores can be

obtained. Generally, the water permeabilities of these films are very low, ~ 0.5 L m^{-2} h^{-1} bar^{-1}, due to the large film thickness, ~300 μm.[111] Thinner films, ~100 nm to 1 μm, are required for obtaining water permeabilities comparable to commercial UF membranes with similar average pore sizes, but the relatively high volatility of typical liquid monomer reaction mixtures has hindered this goal.

2.5.2 Kinetically Trapped Morphologies Above the Order-Disorder Transition

To address the processing challenges inherent to PIMS, our group has recently developed a new method to obtain similar morphologies from pre-formed block polymers amenable to solution processing.[89,90,113,117] Above the order-disorder transition temperature (T_{ODT}), composition fluctuations in block polymer melts result in a disordered, yet microphase separated morphology that resembles spinodal decomposition.[70,118] This morphology exists at a much smaller length scale than in immiscible polymer blends, resulting in inherently co-continuous domains with sizes appropriate for UF membranes. Kinetic trapping of disordered state composition fluctuations requires an ordered and chemically reactive block polymer that can be heated into the disordered state and subsequently cross-linked (Figure 2.4a).[89,113] Stable pores can then be generated by selectively removing the uncross-linked, sacrificial domain (Figure 2.4b). Polymers that contain pendant epoxide or unsaturated moieties, such as poly(glycidyl methacrylate)[89,90] and polybutadiene[113], have proven successful for introducing latently cross-linkable functionalities into the matrix. Epoxide-containing domains are cured using thermal[89] or photoacid generators,[90] while unsaturated systems can be cured through a radical process.[113] Unlike PIMS, the uncross-linked precursor is polymeric and non-volatile, enabling the fabrication of thin films by

solution processing. Consequently, composite membranes with block polymer selective layers on the order of 100 nm to 1 μm thick have been obtained using blade and spin coating methods (Figure 2.4c and 2.4d).[89,90,113] The ability to produce thinner block polymer films has permitted fabrication of highly selective membranes with higher water permeabilities than PIMS membranes.

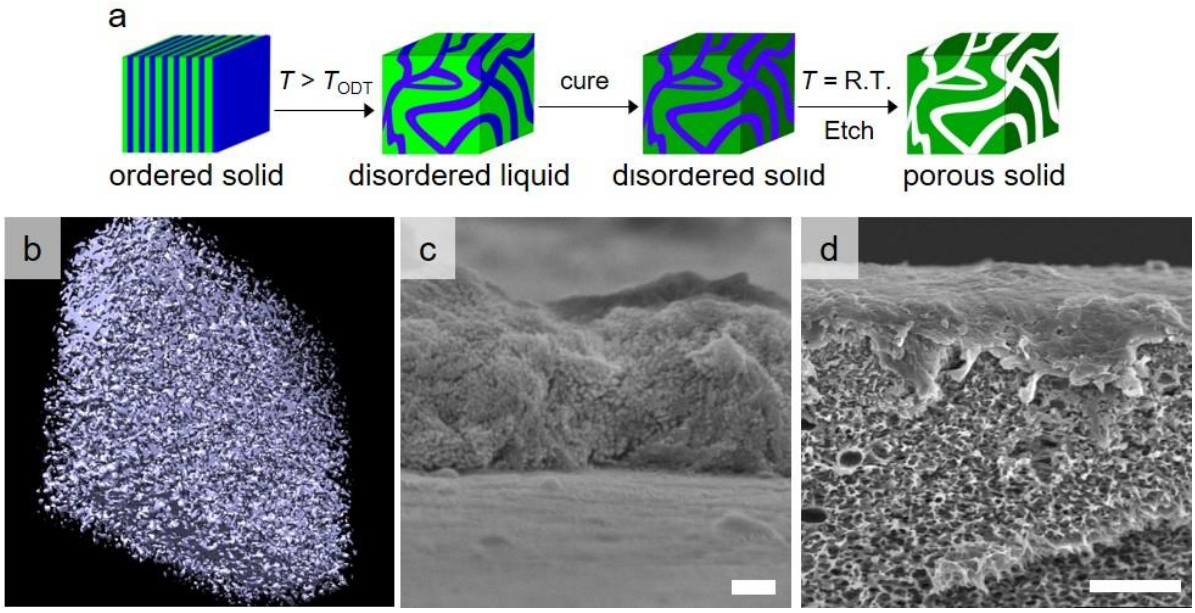

Figure 2.4. An illustration of the process used to kinetically trap disordered state composition fluctuations for the purpose of generating co-continuous pores is presented in (a). The three-dimensional connectivity of these pores has been demonstrated by a transmission electron microtomographic reconstruction of a cross-linked P(S-*s*-GMA)-*b*-PLA diblock (b).[89] The use of the disordered state also helps facilitate co-casting techniques that can be integrated with existing NIPS processes, as has been demonstrated for dual layer membranes comprising a kinetically trapped P(MMA-*s*-S)-*b*-PLA selective layer and a PSF support layer (c).[90] The block polymer derived selective layers of these composite membranes maintain the bicontinuous pore structure observed in bulk monoliths across the entire thickness, where the pores generated from a photocured P(S-*s*-GMA)-*b*-PLA were observed to span the entire thickness of the selective layer (d). The scale bar corresponds to 2 μm in (c) and to 200 nm in (d).

In addition to chemical cross-linking reactions, thermal quenching of high T_g polymers can be used to trap the fluctuating disordered state. By first heating the block polymer above the T_{ODT} and then rapidly quenching below T_g, the disordered state is kinetically trapped

by vitrification before it can re-order.[117] The low mobility of the chains in the glassy state and the relatively high modulus preserves the disordered and co-continuous network of pores. This method has allowed for comparable porosities to the cross-linked systems, while also reducing the processing time and expanding the scope of the ODT approach to more diverse chemistries.[117]

Membranes with kinetically trapped disordered morphologies can be produced using similar membrane casting protocols to those previously discussed for equilibrium ordered morphologies. Early studies directly coated block polymer solutions onto pre-formed NIPS supports using blade or spin coating techniques (Figure 2.4c).[89,90,113] After drying, these films were heated above the T_{ODT} of the block polymer and cross-linked in the disordered state. However, high temperatures, harsh conditions, and long curing times are often needed for these cross-linking reactions, which may lead to densification of the support layer pores. Consequently, the observed water permeabilities for these membranes were lower than expected, although they still exhibited high size-selectivities.[89,90,113] In contrast, the vitrification method uses milder processing conditions that eliminate the need for subsequent cross-linking steps.

The thermal quenching method can also be combined with NIPS to produce composite membrane in a single process. In a proof of concept, a dilute solution of a P(MMA-*s*-S)-*b*-PLA diblock was directly coated on top of a solvent-swollen polysulfone support layer. This dual layer liquid film was then heated above the T_{ODT} of the block polymer. Subsequently immersing this film in an ice water coagulation bath precipitated the

polysulfone layer by NIPS and kinetically trapped the fluctuating disordered state of the block polymer. Removal of the PLA domains in the selective layer resulted in the formation of a composite membrane (Figure 2.4d), with a high size-selectivity and a water permeability of ~150 L m^{-2} h^{-1} bar^{-1}. This process can be realized at a large scale using existing industrial membrane fabrication infrastructure. Further refinement is expected to enable roll-to-roll production of highly selective membranes competitive with commercial technologies in terms of water permeability, scalability, and cost.

2.6 Selective Swelling of Self-assembled Block Polymers

An emerging method of fabricating UF membranes from self-assembled block polymers uses the selective solvent swelling of one block to generate pores.[119,120] Like the previously discussed method of selective degradation, selective swelling induced pore generation is performed on solid block polymer films that are self-assembled into their thermodynamically favored morphology (spheres, cylinders, gyroid, lamellae). However, instead of chemically etching one domain, pores are produced through the volumetric expansion of one block in the presence of a highly selective solvent.[119,120] This method eliminates the formation of degradation byproducts inherent to selective etching and simplifies membrane production. One of the major advantages of the selective swelling strategy is that the swellable polar block remains intact in the final membrane, which can result in a hydrophilic surface and pore walls that improve the wettability and fouling resistance of the membrane.[15,121] Additionally, pore generation proceeds significantly faster than for selectively etched membranes, notably producing uniform pores in less than one minute using microwave heating.[122]

2.6.1 Scope of Polymer Chemistries

Selective swelling induced pore generation requires the constituent polymer blocks to have relatively different polarities. This ensures that the solvent is highly preferential for only one block and non-preferential (or highly unfavorable) for the other(s). The first known report of selective swelling induced pore generation in UF membrane fabrication used a PS-*b*-PMMA diblock to produce UF membranes with high water permeabilities and narrow pore size distributions.[123] Contemporary efforts have focused heavily on PS-*b*-P2VP diblocks due to their lower water contact angle and improved pore wettability post-swelling.[18,121,124] The hydrophilicity has been further improved by employing PS-*b*-PEO diblocks, as the presence of the hydrophilic PEO chains along the membrane surface and pore walls imparts a high degree of fouling resistance.[15,125,126]

Recent research has focused on replacing the brittle PS block with a mechanically robust PSF block (e.g. PSF-*b*-PEO) in an effort to make a more commercially relevant membrane.[120,127,128] Produced by step growth synthesis, these PSF-containing block polymers have an inherently higher molar mass dispersity than block polymers synthesized using controlled chain-growth polymerization. However, the effect of this high dispersity on the pore size distribution has received little attention. Future research efforts are likely to continue the development of block polymers chemistries similar to those that are currently used in membrane fabrication.

2.6.2 Detailed Mechanistic Description

The detailed mechanism for selective swelling induced pore generation will be described for the well-studied PS-*b*-P2VP diblock polymer in ethanol (Figure 2.5a).[119,121] Ethanol is highly selective for the P2VP block, yet a very poor solvent for the PS matrix block. Consequently, ethanol partitions into the P2VP block almost exclusively, while the PS block remains comparatively rigid and unaffected. As the P2VP chains swell, an osmotic driving force causes them to stretch and deform. This results in an increase in the film thickness to accommodate the volumetric expansion of the swollen chains, as confirmed by spectroscopic ellipsometry (Figure 2.5b).[119,121] Swelling is typically performed at elevated temperatures to facilitate some plastic deformation of the PS matrix (the T_g of PS decreases from ~100 °C in bulk to ~85 °C in the presence of ethanol).[119,120] However, the swelling temperature is still typically below the T_g of PS in the presence of ethanol.[121] Therefore, deformation of the PS matrix is expected to occur locally at the domain interface, as mixing between the highly swollen P2VP block and the PS block further depresses T_g near the block junction.[120] When the swollen film is removed from the selective solvent, the PS chains immediately vitrify and the previously swollen P2VP chains collapse against the glassy matrix. The collapsed P2VP chains are enriched on the membrane surface as well as the pore walls, as evidenced by a decrease in the water contact angle of the films post-swelling.[123] The volume that was previously occupied by ethanol in the P2VP domains is converted into pores, as supported by the strong correlation between increased film thickness and increased porosity and pore size. Higher swelling temperatures increase the mobility of the PS chains, facilitating plastic deformation and

greatly increasing the degree of swelling.[121] Therefore, adjusting the swelling time and temperature can tune the average pore size and overall film porosity (Figure 2.5c).[121]

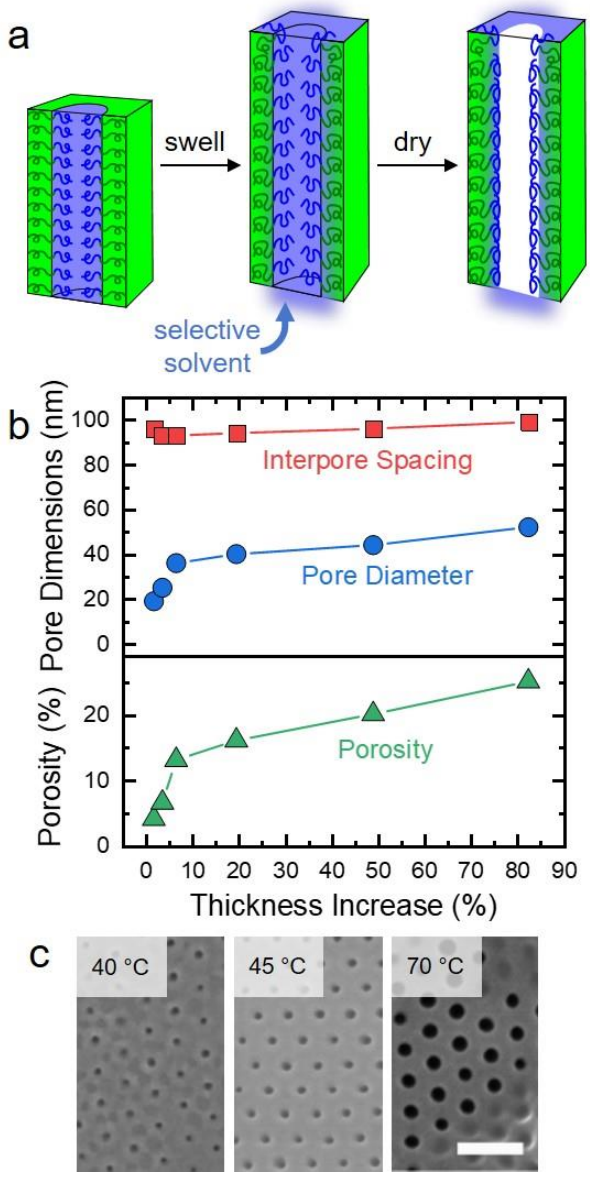

Figure 2.5. A side-view (top panel) and a top-view (bottom panel) illustration of selective swelling induced pore generation is presented in (a). This proposed mechanism has been supported by the strong correlation between the increase in film porosity (green triangles) and pore diameter (blue circles) with the increase in film thickness upon swelling PS-*b*-P2VP (b).[119] Conversely, the interpore spacing (red squares) remains constant, indicating that swelling is confined in the lateral direction. The effect of swelling temperature at a constant swelling time for a PS-*b*-P2VP diblock in ethanol is presented in (c).[121] Generally, higher swelling temperatures (40, 45, and 70 °C from left to right) results in larger pores due to an increased degree of swelling. The scale bar in (c) corresponds to 200 nm.

2.6.3 Film Casting Strategies

Both free-standing[127–129] and composite membranes[18,123,124,130,131] have been reported, but the higher water permeabilities and lower materials requirements of composite membranes are preferred. Melt extrusion of UF membranes from PSF-*b*-PEO has also been reported, where microwave heating the extrudate in the solvent bath can significantly reduce the time required for pore generation from several hours to several seconds.[132] While this process has been primarily applied to thick films (ca. 50 μm) thus far, it can be a promising strategy for practical membrane production, provided that it can be extended to sufficiently thin films (ca. 100 nm).[122]

2.6.4 Domain Alignment and Morphological Control

As discussed for selectively etched block polymer UF membranes, the self-assembled domains must be converted into continuous pores. One notable feature of the selective swelling mechanism is that cylindrical domains do not necessarily have to be perpendicularly aligned through the thickness of the film to obtain continuous pores. Instead, randomly oriented cylindrical domains merge and interconnect to form bicontinuous pores upon the selective swelling of PS-*b*-P2VP.[18,131,133] This facilitates the fabrication of highly permeable UF membranes without having to execute complicated alignment procedures. Bicontinuous structures with a percolating pore network can also be produced by selectively swelling disordered block polymers that still exhibit locally microphase separated domains, as has been demonstrated for PSF-*b*-PEO.[127,128]

For certain applications, it may be advantageous to align cylindrical domains to reduce pore tortuosity by using the previously discussed techniques. Continuous pores have been reported for cylinders with both parallel[134] and perpendicular[125] orientations in PS-*b*-P2VP, offering the possibility of tuning the pore topology from slits to cylinders respectively. This may be an interesting platform for examining the relationship between pore morphology and water transport at the nanoscale, informing the development of transport models specifically tailored towards UF and NF.

2.7 Evaporation-Induced Self-assembly Followed by Non-solvent Induced Phase Separation

One of the most promising fabrication strategies for block polymer UF membranes combines the principles of block polymer thermodynamic self-assembly with traditional non-solvent induced phase separation – a process termed evaporation induced self-assembly followed by non-solvent induced phase separation (SNIPS).[7,19,135] The presence of solvent in SNIPS drives the block polymer molecules to self-assemble into micelles rather than the previously discussed morphologies in solid films. The SNIPS process follows a similar protocol as traditional NIPS.[19] Briefly, a concentrated block polymer solution is cast into a film and immersed in non-solvent after a short evaporation time to induce phase separation and pore formation. By virtue of this similarity, the SNIPS process should be readily integrated into existing industrial coating methods, potentially enabling commercially viable roll-to-roll membrane fabrication.[7,136] In comparison to NIPS membranes, the microphase separated nanostructures inherent to block polymers result in more regular and uniform surface pores and enable more precise solute separation.

Like NIPS membranes, SNIPS membranes exhibit an asymmetric and integral architecture with a thin active layer that gradually transitions into a thicker and more porous substructure.[135] In effect, both the selective and the support layers are composed of block polymer in SNIPS. Such an integral structure eliminates the need to coat a separate block polymer layer on top of a porous support, significantly simplifying the coating process. This architecture also guarantees that the small pores that actively separate the targeted contaminants in the selective layer are well-connected to the much larger pores in the membrane substructure. High water permeabilities can thus be obtained without having to orient the domains, in direct contrast to ordered block polymer solid films (see section 4). The ultimate membrane properties are highly dependent upon the choice of block polymer chemistry and composition, solution concentration, evaporation time, and solvent.

2.7.1 Scope of Polymer Chemistries

In general, the block polymer used in SNIPS contain a polar block and a non-polar block. The non-polar block forms the membrane matrix, and typically PS has been used due to its easy synthesis and high T_g. The SNIPS mechanism allows flexibility in the choice of the polar block, enabling membrane properties (e.g. pore size, stimuli responsiveness, and fouling resistance) to be precisely tailored toward the targeted application. The most highly studied and arguably most mature system is PS-*b*-P4VP. However, many other polymers have been successfully used for the polar block, including poly(dimethylacrylamide),[137–140] poly(2-vinylpyridine),[141] poly(2-hydroxyethyl methacrylate),[142,143] and poly(ethylene oxide).[144,145] Including a low T_g end block (such as isoprene) can produce more mechanically robust membranes, where PI-*b*-PS-*b*-P4VP membranes displayed toughness

values three times higher than PS-*b*-P4VP.[146] Triblock polymers have also been used to introduce more hydrophilic chemistries, such as PEO[147] and PAA,[139] into the block polymer to improve fouling resistance.

One intriguing feature of using P4VP-containing block polymers is that the pore walls are lined with pyridine moieties. These pyridine groups can serve as a reactive handle for pore wall functionalization, facilitating the introduction of cysteine,[16] dopamine,[16,148,149] and graphene oxide[150] to improve fouling resistance and bactericidal properties. Additionally, reaction of the pyridine groups with either methyl iodide or propane sultone results in cationic or zwitterionic pores, respectively, which can be used to selectively bind charged organic dyes with sizes of ~1 nm, which would otherwise be too small to remove by UF.[33]

P4VP has a pKa of 4.6, resulting in the protonation of the pyridine moieties at lower pH.[151]. These protonated chains swell in water, constricting the pores and resulting in pore sizes below 5 nm.[151,152] Pore sizes below 10 nm are otherwise difficult to obtain from PS-*b*-P4VP, as a sufficiently high molar mass is needed to obtain well-structured pores.[153] Additionally, this pH-responsiveness allows for the possibility of pore gating.[152] However, in most applications, variability in pore size is disadvantageous and results in an undesirable decrease in water permeability at low pH. For such applications, PEO has been shown to result in pore sizes that are significantly more stable across a range of pH than P4VP.[144] Furthermore, the hydrophilicity of PEO inherently improves the fouling resistance of these membranes without the need for pore wall functionalization.[144,145]

An emerging chemistry for use in SNIPS membranes replaces the P4VP block with poly(*N*, *N*-dimethylacrylamide) (PDMA).[137,138,140] Treatment of PI-*b*-PS-*b*-PDMA triblocks with concentrated acid hydrolyzes the PDMA block to form poly(acrylic acid) (PAA).[137,139,140,154] The acrylic acid groups are largely deprotonated above pH = 3.5, resulting in negatively charged chains that swell into the pores to reduce repulsive interactions. Consequently, effective pore sizes as small as ~1 nm can be obtained at neutral pH, potentially enabling these membranes to be used in size-selective NF.[137,140] Below pH ~ 3.5, the acrylic acid groups are largely protonated and collapse against the matrix, increasing the pore size to the UF range.[139] Similar features have been obtained by blending PS-*b*-PAA into a PS-*b*-P4VP casting solution.[155] Additionally, PAA containing SNIPS membranes have been shown to strongly and selectively bind Cu^{2+} which may enable heavy metal removal in addition to traditional UF separations.[32,137]

2.7.2 Detailed Mechanistic Description

The precise membrane formation mechanism for SNIPS is complex, due to its strong dependence on the selected casting parameters. The two most widely studied systems, PS-*b*-P4VP in DMF/THF and PI-*b*-PS-*b*-P4VP in DOX/THF, will be examined in detail here as representative examples. To understand the entire SNIPS mechanism for PS-*b*-P4VP in DMF/THF, it is critical to first establish the self-assembly of the block polymer molecules in the casting solution. Based on their solubility parameters, DMF is a preferential solvent for P4VP and THF is a relatively neutral solvent for both PS and P4VP.[156] These purely enthalpic considerations suggest that the P4VP block will form the corona to minimize less favorable PS-solvent interactions.

However, typical diblocks used in SNIPS membranes are highly asymmetric, containing approximately 65 to 85 wt.% PS.[19,135] Packing these longer PS chains into the micelle core requires a large degree of entropically unfavorable chain stretching.[157,158] Since DMF is a theta solvent for PS rather than a very poor solvent, the enthalpic cost of exposing the PS chains to solvent is lower than the entropic cost of packing these chains into the micelle core. Therefore, it is thermodynamically favorable to form a spherical micelle with a PS corona and a P4VP core (Figure 2.6a).[159] Small angle neutron scattering (SANS) experiments of representative solutions support this hypothesis.[158] Contrast matching the P4VP block of PS-*b*-P4VP to DMF made the P4VP domains "invisible" to the incident neutron beam, and an almost complete disappearance of the inter-micellar scattering was observed,[158] clearly suggesting that the micelles comprise a solvent-swollen spherical P4VP core that is surrounded by a PS corona in DMF.[159]

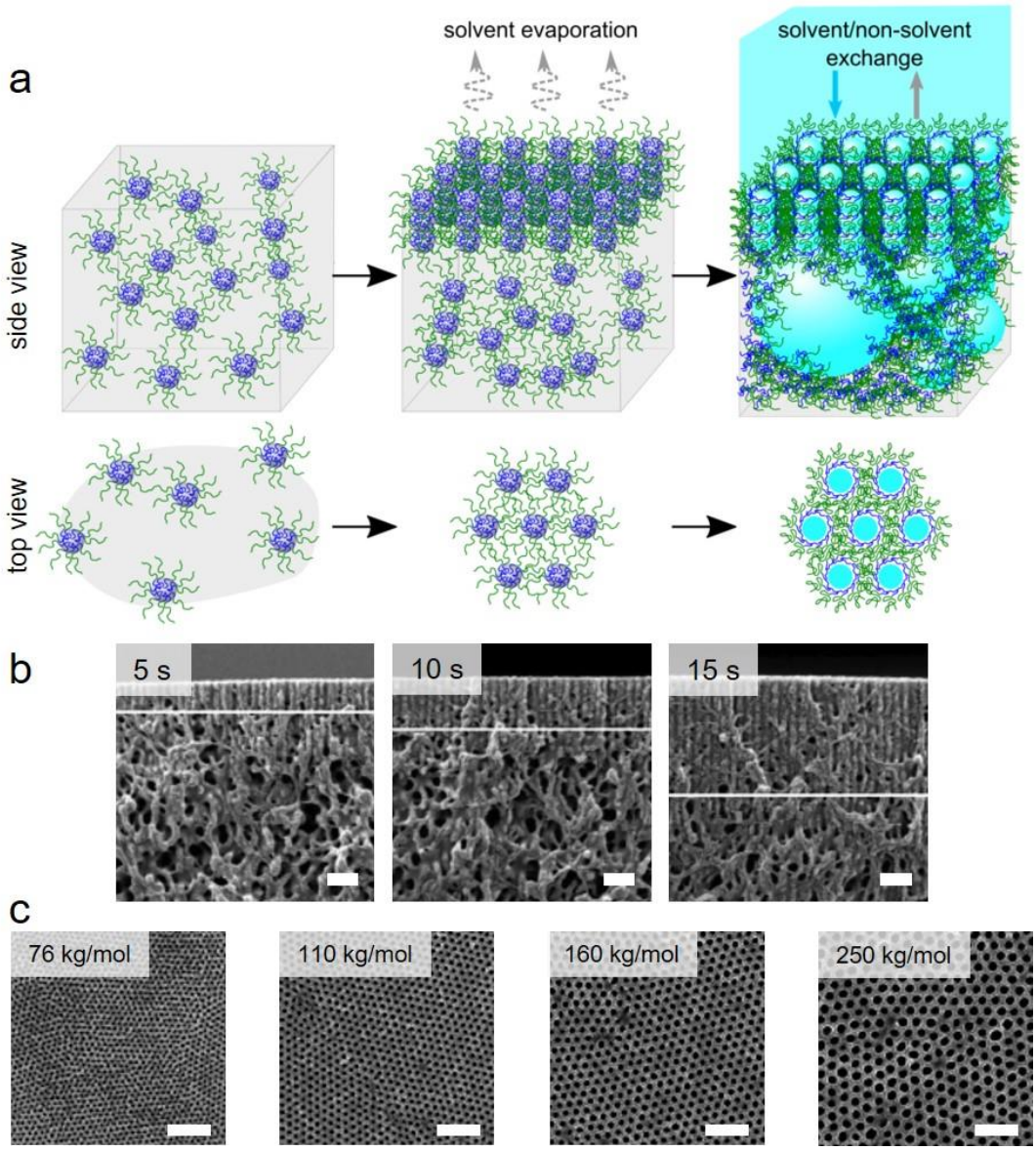

Figure 2.6. In the SNIPS mechanism (a), a concentrated solution of PS-*b*-P4VP in DMF/THF self-assembles into micelles composed of a P4VP core (blue) and a PS corona (green). After casting a film, a disordered packing of micelles is initially obtained. A short solvent evaporation step drives the micelles to pack an ordered hexagonal arrangement of cylindrical channels at the film-air interface. Immersing the film into non-solvent exchanges the casting solvent for the non-solvent, resulting in the precipitation of the polymer into a solid film with P4VP-lined pores supported by a solid PS matrix. The development of the cross-sectional morphology for a PS-*b*-P4VP membrane with increasing evaporation time is presented in (b).[160] Active layer thickness increases with the evaporation time due to increased inter-micellar interactions that drive cylinder growth. The tunability of the average pore size is demonstrated in (c) for a PS-*b*-P4VP system.[161] Increasing the molar mass of the block polymer, results in a larger average pore size. The scale bars in (b and c) correspond to 200 nm.

After this solution is cast into a film, solvent evaporation primarily occurs at the film-air interface, increasing the local polymer concentration and thus the micelle-micelle interactions. This causes the initially disordered micelles to first coalesce and then arrange into a regularly ordered packing in the surface layer (Figure 2.6a).[162–164] The structure of this packing is highly dependent upon the choice of solvent, polymer composition, and concentration. For PS-*b*-P4VP in DMF/THF, grazing incidence small angle X-ray scattering (GISAXS) experiments support a transition from a disordered packing of spherical micelles at the surface to an ordered hexagonal packing with increasing polymer concentration, representing the expected concentration evolution upon film drying.[156,162,163] Solvent evaporation also creates a concentration gradient in the direction normal to the film-air interface that causes the initially spherical micelles to coalesce into perpendicularly oriented cylindrical channels at the film surface (Figure 2.6b).[160,162,163] Below the film-air interface, solvent evaporation is significantly slower, resulting in a lower concentration of micelles in the substructure. These micelles remain loosely packed in a disordered arrangement.[159,163]

After the evaporation step, the P4VP cores of the cylindrical channels at the film surface remain slightly swollen in solvent.[158] When the film is immersed in water, there is an influx of non-solvent into the P4VP cores (Figure 2.6a).[136,163] The volumetric expansion caused by the solvent/non-solvent exchange is accommodated by the concomitant contraction of the PS chains in the corona to fill the interstitial space between the micelles.[159] The coalescence of these PS chains physically traps the morphology and prevents further coarsening.[159] Removal of the non-solvent generates uniformly sized surface pores lined

by P4VP. The lower concentration and looser micelle packing below the film surface results in a significantly different substructure morphology, resembling traditional NIPS membranes with larger pores and a more disperse size distribution.[156,159,163] Due to the concentration gradient that developed during solvent evaporation, there is a gradual transition from the small and uniform pores at the film surface to the large and irregular pores in the substructure.[165] Consequently, these membranes exhibit an integral and asymmetric structure with a thin active layer on top of a thicker support layer.

The average pore size at the surface can be rationally tuned by adjusting the molar mass of the PS-*b*-P4VP block polymers (Figure 2.6c).[161] Additionally, the evaporation time strongly influences the size and regularity of the membrane surface pores and the active layer thickness (Figure 2.6b).[19,135,146,160] For short evaporation times, the surface layer will be highly swollen, and the micelles will have not yet packed into a regularly ordered arrangement.[146] These membranes closely resemble NIPS membranes and have an irregular arrangement of surface pores with a broad size distribution. Longer evaporation times improve the ordered packing of the micelles at the film surface, resulting in progressively smaller and more regularly arranged pores in the active layer. However, very long evaporation times prevent the solvent/non-solvent exchange required for pore generation, resulting in a non-porous surface that is undesirable for UF membranes.

Chemically similar triblock polymers containing a poly(isoprene) endblock (PI-*b*-PS-*b*-P4VP) have also received significant attention, as the rubbery PI block can improve upon the mechanical robustness of PS-*b*-P4VP membranes.[146] These triblock systems are

commonly cast from DOX/THF mixtures using similar strategies to those previously discussed for diblocks.[146,151,166,167] While the overall mechanism is generally similar to PS-*b*-P4VP in DMF/THF, the specific details related to the initial micellar assembly and their packing following solvent evaporation are quite different.

The presence of the highly solvophobic PI endblock introduces an additional enthalpic drive to minimize PI-solvent contact. The resulting micelles thus likely contain a P4VP corona that encases a sphere composed of a PI core and a PS shell, supported by selectively stained TEM micrographs.[146] In contrast to the hexagonal packing of PS-*b*-P4VP, GISAXS studies suggest that cubic packings, and in particular a BCC packing, are preferred for PS-*b*-PI-*b*-P4VP in DOX/THF upon solvent evaporation.[151] After immersing these films in water, solvent/non-solvent exchange in the swollen P4VP coronae causes the chains to collapse along the significantly less swollen PS/PI cores. The collapse of the P4VP chains creates voids in the interstitial space between micelles, which are filled with non-solvent.[146] This process occurs in the top several layers of micelles at the film surface, converting the interstitial space between the micelles into a co-continuous network of channels both perpendicular and parallel to the film surface.[151,168] SEM images of the top surface of dried PS-*b*-PI-*b*-P4VP membranes demonstrate a square packing of surface pores with center-to-center distances that are consistent with the symmetry and lattice parameter of the initial cubic packing of micelles, suggesting that the evaporation-induced surface morphology is trapped upon precipitation.[146,151] The substructure retains a similar morphology to the previously discussed NIPS and PS-*b*-P4VP SNIPS membranes.

2.7.3 Film Casting Strategies

The primary advantage of the SNIPS mechanism is that the resultant membranes contain integral selective and support layers. As a result, the desired architecture of a thin and highly size-selective active layer supported by a thicker and highly porous substructure is inherent to the process, eliminating the need for complex coating protocols involving porous substrates.[7,135,159] Instead, a concentrated solution of block polymer can be easily blade cast into a free-standing film using identical procedures to those commercially used in NIPS membranes. While these free-standing SNIPS membranes often exhibit similar water permeabilities and improved size-selectivities as compared to NIPS membranes with similar average pore sizes, they typically require large quantities of block polymer which can significantly raise the materials cost.[7] Furthermore, a large portion of the block polymer mass forms the highly porous substructure and does not significantly contribute to the overall size-selectivity. The use of commercially produced block polymers (e.g. PS-*b*-PB-*b*-PS) for SNIPS membranes could potentially reduce materials costs, but few reports have fully explored these polymers for membrane fabrication.[169] Therefore, processing methods that can reduce the thickness of this substructure without compromising the size-selectivity and mechanical integrity are of high interest.

As discussed previously for selectively etched and selectively swollen systems, composite membranes are perhaps the most attractive solution. This can significantly reduce the thickness of the non-selective block polymer substructure without adversely affecting either the overall mechanical robustness or the high size-selectivity. Thin selective layers layer of PS-*b*-P4VP have been spray coated onto PVDF or PAN membranes, reducing the

total block polymer thickness from ~50 μm for a free-standing membrane to 1 μm for the composite membrane without compromising solute rejection.[170] Additionally, roller casting methods that more closely resemble traditional membrane casting processes have been used to coat a thin PS-*b*-P4VP SNIPS layer on top of a PAN membrane.[171]

Due to the similarities between the pore formation mechanisms in SNIPS and NIPS, it is also possible to co-cast a NIPS-based solution and a SNIPS-based solution into a composite architecture.[172,173] This strategy follows a similar protocol as previously discussed for UF membranes derived from selectively etched disordered block polymers. Briefly, a homopolymer solution is first cast into a film followed by coating a block polymer solution on top of the nascent support layer. A partial evaporation step drives block polymer self-assembly at the surface of the active (top) layer, while the film remains highly swollen in solvent closer to the substrate. This film can then be immersed into a non-solvent bath to simultaneously induce pore formation in the homopolymer-derived support layer by NIPS and in the block polymer-derived selective layer by SNIPS. Such a strategy has been successfully reported for a PS-*b*-P4VP block polymer solution on top of a PS homopolymer solution.[172] However, adoption of this technique has been limited by the poor adhesion of the block polymer solution to commercially relevant NIPS solutions, such as PAN.[172]

All of the coating methods discussed thus far have targeted flat sheet membrane configurations, but many industrially relevant separations processes use hollow fiber modules due to their higher packing efficiency and easier cleaning.[136] These hollow fiber configurations are usually obtained by extruding polymer solutions through a spinneret and

into a coagulation bath. Due to its mechanistic similarities to NIPS, the SNIPS process should be readily integrated into the existing fiber spinning infrastructure.[154,172,173] There are numerous reports focused on the fabrication of hollow fiber SNIPS membranes, and they have been comprehensively discussed in a recent review.[136] In general, the overall mechanism is similar to the flat sheet configuration. A concentrated block polymer solution is extruded though an annular spinneret followed by a partial solvent evaporation step before the fiber enters the non-solvent bath. In addition to the key processing parameters discussed previously, the morphology of fiber-spun SNIPS membranes depends upon the shear stresses in the spinneret, the block polymer flow rate, and the distance and time between the spinneret die and the non-solvent bath.[136] Either free-standing[154,174–177] or composite[170,172,173] hollow fiber SNIPS membranes can be fabricated. Hollow fiber composite membranes can be obtained by spray coating or dip coating a thin block polymer layer onto a porous substrate.[170] Additionally, co-casting techniques can be used to fabricate dual layer hollow fibers by passing both a block polymer solution and a homopolymer solution through a triple orifice spinneret followed by extrusion into a non-solvent bath, as has been demonstrated for PS-*b*-P4VP.[113]

2.7.4 Domain Alignment and Morphological Control

Regardless of the fabrication procedure, an appealing feature of the SNIPS process is that continuous pores are routinely obtained in the selective layer without having to orient the block polymer domains.[7,19,135] The evaporation of solvent from the film-air interface creates a driving force for self-assembly perpendicular to the film surface. Furthermore, the integral nature of the selective and support layers ensures that the pores in the selective

layer are directly connected to the pores in the support layer with a gradient in pore sizes across the membrane thickness.[165] These features can significantly reduce membrane processing costs associated with the previously discussed magnetic field and SVA protocols, and these processing savings could potentially compensate for the increased materials cost of SNIPS membranes.

2.8 Structure-Property-Performance Relationships in Block Polymer UF Membrane

While the lab-scale preparation of block polymer UF membranes is relatively mature and enhanced size-selectivity over traditional UF membranes has been demonstrated, block polymer membranes must be economically competitive with existing NIPS membranes to be commercially viable. This requires water permeability comparable to NIPS membranes, tunable and sharp molecular weight cutoff values, high fouling resistance to minimize membrane cleaning and maximize operation lifetime, and rapid fabrication at a large scale and a low cost. To identify the core research areas, critical analysis of key structure-property-performance relationships must be performed. In this section, we will evaluate the water permeability, size-selectivity, fouling resistance, and process scalability of state-of-the-art block polymer UF membranes to help guide future research.

2.8.1 Water Permeability

The water permeability of UF membranes is one of the most important considerations for commercial viability. Membranes with high water permeability require smaller membrane areas, shorter filtration times, and lower applied pressures, resulting in a small system footprint and high energy efficiency.[3] Based on the Hagen-Poiseuille model (eq. 1), the

water permeability for a free-standing block polymer membrane can be increased by decreasing the film thickness, by increasing the pore size, and by increasing the total porosity.[25] Generally, the pore size can be increased by increasing the block polymer molar mass.[20,119,150] However, large adjustments in the average pore size significantly alter the MWCO. Therefore, increasing the porosity could be a more robust approach that does not alter solute rejection. For selectively etched and selectively swollen membranes, this can be easily achieved by increasing the volume fraction of the pore-forming block, but very high porosities ($\varepsilon > 0.5$) are susceptible to pore collapse.[110]

Decreasing the thickness of the block polymer layer can also significantly increase the water permeability. Composite membranes with a thin block polymer layer on top of a thicker and more porous support can accomplish this objective without compromising the mechanical integrity, reducing the thickness of the block polymer from several microns to below 100 nm.[20,124,170] Modeling the water permeability for composite membranes is more challenging than for free-standing membranes, but a resistors-in-series approach is useful[178,179]:

$$P_{\text{dual}}^{-1} = P_{\text{support}}^{-1} + P_{\text{selective}}^{-1} \quad \text{(eq. 2)}$$

This model inversely relates the resistance to water flow to the permeability (P) for each layer.

Applying this model framework to composite membranes with selectively swollen or selectively etched block polymer selective layers is relatively straightforward. The water permeability of the block polymer selective layer can be calculated using the Hagen-

Poiseuille equation (eq. 1), while the water permeability of the support layer can be independently measured. The theoretical water permeability of these membranes calculated using eq. 1 and 2 can then be compared to the experimental water permeabilities that are widely reported in the literature (Figure 2.7a). Despite accounting for resistance from the support layer, the experimental water permeabilities are still significantly lower than the resistors-in-series model predicts, particularly for selectively etched membranes.

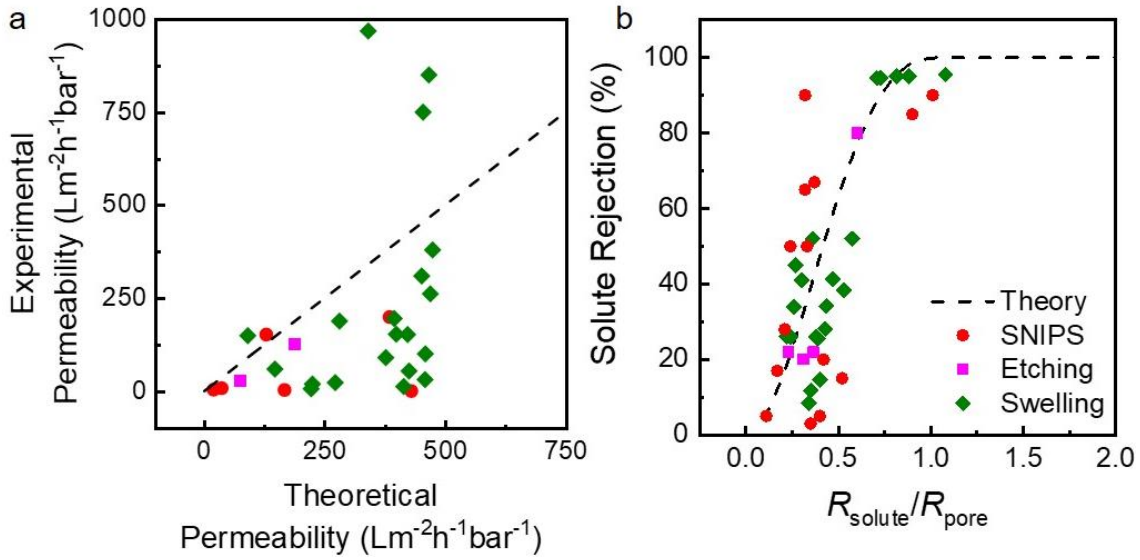

Figure 2.7. Scatter plot comparing the experimentally measured water permeability to the theoretical water permeability as estimated by the Hagen-Poiseuille equation for several block polymer membranes (a). The theoretical permeability was calculated according to a resistors-in-series model based on SEM images of the selective layer and the reported support layer permeability. The dashed line denotes the ideal case, where the experimental water permeability exactly matches the theoretical prediction. BSA rejection (R_h ~ 4 nm) as a function of R_{solute}/R_{pore} is presented for several different block polymer derived UF membranes (b). The dashed line denotes the theoretical rejection curve for an isoporous membrane.

Applying the resistors-in-series model to SNIPS membranes is more challenging due to the integral selective and support layers. This makes an independent measurement of the support layer water permeability impossible, but the water permeability of the selective layer can still be estimated based on the surface porosity, average pore size, and active

layer thickness observed by SEM. The substructure permeability was conservatively estimated as 500 L m^{-2} h^{-1} bar^{-1} for the data presented in Figure 2.7a based on typical support layer permeabilities reported for other block polymer membranes. Plasma etching of the active layer could potentially reveal the underlying substructure, enabling more accurate measurements of the substructure permeability. However, such studies have not been reported to the best of our knowledge. The substructure morphology of SNIPS membranes is highly process dependent; therefore, our rough estimate of the support layer permeability likely accounts for the larger variability in the data as compared to the other block polymer membranes. In general, the experimental permeabilities were lower than the resistors-in-series model predicts with a few notable exceptions where the experimental permeability was higher than the model prediction. For those systems, the selected support layer permeability likely underestimated the true permeability.

These lower than expected water permeabilities have hindered the development of block polymer membranes, as they are unable to match the performance of NIPS membranes. The inability of the resistors-in-series model to accurately predict the experimental water permeability suggests that additional factors contribute a significant resistance to water transport, regardless of the pore formation mechanism. For composite membranes, the block polymer casting solvent could partially dissolve or swell the NIPS support, significantly reducing the support layer water permeability and porosity compared to measurements obtained prior to coating.[89,90]

Additionally, pore size is typically measured by SEM in the dry state, while membrane processes are performed in the wet state. The presence of water may partially swell the polymer chains lining the pores, effectively decreasing the pore size.[180,181] This phenomenon may be particularly pronounced for pores lined by polar and hydrophilic moieties (such as PEO, P2VP, and P4VP), which are predominant in selectively swollen and SNIPS membranes.[180] Equation 1 predicts a d^4 dependence of the water permeability on the pore diameter (porosity scales as d^2 for a fixed pore density), so only minor differences in the measured pore size have a significant impact on the predicted water permeability. For example, a 10% overestimate in the measured pore size results in a 35% decrease in the theoretical water permeability.

Pore tortuosity could also have a significant impact on the experimental water permeability, increasing the effective path length for water transport and decreasing the permeability as compared to a perfectly straight pore. The experimental data more closely follows the theoretical prediction after accounting for a reasonable degree of pore tortuosity ($\tau \sim 1.5 – 3$), but the experimental permeabilities are still generally lower than expected. Additionally, the effective porosity of the block polymer selective layer could also be lower than inferred based on SEM of the membrane surface. As discussed earlier, water permeation requires pores that are continuous through the entire thickness of the selective layer, but many block polymer morphologies exhibit discontinuous grain boundaries that interrupt water transport and significantly reduce the water permeability. This is particularly evident in selectively etched cylindrical block polymers, where challenges in orienting the domains and achieving high water permeabilities are well-documented.[17,20,21]

The selective swelling mechanism partially mitigates this challenge, as misaligned domains merge into continuous pores upon swelling.[18,124,128] This may explain the generally higher water permeabilities observed for selectively swollen membranes compared to selectively etched membranes, but this comes at the cost of increased tortuosity. The presence of discontinuous pores in the selective layer is less obvious for SNIPS membranes, but the possibility cannot be dismissed. Due to the kinetic nature of SNIPS, active layer pore growth may be arrested before these pores connect to those in the substructure, resulting in a dense interlayer that impedes water transport.[141,182]

To address these hypotheses, significant advances in membrane metrology are needed. Electron microtomography is expected to grow in importance as a powerful tool that enables the 3D reconstruction of the selective layer morphology at the nanoscale, facilitating quantitative analysis of pore continuity.[165,183] The FIB-SEM technique is particularly intriguing, as it is compatible with > 100 nm thick films and can thus be used to reconstruct the entire selective layer morphology with high fidelity and a wide depth of field.[182,183] Additionally, developments in liquid cell electron microscopy can facilitate sample imaging in environments that better represent real membrane processes, which is critical for obtaining more accurate measurements of the pore size.[184] Nanoscale diffusion experiments, such as PFG-NMR, can directly monitor the tracer diffusion of isotopically labelled water through the membrane pores to investigate the presence of misaligned and discontinuous pores, estimate the pore tortuosity, and reveal nanoscale confinement effects.[185] Finally, simulations that accurately describe the non-equilibrium morphologies obtained after block polymer coating can illuminate nanostructure development.[186,187] Such

advances can reveal the factors currently limiting the water permeability of block polymer membranes and guide the development of higher performing systems.

2.8.2 Size-selectivity

While high water permeability is necessary, the primary motivation for the development of block polymer membranes is their potential for highly size-selective separations.[3,7] Many emerging applications for UF require precise discrimination between contaminants of nearly identical sizes, which is currently impossible to achieve in a single pass for NIPS membranes.[3,42,43]

As discussed previously, UF membranes operate by a size-exclusion mechanism, where particles that are larger than the membrane pores are rejected. For a solute of hydrodynamic radius, a, permeating a membrane pore of radius, r_p, the size-dependent rejection profile can be accurately predicted by equation 3:[10]

$$R = 1 - \left[2\left(1 - \frac{a}{r_p}\right)^2 - \left(1 - \frac{a}{r_p}\right)^4\right] \exp\left[-0.7146\left(\frac{a}{r_p}\right)^2\right] \text{ (eq. 3)}$$

Equation 3 was derived from hindered transport theory and represents the convective flow of a spherical solute as it approaches a cylindrical capillary.[10] Complete rejection of a solute requires that all the membrane pores are smaller than the contaminant targeted for removal. Equation 3 assumes an isoporous size distribution, where all pores are identical with a radius of r_p. Such behavior is expected for block polymer UF membranes, but commercial NIPS membranes exhibit a broad distribution of pore sizes. For these systems, eq. 3 can be integrated across the pore size distribution, typically assuming a log-normal pore size distribution.[3,10] Using the isoporous model along with reported average pore sizes obtained

in the dry state for select block polymer UF membranes, we compared the experimental rejections of bovine serum albumin (BSA) to the theoretical prediction of eq. 3 (Figure 2.7b). The experimental data closely follows theory, consistent with the expectation that block polymer selective layers are indeed composed of nearly uniform pore sizes.

These conclusions are corroborated by the significantly smaller pore size coefficient of variation (standard deviation divided by mean pore size) of block polymer UF membranes as compared to NIPS membranes based on measurements that we made from reported SEM images in the dry state (Figure 2.8a). Interestingly, the pore size distribution of block polymer membranes also appears to depend upon the pore formation mechanism. SNIPS membranes tend to have a broader pore size distribution than selectively etched and selectively swollen membranes, although the pore size distribution is generally still narrower than for NIPS membranes. This may be related to the hybrid nature of the SNIPS mechanism, which combines aspects of both NIPS and block polymer self-assembly.[135,136] In contrast, selective swelling and selective etching of block polymer films are performed at thermodynamic equilibrium, where pores are formed from well-defined and uniform domains. Selectively etched disordered morphologies also exhibit comparatively narrow pore size distributions, as they have been kinetically trapped in the equilibrium morphology associated with the processing temperature and conditions.[90,117] Overall, these high selectivities and nearly uniform pore sizes are encouraging, indicating that block polymer UF membranes satisfy their primary technological objective despite their lower than expected water permeabilities.

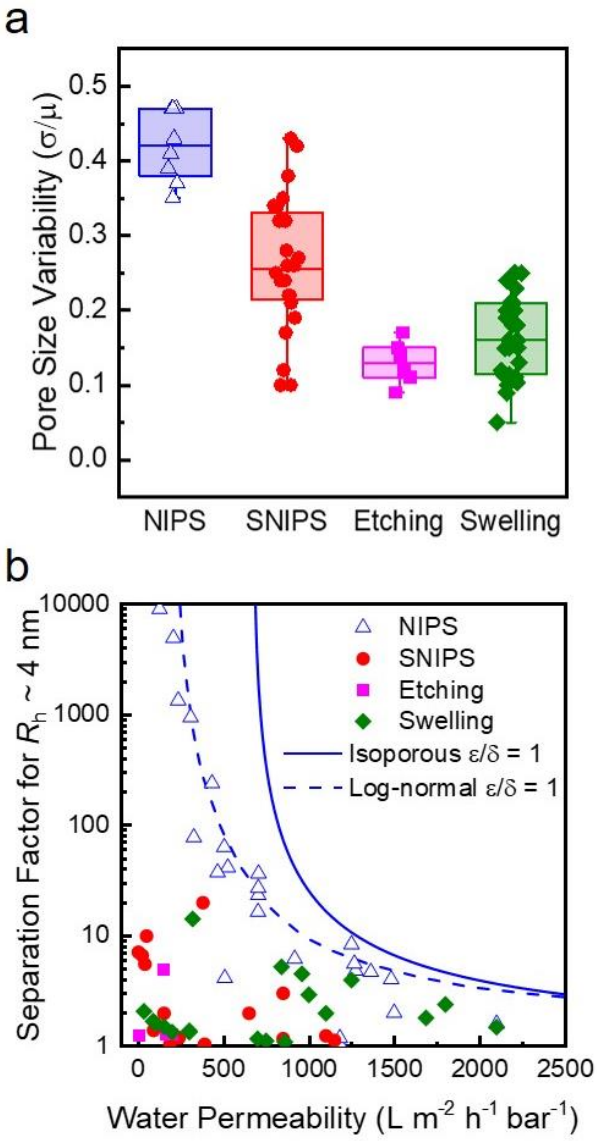

Figure 2.8. The pore size coefficient of variation (standard deviation divided by mean pore size) is presented for traditional NIPS as well as block polymer derived UF membranes (a). The separation factor, (1 - rejection)$^{-1}$, for BSA (R_h ~ 4 nm) is presented against water permeability (b). All points correspond to experimentally reported values of permeability and rejection. Open blue triangles correspond to traditional NIPS membranes, while the filled symbols correspond to block polymer membranes. The solid line represents the theoretical permselectivity calculated for an isoporous pore size distributions, and the dashed line corresponds to a log-normal distribution, assuming a fixed ratio of surface porosity to active layer thickness (ε/δ).

The ideal UF membrane would have both high water permeability and high size-selectivity.

However, examining the equations that describe the water permeability (eq. 1) and the

solute rejection (eq. 3), it becomes apparent that small changes in the pore size will have a much larger effect on the permeability than on the rejection for a constant ratio of surface porosity to active layer thickness (ε/δ). Practically, this reflects the well-discussed permeability-selectivity trade-off.[10] By simultaneously solving eq. 1 and 3, it is possible to generate a permselectivity curve for a given solute. Such a theoretical curve is presented in Figure 2.8b along with BSA rejection from both commercial NIPS and block polymer UF membranes. BSA was selected as a standard solute due to its ubiquity in the UF membrane literature.

Experimental data for NIPS membranes generally fall along a permselectivity curve calculated assuming a log-normal pore size distribution and $\varepsilon/\delta = 1\ \mu m^{-1}$. These assumptions reflect the broad pore size distributions and thin active layers of NIPS membranes.[3] Based on the reported range of porosities and selective layer thicknesses, block polymer membranes are expected to have ε/δ in the range of approximately 0.2 to 1 μm^{-1}. However, the experimental data generally fall well below this prediction. The sharp rejection curve shown in Figure 2.7b and the low pore size coefficient of variations shown in Figure 2.8a for block polymer membranes suggests that their comparatively poor performance does not reflect a low size-selectivity. Instead, the lower permselectivity likely results from a lower than expected water permeability. The low ratio of surface porosity to active layer thickness could reflect the well-documented challenges of coating very thin block polymer films and aligning the domains to generate continuous pores.[17] Additionally, as discussed in the previous section, the support layer has a significant effect

on the overall permeability and may ultimately limit the permeability of composite membranes.

While BSA is an industry standard for evaluating UF membrane rejection, the R_h of BSA (~4 nm) is significantly smaller than the typical pore sizes of block polymer membranes, resulting in low separation factors. Virus filtration requires the rejection of solutes with R_h ~ 10 nm. Therefore, PEO with a molar mass of 100 kg mol^{-1} and R_h of ~10 nm (PEO-100k) is a more representative standard to evaluate rejection for block polymer membranes (Figure 2.9). In general, the permselectivity was notably higher for PEO-100k than for BSA, indicating that block polymer membranes are more suitable for virus filtration than for the removal of small organic molecules, which is consistent with their typical pore sizes. However, the data still fall significantly below the predicted performance based on values of ε and δ obtained by SEM. For reference, a theoretical curve generated assuming $\varepsilon = 0.3$ and $\delta = 1$ μm (i.e. typical values for block polymer UF membranes) is included in Figure 2.9. Again, this likely reflects significant contributions from the support layer to the overall permeability. Furthermore, support layer compaction may occur during operation. Highly permeable NIPS membranes undergo compaction during prolonged operation, resulting in a decline in permeability over time due to a loss in porosity.[188,189] For composite block polymer membranes, this can result in water permeabilities that are significantly lower than expected. Additionally, most block polymer membranes have PS-based matrices with low toughness, which may exacerbate membrane compaction and flux decline. To advance block polymer membranes, their permselectivites will need to become competitive with NIPS membranes. Fundamental studies investigating the role of the

support layer in membrane performance are critical, with a particular focus on better understanding the morphological evolution during membrane operation. Future research should also focus on developing membrane matrix materials with improved toughness as well as new fabrication methods for obtaining thinner selective layers with more continuous pores.

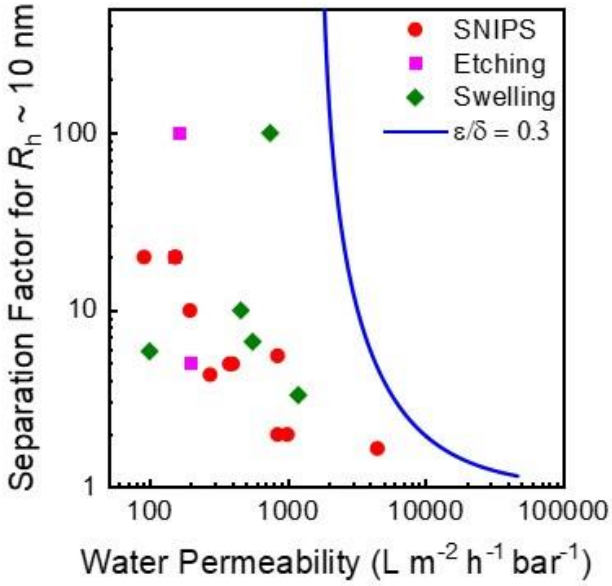

Figure 2.9. The separation factor, (1 - rejection)$^{-1}$, for PEO with a molar mass of 100 kg mol^{-1} and R_h of ~10 nm that reasonably approximates the hydrodynamic size of viruses targeted in virus filtration. All points correspond to experimentally reported values of permeability and PEO-100k rejection. The theoretical curve was calculated assuming $\varepsilon = 0.3$ and $\delta = 1$ μm, which are typical values for block polymer UF membranes.

2.8.3 Fouling Resistance

Poor fouling resistance is a major limitation of commercial NIPS membranes due to their hydrophobic surfaces. Incorporating surface segregating amphiphilic block or comb polymers into the NIPS casting solution represents a straightforward strategy for easily improving the fouling resistance (Section 2.3.2). These surface segregating block polymer additives can be readily integrated into the existing membrane casting infrastructure at low concentrations without requiring the often-complex coating procedures needed for block

polymer selective layers. Consequently, these block polymer technologies are currently being incorporated into commercial membranes (see Ultramem produced by Clean Membranes), serving as a bridge between existing homopolymer NIPS membranes and next-generation block polymer membranes.[190]

The increased surface functionality of block polymers enables antifouling moieties to be chemically grafted to the membrane surface, improving their long-term stability over the physically bound additives employed in homopolymer NIPS membranes. Pyridine groups in P4VP-based SNIPS membranes are amenable to chemical functionalization, as demonstrated by the oxidation of a PS-*b*-P4VP membrane to form polyanionic PS-*b*-P4VPN-oxide.[191] Reactive handles can also be introduced along the pore walls of selectively etched membranes by incorporating a functional midblock or junction between the matrix-forming and sacrificial blocks. For example, the PI block of PS-*b*-PI-*b*-PLA was oxidized post-etching to produce reactive epoxide moieties along the pore walls.[192] Furthermore, selecting polymer segments with the desired functionality can eliminate the need for costly and often challenging functionalization steps. The SNIPS process is particularly attractive in this regard, as the pores are lined by a polar block (e.g. P4VP, PAA, P2VP, PDMA). Inherently hydrophilic membranes have also been prepared through the selective swelling of block polymers, resulting in the enrichment of the polar block (e.g. P2VP, PEO) along the membrane surface and pore walls.[128,133] Notably, a composite membrane prepared from an active layer of selectively swollen PS-b-PEO on a PVDF substrate displayed ~100% recovery of the initial water flux after BSA filtration.[15] Blending amphiphilic block polymers into selectively etched membranes can also improve

fouling resistance. This has been demonstrated for binary blends of PS-*b*-PEO and PS-*b*-PLA, where the miscibility between the PEO and PLA blocks resulted in a mixed PLA/PEO domain that was converted into PEO-lined pores upon PLA removal.[193] Overall, the potential for drastically improving the fouling resistance of UF membranes with block polymers represents a major advantage, potentially decreasing cleaning expenses and increasing membrane lifetime.

2.8.4 Process Scalability

Commercialization of block polymer UF membranes likely requires the continuous and roll-to-roll production of membranes at large size scales (> 100 m^2) and low costs. Curtain coating represents the current industry standard for producing NIPS membranes. However, high performing membranes fabricated from selectively etched or selectively swollen block polymers are typically obtained by difficult-to-scale processes, such as spin coating.[26,36] Furthermore, pore generation in these membranes often requires hours to days in contrast to the instantaneous pore formation in NIPS. Recent advances have reduced the pore formation time to seconds by using microwave heating in conjunction with selective swelling, which is a promising development for more scalable fabrication.[132]

In this context, SNIPS membranes have risen to prominence, as they can be easily fabricated into highly permeable systems using blade coating techniques with near instantaneous pore formation. Due to the mechanistic similarities with NIPS, SNIPS membranes can be produced in a roll-to-roll process using existing industrial infrastructure, significantly increasing production throughput and reducing capital costs. A major

disadvantage of SNIPS membranes is their high materials cost, which is directly related to their integral and asymmetric architecture. Block polymer forms both the selective and support layers, yet only the thin selective layer contributes to the size-selectivity. High materials costs may limit SNIPS membranes to high value UF applications, but the ease and scalability of fabrication could potentially compensate for their high expenses. Additionally, composite SNIPS membranes can reduce the consumption of block polymer by up to 95%,[170,171] while co-casting strategies could potentially streamline production and lower costs even further.[172,173] Significant improvements in fouling resistance and toughness can also increase the operation lifetime of block polymer membranes compared to NIPS membranes, potentially mitigating their higher initial cost.

2.9 Future Outlook

Achieving the technological objectives of block polymer membranes will require both fundamental research and practical advances in chemistry and processing. A number of open fundamental questions must be addressed to optimize membrane fabrication. Detailed studies of the non-equilibrium self-assembly and nanostructure formation during the SNIPS process can significantly guide membrane processing, reducing experimental time and costs and ensuring the reproducible fabrication of high performing systems at an industrially relevant size-scale. Understanding the contribution of the support layer to the overall performance of composite membranes is also necessary for optimizing membrane design. Furthermore, advances in characterization techniques are needed to provide robust and reliable data for more accurate predictions of the permeability and size-selectivity of block polymer membranes. This will entail the continued development of microscopy

techniques that facilitate imaging in 3D and in sample environments that better represent membrane operations.

The information gained from these fundamental studies is expected to significantly inform the synthetic design of block polymers specifically tailored for UF applications. The currently ubiquitous styrenic block polymers typically lack the necessary mechanical properties for commercial membrane processes. New polymer chemistries that replicate the performance of existing NIPS membranes are therefore required to achieve membranes that can withstand prolonged operation. These chemistries should be relatively cost effective and transferable to industrial synthetic capabilities.

Furthermore, advances in membrane fabrication are critical. Many academic systems rely upon non-scalable coating process (e.g. spin coating) or require large quantities of costly block polymer (e.g. SNIPS membranes). Additionally, academic research has generally focused on the fabrication of flat sheet membranes; however, hollow fiber membranes are generally preferred by industry. Translation of lab-scale research to more commercially relevant membrane coating processes and configurations is crucial. Future developments must focus on reducing the cost or quantity of block polymer, reducing the time required for pore formation, and identifying coating methods that can be integrated into existing industrial membrane fabrication processes.

In summary, block polymer membranes represent a potentially transformative technology in water filtration. Superior size-selectivities to existing NIPS membranes have been routinely demonstrated at the lab-scale, introducing the possibility for more efficient and

precise separations. This can improve process efficiency and foster the development of new applications. Furthermore, the enhanced functionality of block polymers allows for the incorporation of fouling resistant moieties that can significantly reduce cleaning expenses and extend membrane lifetimes. However, despite their immense potential, further progress is needed before block polymer membranes can supplant NIPS membranes. Identifying the optimal balance between maximizing water permeability and process scalability and minimizing materials costs is critical. Block polymer membranes are slowly being commercialized at the start-up level, and continued progress may transform these systems into commercially viable technologies.

2.10 Thesis Overview

This thesis primarily focuses on incorporating disordered block polymer morphologies into the production of ultrafiltration membranes with both high water permeability and high size-selectivity. Achieving these objectives requires the development of block polymer chemistries that can be solution processed into thin films and subsequently heated above their order-disorder transition temperatures to access the fluctuating disordered state. Disordered state composition fluctuations can then be kinetically trapped by either curing or rapidly vitrifying the morphology that exists above T_{ODT}. This preserves the co-continuous domains associated with the fluctuating disordered state, and these domains can then be converted into uniform pores following the selective removal of one of the blocks.

Chapter 3 describes the synthetic, processing, and characterization methods used throughout this thesis. Chapter 4 details proof-of-concept results that demonstrate the

generation of co-continuous pores from block polymers that were thermally cross-linked above T_{ODT}. In Chapter 5, these findings were extended to a system that can be photocured in the disordered state, decoupling the stimuli used to disorder and cross-link the block polymer. Chapter 6 describes the development of a non-cross-linkable block polymer that can be kinetically trapped by rapid vitrification from above T_{ODT}. This system was then used to probe the temperature dependent morphological development above T_{ODT}, revealing a transition from the desired disordered and co-continuous morphology to an undesirable and relatively unstructured morphology far above T_{ODT}. Chapter 7 details the use of large amplitude oscillatory shear as an additional stimulus for controlling the domain structure near the T_{ODT}. Finally, the findings from each of these chapters were incorporated into the development of a novel co-casting strategy for obtaining ultrafiltration membranes, which is described in Chapter 8. This co-casting technique represents a potentially scalable process for obtaining both high water permeability and high size-selectivity, achieving the primary technological objective of this thesis.

2.11 References

1) Mekonnen, M. M.; Hoekstra, A. Y. Four Billion People Facing Severe Water Scarcity. *Sci Adv* **2016**, *2*, e1500323.

2) Ercin, A. E.; Hoekstra, A. Y. Water Footprint Scenarios for 2050: A Global Analysis. *Environment International* **2014**, *64*, 71–82.

3) Werber, J. R.; Osuji, C. O.; Elimelech, M. Materials for next-Generation Desalination and Water Purification Membranes. *Nature Reviews Materials* **2016**, *1*, 16018.

4) Park, H. B.; Kamcev, J.; Robeson, L. M.; Elimelech, M.; Freeman, B. D. Maximizing the Right Stuff: The Trade-off between Membrane Permeability and Selectivity. *Science* **2017**, *356*, eaab0530.

5) Guillen, G. R.; Pan, Y.; Li, M.; Hoek, E. M. V. Preparation and Characterization of Membranes Formed by Nonsolvent Induced Phase Separation: A Review. *Ind. Eng. Chem. Res.* **2011**, *50*, 3798–3817.

6) Nunes, S. P. Block Copolymer Membranes for Aqueous Solution Applications. *Macromolecules* **2016**, *49*, 2905–2916.

7) Zhang, Y.; Sargent, J. L.; Boudouris, B. W.; Phillip, W. A. Nanoporous Membranes Generated from Self-Assembled Block Polymer Precursors: Quo Vadis? *Journal of Applied Polymer Science* **2015**, *132*.

8) Sadeghi, I.; Kaner, P.; Asatekin, A. Controlling and Expanding the Selectivity of Filtration Membranes. *Chem. Mater.* **2018**, *30*, 7328–7354.

9) van de Witte, P.; Dijkstra, P. J.; van den Berg, J. W. A.; Feijen, J. Phase Separation Processes in Polymer Solutions in Relation to Membrane Formation. *Journal of Membrane Science* **1996**, *117*, 1–31.

10) Mehta, A.; Zydney, A. L. Permeability and Selectivity Analysis for Ultrafiltration Membranes. *Journal of Membrane Science* **2005**, *249*, 245–249.

11) Mochizuki, S.; Zydney, A. L. Theoretical Analysis of Pore Size Distribution Effects on Membrane Transport. *Journal of Membrane Science* **1993**, *82*, 211–227.

12) Bates, F. S.; Frederickson, G. Block Copolymers - Designer Soft Materials. *Phys. Today* **1999**, *52* (2), 32–38.

13) Bates, C. M.; Bates, F. S. 50th Anniversary Perspective: Block Polymers—Pure Potential. *Macromolecules* **2017**, *50*, 3–22.

14) Jackson, E. A.; Hillmyer, M. A. Nanoporous Membranes Derived from Block Copolymers: From Drug Delivery to Water Filtration. *ACS Nano* **2010**, *4*, 3548–3553.

15) Yang, H.; Wang, Z.; Lan, Q.; Wang, Y. Antifouling Ultrafiltration Membranes by Selective Swelling of Polystyrene/poly(ethylene Oxide) Block Copolymers. *Journal of Membrane Science* **2017**, *542*, 226–232.

16) Shevate, R.; Kumar, M.; Karunakaran, M.; Hedhili, M. N.; Peinemann, K.-V. Polydopamine/Cysteine Surface Modified Isoporous Membranes with Self-Cleaning Properties. *Journal of Membrane Science* **2017**, *529*, 185–194.

17) Phillip, W. A.; O'Neill, B.; Rodwogin, M.; Hillmyer, M. A.; Cussler, E. L. Self-Assembled Block Copolymer Thin Films as Water Filtration Membranes. *ACS Appl. Mater. Interfaces* **2010**, *2*, 847–853.

18) Shi, X.; Wang, Z.; Wang, Y. Highly Permeable Nanoporous Block Copolymer Membranes by Machine-Casting on Nonwoven Supports: An Upscalable Route. *Journal of Membrane Science* **2017**, *533*, 201–209.

19) Peinemann, K.-V.; Abetz, V.; Simon, P. F. W. Asymmetric Superstructure Formed in a Block Copolymer via Phase Separation. *Nature Materials* **2007**, *6*, 992.

20) Querelle, S. E.; Jackson, E. A.; Cussler, E. L.; Hillmyer, M. A. Ultrafiltration Membranes with a Thin Poly(styrene)-B-Poly(isoprene) Selective Layer. *ACS Appl. Mater. Interfaces* **2013**, *5*, 5044–5050.

21) Jackson, E. A.; Lee, Y.; Hillmyer, M. A. ABAC Tetrablock Terpolymers for Tough Nanoporous Filtration Membranes. *Macromolecules* **2013**, *46*, 1484–1491.

22) Yang, S. Y.; Park, J.; Yoon, J.; Ree, M.; Jang, S. K.; Kim, J. K. Virus Filtration Membranes Prepared from Nanoporous Block Copolymers with Good Dimensional Stability under High Pressures and Excellent Solvent Resistance. *Advanced Functional Materials* **2008**, *18*, 1371–1377.

23) Phillip, W. A.; Amendt, M.; O'Neill, B.; Chen, L.; Hillmyer, M. A.; Cussler, E. L. Diffusion and Flow Across Nanoporous Polydicyclopentadiene-Based Membranes. *ACS Appl. Mater. Interfaces* **2009**, *1*, 472–480.

24) Epstein, N. On Tortuosity and the Tortuosity Factor in Flow and Diffusion through Porous Media. *Chemical Engineering Science* **1989**, *44*, 777–779.

25) Phillip, W. A.; Rzayev, J.; Hillmyer, M. A.; Cussler, E. L. Gas and Water Liquid Transport through Nanoporous Block Copolymer Membranes. *Journal of Membrane Science* **2006**, *286*, 144–152.

26) Baker, R. W. *Membrane Technology and Applications*, 2nd ed.; John Wiley & Sons, 2012.

27) Wu, D.; Howell, J. .; Field, R. . Critical Flux Measurement for Model Colloids. *Journal of Membrane Science* **1999**, *152*, 89–98. h

28) Zhang, R.; Liu, Y.; He, M.; Su, Y.; Zhao, X.; Elimelech, M.; Jiang, Z. Antifouling Membranes for Sustainable Water Purification: Strategies and Mechanisms. *Chem. Soc. Rev.* **2016**, *45*, 5888–5924.

29) Asatekin, A.; Kang, S.; Elimelech, M.; Mayes, A. M. Anti-Fouling Ultrafiltration Membranes Containing Polyacrylonitrile-Graft-Poly(ethylene Oxide) Comb Copolymer Additives. *Journal of Membrane Science* **2007**, *298*, 136–146.

30) Maruf, S. H.; Wang, L.; Greenberg, A. R.; Pellegrino, J.; Ding, Y. Use of Nanoimprinted Surface Patterns to Mitigate Colloidal Deposition on Ultrafiltration Membranes. *Journal of Membrane Science* **2013**, *428*, 598–607.

31) Cheryan, M. *Ultrafiltration and Microfiltration Handbook*; CRC Press, 1998.

32) Zhang, Y.; Vallin, J. R.; Sahoo, J. K.; Gao, F.; Boudouris, B. W.; Webber, M. J.; Phillip, W. A. High-Affinity Detection and Capture of Heavy Metal Contaminants Using Block Polymer Composite Membranes. *ACS Cent. Sci.* **2018**, *4*, 1697–1707.

33) Zhang, Z.; Rahman, M. M.; Abetz, C.; Höhme, A.-L.; Sperling, E.; Abetz, V. Chemically Tailored Multifunctional Asymmetric Isoporous Triblock Terpolymer Membranes for Selective Transport. *Advanced Materials* **2020**, *32*, 1907014.

34) Greenlee, L. F.; Lawler, D. F.; Freeman, B. D.; Marrot, B.; Moulin, P. Reverse Osmosis Desalination: Water Sources, Technology, and Today's Challenges. *Water Research* **2009**, *43*, 2317–2348.

35) Tchobanoglous, G.; Darby, J.; Bourgeous, K.; McArdle, J.; Genest, P.; Tylla, M. Ultrafiltration as an Advanced Tertiary Treatment Process for Municipal Wastewater. *Desalination* **1998**, *119*, 315–321.

36) *Microfiltration and Ultrafiltration Membranes for Drinking Water*; AWWA, 2016.

37) Wen, C.; Huang, X.; Qian, Y. Domestic Wastewater Treatment Using an Anaerobic Bioreactor Coupled with Membrane Filtration. *Process Biochemistry* **1999**, *35*, 335–340.

38) Urgun-Demirtas, M.; Stark, B. C.; Pagilla, K. R. Comparison of 2-Chlorobenzoic Acid Biodegradation in a Membrane Bioreactor by B. Cepacia and B. Cepacia Bearing the Bacterial Hemoglobin Gene. *Water Research* **2006**, *40*, 3123–3130.

39) Salazar-Peláez, M. L.; Morgan-Sagastume, J. M.; Noyola, A. Influence of Hydraulic Retention Time on Fouling in a UASB Coupled with an External Ultrafiltration Membrane Treating Synthetic Municipal Wastewater. *Desalination* **2011**, *277*, 164–170.

40) Cote, P.; Alam, Z.; Penny, J. Hollow Fiber Membrane Life in Membrane Bioreactors (MBR). *Desalination* **2012**, *288*, 145–151.

41) Jiang, Z.; Karan, S.; Livingston, A. G. Water Transport through Ultrathin Polyamide Nanofilms Used for Reverse Osmosis. *Advanced Materials* **2018**, *30*, 1705973.

42) Fallahianbijan, F.; Giglia, S.; Carbrello, C.; Bell, D.; Zydney, A. L. Impact of Protein Fouling on Nanoparticle Capture within the Viresolve® Pro and Viresolve® NFP Virus Removal Membranes. *Biotechnology and Bioengineering* **2019**, *116*, 2285–2291.

43) van Reis, R.; Zydney, A. Bioprocess Membrane Technology. *Journal of Membrane Science* **2007**, *297*, 16–50.

44) Wintgens, T.; Melin, T.; Schäfer, A.; Khan, S.; Muston, M.; Bixio, D.; Thoeye, C. The Role of Membrane Processes in Municipal Wastewater Reclamation and Reuse. *Desalination* **2005**, *178*, 1–11.

45) Laîné, J.-M.; Vial, D.; Moulart, P. Status after 10 Years of Operation — Overview of UF Technology Today. *Desalination* **2000**, *131*, 17–25.

46) Kimura, K.; Hane, Y.; Watanabe, Y.; Amy, G.; Ohkuma, N. Irreversible Membrane Fouling during Ultrafiltration of Surface Water. *Water Research* **2004**, *38*, 3431–3441.

47) Xiao, K.; Liang, S.; Wang, X.; Chen, C.; Huang, X. Current State and Challenges of Full-Scale Membrane Bioreactor Applications: A Critical Review. *Bioresource Technology* **2019**, *271*, 473–481. https://doi.org/10.1016/j.biortech.2018.09.061.

48) Lousada-Ferreira, M.; Geilvoet, S.; Moreau, A.; Atasoy, E.; Krzeminski, P.; van Nieuwenhuijzen, A.; van der Graaf, J. MLSS Concentration: Still a Poorly Understood Parameter in MBR Filterability. *Desalination* **2010**, *250*, 618–622.

49) Drews, A.; Kraume, M. Process Improvement by Application of Membrane Bioreactors. *Chemical Engineering Research and Design* **2005**, *83*, 276–284.

50) Budd, W. E.; Oakey, R. W. Membrane Separation in Biological-Reactor Systems. 3472765A.

51) Lesjean, B.; Huisjes, E. H. Survey of the European MBR Market: Trends and Perspectives. *Desalination* **2008**, *231*, 71–81.

52) Tang, S.; Wang, Z.; Wu, Z.; Zhou, Q. Role of Dissolved Organic Matters (DOM) in Membrane Fouling of Membrane Bioreactors for Municipal Wastewater Treatment. *Journal of Hazardous Materials* **2010**, *178*, 377–384.

53) Ping Chu, H.; Li, X. Membrane Fouling in a Membrane Bioreactor (MBR): Sludge Cake Formation and Fouling Characteristics. *Biotechnology and Bioengineering* **2005**, *90*, 323–331.

54) Kim, J.; Kim, K.; Ye, H.; Lee, E.; Shin, C.; McCarty, P. L.; Bae, J. Anaerobic Fluidized Bed Membrane Bioreactor for Wastewater Treatment. *Environ. Sci. Technol.* **2011**, *45*, 576–581.

55) Ho, J.; Sung, S. Anaerobic Membrane Bioreactor Treatment of Synthetic Municipal Wastewater at Ambient Temperature. *Water Environment Research* **2009**, *81*, 922–928.

56) Choi, J.-G.; Bae, T.-H.; Kim, J.-H.; Tak, T.-M.; Randall, A. . The Behavior of Membrane Fouling Initiation on the Crossflow Membrane Bioreactor System. *Journal of Membrane Science* **2002**, *203*, 103–113.

57) Tiraferri, A.; Yip, N. Y.; Phillip, W. A.; Schiffman, J. D.; Elimelech, M. Relating Performance of Thin-Film Composite Forward Osmosis Membranes to Support Layer Formation and Structure. *Journal of Membrane Science* **2011**, *367*, 340–352.

58) Vrijenhoek, E. M.; Hong, S.; Elimelech, M. Influence of Membrane Surface Properties on Initial Rate of Colloidal Fouling of Reverse Osmosis and Nanofiltration Membranes. *Journal of Membrane Science* **2001**, *188*, 115–128.

59) Hester, J. F.; Olugebefola, S. C.; Mayes, A. M. Preparation of pH-Responsive Polymer Membranes by Self-Organization. *Journal of Membrane Science* **2002**, *208*, 375–388.

60) Hester, J. F.; Banerjee, P.; Mayes, A. M. Preparation of Protein-Resistant Surfaces on Poly(vinylidene Fluoride) Membranes via Surface Segregation. *Macromolecules* **1999**, *32*, 1643–1650.

61) Hester, J. F.; Mayes, A. M. Design and Performance of Foul-Resistant Poly(vinylidene Fluoride) Membranes Prepared in a Single-Step by Surface Segregation. *Journal of Membrane Science* **2002**, *202*, 119–135.

62) Akthakul, A.; Salinaro, R. F.; Mayes, A. M. Antifouling Polymer Membranes with Subnanometer Size Selectivity. *Macromolecules* **2004**, *37*, 7663–7668.

63) Kaner, P.; Dudchenko, A. V.; Mauter, M. S.; Asatekin, A. Zwitterionic Copolymer Additive Architecture Affects Membrane Performance: Fouling Resistance and Surface Rearrangement in Saline Solutions. *J. Mater. Chem. A* **2019**, *7*, 4829–4846.

64) Zhao, W.; Su, Y.; Li, C.; Shi, Q.; Ning, X.; Jiang, Z. Fabrication of Antifouling Polyethersulfone Ultrafiltration Membranes Using Pluronic F127 as Both Surface Modifier and Pore-Forming Agent. *Journal of Membrane Science* **2008**, *318*, 405–412.

65) Chen, W.; Su, Y.; Peng, J.; Zhao, X.; Jiang, Z.; Dong, Y.; Zhang, Y.; Liang, Y.; Liu, J. Efficient Wastewater Treatment by Membranes through Constructing Tunable Antifouling Membrane Surfaces. *Environ. Sci. Technol.* **2011**, *45*, 6545–6552. https://doi.org/10.1021/es200994n.

66) Zhao, X.; Su, Y.; Chen, W.; Peng, J.; Jiang, Z. pH-Responsive and Fouling-Release Properties of PES Ultrafiltration Membranes Modified by Multi-Functional Block-like Copolymers. *Journal of Membrane Science* **2011**, *382*, 222–230.

67) Chen, W.; Su, Y.; Peng, J.; Dong, Y.; Zhao, X.; Jiang, Z. Engineering a Robust, Versatile Amphiphilic Membrane Surface Through Forced Surface Segregation for Ultralow Flux-Decline. *Advanced Functional Materials* **2011**, *21*, 191–198.

68) Zhao, X.; Su, Y.; Li, Y.; Zhang, R.; Zhao, J.; Jiang, Z. Engineering Amphiphilic Membrane Surfaces Based on PEO and PDMS Segments for Improved Antifouling Performances. *Journal of Membrane Science* **2014**, *450*, 111–123.

69) Bates, F.; Frederickson, G. Block Copolymer Thermodynamics: Theory and Experiments. *Annu. Rev. Phys. Chem.* **1990**, *41*, 525–557.

70) Rosedale, J. H.; Bates, F. S.; Almdal, K.; Mortensen, K.; Wignall, G. D. Order and Disorder in Symmetric Diblock Copolymer Melts. *Macromolecules* **1995**, *28*, 1429–1443.

71) Sinturel, C.; Bates, F. S.; Hillmyer, M. A. High χ–Low N Block Polymers: How Far Can We Go? *ACS Macro Lett.* **2015**, *4*, 1044–1050.

72) Schmitt, A. K.; Mahanthappa, M. K. Characteristics of Lamellar Mesophases in Strongly Segregated Broad Dispersity ABA Triblock Copolymers. *Macromolecules* **2014**, *47*, 4346–4356.

73) Widin, J. M.; Schmitt, A. K.; Im, K.; Schmitt, A. L.; Mahanthappa, M. K. Polydispersity-Induced Stabilization of a Disordered Bicontinuous Morphology in ABA Triblock Copolymers. *Macromolecules* **2010**, *43*, 7913–7915.

74) Matsen, M. W.; Bates, F. S. Conformationally Asymmetric Block Copolymers. *J. Polym. Sci. B Polym. Phys.* **1997**, *35*, 945–952.

75) Bates, F. S.; Hillmyer, M. A.; Lodge, T. P.; Bates, C. M.; Delaney, K. T.; Fredrickson, G. H. Multiblock Polymers: Panacea or Pandora's Box? *Science* **2012**, *336*, 434.

76) Lequieu, J.; Koeper, T.; Delaney, K. T.; Fredrickson, G. H. Extreme Deflection of Phase Boundaries and Chain Bridging in A(BA′)n Miktoarm Star Polymers. *Macromolecules* **2020**, *53*, 513–522.

77) Tang, P.; Qiu, F.; Zhang, H.; Yang, Y. Morphology and Phase Diagram of Complex Block Copolymers: ABC Star Triblock Copolymers. *J. Phys. Chem. B* **2004**, *108*, 8434–8438.

78) Grason, G. M.; Kamien, R. D. Interfaces in Diblocks: A Study of Miktoarm Star Copolymers. *Macromolecules* **2004**, *37*, 7371–7380.

79) Matsen, M. W. Fast and Accurate SCFT Calculations for Periodic Block-Copolymer Morphologies Using the Spectral Method with Anderson Mixing. *The European Physical Journal E* **2009**, *30*, 361.

80) Lodge, T. P. Block Copolymers: Long-Term Growth with Added Value. *Macromolecules* **2020**, *53*, 2–4.

81) Li, L.; Szewczykowski, P.; Clausen, L. D.; Hansen, K. M.; Jonsson, G. E.; Ndoni, S. Ultrafiltration by Gyroid Nanoporous Polymer Membranes. *Journal of Membrane Science* **2011**, *384*, 126–135.

82) Zhou, H.-J.; Yang, G.-W.; Zhang, Y.-Y.; Xu, Z.-K.; Wu, G.-P. Bioinspired Block Copolymer for Mineralized Nanoporous Membrane. *ACS Nano* **2018**, *12*, 11471–11480.

83) Ting, Y.-H.; Park, S.-M.; Liu, C.-C.; Liu, X.; Himpsel, F. J.; Nealey, P. F.; Wendt, A. E. Plasma Etch Removal of Poly(methyl Methacrylate) in Block Copolymer Lithography. *Journal of Vacuum Science & Technology B: Microelectronics and Nanometer Structures Processing, Measurement, and Phenomena* **2008**, *26*, 1684–1689.

84) Li, L.; Schulte, L.; Clausen, L. D.; Hansen, K. M.; Jonsson, G. E.; Ndoni, S. Gyroid Nanoporous Membranes with Tunable Permeability. *ACS Nano* **2011**, *5*, 7754–7766.

85) Schulte, L.; Grydgaard, A.; Jakobsen, M. R.; Szewczykowski, P. P.; Guo, F.; Vigild, M. E.; Berg, R. H.; Ndoni, S. Nanoporous Materials from Stable and Metastable Structures of 1,2-PB-B-PDMS Block Copolymers. *Polymer* **2011**, *52*, 422–429.

86) Vriezekolk, E. J.; Kudernac, T.; de Vos, W. M.; Nijmeijer, K. Composite Ultrafiltration Membranes with Tunable Properties Based on a Self-Assembling Block Copolymer/homopolymer System. *Journal of Polymer Science Part B: Polymer Physics* **2015**, *53*, 1546–1558.

87) Lefèvre, N.; Daoulas, K. C.; Müller, M.; Gohy, J.-F.; Fustin, C.-A. Self-Assembly in Thin Films of Mixtures of Block Copolymers and Homopolymers Interacting by Hydrogen Bonds. *Macromolecules* **2010**, *43*, 7734–7743.

88) Mao, H.; Hillmyer, M. A. Nanoporous Polystyrene by Chemical Etching of Poly(ethylene Oxide) from Ordered Block Copolymers. *Macromolecules* **2005**, *38*, 4038–4039.

89) Vidil, T.; Hampu, N.; Hillmyer, M. A. Nanoporous Thermosets with Percolating Pores from Block Polymers Chemically Fixed above the Order–Disorder Transition. *ACS Cent. Sci.* **2017**.

90) Hampu, N.; Hillmyer, M. A. Temporally Controlled Curing of Block Polymers in the Disordered State Using Thermally Stable Photoacid Generators for the Preparation of Nanoporous Membranes. *ACS Appl. Polym. Mater.* **2019**, *1*, 1148–1154.

91) Cavicchi, K. A.; Zalusky, A. S.; Hillmyer, M. A.; Lodge, T. P. An Ordered Nanoporous Monolith from an Elastomeric Crosslinked Block Copolymer Precursor. *Macromol. Rapid Commun.* **2004**, *25*, 704–709.

92) Chen, L.; Hillmyer, M. A. Mechanically and Thermally Robust Ordered Nanoporous Monoliths Using Norbornene-Functional Block Polymers. *Macromolecules* **2009**, *42*, 4237–4243.

93) Phillip, W. A.; Hillmyer, M. A.; Cussler, E. L. Cylinder Orientation Mechanism in Block Copolymer Thin Films Upon Solvent Evaporation. *Macromolecules* **2010**, *43*, 7763–7770.

94) Hamley, I. W. Ordering in Thin Films of Block Copolymers: Fundamentals to Potential Applications. *Progress in Polymer Science* **2009**, *34*, 1161–1210.

95) Fasolka, M. J.; Mayes, A. M. Block Copolymer Thin Films: Physics and Applications. *Annual Review of Materials Science* **2001**, *31*, 323–355.

96) Segalman, R. A. Patterning with Block Copolymer Thin Films. *Materials Science and Engineering: R: Reports* **2005**, *48*, 191–226.

97) Sinturel, C.; Vayer, M.; Morris, M.; Hillmyer, M. A. Solvent Vapor Annealing of Block Polymer Thin Films. *Macromolecules* **2013**, *46*, 5399–5415.

98) Baruth, A.; Seo, M.; Lin, C. H.; Walster, K.; Shankar, A.; Hillmyer, M. A.; Leighton, C. Optimization of Long-Range Order in Solvent Vapor Annealed Poly(styrene)-Block-Poly(lactide) Thin Films for Nanolithography. *ACS Appl. Mater. Interfaces* **2014**, *6*, 13770–13781.

99) Feng, X.; Tousley, M. E.; Cowan, M. G.; Wiesenauer, B. R.; Nejati, S.; Choo, Y.; Noble, R. D.; Elimelech, M.; Gin, D. L.; Osuji, C. O. Scalable Fabrication of Polymer Membranes with Vertically Aligned 1 Nm Pores by Magnetic Field Directed Self-Assembly. *ACS Nano* **2014**, *8*, 11977–11986.

100) Feng, X.; Kawabata, K.; Cowan, M. G.; Dwulet, G. E.; Toth, K.; Sixdenier, L.; Haji-Akbari, A.; Noble, R. D.; Elimelech, M.; Gin, D. L.; Osuji, C. O. Single Crystal Texture by Directed Molecular Self-Assembly along Dual Axes. *Nature Materials* **2019**, *18*, 1235–1243.

101) Gopinadhan, M.; Deshmukh, P.; Choo, Y.; Majewski, P. W.; Bakajin, O.; Elimelech, M.; Kasi, R. M.; Osuji, C. O. Thermally Switchable Aligned Nanopores by Magnetic-Field Directed Self-Assembly of Block Copolymers. *Advanced Materials* **2014**, *26*, 5148–5154.

102) Majewski, P. W.; Gopinadhan, M.; Osuji, C. O. Magnetic Field Alignment of Block Copolymers and Polymer Nanocomposites: Scalable Microstructure Control in Functional Soft Materials. *Journal of Polymer Science Part B: Polymer Physics* **2012**, *50*, 2–8.

103) Choo, Y.; Mahajan, L. H.; Gopinadhan, M.; Ndaya, D.; Deshmukh, P.; Kasi, R. M.; Osuji, C. O. Phase Behavior of Polylactide-Based Liquid Crystalline Brushlike Block Copolymers. *Macromolecules* **2015**, *48*, 8315–8322.

104) Rokhlenko, Y.; Gopinadhan, M.; Osuji, C. O.; Zhang, K.; O'Hern, C. S.; Larson, S. R.; Gopalan, P.; Majewski, P. W.; Yager, K. G. Magnetic Alignment of Block Copolymer Microdomains by Intrinsic Chain Anisotropy. *Phys. Rev. Lett.* **2015**, *115*, 258302.

105) Cochran, E. W.; Garcia-Cervera, C. J.; Fredrickson, G. H. Stability of the Gyroid Phase in Diblock Copolymers at Strong Segregation. *Macromolecules* **2006**, *39*, 2449–2451.

106) Matsen, M. W.; Bates, F. S. Origins of Complex Self-Assembly in Block Copolymers. *Macromolecules* **1996**, *29*, 7641–7644.

107) Matsen, M. W.; Schick, M. Microphase Separation in Starblock Copolymer Melts. *Macromolecules* **1994**, *27*, 6761–6767.

108) She, M.-S.; Lo, T.-Y.; Ho, R.-M. Controlled Ordering of Block Copolymer Gyroid Thin Films by Solvent Annealing. *Macromolecules* **2014**, *47*, 175–182.

109) Jung, J.; Park, H.-W.; Lee, S.; Lee, H.; Chang, T.; Matsunaga, K.; Jinnai, H. Effect of Film Thickness on the Phase Behaviors of Diblock Copolymer Thin Film. *ACS Nano* **2010**, *4*, 3109–3116.

110) Feng, X.; Imran, Q.; Zhang, Y.; Sixdenier, L.; Lu, X.; Kaufman, G.; Gabinet, U.; Kawabata, K.; Elimelech, M.; Osuji, C. O. Precise Nanofiltration in a Fouling-Resistant

Self-Assembled Membrane with Water-Continuous Transport Pathways. *Sci Adv* **2019**, *5*, eaav9308.

111) Seo, M.; Hillmyer, M. A. Reticulated Nanoporous Polymers by Controlled Polymerization-Induced Microphase Separation. *Science* **2012**, *336*, 1422.

112) Seo, M.; Moll, D.; Silvis, C.; Roy, A.; Querelle, S.; Hillmyer, M. A. Interfacial Polymerization of Reactive Block Polymers for the Preparation of Composite Ultrafiltration Membranes. *Ind. Eng. Chem. Res.* **2014**, *53*, 18575–18579.

113) Hampu, N.; Bates, M. W.; Vidil, T.; Hillmyer, M. A. Bicontinuous Porous Nanomaterials from Block Polymers Radically Cured in the Disordered State for Size-Selective Membrane Applications. *ACS Appl. Nano Mater.* **2019**.

114) Schulze, M. W.; Hillmyer, M. A. Tuning Mesoporosity in Cross-Linked Nanostructured Thermosets via Polymerization-Induced Microphase Separation. *Macromolecules* **2017**, *50*, 997–1007.

115) Saba, S. A.; Mousavi, M. P. S.; Bühlmann, P.; Hillmyer, M. A. Hierarchically Porous Polymer Monoliths by Combining Controlled Macro- and Microphase Separation. *J. Am. Chem. Soc.* **2015**, *137*, 8896–8899.

116) Oh, J.; Seo, M. Photoinitiated Polymerization-Induced Microphase Separation for the Preparation of Nanoporous Polymer Films. *ACS Macro Lett.* **2015**, *4*, 1244–1248.

117) Hampu, N.; Hillmyer, M. A. Molecular Engineering of Nanostructures in Disordered Block Polymers. *ACS Macro Lett.* **2020**, *9*, 382–388.

118) Yadav, M.; Bates, F. S.; Morse, D. C. Network Model of the Disordered Phase in Symmetric Diblock Copolymer Melts. *Phys. Rev. Lett.* **2018**, *121*, 127802.

119) Wang, Y. Nondestructive Creation of Ordered Nanopores by Selective Swelling of Block Copolymers: Toward Homoporous Membranes. *Acc. Chem. Res.* **2016**, *49*, 1401–1408.

120) Zhou, J.; Wang, Y. Selective Swelling of Block Copolymers: An Upscalable Greener Process to Ultrafiltration Membranes? *Macromolecules* **2020**, *53*, 5–17.

121) Yin, J.; Yao, X.; Liou, J.-Y.; Sun, W.; Sun, Y.-S.; Wang, Y. Membranes with Highly Ordered Straight Nanopores by Selective Swelling of Fast Perpendicularly Aligned Block Copolymers. *ACS Nano* **2013**, *7*, 9961–9974.

122) Shi, X.; Wang, X.; Wang, Y.; Wang, Y. Producing Nanoporosities in Block Copolymers within 30 S by Microwave-Boosted Selective Swelling. *Macromolecules* **2020**. *In Press*.

123) Ahn, H.; Park, S.; Kim, S.-W.; Yoo, P. J.; Ryu, D. Y.; Russell, T. P. Nanoporous Block Copolymer Membranes for Ultrafiltration: A Simple Approach to Size Tunability. *ACS Nano* **2014**, *8*, 11745–11752.

124) Yan, N.; Wang, Z.; Wang, Y. Highly Permeable Membranes Enabled by Film Formation of Block Copolymers on Water Surface. *Journal of Membrane Science* **2018**, *568*, 40–46.

125) Guo, L.; Wang, Z.; Wang, Y. Perpendicular Alignment and Selective Swelling-Induced Generation of Homopores of Polystyrene-B-poly(2-Vinylpyridine)-B-Poly(ethylene Oxide) Triblock Terpolymer. *Macromolecules* **2018**, *51*, 6248–6256.

126) Yang, H.; Guo, L.; Wang, Z.; Yan, N.; Wang, Y. Nanoporous Films with Superior Resistance to Protein Adsorption by Selective Swelling of Polystyrene-Block-Poly(ethylene Oxide). *Ind. Eng. Chem. Res.* **2016**, *55*, 8133–8140.

127) Wang, Z.; Liu, R.; Yang, H.; Wang, Y. Nanoporous Polysulfones with in Situ PEGylated Surfaces by a Simple Swelling Strategy Using Paired Solvents. *Chem. Commun.* **2017**, *53*, 9105–9108.

128) Zhong, D.; Wang, Z.; Lan, Q.; Wang, Y. Selective Swelling of Block Copolymer Ultrafiltration Membranes for Enhanced Water Permeability and Fouling Resistance. *Journal of Membrane Science* **2018**, *558*, 106–112.

129) Shi, X.; Xu, Z.; Huang, C.; Wang, Y.; Cui, Z. Selective Swelling of Electrospun Block Copolymers: From Perforated Nanofibers to High Flux and Responsive Ultrafiltration Membranes. *Macromolecules* **2018**, *51*, 2283–2292.

130) Ma, D.; Zhou, J.; Wang, Z.; Wang, Y. Block Copolymer Ultrafiltration Membranes by Spray Coating Coupled with Selective Swelling. *Journal of Membrane Science* **2020**, *598*, 117656.

131) Wang, Z.; Guo, L.; Wang, Y. Isoporous Membranes with Gradient Porosity by Selective Swelling of UV-Crosslinked Block Copolymers. *Journal of Membrane Science* **2015**, *476*, 449–456.

132) Wang, Y.; Shi, X. S. Method to Enhance the Process of Selective Swelling-Induced Pores Generation for Separation Membrane. CN110124539 A.

133) Wang, Z.; Yao, X.; Wang, Y. Swelling-Induced Mesoporous Block Copolymer Membranes with Intrinsically Active Surfaces for Size-Selective Separation. *J. Mater. Chem.* **2012**, *22*, 20542–20548.

134) Guo, L.; Wang, Y. Nanoslitting of Phase-Separated Block Copolymers by Solvent Swelling for Membranes with Ultrahigh Flux and Sharp Selectivity. *Chem. Commun.* **2014**, *50*, 12022–12025.

135) Abetz, V. Isoporous Block Copolymer Membranes. *Macromolecular Rapid Communications* **2015**, *36*, 10–22.

136) Radjabian, M.; Abetz, V. Advanced Porous Polymer Membranes from Self-Assembling Block Copolymers. *Progress in Polymer Science* **2020**, *102*, 101219.

137) Weidman, J. L.; Mulvenna, R. A.; Boudouris, B. W.; Phillip, W. A. Nanostructured Membranes from Triblock Polymer Precursors as High Capacity Copper Adsorbents. *Langmuir* **2015**, *31*, 11113–11123.

138) Zhang, Y.; Mulvenna, R. A.; Qu, S.; Boudouris, B. W.; Phillip, W. A. Block Polymer Membranes Functionalized with Nanoconfined Polyelectrolyte Brushes Achieve Sub-Nanometer Selectivity. *ACS Macro Lett.* **2017**, *6*, 726–732.

139) Weidman, J. L.; Mulvenna, R. A.; Boudouris, B. W.; Phillip, W. A. Unusually Stable Hysteresis in the pH-Response of Poly(Acrylic Acid) Brushes Confined within Nanoporous Block Polymer Thin Films. *J. Am. Chem. Soc.* **2016**, *138*, 7030–7039.

140) Mulvenna, R. A.; Weidman, J. L.; Jing, B.; Pople, J. A.; Zhu, Y.; Boudouris, B. W.; Phillip, W. A. Tunable Nanoporous Membranes with Chemically-Tailored Pore Walls from Triblock Polymer Templates. *Journal of Membrane Science* **2014**, *470*, 246–256.

141) Jung, A.; Rangou, S.; Abetz, C.; Filiz, V.; Abetz, V. Structure Formation of Integral Asymmetric Composite Membranes of Polystyrene-Block-Poly(2-Vinylpyridine) on a Nonwoven. *Macromolecular Materials and Engineering* **2012**, *297*, 790–798.

142) Schöttner, S.; Brodrecht, M.; Uhlein, E.; Dietz, C.; Breitzke, H.; Tietze, A. A.; Buntkowsky, G.; Gallei, M. Amine-Containing Block Copolymers for the Bottom-Up Preparation of Functional Porous Membranes. *Macromolecules* **2019**, *52*, 2631–2641.

143) Schöttner, S.; Schaffrath, H.-J.; Gallei, M. Poly(2-Hydroxyethyl Methacrylate)-Based Amphiphilic Block Copolymers for High Water Flux Membranes and Ceramic Templates. *Macromolecules* **2016**, *49*, 7286–7295.

144) Karunakaran, M.; Nunes, S. P.; Qiu, X.; Yu, H.; Peinemann, K.-V. Isoporous PS-B-PEO Ultrafiltration Membranes via Self-Assembly and Water-Induced Phase Separation. *Journal of Membrane Science* **2014**, *453*, 471–477.

145) Hahn, J.; Filiz, V.; Rangou, S.; Clodt, J.; Jung, A.; Buhr, K.; Abetz, C.; Abetz, V. Structure Formation of Integral-Asymmetric Membranes of Polystyrene-Block-Poly(ethylene Oxide). *Journal of Polymer Science Part B: Polymer Physics* **2013**, *51* (4), 281–290.

146) Phillip, W. A.; Dorin, R. M.; Werner, J.; Hoek, E. M. V.; Wiesner, U.; Elimelech, M. Tuning Structure and Properties of Graded Triblock Terpolymer-Based Mesoporous and Hybrid Films. *Nano Lett.* **2011**, *11*, 2892–2900.

147) Sutisna, B.; Polymeropoulos, G.; Musteata, V.; Peinemann, K.-V.; Avgeropoulos, A.; Smilgies, D.-M.; Hadjichristidis, N.; Nunes, S. P. Design of Block Copolymer Membranes Using Segregation Strength Trend Lines. *Mol. Syst. Des. Eng.* **2016**, *1* (3), 278–289.

148) Clodt, J. I.; Filiz, V.; Rangou, S.; Buhr, K.; Abetz, C.; Höche, D.; Hahn, J.; Jung, A.; Abetz, V. Double Stimuli-Responsive Isoporous Membranes via Post-Modification of

pH-Sensitive Self-Assembled Diblock Copolymer Membranes. *Advanced Functional Materials* **2013**, *23*, 731–738.

149) Höhme, C.; Filiz, V.; Abetz, C.; Georgopanos, P.; Scharnagl, N.; Abetz, V. Postfunctionalization of Nanoporous Block Copolymer Membranes via Click Reaction on Polydopamine for Liquid Phase Separation. *ACS Appl. Nano Mater.* **2018**, *1*, 3124–3136.

150) Shevate, R.; Kumar, M.; Cheng, H.; Hong, P.-Y.; Behzad, A. R.; Anjum, D.; Peinemann, K.-V. Rapid Size-Based Protein Discrimination inside Hybrid Isoporous Membranes. *ACS Appl. Mater. Interfaces* **2019**, *11*, 8507–8516.

151) Gu, Y.; Wiesner, U. Tailoring Pore Size of Graded Mesoporous Block Copolymer Membranes: Moving from Ultrafiltration toward Nanofiltration. *Macromolecules* **2015**, *48*, 6153–6159.

152) Zhang, Q.; Gu, Y.; Li, Y. M.; Beaucage, P. A.; Kao, T.; Wiesner, U. Dynamically Responsive Multifunctional Asymmetric Triblock Terpolymer Membranes with Intrinsic Binding Sites for Covalent Molecule Attachment. *Chem. Mater.* **2016**, *28*, 3870–3876.

153) Zhu, G.; Ying, Y.; Li, X.; Liu, Y.; Yang, C.; Yi, Z.; Gao, C. Isoporous Membranes with Sub-10 Nm Pores Prepared from Supramolecular Interaction Facilitated Block Copolymer Assembly and Application for Protein Separation. *Journal of Membrane Science* **2018**, *566*, 25–34.

154) Zhang, Y.; Mulvenna, R. A.; Boudouris, B. W.; Phillip, W. A. Nanomanufacturing of High-Performance Hollow Fiber Nanofiltration Membranes by Coating Uniform Block Polymer Films from Solution. *J. Mater. Chem. A* **2017**, *5*, 3358–3370.

155) Yu, H.; Qiu, X.; Moreno, N.; Ma, Z.; Calo, V. M.; Nunes, S. P.; Peinemann, K.-V. Self-Assembled Asymmetric Block Copolymer Membranes: Bridging the Gap from Ultra- to Nanofiltration. *Angewandte Chemie International Edition* **2015**, *54*, 13937–13941.

156) Marques, D. S.; Vainio, U.; Chaparro, N. M.; Calo, V. M.; Bezahd, A. R.; Pitera, J. W.; Peinemann, K.-V.; Nunes, S. P. Self-Assembly in Casting Solutions of Block Copolymer Membranes. *Soft Matter* **2013**, *9*, 5557–5564.

157) Capone, B.; Hansen, J.-P.; Coluzza, I. Competing Micellar and Cylindrical Phases in Semi-Dilute Diblock Copolymer Solutions. *Soft Matter* **2010**, *6*, 6075–6078.

158) Oss-Ronen, L.; Schmidt, J.; Abetz, V.; Radulescu, A.; Cohen, Y.; Talmon, Y. Characterization of Block Copolymer Self-Assembly: From Solution to Nanoporous Membranes. *Macromolecules* **2012**, *45*, 9631–9642.

159) Radjabian, M.; Abetz, C.; Fischer, B.; Meyer, A.; Abetz, V. Influence of Solvent on the Structure of an Amphiphilic Block Copolymer in Solution and in Formation of an Integral Asymmetric Membrane. *ACS Appl. Mater. Interfaces* **2017**, *9*, 31224–31234.

160) Dreyer, O.; Wu, M.-L.; Radjabian, M.; Abetz, C.; Abetz, V. Structure of Nonsolvent-Quenched Block Copolymer Solutions after Exposure to Electric Fields during Solvent Evaporation. *Advanced Materials Interfaces* **2019**, *6*, 1900646.

161) Hahn, J.; Clodt, J. I.; Filiz, V.; Abetz, V. Protein Separation Performance of Self-Assembled Block Copolymer Membranes. *RSC Adv.* **2014**, *4*, 10252–10260.

162) Dorin, R. M.; Marques, D. S.; Sai, H.; Vainio, U.; Phillip, W. A.; Peinemann, K.-V.; Nunes, S. P.; Wiesner, U. Solution Small-Angle X-Ray Scattering as a Screening and Predictive Tool in the Fabrication of Asymmetric Block Copolymer Membranes. *ACS Macro Lett.* **2012**, *1*, 614–617.

163) Marques, D. S.; Dorin, R. M.; Wiesner, U.; Smilgies, D.-M.; Behzad, A. R.; Vainio, U.; Peinemann, K.-V.; Nunes, S. P. Time-Resolved GISAXS and Cryo-Microscopy Characterization of Block Copolymer Membrane Formation. *Polymer* **2014**, *55*, 1327–1332. https://doi.org/10.1016/j.polymer.2013.11.010.

164) Stegelmeier, C.; Filiz, V.; Abetz, V.; Perlich, J.; Fery, A.; Ruckdeschel, P.; Rosenfeldt, S.; Förster, S. Topological Paths and Transient Morphologies during Formation of Mesoporous Block Copolymer Membranes. *Macromolecules* **2014**, *47*, 5566–5577.

165) Sundaramoorthi, G.; Hadwiger, M.; Ben-Romdhane, M.; Behzad, A. R.; Madhavan, P.; Nunes, S. P. 3D Membrane Imaging and Porosity Visualization. *Ind. Eng. Chem. Res.* **2016**, *55*, 3689–3695.

166) Dorin, R. M.; Phillip, W. A.; Sai, H.; Werner, J.; Elimelech, M.; Wiesner, U. Designing Block Copolymer Architectures for Targeted Membrane Performance. *Polymer* **2014**, *55*, 347–353.

167) Zhang, Q.; Li, Y. M.; Gu, Y.; Dorin, R. M.; Wiesner, U. Tuning Substructure and Properties of Supported Asymmetric Triblock Terpolymer Membranes. *Polymer* **2016**, *107*, 398–405.

168) Pendergast, M. M.; Mika Dorin, R.; Phillip, W. A.; Wiesner, U.; Hoek, E. M. V. Understanding the Structure and Performance of Self-Assembled Triblock Terpolymer Membranes. *Journal of Membrane Science* **2013**, *444*, 461–468.

169) Sutisna, B.; Polymeropoulos, G.; Musteata, V.; Sougrat, R.; Smilgies, D.-M.; Peinemann, K.-V.; Hadjichristidis, N.; Nunes, S. P. Functionalized Nanochannels from Self-Assembled and Photomodified Poly(Styrene-B-Butadiene-B-Styrene). *Small* **2018**, *14*, 1701885.

170) Hahn, J.; Clodt, J. I.; Abetz, C.; Filiz, V.; Abetz, V. Thin Isoporous Block Copolymer Membranes: It Is All about the Process. *ACS Appl. Mater. Interfaces* **2015**, *7*, 21130–21137.

171) Bucher, T.; Filiz, V.; Abetz, C.; Abetz, V. Formation of Thin, Isoporous Block Copolymer Membranes by an Upscalable Profile Roller Coating Process—A Promising Way to Save Block Copolymer. *Membranes* **2018**, *8*.

172) Hilke, R.; Pradeep, N.; Behzad, A. R.; Nunes, S. P.; Peinemann, K.-V. Block Copolymer/homopolymer Dual-Layer Hollow Fiber Membranes. *Journal of Membrane Science* **2014**, *472*, 39–44.

173) Liu, Y.; Liu, T.; Su, Y.; Yuan, H.; Hayakawa, T.; Wang, X. Fabrication of a Novel PS4VP/PVDF Dual-Layer Hollow Fiber Ultrafiltration Membrane. *Journal of Membrane Science* **2016**, *506*, 1–10.

174) Radjabian, M.; Koll, J.; Buhr, K.; Vainio, U.; Abetz, C.; Handge, U. A.; Abetz, V. Tailoring the Morphology of Self-Assembled Block Copolymer Hollow Fiber Membranes. *Polymer* **2014**, *55*, 2986–2997.

175) Radjabian, M.; Koll, J.; Buhr, K.; Handge, U. A.; Abetz, V. Hollow Fiber Spinning of Block Copolymers: Influence of Spinning Conditions on Morphological Properties. *Polymer* **2013**, *54*, 1803–1812.

176) Hilke, R.; Pradeep, N.; Madhavan, P.; Vainio, U.; Behzad, A. R.; Sougrat, R.; Nunes, S. P.; Peinemann, K.-V. Block Copolymer Hollow Fiber Membranes with Catalytic Activity and pH-Response. *ACS Appl. Mater. Interfaces* **2013**, *5*, 7001–7006.

177) Sankhala, K.; Koll, J.; Radjabian, M.; Handge, U. A.; Abetz, V. A Pathway to Fabricate Hollow Fiber Membranes with Isoporous Inner Surface. *Advanced Materials Interfaces* **2017**, *4*, 1600991.

178) Werber, J. R.; Porter, C. J.; Elimelech, M. A Path to Ultraselectivity: Support Layer Properties To Maximize Performance of Biomimetic Desalination Membranes. *Environ. Sci. Technol.* **2018**, *52*, 10737–10747.

179) Henis, J. M. S.; Tripodi, M. K. Composite Hollow Fiber Membranes for Gas Separation: The Resistance Model Approach. *Journal of Membrane Science* **1981**, *8*, 233–246.

180) Rangou, S.; Buhr, K.; Filiz, V.; Clodt, J. I.; Lademann, B.; Hahn, J.; Jung, A.; Abetz, V. Self-Organized Isoporous Membranes with Tailored Pore Sizes. *Journal of Membrane Science* **2014**, *451*, 266–275.

181) Wang, J.; Rahman, M. M.; Abetz, C.; Abetz, V. Bovine Serum Albumin Selective Integral Asymmetric Isoporous Membrane. *Journal of Membrane Science* **2020**, *604*, 118074.

182) Nunes, S. P.; Sougrat, R.; Hooghan, B.; Anjum, D. H.; Behzad, A. R.; Zhao, L.; Pradeep, N.; Pinnau, I.; Vainio, U.; Peinemann, K.-V. Ultraporous Films with Uniform Nanochannels by Block Copolymer Micelles Assembly. *Macromolecules* **2010**, *43*, 8079–8085.

183) Feng, X.; Burke, C. J.; Zhuo, M.; Guo, H.; Yang, K.; Reddy, A.; Prasad, I.; Ho, R.-M.; Avgeropoulos, A.; Grason, G. M.; Thomas, E. L. Seeing Mesoatomic Distortions in Soft-Matter Crystals of a Double-Gyroid Block Copolymer. *Nature* **2019**, *575*, 175–179.

184) Parent, L. R.; Bakalis, E.; Proetto, M.; Li, Y.; Park, C.; Zerbetto, F.; Gianneschi, N. C. Tackling the Challenges of Dynamic Experiments Using Liquid-Cell Transmission Electron Microscopy. *Acc. Chem. Res.* **2018**, *51*, 3–11.

185) Timachova, K.; Sethi, G. K.; Bhattacharya, R.; Villaluenga, I.; Balsara, N. P. Ion Diffusion across a Disorder-to-Order Phase Transition in a Poly(ethylene Oxide)-B-Poly(silsesquioxane) Block Copolymer Electrolyte. *Mol. Syst. Des. Eng.* **2019**, *4*, 357–364.

186) Howard, M. P.; Lequieu, J.; Delaney, K. T.; Ganesan, V.; Fredrickson, G. H.; Truskett, T. M. Connecting Solute Diffusion to Morphology in Triblock Copolymer Membranes. *Macromolecules* **2020**. *In Press*.

187) Wang, C.; Quan, X.; Liao, M.; Li, L.; Zhou, J. Computer Simulations on the Channel Membrane Formation by Nonsolvent Induced Phase Separation. *Macromolecular Theory and Simulations* **2017**, *26*, 1700027.

188) Bohonak, D. M.; Zydney, A. L. Compaction and Permeability Effects with Virus Filtration Membranes. *Journal of Membrane Science* **2005**, *254*, 71–79.

189) Persson, K. M.; Gekas, V.; Trägårdh, G. Study of Membrane Compaction and Its Influence on Ultrafiltration Water Permeability. *Journal of Membrane Science* **1995**, *100*, 155–162.

190) Lorain, O.; Espenan, J.-M.; Remigy, J.-F.; Rouch, J.-C.; Savart, T.; Gerard, P.; Magnet, S. Copolymer Having Amphiphilic Blocks, and Use Thereof for Manufacturing Polymer Filtration Membranes. US20160030896A1.

191) Shevate, R.; Karunakaran, M.; Kumar, M.; Peinemann, K.-V. Polyanionic pH-Responsive Polystyrene-B-poly(4-Vinyl Pyridine-N-Oxide) Isoporous Membranes. *Journal of Membrane Science* **2016**, *501*, 161–168.

192) Bailey, T. S.; Rzayev, J.; Hillmyer, M. A. Routes to Alkene and Epoxide Functionalized Nanoporous Materials from Poly(styrene-B-Isoprene-B-Lactide) Triblock Copolymers. *Macromolecules* **2006**, *39*, 8772–8781.

193) Mao, H.; Hillmyer, M. A. Morphological Behavior of Polystyrene-Block-Polylactide/Polystyrene-Block-Poly(ethylene Oxide) Blends. *Macromol. Chem. Phys.* **2008**, *209*, 1647–1656.

Chapter 3. Experimental Techniques and Data Processing

Based on its critical relevance to the work described throughout this thesis, this chapter (Chapter 3) details the experimental techniques, data processing, and data interpretation that is used throughout. These methods are included to aid interested readers in the reproduction of certain experiments. This chapter will first describe the synthetic methods used for the polymers examined in this thesis, providing representative examples and directing the reader to the pertinent chapters where these polymers are discussed in detail. Next, the various cross-linking and quenching strategies used to kinetically trap the fluctuating disordered state for the block polymers that are analyzed in Chapters 4 – 8 will be described. Then the membranes fabrication strategies employed to achieve the technological objectives outlined in Chapter 2 are discussed. These methods were used in Chapters 4, 5, and 8. Finally, the characterization techniques and data analyses used throughout the thesis are described.

3.1 Polymerization Methods

3.1.1 Synthesis of P(S-*s*-B)-OH

The anionic copolymerization of styrene and butadiene was performed in a custom-made 1 L glass reactor with 5 ACE-threaded ports and Teflon-coated stir bar. A description of the equipment employed in anionic synthesis is provided elsewhere.[1,2] Synthesis of the P(S-*s*-B)-OH was performed using a modified procedure to end-cap with a hydroxyl group, employing potassium *tert*-butoxide (KOtBu, 1.0 M in THF) at a molar ratio of 0.05 relative to the initiator to facilitate statistical copolymerization of the two monomers.[3,4] The addition of KOtBu to the reactor was followed by the removal of THF under dynamic

vacuum, and the contents of the reactor were dried overnight. Cyclohexane was then added and followed by the addition of *sec*-butyllithium (1.4 M in cyclohexane). The solution was heated to 40 °C and stirred for 15 min prior to the addition of styrene and butadiene monomer, which were added in concert. The polymerization proceeded for 8 h followed by the addition of 10 molar equivalents of ethylene oxide. After 10 h, the reaction was quenched with the addition of acidic methanol. The product, P(S-*s*-B)-OH, was twice precipitated in a 10-fold volume excess of methanol, filtered, and dried under reduced pressure. A representative ^{1}H NMR spectrum is presented in Figure 4.2. This polymer is further analyzed in Chapter 4.

3.1.2 Synthesis of P(S-*s*-B)-*b*-PLA

The polymerization of (±)-lactide proceeded via initiation from the hydroxyl functionality of P(S-*s*-B)-OH in the presence of DBU catalyst.[5] In a representative synthesis, (±)-lactide (2.5 g, 17.4 mmol, 30 eq.) and P(S-*s*-B)-OH (2.5 g, 0.58 mmol, 1 eq.) were added to a pressure vessel equipped with a stir bar and dissolved in DCM (40 mL) under the nitrogen atmosphere of a glovebox. The reaction mixture was stirred for approximately 20 min. The organocatalyst DBU (0.088 g, 0.58 mmol, 1 eq.) was subsequently added using a microsyringe, and the pressure vessel was hermetically sealed using a threaded PTFE bushing and Viton O-ring. After stirring the reaction for 20 min at room temperature, the solution was exposed to air and the reaction quenched by the addition of benzoic acid (0.18 g, 1.45 mmol, 2.5 eq.). The product P(S-*s*-B)-*b*-PLA was precipitated into methanol, filtered, and dried overnight at room temperature under reduced pressure (4.25 g, 85 %

yield). A representative ^{1}H NMR is presented in Figure 4.5. These diblock polymers are extensively studied in Chapter 4.

3.1.3 Synthesis of PLA-CTA

The trithiocarbonate terminated PLAs (PLA-CTA) were prepared in a nitrogen filled glovebox by using 4-cyano-4-[(dodecylsulfanylthiocarbonyl) sulfanyl]pentanol as an initiator and DBU as a catalyst.[6–8] In a N_2 filled glovebox, ±-lactide (10.0 g, 125 molar eq.) and DCM (60 mL) are mixed in a 100 mL pressure vessel. In a separate vial, 4-cyano-4-[(dodecylsulfanylthiocarbonyl) sulfanyl]pentanol (0.22 g, 1 mol. eq.) was dissolved in DCM (5 mL). After the ±-lactide was completely dissolved, the CTA solution was added to the pressure vessel and the mixture was stirred for several minutes to ensure homogenization. The catalyst DBU (0.083 mL, 1 mol. eq.) was added to the solution and the pressure vessel was hermetically sealed. The reaction was removed from the glovebox and stirred at room temperature for 20 minutes. The polymerization was then terminated by exposing the reaction to air and adding benzoic acid (0.17 g, 2.5 mol. eq.). The solution was added dropwise to excess methanol to precipitate the solid polymer, filtered to isolate the product, and dried overnight under reduced pressure at room temperature. The overall yield was 9.3 g. A representative ^{1}H NMR spectrum is presented in Figure 5.5. This reaction was used to synthesize the polymers examined in Chapters 5 – 8.

3.1.4 Synthesis of P(S-*s*-GMA)-*b*-PLA

The P(S-*s*-GMA) block was synthesized via a RAFT copolymerization of S and GMA in bulk using PLA-CTA as a macro-CTA.[6,7] A detailed description of the P(S-*s*-GMA)-14-

PLA-18-XS-29 synthesis is provided here. PLA-CTA (18 kg mol^{-1}, 2.5 g, 0.143 mmol, 1 eq.) was dissolved in a monomer mixture of S (4.19 g, 40.3 mmol, 282 eq.) and GMA (1.62 g, 11.4 mmol, 80 eq.) in a 100 mL round bottom flask equipped with a septum. After the PLA-CTA was completely dissolved, the free radical initiator AIBN (5.9 mg, 35.7 μmol, 0.25 eq., 0.34 mL as a 2 wt % solution in toluene) was introduced via a microsyringe. The mixture was then sealed and sparged with Ar gas for approximately 20 minutes before immersing the vial in a pre-heated silicone oil bath set to 70 ˚C. The polymerization was run to approximately 40 % conversion of GMA (typically about 5 h) and the reaction was terminated by exposure to air. The polymer was then diluted in THF, precipitated in methanol, and dried overnight under reduced pressure at 100 ˚C. A representative ^{1}H NMR spectrum is presented in Figure 5.6. Similar diblock polymers were investigated in Chapters 5 and 7.

3.1.5 Synthesis of P(MMA-*s*-S)-*b*-PLA

The P(MMA-*s*-S) block was synthesized via a RAFT copolymerization of S and MMA in bulk using PLA-CTA as a macro-CTA.[8] PLA-CTA was synthesized following the protocol outlined in section 3.1.3. A detailed description of the P(MMA-*s*-S)-23-PLA-24-XS-27 synthesis is provided here. PLA-CTA (24 kg mol^{-1}, 0.25 g, 0.017 mmol, 1 eq.) was dissolved in a monomer mixture of S (0.09 g, 0.88 mmol, 53 eq.) and MMA (0.35 g, 3.5 mmol, 212 eq.) in a 2 dram vial equipped with a septum. After the PLA-CTA was completely dissolved, the free radical initiator AIBN (0.7 mg, 4.2 μmol, 0.25 eq., 34 μL as a 2 wt % solution in toluene) was introduced via a microsyringe. The mixture was then

sealed and sparged with Ar gas for approximately 20 minutes before immersing the vial in a pre-heated silicone oil bath set to 80 ˚C. The polymerization was run to approximately 40 % conversion of MMA (typically 4 to 5 h) and the reaction was terminated by exposure to air. The polymer was then diluted in THF, precipitated in methanol, and dried overnight under reduced pressure at 100 ˚C. A representative ^{1}H NMR spectrum is presented in Figure 6.4. Similar diblock polymers were used in Chapters 6 and 8.

3.2 Cross-linking and Quenching Methods

3.2.1 Preparation of Cross-linkable films

To prepare cross-linkable block polymer films, the block polymer and cross-linking agent were co-dissolved in THF at a concentration of 0.25 g/mL. After dissolution and homogenization, the solution was poured into a silicone mold. Solvent was slowly evaporated overnight under ambient temperature and pressure. The film was then dried overnight at 100 °C under reduced pressure. This technique was used to cast monolithic films in all subsequent chapters

3.2.2 Radical Cross-linking of P(S-*s*-B)-*b*-PLA

To cure the sample, a dry monolithic film of P(S-*s*-B)-*b*-PLA and peroxide was transferred to the convection oven of an ARES rheometer equipped with a parallel plate geometry covered using a Teflon sheet. The convection oven was pre-heated to the desired cure temperature (T_{cure}) under a nitrogen atmosphere prior to sample loading to minimize sub-T_{cure} cross-linking. Cure times (t_{cure}) were chosen based on the calculated $t_{1/2}$ for DCP and BPO at the desired cure temperature such that $t_{cure} > 8t_{1/2}$ to ensure near quantitative

dissociation of the peroxide (>99.6% conversion). Values for $t_{1/2}$ were calculated using the expressions:

$$k = Ae^{-E_a/RT} \quad \text{(Equation 1)}$$

$$t_{1/2} = \frac{ln2}{k} \quad \text{(Equation 2)}$$

where A and E_a is 7.47×10^{15} s^{-1} and 153.79 kJ mol^{-1}, respectively, for DCP (0.2 M in decane).[9] It should be noted that the necessary cure times for DCP are impractical for temperatures below 115 °C (ca. > 1 week). To probe low temperature phenomena, BPO (A = 6.94×10^{13} s^{-1}, E_a = 122.35 kJ mol^{-1} for 0.2 M BPO in benzene) was used as a cross-linking agent.[9] The application of these curing protocols is described in detail in Chapter 4.

3.2.3 Photocuring of P(S-*s*-GMA)-*b*-PLA

UV curing experiments were performed using a UVP Blak-Ray B-100AP lamp equipped with a 100 W longwave (365 nm) bulb. The lamp is rated to provide an intensity of approximately 8,900 μW/cm^2 at a distance of 10 inches from the target, which is reasonably close to the experimental set-up used here. The lamp was positioned so that it pointed directly onto the surface of a hot plate pre-heated to the desired curing temperature. Prior to irradiating, the sample was loaded into a glass vial, sealed with a rubber septum, and sparged with inert gas for 10 minutes.[10,11] The sample was then placed on the hot plate, allowed to reach thermal equilibrium after several minutes, and subsequently irradiated. The application of these curing protocols is described in detail in Chapter 5.

3.2.4 Quenching of P(MMA-*s*-S)-*b*-PLA

Samples were initially annealed overnight under reduced pressure at 100 °C. Vitrification of disordered block polymers was achieved by first annealing the block polymer at a temperature above its T_{ODT} (180 °C) in the forced convection oven of a Rheometrics ARES mechanical spectrometer for 1 h. Quenched samples were obtained by removing the sample from the oven and immediately submerging it in liquid nitrogen to kinetically trap the morphology associated with that temperature. Other samples were cooled at a pre-defined and controlled rate to a temperature below T_g using the oven of the rheometer. Care was taken to ensure that the sample was not subjected to shear during the experiment. These vitrification protocols are used in Chapters 6 and 8.

3.2.5 Thermal Cross-linking of P(S-*s*-GMA)-*b*-PLA

The P(S-*s*-GMA)-*b*-PLA + 0.3 wt.% BTPH film was formed into a circular disc prior to curing. For samples that were cross-linked without shear, the disc was placed in a rheometer that was pre-heated to the desired curing temperature. The oven was sealed, and the sample was cured without applying shear.

For samples that were cross-linked under shear, the polymer was loaded into the rheometer at 130 °C and molded to the plates. The sample was then rapidly heated to the desired curing temperature. Once thermal equilibrium was reached at the curing temperature, oscillatory shear was applied. Isothermal time sweeps were obtained to measure the progression of the cross-linking reaction and to monitor the rheological properties of the

cross-linked network. The application of these curing protocols is described in detail in Chapter 7.

3.3 PLA Etching

Cross-linked monolithic films were etched via immersion in 2.0 M NaOH solution (60/40 methanol/water (v/v)) at room temperature for 1 day.[12] Etched samples were thoroughly washed with water and methanol, filtered, and dried at room temperature overnight under reduced pressure. This process was used to generate porous materials for the research described in all subsequent chapters.

3.4 Membrane Casting

3.4.1 Spin Coating Directly onto a Porous Substrate

A polyethersulfone (PES) support membrane (obtained from Sterlitech, 100 nm average pore size, 47 mm diameter) was immersed in water for 1 min to backfill the pores. The wetted support was then placed onto a glass plate mounted on the chuck of a spin coater. A solution containing 2 wt. % block polymer + cross-linking agent in chlorobenzene was then deposited on the PES support and spin coated at 1500 rpm for 1 min.[13] The composite membrane was dried for 1 h at 80 °C and cured. These procedures were used to fabricate the membranes described in Chapters 4 and 5.

3.4.2 Co-casting Dual Layer Membranes

An approximately 6 cm by 6 cm square of a non-woven polyester support was cut from a larger sheet using scissors. This piece was then mounted on top of a 7.5 cm by 7.5 cm

square glass plate and secured using electrical tape. Care was taken to ensure that the polyester support remained flat against the glass plate to prevent bubble and hole formation during membrane casting. The glass plate was then placed on top of a spin coater and secured by pulling vacuum. The polyester film was pre-wet with a small amount of DMF (approximately 0.1 mL) to promote spreading of the PSF solution across the support and to prevent defect formation.[14] The PSF support layer solution (approximately 1 mL) was dropped onto the center of the static polyester film. The film was accelerated at a rate of 500 rpm s^{-1} and spin coated at 500 rpm for 5 s using a Brewer Science Cee 200 spin coater. Immediately following the completion of the process, the block polymer selective layer solution was filtered through a 0.22 μm syringe and dropped in the center of the DMF-swollen PSF layer in a static dispense. the film was accelerated at a rate of 500 rpm s^{-1} and spin coated at 500 rpm for 5 s. Following both coating steps, liquid was observed on the walls of the spin coater, suggesting that solvent was lost by viscous flow (i.e. "spin off").

Following the completion of both spin coating steps, two liquid layers should be present: a denser and more viscous PSF layer swollen in DMF on the bottom and a less viscous P(MMA-*s*-S)-*b*-PLA layer swollen in THF on the top. Two different thermal processing methods were then examined to generate the final membrane. In the thermally annealed system, the film was moved to a pre-heated hot plate set to 150 °C for 10 s to ensure complete THF removal and then immersed in an ice water coagulation bath to precipitate the PSF support layer by NIPS and vitrify the P(MMA-*s*-S)-*b*-PLA selective layer. In the as-cast system, the film sat for 10 s at room temperature before immersing in the ice water coagulation bath. These procedures were used to cast the membranes studied in Chapter 8.

3.5 Characterization Methods

This section describes the experimental protocols used to characterize the polymers and membranes analyzed in all subsequent sections. A detailed description of each experimental method is described here for reference.

^{1}H NMR Spectroscopy

^{1}H NMR spectroscopy experiments were performed on a Bruker Avance III HD nanobay AX-400 spectrometer equipped with a 5mm BBO SmartProbe and a SampleXpress autosampler. Spectra of the polymers were acquired in $CDCl_3$ using tetramethylsilane as a reference.

SEC

SEC analysis was performed in tetrahydrofuran at 25 °C using an Agilent 1260 Infinity liquid chromatograph system equipped with three Waters Styragel columns in series, as well as a Wyatt DAWN Heleos II 18-angle laser light scattering detector S4 and a Wyatt OPTILAB T-rEX refractive index detector.

DSC

Differential scanning calorimetry (DSC) analyses were performed on a TA Instruments Discovery DSC using standard aluminum T-zero pans with hermetic lids. Scans were conducted under a nitrogen atmosphere at a rate of 20 °C min^{-1}. Glass transition

temperatures (T_g) were determined using the final heating ramp typically within the temperature range of 0–200 °C.

Dynamic mechanical analysis (DMA)

The low frequency rheological response of each SBL block polymer was evaluated on a Rheometrics ARES mechanical spectrometer equipped with an 8 or 25 mm parallel plate geometry. The oven was operated under a nitrogen atmosphere to prevent thermal degradation of the sample. The order-disorder transition temperature (T_{ODT}) of each block polymer was determined from a linear dynamic temperature sweep acquired at a heating rate of 2 °C min^{-1} with an applied angular frequency (ω) of 1 rad s^{-1} and a shear strain (γ) within the linear viscoelastic regime ($\gamma \approx 1–5\%$). A precipitous drop in the storage modulus (G') indicated the transition of the ordered microstructure to a disordered state.[15–17] Frequency sweeps were performed below T_{ODT} with a shear strain of 1 % for frequencies from 0.01 to 100 rad s^{-1}, and the frequency dependence of G' was extracted by fitting a power law to the low frequency data (typically 0.01 to 0.1 rad s^{-1}), $G' \sim \omega^n$.[18]

SAXS

SAXS profiles were collected at the Advanced Photon Source (APS) at Argonne National Laboratories using the Sector 5-ID-D beamline, which is maintained by the DuPont-Northwestern-Dow Collaborative Access Team. Scattering experiments were performed using X-rays of wavelength 0.76 Å and the scattering intensity was collected on a 2D Mar CCD detector. Sample-to-detector distances were calibrated using a silver behenate standard. Intensity as a function of the wave vector, q, where $q = (4\pi/\lambda) \sin(\theta/2)$ (θ is the

scattering angle and λ is the X-ray wavelength), was obtained by azimuthally integrating the 2D patterns. For the cross-linked and quenched samples, SAXS profiles were collected at room temperature by directly using a monolith of the materials. For the measurement of the T_{ODT}, samples were hermetically sealed in T-zero DSC pans (TA Instruments). DSC pans were mounted in a Linkam heating stage for variable temperature control. Samples were equilibrated for at least 2 min at each temperature prior to data collection. 2D scattering patterns were analyzed using the software Datasqueeze.

SEM

SEM micrographs were obtained on a Hitachi SU8230 cold FEG-SEM with an accelerating voltage of 3 kV, an upper secondary electron detector, and a lateral resolution of 1.1 nm at a working distance of 5 mm. Before imaging, samples were coated with approximately 2 nm of Ir via sputtering using an ACE600 coater.

N_2 Sorption

The nitrogen adsorption isotherm was obtained on a Quantachrome Autosorb iQ (Boynton Beach, FL) at the temperature of liquid nitrogen (77.3 K). The sample was loaded in 6 mm stems and degassed for 20 h at room temperature before measurement using a turbomolecular pump. The BET specific surface area was obtained from the adsorption branch from P/P_0 = 0.05-0.35. The mesopore size distribution was estimated using a quenched solid density functional theory (QSDFT) kernel for the adsorption branch of nitrogen on carbon using a cylindrical pore model.[19]

Water Flux Measurements

A 2.5 cm diameter disc of the etched UF membrane was loaded into an Amicon 8010 stirred cell. The cell was pressurized using N_2 gas to induce water flow through the membrane. The permeate was collected in a glass vessel placed on top of a mass balance that was interfaced to a computer.[13,20,21] Water flux was measured based on the change in the mass of permeated water over the experimental time scale. Three different pressure differences were applied to the cell (0.25, 0.5, and 1 bar) to determine the relationship between applied pressure and water flux. Water permeability was calculated based on the slope of a linear fit to the water flux vs. applied pressure data.

Dextran Rejection Measurements

Size rejection experiments were performed using fluorescently labeled dextran standards of varying molar masses. Each dextran standard was dissolved in deionized water to a concentration of 0.5 mg cm^{-3} to form separate solutions. The solution was then added to the dry Amicon 8010 stirred cell containing the dual layer membrane, stirred at 500 rpm, and pressurized to 0.5 bar. The permeate was collected in a clean glass vial. Rejection was determined using UV-Vis spectroscopy based on the ratio of the absorbance of the permeate solution to the absorbance of the feed solution at the wavelength corresponding to maximum absorbance.[13] This experimental protocol was repeated for every dextran molar mass to generate a rejection curve.

3.6 References

1) Hillmyer, M. A.; Bates, F. S. Synthesis and Characterization of Model Polyalkane−Poly(ethylene Oxide) Block Copolymers. *Macromolecules* **1996**, *29*, 6994–7002.

2) Wolf, J. H.; Hillmyer, M. A. Ordered Nanoporous Poly(cyclohexylethylene). *Langmuir* **2003**, *19*, 6553–6560.

3) Sardelis, K.; Michels, H. J.; Allen, J. Graded Block and Randomized Copolymers of butadienHtyrene. *Polymer* **1984**, *25*, 1011–1019.

4) Xu, J.; Mittal, V.; Bates, F. S. Toughened Isotactic Polypropylene: Phase Behavior and Mechanical Properties of Blends with Strategically Designed Random Copolymer Modifiers. *Macromolecules* **2016**, *49*, 6497–6506.

5) Touris, A.; Chanpuriya, S.; Hillmyer, M. A.; Bates, F. S. Synthetic Strategies for the Generation of ABCA' Type Asymmetric Tetrablock Terpolymers. *Polym. Chem.* **2014**, *5*, 5551–5559.

6) Vidil, T.; Hampu, N.; Hillmyer, M. A. Nanoporous Thermosets with Percolating Pores from Block Polymers Chemically Fixed above the Order–Disorder Transition. *ACS Cent. Sci.* **2017**, *3*, 1114-1120.

7) Hampu, N.; Hillmyer, M. A. Temporally Controlled Curing of Block Polymers in the Disordered State Using Thermally Stable Photoacid Generators for the Preparation of Nanoporous Membranes. *ACS Appl. Polym. Mater.* **2019**, *1*, 1148–1154.

8) Hampu, N.; Hillmyer, M. A. Molecular Engineering of Nanostructures in Disordered Block Polymers. *ACS Macro Lett.* **2020**, *9*, 382–388.

9) Akiba, M.; Hashim, A. S. Vulcanization and Crosslinking in Elastomers. *Progress in Polymer Science* **1997**, *22*, 475–521.

10) Scalfani, V. F.; Bailey, T. S. Access to Nanostructured Hydrogel Networks through Photocured Body-Centered Cubic Block Copolymer Melts. *Macromolecules* **2011**, *44*, 6557–6567.

11) Scalfani, V. F.; Bailey, T. S. Thermally Stable Photocuring Chemistry for Selective Morphological Trapping in Block Copolymer Melt Systems. *Chem. Mater.* **2010**, *22*, 5992–6000.

12) Zeng, D.; Ribbe, A.; Hayward, R. C. Anisotropic and Interconnected Nanoporous Materials from Randomly End-Linked Copolymer Networks. *Macromolecules* **2017**, *50*, 4668–4676.

13) Jackson, E. A.; Lee, Y.; Hillmyer, M. A. ABAC Tetrablock Terpolymers for Tough Nanoporous Filtration Membranes. *Macromolecules* **2013**, *46*, 1484–1491.

14) Tiraferri, A.; Yip, N. Y.; Phillip, W. A.; Schiffman, J. D.; Elimelech, M. Relating Performance of Thin-Film Composite Forward Osmosis Membranes to Support Layer Formation and Structure. *Journal of Membrane Science* **2011**, *367*, 340–352.

15) Rosedale, J. H.; Bates, F. S. Rheology of Ordered and Disordered Symmetric Poly(ethylenepropylene)-Poly(ethylethylene) Diblock Copolymers. *Macromolecules* **1990**, *23*, 2329–2338.

16) Bates, F. S.; Rosedale, J. H.; Fredrickson, G. H. Fluctuation Effects in a Symmetric Diblock Copolymer near the Order–disorder Transition. *The Journal of Chemical Physics* **1990**, *92*, 6255–6270.

17) Bates, F. S. Block Copolymers near the Microphase Separation Transition. 2. Linear Dynamic Mechanical Properties. *Macromolecules* **1984**, *17*, 2607–2613.

18) Kossuth, M. B.; Morse, D. C.; Bates, F. S. Viscoelastic Behavior of Cubic Phases in Block Copolymer Melts. *Journal of Rheology* **1998**, *43*, 167–196.

19) Gor, G. Y.; Thommes, M.; Cychosz, K. A.; Neimark, A. V. Quenched Solid Density Functional Theory Method for Characterization of Mesoporous Carbons by Nitrogen Adsorption. *Carbon* **2012**, *50*, 1583–1590. https://doi.org/10.1016/j.carbon.2011.11.037.

20) Phillip, W. A.; O'Neill, B.; Rodwogin, M.; Hillmyer, M. A.; Cussler, E. L. Self-Assembled Block Copolymer Thin Films as Water Filtration Membranes. *ACS Appl. Mater. Interfaces* **2010**, *2*, 847–853.

21) Querelle, S. E.; Jackson, E. A.; Cussler, E. L.; Hillmyer, M. A. Ultrafiltration Membranes with a Thin Poly(styrene)-B-Poly(isoprene) Selective Layer. *ACS Appl. Mater. Interfaces* **2013**, *5*, 5044–5050.

Chapter 4. Bicontinuous Porous Nanomaterials from Block Polymers Radically Cured in the Disordered State for Size-Selective Membrane Applications[2]

4.1 Introduction

Nanoscale structural co-continuity is a key material feature expected to present new engineering opportunities in emerging technologies across medicine, energy, separations, and catalysis.[1-5] Block polymers, comprising two chemically distinct polymeric segments, are endowed with natural mechanisms to produce nanoscale structure through self-assembly. Precision synthesis is typically necessary to satisfy the stringent requirements on block polymer molar mass (N), segmental interaction parameter (χ), and composition (f_A) to achieve an ordered co-continuous state (i.e., the bicontinuous double gyroid).[6-7] Consequently, recent efforts have instead targeted non-equilibrium states to produce continuous and independent nanodomains, i.e. polymerization induced microphase separation (PIMS)[8-12], randomly end-linked copolymer networks (RECNs)[13-14], interpenetrating polymer networks[15], and microemulsion templated polymerizations.[16-17] These systems rely upon trapping transient compositional fluctuations that evolve as a block polymer grows *in-situ* amid multifunctional cross-linkers. These strategies rely upon achieving a fine balance between the kinetics of phase separation and the synchronous

[2] Reproduced with permission from Hampu, N.; Bates, M. W.; Vidil, T.; Hillmyer, M. A. Bicontinuous Porous Nanomaterials from Block Polymers Radically Cured in the Disordered State for Size-Selective Membrane Applications. *ACS Appl. Nanomater*. **2019**, *2*, 4567-4577. Copyright 2019 American Chemical Society.

cross-linking reactions that lock the growing phase separated domains into a spatially heterogeneous and percolating network. Despite these challenges, chemistries have been successfully adapted to produce materials with optimal combinations of properties (e.g., high transport and mechanical stiffness) that are critical to applications involving, for example, porous media and ionically conductive electrolytes.[1, 18-19] The bicontinuity of these high-performing materials has been correlated to their disordered structures.

An alternative strategy to access co-continuous nanostructures could exploit the disordered state of block polymers attained via thermodynamic equilibrium rather than competing kinetic phenomena. Mean-field treatments of the disordered state predict the existence of a homogeneous melt of molecularly mixed segments at elevated temperatures. Such a morphology lacks the nanoscale, microphase separated domains required for many applications, and consequently, there has been little effort to utilize the order-disorder transition in the development of technologically relevant innovations. However, these mean-field treatments neglect the presence of thermally-induced composition fluctuations in the disordered state. These fluctuations produce a dynamic and rearranging state of locally microphase segregated domains with a characteristic length-scale set by the overall size of the polymer coil even above the order-disorder transition temperature (T_{ODT}). A variety of experimental techniques, including small-angle X-ray and neutron scattering (SAXS and SANS),[20-25] transmission electron microscopy (TEM),[24-27] and rheology,[20, 27-28] have demonstrated the existence of such fluctuations in the vicinity of the T_{ODT}. Recent theoretical simulations[29] have further refined the physical depiction of the disordered state as a structure with rather similar domain characteristics (size and composition) as the

ordered phase, lacking only long-range spatial correlations. Therefore, unlike non-equilibrium processes, chemical fixation of a disordered block polymer above the T_{ODT} could offer an opportunity to precisely dictate the properties of the cross-linked thermoset through the chemical design of the polymer molecule. To this end, we have recently described the utility of the ODT of a reactive block polymer, comprising an epoxy-functionalized thermosetting block, poly(styrene-*stat*-glycidyl methacrylate), to prepare mesoporous materials with well-defined and co-continuous three-dimensional network structures using both thermal and photochemical cross-linking agents.[30-31]

4.2 Experimental Methods

Here, we expand the scope of thermosetting blocks and cross-linking chemistries by using a reactive styrene-butadiene, P(S-*s*-B), segment cured using a thermally latent peroxide. This system utilizes an industrially relevant curing strategy in thermoset technologies, namely the radical cross-linking of unsaturated copolymers. Moreover, the high interaction parameter between PB and PLA as compared to PGMA and PLA should enable the use of lower molar mass precursors to access smaller pores, thus enabling size-selective membranes with enhanced rejection of smaller water solutes and contaminants. The curing process, schematically depicted in Figure 4.1, begins with a homogeneous mixture of block polymer, poly(styrene-*stat*-butadiene)-*block*-polylactide (P(S-*s*-B)-*b*-PLA), and dicumyl peroxide (DCP). Inclusion of the high T_g styrene units in the thermosetting block improves its thermal resistance and mechanical properties as compared to pure poly(butadiene). It also effectively lowers the segment-segment interaction parameter (χ) with the polylactide block, leading to a thermally accessible T_{ODT}. At curing temperatures $T_{cure} \sim T_{ODT}$, the

peroxide decomposes, initiating radical coupling and addition reactions largely through the vinyl groups of the unsaturated copolymer. Upon cooling, the peroxide-cured network remains kinetically trapped in the disordered state. Selective hydrolysis of the PLA block renders a porous material at room temperature and enables facile characterization of the morphology. Using a combination of SAXS, scanning electron microscopy (SEM), and nitrogen sorption analyses, the porosity produced for a given block polymer-peroxide pair was investigated as a function of peroxide loading and cure temperature. In this study, the cross-linking of the block polymer in the vicinity of the order-disorder transition temperature is examined as a new approach for the control of the morphology and the design of new functional materials, which we highlight via the performance of this system in the ultrafiltration of macromolecular test substances in water.

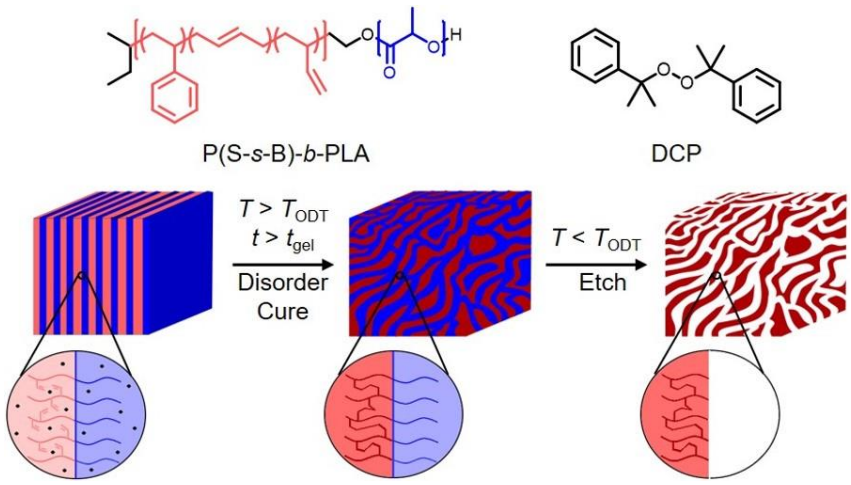

Figure 4.1. Strategy employed to produce a bicontinuous nanoporous network via chemically cross-linking a reactive diblock copolymer in the disordered state. Chemical structures of the block polymer, comprising an etchable PLA (blue) block and a cross-linkable poly(styrene-*stat*-butadiene) block (red), and dicumyl peroxide (DCP) are displayed at the top. Mixtures of the block polymer and DCP initially form a lamellar morphology at room temperature. Heating to a curing temperature (T_{cure}) above the order-disorder transition temperature (T_{ODT}) triggers the decomposition of the thermally latent peroxide and produces polymer radicals that result in chemical cross-links. These cross-links kinetically trap a locally segregated but macroscopically disordered and co-continuous morphology and prevent the block polymer from re-ordering upon cooling to room temperature. The PLA block (blue) is subsequently removed via a mild basic hydrolysis to render the matrix (red) porous.

Anionic synthesis of the P(S-*s*-B)-OH copolymer was performed in the presence of potassium *tert*-butoxide, a polarity modifier that ensures a statistical incorporation of the two monomers.[35,36] The reactive chain-ends were end-capped with a hydroxyl unit to initiate the subsequent ring-opening transesterification polymerization of (±)-lactide (see Chapter 3 for full synthetic details). According to ^{1}H NMR analysis (Figure 4.2), the isolated P(S-*s*-B)-OH precursor was determined to be 4.2 kg mol^{-1} and consisted of 27 mol % butadiene comprising 80 % in-chain double-bonds from a predominantly 1,4-mode of addition. The LS-SEC chromatogram obtained in THF at room temperature displayed a single peak of narrow molar mass distribution ($Đ$ = 1.19), Figure 4.3. In accordance with a statistical microstructure, a single glass transition temperature ($T_{g,SB}$ = 41 °C, Figure 4.4) was observed that was consistent with the prediction from the Fox equation using $T_{g,PS} \approx$ 100 °C and $T_{g,PB} \approx$ –112 °C.[41,42] Subsequent growth of PLA from the SB macroinitiator produced a library of poly(styrene-*stat*-butadiene)-*block*-poly(lactide) (SBL) diblock polymers of varying PLA molar mass ($M_{n,PLA}$ = 2.7–7.1 kg mol^{-1}) and block compositions spanning the width of the lamellar window (f_{PLA} = 0.36–0.59) with a range of thermally accessible order-disorder transition temperatures (T_{ODT} = 115–205 °C), Table 4.1 and Figure 4.5. Each sample is hereafter referred to as SBL(x, y) where x is the volume fraction of PLA in the diblock, and y is the T_{ODT} as determined by dynamic mechanical analysis. Although each material is microphase-separated, a single T_g ~ 44 °C was observed for all SBL diblock copolymers, which is attributed to an overlap of the nearly identical T_g's for low molar mass PLA[13] and P(S-*s*-B), Figure 4.4.

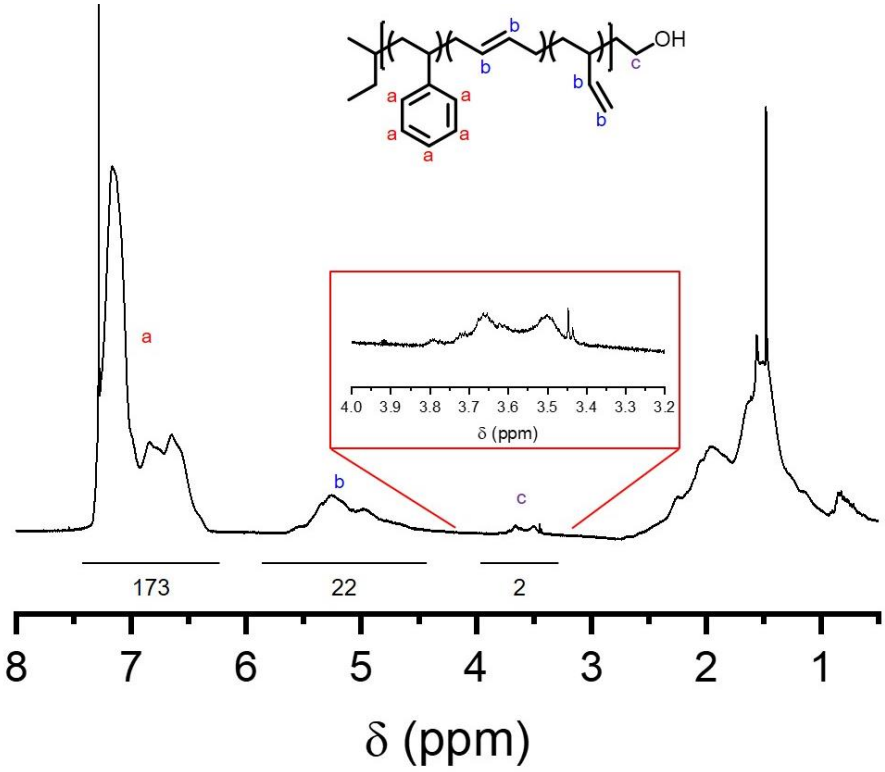

Figure 4.2. ^{1}H NMR spectrum of the statistical copolymer precursor, P(S-*s*-B)-OH. Regions of integration for the PS aromatic protons (7.2–6.3 ppm, 5*H* per repeat unit) and PB vinylic protons (5.4–5.0 ppm, 2*H* per repeat unit) relative to the methylene protons (3.5 ppm, 2*H*) adjacent to the hydroxyl end-group are indicated, and the integral values are provided below the corresponding peak (M_n = 4200 g mol^{-1}, 73 wt. % PS).

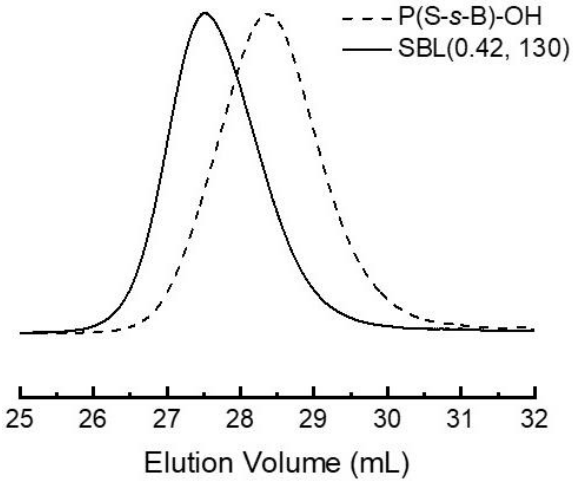

Figure 4.3. Representative SEC elugrams for the P(S-*s*-B)-OH macroinitiator ($Đ$ = 1.19, dashed curve) and the diblock copolymer SBL(0.42, 130) ($Đ$ = 1.09, solid curve).

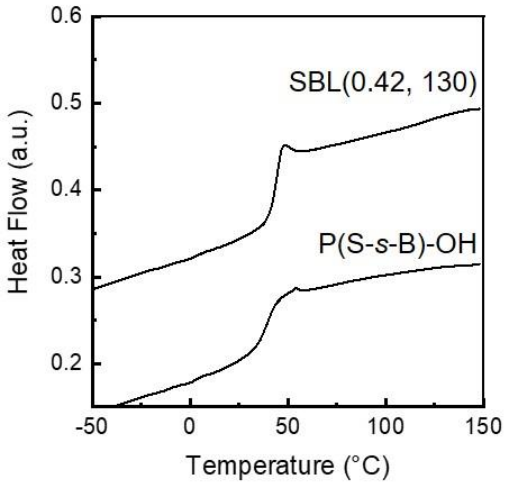

Figure 4.4. DSC thermograms obtained on the second heating cycle at a ramp rate of 10 °C min^{-1} for the P(S-*s*-B)-OH macroinitiator and a representative diblock copolymer, SBL(0.42, 130). A T_g of 41 °C was observed for P(S-*s*-B)-OH and a T_g of 54 °C was observed for SBL(0.42, 130). Thermograms were vertically shifted for clarity.

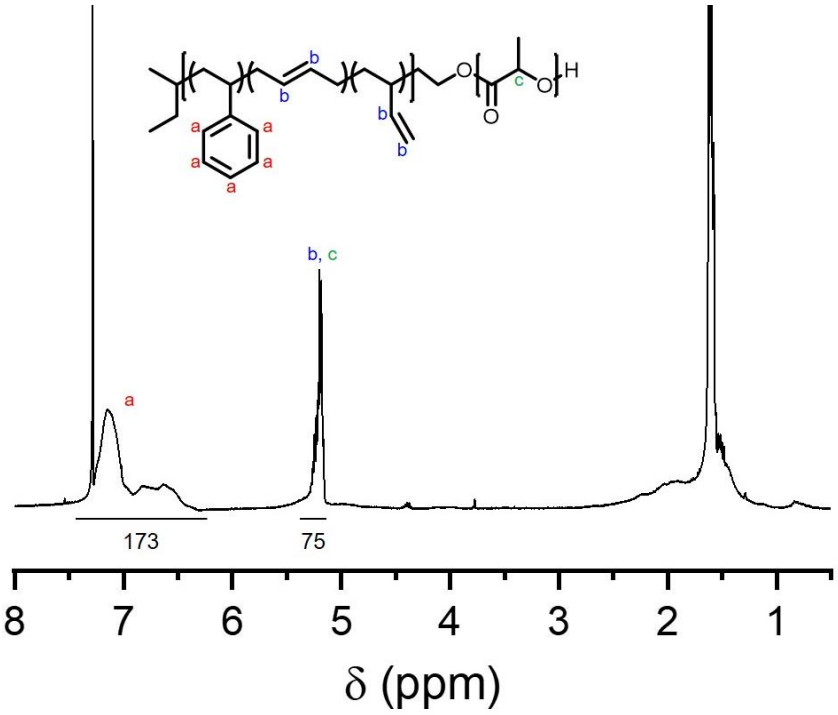

Figure 4.5. Representative ^{1}H-NMR spectrum of the P(S-*s*-B)-*b*-PLA block polymer SBL(0.42, 130). Regions of integration for the PS aromatic protons (7.2–6.3 ppm, 5*H*) relative to the PB vinylic protons (5.4–5.0 ppm, 2*H)* and the overlapping methine protons of the PLA backbone (5.4–5.0 ppm, 1*H*) are indicated, and the corresponding integral values are provided below the corresponding peak (M_n = 7800 g mol^{-1}, f_{PLA} = 0.42).

Table 4.1. Molecular characterization of SBL block polymers.[a]

SBL Sample ID[b]	$M_{n,PLA}$[c]	f_{PLA}[d]	$Đ$[e]	Morphology[f]	d (nm)[g]	T_{ODT} (°C)[h]
SBL(0.34, dis)	2.7	0.34	1.08	Disordered	17.2	- (-)
SBL(0.36, 115)	2.8	0.36	1.09	Lamellar	14.8	115 (120<T<130)
SBL(0.42, 130)	3.6	0.42	1.06	Lamellar	13.7	130 (125<T<130)
SBL(0.43, 135)	4.0	0.43	1.07	Lamellar	14.0	135 (130<T<135)
SBL(0.45, 180)	4.2	0.45	1.08	Lamellar	17.4	180 (190<T<192)
SBL(0.56, 205)	6.5	0.56	1.09	HPL	17.3	205 (191<T<193)
SBL(0.59, 185)	7.1	0.59	1.05	Lamellar	19.0	185 (180<T<190)

[a]P(S-*s*-B)-OH precursor: $M_{n,NMR}$ = 4200 g mol^{-1}, $Đ$ = 1.19, 73 wt% PS. [b]Samples are referred to as SBL(X,Y) where X specifies the volume fraction the PLA block and Y is the order-disorder transition temperature, T_{ODT}, identified rheologically. [c]Number-average molar mass of the PLA block from ^{1}H NMR analysis reported in kg mol^{-1}. [d]Volume fraction of PLA based on reported homopolymer densities and ^{1}H NMR. [e]Molar mass dispersity evaluated using LS-SEC in THF. [f]Evaluated via SAXS. [g]Principal domain spacing determined from SAXS patterns obtained at 25 °C. [h]T_{ODT} was determined via dynamic mechanical thermal analysis performed on heating at 1 °C min^{-1}. Values in parentheses are estimated from SAXS based on the increment between the highest temperature where a sharp peak is observed and the lowest temperature where a broad peak is observed. Samples were annealed at least 2 minutes at each temperature prior to data acquisition.

4.3 Results and Discussion

4.3.1 Morphological Characterization of Diblock Polymers

The series of near-symmetric SBL diblock copolymers were characterized using a combination of SAXS and DMA (Table 4.1). Figure 4.6a displays the temperature dependence of the storage modulus, G', for a representative diblock, SBL(0.42, 130). The T_{ODT} was identified by the precipitous drop in G' around 130 °C, indicating the transition of a soft solid to the liquid-like behavior of a disordered melt. The low frequency linear viscoelastic response for SBL(0.42, 130) at T = 80 °C, Figure 4.7, is consistent with the expected frequency dependence ($G' \sim \omega^{1/2}$) for a lamellar morphology, and it transitions to terminal behavior expected for a disordered melt ($G' \sim \omega^2$) above T_{ODT} (T = 140 °C).[43] Variable temperature SAXS data obtained on heating from 25 to 130 °C are presented in Figure 4.6b. The SAXS pattern obtained at 25 °C exhibits a sharp principal scattering peak

located at q^* = 0.46 nm^{-1} as well as higher ordering scattering maxima at $2q^*$ (0.92 nm^{-1}) and $3q^*$ (1.38 nm^{-1}), indicative of lamellar order with a domain periodicity d = 13.7 nm. As SBL(0.42, 130) is heated, the intensity of the principal scattering peak decreases until a single broad reflection remains at 130 °C, consistent with the transition from the ordered to the disordered state and the T_{ODT} obtained from DMA. A plot of the inverse intensity of the principal scattering peak, $I(q^*)$, vs. the inverse of the temperature, T^{-1} (Figure 4.6b, inset), demonstrates an abrupt increase in I^{-1} above T_{ODT}, which is consistent with the transition from an ordered to a disordered microstructure. The experimentally measured T_{ODT} corresponded reasonably well with the theoretical prediction from a binary interaction model, which suggests that the molar mass and composition of P(S-*s*-B)-*b*-PLA diblocks can be rationally tuned to target a desired T_{ODT} and T_{cure} (Figure 4.8).[44]

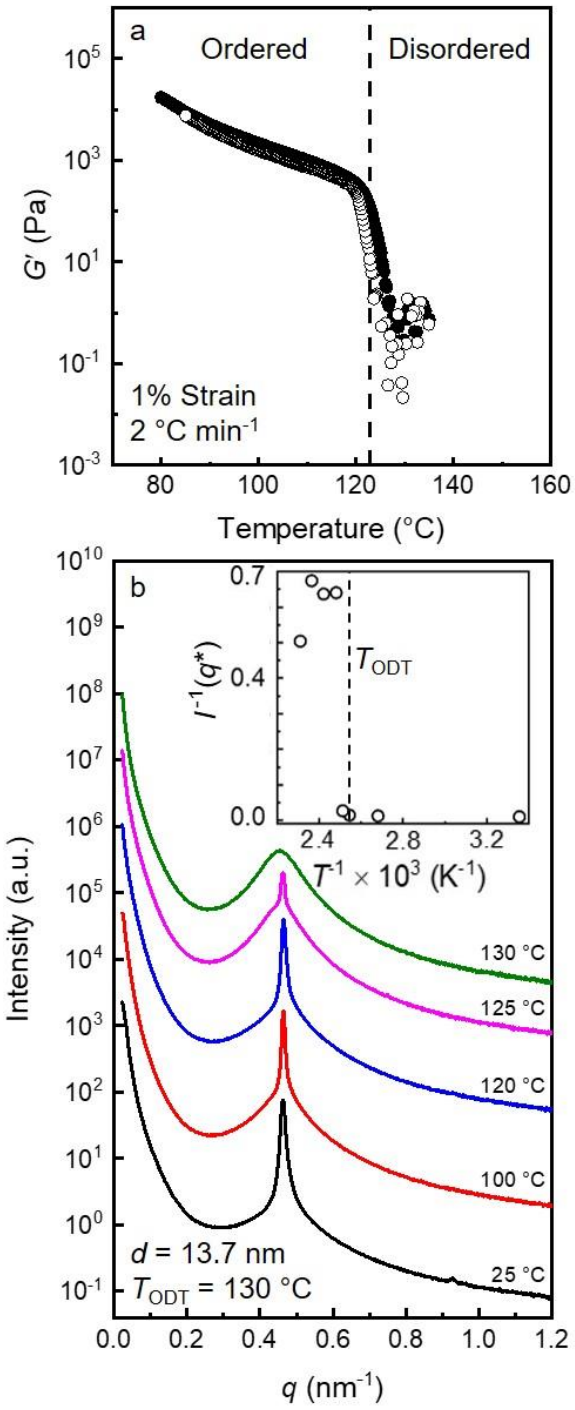

Figure 4.6. (a) Temperature dependence of the storage modulus G' for SBL(0.42, 130) (1 rad s^{-1}, 1% strain) on heating (●) and on cooling (○) at a ramp rate of 2 °C min^{-1}. A precipitous drop in G' around 130 °C indicates the onset of the order-disorder transition. (b) Variable temperature SAXS data acquired after thermal equilibration at each temperature for 2 min. The sample was annealed for 1 hour at 80 °C prior to measurement. The inset presents the inverse intensity of the principal scattering peak, $I^{-1}(q^*)$, vs. the inverse of the temperature, T^{-1}.

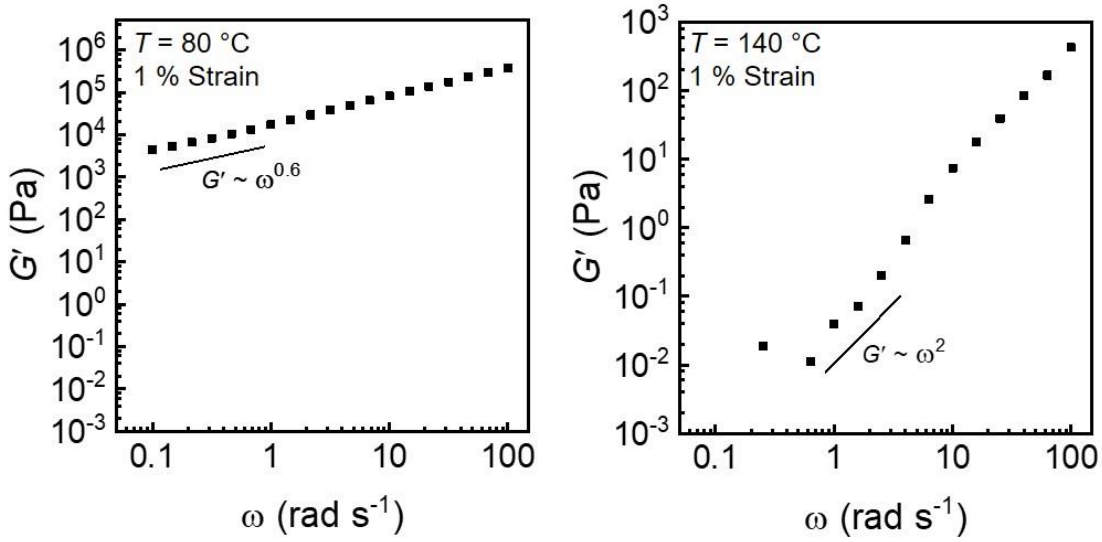

Figure 4.7. Dynamic frequency sweeps for SBL(0.42, 130) at 80 °C and 140 °C (1 % strain). Power law fits for the low frequency dependence of G' are indicated on the respective plots.

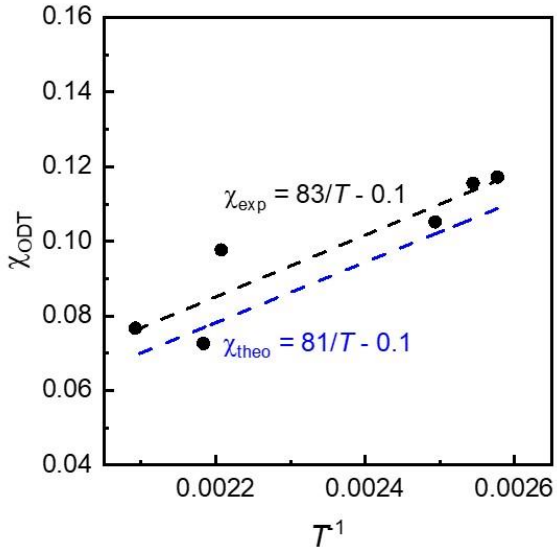

Figure 4.8. Temperature dependence, $\chi_{SBL}(T)$, estimated using the order-disorder transition temperatures of the series of compositionally symmetric P(S-*s*-B)-*b*-PLA diblock polymers presented in Table 4.1. A linear fit to the experimental data, $\chi_{exp,}$ is presented as the dashed black line. The theoretical prediction, χ_{theo}, based on a binary interaction model is presented as a dashed blue line for comparison. Data are reported using a fixed monomer reference volume (v_o = 118 Å^3).

4.3.2 Cross-linking Block Polymer Films Near T_{ODT}

The radical initiator DCP was selected as a suitable cross-linking agent given its established reactivity at temperatures in the vicinity of the T_{ODT} for SBL(0.42, 130).[38] Blends of block polymer and radical initiator were prepared by film casting a 25 wt. % solution of SBL(0.42, 130) co-dissolved with prescribed amount of DCP in THF followed by slow solvent evaporation overnight under ambient conditions (see Chapter 3 for a detailed description of film preparation and curing). The resulting films were optically transparent discs with a diameter of approximately 1 inch. The films were heated under nitrogen at 80 °C for 2 h to remove any residual THF as well as to anneal the sample. SEC chromatograms of the prepared films did not display any significant change in elution volume or peak breadth as compared to neat SBL(0.42, 130), which indicates that this low-temperature film preparation procedure does not induce any premature cross-linking of the macromolecular precursor (Figure 4.9). Furthermore, room temperature SAXS patterns for SBL(0.42, 130) samples containing DCP exhibit little change in the peak intensity or location of q^* for samples containing up to 15 wt. % DCP, suggesting that DCP addition does not significantly perturb the lamellar state nor lead to a highly selective swelling of a single domain, Figure 4.10. This suggests that DCP is a good diluent for both blocks and is likely distributed fairly evenly in both domains.[45-46]

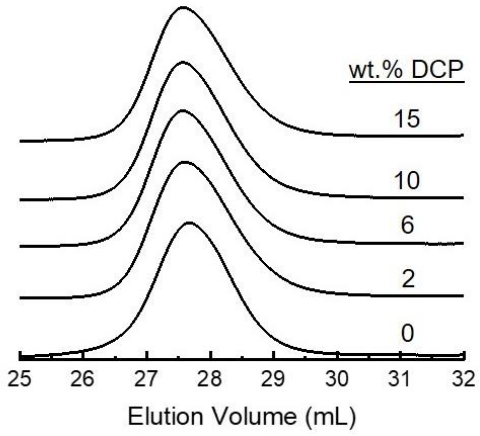

Figure 4.9. SEC traces for a prepared SBL(0.42, 130) film and films containing 0, 2, 6, 10, and 15 wt. % DCP following the annealing procedure. Elugrams were vertically shifted for clarity.

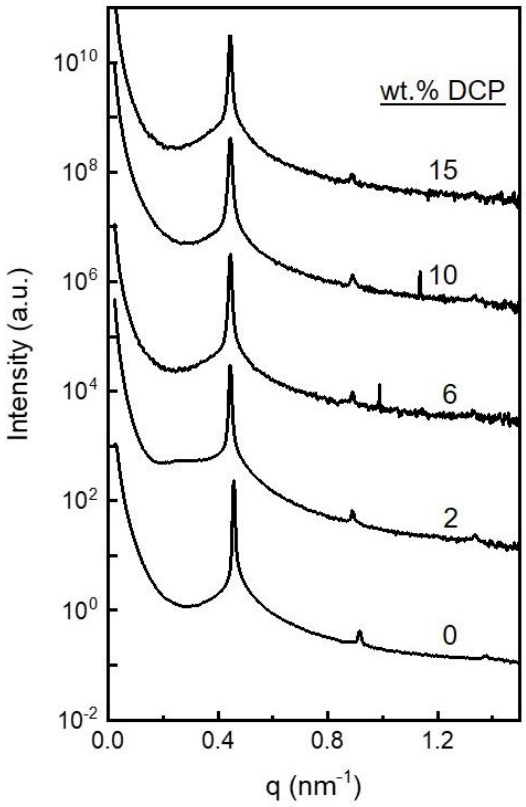

Figure 4.10. Room temperature SAXS patterns obtained for neat SBL(0.42, 130) and dried monolithic films containing 0, 2, 6, 10, and 15 wt. % DCP. All data were obtained at room temperature after annealing for 1 hour at 80 °C.

However, both variable temperature SAXS (Figure 4.11) and DMA (Figure 4.12) indicate a trend of decreasing T_{ODT} with increasing amounts of added DCP in SBL blends, leading to a reduced T_{ODT} of 105 °C at 10 wt. % loading for SBL(0.42, 130), Tables 4.2 and 4.3. Reductions in T_{ODT} with DCP content are attributed to a reasonably uniform distribution of DCP within the block polymer, effectively introducing a mostly neutral diluent that screens interfacial contacts between the PLA and P(S-*s*-B) segments and stabilizes the disordered state.[47] We note that these results may also suggest that peroxide content can be used as a tool to modulate the available thermal processing window defined by the location of the effective T_{ODT}, without needing to synthesize a new block polymer. In all subsequent analyses, we refer to each T_{ODT} as that for a particular SBL block polymer and specified DCP content.

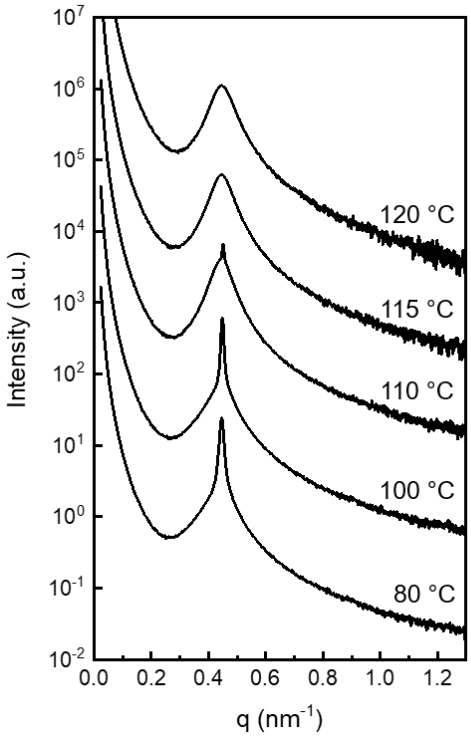

Figure 4.11. Variable temperature SAXS obtained for SBL(0.42, 130) containing 6 wt. % DCP. The sample was annealed for 1 hour at 80 °C prior to data collection and thermally equilibrated for 2 min at each temperature.

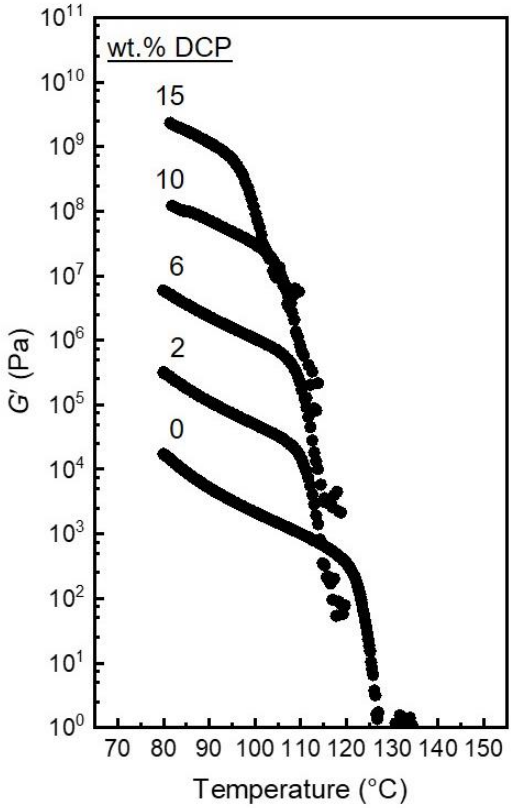

Figure 4.12. Temperature dependence of the storage modulus for neat SBL(0.42, 130) and dried films containing 2, 6, 10, and 15 wt. % DCP. All data were obtained using a frequency of 1 rad s^{-1}, 1 % strain, and a heating rate of 2 °C min^{-1}. Data are vertically shifted for clarity.

Table 4.2. T_{ODT} of SBL(0.42, 130) mixtures of varied DCP concentration.

DCP (wt. %)	T_{ODT} (°C)
0	130
2	117
6	112
10	105
15	95

Table 4.3. T_{ODT} of varied SBL precursors containing 6 wt. % DCP.

Block Polymer	T_{ODT} (°C)
SBL(0.42, 130)	112
SBL(0.45, 180)[a]	170
SBL(0.56, 205)[a]	170
SBL(0.59, 185)	145

[a] T_{ODT} estimated using SAXS.

Composite films of SBL(0.42, 130) and DCP were cured under a nitrogen atmosphere in the vicinity of T_{ODT} to arrest the morphology present at each curing temperature, T_{cure}. Once cured, the efficiency of the cross-linking reaction was estimated via measurement of the gel fraction. Cross-linked samples were immersed in THF overnight, and the swelled gels were subsequently dried under vacuum and massed. The gel fractions (f_{gel}), defined as the ratio of the mass of the dry network prior swelling to the mass of the dry network after swelling, are provided in Table 4.4. It was found that an increase in T_{cure} or higher DCP loadings led to an increase in gel fraction, likely due to an increased number of radicals and thus potential cross-linking reactions.

Table 4.4. Gel fraction (f_{gel}) of cured SBL(0.42,130) and DCP blends and gravimetric analysis after etching as a function of crosslinker content and cure temperature.

wt. % DCP	T_{cure} (°C)	t_{cure} (h)	*Before Etching*	*After Etching*
			f_{gel}	Mass Loss (%)
2	120	120	0.00	45
	130	18	0.00	50
	150	4	0.00	44
	170	2	0.00	46
6	90	300	0.40	56
	115	120	0.44	40
	130	18	0.57	50
	150	4	0.70	48
	170	2	0.68	44
	190	2	0.83	60
10	90	300	0.80	55
	110	120	0.85	54
	130	18	0.88	51
	150	4	0.98	52
	170	2	0.94	50
15	130	18	0.90	53
	150	4	0.92	48
	170	2	0.95	51

Samples of SBL(0.42,130) and 6 wt% DCP (T_{ODT} = 112 °C) were cured at temperatures within the ordered and disordered states and subsequently examined using room-temperature SAXS to assess the resulting morphology. For T_{cure} = 90 °C, the cross-linked material displays a sharp scattering maximum at a slightly decreased q^* as compared to the uncured system (q^* = 0.39 nm^{-1}) and a higher order reflection at $2q^*$, thus retaining the lamellar order of the pristine block polymer (Figure 4.13). In contrast, each sample cross-linked above T_{ODT} (T_{cure} = 115, 130, 150, 170, and 190 °C) presents a single broad reflection upon cooling that is characteristic of a disordered microphase separated state (Figure 4.13, solid curves), suggesting that the cross-linking reactions arrest the microstructure adopted at the curing temperature.

Selective removal of the PLA domains was achieved via mild hydrolysis following immersion of the cured samples in a 0.5 M NaOH solution of methanol/water (60/40 v/v). For all samples, the mass loss (40–60 %) following etching was reasonably consistent with the initial PLA content in the blend (Table 4.4). FTIR spectra corroborated the complete removal of PLA with the disappearance of a characteristic carbonyl stretch at 1750 cm^{-1} (Figure 4.14). Room temperature SAXS data obtained post-etch indicate a significant change in nanostructure for SBL(0.42, 130) blends cured with DCP in the ordered state ($\Delta T = T_{cure} - T_{ODT}$ = –22 °C) (Figure 4.13, dashed curve). The absence of the sharp lamellar principal scattering maximum after etching suggests a loss of any porosity generated from the degradation of PLA lamellae.[12,48] Further examination of the etched monolith morphology using SEM supports this interpretation. The corresponding micrograph

(Figure 4.13) displays an array of sheet-like features, suggesting a collapsed arrangement of cross-linked P(S-*s*-B) layers.

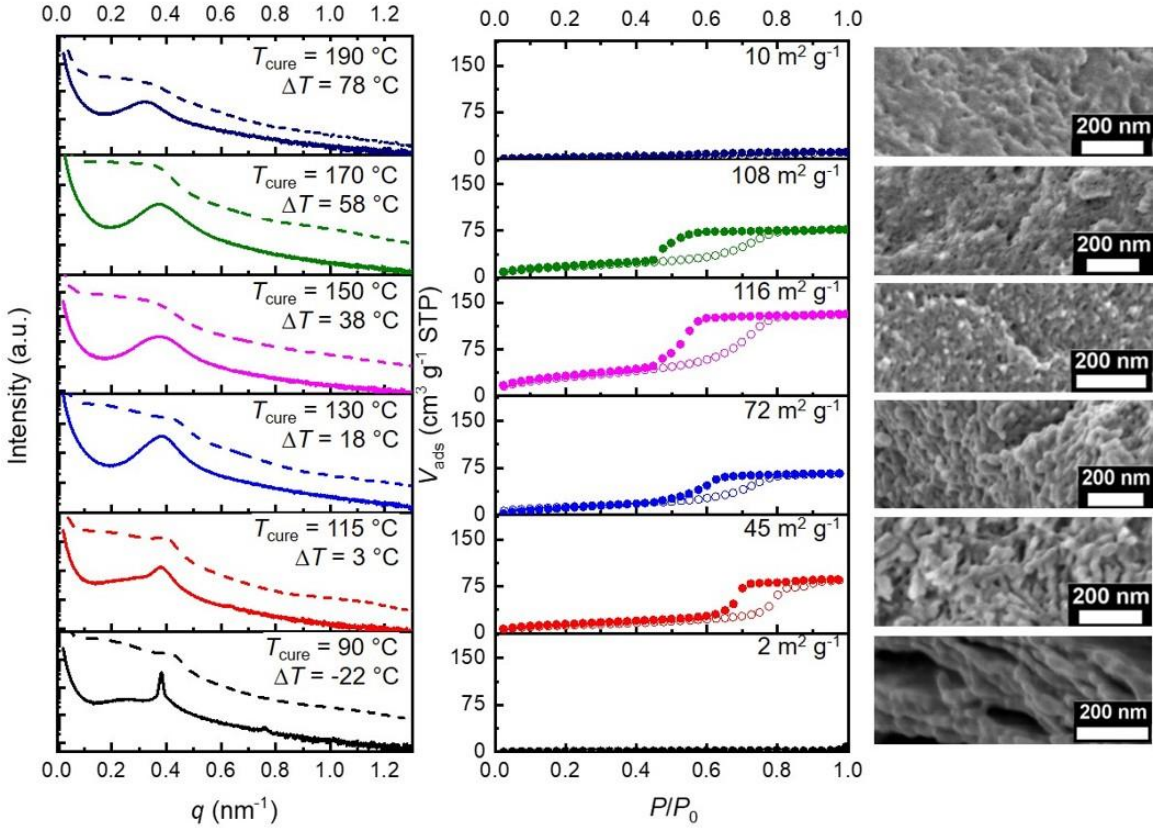

Figure 4.13. Room temperature SAXS patterns (left), nitrogen sorption isotherms (middle), and SEM micrographs (right) for SBL(0.42, 130) and 6 wt. % DCP blends. Curing temperatures, T_{cure}, are indicated on each set of SAXS patterns. Dashed and solid curves were obtained prior to and after etching, respectively, and all data are vertically shifted for clarity. The absence of sharp scattering peaks for blends cured above the effective $T_{ODT} \approx 112$ °C suggests that the cross-links formed prevent recovery of the ordered phase on cooling. Nitrogen sorption isotherms were obtained under adsorption (○) and desorption (●) for etched samples. Sorption hysteresis evident for $T_{cure} \geq 115$ °C indicates the presence of a continuous mesoporous network. BET specific surface areas are indicated for each sample. The SEM micrographs compare etched samples that were cryo-fractured and sputter-coated with ~3 nm of Pt prior to imaging. The collapse of the residual P(S-*s*-B) lamellae for T_{cure} = 90 °C corresponds to cross-linking below T_{ODT}. All samples cross-linked above T_{ODT} produce a disordered surface morphology after etching $T_{cure} \geq 115$ °C.

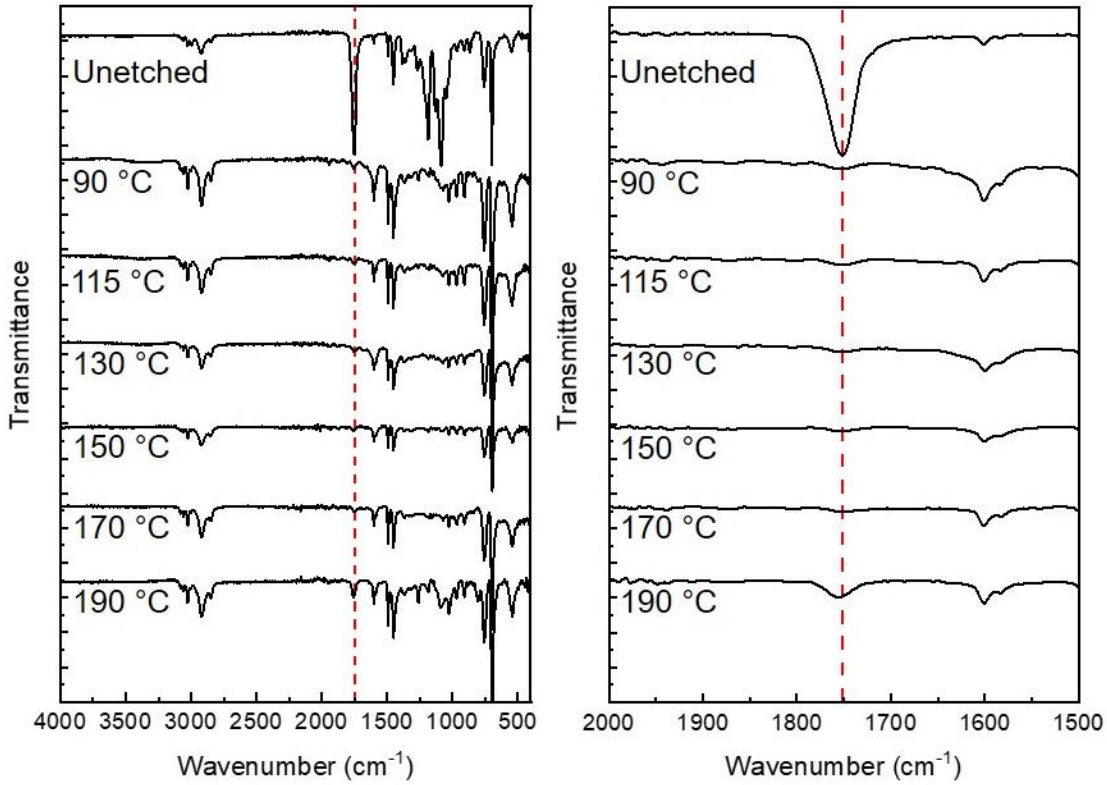

Figure 4.14. Post-etch FTIR spectra for SBL(0.42, 130) cured with 6 wt. % DCP at temperatures in the vicinity of the effective order-disorder transition temperature (T_{ODT} = 112 °C). The unetched material is shown for comparison. Spectra are vertically shifted for clarity. The full spectra are presented on the left and the right emphasize the disappearance of the carbonyl stretch characteristic of PLA at 1750 cm^{-1} after exposure to aqueous base.

In contrast, etched monoliths of SBL(0.42, 130) and 6 wt. % DCP cross-linked at temperatures within the disordered state retain a broad reflection at similar values of q^* (0.34 to 0.43 nm^{-1}) to the unetched state. After PLA hydrolysis, the observed increase in scattering intensity for all q is consistent with an increased electron density contrast between the residual P(S-*s*-B) matrix and a generated network of mesopores (Figure 4.13, dashed curves). Low q ($q < q^*$) scattering also emerges in some samples, signaling the development of larger-scale inhomogeneities after etching. These features have been previously attributed to a fraction of lost porosity due to pore collapse, although some low

q scattering is also observed prior to etching for T_{cure} = 90 and 115 °C. Its presence may suggest that thermal degradation of the PLA block contributes to this observation given the long curing times employed at these temperatures.[12, 49] The SEM images (Figure 4.13) generally indicate that the etched sample series of cross-linked and disordered block polymers produces a disorganized pore structure, resembling the previously reported bicontinuous porous networks from PIMS[8-12] and RECNS.[13-14] Overall, the images are consistent with the notion that the DCP initiated cross-linking reactions effectively trap the disordered morphology adopted above T_{ODT}. Differences in surface topography observed in the micrographs for samples cross-linked in the disordered state may reflect a decrease in the segregation strength as $T_{cure} - T_{ODT}$ increases. For example, the sample cured in close proximity to the T_{ODT} at T_{cure} = 115 °C displays an elongated topography. This may reflect that the disordered melt remains rather similar structurally to the ordered phase at the local level, with well-defined domains, yet increased interfacial curvature.[28, 50] For T_{cure} spanning 130–170 °C, pores are observed within a roughened surface of cross-linked globules, which may reflect a tightening of the cross-linked mesh due to shorter range spatial correlations within the melt at these higher temperatures (lower segregation strengths). Interestingly, for T_{cure} = 190 °C, the surface appears flatter and relatively featureless, which may reflect the effectively homogenized state of the disordered melt *far* above T_{ODT} or may signal a possible material sensitivity to the curing process at the highest temperature investigated.

Nitrogen sorption measurements of the etched sample series obtained at 77 K were used to further characterize the materials (Figure 4.13). The featureless isotherm formed from cross-linking in the ordered state confirms the non-porous nature of the collapsed P(S-*s*-B)

lamellae. For samples cross-linked within the window $T_{ODT} < T \leq 170$ °C, Type IV isotherms with H2 hysteresis indicative of bicontinuous mesoporosity are observed.[51-52] Quenched solid density functional theory (QSDFT) analysis was used to fit each adsorption branch with a cylindrical pore model to estimate the pore size distribution.[31] For this sample set, all mesopore populations exhibit a principal pore mode of approximately 8 nm (Figure 4.15). The sample produced at the highest curing temperature (190 °C) forms an exception with no measurable porosity (Figure 4.13), although the result is qualitatively consistent with the distinguishing features noted in the SEM micrograph (Figure 4.13).

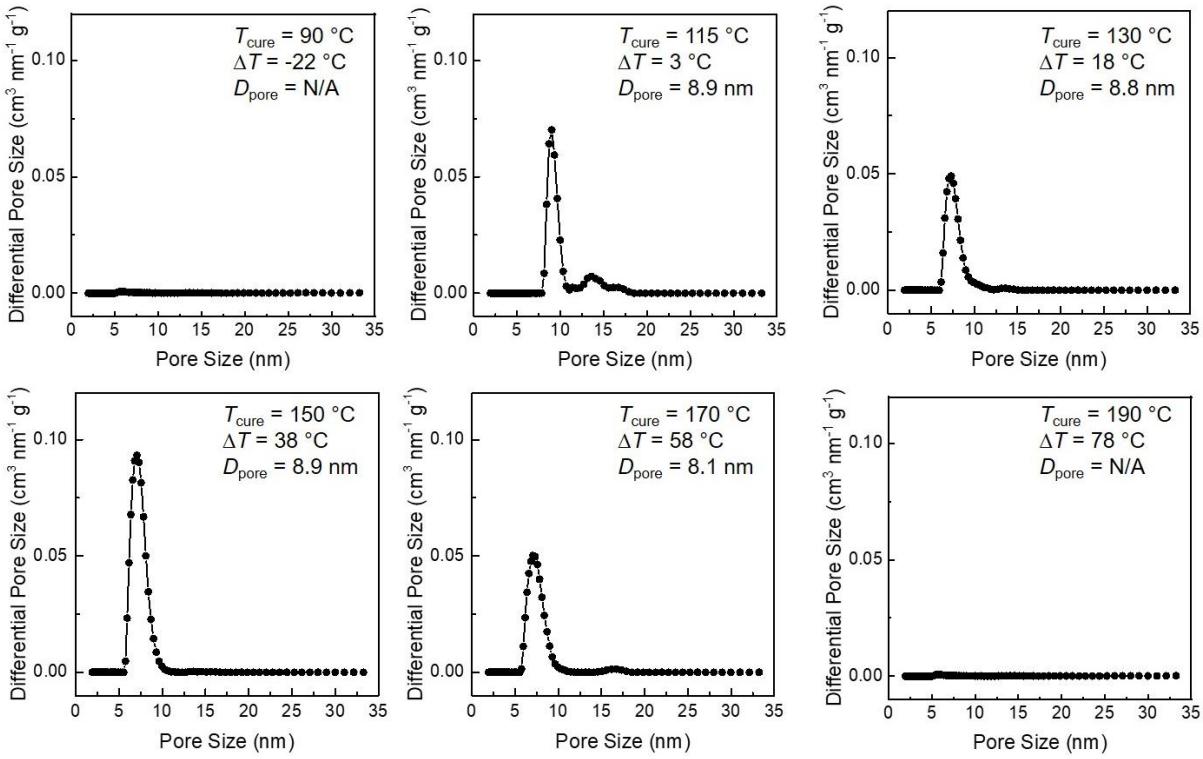

Figure 4.15. Pore size distributions for monolithic films prepared from SBL(0.42, 130) cured using 6 wt. % DCP at 90 °C, 115 °C, 130 °C, 150 °C, 170 °C, and 190 °C based on QSDFT analysis of the adsorption branch. Curing temperatures, T_{cure}, for each sample are indicated on each pore size distribution. The pore mode is approximately 8-9 nm for all porous samples.

Specific surface areas estimated using the Brunauer–Emmett–Teller (BET) analysis and total pore volumes (evaluated at $P/P_o = 0.95$) as a function of the relative temperature

difference between the curing conditions and the ODT in °C ($\Delta T = T_{cure} - T_{ODT}$) are presented in Figure 4.16. Porosity and BET surface area reach a maximum for ΔT = 40 °C, which suggests optimal domain connectivity and pore stability are achieved under these conditions. These results reveal an increase in porosity as T_{cure} crosses T_{ODT}, likely due to the distinct nanostructures of the periodic lamellar and the isotropic disordered states which affects the continuity of porous and cross-linked domains. The increase in porosity as ΔT increases from 3 to 18 °C highlights this point. The sample cured just above T_{ODT} (ΔT = 3 °C) recovers some lamellar character on cooling, as evidenced by the observance of an intense primary peak within the broader disordered peak in the room temperature SAXS pattern (Figure 4.13). At ΔT = 18 °C, a less intense primary peak results upon cooling, which may suggest that the increase in the curing temperature facilitates the cross-linking reactions to more efficiently trap the disordered state. This conclusion is consistent with the larger gel fraction evaluated in the unetched material (Table 4.4). A steady increase in porosity is noted for samples cured at higher temperature up to 150 °C, with a slight decrease in porosity noted at T_{cure} = 170 °C. Although the gel fraction increased as the cure temperature increased to 190 °C, the cross-linked product was non-porous.

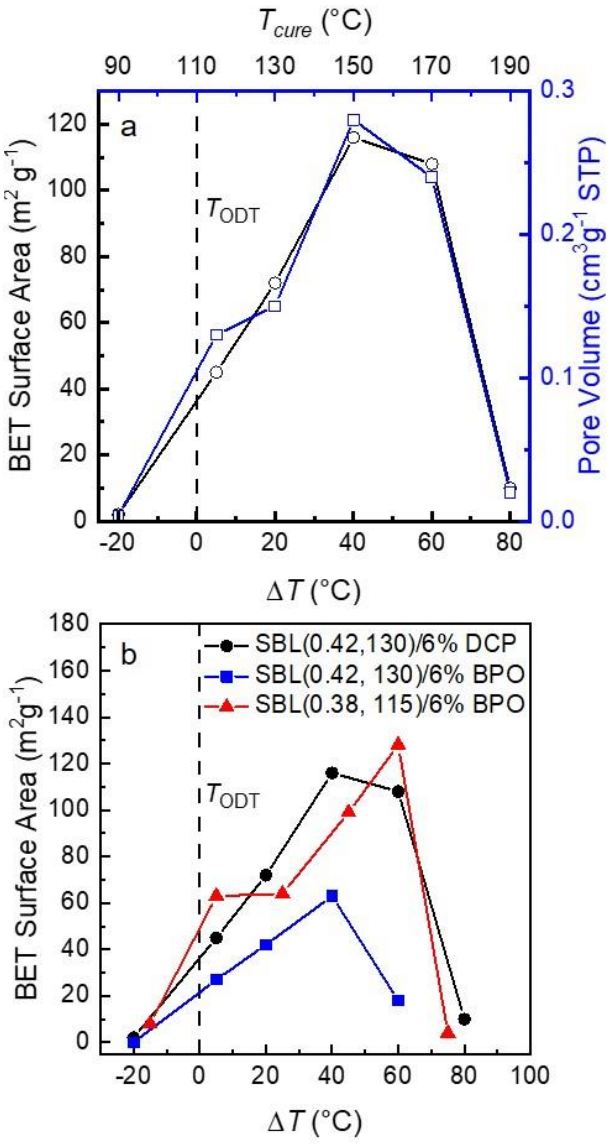

Figure 4.16. (a) BET surface area (black curve) and pore volume (blue curve) for etched SBL(0.42, 130) samples cured with 6 wt.% DCP at various temperatures relative to T_{ODT}. Relative curing temperatures ($\Delta T = T_{curing} - T_{ODT}$) and T_{cure} are indicated on the lower and upper *x*-axes, respectively. A noticeable increase in porosity is observed for samples cross-linked in the disordered state due to enhanced domain connectivity. (b) A comparison of BET surface areas for SBL(0.42, 130)/6 wt. % DCP (T_{ODT} = 112 °C), SBL(0.42, 130)/6 wt. % BPO (T_{ODT} = 95 °C), and SBL(0.38, 115)/6 wt. % BPO (T_{ODT} = 90 °C) cross-linked at various ΔT.

A complex dependence of material properties on temperature is not uncommon in peroxide cross-linking reactions of polymers. Studies on commercially relevant (and chemically related) styrene-butadiene rubber (SBR) have demonstrated that as curing temperature

increases, DCP cross-linking efficiencies first gradually increase and then decrease abruptly.[53] However, we recognize that thermal effects associated with the cross-linking reaction, thermal material stability, and the strength of composition fluctuations at T_{cure} may also contribute to the observed trends in surface area and pore volume (Figure 4.16). Consequently, we note that the specific outcome for the SBL(0.42, 130)/6 wt. % DCP cured at 190 °C may be related to two additional phenomena: (i) a progression to a homogeneous mean-field-like state at temperatures *far* above T_{ODT}, and/or (ii) the promotion of significant side-reactions at rather high temperature that compromise the efficiency of the cross-linking reaction and the mechanical properties of the matrix and/or pore structure.[53-54] Preceding experiments[30-31] with PLA-*b*-P(S-*s*-GMA) samples cured via a cationic mechanism did not exhibit a similar sudden decrease in porosity *far* above T_{ODT} but instead a plateau, which may preclude the former interpretation. However, curing temperatures in excess of ΔT = 40 °C were not explored. With respect to the latter hypothesis, isothermal gravimetric analysis performed at each curing temperature (Figure 4.17) found a decomposition profile exhibiting a much more rapid mass loss at 190 °C, which may suggest side reactions and/or thermal decomposition are potentially important factors.

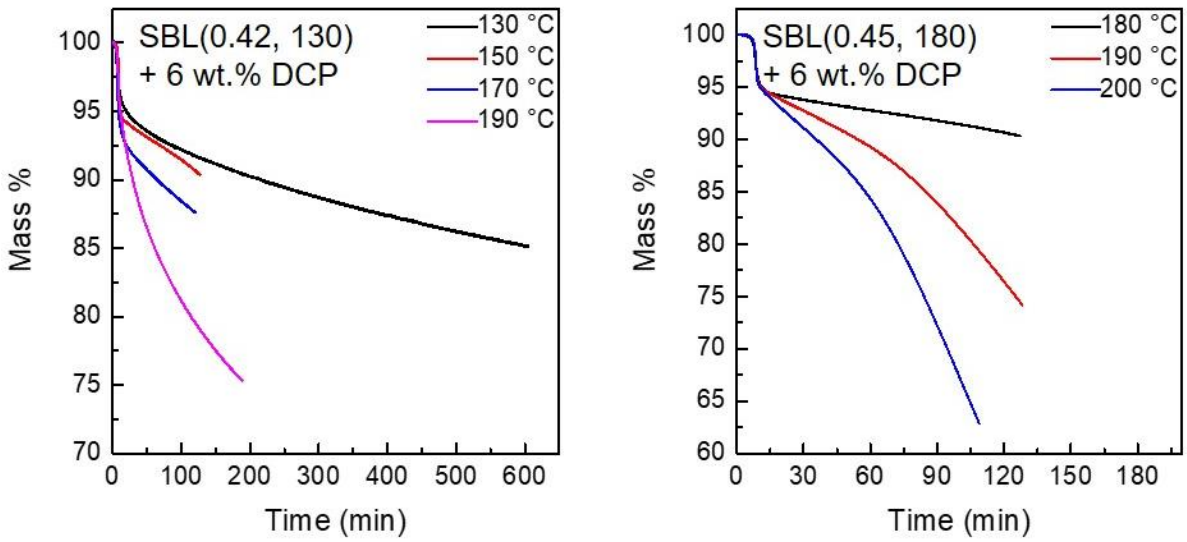

Figure 4.17. Isothermal gravimetric analysis for (a) SBL(0.42, 130) and (b) SBL(0.45, 180) blends containing 6 wt. % DCP at several cure temperatures obtained under a nitrogen atmosphere.

4.3.3 Effect of Peroxide Concentration

Further experiments were therefore conducted to explore the effect of peroxide content and curing temperature on sample porosity. Peroxide-block polymer mixtures exhibited a steady reduction in T_{ODT} with increased DCP concentration, decreasing from the nominal 130 °C for the pure diblock copolymer SBL(0.42, 13) (Figure 4.12) to 95 °C at 15 wt. % loading. Similar cure temperatures (130–170 °C) were consequently suitable to survey structures formed in the ordered and disordered states at each peroxide concentration. Although no measurable gel fraction was obtained in all materials cured using the lowest peroxide content of 2 wt. % DCP (T_{ODT} = 117 °C), each sample lost a comparable mass fraction after exposure to aqueous base, corresponding to the removal of the PLA block (Table 4.4). The corresponding SAXS profiles, nitrogen sorption isotherms, and SEM micrographs of the etched monolithic films are presented in Figures 4.18–4.20.

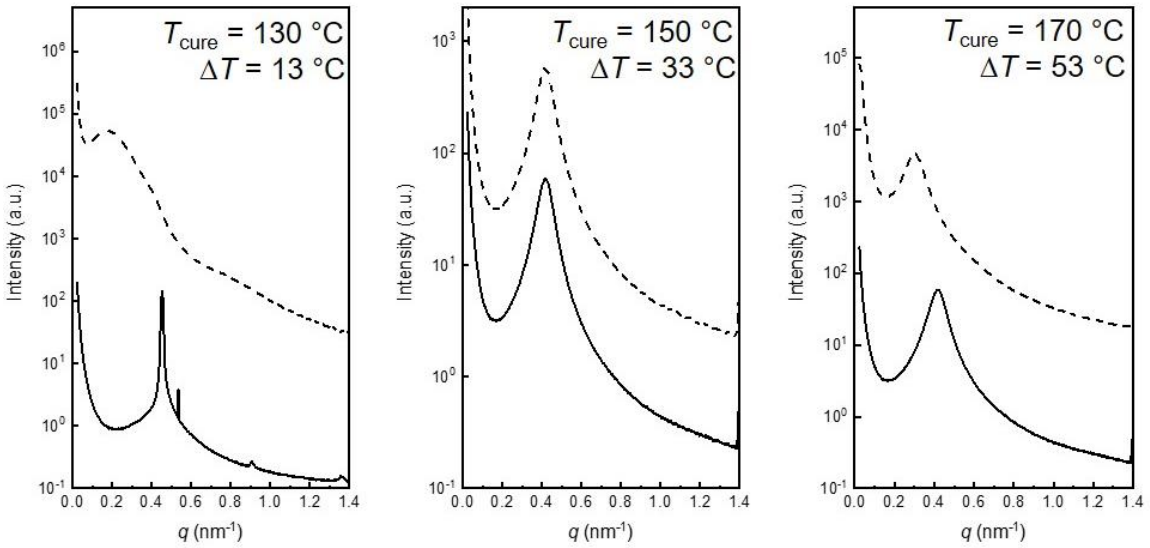

Figure 4.18. Room temperature SAXS patterns before (solid) and after (dashed) etching for SBL(0.42, 130) and 2 wt. % DCP blends cured at 130 °C, 150 °C, and 170 °C. Curing temperatures, T_{cure}, for each sample are indicated on each set of patterns. Curves have been vertically shifted for clarity.

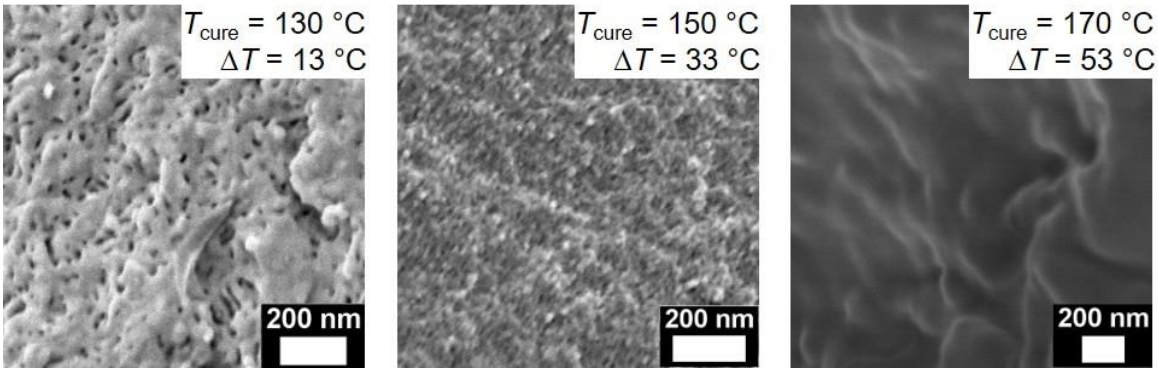

Figure 4.19. SEM images for etched SBL(0.42, 130) samples crosslinked using 2 wt. % DCP at 130 °C, 150 °C, and 170 °C. Curing temperatures, T_{cure}, for each sample are indicated on each micrograph. All samples were coated with approximately 3 nm of Pt prior to imaging.

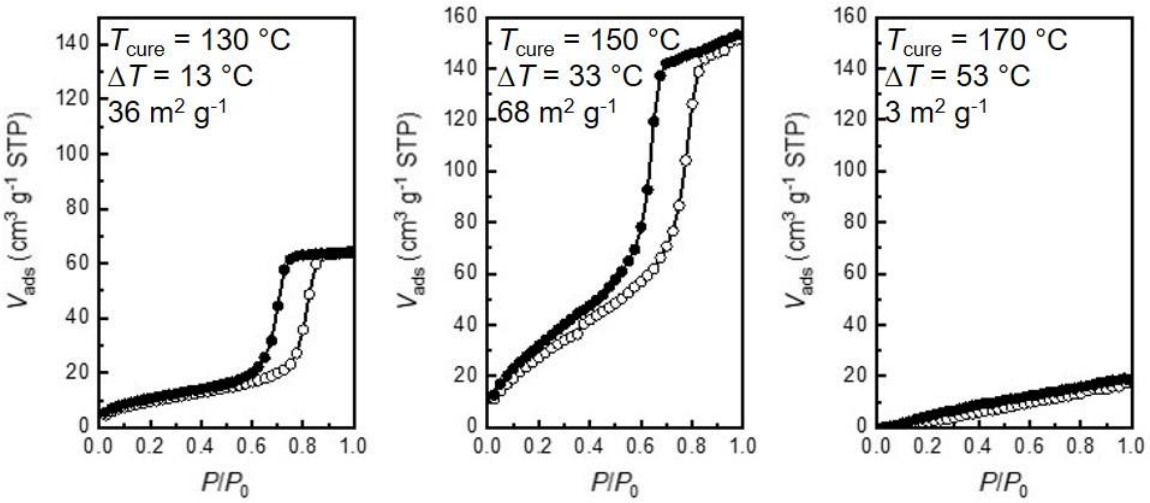

Figure 4.20. Nitrogen sorption isotherms obtained under adsorption (○) and desorption (●) for etched SBL(0.42, 130) samples crosslinked using 2 wt. % DCP at 130 °C, 150 °C, and 170 °C. Curing temperatures, T_{cure}, for each sample are indicated on each isotherm. The BET specific surface areas are indicated for each sample.

Despite the lack of a gel network, the etched material supports a porous monolith likely due to the glassy nature of the P(S-*s*-B) matrix, achieving a maximum porosity at 150 °C, while higher temperatures (T_{cure} = 170 °C, ΔT = 53 °C) led to an abrupt drop in porosity similarly noted in the 6 wt. % DCP case. Additionally, the pore mode as determined by QSDFT for these samples was nearly identical to those cross-linked using 6 wt.% DCP, indicating that DCP concentration (in the limit examined here) does not significantly influence the pore size distribution. On the other hand, greater DCP contents (≥ 10 wt. %) produced the highest gel fractions ($f_{gel} \geq 0.8$) but no pore structure after etching for all T_{cure}. Weak scattering in the SAXS profiles of samples formed using 10 wt. % DCP, both before and after etching, suggests a weakening of the compositional fluctuations present in the disordered state (Figure 4.21).[53] Non-selective partitioning of DCP in both domains likely lowered the segregation strength of the block polymer, which was then cross-linked in a homogenized state that produced no pore structure upon etching (Figures 4.22 and 4.23).[45]

Therefore, there is an apparent trade-off between using higher concentrations of peroxide to produce a gelled network and the arrest of a well-defined nanostructured state.

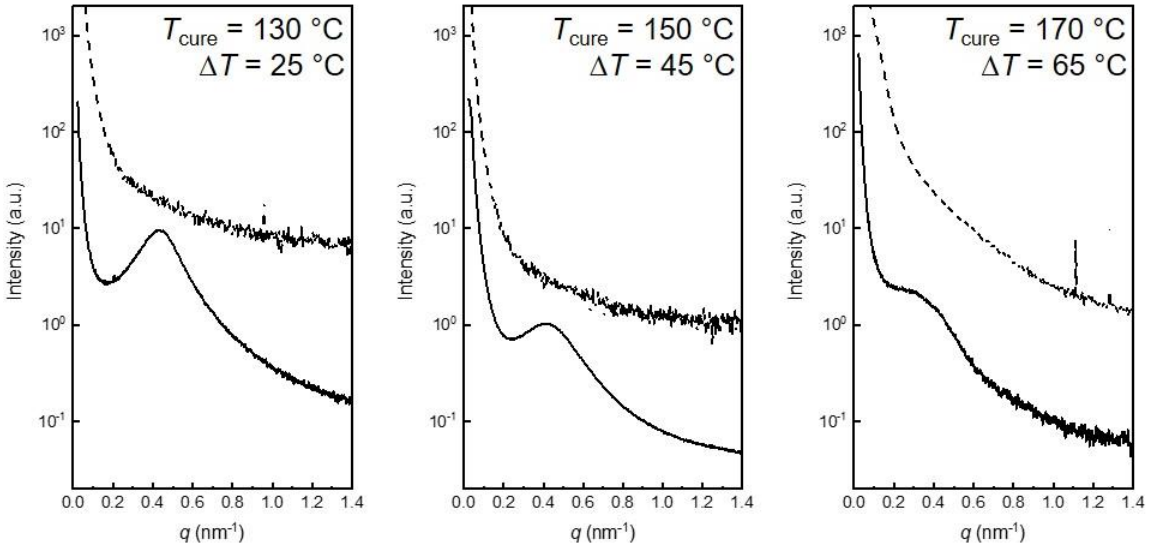

Figure 4.21. Room temperature SAXS before (solid lines) and after (dashed lines) etching for SBL(0.42, 130) and 10 wt. % DCP blends cured at 130 °C, 150 °C, and 170 °C. Curing temperatures, T_{cure}, for each sample are indicated on each set of patterns. Curves have been vertically shifted for clarity.

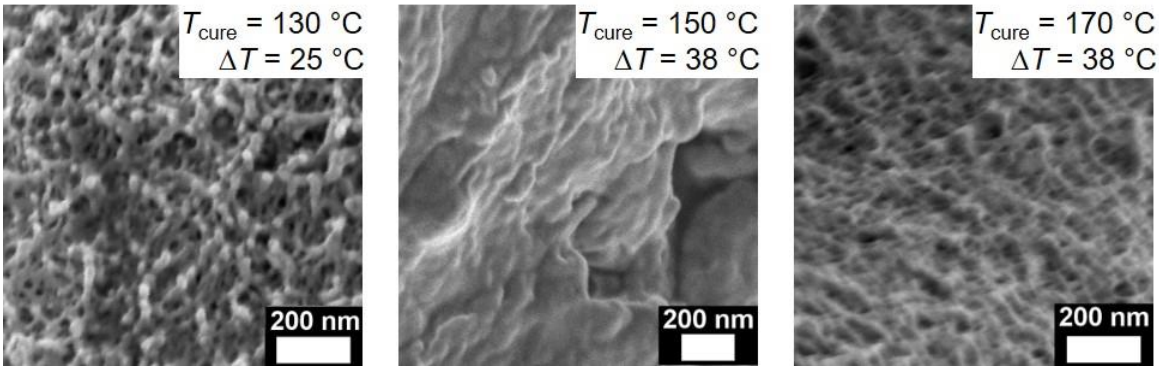

Figure 4.22. SEM images for etched SBL(0.42, 130) samples crosslinked using 10 wt. % DCP at (a) 130 °C, (b) 150 °C, and (c) 170 °C.

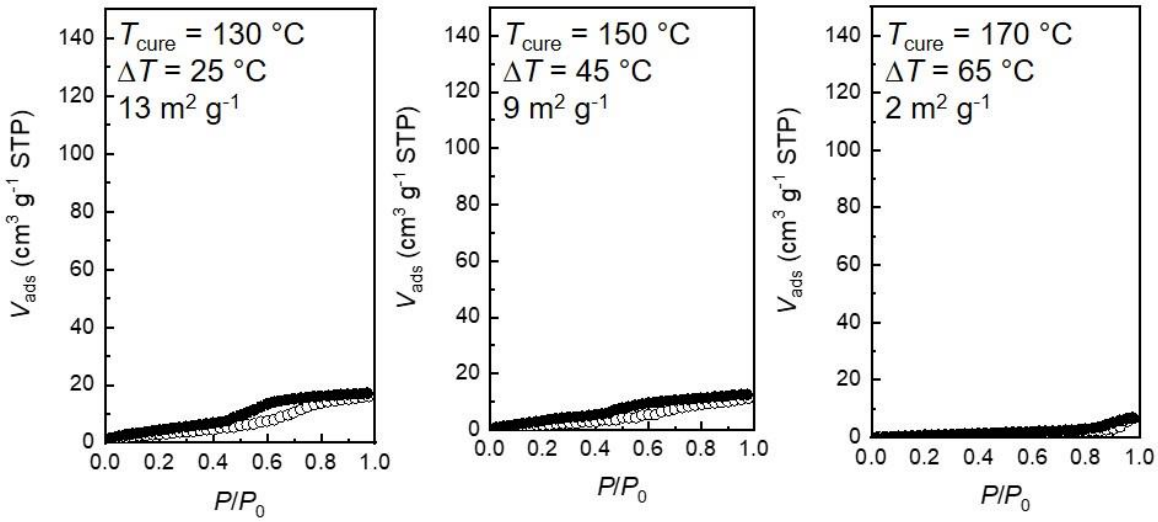

Figure 4.23. Nitrogen sorption isotherms obtained under adsorption (○) and desorption (●) for etched SBL(0.42, 130) samples crosslinked using 10 wt. % DCP at 130 °C, 150 °C, and 170 °C. Curing temperatures, T_{cure}, for each sample are indicated on each isotherm. The BET specific surface area is indicated for each sample.

4.3.4 Effect of Peroxide Chemistry

We further explored the generality of the radical curing strategy through the use of an alternative commercially available cross-linker, benzoyl peroxide (BPO), mixed at a 6 wt. % loading with SBL(0.42, 130). SAXS and SEC analyses indicate that the incorporation of BPO does not alter the morphology or molar mass distribution prior to curing. However, substitution of BPO in SBL(0.42, 130) at fixed mass concentration does significantly alter the segregation strength, reducing the T_{ODT} from 112 °C for the corresponding DCP mixture to 95 °C for SBL(0.42, 130)/6 wt. % BPO. In comparison to DCP, BPO exhibits a half-life that is roughly half the value of DCP (e.g., $t_{1/2}$ = 60 min for BPO (0.2 M in benzene) versus 130 min for DCP at 130 °C (0.2 M in decane)) and is conveniently also appropriate for cross-linking processes employed at lower temperature. Qualitatively, cured SBL(0.42, 130)/6 wt. % BPO products (T_{cure} = 75–170 °C) appear similar to samples produced using DCP. The SAXS pattern of the sample cured at 75 °C (below T_{ODT}) appears ordered with

a sharp maximum at $q^* = 0.46$ nm^{-1} (Figure 4.24), and accordingly, the collapsed lamellae are deemed nonporous (Figure 4.25). For T_{cure} = 115 °C (above T_{ODT}), the block polymer partially re-orders on cooling, as evinced by the strong scattering reflection at $q^* = 0.47$ nm^{-1} within the predominantly broad peak (Figure 4.24). Higher cure temperatures promote cross-linking reactions that adequately fix the disordered state on cooling to room temperature (Figure 4.24, solid curves). Etched materials typically display a local maximum in SAXS, indicative of a primary correlation length, and some low q scattering at larger length-scales (Figure 4.24, dashed curves). Corresponding SEM images (Figure 4.25) and nitrogen sorption analyses (Figures 4.16 and 4.26) support the formation of a disordered pore network that exhibits a steady increase in porosity with curing temperature up to 150 °C. Again, the pore mode for these materials as determined by QSDFT is nearly identical to those cross-linked with 6 wt.% DCP, suggesting that the pore size distribution is governed by the block polymer rather than the structure or reactivity of the peroxide cross-linking agent. As noted for the DCP samples, a consistent drop in porosity is observed for products cured *far* above T_{ODT} at 170 °C using BPO. The qualitatively similar results for both DCP and BPO cured samples supports the conclusion that the observed morphologies reflect an inherent thermodynamic structure rather than a kinetic phenomenon.

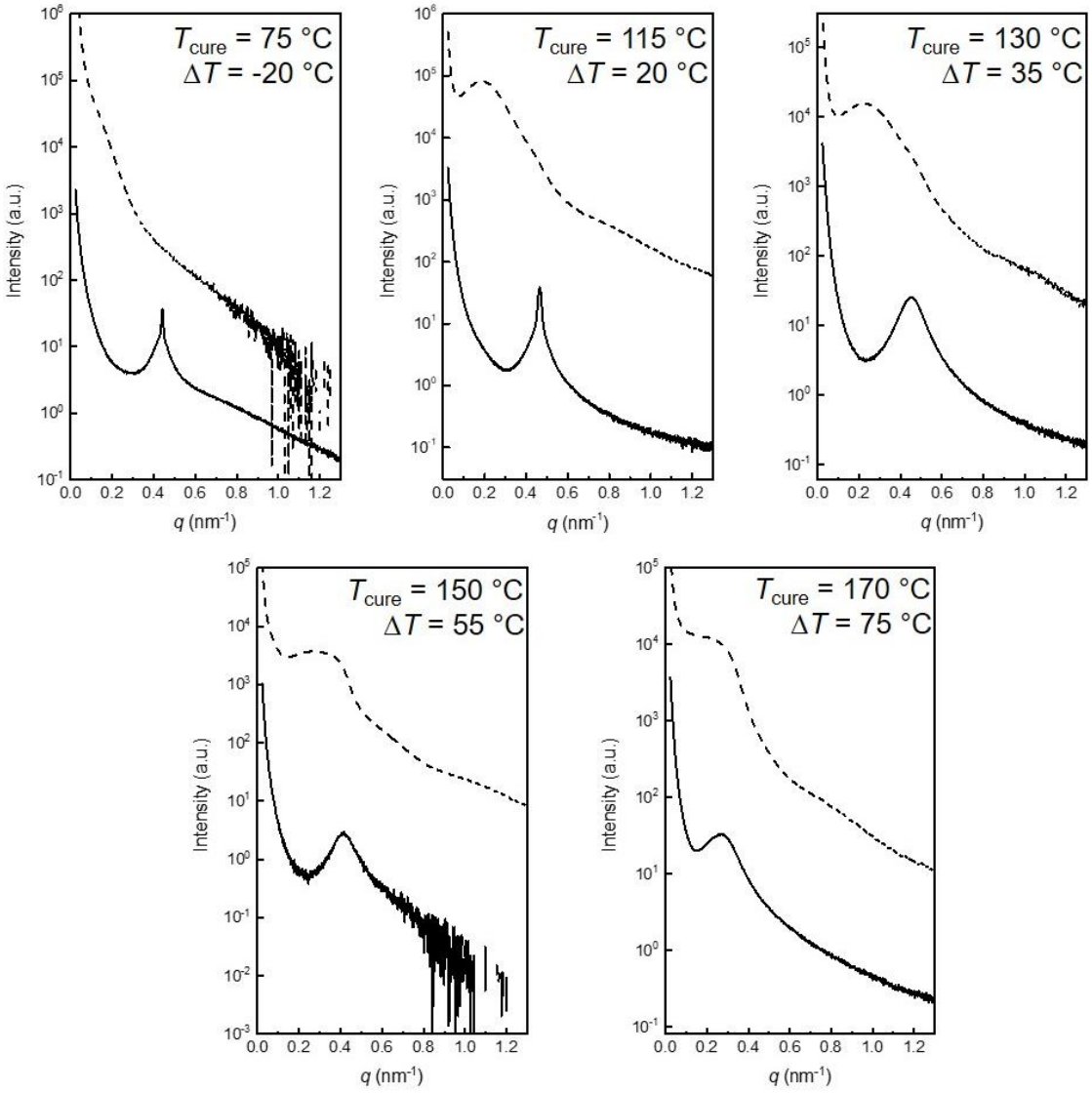

Figure 4.24. Room temperature SAXS patterns before (solid curves) and after (dashed curves) etching for SBL(0.42, 130) and 6 wt. % BPO blends cured at 75 °C, 115 °C, 130 °C, 150 °C, and 170 °C. Curing temperatures, T_{cure}, for each sample are indicated on each set of patterns. Curves are vertically shifted for clarity.

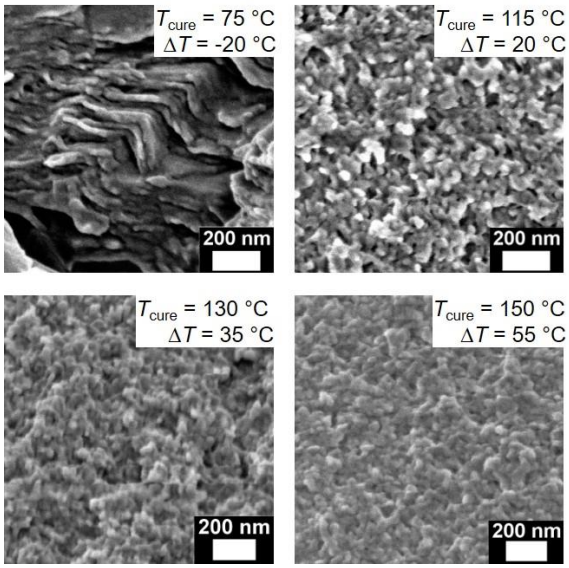

Figure 4.25. SEM images for etched SBL(0.42, 130) samples crosslinked using 6 wt. % BPO at 75 °C, 115 °C, 130 °C, and 150 °C. Curing temperatures, T_{cure}, for each sample are indicated on each micrograph. All samples were coated with ~3 nm of Pt prior to imaging.

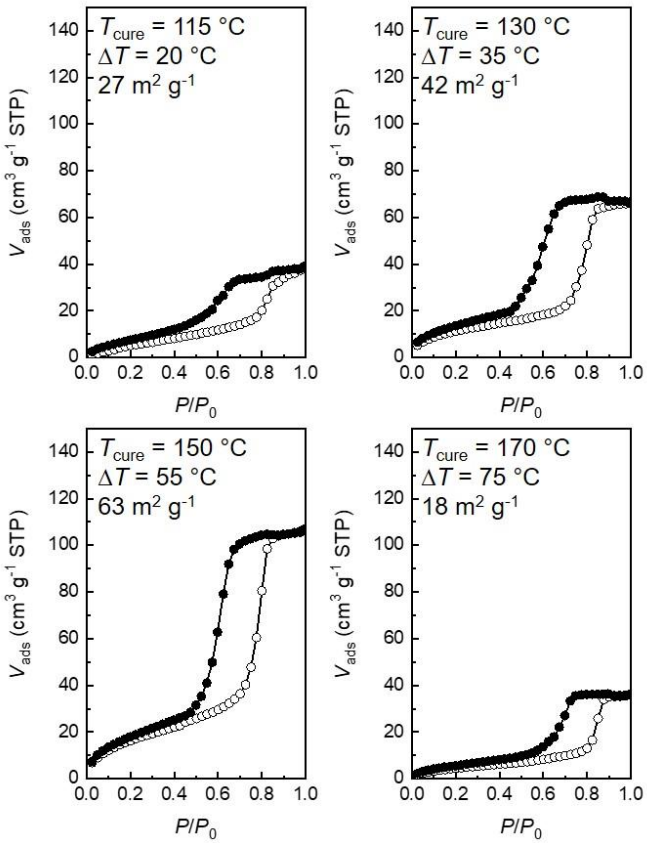

Figure 4.26. Nitrogen sorption isotherms obtained under adsorption (○) and desorption (●) for etched SBL(0.42, 130) samples crosslinked using 6 wt. % BPO at 115 °C, 130 °C, 150 °C, and 170 °C. Curing temperatures, T_{cure}, for each sample are indicated on each isotherm.

A non-monotonic dependence of cross-linking efficiency on temperature has been previously elucidated in peroxide curing of unsaturated polymers.[55] In such systems, there is an ultimate decline in the reactions that produce cross-links due to hydrogen abstraction and an increased termination of the chain reactions propagating through the double bond, leading to a designated *highest efficiency temperature* (HET). We speculate that similar phenomena give rise to the non-monotonic temperature dependence observed in peroxide cured SBL. Optimal domain connectivity and pore stabilities are consistently achieved in SBL samples cured at 150 °C, revealing a unique system parameter akin to the HET of conventional peroxide systems. While the location of the HET is unique to a peroxide-polymer pair,[53] optimal porosity with respect to temperature does not seem to vary with concentration (i.e., for < 10 wt. %) or identity of the peroxide for a particular SBL diblock. Furthermore, despite BPO generally demonstrating a lower cross-linking efficiency than DCP in the literature, the present results suggest that BPO produces comparably porous materials, thereby augmenting the available palette of functional peroxides.

4.3.5 Effect of Block Polymer T_{ODT}

Three additional SBL block polymers synthesized from the same macromolecular SB precursor were prepared to probe the influence of PLA molar mass. A longer PLA block resulted in a higher f_{PLA} and correlated with a considerable increase in the order-disorder transition temperature (T_{ODT} = 180 °C) for the pristine block polymer SBL(0.45, 180) (Figure 4.27). Mixing this block polymer with DCP at 6 wt. % required high curing temperatures above 170 °C (the T_{ODT} for the block polymer-peroxide blend by SAXS, Figure 4.28) to arrest a disordered but microphase-separated state, according to similar

SAXS (Figure 4.29) and SEM (Figure 4.30) analyses. However, nitrogen sorption measurements indicated unexpectedly low pore volumes (≤ 0.07 cm^3 g^{-1}) and BET surface areas (≤ 20 m^2 g^{-1}) for all curing temperatures (Figure 4.31). Importantly, we note that curing temperatures within the disordered state (180–210 °C) for SBL(0.45, 180) exceed the temperature of optimal porosity found in SBL(0.42, 130)/DCP mixtures (ca. 150 °C). Furthermore, it is possible the rapid decomposition of DCP at 170 °C (ca. $t_{1/2} \approx 2$ min) adversely influences the properties of the final product by chemically fixing the block polymer prior to equilibration as a disordered melt at T_{cure}. Despite $\leq 5\%$ mass loss under the curing conditions employed (Figure 4.17), the reduced porosity may also demonstrate that high curing temperatures, in general, sacrifice material integrity,[55] leading to decreased pore connectivity and/or pore collapse.

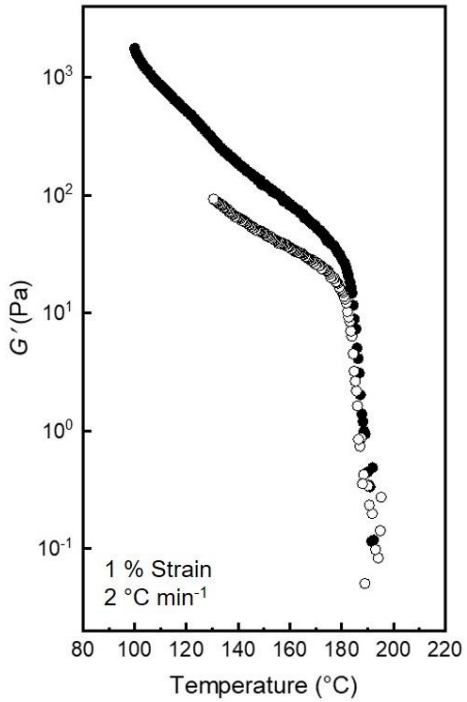

Figure 4.27. (a) Temperature dependence of the storage modulus for SBL(0.45, 180) (1 rad s^{-1}, 1% strain, and 2 °C min^{-1}) on heating (●) and on cooling (○). A precipitous drop in G' around 180 °C indicates the onset of the order-disorder transition.

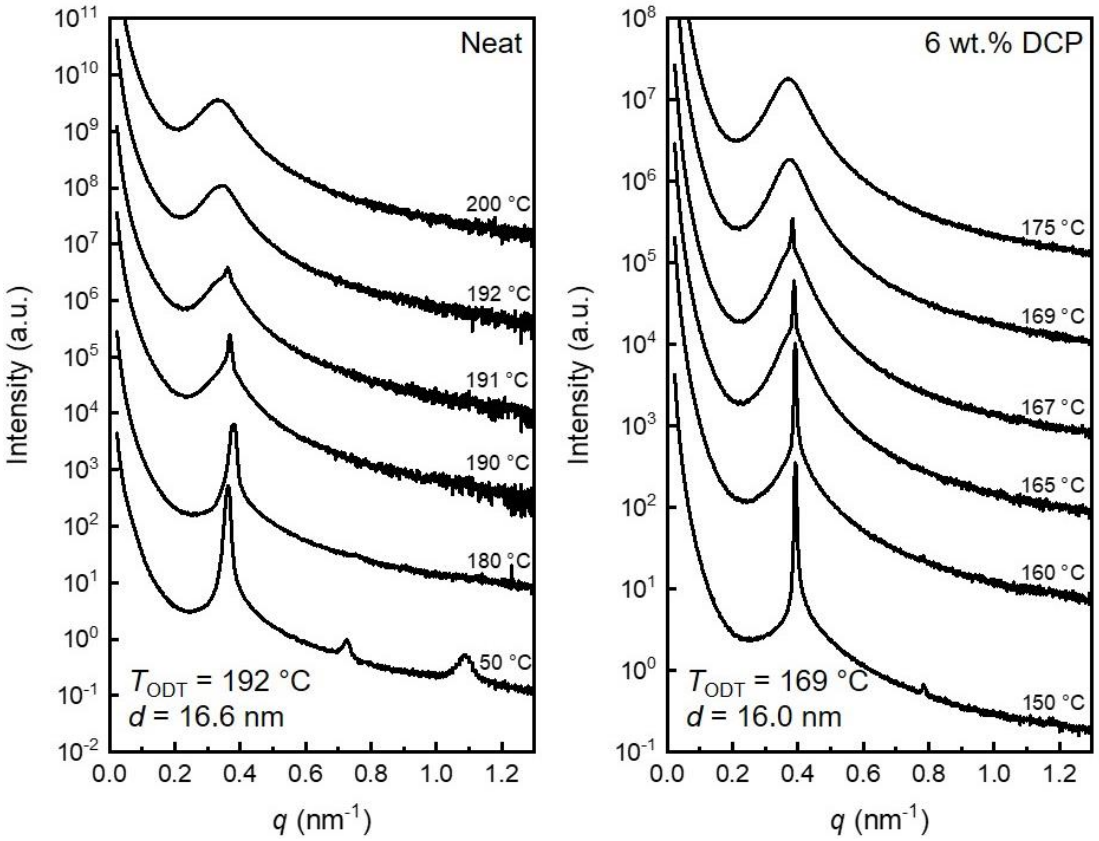

Figure 4.28. Variable temperature SAXS data for (a) SBL(0.45, 180) and (b) SBL(0.45, 180) containing 6 wt.% DCP acquired after thermal equilibration at each temperature for 2 min. The samples were annealed for 1 hour at 80 °C prior to measurement. The T_{ODT}'s were determined to be 192 °C for the neat polymer and 169 °C for the DCP containing polymer based on the widening of the principal scattering peak.

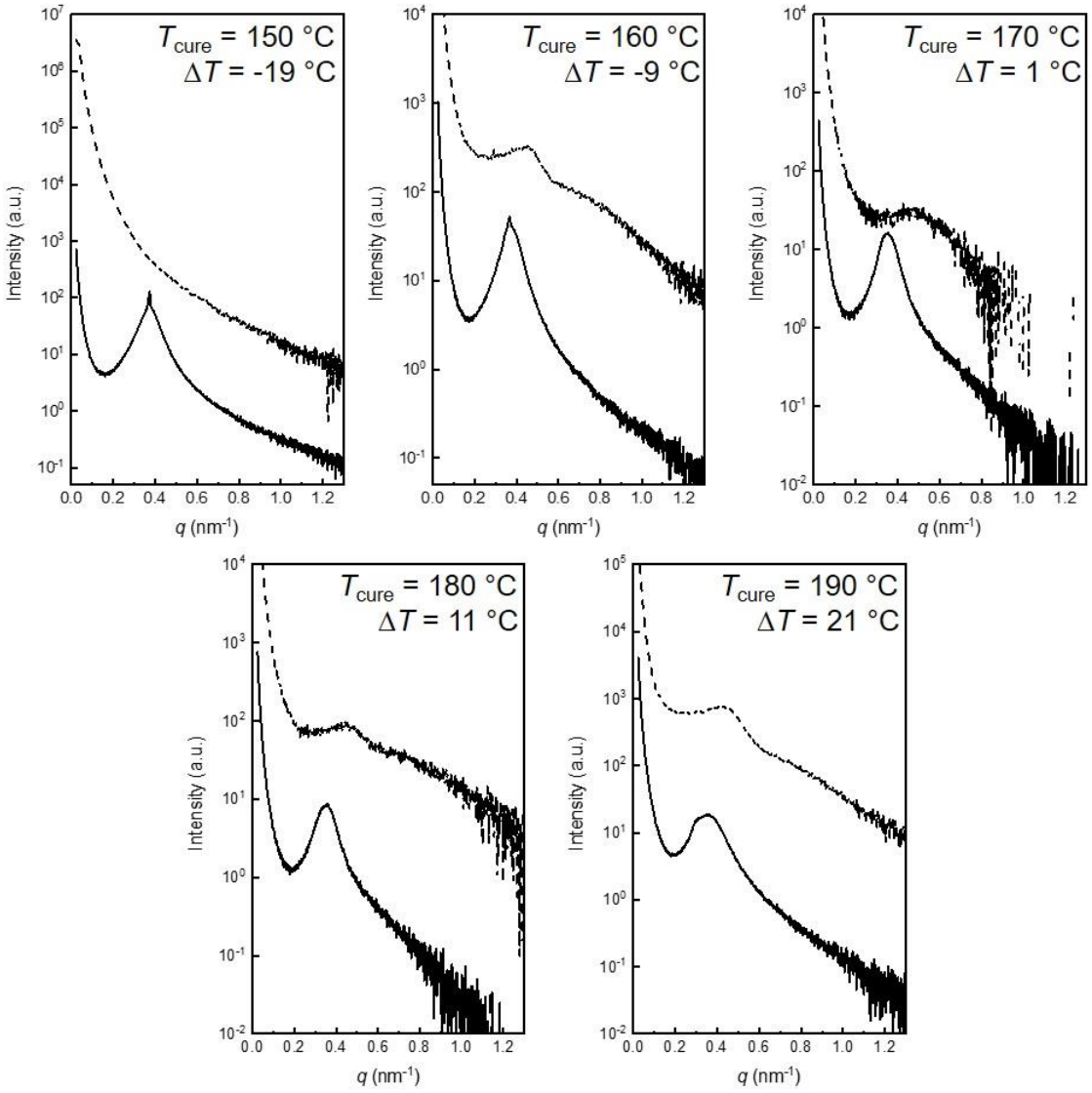

Figure 4.29. Room temperature SAXS patterns before (solid curves) and after (dashed curves) etching for SBL(0.45, 180) and 6 wt. % DCP blends cured at 150 °C, 160 °C, 170 °C, 180 °C, and 190 °C. Curing temperatures, T_{cure}, for each sample are indicated on each set of patterns. Curves are vertically shifted for clarity.

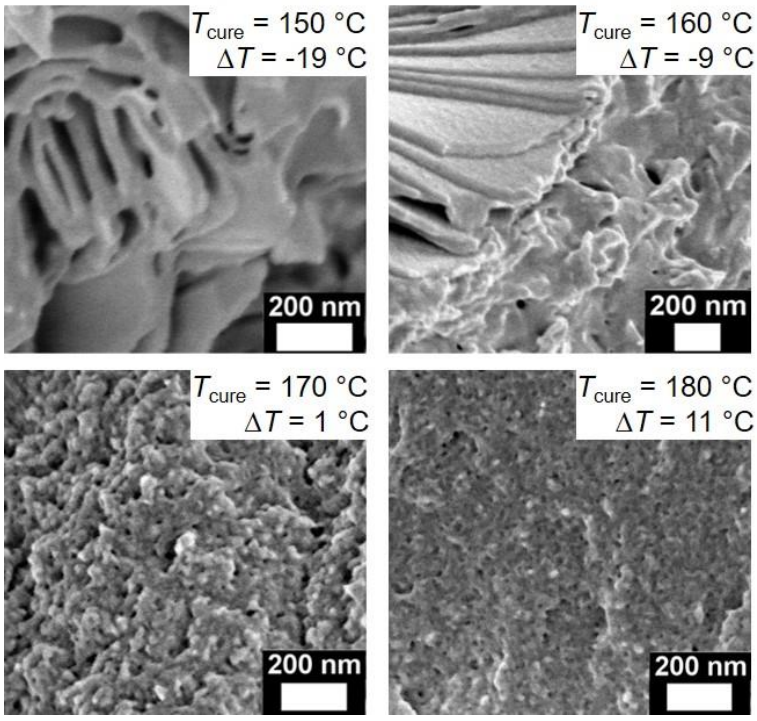

Figure 4.30. Representative SEM micrographs for etched SBL(0.45, 180) samples cured using 6 wt. % DCP at 150 °C, 160 °C, 170 °C, and 180 °C. Curing temperatures, T_{cure}, for each sample are indicated on each micrograph. All samples were sputter coated with approximately 3 nm of Pt prior to imaging.

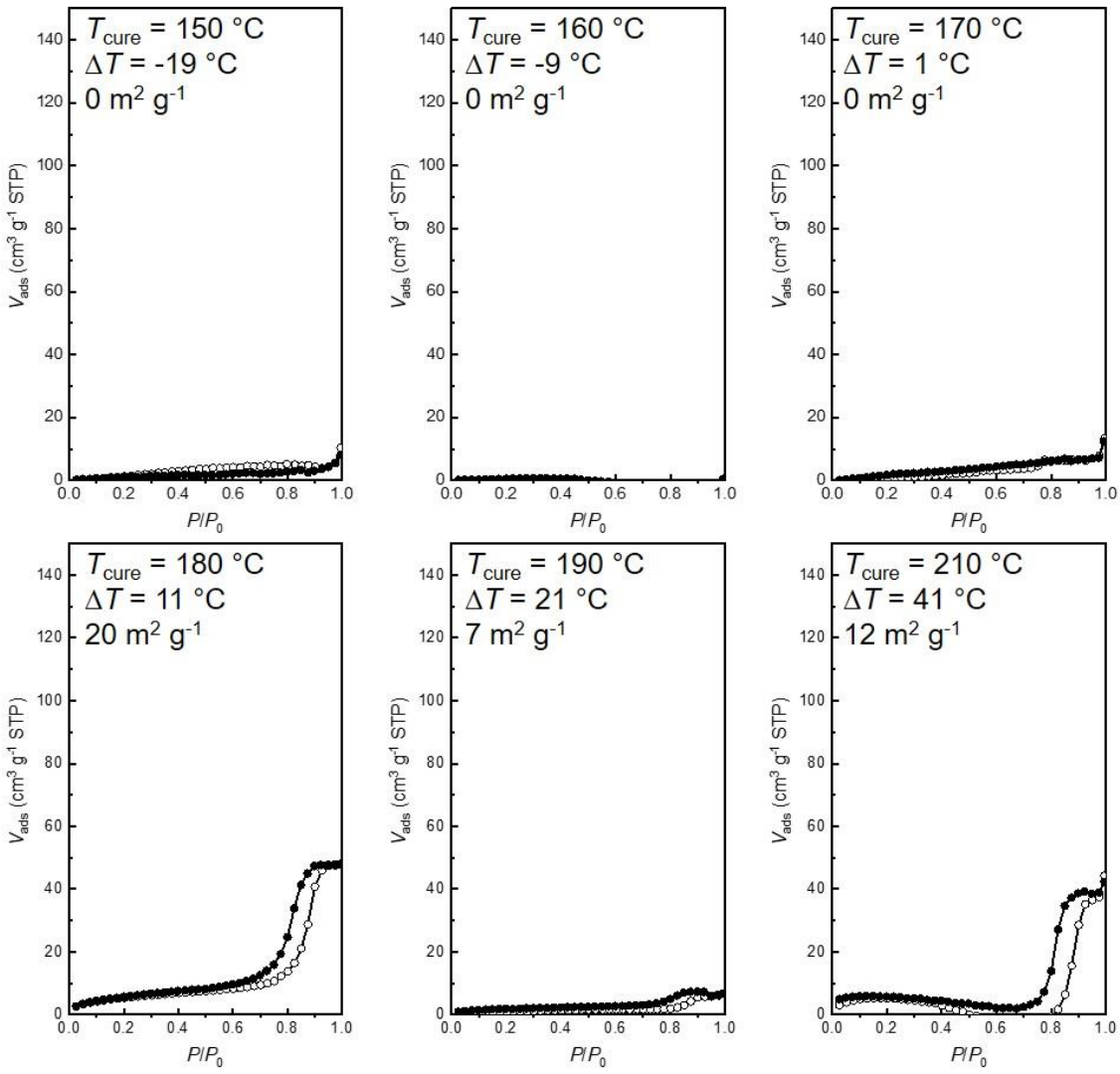

Figure 4.31. Nitrogen sorption isotherms obtained under adsorption (○) and desorption (●) for SBL(0.45, 180) cured using 6 wt. % DCP at 150 °C, 160 °C, 170 °C, 180 °C, 190 °C, and 210 °C. Curing temperatures, T_{cure}, for each sample are indicated on each isotherm. The BET specific surface area for each sample is indicated.

SBL(0.36, 115), a block polymer of lower PLA molar mass, exhibited a shift in the nominal T_{ODT} from 120 °C to 90 °C with the addition of 6 wt. % BPO (Figures 4.32 and 4.33). In contrast to SBL(0.45, 180), the low T_{ODT} of this shorter diblock rendered the use of DCP kinetically infeasible, requiring $t_{cure} \geq 300$ h at 90 °C.[38] Comparison of the cured and etched SAXS profiles indicated an improved preservation of the disordered microstructure with minimal low-angle scattering below q^* after etching for curing temperatures ≥ 100 °C,

Figure 4.34. Accordingly, small pores remain evident in the SEM micrographs (Figure 4.35) and sorption isotherms (Figure 4.36) until a precipitous drop in porosity is achieved for T_{cure} = 190 °C, revealing a similar temperature dependence as previously discussed in the other starting materials explored. In spite of the reduced efficiency of BPO established in network curing in the literature, the highest porosities are achieved using BPO as a cross-linker, reaching a total pore volume of 0.34 $cm^3\ g^{-1}$ and surface area of 128 $m^2\ g^{-1}$ at 170 °C (Figure 4.16). Interestingly, the pore mode for the samples prepared from SBL(0.36, 115) and 6 wt.% BPO was rather similar to the pore mode from SBL(0.42, 130) and 6 wt.% DCP. However, it is important to note that these two diblock polymers are of comparable molar mass (7.0 and 7.8 kg mol^{-1}, respectively) despite having rather different T_{ODT}'s. Larger variations in the composition of the P(S-*s*-B)-OH macroinitiator and the molar mass of the product block polymer are expected to lead to larger differences in the pore size distribution, in accordance with our previous results.[12, 30] The combined results suggest that the chemical identity of the cross-linker is perhaps secondary to other factors of the system such as location of the pristine block polymer T_{ODT} in further improving the porous properties of the matrix.

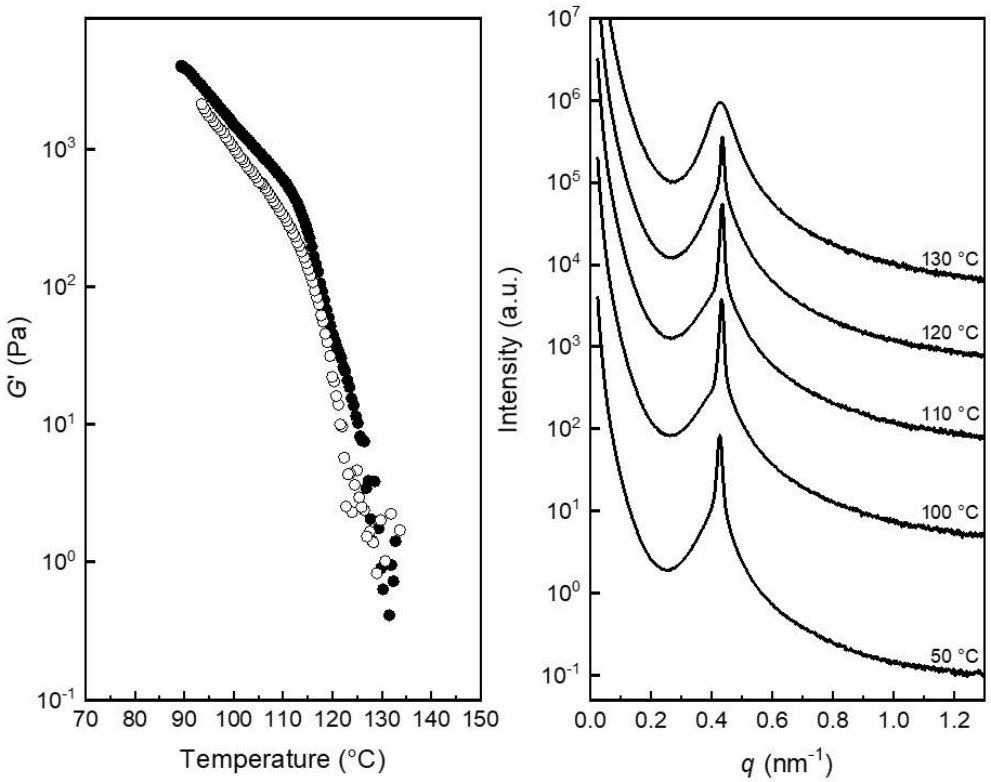

Figure 4.32. (a) Temperature dependence of the storage modulus for SBL(0.36, 115) (1 rad s^{-1}, 1 % strain, and 2 °C min^{-1}) on heating (●) and on cooling (○). A precipitous drop in G' around 115 °C indicates the onset of the order-disorder transition. (b) Variable temperature SAXS data acquired after thermal equilibration at each temperature for 2 min. The sample was annealed for 1 hour at 80 °C prior to measurement. The T_{ODT} was determined to be approximately 120 °C based on the broadening of the principal scattering peak.

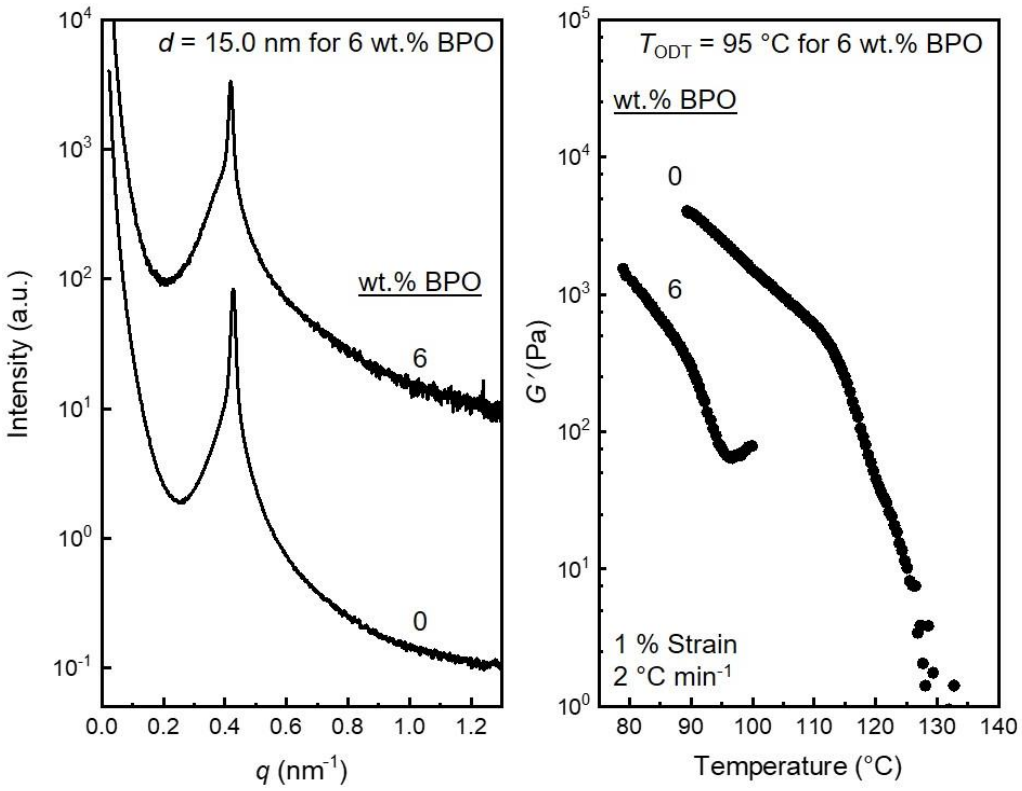

Figure 4.33. (a) Room temperature SAXS patterns and (b) temperature dependence of the storage modulus for neat SBL(0.36, 115) and a 6 wt. % BPO blend obtained after annealing for 1 hour at 80 °C.

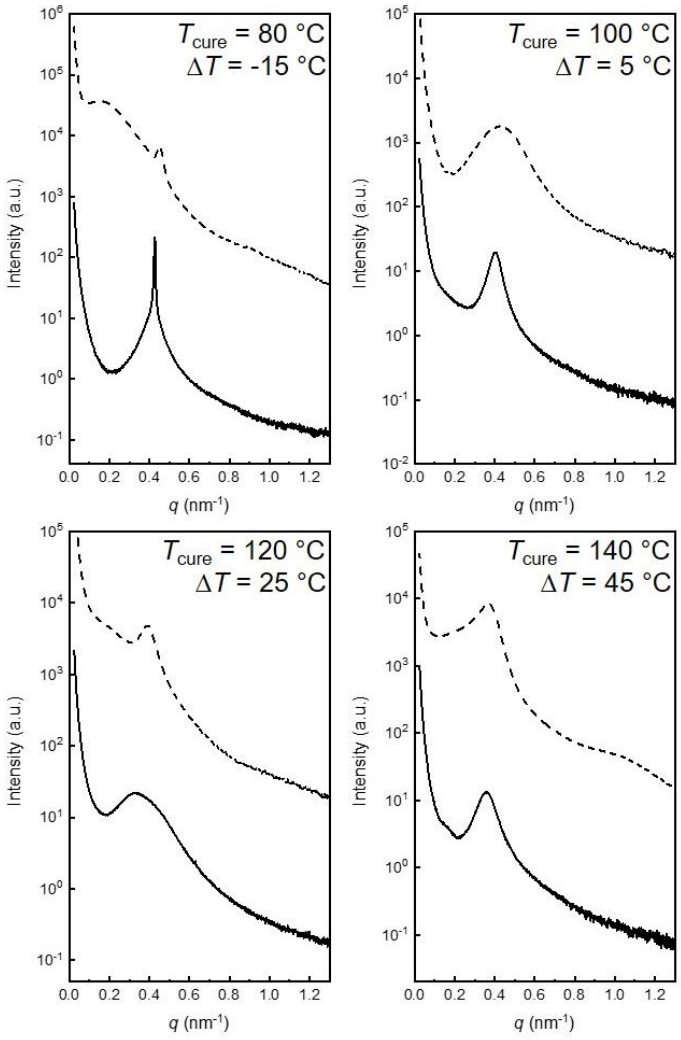

Figure 4.34. Room temperature SAXS patterns before (solid curves) and after (dashed curves) etching for SBL(0.36, 115) and 6 wt. % BPO blends cured at 80 °C, 100 °C, 120 °C, and 140 °C. Curing temperatures, T_{cure}, for each sample are indicated for each set of patterns. Curves are vertically shifted for clarity.

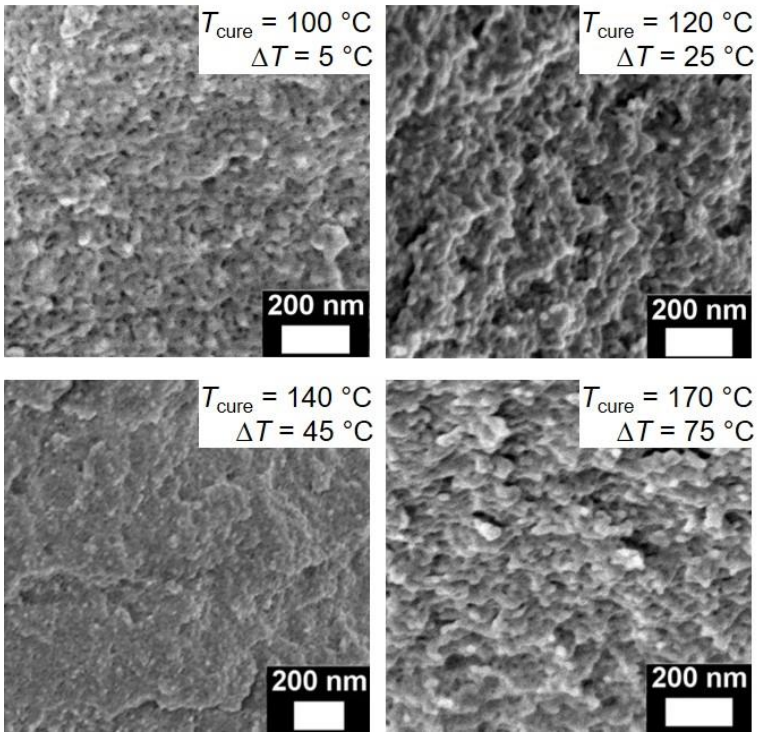

Figure 4.35. Representative SEM images for etched SBL(0.36, 115) samples cured using 6 wt. % BPO at 100 °C, 120 °C, 140 °C, and 170 °C. Curing temperatures, T_{cure}, for each sample are indicated on each micrograph. All samples were coated with approximately 3 nm of Pt prior to imaging.

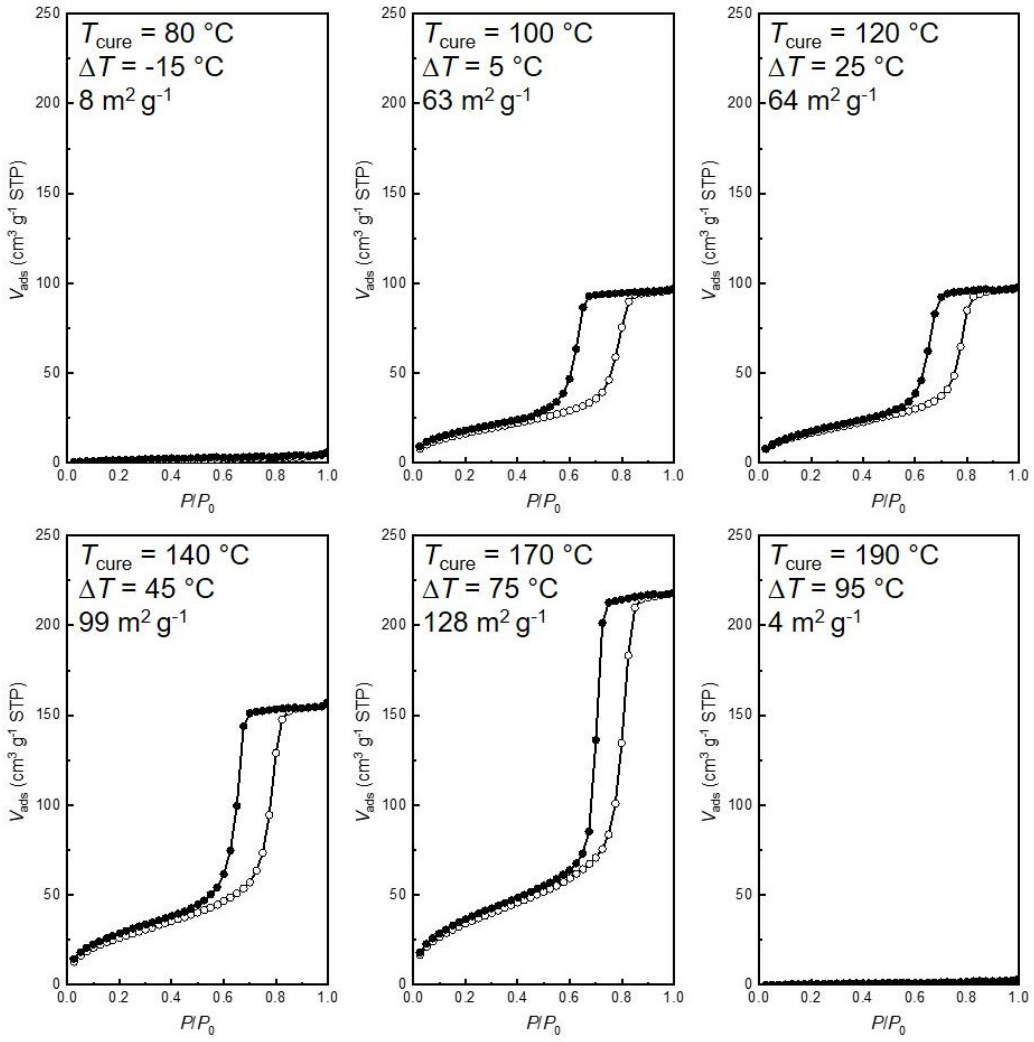

Figure 4.36. Nitrogen sorption isotherms obtained under adsorption (○) and desorption (●) for SBL(0.36, 115) cured using 6 wt. % BPO at 90 °C, 100 °C, 120 °C, 140 °C, 170 °C, and 190 °C. Curing temperatures, T_{cure}, for each sample are indicated on each isotherm. The specific BET surface area of each sample is indicated.

To determine whether self-assembly into a long-range ordered lamellar morphology at ambient temperature is a necessary condition to achieve porous materials after cross-linking and etching, a disordered diblock polymer with no observable T_{ODT} from SAXS and DMA, SBL(0.34, dis), was explored (Figure 4.37). Monoliths prepared from SBL(0.34, dis) cross-linked with 6 wt.% BPO displayed rather high BET surface areas (123 m^2 g^{-1} at 105 °C) despite lacking adequate segregation strength to induce ordering at room

temperature (Figure 4.38). However, we suspect that if the segregation strength of a given diblock is too low ($\chi N << (\chi N)_{ODT}$) due to a combination of high curing temperature and/or low molar mass, porous materials would not be obtainable as the requisite continuous domains would likely not form in a mean-field homogeneous state. The observed decrease in porosity for SBL(0.42, 130)/6 % DCP cross-linked at 190 °C and for SBL(0.38, 115)/6% BPO cross-linked at 170 °C may possibly reflect a transition to such a state given the very low segregation strengths, although the possibility of thermal degradation should be recognized.

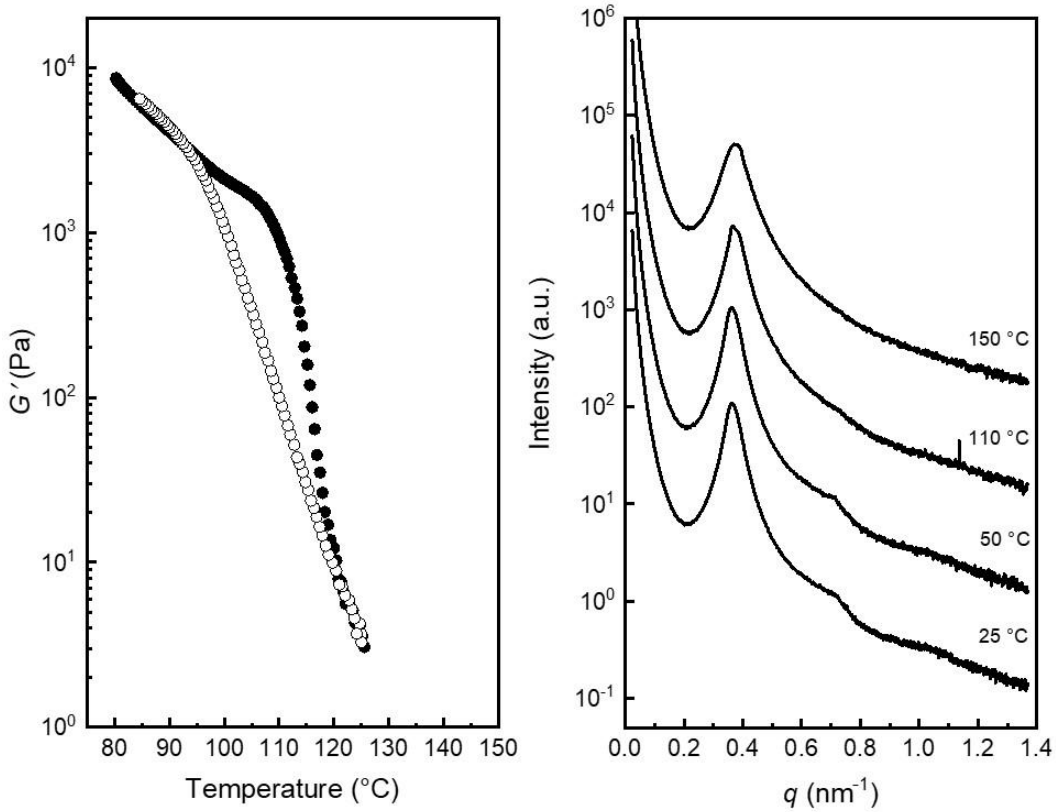

Figure 4.37. (left) Temperature dependence of the storage modulus for SBL(0.34, dis) (1 rad s^{-1}, 1 % strain, and 2 °C min^{-1}) on heating (●) and on cooling (○). No precipitous drop in G' was observed indicating that the sample did not undergo an the order-disorder transition. (right) Variable temperature SAXS data acquired after thermal equilibration at each temperature for 2 min. The sample was annealed for 1 hour at 80 °C prior to measurement.

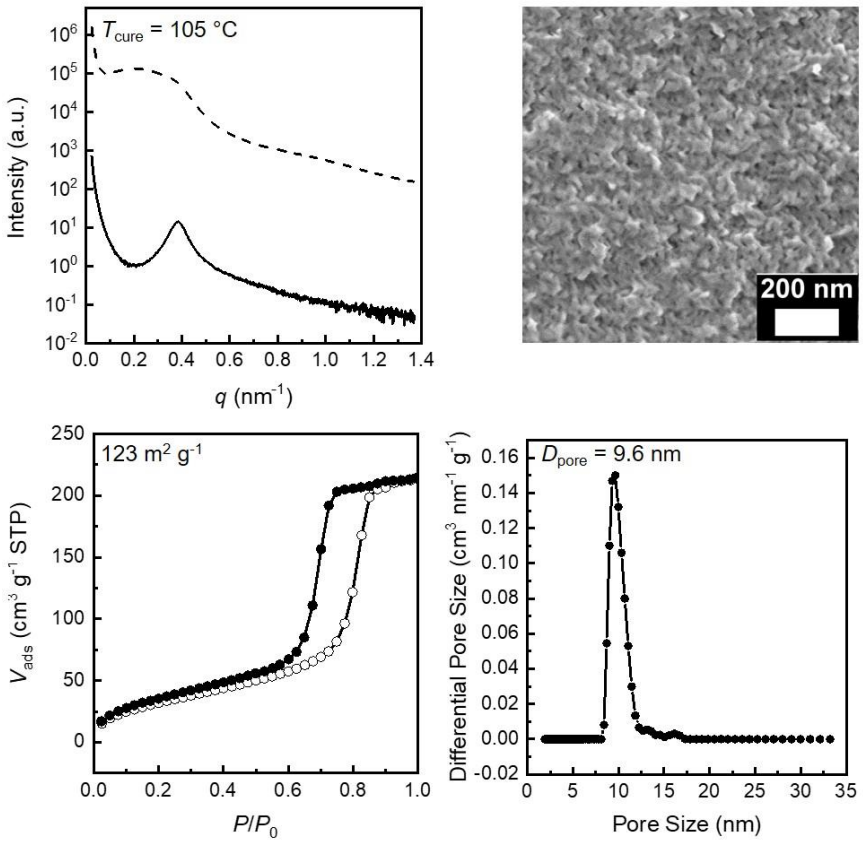

Figure 4.38. Small angle X-ray scattering patterns (top left panel) for SBL(0.34, dis) cross-linked at 105 °C with 6 wt.% BPO before (solid curve) and after (dashed curve) etching. Representative SEM image (top right panel), nitrogen sorption isotherm (bottom left panel), and QSDFT pore size distribution (bottom right panel) for the same sample after etching. BET specific surface is included with the isotherm and QSDFT pore mode is included with the pore size distribution

4.3.6 UF Membrane Fabrication

The materials described thus far employed a low-temperature and solution-based casting protocol to incorporate a thermally active peroxide, enabling advantageous control of the pore size and pore size distribution predominantly through the pre-formed characteristics of the block polymer (i.e., molar mass and chemical composition) cured upon heating into the disordered state. We chose to demonstrate the versatility and technological potential of these materials in thin films (< 200 nm thickness), exploiting the nanoscale pores and narrow pore size distributions as a highly selective ultrafiltration membrane as compared

to commercial NIPS membranes[56-57]. To produce the thin film, a 2 wt. % solution of SBL(0.42, 130) and 6 w/w % DCP in chlorobenzene was spin coated onto a water-filled commercial polyethersulfone (PES) support[39-40] and subsequently cured at 150 °C. After selective removal of the PLA, SEM images of the composite membrane obtained in cross-section indicated an effective film thickness of approximately 150 nm for the deposited layer (Figure 4.39). Top-view SEM images of the bare PES support and the composite surface are presented in Figure 4.39. Additional surface coverage and small pores from the block polymer coating are visible within the larger pores of the PES support.

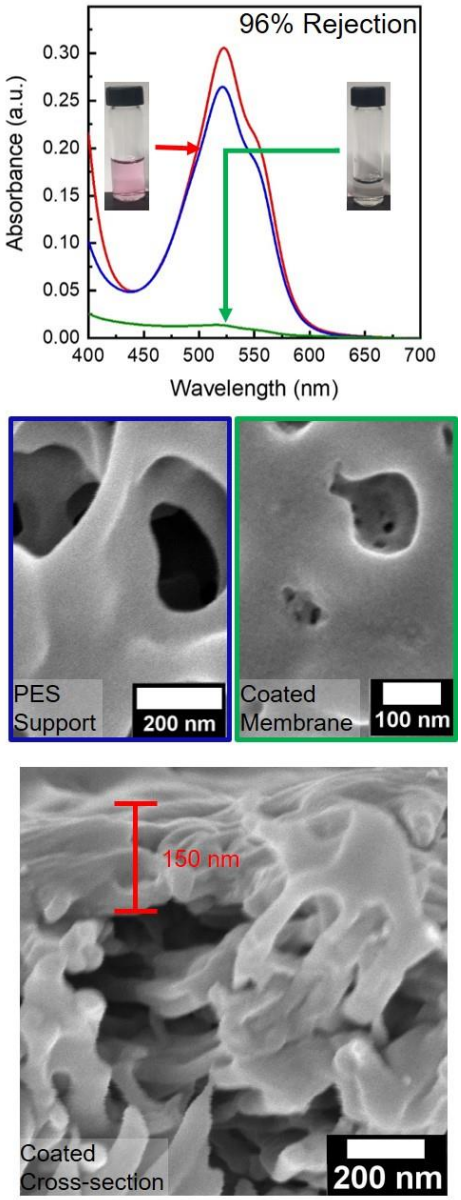

Figure 4.39. Characterization of the composite membrane formed using a 2 wt. % solution of SBL(0.42, 130) (6 w/w % DCP) spin-coated on top of a macroporous PES support and cured at 150 °C. UV-vis absorbance (top panel) of a feed solution (red curve) comprising a fluorescent TRITC-dextran (0.5 mg cm^{-3}, M = 150 kg mol^{-1}, R_h ~ 7 nm) and the corresponding filtrate after passing the feed solution through the bare PES support (blue curve) and the composite membrane (green curve).TRITC-dextran rejection for the composite membrane is established based on 96% solute rejection calculated using the relative absorbance of the feed and filtrate solutions at 521 nm. Photographs of the feed and the filtrate solutions are included in the insets of the top panel. Top-view SEM images contrast (middle left panel, blue border) the bare PES support and (middle right panel, green border) the nanoporous composite membrane after removal of the PLA domain. A cryo-fractured cross-section of the nanoporous composite membrane displayed a selective layer that was approximately 150 nm thick (bottom panel).

Based on linear fits of measured water flux versus transmembrane pressure, the nanoporous layer significantly reduced the hydraulic permeability from 3700 L m^{-2} h^{-1} bar^{-1} for the PES support to 10 L m^{-2} h^{-1} bar^{-1} (Figure 4.40). This permeability is lower than the expected 2000 L m^{-2} h^{-1} bar^{-1} based on the Hagen-Poiseuille equation for the selective layer thickness, pore diameter, and porosity (f_{PLA}) observed here. This discrepancy may indicate that the solution processing method and thermal cross-linking conditions employed may have adversely affected the porosity of the underlying PES support, particularly at the [selective layer]/[support layer] interface, effectively reducing the permeability. Indeed, exposure of the bare PES support to chlorobenzene resulted in an approximate five-fold decrease in water permeability from 3700 to 700 L m^{-2} h^{-1} bar^{-1}. Further developments in the design of the coating and curing processes may result in improved permeability. To demonstrate the size selectivity of the composite membrane, we measured the retention of a solution of TRITC-dextran, a fluorescently labelled polysaccharide with a hydrodynamic radius, $R_h \approx 7$ nm, greater than the average pore radius, ~ 4 nm), estimated from QSDFT analysis of the corresponding monolithic sample. UV−vis analysis of the filtrate passed through the membrane demonstrated near-complete rejection (96 %, Figure 4.39), thereby illustrating the potential of the produced co-continuous and porous network to serve as a selective layer for ultrafiltration.

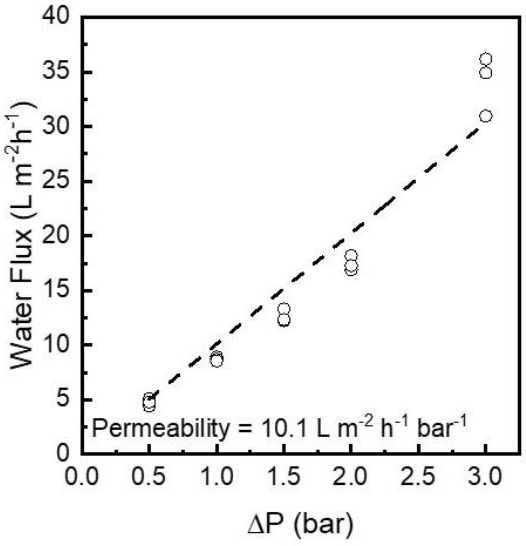

Figure 4.40. Pure water flux versus pressure drop measured across a thin porous layer (150 nm) formed from SBL(0.42, 130) cured using 6 wt. % DCP at 150 °C atop a PES support. Flux measurements were performed in triplicate. The hydraulic permeability corresponds to the slope of the linear regression (dashed line).

4.4 Conclusions

In this work, we examined the utility of a radical curing process to chemically fix block polymers in the disordered state at elevated temperatures near T_{ODT}. The porosity of SBL networks produced after thermal cross-linking of the P(S-*s*-B) domains and subsequent hydrolysis of the PLA domain was investigated and shown to have a strong dependence on the reaction conditions, particularly the curing temperature and the peroxide concentration. Sensitivity of the block polymer segregation strength to peroxide loading was demonstrated for a series of lamellar-forming block polymers, with a reproducible trend of decreasing T_{ODT} as DCP or BPO concentration increased. Nanostructured bicontinuous thermosets were formed via cross-linking at temperatures above T_{ODT}. Increases in BET specific surface area were observed for both BPO and DCP cured networks for curing temperatures up to 150 °C, while the pore size mode was generally consistent with the domain spacing of the uncross-linked precursor. Due to their narrow pore size distribution, these systems

could potentially be useful for ultrafiltration, which was highlighted via the formation of a composite membrane. The bicontinuous and cross-linked surface layer of etched SBL deposited on a PES support provided excellent solute rejection. Overall, this study indicates that the disordered state is well-segregated and bicontinuous. Cross-linking the structure of the disordered melt provides a new material strategy with readily generalizable chemistry tolerant of a diverse array of cross-linkable functionalities, including unsaturation. Revamping the view of disordered block polymers and their utility will have profound impact in both practical applications and in the fundamental understanding of the disordered state.

4.5 References

1) Allen, S. D.; Bobbala, S.; Karabin, N. B.; Scott, E. A., On the advancement of polymeric bicontinuous nanospheres toward biomedical applications. *Nanoscale Horizons* **2019**. *4*, 258-272.

2) Zhang, Q.; Huang, S.-Z.; Jin, J.; Liu, J.; Li, Y.; Wang, H.-E.; Chen, L.-H.; Wang, B.-J.; Su, B.-L., Engineering 3D bicontinuous hierarchically macro-mesoporous LiFePO4/C nanocomposite for lithium storage with high rate capability and long cycle stability. *Scientific Reports* **2016,** *6*, 25942.

3) Lu, G. Q.; Zhao, X. S., Nanoporous Materials - Science and Engineering. World Scientific.

4) Ulbricht, M., Advanced functional polymer membranes. *Polymer* **2006,** *47*, 2217-2262.

5) Peinemann, K.; Abetz, V.; Simon, P. F. W.. Asymmetric Superstructure Formed in a Block Copolymer via Phase Separation. *Nature Materials* **2007**, *6*, 992-996.

6) Meuler, A. J.; Hillmyer, M. A.; Bates, F. S., Ordered Network Mesostructures in Block Polymer Materials. *Macromolecules* **2009,** *42*, 7221-7250.

7) Bates, C. M.; Bates, F. S., 50th Anniversary Perspective: Block Polymers—Pure Potential. *Macromolecules* **2017,** *50*, 3-22.

8) Seo, M.; Hillmyer, M. A., Reticulated Nanoporous Polymers by Controlled Polymerization-Induced Microphase Separation. *Science* **2012,** *336*, 1422-1425.

9) Saba, S. A.; Mousavi, M. P. S.; Bühlmann, P.; Hillmyer, M. A., Hierarchically Porous Polymer Monoliths by Combining Controlled Macro- and Microphase Separation. *Journal of the American Chemical Society* **2015,** *137*, 8896-8899.

10) Saba, S. A.; Lee, B.; Hillmyer, M. A., Tricontinuous Nanostructured Polymers via Polymerization-Induced Microphase Separation. *ACS Macro Letters* **2017,** *6*, 1232-1236.

11) Schulze, M. W.; McIntosh, L. D.; Hillmyer, M. A.; Lodge, T. P., High-Modulus, High-Conductivity Nanostructured Polymer Electrolyte Membranes via Polymerization-Induced Phase Separation. *Nano Letters* **2013,** *14*, 122-126.

12) Schulze, M. W.; Hillmyer, M. A., Tuning Mesoporosity in Cross-Linked Nanostructured Thermosets via Polymerization-Induced Microphase Separation. *Macromolecules* **2017,** *50*, 997-1007.

13) Zeng, D.; Ribbe, A.; Hayward, R. C., Anisotropic and Interconnected Nanoporous Materials from Randomly End-Linked Copolymer Networks. *Macromolecules* **2017,** *50*, 4668-4676.

14) Walker, C. N.; Bryson, K. C.; Hayward, R. C.; Tew, G. N., Wide Bicontinuous Compositional Windows from Co-Networks Made with Telechelic Macromonomers. *ACS Nano* **2014,** *8*, 12376-12385.

15) Utroša, P.; Žagar, E.; Kovačič, S.; Pahovnik, D. Porous Polystyrene Monoliths Prepared from in Situ Simultaneous Interpenetrating Polymer Networks: Modulation of Morphology by Polymerization Kinetics. *Macromolecules* **2019**, *52*, 819-826.

16) Antonietti, M.; Hentze, H.P. Synthesis of Sponge-like Polymer Dispersions via Polymerization of Bicontinuous Microemulsions. *Colloid and Polymer Science* **1996**, *274*, 696–702.

17) Breulmann, M.; Davis, S. A.; Mann, S.; Hentze, H. P.; Antonietti, M. Polymer–Gel Templating of Porous Inorganic Macro-Structures Using Nanoparticle Building Blocks. Advanced Materials 2000, 12, 502-507.

18) Chopade, S. A.; Au, J. G.; Li, Z.; Schmidt, P. W.; Hillmyer, M. A.; Lodge, T. P., Robust Polymer Electrolyte Membranes with High Ambient-Temperature Lithium-Ion Conductivity via Polymerization-Induced Microphase Separation. *ACS Applied Materials & Interfaces* **2017,** *9*, 14561-14565.

19) Chopade, S. A.; So, S.; Hillmyer, M. A.; Lodge, T. P., Anhydrous Proton Conducting Polymer Electrolyte Membranes via Polymerization-Induced Microphase Separation. *ACS Applied Materials & Interfaces* **2016,** *8*, 6200-6210.

20) Bates, F. S.; Rosedale, J. H.; Fredrickson, G. H., Fluctuation effects in a symmetric diblock copolymer near the order--disorder transition. *The Journal of Chemical Physics* **1990,** *92*, 6255-6270.

21) Zhao, Y.; Sivaniah, E.; Hashimoto, T., SAXS Analysis of the Order−Disorder Transition and the Interaction Parameter of Polystyrene-block-poly(methyl methacrylate). *Macromolecules* **2008,** *41*, 9948-9951.

22) Bates, F. S.; Rosedale, J. H.; Fredrickson, G. H.; Glinka, C. J., Fluctuation-Induced First-Order Transition of an Isotropic System to a Periodic State. *Physical Review Letters* **1988,** *61*, 2229-2232.

23) Rosedale, J. H.; Bates, F. S.; Almdal, K.; Mortensen, K.; Wignall, G. D., Order and Disorder in Symmetric Diblock Copolymer Melts. *Macromolecules* **1995,** *28*, 1429-1443.

24) Sakamoto, N.; Hashimoto, T., Ordering Dynamics of a Symmetric Polystyrene-block-polyisoprene. 2. Real-Space Analysis on the Formation of Lamellar Microdomain. *Macromolecules* **1998,** *31*, 3815-3823.

25) Sakamoto, N.; Hashimoto, T., Ordering Dynamics of a Symmetric Polystyrene-block-polyisoprene. 1. Ordering Mechanism from the Disordered State. *Macromolecules* **1998,** *31*, 3292-3302.

26) Hashimoto, T., Phase transition and self-assembly in block copolymers. *Macromolecular Symposia* **2001,** *174*, 69-84.

27) Kennemur, J. G.; Hillmyer, M. A.; Bates, F. S., Rheological Evidence of Composition Fluctuations in an Unentangled Diblock Copolymer Melt near the Order–Disorder Transition. *ACS Macro Letters* **2013,** *2*, 496-500.

28) Hickey, R. J.; Gillard, T. M.; Lodge, T. P.; Bates, F. S., Influence of Composition Fluctuations on the Linear Viscoelastic Properties of Symmetric Diblock Copolymers near the Order–Disorder Transition. *ACS Macro Letters* **2015,** *4*, 260-265.

29) Medapuram, P.; Glaser, J.; Morse, D. C., Universal Phenomenology of Symmetric Diblock Copolymers near the Order–Disorder Transition. *Macromolecules* **2015,** *48*, 819-840.

30) Vidil, T.; Hampu, N.; Hillmyer, M. A., Nanoporous Thermosets with Percolating Pores from Block Polymers Chemically Fixed above the Order–Disorder Transition. *ACS Central Science* **2017,** *3*, 1114-1120.

31) Hampu, N.; Hillmyer, M.A., Temporally Controlled Curing of Block Polymers in the Disordered State Using Thermally Stable Photoacid Generators for the Preparation of Nanoporous Membranes. *ACS Appl. Polym. Mater*. **2019**, *1*, 1148-1154.

32) Gor, G. Y.; Thommes, M.; Cychosz, K. A.; Neimark, A. V., Quenched solid density functional theory method for characterization of mesoporous carbons by nitrogen adsorption. *Carbon* **2012,** *50*, 1583-1590.

33) Hillmyer, M. A.; Bates, F. S., Synthesis and Characterization of Model Polyalkane−Poly(ethylene oxide) Block Copolymers. *Macromolecules* **1996,** *29* (22), 6994-7002.

34) Wolf, J. H.; Hillmyer, M. A., Ordered Nanoporous Poly(cyclohexylethylene)†. *Langmuir* **2003,** *19*, 6553-6560.

35) Sardelis, K.; Michels, H. J.; Allen, G.; F.R.S, Graded block and randomized copolymers of butadiene-styrene. *Polymer* **1984,** *25*, 1011-1019.

36) Xu, J.; Mittal, V.; Bates, F. S., Toughened Isotactic Polypropylene: Phase Behavior and Mechanical Properties of Blends with Strategically Designed Random Copolymer Modifiers. *Macromolecules* **2016,** *49*, 6497-6506.

37) Touris, A.; Chanpuriya, S.; Hillmyer, M. A.; Bates, F. S., Synthetic strategies for the generation of ABCA' type asymmetric tetrablock terpolymers. *Polymer Chemistry* **2014,** *5*, 5551-5559.

38) Akiba, M.; Hashim, A. S., Vulcanization and crosslinking in elastomers. *Progress in Polymer Science* **1997,** *22*, 475-521.

39) Querelle, S. E.; Jackson, E. A.; Cussler, E. L.; Hillmyer, M. A., Ultrafiltration Membranes with a Thin Poly(styrene)-b-poly(isoprene) Selective Layer. *ACS Applied Materials & Interfaces* **2013,** *5*, 5044-5050.

40) Jackson, E. A.; Lee, Y.; Hillmyer, M. A., ABAC Tetrablock Terpolymers for Tough Nanoporous Filtration Membranes. *Macromolecules* **2013,** *46*, 1484-1491.

41) Ellison, C. J.; Mundra, M. K.; Torkelson, J. M., Impacts of Polystyrene Molecular Weight and Modification to the Repeat Unit Structure on the Glass Transition−Nanoconfinement Effect and the Cooperativity Length Scale. *Macromolecules* **2005,** *38*, 1767-1778.

42) Hiemenz, P. C.; Lodge, T. P., *Polymer Chemistry*, *Second Edition*. CRC Press: 2007.

43) Bates, F. S., Block copolymers near the microphase separation transition. 2. Linear dynamic mechanical properties. *Macromolecules* **1984,** *17*, 2607-2613.

44) Ren, Y.; Lodge, T. P.; Hillmyer, M.A., Synthesis, Characterization, and Interaction Strengths of Difluorocarbene-Modified Polystyrene−Polyisoprene Block Copolymers. Macromolecules 2000, 33, 866-876.45.

45) Hashimoto, T.; Shibayama, M.; Kawai, H., Ordered structure in block polymer solutions. 4. Scaling rules on size of fluctuations with block molecular weight, concentration, and temperature in segregation and homogeneous regimes. *Macromolecules* **1983**, *16*, 1093-1101.

46) Naughton, J.R.; Matsen, M.W., Limitations of the Dilution Approximation for Concentrated Block Copolymer/Solvent Mixtures. *Macromolecules* **2002**, *35*, 5688-5696.

47) Lodge, T. P.; Hanley, K. J.; Pudil, B.; Alahapperuma, V., Phase Behavior of Block Copolymers in a Neutral Solvent. *Macromolecules* **2003,** *36*, 816-822.

48) Bertrand, A.; Hillmyer, M. A., Nanoporous Poly(lactide) by Olefin Metathesis Degradation. *Journal of the American Chemical Society* **2013,** *135*, 10918-10921.

49) Roe, R. J.; Nojima, S., Small-Angle X-Ray Scattering Study of Microand Macro-Phase Separations in Blends of Block Copolymer with Homopolymer. *MRS Online Proceedings Library Archive* **1986,** *79*, null-null.

50) Lee, S.; Gillard, T. M.; Bates, F. S., Fluctuations, Order, and Disorder in Short Diblock Copolymers. *Aiche J* **2013,** *59*, 3502-3513.

51) Sing, K. S. W.; Everett, D. H.; Haul, R. A. W.; Moscou, L.; Pierotti, R. A.; Rouquerol, J.; Siemieniewska, T., Reporting Physisorption Data for Gas Solid Systems with Speical Reference to the Determination of Surface-area and Porosity (Recommendations 1984). *Pure Appl. Chem.* **1985,** *57*, 603-619.

52) Lowell, S.; Shields, J. E.; Thomas, M. A.; Thommes, M., *Characterization of porous solids and powders: surface area, pore size and density*. Springer Science & Business Media: 2012; Vol. 16.

53) Basfar, A. A.; Abdel-Aziz, M. M.; Mofti, S., Influence of different curing systems on the physico-mechanical properties and stability of SBR and NR rubbers. *Radiation Physics and Chemistry* **2002,** *63*, 81-87.

54) Kruželák, J.; Sýkora, R.; Hudec, I., Peroxide vulcanization of natural rubber. Part I: effect of temperature and peroxide concentration. **2014,** *34*, 617-624.

55) Nobuyuki, A.; Izumi, K.; Takehisa, K., Dependence of the Crosslinking Efficiency on the Reaction Conditions in the Peroxide Crosslinking of Unsaturated Polyolefins. *Bulletin of the Chemical Society of Japan* **1967,** *40*, 2597-2603.

56) Yang, S. Y.; Park, J.; Yoon, J.; Ree, M.; Jang, S. K.; Kim, J. K. Virus Filtration Membranes Prepared from Nanoporous Block Copolymers with Good Dimensional Stability under High Pressures and Excellent Solvent Resistance." *Advanced. Functional Materials* **2008**, *18*, 1371-1377.

57) Abetz, V. Isoporous Block Copolymer Membranes. *Macromolecular Rapid Communications* **2015**, *36*, 10-22.

Chapter 5. Temporally Controlled Curing of Block Polymers in the Disordered State Using Thermally-Stable Photoacid Generators for the Preparation of Nanoporous Membranes[3]

5.1 Introduction

The self-assembly of block polymers into well-defined domains with a narrow size distribution has led to numerous potential applications due to their ability to marry disparate properties into a single material.[1–5] One application of particular interest is in separations technologies, especially water purification.[1,6–8] By designing a block polymer that contains one block which can be selectively etched to generate pores and a second block that provides sufficient mechanical integrity to the matrix, porous materials comprising continuous channels have been reported.[6,9] However, commonly reported equilibrium morphologies are either anisotropic cylinders, which require costly post-processing alignment to orient domains, or are isotropic and bicontinuous (gyroid), but exist in a narrow window of morphology space.[10–14]

---

[3] Reproduced with permission from Hampu, N.; Hillmyer, M. A. Temporally Controlled Curing of Block Polymers in the Disordered State Using Thermally Stable Photoacid Generators for the Preparation of Nanoporous Membranes. *ACS Appl. Polym. Mater.* **2019**, *1*, 1148-1154. Copyright 2019 American Chemical Society.

Recently, significant research effort has focused on circumventing these challenges by kinetically trapping disordered morphologies comprised of bicontinuous domains (polymerization induced microphase separation,[15] randomly end-linked copolymer networks,[16] bicontinuous microemulsions[17]). One such system that we have recently reported in our group involves heating an initially ordered and reactive polylactide-*block*-poly(styrene-*stat*-glycidyl methacrylate), PLA-*b*-P(S-*s*-GMA), diblock polymer above its order-disorder transition temperature (T_{ODT}) and subsequently cross-linking to kinetically trap the well-established bicontinuous morphology associated with disordered state composition fluctuations.[18–20] Due to their tortuous and isotropic domains, the resulting materials displayed high porosity without the need for post-synthetic alignment. Additionally, they remained solution processable prior to the initiation of the cross-linking reaction. This previous report relied upon utilizing a thermal stimulus to initiate both the disordering and the cross-linking processes. Consequently, this system is limited to diblock polymers with T_{ODT}'s that are in the temperature range of efficient catalytic activity to ensure favorable cross-linking kinetics.[21]

5.2 Experimental Methods

Here, we have investigated a strategy to temporally control the onset of cross-linking for PLA-*b*-P(S-*s*-GMA) across a broad temperature range by using a thermally stable photoacid generator, 4-iodophenyldiphenylsulfonium triflate (IST).[22] This allows for the independent and orthogonal control over the onset of the disordering process and the initiation of the cross-linking reaction, such that PLA-*b*-P(S-*s*-GMA) + IST can initially be

heated above T_{ODT} to induce disordering, subsequently irradiated to initiate curing, cooled to room temperature, and selectively etched (Figure 5.1).

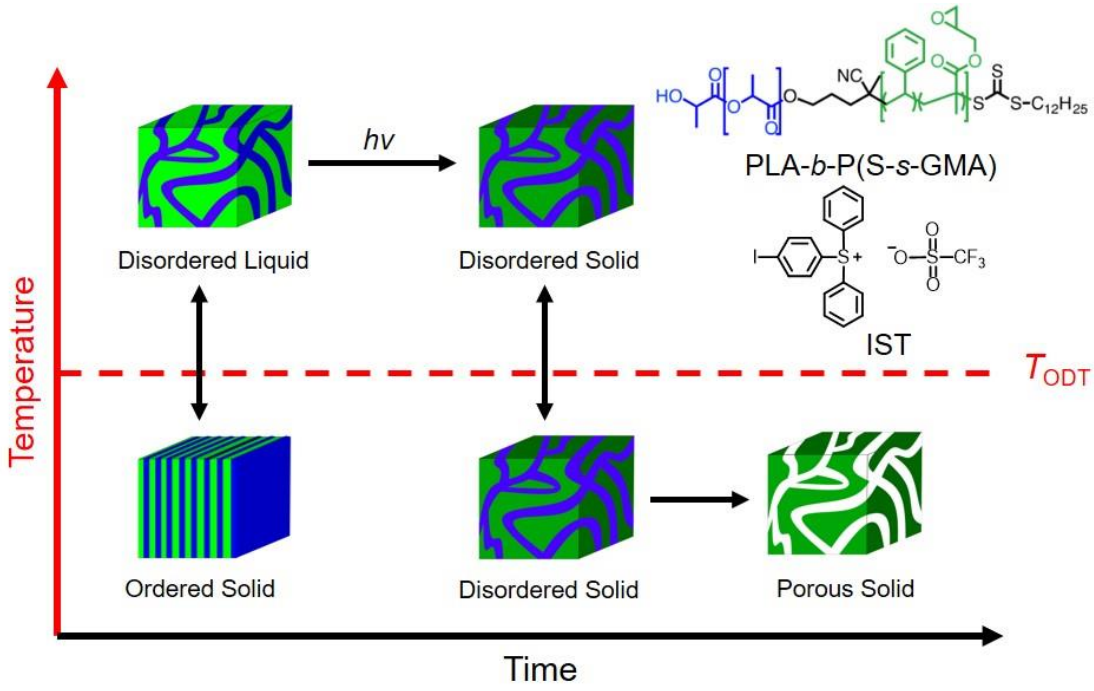

Figure 5.1. A lamellar forming PLA-*b*-P(S-*s*-GMA) diblock polymer is combined with 1 wt.% IST. The system is then heated above T_{ODT} to induce disordering. In a subsequent step, the sample is irradiated with UV light above the T_{ODT} to initiate the cross-linking reaction. The sample is then cooled to room temperature and the PLA block is selectively removed to generate a porous material.

5.3 Results and Discussion

5.3.1 Identification of an Appropriate Photoacid Generator

This strategy requires that the photoacid generator remains stable at elevated temperatures and does not thermally degrade into acids that can initiate undesired, premature cross-linking reactions.[23] To identify a PAG with the requisite thermal stability, a series of commercially available iodonium and sulfonium salts with varying cation and counter-anion structures were screened by blending with a commercially available P(S-*s*-GMA) statistical copolymer, Joncryl ADR-4368 (M_w = 6.8 kg mol^{-1}, approximately 4 epoxide

units per chain), at a concentration of 1 wt.%. The thermal stability of each PAG was then evaluated by heating the blends to 190 °C for 45 minutes without UV irradiation as a representative curing temperature and time. Following this thermal treatment, the samples were swollen in THF overnight at room temperature and the gel fraction (defined as the ratio of the dry polymer mass after swelling to the dry polymer mass prior to swelling) was measured. IST was found to be the only PAG that displayed a gel fraction of 0, indicating that a significant degree of thermal cross-linking did not occur in this system. Additionally, this sample displayed a negligible shift in peak elution time by SEC as compared to the sample prior to heating, further supporting this conclusion (Figure 5.2). These results correspond well with previous experimental results, which have demonstrated that IST remained thermally stable in epoxide containing block polymers up to 200 °C.[22] Conversely, all of the other PAG's that were screened (diphenyliodonium hexafluorophosphate, bis(4-tert-butylphenyl)iodonium hexaflurophosphate, and triarylsulfonium hexafluoroantimonate) displayed relatively high gel fractions between 0.7 and 0.85, indicating that they thermally dissociated into acids that subsequently initiated a significant degree of cross-linking (Table 5.1). Consequently, it was concluded that IST was the only PAG that we examined which exhibited the necessary thermal stability to

enable the orthogonal control over the onset of the disordering process and the initiation of the cross-linking reaction.

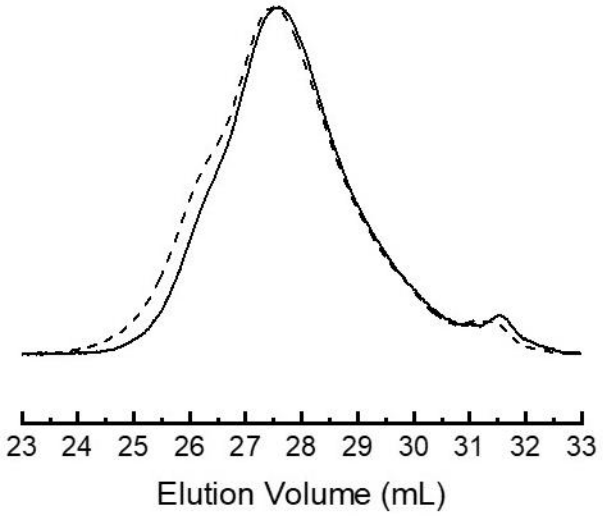

Figure 5.2. THF SEC elugrams for Joncryl-ADR4368 + 1 wt.% IST blends obtained prior to heating (solid curve) and after heating for 45 minutes at 190 °C (dashed curve).

Table 5.1. Gel fractions obtained from Joncryl-ADR4368 containing 1 wt.% of various photoacid generators after heating and/or irradiating with UV light.

Photoacid Generator (PAG)	Wt. % PAG	Temperature (°C)	Irradiation Time (min)	Gel Fraction (%)
Diphenyliodonium hexafluorophosphate	1	190	0	80
Triarylsulfonium hexafluoroantimonate	1	190	0	85
4-iodophenyldiphenyl hexafluoroantimonate	0.5	190	10	0
	1	190	0	0
			5	54
			5 + 5 post-exposure	60
			10	89
			45	93
Bis(4-tert-butylphenyl)iodonium hexaflurophosphate	1	190	0	70

After demonstrating the thermal stability of IPDPST, its ability to efficiently initiate cross-linking upon UV irradiation was examined. Films of Joncryl-ADR4368 + 1 wt.% IST (~ 2 mm thick) were heated to 190 °C and subsequently irradiated with 350 nm UV light for either 5, 10, or 45 minutes. Although PS has been shown to absorb UV radiation, the absorption band is centered around 260 to 290 nm which lies outside of the wavelength range generated by the UV source used here, so absorption by PS is expected to be minimal.[23] After a 10 min irradiation time, the gel fraction was measured as 0.89 (Table 5.1). A similar gel fraction was observed after an irradiation time of 45 min. However, a shorter irradiation time of 5 min resulted in a noticeably lower gel fraction of 0.54. Additionally, a 5 min irradiation followed by continued heating in the absence of UV irradiation for 5 min at 190 °C did not significantly increase the gel fraction (Table 5.1). Furthermore, reducing the loading of IST to 0.5 wt.% resulted in a gel fraction of 0 following a 10 min irradiation (Table 5.1). These results suggest that longer irradiation times and higher loadings of IST are required to generate a sufficient number of acidic species that can initiate the cross-linking reaction. Therefore, the loading of IST was maintained at 1 wt.% with a 10 min irradiation time for further experiments.

Next, IST was investigated for the photocuring of a PLA-*b*-P(S-*s*-GMA) diblock polymer at elevated temperatures. The diblocks investigated in this study are labelled according to the nomenclature PLA-α-P(S-*s*-GMA)-β-XGMA-γ where α and β are the molar masses (in kg mol^{-1}) of the PLA and P(S-*s*-GMA) blocks, respectively, and γ is the molar percentage of GMA in the P(S-*s*-GMA) block (XGMA) (see Chapter 3 for full synthetic details). A previously reported PLA-17-P(S-*s*-GMA)-11-XGMA-29 diblock ($M_{n,\,PLA}$ = 17

kg mol^{-1}, $M_{n,\,P(S\text{-}s\text{-}GMA)}$ = 11 kg mol^{-1}, molar fraction of GMA in the P(S-*s*-GMA) statistical copolymer block = 29 %) was blended with 1 wt.% IST to form approximately 2 mm thick films which were then irradiated at 190 °C (T_{ODT} + 15 °C) for 10 minutes (see Chapter 3 for a detailed description of the photocuring procedure).[18] The cross-linked samples were cooled and then immersed overnight at room temperature in a 2 M solution of NaOH (40/60 H_2O/MeOH v/v) to selectively etch the PLA domains. The total pore volume, 0.45 cm^{3}g^{-1}, and morphology obtained from PLA-17-P(S-s-GMA)-11-XGMA-29 + 1% IST irradiated for 10 minutes at 190 °C were comparable to those obtained for the same polymer thermally cross-linked with 0.3 wt.% benzyl triphenylphosphonium hexafluorantimonate (BTPH) for 1 hour at 190 °C, 0.39 cm^{3}g^{-1} (see Figures 5.3 and 5.4).[18] This suggests photocuring can be used to efficiently initiate the cross-linking reaction at elevated temperatures without compromising the high porosity previously observed with thermally cross-linked systems.

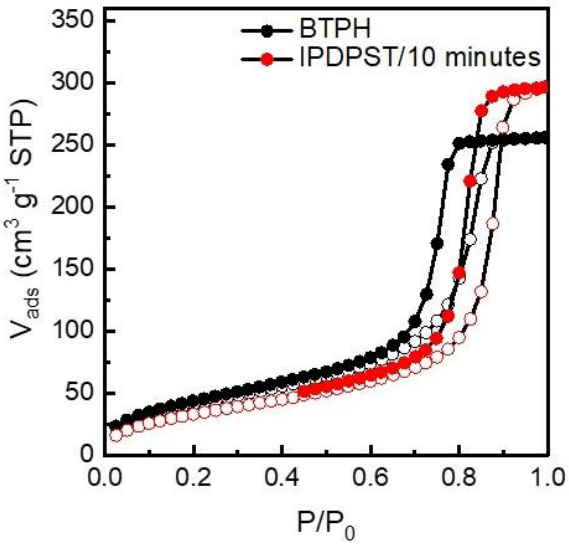

Figure 5.3. N_2 sorption isotherms for PLA-17-P(S-*s*-GMA)-11-XGMA-29 cured at 190 °C with either 0.3 wt.% BTPH for 1 hour (black) or 1 wt.% IST for 10 minutes (red).

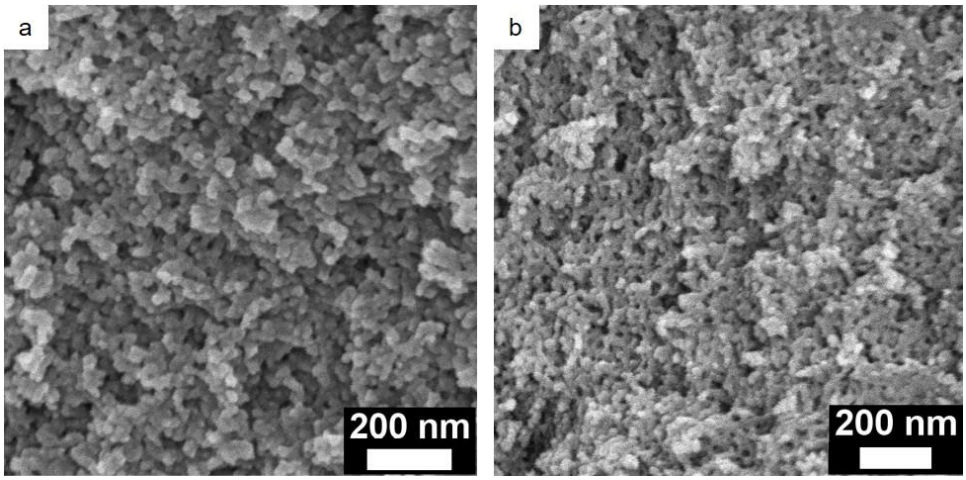

Figure 5.4. SEM images for PLA-17-P(S-s-GMA)-11-XGMA-29 cured at 190 °C with 0.3 wt.% BTPH for 1 hour or with 1 wt.% IST for 10 minutes (b). All samples were coated with approximately 2 nm of Ir prior to imaging.

5.3.2 Temperature Dependence of Porosity in the Disordered State

One of the notable features of photocuring is that the cross-linking reaction can be temporally controlled across a wide temperature range while maintaining a high efficiency, provided that the photoacid generator remains thermally stable. In contrast, the use of thermal cross-linking agents is limited to a much narrower temperature range where the catalytic activity is efficient, *and* the reaction kinetics are favorable. To demonstrate the increased breadth of the curing window for photoacid generators, a lamellar-forming diblock polymer, PLA-20-P(S-*s*-GMA)-12-XGMA-38 (Figures 5.5, 5.6, and 5.7), with a relatively low T_{ODT} of 105 °C, as determined by variable temperature small angle X-ray scattering (SAXS) (Figure 5.8), was selected.

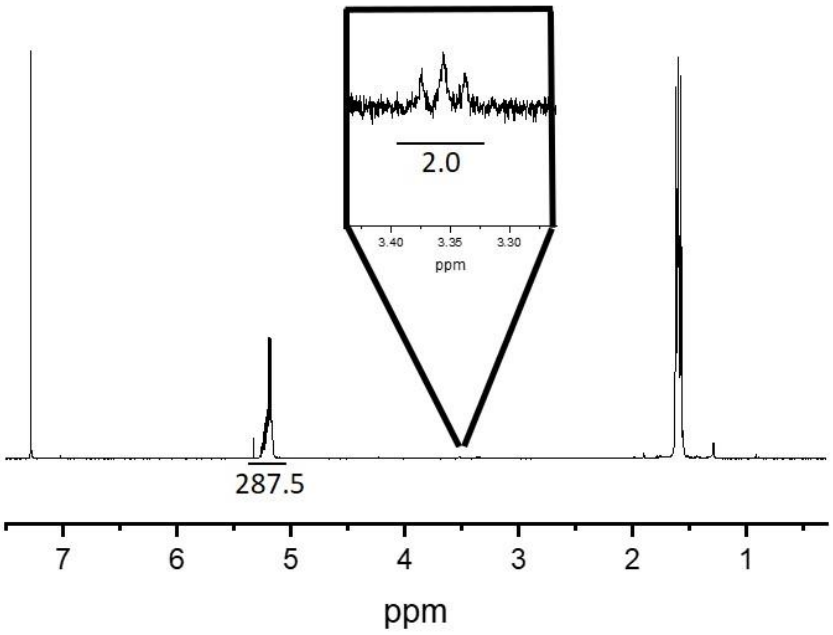

Figure 5.5. [1]H NMR spectrum for PLA-20. Integral values correspond to the methine protons of PLA (5-5.4 ppm) and the methylene protons adjacent to the trithiocarbonate of the CTA(3.30-3.40 ppm). The inset presents a higher magnification image of the methylene protons from the CTA.

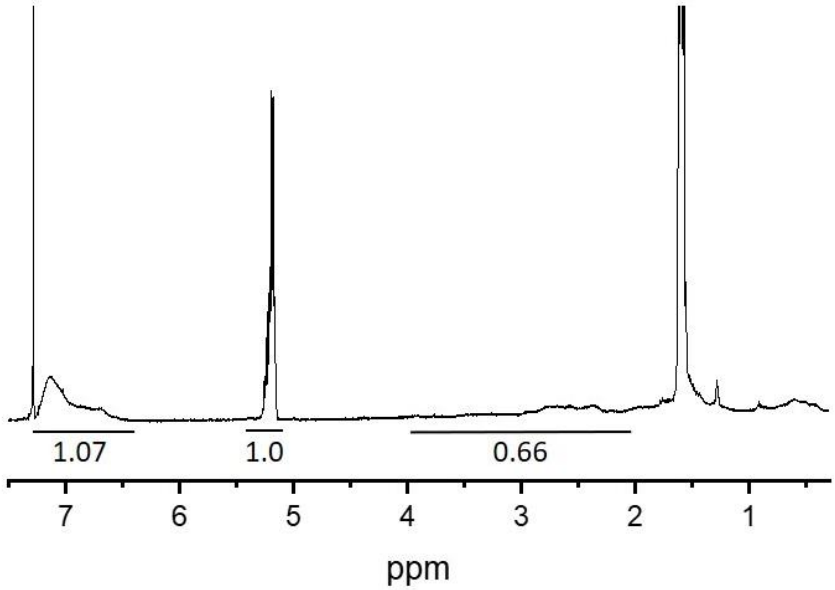

Figure 5.6. [1]H NMR spectrum for PLA-20-P(S-*s*-GMA)-12-XGMA-38. Integral values correspond to the methine protons of PLA(5-5.4 ppm), the aromatic protons of PS (6.3-7.2 ppm), and the glycidyl protons of PGMA (2.1-4.2 ppm). The integral of the methine protons of PLA was set to 1 as a reference.

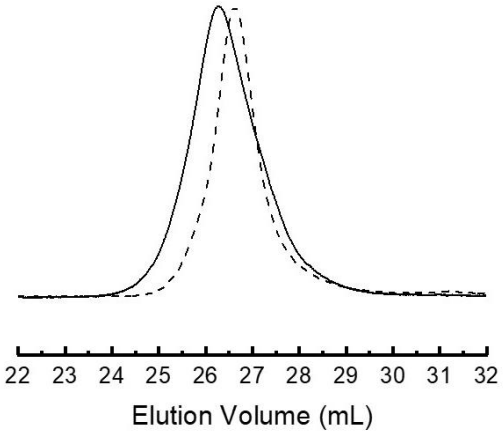

Figure 5.7. THF SEC elugrams for PLA-20 (dashed curve) and PLA-20-P(S-*s*-GMA)-12-XGMA-38 (solid curve).

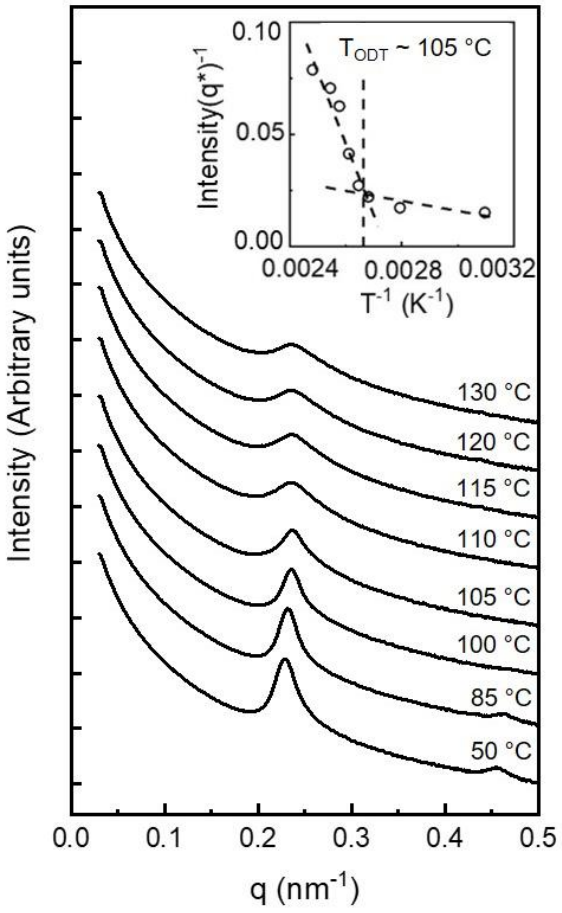

Figure 5.8. Variable temperature SAXS for PLA-20-P(S-s-GMA)-12-XGMA-38 + 1 wt.% IST. Samples were equilibrated for 2 minutes at each temperature prior to data collection. Inset displays a plot of $I^{-1}(q^*)$ vs T^{-1}. T_{ODT} was determined to be approximately 105 °C based on the temperature corresponding to the change in slope (dashed lines).

The temperature dependence of the porosity and morphology of the photocured samples was then examined. Blends of PLA-20-P(S-*s*-GMA)-12-XGMA-38 + 1 wt.% IST (with a film thickness of several millimeters) were sealed in glass vials, sparged with Ar gas, and placed on a hot plate pre-heated to the desired curing temperature. After the films thermally equilibrated for 5 minutes at the desired curing temperature, a 365 nm UV lamp was used to irradiate the samples for 10 minutes. The samples were cooled to room temperature and gel fractions of approximately 0.98 were obtained. The PLA domains were subsequently etched to generate porous materials.

The porosity of these samples was then examined using N_2 sorption analysis. A featureless isotherm consistent with negligible porosity was observed for a sample photocured below T_{ODT}. In contrast, all samples irradiated above T_{ODT} displayed type IV isotherms with H2 hysteresis (Figure 5.9), characteristic of bicontinuous mesoporosity and consistent previous results from a thermally cross-linked system.[18] Additionally, narrow pore size distributions were obtained by quenched solid density functional theory, QSDFT (Figure 5.10).[24,25] Intriguingly, the porosity remained high even for samples cured *far* above T_{ODT} (Figure 5.11). This suggests that composition fluctuations persist well above T_{ODT}, resulting in well-defined, nanostructured domains across a broad range of temperatures. Such behavior is particularly appealing from a practical perspective, as it enables flexibility in both the selection of photocuring temperature and the design of the block polymer's T_{ODT}. Furthermore, from a fundamental perspective, these results suggest that the more molecularly homogeneous mean-field limit, which we expect would be challenging to quantitatively etch to generate porous materials, has not been reached even 75 °C above

T_{ODT} in this particular case. Although it should be noted that the slight decrease in porosity observed for the highest photocuring temperature may possibly reflect the onset of a transition from a fluctuating disordered to a more mean-field-like state.[26]

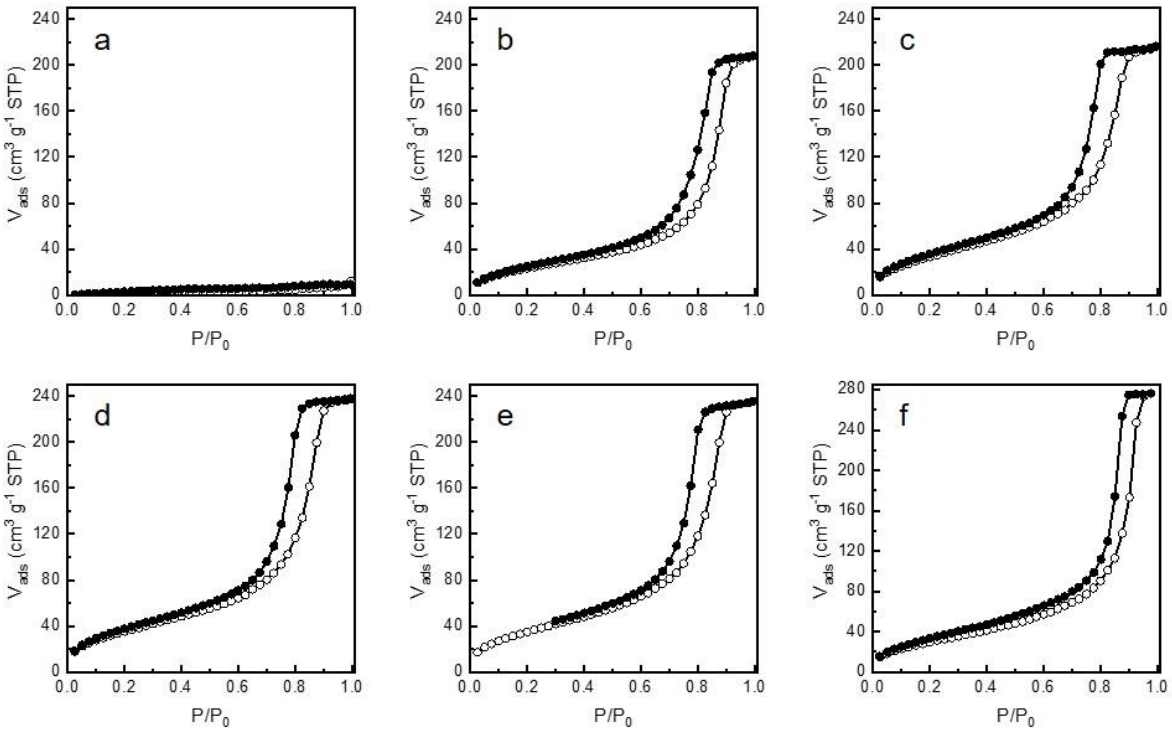

Figure 5.9. N_2 sorption isotherms for PLA-20-P(S-*s*-GMA)-12-XGMA-38 + 1 wt.% IST irradiated for 10 minutes at 85 °C (a), 107 °C (b), 117 °C (c), 130 °C (d), 150 °C (e), and 170 °C (f). Open symbols correspond to adsorption and closed symbols to desorption.

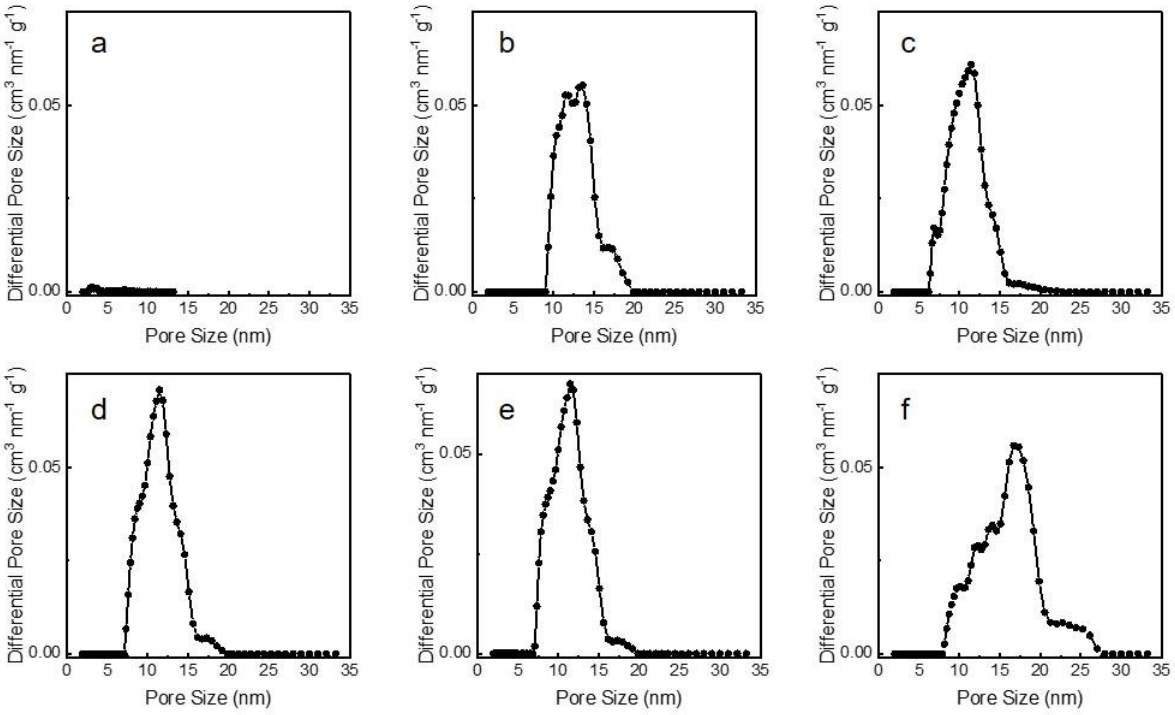

Figure 5.10. QSDFT pore size distributions for PLA-20-P(S-*s*-GMA)-12-XGMA-38 + 1 wt.% IST irradiated for 10 minutes at 85 °C (a), 107 °C (b), 117 °C (c), 130 °C (d), 150 °C (e), and 170 °C (f).

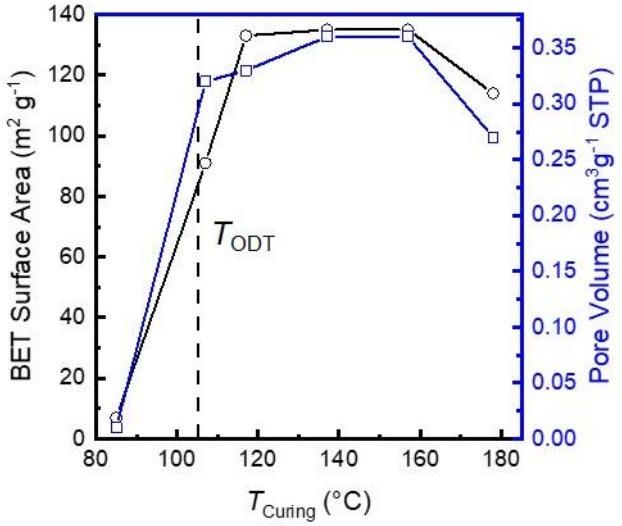

Figure 5.11. N_2 sorption analysis of BET surface area (black curve, ○) and pore volume (blue curve, □) for PLA-20-P(S-*s*-GMA)-12-XGMA-38 photocured with 1 wt.% IST at various temperatures relative to T_{ODT} following the selective etching of PLA. The T_{ODT} is indicated by the dashed line.

Notably, lower porosities were observed for the same polymer thermally cross-linked with BTPH at comparable temperatures (Figure 5.12). The lower catalytic activity of BTPH in this temperature range results in inefficient curing kinetics. Consequently, thermal degradation of the PLA domains may occur in the melt state prior to gelation during the long curing times needed for BTPH, resulting in significant pore collapse.[9] Additionally, the change in chemistry associated with epoxide ring opening may significantly depress χN when the curing kinetics are slow, decreasing the extent of phase separation. These results demonstrate that the high catalytic efficiency and the temporal control of IST offers the distinct advantage of broadening the processing window for this cross-linkable block polymer system.

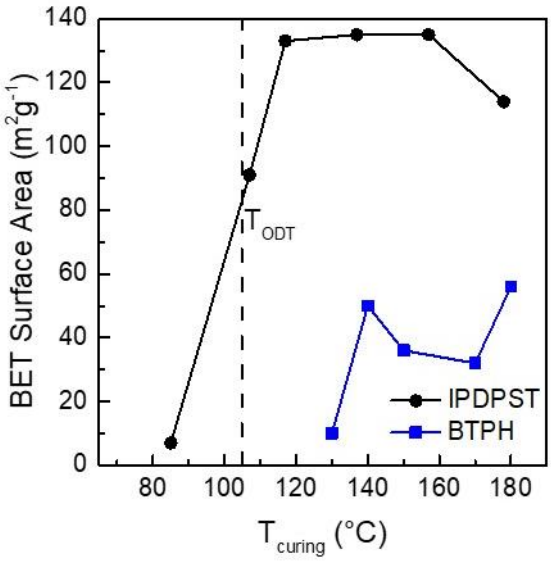

Figure 5.12. BET surface area for PLA-20-P(S-*s*-GMA)-12-XGMA-38 photocured with 1 wt.% IST (black circles) and 0.3 wt.% BTPH (blue squares) at various temperatures below and above T_{ODT}.

SEM and room temperature SAXS were then used to examine the morphology of samples cross-linked below and above T_{ODT}. For a sample irradiated below T_{ODT} at 85 °C (T_{ODT} – 20 °C), a collapsed layered and sheet-like morphology was observed by SEM (Figure 5.13).

Additionally, a sharp peak at q^* was observed in SAXS prior to etching, consistent with an ordered morphology (Figure 5.13, blue curves). After etching, the primary peak was noticeably broader, which suggests that the lack of domain continuity was insufficient to support the free-standing lamellae. These mechanically unstable lamellae collapsed, resulting in a loss of long-range spatial correlations as compared to the unetched sample. This is in qualitative agreement with the observations from SEM.[27,28] The extent of peak broadening is likely related to the degree of pore collapse, and the case of severe or complete pore collapse the peak may result in a featureless scattering pattern where no peak is observed, as was previously observed for thermally cross-linked systems with BTPH.[18] For a sample cross-linked at 130 °C (T_{ODT} + 25 °C), a disordered morphology that topologically resembles other bicontinuous morphologies was observed by SEM (Figure 5.13).[3,15,16] Furthermore, SAXS patterns obtained prior to etching displayed a broad peak without sharp higher order reflections, supporting the assignment of a disordered morphology. In contrast to the sample cured below T_{ODT}, the peak breadth remained relatively unchanged following etching. This demonstrates that the bicontinuous domains associated with composition fluctuations result in a significant enhancement in the mechanical robustness of the disordered porous network as compared to the lamellar case (Figure 5.13, red curves). Similar observations were made for all samples irradiated above T_{ODT} and are consistent with those reported for similar diblock polymers thermally cross-linked with BTPH.[18]

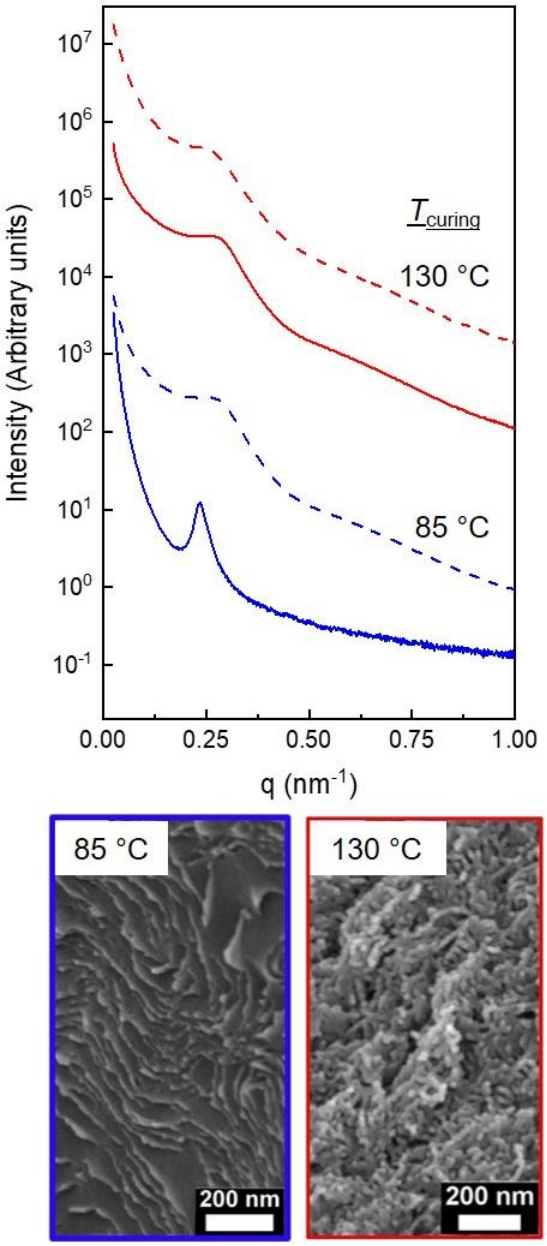

Figure 5.13. Room temperature SAXS patterns (top panel) for PLA-20-P(S-*s*-GMA)-12-XGMA-38 + 1 wt.% IST for samples irradiated for 10 minutes at 85 °C (T_{ODT} – 20 °C) (blue curves) and at 130 °C (T_{ODT} + 25 °C) (red curves). Solid curves are for unetched samples and dashed curves for etched samples. SEM images (bottom panels) for PLA-20-P(S-*s*-GMA)-12-XGMA-38 + 1% IST for samples (bottom left) irradiated for 10 minutes at 85 °C (T_{ODT} – 20 °C) and (bottom right) at 130 °C (T_{ODT} + 25 °C).

5.3.3 In-situ SAXS During Photocuring in the Disordered State

As the described system involves photocuring in the disordered state, the cross-linking reaction may have a noticeable influence on the observed morphology. It is possible that the cross-linking reaction can effectively sharpen the interfaces between domains, as has been explored in other systems, i.e. reaction-induced microphase separation (RIMPS).[29–31] To investigate this possibility, a UV lamp was set-up in a SAXS beamline and time-resolved SAXS patterns were obtained at 130 °C both with and without UV irradiation.

Two separate samples were prepared in quartz capillaries: neat PLA-20-P(S-*s*-GMA)-12-XGMA-38 as a non-cross-linkable control and PLA-20-P(S-*s*-GMA)-12-XGMA-38 + 1 wt.% IST. Each time point was acquired using a 1 s exposure of X-rays to a different region of the sample to minimize the potential effects from repeated and prolonged exposures. Both samples were heated to 130 °C and held at a constant temperature for approximately 25 minutes without irradiating the sample to isolate any effects from temperature alone. The UV lamp was then turned on for 35 minutes to initiate photocuring.

Following irradiation, both capillaries were opened, and the samples were immersed in THF to evaluate the occurrence of network formation. The neat sample completely dissolved, consistent with an uncross-linked system, while the sample containing IST remained insoluble over the course of several days, consistent with a cured system. Furthermore, no obvious qualitative change in the shape of the scattering patterns was observed for either sample upon irradiation (Figure 5.14). Although there is some noise in the data, there was little quantitative change in either $I(q^*)$ or full width at half max

(FWHM) throughout the duration of UV irradiation (Figure 5.15). Additionally, q^* remained reasonably constant throughout the duration of the experiment, consistent with previous observations regarding the ODT in diblock polymers and with minimal domain swelling upon cross-linking (Figure 5.16).

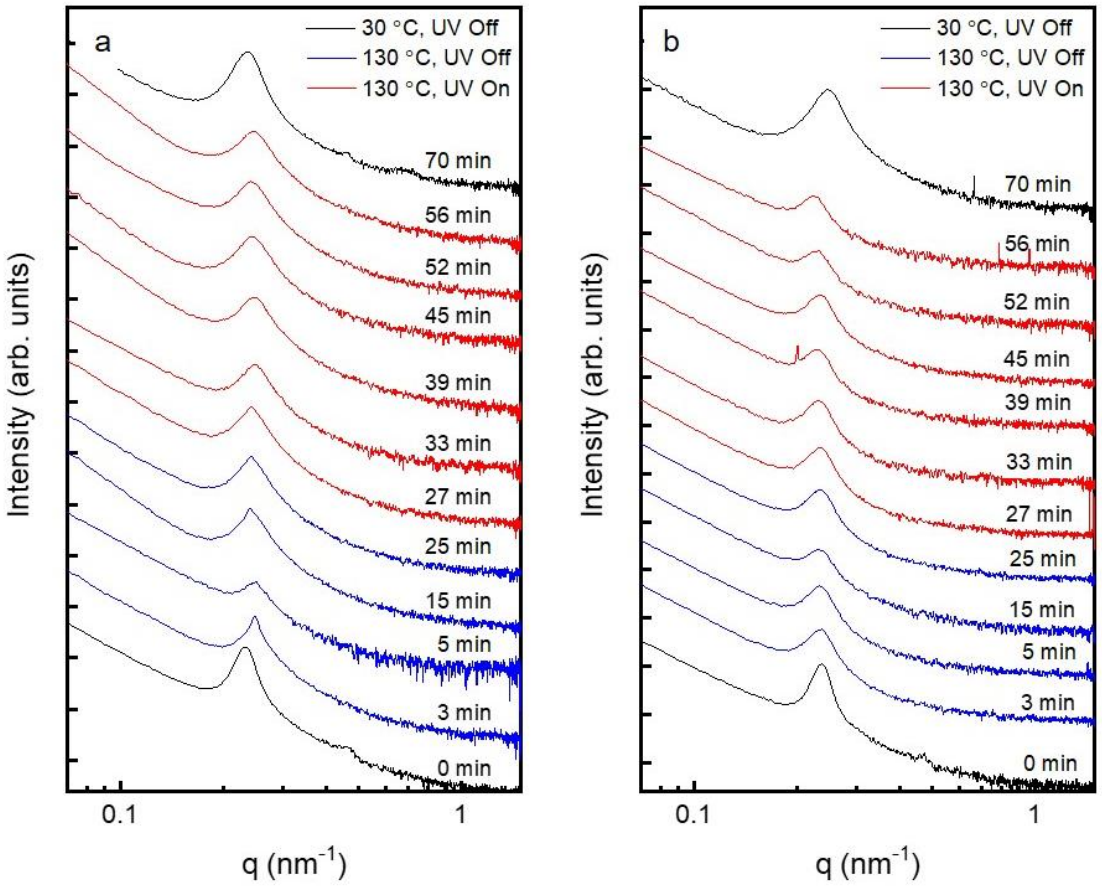

Figure 5.14. In-situ photocuring SAXS patterns for neat PLA-20-P(S-*s*-GMA)-11-XGMA-38 (a) and PLA-20-P(S-*s*-GMA)-11-XGMA-38 + 1 wt.% IST (b). Patterns were initially taken at 30 °C (time = 0 min, black curves). The samples were then rapidly heated to 130 °C at a rate of 50 °C min^{-1} and held at a constant temperature for 25 minutes with the UV lamp turned off (blue curves, 3 min to 25 min). The UV lamp was then switched on for 30 minutes while a constant temperature of 130 °C was maintained (red curves, 27 min to 56 min). The samples were then cooled to 30 °C and annealed for 10 minutes (black curves, 70 min). The reported patterns are representative examples of the full data set.

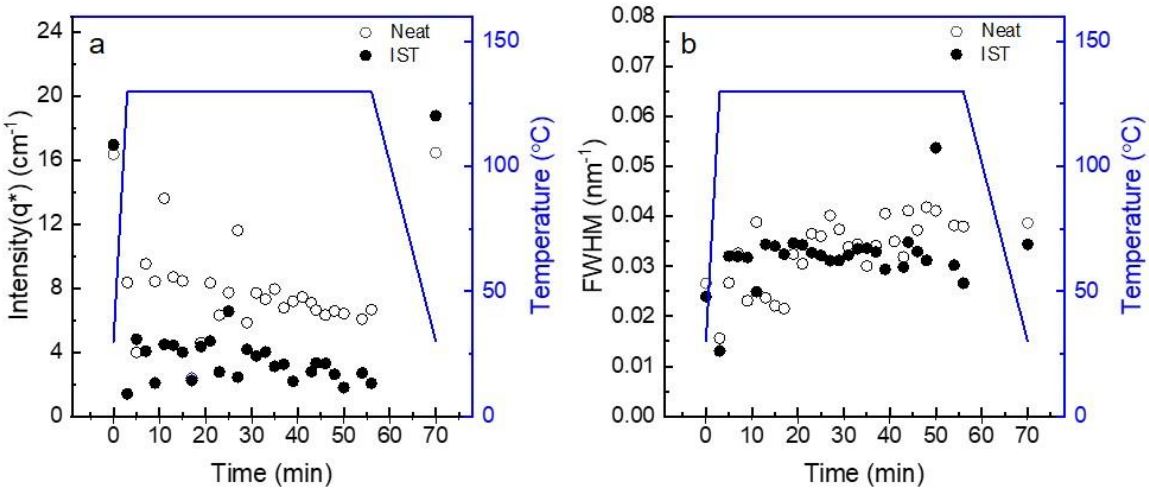

Figure 5.15. The intensity of the principal scattering peak, $I(q^*)$, (a) and the full width at half max of the principal scattering peak, FWHM, (b) for neat PLA-20-P(S-*s*-GMA)-11-XGMA-38 (open circles) and PLA-20-P(S-*s*-GMA)-11-XGMA-38 + 1 wt.% IST (closed circles). Patterns were initially taken at 30 °C (time = 0 min). The samples were then rapidly heated to 130 °C at a rate of 50 °C min^{-1} and held at a constant temperature for 25 minutes with the UV lamp turned off. The UV lamp was then switched on for 30 minutes while a constant temperature of 130 °C was maintained. The samples were then cooled to 30 °C and patterns were acquired after 10 minutes (time = 70 min).

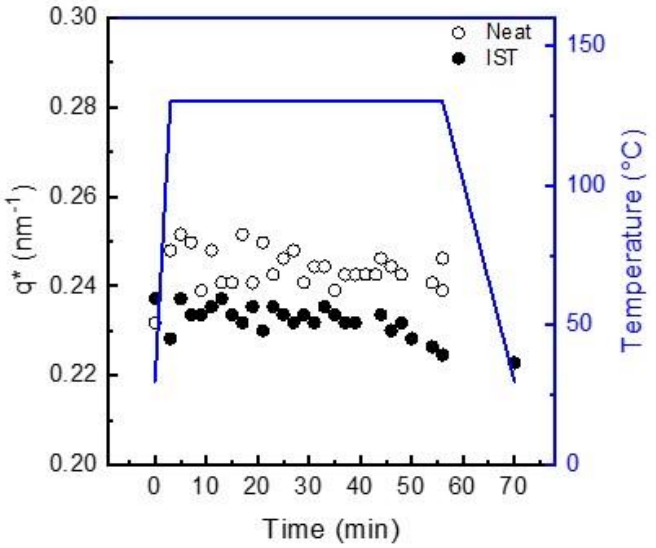

Figure 5.16. The principal scattering vector, q^*, for neat PLA-20-P(S-*s*-GMA)-11-XGMA-38 (open circles) and PLA-20-P(S-*s*-GMA)-11-XGMA-38 + 1 wt.% IST (closed circles). Patterns were initially taken at 30 °C (time = 0 min). The samples were then rapidly heated to 130 °C at a rate of 50 °C min^{-1} and held at a constant temperature for 25 minutes with the UV lamp turned off. The UV lamp was then switched on for 30 minutes while a constant temperature of 130 °C was maintained. The samples were then cooled to 30 °C and annealed for 10 minutes.

The uncross-linked diblock polymer displayed a slightly lower intensity and a higher FWHM than the cross-linked sample upon cooling to 30 °C at a rate of approximately 20 °C min^{-1} following irradiation. This would seem to suggest that the cross-linked sample displayed a higher degree of long-range spatial correlations despite being kinetically trapped in the disordered state. This counterintuitive observation may reflect that the annealing time for the uncross-linked sample was insufficient to recover its initial degree of long-range order upon cooling. Indeed, the initial pattern (time = 0 min) was acquired after 8 h of thermal annealing at 95 °C (between T_g and T_{ODT}), while the pattern obtained upon cooling from above T_{ODT} experienced a significantly shorter annealing time of approximately 2-3 min in the same temperature range. It is expected that a more noticeable increase in $I(q^*)$ and decrease in FWHM would have been observed following a prolonged annealing procedure upon cooling, although the possibility of beam damage and/or thermal degradation cannot be completely excluded. Overall, the observation that $I(q^*)$ and FWHM remain reasonably constant during the cross-linking reaction is consistent with the conclusion that no significant changes in the morphology or the extent of nanoscale spatial correlations occurred during photocuring. Instead, these results support the conclusion that the cross-linking reaction effectively traps the morphology that exists at the curing temperature with high fidelity.

5.3.4 Fabrication of Thin Films and Ultrafiltration Membranes

One notable feature of this system is that the uncross-linked precursor is soluble in common organic solvents, which enables solution processing into thin films. Grazing incidence

small angle X-ray scattering (GISAXS) patterns were obtained for PLA-20-P(S-*s*-GMA)-11-XGMA-38 + 1 wt.% IST thin films spin coated onto silicon wafers (~ 70 nm film thickness). The films were irradiated both below and above the T_{ODT} and the results were qualitatively consistent with those obtained for bulk samples (Figure 5.17). This suggests that thin film confinement does not significantly influence the extent of composition fluctuations, consistent with previous observations.[33]

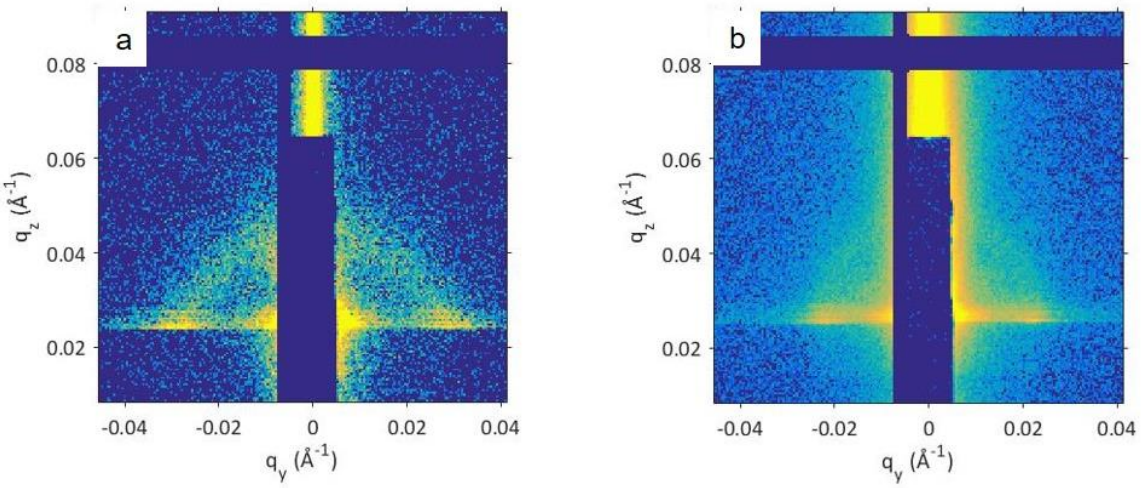

Figure 5.17. GISAXS patterns for approximately 70 nm thick films of PLA-20-P(S-*s*-GMA)-12-XGMA-38 + 1 wt.% IST spin coated from a 2 wt.% solution in acetonitrile onto Si wafers and irradiated at 80 °C (a) and 130 °C (b).

The suitability of this system for ultrafiltration (UF) membranes was then demonstrated by spin coating a 2 wt.% solution of PLA-20-P(S-*s*-GMA)-12-XGMA-38 + 1 wt.% IST in acetonitrile onto a water-filled PSF support (average pore size ~ 30 nm) following a previously reported procedure (see Chapter 3 for a detailed description of membrane fabrication).[6] This composite membrane was then heated to 150 °C (above the T_{ODT} of the selective layer), irradiated to cross-link, and selectively etched as in the bulk case. Top view SEM revealed a morphology that resembles the bulk system (Figure 5.18, top left panel), while cross-sectional SEM of a cryo-fractured membrane displayed an

approximately 800 nm thick film with domains that appear to percolate throughout the thickness of the film (Figure 5.18, top right panel). The hydraulic permeability of the resulting membrane was 4 $Lm^{-2}h^{-1}bar^{-1}$ as compared to 280 $Lm^{-2}h^{-1}bar^{-1}$ for the bare PSF support (Figure 5.19). The relatively low permeability of the UF membrane is possibly a result of the relatively thick selective layer. Further refinement of the coating process should result in thinner and more permeable UF membranes.

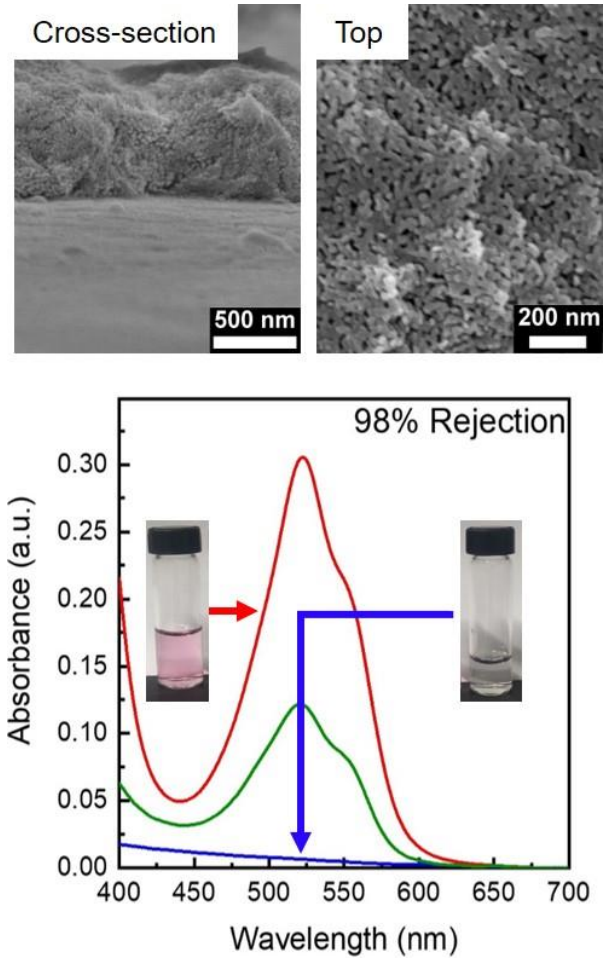

Figure 5.18. Cross-sectional SEM (top left panel) and top view SEM (top right panel) of an approximately 800 nm thick PLA-20-P(S-*s*-GMA)-12-XGMA-38 + 1 wt.% IST membrane spin coated from a 2 wt.% solution in acetonitrile onto a PSF support and irradiated at 150 °C for 10 minutes. UV-Vis spectra (bottom panel) for a feed solution (red curve) comprised of 0.5 mg/mL of TRITC-dextran (R_h ~ 7 nm) and the corresponding permeates from the bare PSF support (green curve) and from the composite membrane (blue curve). Rejection was 98% for the composite membrane as compared to 65% for the bare PSF support based on the ratio of maximum permeate absorbance to maximum feed absorbance.

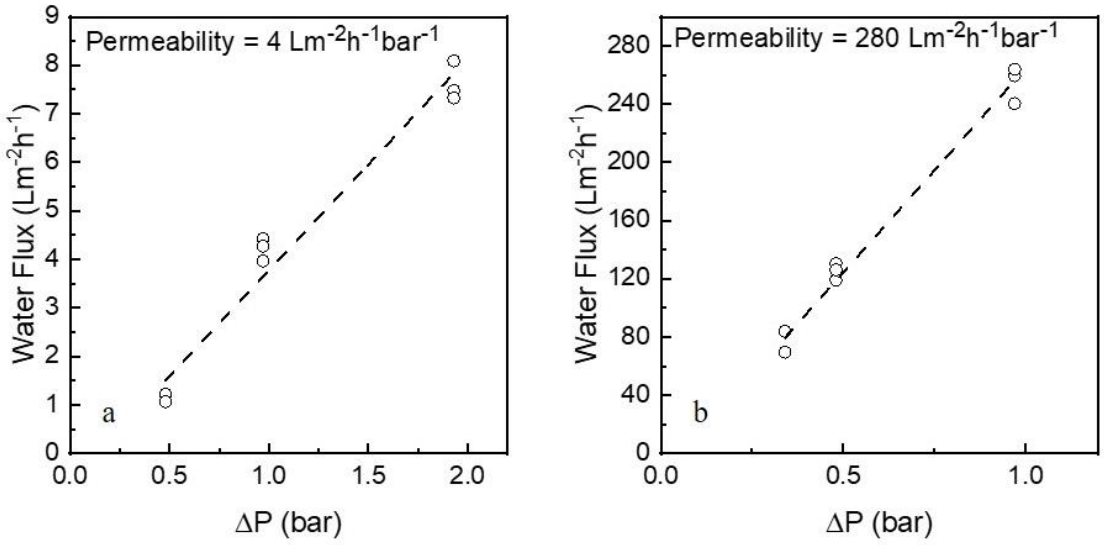

Figure 5.19. Water flux vs. pressure difference for a selective layer of PLA-20-P(S-*s*-GMA)-12-XGMA-38+ 1% IST spin coated from a 2 wt.% solution in acetonitrile onto a PSF support. The composite membrane was irradiated for 10 minutes at 150 °C (a). Water flux vs. pressure difference for the bare PSF support is presented in (b).

The high selectivity of the composite membrane was then demonstrated by passing an aqueous solution of a fluorescently labelled polysaccharide, TRITC-dextran, with an average R_h ~ 7 nm (larger than the pore radius of the selective layer as estimated by N_2 sorption) through the UF membrane. Rejection was calculated from the ratio of the UV-Vis absorbance of the permeate solution to that of the feed solution.[34] A rejection of 98% was observed for the composite membrane as compared to 65 % for the bare support, demonstrating the superior size-selectivity of the block polymer UF membrane (Figure 5.18, bottom panel). Additionally, a rejection curve was constructed using dextran standards of varying molar mass. A R_h cut-off of approximately 6 nm was found (Figure 5.20), consistent with the average pore size from QSDFT based on N_2 sorption for a bulk monolithic sample.

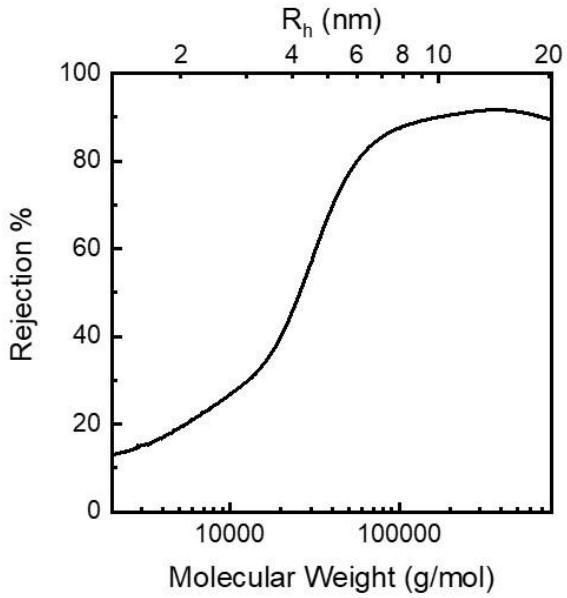

Figure 5.20. Rejection curve for a selective layer of PLA-20-P(S-*s*-GMA)-12-XGMA-38 + 1% IST spin coated from a 2 wt.% solution in acetonitrile onto a PSF support. The composite membrane was irradiated for 10 minutes at 150 °C. Rejection was calculated from aqueous SEC based on the permeate from a mixed feed of dextran standards.

5.4 Conclusions

We describe a method that enables a PLA-*b*- P(S-*s*-GMA) diblock containing the photoacid generator IST to be heated above its T_{ODT} and subsequently irradiated with UV light to kinetically trap the disordered state in a temporally controlled manner. Consequently, this system allows for the independent control over both the disordering process and the onset of the cross-linking reaction, effectively extending the temperature window where cross-linking is kinetically feasible. A diblock polymer with a low T_{ODT} was photocured with IST to demonstrate the ability to extend the temperature range where highly porous materials are accessible beyond a previously reported thermal cross-linking agent. Finally, the applicability of the photocured system in the design of highly selective UF membranes was demonstrated.

5.5 References

1) Jackson, E. A.; Hillmyer, M. A. Nanoporous Membranes Derived from Block Copolymers: From Drug Delivery to Water Filtration. *ACS Nano* **2010**, *4*, 3548–3553.

2) Phillip, W. A.; O'Neill, B.; Rodwogin, M.; Hillmyer, M. A.; Cussler, E. L. Self-Assembled Block Copolymer Thin Films as Water Filtration Membranes. *ACS Appl. Mater. Interfaces* **2010**, *2*, 847–853.

3) Schulze, M. W.; McIntosh, L. D.; Hillmyer, M. A.; Lodge, T. P. High-Modulus, High-Conductivity Nanostructured Polymer Electrolyte Membranes via Polymerization-Induced Phase Separation. *Nano Lett.* **2014**, *14*, 122–126.

4) Teran, A. A.; Mullin, S. A.; Hallinan, D. T.; Balsara, N. P. Discontinuous Changes in Ionic Conductivity of a Block Copolymer Electrolyte through an Order–Disorder Transition. *ACS Macro Lett.* **2012**, *1*, 305–309.

5) Bates, F. S.; Frederickson, G. Block Copolymers - Designer Soft Materials. *Phys Today* **1999**, *52*, 32–38.

6) Querelle, S. E.; Jackson, E. A.; Cussler, E. L.; Hillmyer, M. A. Ultrafiltration Membranes with a Thin Poly(styrene)-B-Poly(isoprene) Selective Layer. *ACS Appl. Mater. Interfaces* **2013**, *5*, 5044–5050.

7) Akthakul, A.; Salinaro, R. F.; Mayes, A. M. Antifouling Polymer Membranes with Subnanometer Size Selectivity. *Macromolecules* **2004**, *37*, 7663–7668.

8) Werber, J. R.; Osuji, C. O.; Elimelech, M. Materials for next-Generation Desalination and Water Purification Membranes. *Nat. Rev. Mater.* **2016**, *1*, 16018.

9) Cavicchi, K. A.; Zalusky, A. S.; Hillmyer, M. A.; Lodge, T. P. An Ordered Nanoporous Monolith from an Elastomeric Crosslinked Block Copolymer Precursor. *Macromol. Rapid Commun.* **2004**, *25*, 704–709.

10) Cochran, E. W.; Garcia-Cervera, C. J.; Fredrickson, G. H. Stability of the Gyroid Phase in Diblock Copolymers at Strong Segregation. *Macromolecules* **2006**, *39*, 2449–2451.

11) Matsen, M. W.; Bates, F. Unifying Weak- and Strong-Segregation Block Copolymer Theories. *Macromolecules* **1996**, *29*, 1091–1098.

12) Gopinadhan, M.; Deshmukh, P.; Choo, Y.; Majewski, P. W.; Bakajin, O.; Elimelech, M.; Kasi, R. M.; Osuji, C. O. Thermally Switchable Aligned Nanopores by Magnetic-Field Directed Self-Assembly of Block Copolymers. *Adv. Mater.* **2014**, *26*, 5148–5154.

13) Hadziioannou, G.; Mathis, A.; Skoulios, A. Obtention de ≪ Monocristaux ≫ de Copolymères Triséquencés Styrène/isoprène/styrène Par Cisaillement Plan. *Colloid Polym. Sci.* **1979**, *257*, 136–139.

14) Sinturel, C.; Vayer, M.; Morris, M.; Hillmyer, M. A. Solvent Vapor Annealing of Block Polymer Thin Films. *Macromolecules* **2013**, *46*, 5399–5415.

15) Seo, M.; Hillmyer, M. A. Reticulated Nanoporous Polymers by Controlled Polymerization-Induced Microphase Separation. *Science* **2012**, *336*, 1422-1425.

16) Zeng, D.; Ribbe, A.; Hayward, R. C. Anisotropic and Interconnected Nanoporous Materials from Randomly End-Linked Copolymer Networks. *Macromolecules* **2017**, *50*, 4668–4676.

17) Zhou, N.; Bates, F. S.; Lodge, T. P. Mesoporous Membrane Templated by a Polymeric Bicontinuous Microemulsion. *Nano Lett.* **2006**, *6*, 2354–2357.

18) Vidil, T.; Hampu, N.; Hillmyer, M. A. Nanoporous Thermosets with Percolating Pores from Block Polymers Chemically Fixed above the Order–Disorder Transition. *ACS Cent. Sci.* **2017**. *3*, 1114-1120.

19) Bates, F. S.; Rosedale, J. H.; Fredrickson, G. H. Fluctuation Effects in a Symmetric Diblock Copolymer near the Order–disorder Transition. *J. Chem. Phys.* **1990**, *92*, 6255–6270.

20) Lee, S.; Gillard, T.; Bates, F. Fluctuations, Order, and Disorder in Short Diblock Copolymers. *AIChE* **2013**, *59*, 3502–3513.

21) Takuma, K.; Takata, T.; Endo, T. Cationic Polymerization of Epoxide with Benzyl Phosphonium Salts as the Latent Thermal Initiator. *Macromolecules* **1993**, *26*, 862–863.

22) Scalfani, V. F.; Bailey, T. S. Thermally Stable Photocuring Chemistry for Selective Morphological Trapping in Block Copolymer Melt Systems. *Chem. Mater.* **2010**, *22*, 5992–6000.

23) Li, T.; Zhou, C.; Jiang, M. UV Absorption Spectra of Polystyrene. *Polym. Bull.* **1991**, *25*, 211–216.

24) Gor, G. Y.; Thommes, M.; Cychosz, K. A.; Neimark, A. V. Quenched Solid Density Functional Theory Method for Characterization of Mesoporous Carbons by Nitrogen Adsorption. *Carbon* **2012**, *50*, 1583–1590.

25) Neimark, A. V.; Lin, Y.; Ravikovitch, P. I.; Thommes, M. Quenched Solid Density Functional Theory and Pore Size Analysis of Micro-Mesoporous Carbons. *Carbon* **2009**, *47*, 1617–1628.

26) Almdal, K.; Rosedale, J. H.; Bates, F. S.; Wignall, G. D.; Fredrickson, G. H. Gaussian- to Stretched-Coil Transition in Block Copolymer Melts. *Phys. Rev. Lett.* **1990**, *65*, 1112–1115.

27) Bertrand, A.; Hillmyer, M. A. Nanoporous Poly(lactide) by Olefin Metathesis Degradation. *J. Am. Chem. Soc.* **2013**, *135*, 10918–10921.

28) Schulze, M. W.; Hillmyer, M. A. Tuning Mesoporosity in Cross-Linked Nanostructured Thermosets via Polymerization-Induced Microphase Separation. *Macromolecules* **2017**, *50*, 997–1007.

29) Zofchak, E. S.; LaNasa, J. A.; Mei, W.; Hickey, R. J. Polymerization-Induced Nanostructural Transitions Driven by In Situ Polymer Grafting. *ACS Macro Lett.* **2018**, *7*, 822–827.

30) Amendt, M. A.; Chen, L.; Hillmyer, M. A. Formation of Nanostructured Poly(dicyclopentadiene) Thermosets Using Reactive Block Polymers. *Macromolecules* **2010**, *43*, 3924–3934.

31) Lipic, P. M.; Bates, F. S.; Hillmyer, M. A. Nanostructured Thermosets from Self-Assembled Amphiphilic Block Copolymer/Epoxy Resin Mixtures. *J. Am. Chem. Soc.* **1998**, *120*, 8963–8970.

32) Morell, M.; Ramis, X.; Ferrando, F.; Serra, À. Effect of Polymer Topology on the Curing Process and Mechanical Characteristics of Epoxy Thermosets Modified with Linear or Multiarm Star Poly(ε-Caprolactone). *Polymer* **2011**, *52*, 4694–4702.

33) Kim, S.; Nealey, P. F.; Bates, F. S. Directed Assembly of Lamellae Forming Block Copolymer Thin Films near the Order–Disorder Transition. *Nano Lett.* **2014**, *14*, 148–152.

34) Jackson, E. A.; Lee, Y.; Hillmyer, M. A. ABAC Tetrablock Terpolymers for Tough Nanoporous Filtration Membranes. *Macromolecules* **2013**, *46*, 1484–1491.

Chapter 6. Molecular Engineering of Nanostructure in Disordered Block Polymers[4]

6.1 Introduction

Block polymers comprise two or more chemically distinct polymers covalently linked into a single chain.[1–3] These materials can self-assemble into long-range ordered morphologies due to a combination of unfavorable enthalpic contacts and chain connectivity – a phenomena termed microphase separation.[2,4] In typical block polymers, entropic factors associated with unfavorable chain stretching in the ordered state become increasingly significant at higher temperatures, eventually leading to a loss in long-range order at the order-disorder transition (ODT) temperature (T_{ODT}).[2,4,5]

Intuitively, one might imagine a very weakly structured and mostly homogeneous melt in the disordered state just above T_{ODT}, with low amplitude fluctuations around the mean composition (f) at the length scale of R_g. However, numerous experimental[6–9] and theoretical studies[10,11] have shown that composition fluctuations exist just above T_{ODT}, resulting in a system that remains locally microphase segregated despite a lack of long-range spatial correlations. Indeed, it has been shown that there is a significant change in

[4] Reproduced with permission from Hampu, N.; Hillmyer, M. A. Molecular Engineering of Nanostructures in Disordered Block Polymers. *ACS Macro Let.* **2020**, *9*, 382-388. Copyright 2020 American Chemical Society.

interfacial Gaussian curvature, yet little change in domain purity or interfacial area across T_{ODT}, resulting in a dynamic pattern that resembles the late stages of spinodal decomposition.[8,11–13]

Recently, we have reported direct experimental evidence confirming the bicontinuous nature of the fluctuating disordered state for symmetric diblock polymers by cross-linking reactive block polymers above T_{ODT} and selectively removing one domain to give nanoporous materials.[14–16] However, kinetic and thermal limitations of these cross-linking reactions[15,16] have prevented the investigation of the domain structure *far* above T_{ODT} (at segregation strengths of $\chi N << 10$), where a homogeneous, mean-field-like melt is expected.[11,17] To integrate the inherent nanostructure of disordered block polymers into the design of advanced materials, a greater understanding of the experimental parameters governing this transition from a fluctuating disordered to a mean-field disordered state is required.[3,14,18]

6.2 Experimental Methods

To this end, we have designed poly(methyl methacrylate-*stat*-styrene)-*block*-polylactide, P(MMA-*s*-S)-*b*-PLA, diblock terpolymers that can be heated above their T_{ODT}, lack readily cross-linkable moieties, and can be vitrified by quenching at low temperature. By tuning the molar fraction of styrene in these diblocks, a wide range of χN can be accessed with minimal variation in the degree of polymerization, N, as $\chi_{S\text{-}LA} >> \chi_{MMA\text{-}LA}$.[19,20] Consequently, the entire range from ordered to fluctuating disordered to mean-field disordered states can be obtained through this molecular engineering approach without

encountering previous kinetic and thermal complications associated with chemically cross-linkable systems (Figure 6.1). A series of P(MMA-*s*-S)-*b*-PLA diblock polymers was synthesized using reversible-addition fragmentation chain transfer (RAFT) polymerization from a single PLA macro-chain transfer agent with a number average molar mass of 24 kg mol^{-1}, PLA-24 (Figures 6.2 – 6.4 and Table 6.1) (see Chapter 3 for full synthetic details). Size exclusion chromatography (SEC) analysis for all the P(MMA-*s*-S)-*b*-PLA diblock polymers displayed a single, narrow peak with $Đ \lesssim 1.1$ and similar molar masses. (Figure 6.3). The S/MMA reactivity ratios are both approximately 0.5, so copolymerizations were terminated at low conversions to help mitigate compositional drift along the chain. Therefore, variations in segregation strengths, χN, are primarily the result of differences in χ rather than the overall volume normalized degree of polymerization (N). Thus, these diblocks will be referred to by their respective molar fractions of styrene in the P(MMA-*s*-S) block (XS).

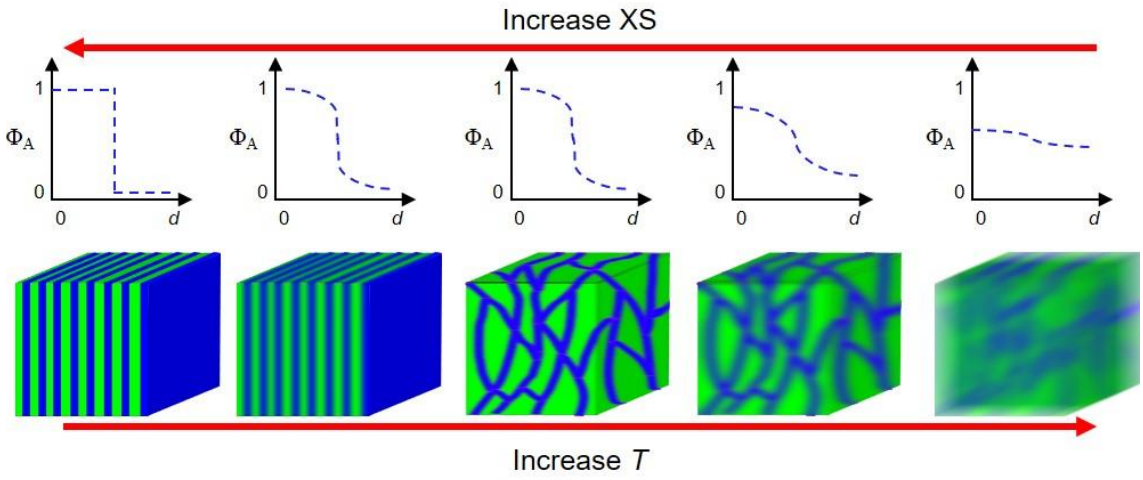

Figure 6.1. A sketch of the anticipated composition profile of the volume fraction of the A block (Φ_A) across one lamellar period (d) for varying χN is provided in the upper panel, while a cartoon representation of the corresponding domain structures is provided in the lower panel. By increasing the molar fraction of styrene in the poly(methyl methacrylate-*stat*-styrene)-*block*-polylactide, P(MMA-*s*-S)-*b*-PLA, diblock terpolymer and/or decreasing the temperature, a broad range of domain structures ranging from a phase-pure

ordered lamellar state (far left) to a weakly structured disordered state (far right) can be obtained.

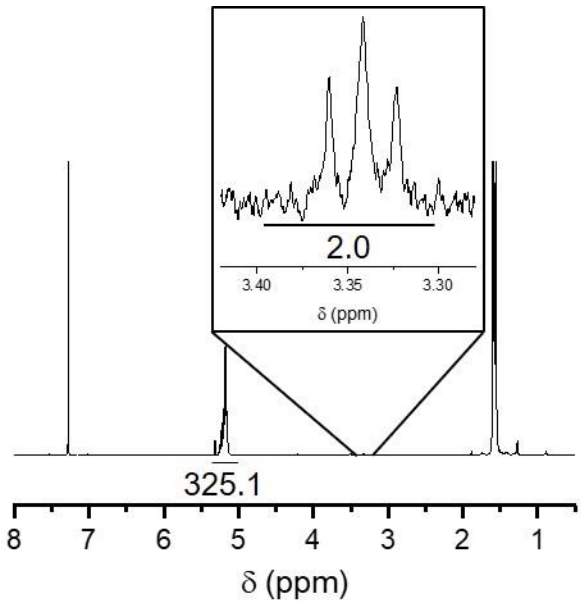

Figure 6.2. ^{1}H NMR spectrum for PLA-24. Regions of integration for the methine protons of the PLA backbone (5.00–5.40 ppm, 1*H*) and the methylene protons adjacent to the trithiocarbonate of the CTA (3.30-3.40 ppm, 2*H*) are indicated, and the corresponding integral values are provided below the corresponding peak (M_n = 24 kg mol^{-1}).

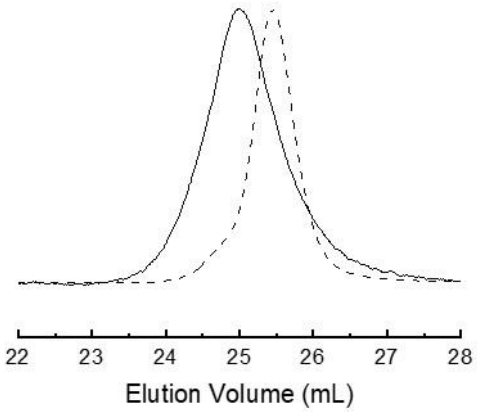

Figure 6.3. THF SEC elugrams for PLA-24 ($Đ$ = 1.07, dashed curve) and P(MMA-*s*-S)-23-PLA-24-XS-27 ($Đ$ = 1.09, solid curve).

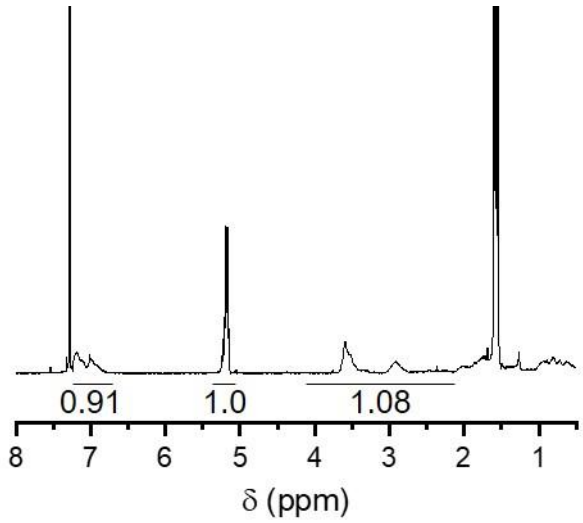

Figure 6.4. ^{1}H NMR spectrum for P(MMA-*s*-S)-23-PLA-24-XS-27 (referred to as XS = 27). Regions of integration for the PS aromatic protons (6.30–7.20 ppm, 5*H*), the methyl protons of PMMA (2.10–4.20 ppm, 3*H*), and the methine protons of the PLA backbone (5.00–5.40 ppm, 1*H*) are indicated along with their corresponding integral values ($M_{n,\ P(MMA\text{-}s\text{-}S)}$ = 23 kg mol^{-1}, XS = 27, f_{PLA} = 0.48).

Table 6.1. Molecular characteristics for all P(MMA-*s*-S)-*b*-PLA diblocks from PLA-24

$M_{n,\ PLA\text{-}CTA}$[a] (kg/mol)	$M_{n,\ P(MMA\text{-}s\text{-}S)}$[b] (kg/mol)	XS (%)	N[c]	f_{PLA}[d]	$Đ$[e]	T_g[f] (°C)	$G'\sim\omega^n$ (95 °C)	$T_{ODT,\ rheo}$[g] (°C)
24	29	0	620	0.43	1.07	50	1.2	-
24	26	8	590	0.45	1.16	56	0.9	-
24	25	17	580	0.46	1.09	55	0.84	-
24	26	19	595	0.45	1.08	53, 72	0.55	-
24	26	20	585	0.46	1.05	54, 74	0.53	-
24	23	26	560	0.48	1.08	52, 75	0.52	130
24	23	27	560	0.48	1.09	52, 75	0.49	140
24	26	32	585	0.45	1.10	54, 85	0.46	160

[a]Number-average molar mass of the PLA block from ^{1}H NMR analysis reported in kg mol^{-1}. [b] Number-average molar mass of the P(MMA-*s*-S) block from ^{1}H NMR analysis reported in kg mol^{-1} [c]Degree of polymerization determined according to M_n and a reference volume of 118 Å^3 [d]Volume fraction of PLA based on reported room temperature homopolymer densities and ^{1}H NMR spectroscopy. [e]Molar mass dispersity evaluated using LS-SEC in THF. [f]T_g determined from the 2nd heating scan from DSC with a ramp rate of 20 °C min^{-1}. [g]$T_{ODT,\ rheo}$ determined from DMA as determined by the discontinuity in G' upon heating with a ramp rate of 2 °C min^{-1}, frequency of 1 rad s^{-1} and strain of 1 %.

6.3 Results and Discussion

6.3.1 Morphological Characterization of Diblock Melts

The existence or absence of well-defined microphase separated domains for the diblock polymers derived from PLA-24 was first investigated using a combination of differential scanning calorimetry (DSC) and dynamic mechanical analysis (DMA). For XS < 19, a single T_g was observed in DSC (Figure 6.5). The frequency dependence of the storage modulus, G', at 95 °C scaled as $G' \sim \omega^{0.84\text{-}1.2}$, which was higher than what is typically observed for ordered block polymers, $G' \sim \omega^{0\text{-}0.5}$ (Figure 6.6). [21–25] Additionally, the frequency dependence of the loss modulus, G'', scaled as $G'' \sim \omega^{0.6\text{-}0.84}$, in general agreement with the expected scaling of $G'' \sim \omega^{1.0}$ for a disordered melt and suggestive of loss dominated viscoelasticity (Figure 6.6). We expect that the low frequency scaling of G' and G'' would be closer to the expected values if the experiments were run to lower frequencies, although technical limitations prohibited such experiments in this work. The XS < 19 diblocks exhibited a continuous and smooth decrease in G' with increasing temperature, signifying that these polymers remained in the disordered state over the entire temperature range (Figure 6.7a).[24] Overall these results suggest that the diblock polymers with low XS lacked well-defined microphase segregated domains due to their low segregation strengths, χN, and likely exhibit a more mean-field-like state with well-mixed blocks at the nanoscale.

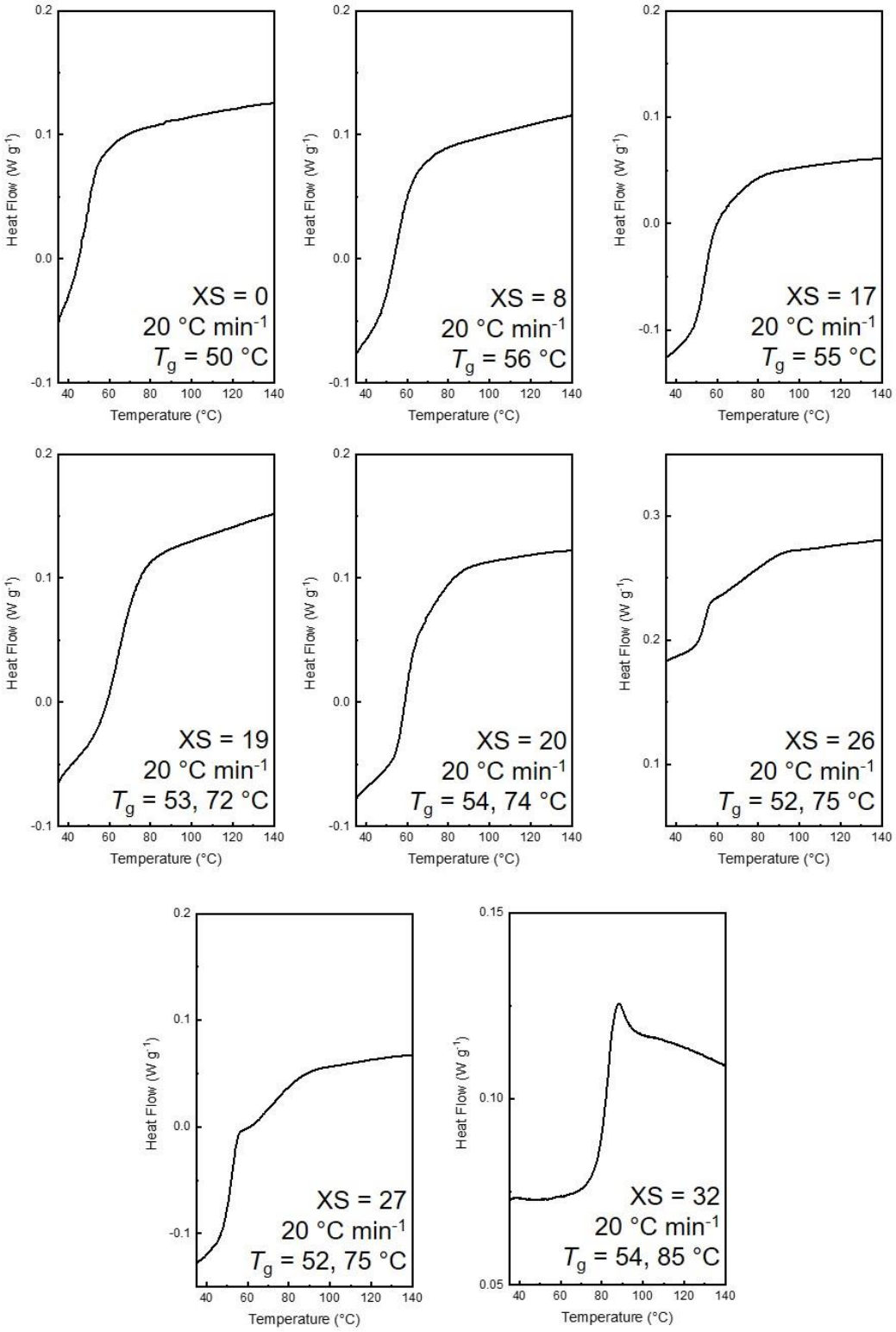

Figure 6.5. DSC thermograms obtained on the second heating cycle at a ramp rate of 20 °C min^{-1} for the P(MMA-*s*-S)-*b*-PLA diblocks derived from PLA-24. The XS and T_g for each diblock is provided on its respective thermogram.

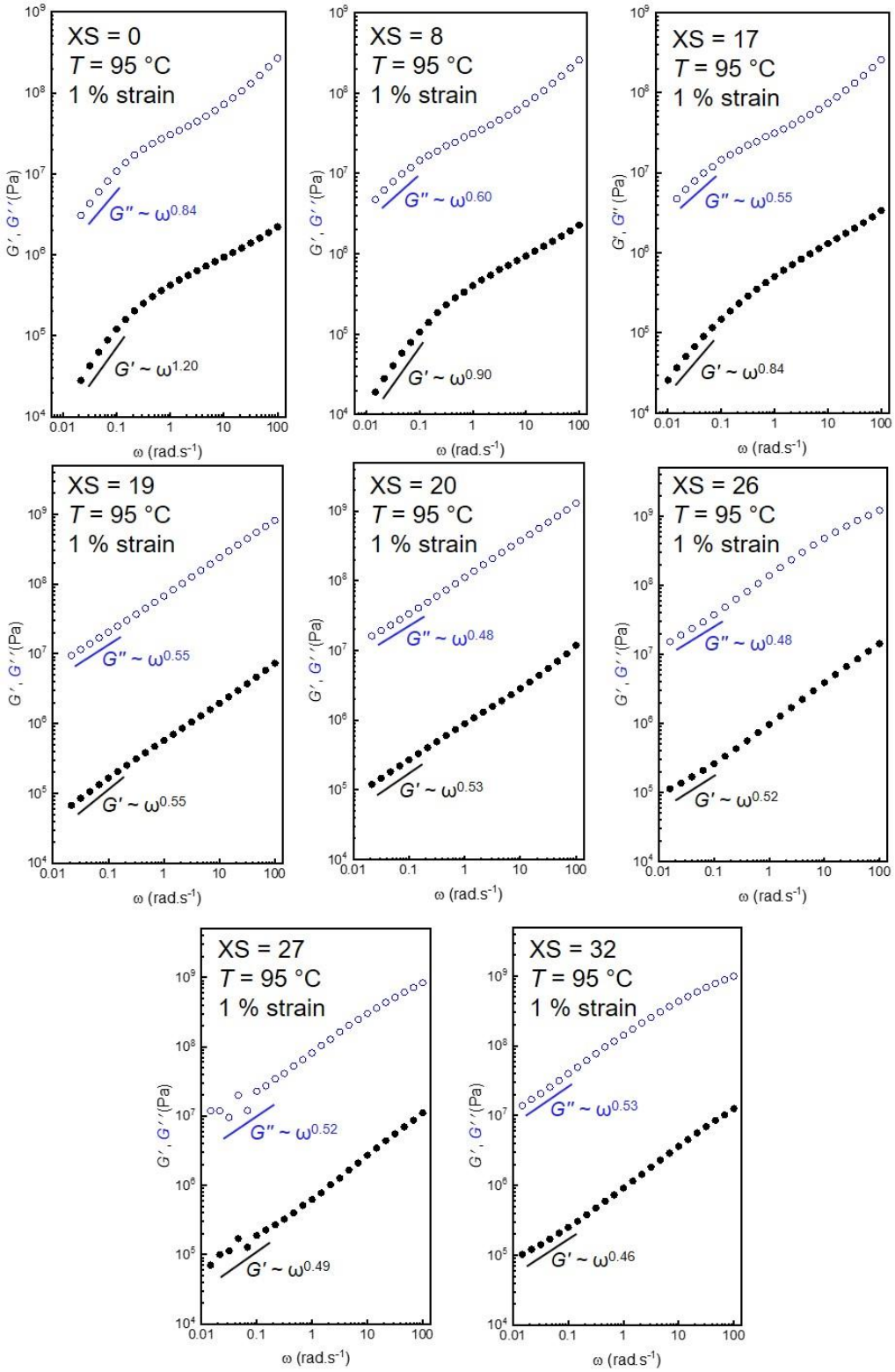

Figure 6.6. Rheological frequency sweeps for the PLA-24 diblocks that were collected from approximately 100 to 0.01 rad s^{-1} at 95 ˚C and 1% strain. The XS and low frequency power law scaling of G' and G'' are inset on the plots. G'' values were vertically shifted by a factor of 100 for clarity.

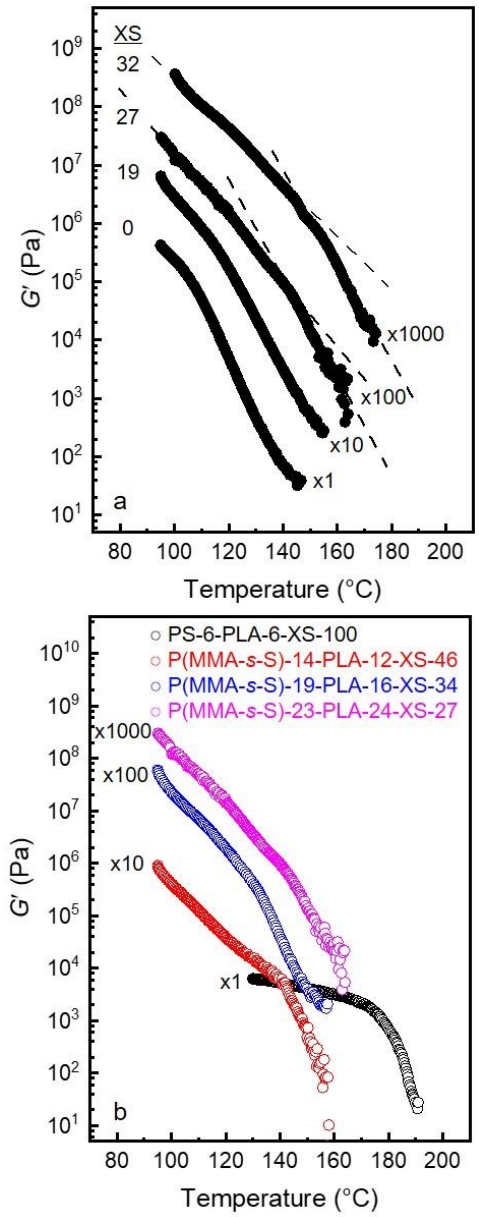

Figure 6.7. Temperature dependence of the storage modulus G' for representative PLA-24 diblocks (a) and for diblocks derived from different molar mass PLA macro-chain transfer agents with varying N and XS (b). All dynamic mechanical analysis temperature sweeps were performed at 1 rad s^{-1}, 1% strain, minimum torque of 0.02 μN m, and with a heating rate of 2 °C min^{-1} on samples annealed overnight at 100 °C. The T_{ODT} was determined based on the change in slope of G' as indicated by the dashed lines inset in (a). Data was vertically translated for clarity, and vertical scaling factors are indicated on the plots.

Conversely, DSC and DMA revealed clear evidence of microphase segregation for the diblocks with XS ≥ 26. Two T_g's were observed in DSC (Figure 6.5) and the low-frequency scaling of the storage modulus at 95 °C, $G' \sim \omega^{0.5}$, was generally consistent with the expected scaling for lamellar-forming diblock polymers (Figure 6.6).[21–25] The temperature dependence of G' exhibited a slight change in slope with increasing temperature, which we attribute to the T_{ODT} (Figure 6.7a).[24] This shoulder became progressively sharper and was shifted to higher temperatures with increasing XS, consistent with an increase in χN. Interestingly, this viscoelastic transition was significantly less sharp than is commonly observed at the ODT.[24] The sharpness of the transition increased with increasing χ (XS) for diblocks with widely varying molar masses (N) yet reasonably similar T_{ODT}'s (Figure 6.7b). This suggests that these low-χ diblocks have relatively thick and diffuse interfaces (and potentially compositional gradients) that resulted in a less drastic change in the viscoelastic properties at the T_{ODT} and thus a broad transition from order to disorder. Similar observations have been reported for block random and tapered copolymers with similarly thick interfacial regions.[26–29] Regardless, the complementary results from DSC and DMA strongly suggest that the diblock polymers with XS ≥ 26 comprise well-structured microphase segregated domains, as is expected for either a fluctuating disordered or an ordered morphology.

The morphologies of the P(MMA-*s*-S)-*b*-PLA diblock polymers were then examined using variable temperature small angle X-ray scattering (SAXS) (Figure 6.8). At 30 °C, intense, narrow scattering peaks were observed for XS ≥ 26 (full width at half max, FWHM = 0.015 nm^{-1}), indicative of an ordered morphology. However, the lack of higher order peaks

suggested only a modest degree of long-range order, possibly due to their relatively thick domain interfaces. Based on f_{PLA} and rheological measurements, it is expected that these diblocks form ordered lamellae.[6,12] For XS = 19, a significantly broader scattering peak (FWHM = 0.051 nm^{-1}) was observed, characteristic of a disordered morphology.

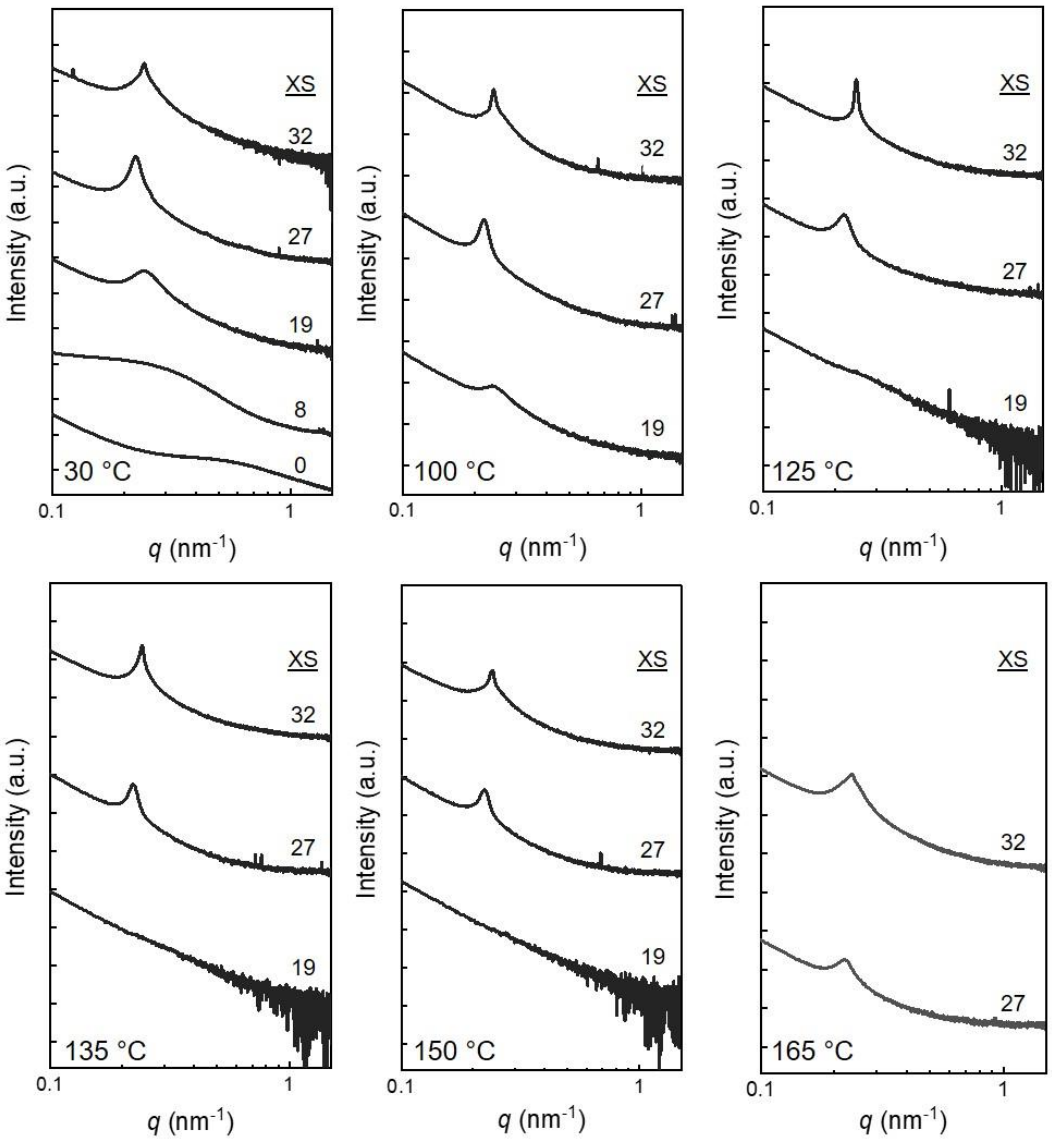

Figure 6.8. Variable temperature SAXS patterns for all PLA-24 diblock polymers obtained at 30 °C, 100 °C, 125 °C, 135 °C, 150 °C, and 165 °C. All samples were annealed for at least 2 minutes at each temperature prior to data acquisition. XS = 0 and 8 were only examined at 30 °C, and only XS = 27 and XS = 32 were examined at 165 °C. Data was vertically translated to ensure clarity. Lower signal to noise at high *q* values likely resulted from low scattered intensity at the edge of the detector.

The two diblocks with the lowest styrene contents, XS = 0 and XS = 8, exhibited very broad peaks (FWHM = 0.1 nm^{-1}) that extend over a large q range at 30 °C, suggesting very short-range spatial correlations. In particular, this peak occurred at a noticeably higher q^* for XS = 0 than for the other diblocks, indicating a significantly smaller domain spacing, $d = 2\pi/q^*$, despite having a slightly higher molar mass. Since all the diblock polymers observed in this study have very similar N, this difference in q^* likely results from the low segregation strength of this diblock ($\chi N \sim 2$, *vide infra*). Theory has predicted a change in scaling from $d \sim N^{0.66}$ for stretched chains in the fluctuating disordered state to $d \sim N^{0.5}$ for Gaussian coils in the mean-field state. These scaling relationships correspond well with the experimental observation that d for XS = 32 (25.6 nm) was approximately twice that of XS = 0 (13.1 nm) for $N \sim 600$, suggesting that XS = 0 exists in an approximately mean-field state.[4,17,30] For XS = 8, the broad peak occurred at an intermediate q ($d \sim 20$ nm), suggesting that this diblock may exist in a transition region between stretched and coiled behavior with low amplitude composition fluctuations.

As XS = 19 was heated from 30 °C, the broad peak eventually shifted to higher q and diminished as the temperature increased, consistent with a transition from fluctuating disordered domains to mean-field-like domains with decreasing χN.[17] For the ordered diblocks with XS ≥ 26, the initially sharp scattering peaks transitioned into broader and less intense peaks at elevated temperatures, consistent with a transition from an ordered to a disordered melt. The T_{ODT}'s from SAXS were determined by identifying the change in slope in I^{-1} vs T^{-1} (Figure 6.9) and T_{ODT} was observed to increase with increasing XS.[8,21] Despite an apparent change in slope for XS = 19 and 26, the low intensity and broad peaks

observed for these polymers likely reflects that this is a transition from a fluctuating to a mean-field-like state rather than an ODT. Additionally, the temperature dependence of the interaction parameter, χ, for the P(MMA-*s*-S)-*b*-PLA diblocks was estimated by fitting the random phase approximation (RPA) to the scattering patterns of XS = 20 and 26 obtained in the disordered state, using a reference volume of 0.118 nm^3 (Figures 6.10 – 6.12).[31] These fitted values of χ were then used to estimate χN for each diblock using a binary interaction model along with previously reported values of $\chi_{S\text{-}LA}$ and $\chi_{S\text{-}MMA}$.

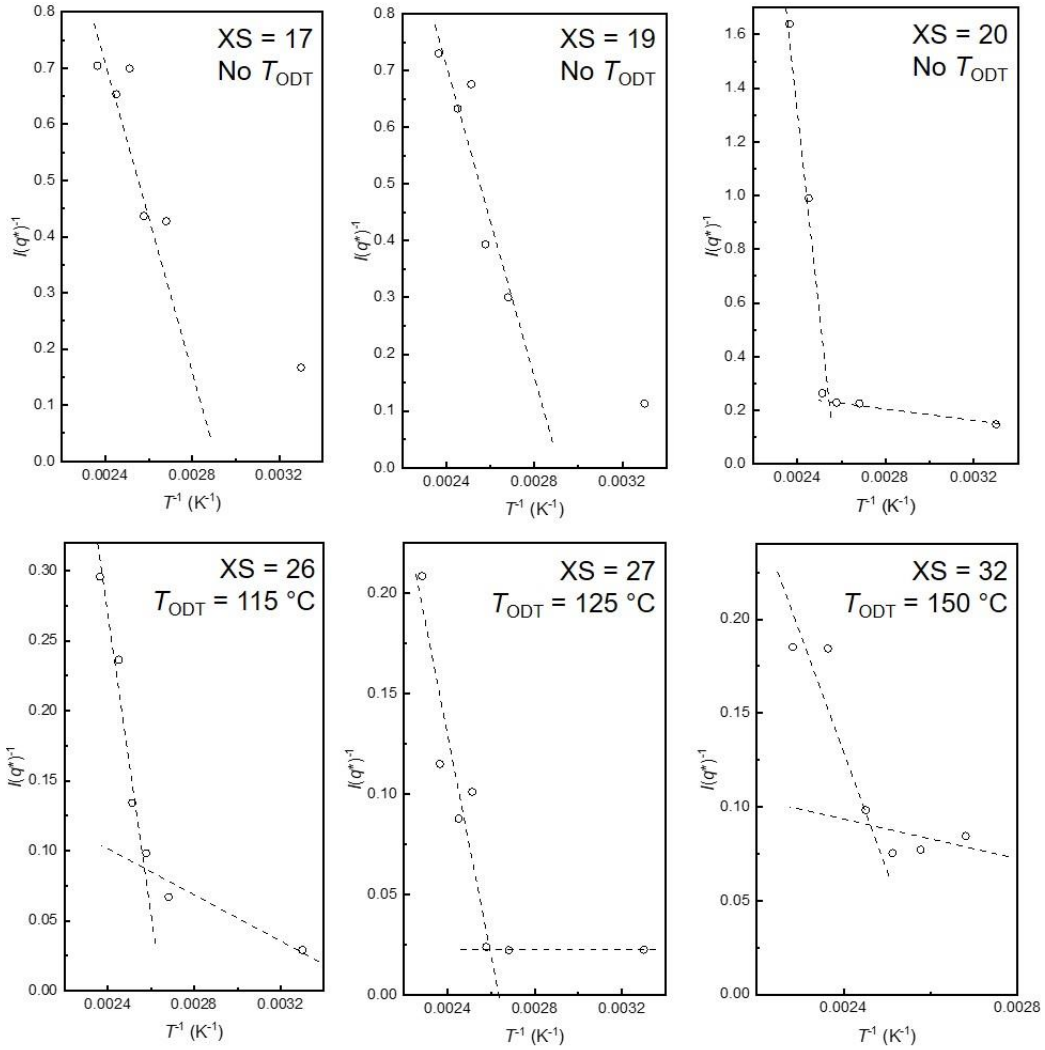

Figure 6.9. The inverse intensity of the principal scattering peak, $I^{-1}(q^*)$ is plotted as a function of the inverse of the temperature where each pattern was obtained, T^{-1}, for the PLA-24 diblocks. The T_{ODT} was determined to be the temperature where a change in the slope of $I^{-1}(q^*)$ was observed and is indicated on each plot.

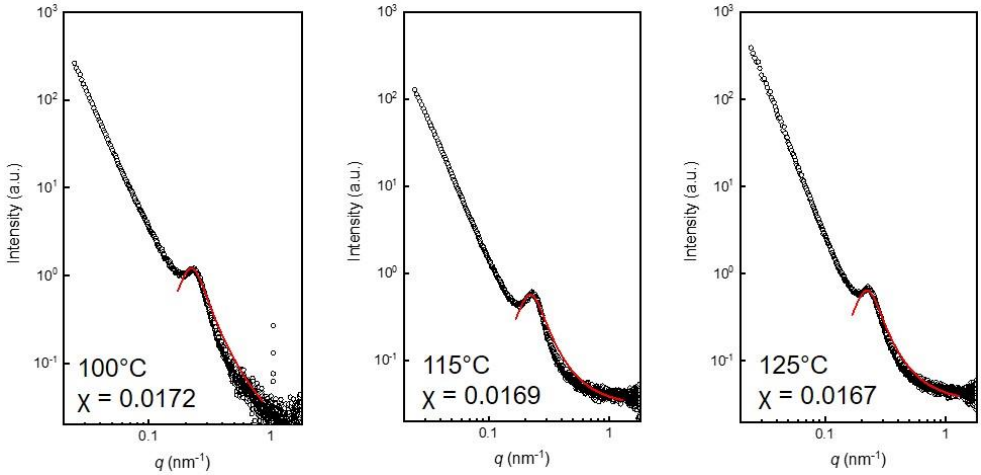

Figure 6.10. Fits of the Random Phase Approximation to scattering patterns obtained at 100, 115, and 125 °C for XS = 20. The fitted values of χ are provided for each temperature. Experimental data is presented as open black circles and model fits as solid red curves.

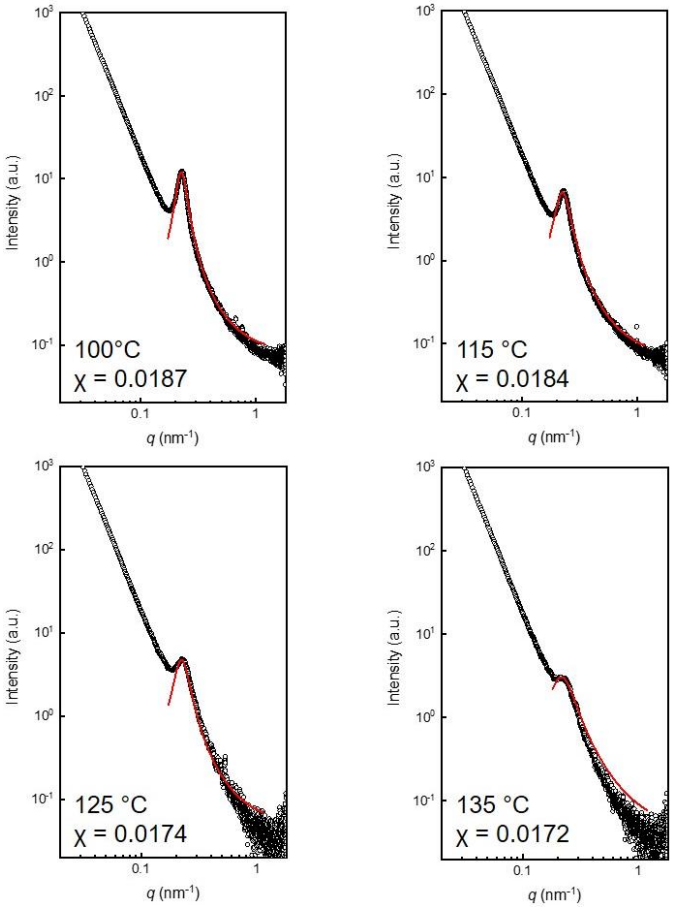

Figure 6.11. Fits of the Random Phase Approximation to scattering patterns obtained at 100, 115, 125, and 135 °C for XS = 26. The fitted values of χ are provided for each temperature. Experimental data is presented as open black circles and model fits as solid red curves.

Table 6.2. RPA fitting parameters for XS = 20 and XS = 26

XS	T (°C)	b_{PLA} (Å)	$b_{P(MMA\text{-}s\text{-}S)}$ (Å)	χ
20	100	7.0	10.5	0.0172
	115	7.0	10.8	0.0169
	125	7.0	11.1	0.0167
26	100	7.0	10.8	0.0187
	115	7.0	10.9	0.0184
	125	7.0	11.6	0.0174
	135	7.0	12.2	0.0172

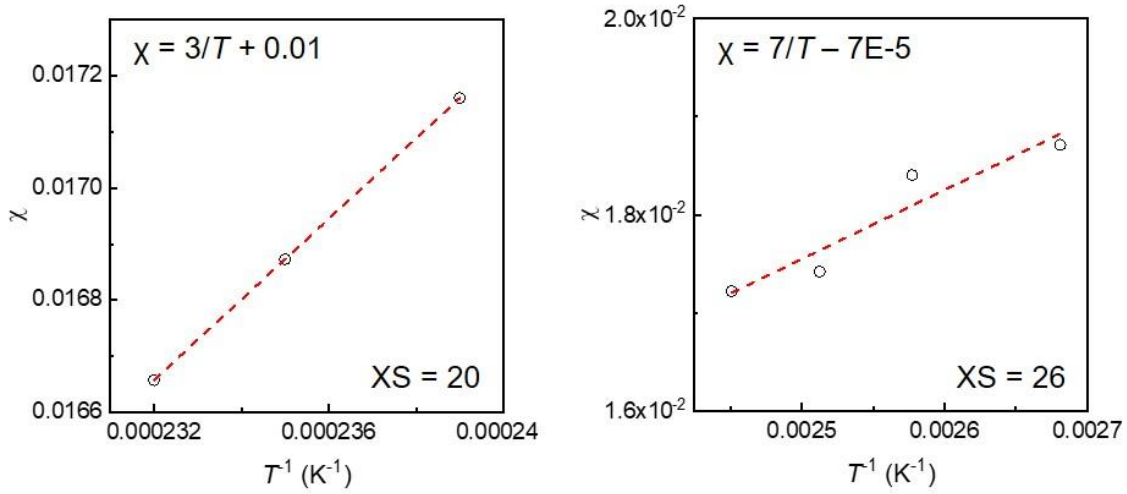

Figure 6.12. Temperature dependence of the interaction parameter, $\chi_{P(MMA\text{-}s\text{-}S)\text{-}b\text{-}PLA}(T)$, estimated using values of χ obtained by fitting the RPA model to disordered SAXS patterns for XS = 20 (left) and XS = 26 (right). A linear fit to the experimental data is presented as the dashed red line. Data are reported using a fixed monomer reference volume (v_o = 118 Å^3).

The continuity of the PLA domains in these diblock polymers was investigated by gravimetric analysis following selective chemical etching of PLA. All samples were annealed overnight at 100 °C (above the T_g), slowly cooled to ambient conditions, and then immersed in a solution of 2 M NaOH in H_2O/MeOH (40/60, v/v) to selectively remove the PLA domains that were readily accessible to the etching solution. For XS ≤ 17 (χN < 6.6 at 100 °C), the mass loss after etching was only about 50 – 60 % of the weight fraction of PLA that was initially present (w_{PLA}) (Table 6.3). This suggests that these PLA domains are not completely continuous and not readily accessible to the etching solution, consistent

with the conclusion that they exhibit a relatively unstructured and mean-field-like morphology based upon the DSC and SAXS analyses discussed previously. Conversely, nearly all the PLA was removed for XS ≥ 19 (χN > 7.3 at 100 °C), with the mass loss after etching representing 85 – 95 % of w_{PLA}. These diblock polymers likely contain mostly continuous PLA domains that are accessible to the etching solution, consistent with the expected domain structure for fluctuating disordered and ordered morphologies.

Table 6.3. Mass loss % of initial PLA present for PLA-24 diblocks with varying XS

XS	Morphology	w_{PLA}	% Total Mass Loss After Etching	% Mass Loss of PLA
0	Dis	0.45	25	55
8	Dis	0.47	27	58
17	Dis	0.48	26	54
19	Dis	0.48	44	92
20	Lam	0.48	42	88
26	Lam	0.50	41	82
27	Lam	0.50	44	88
32	Lam	0.48	45	94

6.3.2 Thermal Processing of Block Polymers Above T_{ODT}

Diblock polymers that exhibit ordered morphologies at room temperature can be kinetically trapped in a disordered state by heating above T_{ODT} and then rapidly cooling below the lowest T_g. To demonstrate this point, the diblock with XS = 27 was annealed at 180 °C (T_{ODT} + 40 °C) and was then rapidly immersed in liquid nitrogen (LN2). SEM (Figure 6.13a), SAXS, and N_2 sorption analysis (Figure 6.14) verified that a kinetically trapped disordered state was obtained. In contrast, a lamellar morphology was observed after annealing below T_{ODT}.[14–16] Slowly cooling the same diblock from 180 °C at a rate of 2 °C

min^{-1} resulted in partial recovery of lamellar ordering (Figures 6.13a and 6.14), suggesting that this cooling rate was insufficient to trap the disordered state prior to re-ordering.

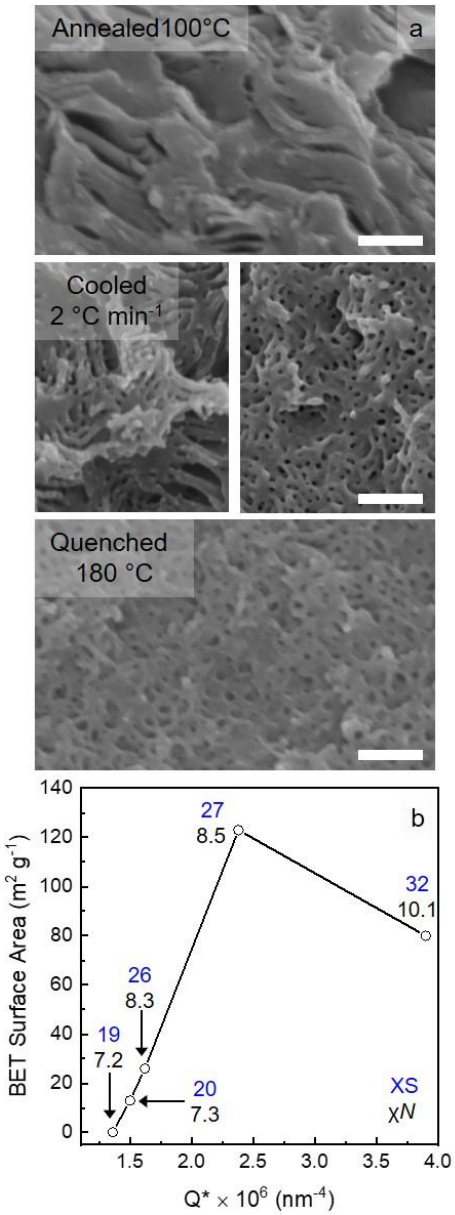

Figure 6.13. SEM images (a) obtained from etched samples of XS = 27 subjected to different thermal treatments: annealed below T_{ODT} (100 °C) (top), annealed above T_{ODT} (180 °C) and cooled below T_g at a rate of 2 °C min^{-1} (middle), and annealed above T_{ODT} (180 °C) and quenched (bottom). The two SEM images in the middle panel were obtained from different regions of the same sample. BET surface area (b) for all PLA-24 diblocks plotted as a function of scattering invariant, Q*. The XS and χN for each sample are indicated in the inset. All samples were annealed at 180 °C before quenching. Q* was calculated from room temperature SAXS patterns before etching.

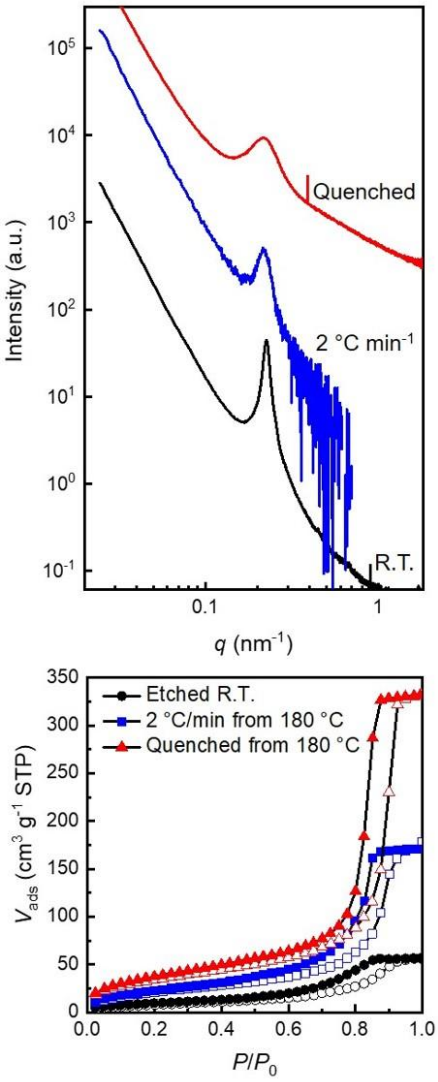

Figure 6.14. SAXS patterns (top) and N_2 sorption isotherms (bottom) for XS = 27 subjected to different thermal treatments. All three samples were annealed overnight at 100 °C (below T_{ODT}). One sample was then cooled to room temperature and analyzed (black). The other two samples were then annealed at 180 °C (above T_{ODT}) for one hour and then either rapidly quenched in LN2 (red) or cooled at a rate of 2°C min^{-1} (blue). SAXS patterns were acquired prior to etching. Isotherms were obtained following PLA removal. Open circles correspond to data taken upon adsorption and closed circles correspond to data taken upon desorption.

6.3.3 Determination of Domain Continuity and Nanostructure in the Disordered State

Based on these results, we postulated that a combination of thermal and chemical (XS) methods can be used to precisely tune the segregation strength of these diblocks while maintaining an identical thermal history. The diblocks with XS ≥ 19, which displayed

quantitative PLA removal following etching at room temperature, were heated to 180 °C (above the T_{ODT}'s for all the diblock polymers examined here) for 1 h before quenching in LN2. The extent of microphase separation present in each of these quenched samples was quantitatively analyzed by calculating the Porod scattering invariant, Q*, from room temperature SAXS patterns acquired prior to PLA removal (Figure 6.15).[13,32] Generally, Q* was observed to decrease with decreasing χN (XS), consistent with weak microphase separation and more homogeneously mixed domains (Figure 6.15).[13,32] On the other hand, diblocks with higher χN (larger XS) gave larger values of Q*, consistent with microphase segregation even at temperatures slightly above T_{ODT} due to the presence of composition fluctuations.[11,13]

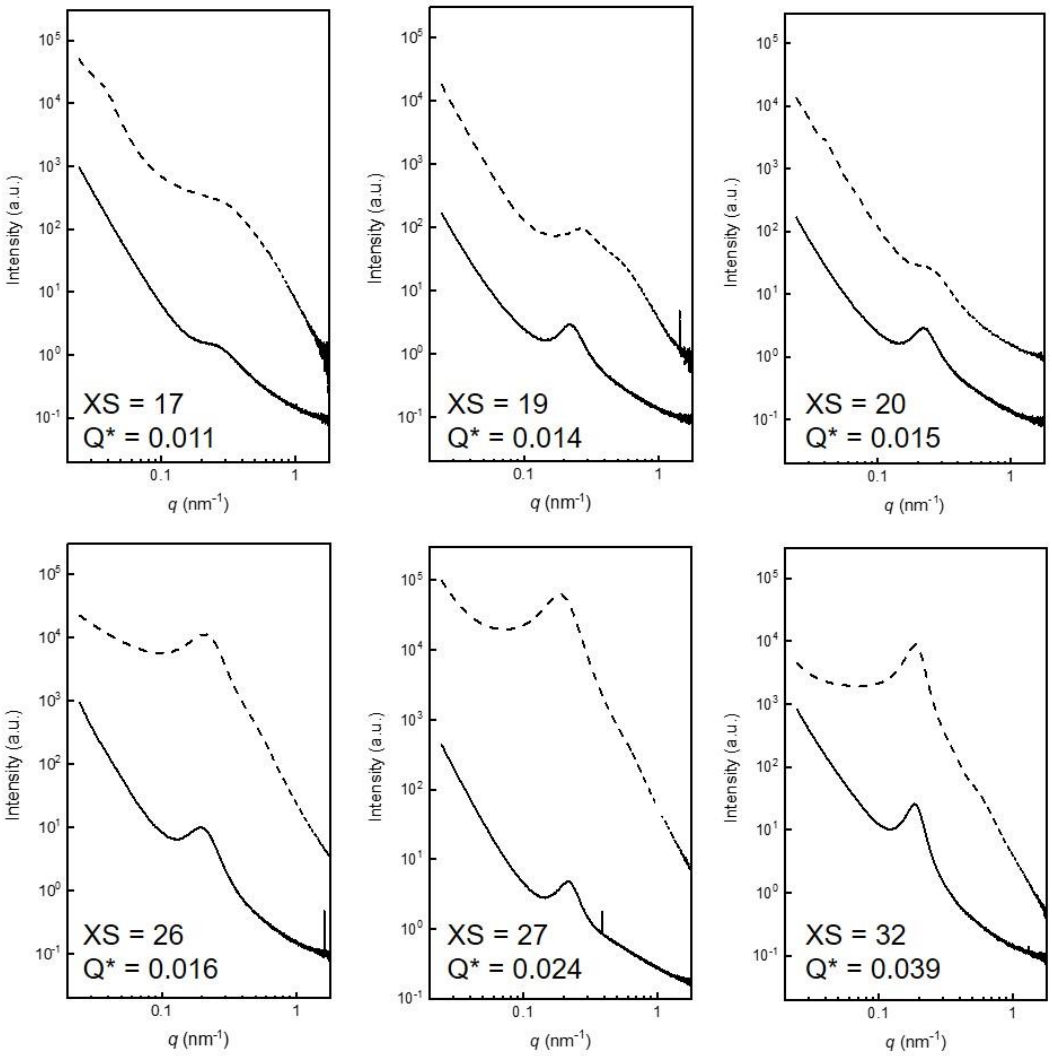

Figure 6.15. Room temperature SAXS for the PLA-24 diblocks quenched from 180 °C before (solid lines) and after (dashed lines) etching. The Porod scattering invariant, Q*, and XS are indicated on each set of patterns. Curves have been vertically shifted for clarity.

Additionally, the SAXS patterns for the unetched samples were fit to the Teubner-Strey (TS) model[33]

$$I(q) = \frac{1}{a_2 + c_1 q^2 + c_2 q^4} \text{ eq. (1)}$$

for q = 0.1 to 1 nm^{-1}. Although the TS model was rigorously derived for ternary mixtures of topologically similar bicontinuous microemulsions, we used it as a qualitative metric to analyze the domain structure in the limit of zero homopolymer and obtained fits that were

in general agreement with the experimental data (Figures 6.16 and 6.17).[34-38] Two parameters of interest can be extracted from the TS fits: the correlation length, ξ, represents the spatial coherence of the domain interfaces and the amphiphilicity factor, f_a, is associated with the interfacial structure.[39,40]

$$\xi = \left[\frac{1}{2}\left(\frac{a_2}{c_2}\right)^{1/2} + \left(\frac{1}{4}\left(\frac{c_1}{c_2}\right)\right)\right]^{-1/2} \quad \text{eq. (2)}$$

$$f_a = \frac{c_1}{\sqrt{4a_2c_2}} \quad \text{eq. (3)}$$

For the polymers with $\chi N > 8.3$ (XS ≥ 26), ξ was relatively large (on the order of the domain spacing), consistent with strong segregated domains. Furthermore, f_a was found to be between -0.8 and -0.94, suggesting that the local interfacial structure of these disordered diblock polymers resembles the ordered lamellar state (f_a = -1). These experimental findings are consistent with the theoretical prediction that the ODT is characterized primarily by a change in Gaussian curvature at the domain interface rather than by a significant change in interfacial area or domain purity.[11,12]

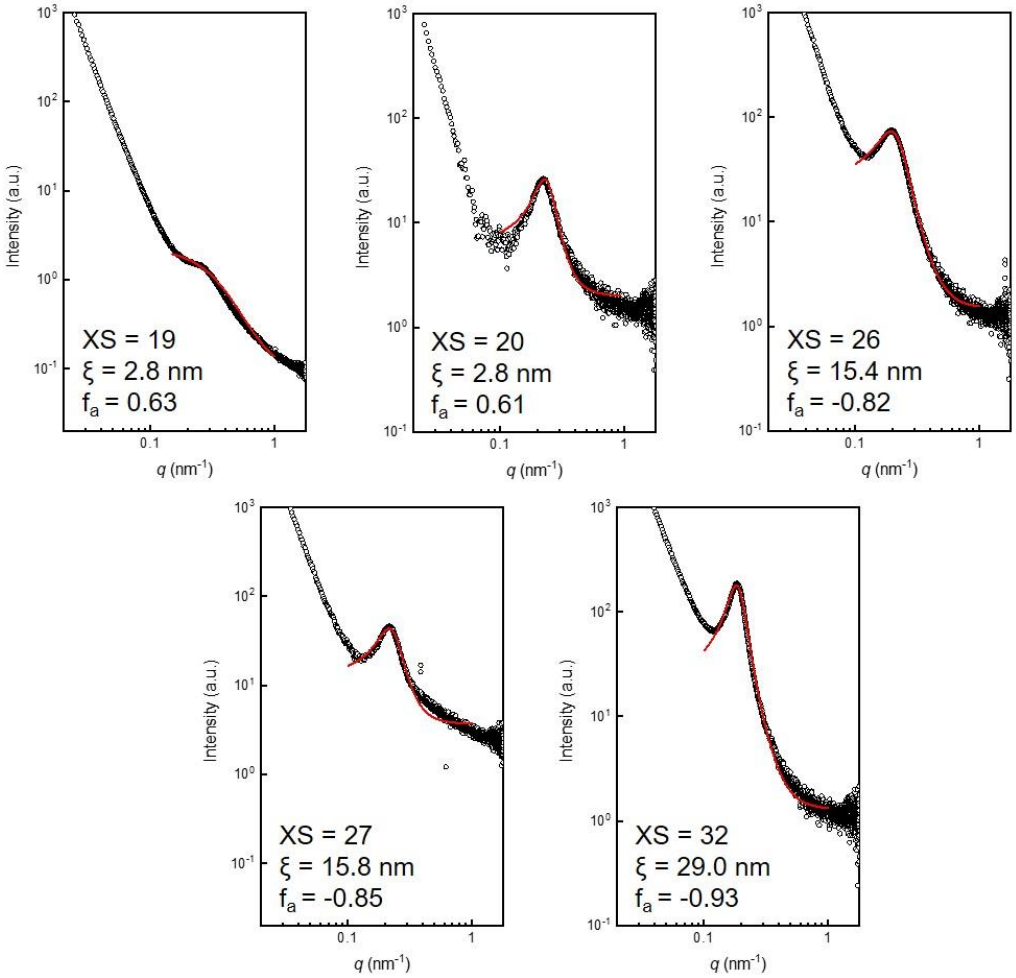

Figure 6.16. Teubner-Strey model fits to the SAXS patterns for the PLA-24 diblocks quenched from 180 °C prior to etching. The XS, ξ, and f_a values for each sample are indicated on their respective plots. Experimental data is presented as open black circles and model fits as solid red curves.

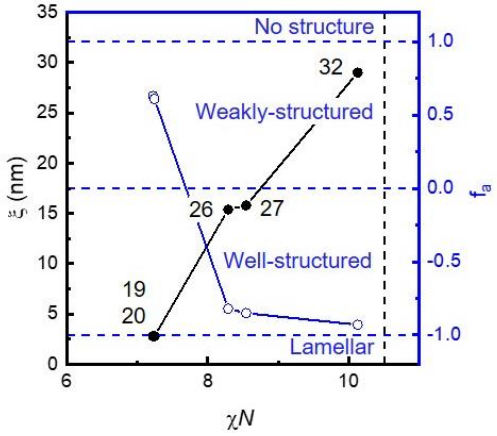

Figure 6.17. Correlation length, ξ, (black closed circles) and amphiphilicity factor, f_a, (blue curve, open circles) obtained from fitting the Teubner-Strey model to SAXS patterns for all quenched samples prior to etching plotted as a function of χN. The XS for each sample is inset next to the respective data point.

Conversely, ξ was significantly smaller for the diblock polymers with lower χN, while f_a was positive. These diblock polymers with low χN only exhibit very short-range spatial correlations (low ξ) and relatively unstructured domains ($f_a > 0$). This is consistent with a homogeneous, mean-field-like melt comprising isolated and uncorrelated domains with sizes on the order of the block radius of gyration, R_g.[17]

While this SAXS analysis provided compelling evidence that corroborated theoretical predictions regarding the extent of spatial correlations in disordered diblocks, it lacked crucial information on the three-dimensional continuity of these domains. N_2 sorption analysis of the porous materials following PLA etching provides a complementary technique better suited to identifying the transition from bicontinuous fluctuating domains to discontinuous mean-field-like domains. Each of the quenched PLA-24 diblock polymers were selectively etched and their BET surface areas as a function of Q* (their respective χN are reported as insets) are presented in Figures 6.13b and 6.18 – 6.19. Very small surface areas were observed for the diblock polymers with $\chi N < 8.3$, suggesting that they lacked a continuous network of pores accessible to N_2. These results are consistent with the low segregation strengths and the weakly structured domains with very short-range spatial correlations revealed by SAXS. In contrast, notably higher BET surface areas were observed for the diblock polymers with $\chi N > 8.3$, reflecting that these materials had a continuous network of pores due to their significantly stronger composition fluctuations and consistent with their higher values of Q* and ξ. This resulted in tortuous and continuous domains that still displayed a high degree of microphase segregation even in the disordered state. Locally, these domains are expected to remain quite similar to an

ordered lamellar system, as predicted by theory and consistent with their $f_a \sim -1$.[11,12] A decrease in surface area for $\chi N = 10.1$ (XS = 32) was observed as compared to $\chi N = 8.5$ (XS = 27) despite having a higher segregation strength. This discrepancy may possibly reflect some degree of re-ordering during the quenching process due to the proximity of T_{quench} to T_{ODT} ($T_{quench} = T_{ODT} + 20$ °C) for this diblock.

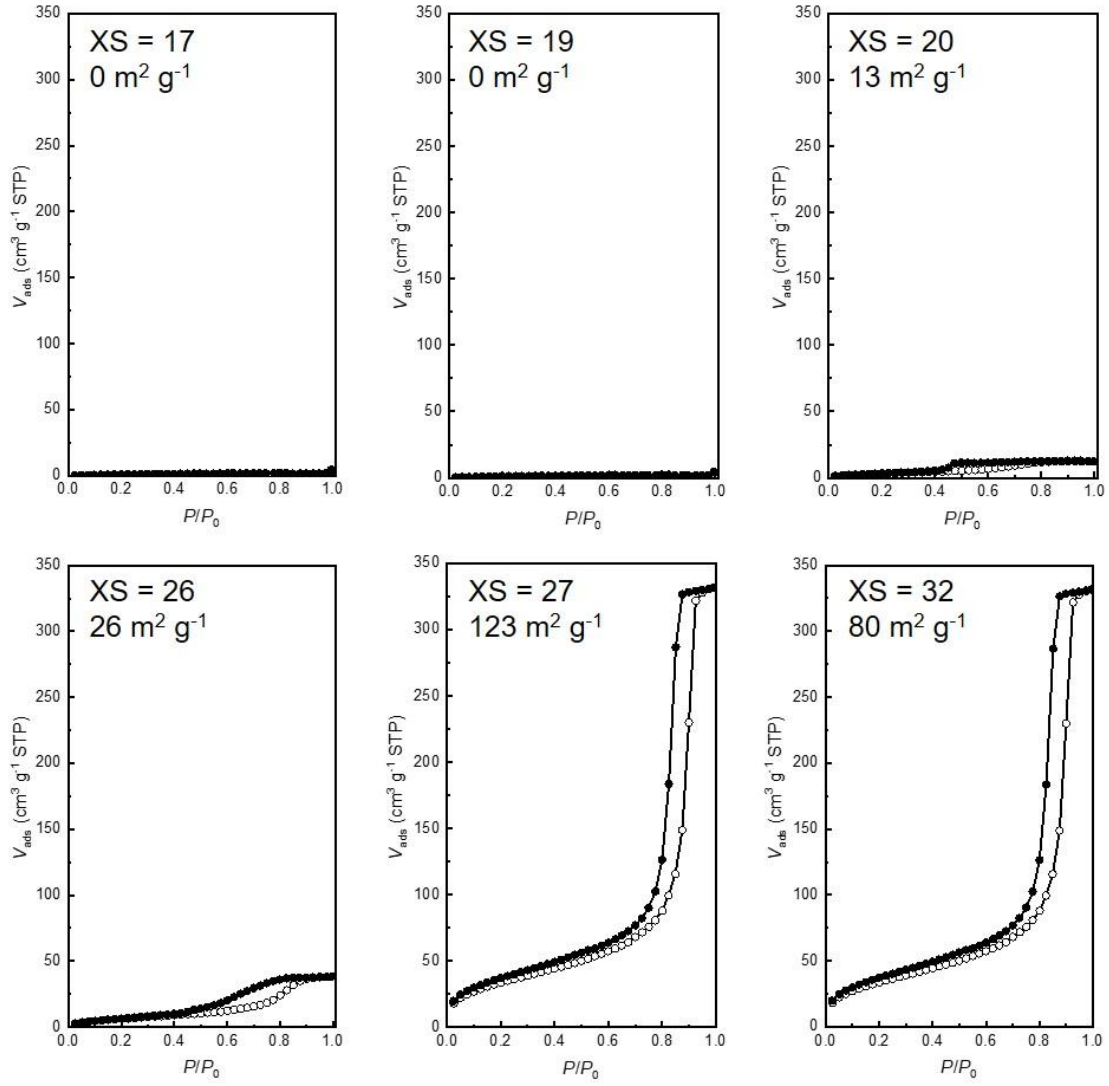

Figure 6.18. Nitrogen sorption isotherms obtained under adsorption (○) and desorption (●) for PLA-24 diblocks quenched from 180 °C and selectively etched in aqueous base. The BET specific surface area and XS are indicated for each sample.

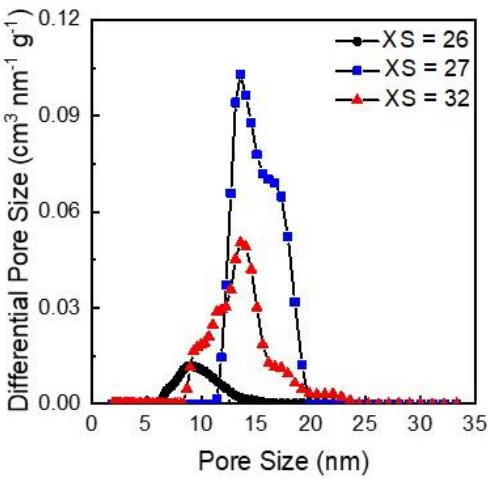

Figure 6.19. Pore size distributions for PLA-24 diblocks quenched from 180 °C based on QSDFT analysis of the adsorption branch. Pore size distributions for XS < 26 are not presented as they displayed negligible pore volumes.

6.4 Conclusions

Collectively, these data support the ability to obtain the full morphological spectrum in diblock polymers from ordered to fluctuating disordered to mean-field disordered through tuning of XS and T_{quench}. These findings have implications in the design of co-continuous morphologies in block polymers across numerous potential applications, demonstrating that the molecular design and thermal processing of diblock polymers can be utilized as a powerful tool to engineer desirable nanostructures into disordered diblock polymers.

6.5 References

1) Bates, F. S.; Frederickson, G. Block Copolymers - Designer Soft Materials. *Phys Today* **1999**, *52*, 32–38.

2) Bates, F.; Frederickson, G. Block Copolymer Thermodynamics: Theory and Experiments. *Annu Rev Phys Chem* **1990**, *41*, 525–557.

3) Bates, C. M.; Bates, F. S. 50th Anniversary Perspective: Block Polymers—Pure Potential. *Macromolecules* **2017**, *50*, 3–22.

4) Leibler, L. Theory of Microphase Separation in Block Copolymers. *Macromolecules* **1980**, *13*, 1602–1617.

5) Rosedale, J. H.; Bates, F. S.; Almdal, K.; Mortensen, K.; Wignall, G. D. Order and Disorder in Symmetric Diblock Copolymer Melts. *Macromolecules* **1995**, *28*, 1429–1443.

6) Bates, F. S.; Rosedale, J. H.; Fredrickson, G. H.; Glinka, C. J. Fluctuation-Induced First-Order Transition of an Isotropic System to a Periodic State. *Phys. Rev. Lett.* **1988**, *61*, 2229–2232.

7) Hahn, H.; Chakraborty, A. K.; Das, J.; Pople, J.; Balsara, N. Order-Disorder Transitions in Cross-Linked Block Copolymer Solids. *Macromolecules* **2005**, *38*, 1277–1285.

8) Bates, F. S.; Rosedale, J. H.; Fredrickson, G. H. Fluctuation Effects in a Symmetric Diblock Copolymer near the Order–disorder Transition. *J. Chem. Phys.* **1990**, *92*, 6255–6270.

9) Sakurai, S.; Iwane, K.; Nomura, S. Morphology of Poly(styrene-Block-Butadiene-Block-Styrene) Triblock Copolymers Cross-Linked in the Disordered State. *Macromolecules* **1993**, *26*, 5479–5486.

10) Frederickson, G.; Helfland, E. Fluctuation Effects in the Theory of Microphase Separation in Block Copolymers. *J Chem Phys* **1987**, *87*, 697–705.

11) Medapuram, P.; Glaser, J.; Morse, D. Universal Phenomenology of Symmetric Diblock Copolymers near the Order−Disorder Transition. *Macromolecules* **2015**, *48*, 819–839.

12) Lee, S.; Gillard, T.; Bates, F. Fluctuations, Order, and Disorder in Short Diblock Copolymers. *AIChE* **2013**, *59*, 3502–3513.

13) Jun, T.; Lee, Y.; Jo, S.; Ryu, C. Y.; Ryu, D. Y. Composition Fluctuation Inhomogeneity of Symmetric Diblock Copolymers: χN Effects at Order-to-Disorder Transition. *Macromolecules* **2018**, *51*, 282–288.

14) Vidil, T.; Hampu, N.; Hillmyer, M. A. Nanoporous Thermosets with Percolating Pores from Block Polymers Chemically Fixed above the Order–Disorder Transition. *ACS Cent. Sci.* **2017**, *3*, 1114-1120.

15) Hampu, N.; Hillmyer, M. A. Temporally Controlled Curing of Block Polymers in the Disordered State Using Thermally Stable Photoacid Generators for the Preparation of Nanoporous Membranes. *ACS Appl. Polym. Mater.* **2019**, *1*, 1148–1154.

16) Hampu, N.; Bates, M. W.; Vidil, T.; Hillmyer, M. A. Bicontinuous Porous Nanomaterials from Block Polymers Radically Cured in the Disordered State for Size-Selective Membrane Applications. *ACS Appl. Nano Mater.* **2019**, *2*, 4567-4577.

17) Almdal, K.; Rosedale, J. H.; Bates, F. S.; Wignall, G. D.; Fredrickson, G. H. Gaussian- to Stretched-Coil Transition in Block Copolymer Melts. *Phys. Rev. Lett.* **1990**, *65*, 1112–1115.

18) Kim, S.; Nealey, P. F.; Bates, F. S. Directed Assembly of Lamellae Forming Block Copolymer Thin Films near the Order–Disorder Transition. *Nano Lett.* **2014**, *14*, 148–152.

19) Zhang, G.; Zhang, J.; Wang, S.; Shen, D. Miscibility and Phase Structure of Binary Blends of Polylactide and Poly(methyl Methacrylate). *J. Polym. Sci. Part B Polym. Phys.* **2003**, *41*, 23–30.

20) Zalusky, A. S.; Olayo-Valles, R.; Wolf, J. H.; Hillmyer, M. A. Ordered Nanoporous Polymers from Polystyrene−Polylactide Block Copolymers. *J. Am. Chem. Soc.* **2002**, *124*, 12761–12773.

21) Hickey, R.; Gillard, T.; Lodge, T.; Bates, F. Influence of Composition Fluctuations on the Linear Viscoelastic Properties of Symmetric Diblock Copolymers near the Order− Disorder Transition. *ACS Macro Lett.* **2015**, *4*, 260–265.

22) Kennemur, J. G.; Hillmyer, M. A.; Bates, F. S. Rheological Evidence of Composition Fluctuations in an Unentangled Diblock Copolymer Melt near the Order–Disorder Transition. *ACS Macro Lett.* **2013**, *2*, 496–500.

23) Kossuth, M. B.; Morse, D. C.; Bates, F. S. Viscoelastic Behavior of Cubic Phases in Block Copolymer Melts. *J. Rheol.* **1998**, *43*, 167–196.

24) Rosedale, J. H.; Bates, F. S. Rheology of Ordered and Disordered Symmetric Poly(ethylenepropylene)-Poly(ethylethylene) Diblock Copolymers. *Macromolecules* **1990**, *23*, 2329–2338.

25) Fox, T. G. Influence of Diluent and of Copolymer Composition on the Glass Temperature of a Polymer System. *Bull Am Phys Soc* **1956**, *1*, 123–125.

26) Ashraf, A. R.; Ryan, J. J.; Satkowski, M. M.; Lee, B.; Smith, S. D.; Spontak, R. J. Bicomponent Block Copolymers Derived from One or More Random Copolymers as an Alternative Route to Controllable Phase Behavior. *Macromol. Rapid Commun.* **2017**, *38*, 1700207.

27) Ashraf, A. R.; Ryan, J. J.; Satkowski, M. M.; Smith, S. D.; Spontak, R. J. Effect of Systematic Hydrogenation on the Phase Behavior and Nanostructural Dimensions of Block Copolymers. *ACS Appl. Mater. Interfaces* **2018**, *10*, 3186–3190.

28) Semenov, A. N. Theory of Block Copolymer Interfaces in the Strong Segregation Limit. *Macromolecules* **1993**, *26*, 6617–6621.

29) Steube, M.; Johann, T.; Galanos, E.; Appold, M.; Rüttiger, C.; Mezger, M.; Gallei, M.; Müller, A. H. E.; Floudas, G.; Frey, H. Isoprene/Styrene Tapered Multiblock Copolymers with up to Ten Blocks: Synthesis, Phase Behavior, Order, and Mechanical Properties. *Macromolecules* **2018**, *51*, 10246–10258.

30) Semenov, A. Microphase Separation in Diblock-Copolymer Melts: Ordering of Micelles. *Macromolecules* **1989**, *22*, 2849–2851.

31) Bates, M. W.; Lequieu, J.; Barbon, S. M.; Lewis, R. M.; Delaney, K. T.; Anastasaki, A.; Hawker, C. J.; Fredrickson, G. H.; Bates, C. M. Stability of the A15 Phase in Diblock Copolymer Melts. *Proc. Natl. Acad. Sci.* **2019**, *116*, 13194.

32) Kang, B.-G.; Kim, D.-G.; Register, R. A. Vinyl Addition Copolymers of Norbornylnorbornene and Hydroxyhexafluoroisopropylnorbornene for Efficient Recovery of N-Butanol from Dilute Aqueous Solution via Pervaporation. *Macromolecules* **2018**, *51*, 3702–3710.

33) Teubner, M.; Strey, R. Origin of the Scattering Peak in Microemulsions. *J. Chem. Phys.* **1987**, *87*, 3195–3200.

34) Hickey, R. J.; Gillard, T. M.; Irwin, M. T.; Lodge, T. P.; Bates, F. S. Structure, Viscoelasticity, and Interfacial Dynamics of a Model Polymeric Bicontinuous Microemulsion. *Soft Matter* **2016**, *12*, 53–66.

35) Hickey, R. J.; Gillard, T. M.; Irwin, M. T.; Morse, D. C.; Lodge, T. P.; Bates, F. S. Phase Behavior of Diblock Copolymer–Homopolymer Ternary Blends: Congruent First-Order Lamellar–Disorder Transition. *Macromolecules* **2016**, *49* (20), 7928–7944.

36) Chen, L.; Hallinan Jr., D. T.; Elabd, Y. A.; Hillmyer, M. A. Highly Selective Polymer Electrolyte Membranes from Reactive Block Polymers. *Macromolecules* 2009, *42*, 6075-6085.

37) Serpico, J. M.; Ehrenberg, S. G.; Fontanella, J. J.; Jiao, X.; Perahia, D.; McGrady, K. A.; Sanders, E. H.; Kellogg, G. E.; Wnek, G. E. Transport and Structural Studies of Sulfonated Styrene−Ethylene Copolymer Membranes. *Macromolecules* **2002**, *35*, 5916-5921.

38) Amendt, M. A.; Chen, L.; Hillmyer, M. A. Formation of Nanostructured Poly(dicyclopentadiene) Thermosets Using Reactive Block Polymers. *Macromolecules* **2010**, *43*, 3924-3934.

39) Schubert, K. -V.; Strey, R.; Kline, S. R.; Kaler, E. W. Small Angle Neutron Scattering near Lifshitz Lines: Transition from Weakly Structured Mixtures to Microemulsions. *J. Chem. Phys.* **1994**, *101* (6), 5343–5355.

40) Silas, J. A.; Kaler, E. W. Effect of Multiple Scattering on SANS Spectra from Bicontinuous Microemulsions. *J. Colloid Interface Sci.* **2003**, *257* (2), 291–298.

Chapter 7. Nanostructural Rearrangement of Lamellar Block Polymers Cured in the Vicinity of the Order-Disorder Transition

7.1 Introduction

Harnessing the self-assembly of materials is crucial for advancing numerous technologies, including energy storage and conversion,[1] water filtration,[2] and drug delivery.[3] Block polymers are particularly attractive for this purpose, as they can be designed to rationally target uniform and periodic patterns of tunable size and symmetry dictated by the molar mass, chemistry, and relative composition of the blocks.[4–6] While strong enthalpic repulsions between the chemically dissimilar blocks drive these materials to microphase separate into ordered nanostructures at low temperatures and/or high degrees of polymerization (N), entropic factors associated with unfavorable chain stretching disrupt the long-range spatial correlations of the ordered state as the system is heated. Eventually, this results in an order to disorder transition (ODT) above T_{ODT}.[7] However, short range microphase separation persists even above T_{ODT} due to composition fluctuations.[8–10]

Continued work is needed to precisely control the orientation and long-range spatial correlations of these self-assembled domains. Next-generation technologies generally rely upon either anisotropic lamellae or cylinders which often require challenging processing methods to precisely orient their domains or isotropic network structures (gyroid) which are difficult to access synthetically. Consequently, significant effort has been invested into manipulating the orientation of anisotropic domains through the application of solvent

vapor annealing[11] and/or magnetic,[12] electric,[13] or shear fields.[14] Shear alignment techniques are particularly appealing as they facilitate uniform orientation of large sample volumes under relatively mild conditions.[15] The successful alignment of ordered lamellar and cylindrical morphologies under shear has been extensively documented in the literature.[14,16–19] However, there has been less work investigating the effect of shear fields on the domain structure of the disordered state.[16,20–22] Recently, our group has explored microphase separation above T_{ODT} as a result of composition fluctuations.[23–26] This fluctuating disordered morphology was shown to exhibit a co-continuous nanostructure with potential practical utility in water filtration,[24] yet the high tortuosity of the domains may impose an undesirable resistance to transport for other applications.[27]

Therefore, we speculated that the application of large amplitude oscillatory shear (LAOS) during the in-situ cross-linking of a lamellar-forming poly(styrene-*stat*-glycidyl methacrylate)-*block*-polylactide, P(S-*s*-GMA)-*b*-PLA, diblock polymer near the T_{ODT} can orient the nanostructured domains while still maintaining their highly desirable continuity. This study was motivated by classic work by Koppi et al., which demonstrated that the application of LAOS above the T_{ODT} can drive a disordered block polymer melt to transiently order into aligned lamellar or cylindrical domains due to a symmetry-breaking field that anisotropically suppresses composition fluctuations and effectively increases the T_{ODT}.[16,17,28] While the expected disordered state was recovered following the cessation of shear for those uncross-linked systems, we believe that cross-linking P(S-*s*-GMA)-*b*-PLA above T_{ODT} under LAOS will kinetically trap this transient anisotropic morphology and allow for possible applications of this state.[16,24] Subsequent chemical etching of the PLA

domains is expected to generate porous materials with tunable pore topologies and tortuosities that can potentially be tailored for targeted applications.

7.2 Experimental Methods

In this work, we examined the effect of strain amplitude at a constant cross-linking temperature above T_{ODT} for a P(S-*s*-GMA)-*b*-PLA diblock terpolymer containing the thermal acid generator benzyl triphenylphosphonium hexafluoroantimonate (BTPH).[24] Furthermore, we investigated the effect that the cross-linking temperature has on the orientation of these domains at a constant strain amplitude. To decouple the relative contributions of cross-linking and shearing on the observed morphologies, experiments were also performed on samples that were first cross-linked at low strain amplitude before applying LAOS. Through a combination of small angle X-ray scattering (SAXS), scanning electron microscopy (SEM), and nitrogen sorption analysis, we revealed crucial processing-structure-property relationships that facilitate the design of tailored nanostructures with morphologies and domain orientations appropriate for a given application.

A readily cross-linkable P(S-*s*-GMA)-*b*-PLA diblock with a thermally accessible T_{ODT} was synthesized using a previously reported procedure (Figures 7.1–7.3) (see Chapter 3 for synthetic details).[23,24] The diblock terpolymer examined in this section was composed of a 18 kg mol^{-1} PLA block and a 14 kg mol^{-1} P(S-*s*-GMA) block with a molar fraction of GMA (XGMA) of 0.29, which will be referred to as P(S-*s*-GMA)-14-PLA-18-XGMA-29. Variable temperature small angle X-ray scattering (SAXS) confirmed the targeted lamellar

morphology with a periodicity of 25.8 nm and a T_{ODT} between 150 and 170 °C (Figures 7.4 and 7.5). Dynamic mechanical analysis (DMA) demonstrated a discontinuity in the temperature dependence of the storage modulus, G', around 160 °C, indicative of the T_{ODT} and in agreement with the results from SAXS (Figure 7.5).

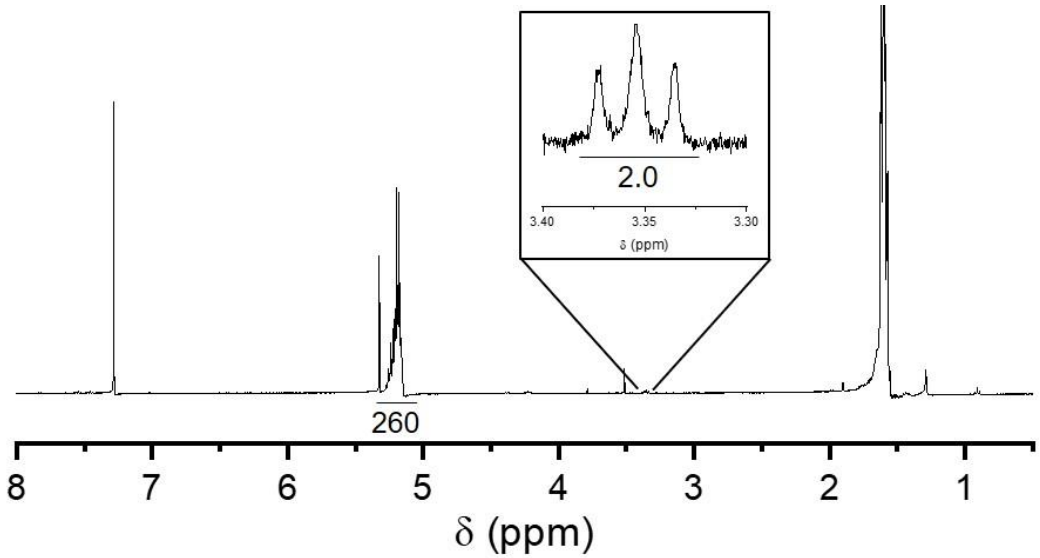

Figure 7.1. ^{1}H NMR spectrum for PLA-18. Integral values correspond to the methine protons of PLA (5-5.4 ppm) and the methylene protons adjacent to the trithiocarbonate of the CTA(3.30-3.40 ppm). The inset presents a higher magnification image of the methylene protons from the CTA.

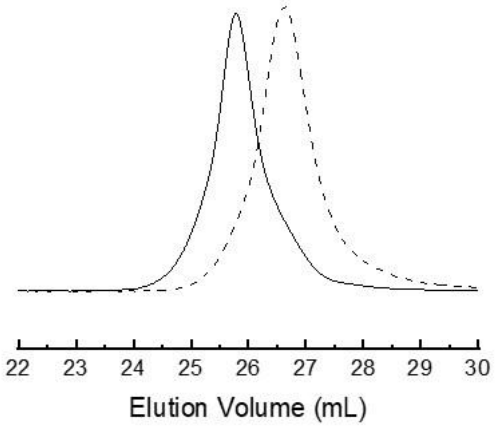

Figure 7.2. SEC elugrams for PLA-18 ($Đ$ = 1.08, dashed curve) and P(S-*s*-GMA)-14-PLA-18-XGMA-29 ($Đ$ = 1.06, solid curve).

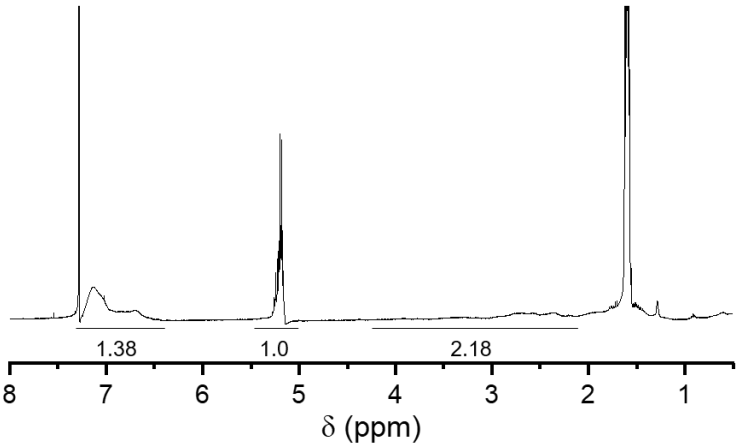

Figure 7.3. ^{1}H NMR spectrum for P(S-*s*-GMA)-14-PLA-18-XGMA-29. Integral values correspond to the methine protons of PLA(5-5.4 ppm), the aromatic protons of PS (6.3-7.2 ppm), and the glycidyl protons of PGMA (2.1-4.2 ppm). The integral of the methine protons of PLA was set to 1 as a reference.

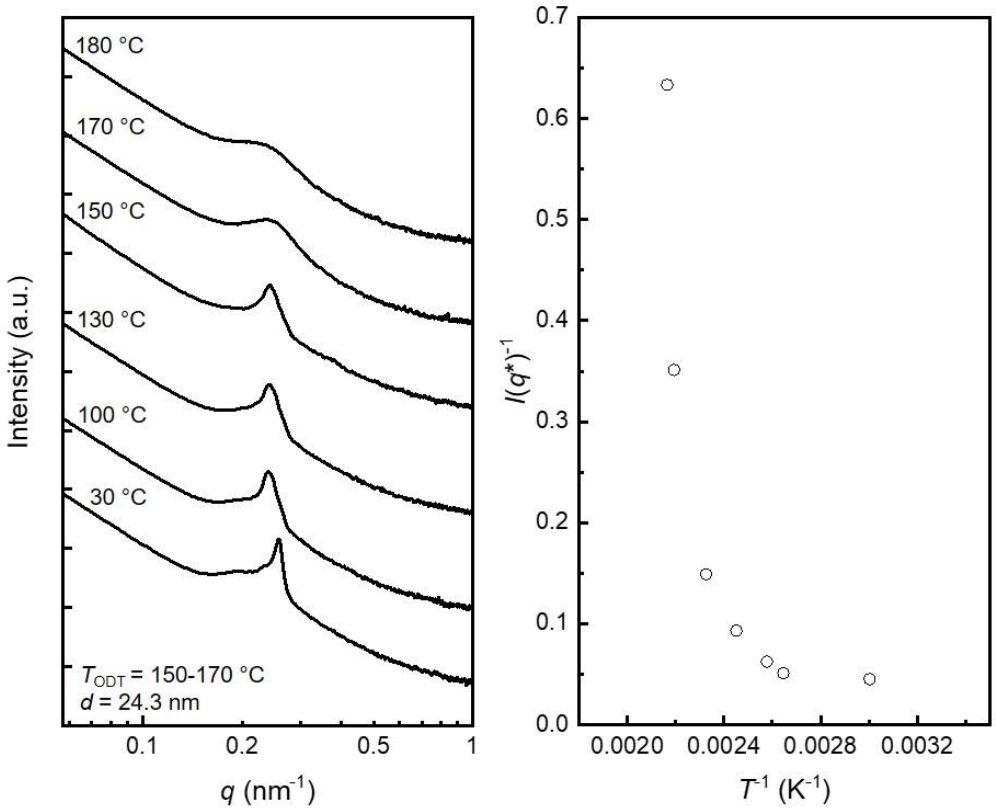

Figure 7.4. Variable temperature SAXS obtained for P(S-*s*-GMA)-14-PLA-18-XGMA-29 (left). The sample was annealed overnight at 100 °C and thermally equilibrated for 2 min at each temperature prior to data collection. The inverse intensity of the principal scattering peak, $I^{-1}(q^*)$ is plotted as a function of the inverse of the temperature where each pattern was obtained, T^{-1}, for P(S-*s*-GMA)-14-PLA-18-XGMA-29 (right). The T_{ODT} was determined to be the temperature where a change in the slope of $I^{-1}(q^*)$.

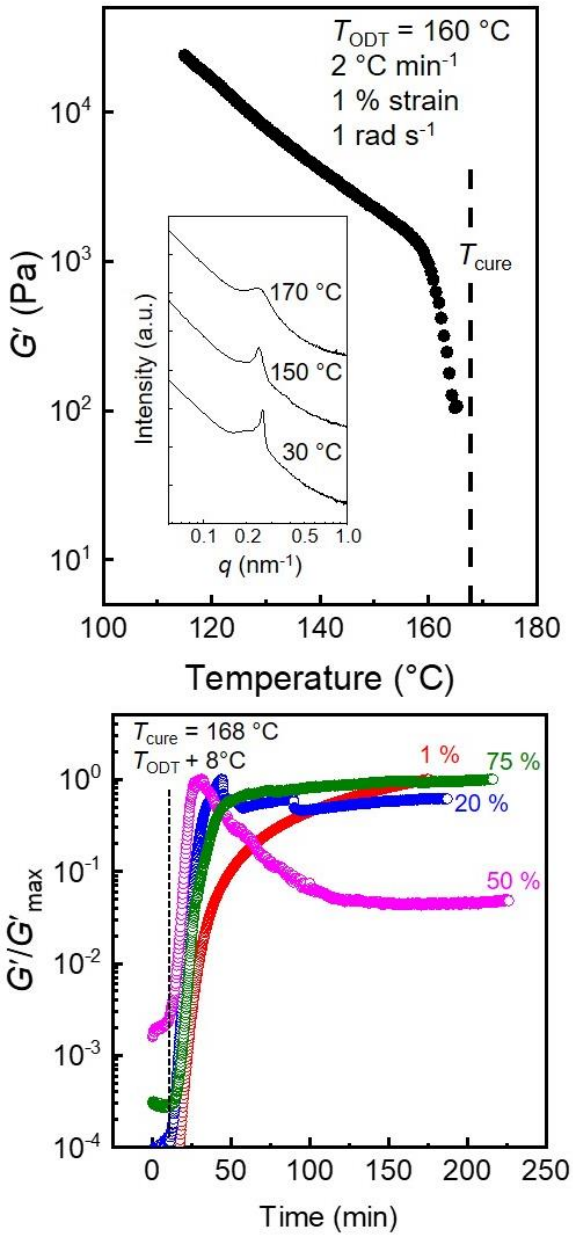

Figure 7.5. Dynamic temperature sweep for P(S-*s*-GMA)-14-PLA-18-XGMA-29 acquired at a strain amplitude of 1 %, frequency of 1 rad s^{-1}, and a heating rate of 2 °C min^{-1} (top). The precipitous drop in G' around 160 °C indicates the $T_{ODT,}$ and the dashed line corresponds to the curing temperature used in subsequent experiments. Variable temperature SAXS patterns are inset and show a T_{ODT} between 150 and 170 °C, as indicated by significant peak broadening. Isothermal time sweeps obtained for P(S-*s*-GMA)-14-PLA-18-XGMA-29 + 0.3 wt.% BTPH cured at 168 °C (bottom). Samples were cured under strain amplitudes of 1 (○), 20 (○), 50 (○), and 75 % (○). To account for shear thinning, G'(t) was normalized by the maximum G' observed for each sample. The gel time is indicated by a dashed black line. P(S-*s*-GMA)-14-PLA-18-XGMA-29 was in the non-linear viscoelastic regime for strain amplitudes of 20 % and above.

7.3 Results and Discussion

7.3.1 Strain Amplitude Dependence on Domain Orientation under LAOS

After identifying the T_{ODT} for P(S-*s*-GMA)-14-PLA-18-XGMA-29, the thermal acid generator BTPH was selected as an appropriate cross-linking agent for the cationic polymerization of the pendant epoxide moieties of GMA.[24] Blends of P(S-*s*-GMA)-14-PLA-18-XGMA-29 containing 0.3 wt.% BTPH were prepared by co-dissolution, solvent casting, and annealing overnight at 100 °C (gel time > 10 days) under reduced pressure prior to loading the samples into a rheometer. The samples were loaded in a parallel plate rheometer at 130 °C where the cross-linking kinetics were slow[24] (gel time > 1 day) and were then rapidly heated after several minutes to 168 °C (T_{ODT} + 8 °C). Upon reaching thermal equilibrium at the experimental temperature, oscillatory shear was applied. The gel time for P(S-*s*-GMA)-*b*-PLA + 0.3 wt.% BTPH was previously found to be approximately 30 min at 170 °C, which is significantly longer than the approximately 1 min needed to reach thermal equilibrium at 168 °C. This ensures that oscillatory shear was applied to these samples prior to gelation, but certainly some cross-linking has begun before reaching 168 °C.[24] Five different strain amplitudes were investigated: 0, 1, 20, 50, and 75 %. Isothermal time sweeps were acquired for each non-zero strain amplitude during the in-situ cross-linking at 168 °C to monitor the evolution of G' over time (Figures 7.5 and 7.6).

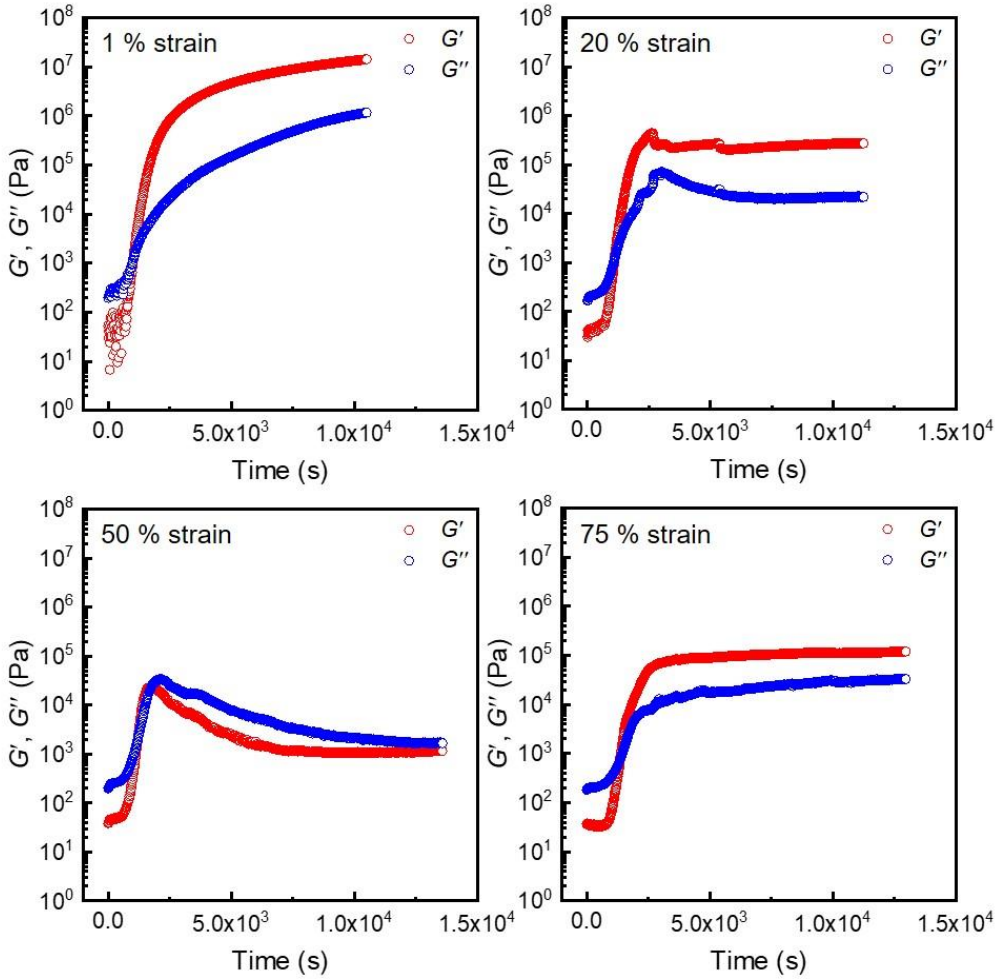

Figure 7.6. Isothermal time sweeps for P(S-*s*-GMA)-14-PLA-18-XGMA-29 + 0.3 wt.% BTPH obtained at 168 °C with strain amplitudes of 1, 20, 50, and 75 %. All samples were loaded into the rheometer at 130 °C before rapidly heating to the experimental temperature.

Each rheological time sweep demonstrated a rapid increase in both G' and G'' at early time points, signaling the onset of the cross-linking reaction (Figures 7.5 and 7.6). The values of G' and G'' cross after approximately 17–20 min for all sample, indicating that the gel time was unaffected by strain amplitude (Figure 7.6). After gelation, G' initially continued to increase with time for all samples , eventually reaching a maximum or a plateau value. Generally, higher values of G'_{max} were observed at lower strain amplitudes, likely due to shear thinning behavior at high strain. In contrast, a sample of P(S-*s*-GMA)-14-PLA-18-XGMA-29 without BTPH displayed no noticeable increase in G' and G'' over time,

confirming that the observed behavior was a direct result of BTPH catalyzed cross-linking (Figure 7.7). We note that P(S-*s*-GMA)-14-PLA-18-XGMA-29 was outside of the linear viscoelastic regime for the experimental strain amplitudes of 20 % and above (Figure 7.8), so we do not make quantitative comparisons across different strain amplitudes. However, a qualitative analysis of the time evolution of G' (and particularly of $G'(t)/G'_{max}$) for a given strain amplitude was still informative.

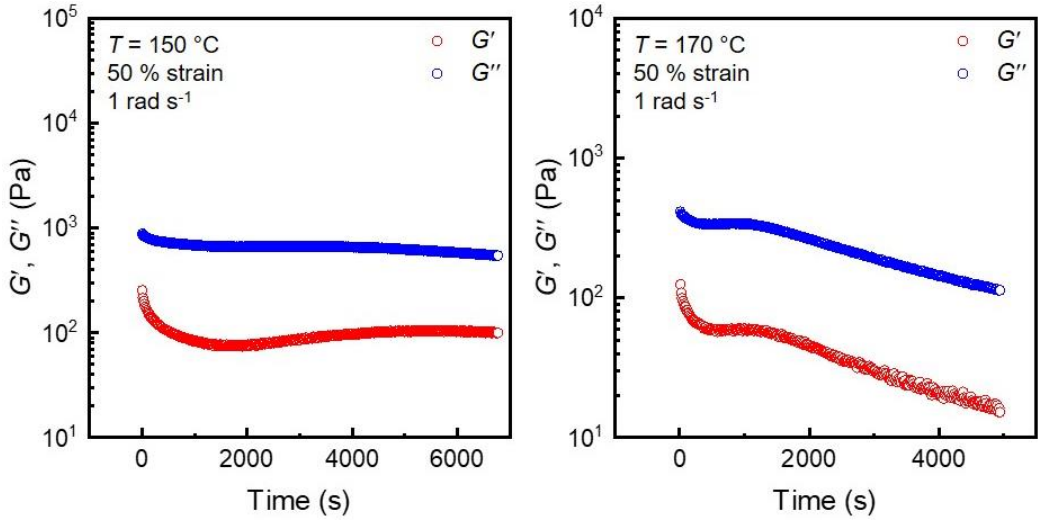

Figure 7.7. Isothermal time sweep for P(S-*s*-GMA)-14-PLA-18-XGMA-29 samples that did not contain BTPH. Data was obtained at 150 °C and 170 °C with a strain amplitude 50 %. The samples were loaded into the rheometer at 130 °C before rapidly heating to the experimental temperature.

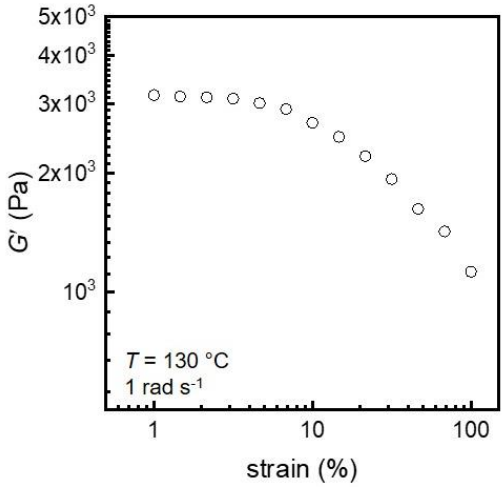

Figure 7.8. Isothermal strain sweep for a P(S-*s*-GMA)-14-PLA-18-XGMA-29 sample that did not contain BTPH. Data was acquired at 130 °C with a frequency of 1 rad s^{-1}.

For the smallest measurable strain amplitude of 1 %, G' plateaued at long experimental times, consistent with the typical behavior of cross-linked materials. In contrast, the samples that were cured under LAOS at 20 and 50 % strain displayed a gradual decrease in apparent G' after reaching an initial maximum. The extent of the decrease in G' was dependent upon the magnitude of the strain amplitude, with higher strain amplitudes generally corresponding to larger decreases in the storage modulus. Since the gel fraction of these samples all approached 1, we posit that the decrease in G' over time represented a change in the extent of domain orientation rather than a change in the degree of cross-linking or sample degradation. Similar behavior has been previously attributed to the parallel alignment of lamellae for uncross-linked block polymers subjected to LAOS in the vicinity of the T_{ODT}, where the introduction of slip planes lowered G'.[29,30] A factor of 15 decrease in G' was observed for a strain amplitude of 50 %, which was significantly greater than the factor of 5 decrease that has been previously observed for uncross-linked systems.[30] Furthermore, no significant change in G' over time was observed at 150 and 170 °C under 50 % strain for samples that did not contain BTPH, consistent with the conclusion that the large decay in the storage modulus was a consequence of the cross-linked nature of these samples (Figure 7.7). We expect that the cross-links introduced spatial and orientational correlations that drove the collective motion of the cured domains under LAOS and ultimately facilitated domain alignment. Interestingly, no such decay in G' was observed over time for the sample cross-linked at highest investigated strain amplitude of 75 %. While this result seems contradictory to the hypothesized rheological signature of domain orientation, the cross-linked lamellar domains may be unable to relax the high local stresses present under these conditions. The different viscoelastic properties

observed at 75 % strain amplitude as compared to 20 and 50 % strain amplitude may reflect changes in the domain nanostructure with increasing strain, which we address below.

To more directly evaluate the effect of strain amplitude on the degree of domain anisotropy, SAXS and scanning electron microscopy (SEM) were performed on each sample (Figures 7.9–7.11). For low strain amplitudes of 0 and 1 %, a single isotropic ring with a scattered intensity independent of the azimuthal angle was observed prior to PLA removal, consistent with unoriented and disordered domains. SEM images of these samples after PLA etching confirmed their disordered nature, as a reticulated morphology that resembled other fluctuating disordered samples was observed.[23,24]

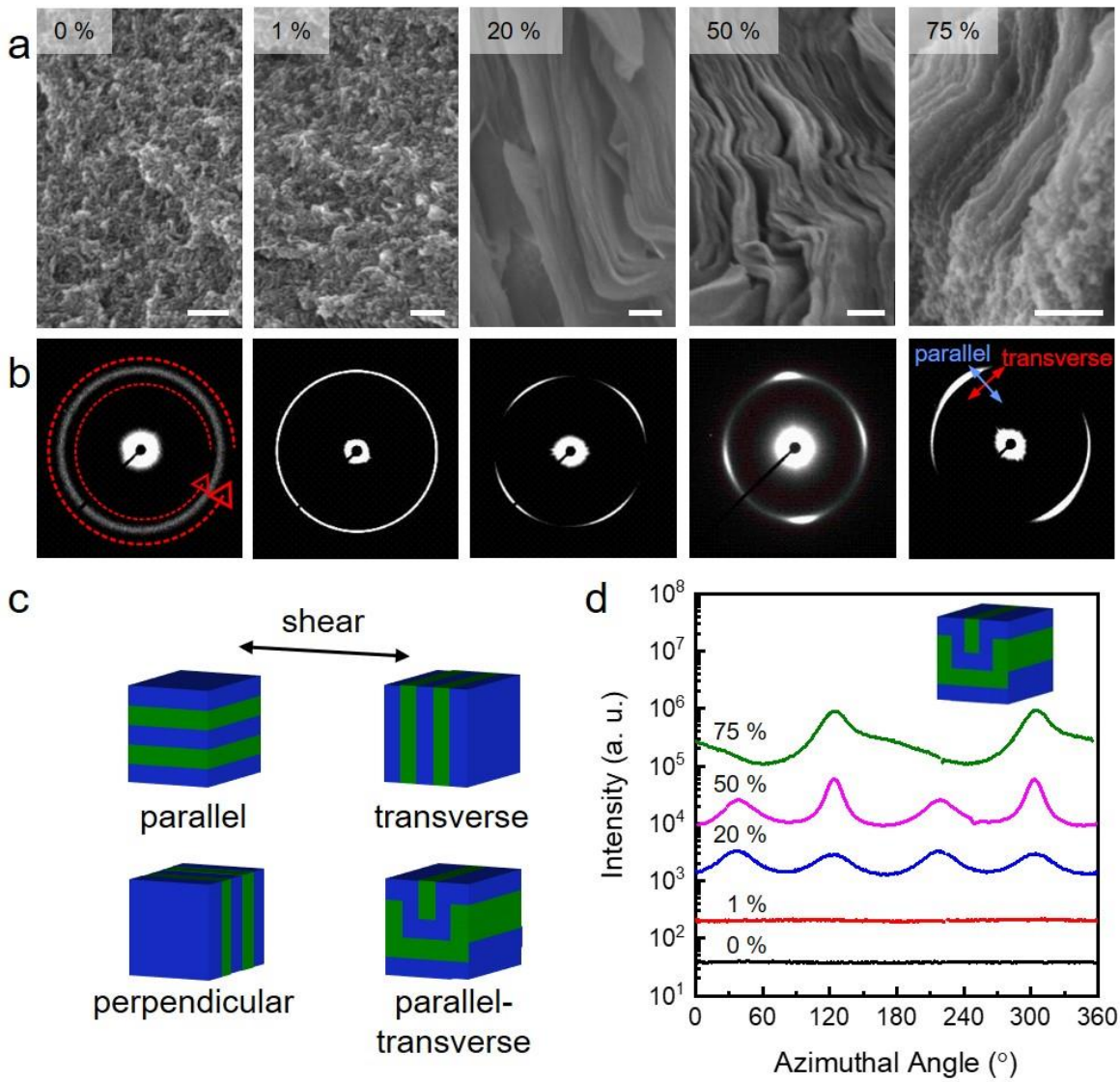

Figure 7.9. SEM images for P(S-*s*-GMA)-14-PLA-18-XGMA-29 + 0.3 wt.% BTPH cured at 168 °C (T_{ODT} + 8 °C) under strain amplitudes of 0, 1, 20, 50, and 75 % following PLA removal (a). The scale bars correspond to 200 nm for each SEM image. All SEM samples were coated with approximately 2 nm of Ir and imaged at 3.0 kV. 2D small angle X-ray scattering patterns of the parallel-transverse plane for the same samples prior to PLA removal are presented in (b). The path corresponding to the azimuthal integration is indicated by the red dashed arrows inset on the first scattering pattern, where the arrow tail represents an azimuthal angle of 0 ° and the arrowhead approaches 360 °. The directions parallel and transverse to the shearing direction are indicated on the final pattern. Slight variations in the azimuthal angles were a result of sample loading into the SAXS geometry. Illustrations of parallel, perpendicular, transverse, and parallel-transverse kinked lamellar orientations with respect to the shearing direction are provided in (c). Integrated intensities of the 2D SAXS patterns as a functional of azimuthal angle along the principal scattering vector for each strain amplitude are presented in (d). An illustration of the proposed parallel-transverse kinked lamellar morphology is presented in the inset.

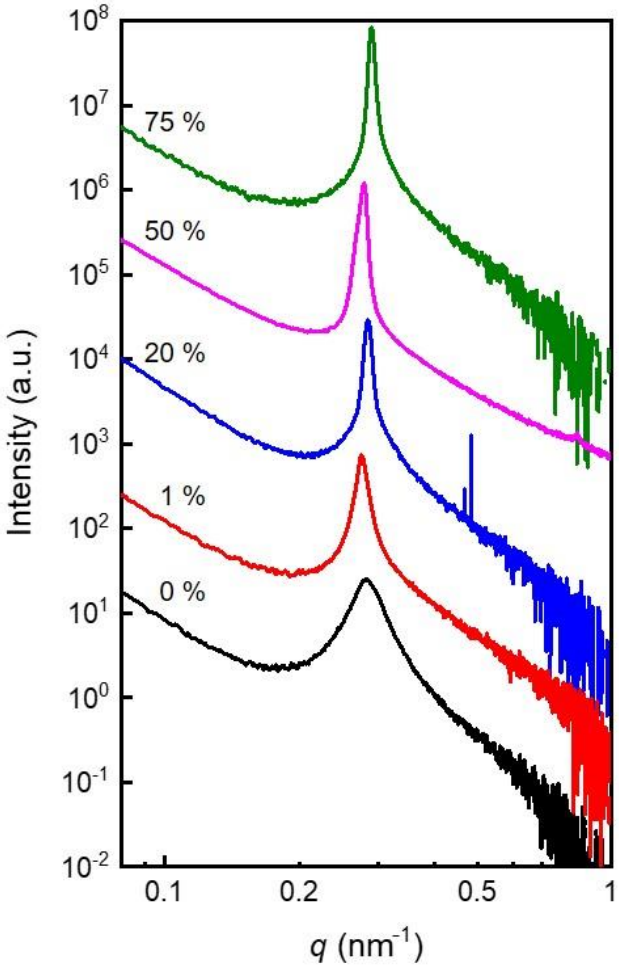

Figure 7.10. Room temperature integrated 1D SAXS patterns for P(S-*s*-GMA)-14-PLA-18-XGMA-29 + 0.3 w.% BTPH cross-linked at 168 °C under strain amplitudes of 0, 1, 20, 50, and 75 % prior to etching. The strain amplitude corresponding to each pattern is indicated next to the respective plot.

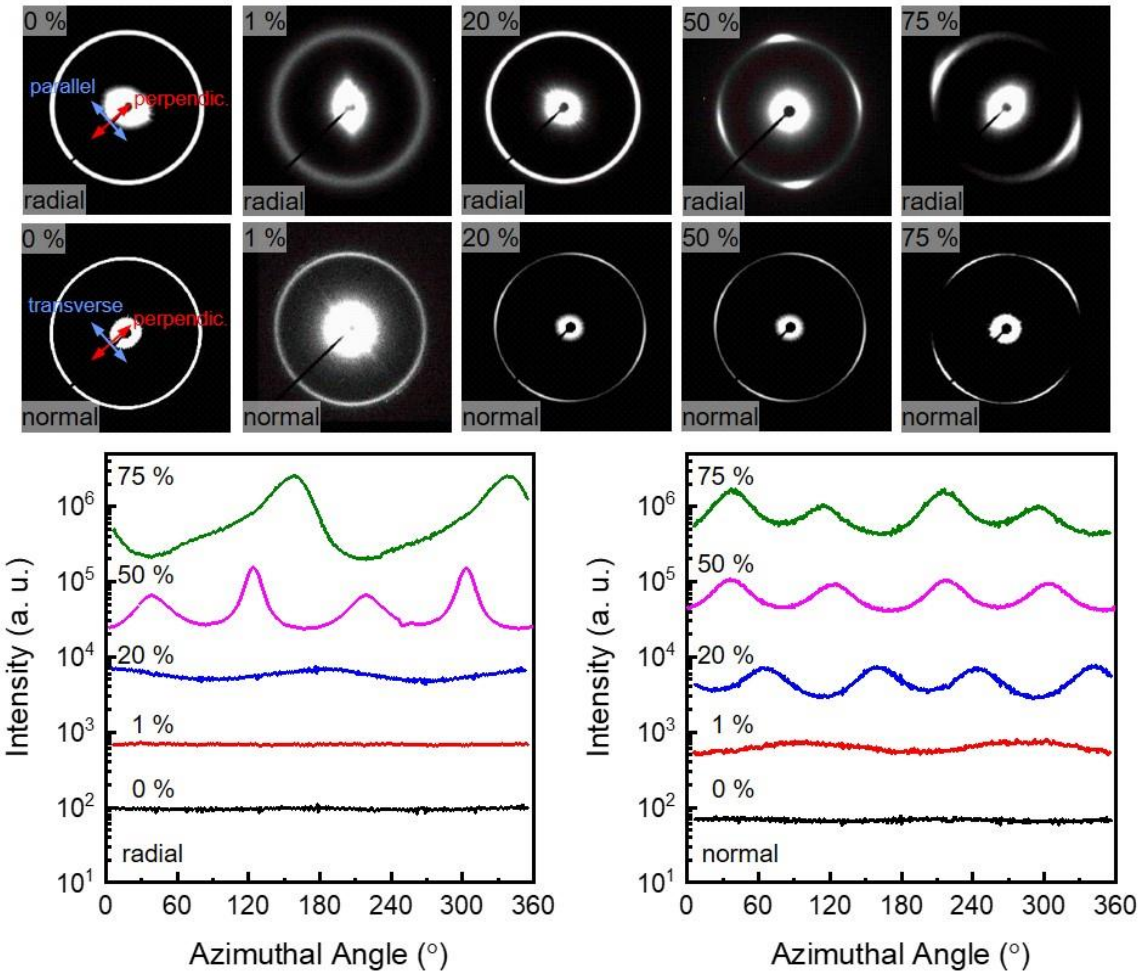

Figure 7.11. 2D small angle X-ray scattering patterns of the parallel-perpendicular (radial) plane (top panel) and the transverse-perpendicular (normal) plane (middle panel) for P(S-*s*-GMA)-14-PLA-18-XGMA-29 + 0.3 wt.% BTPH cured at 168 °C (T_{ODT} + 8 °C) under strain amplitudes of 0, 1, 20, 50, and 75 % prior to PLA removal. The directions that correspond to features that are parallel, perpendicular, and transverse to the shearing direction are indicated on the first pattern of each set. Slight variations in the azimuthal angles were a result of sample loading into the SAXS geometry. Integrated intensities of the 2D SAXS patterns as a functional of azimuthal angle along the principal scattering vector for each strain amplitude are presented in the bottom panel for the radial (left) and normal (right) planes.

However, the samples cross-linked under LAOS with strain amplitudes ≥ 20 % displayed noticeable anisotropy in their 2D SAXS patterns. Strain amplitudes of 20 and 50 % resulted in SAXS patterns comprised of four spots oriented at 90 ° intervals in the parallel-transverse plane, suggestive of aligned domains (Figure 7.9b). SEM images of these

samples post-etching revealed a sheet-like morphology that resembled lamellar ordering despite a cross-linking temperature that was above the T_{ODT} (Figure 7.9a).[31] Consequently, we attributed the lamellar morphology and domain anisotropy of the 20 and 50 % samples to a shear-induced disorder-order transition (DOT).[16,28] The application of LAOS anisotropically suppressed composition fluctuations and effectively raised the T_{ODT}, similar to observations by Koppi et al. for uncross-linked systems.[16,28] In contrast, a sample that did not contain BTPH and was sheared at 170 °C under a strain amplitude of 50 % displayed an unoriented and disordered morphology by SEM after cooling to ambient temperature (Figure 7.12). We expect that this sample also experienced a shear-induced DOT, but the cooling rate was insufficiently fast compared to domain relaxation upon the cessation of shear, resulting in the observed disordered morphology for this uncross-linked system. This demonstrates the critical role that the cross-linking reaction plays in kinetically trapping an otherwise transient shear-induced morphology.

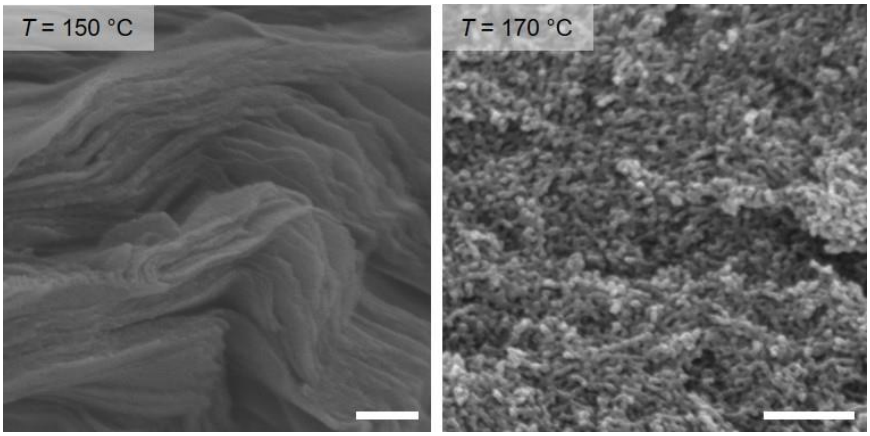

Figure 7.12. SEM for P(S-*s*-GMA)-14-PLA-18-XGMA-29 without BTPH sheared at 150 (T_{ODT} - 10 °C) and 170 °C (T_{ODT} + 10 °C) under a strain amplitude of 50 % after PLA removal. The scale bars correspond to 200 nm.

Curiously, the four-spot pattern observed in the parallel-transverse plane suggested the presence of domains with four-fold symmetry rather than the two-fold symmetry expected

for a uniformly aligned lamellar morphology (see Figure 7.9c for illustrations of possible lamellar orientations with respect to the shearing direction). Additionally, SAXS patterns obtained in the parallel-perpendicular plane generally displayed anisotropic features along the parallel direction (and in some cases along the perpendicular direction), Figure 7.11. Based on these results, we surmised that the domains primarily adopted a parallel-transverse kinked lamellar morphology, where the predominantly parallel lamellae are folded at orthogonal tilt boundaries.[18,19,32,33] . The intermolecular cross-links and significantly higher modulus of the P(S-*s*-GMA) domains resulted in a high mechanical contrast between the domains that limited deformation to the softer PLA domains along preferential slip planes. To relax the high shear stresses present under LAOS, the parallel lamellae likely buckle along these slip planes to form transversely (and also, in some cases, perpendicularly) oriented hinges.[19,32,33] These conclusions are generally consistent with previous work on the orientation of uncross-linked lamellar diblocks under LAOS.[19,32,33]

For an even higher strain amplitude of 75 %, SAXS patterns displayed only two spots parallel to the shear direction that were oriented at 180 ° intervals and displayed small shoulders. This suggested that the lamellae were primarily oriented parallel to the shear direction without the kink bands observed at lower strain amplitude. The SEM image for this sample exhibited some regions consistent with lamellar ordering; however, there were other regions that resembled the disordered state. We hypothesized that these disordered regions reflected the fracturing of the lamellar domains at the transverse hinges due to the high normal stresses present at large strain amplitude. The low intensity shoulders in the

2D SAXS pattern is consistent with this conclusion, as they suggest that the lamellae plastically deform at the kink boundaries, ultimately leading to domain fracture.[15]

The ability to produce porous materials from these shear-oriented materials by removing the PLA domains provided a valuable tool to quantitively probe the continuity of their domains using BET analysis (Figure 7.13).[24,34] The unsheared sample (0 % strain) displayed a N_2 sorption isotherm characteristic of a mesoporous material and consistent with the bicontinuous morphology of the fluctuating disordered state.[24,34] These results corresponded well with the isotropic and disordered morphology revealed by SAXS and SEM. The samples cured under 20 and 50 % strain also exhibited relatively high levels of mesoporosity, albeit slightly lower than for the unsheared sample. The measurable porosity for these samples despite their lamellar ordering was surprising, as we have previously reported that unaligned and etched lamellar morphologies were essentially non-porous due to the collapse of the mechanically unstable free-standing sheets.[24,25,31,35] We believe that the stable pores observed in this work may be a consequence of the parallel-transverse kinked lamellae, where the hinge regions orthogonal to the parallel lamellae reinforce against pore collapse following PLA removal. Furthermore, the comparably high porosities for the disordered morphology obtained in the unsheared case and for the oriented and kinked lamellar morphology obtained under 20 and 50 % strain suggests that the domain continuity of the fluctuating disordered state and the ordered lamellar state are quite similar.[8] From a practical perspective, this strategy could be a useful approach to control the tortuosity of bicontinuous domains and thus remove physical barriers that hinder mass transport without compromising domain continuity. An even higher strain amplitude of 75

% resulted in a significantly lower porosity, likely due to fracturing of the lamellar domains at these high shear stresses as observed in SEM and SAXS. Consequently, the continuity of the domains was interrupted. These results demonstrate the utility of LAOS for precisely controlling the morphology and domain orientation near the T_{ODT}, enabling the engineering of targeted nanostructures.

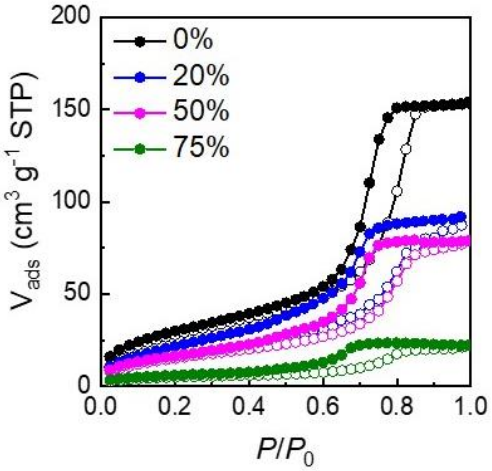

Figure 7.13. Nitrogen sorption isotherms for P(S-*s*-GMA)-14-PLA-18-XGMA-29 + 0.3 wt.% BTPH cured at 168 °C (T_{ODT} + 8 °C) under strain amplitudes of 0, 1, 20, 50, and 75 % following PLA removal.

7.3.2 Temperature dependence of domain orientation under LAOS

In addition to strain amplitude, we expected that the cross-linking temperature would also significantly influence the extent of domain alignment under LAOS. To explore this, we selected the diblock polymer P(S-*s*-GMA)-17-PLA-23-XGMA-27 with a T_{ODT} of approximately 170 °C by DMA (Figure 7.14) and a lamellar morphology with a domain spacing of 28.9 nm by SAXS (Figure 7.15). Three different cross-linking temperatures (155, 175, and 190 °C) were investigated at two different strain amplitudes (0 or 50 %) to study the effect that LAOS had on domain alignment during the in-situ cross-linking in the ordered state (T_{ODT} – 15 °C = 155 °C, t_{gel} = 3.5 h), the strongly fluctuating disordered state

(T_{ODT} + 5 °C = 175 °C, t_{gel} = 0.5 h), and the weakly fluctuating disordered state (T_{ODT} + 20 °C = 190 °C, t_{gel} = 6 min).

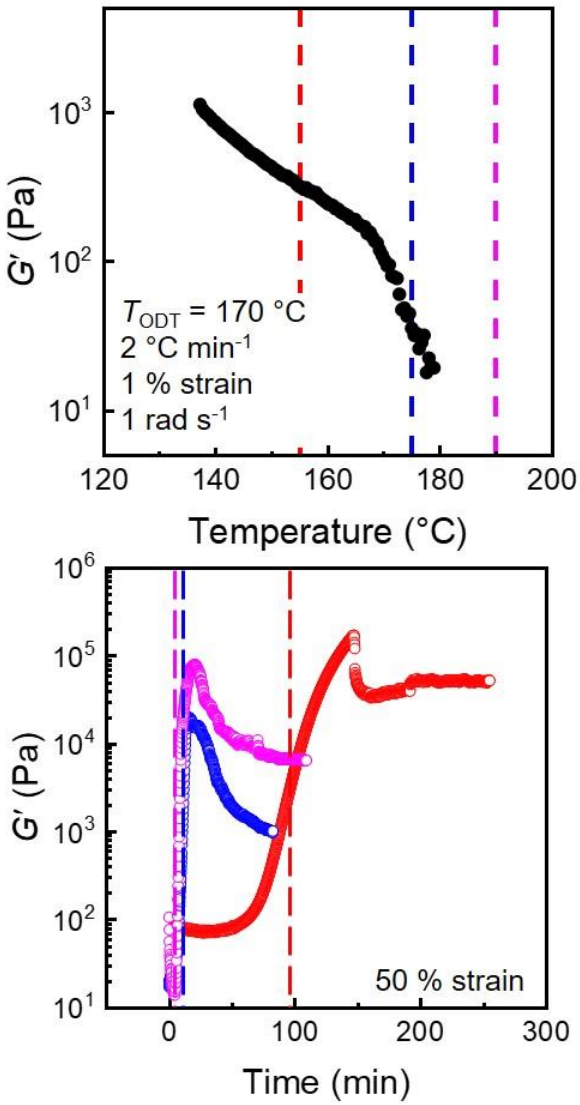

Figure 7.14. Dynamic temperature sweep for P(S-*s*-GMA)-17-PLA-23-XGMA-27 acquired at a strain amplitude of 1 %, frequency of 1 rad s^{-1}, and a heating rate of 2 °C min^{-1} (top). The precipitous drop in G' around 170 °C indicates the T_{ODT} and the dashed lines correspond to the curing temperatures used in subsequent experiments. Isothermal time sweeps for P(S-*s*-GMA)-17-PLA-23-XGMA-27 + 0.3 wt.% BTPH for samples cured at 155 (○), 175 (○), and 190 (○) °C under a strain amplitude of 50 % (bottom). Gel times for each curing temperature are indicated by the dashed lines.

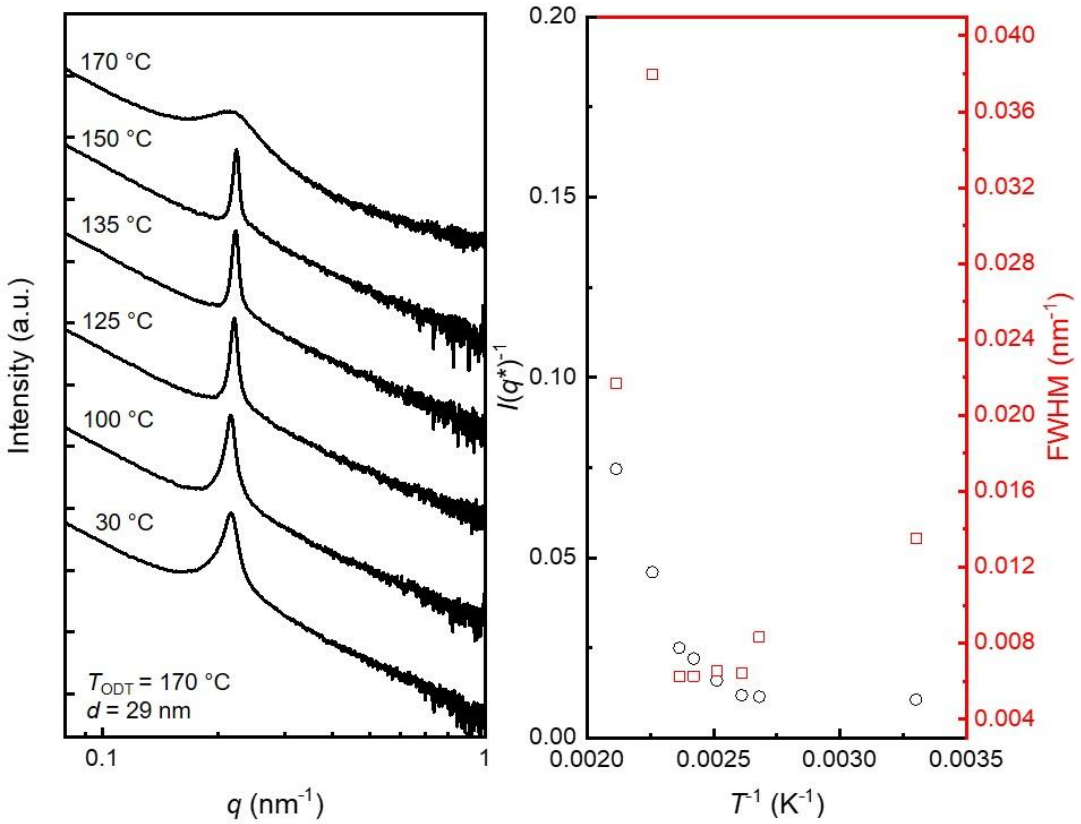

Figure 7.15. Variable temperature SAXS obtained for P(S-*s*-GMA)-17-PLA-23-XGMA-27 (left). The sample was annealed overnight at 100 °C and thermally equilibrated for 2 min at each temperature prior to data collection. The inverse intensity of the principal scattering peak, $I^{-1}(q^*)$ and the full width at half max of the principal scattering peak, FWHM, are plotted as a function of the inverse of the temperature where each pattern was obtained, T^{-1}, for P(S-*s*-GMA)-17-PLA-23-XGMA-27 (right). The T_{ODT} was determined to be the temperature where a change in the slope of $I^{-1}(q^*)$.

All samples were loaded into a parallel plate rheometer at 130 °C and rapidly heated to the targeted cross-linking temperature, as described previously. Upon reaching the desired temperature, isothermal time sweeps were performed under LAOS with a strain amplitude of 50 % (Figures 7.14 and 7.16). Qualitatively similar rheological behavior to the samples cured under variable strain amplitude was observed. The gel time was a function of temperature and ranged from 8 min at 190 °C to 95 min at 155 °C. After the apparent G' reached its initial maximum at intermediate time points, it decayed over time due to domain alignment.[29,30] The extent of this decay was highest for the cross-linking temperatures

closest to the T_{ODT}, where composition fluctuations have the highest amplitude in the unsheared state.[8,36] Qualitatively similar trends were observed for P(S-*s*-GMA)-17-PLA-23-XGMA-27 + 0.3 wt.% BTPH cured under 50 % strain at 165, 180, and 210 °C (Figure 7.16).

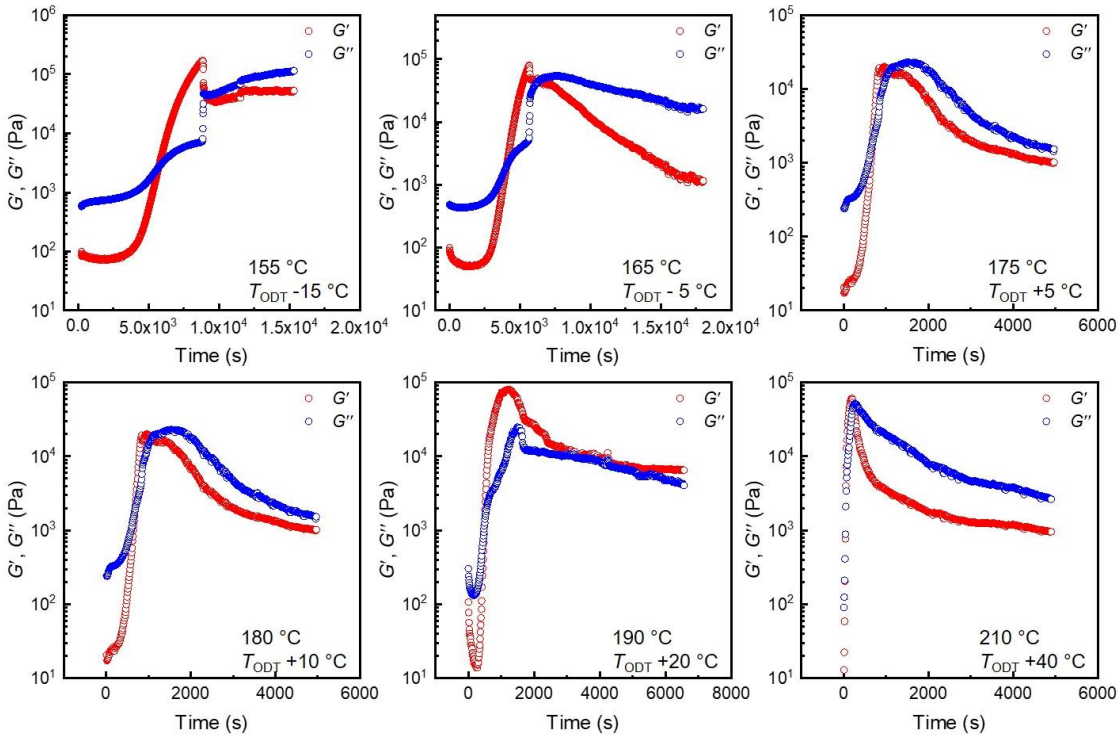

Figure 7.16. Isothermal time sweeps for P(S-*s*-GMA)-17-PLA-23-XGMA-27 + 0.3 wt.% BTPH obtained at 155, 165, 175,180, 190, and 210 °C with a strain amplitude of 50 %. All samples were loaded into the rheometer at 130 °C before rapidly heating to the experimental temperature.

Following curing, SAXS and SEM were used to analyze the morphology and domain anisotropy for the sheared and the unsheared samples (Figures 7.17 and 7.18). For the sample cured at 155 °C (T_{ODT} – 15 °C) without shear, a sharp and isotropic ring was observed in the SAXS pattern prior to PLA removal, characteristic of well-ordered and unaligned lamellae. This was confirmed by the SEM image obtained after etching. The sample cured at the same temperature under LAOS exhibited a noticeably different SAXS

pattern comprised of four spots oriented at 90 ° intervals along with a layered morphology by SEM, consistent with the parallel-transverse kinked lamellae described previously.[18,32] Therefore, the application of LAOS during the in-situ curing of a diblock polymer in the ordered state aligned the lamellae without inducing a phase transition.

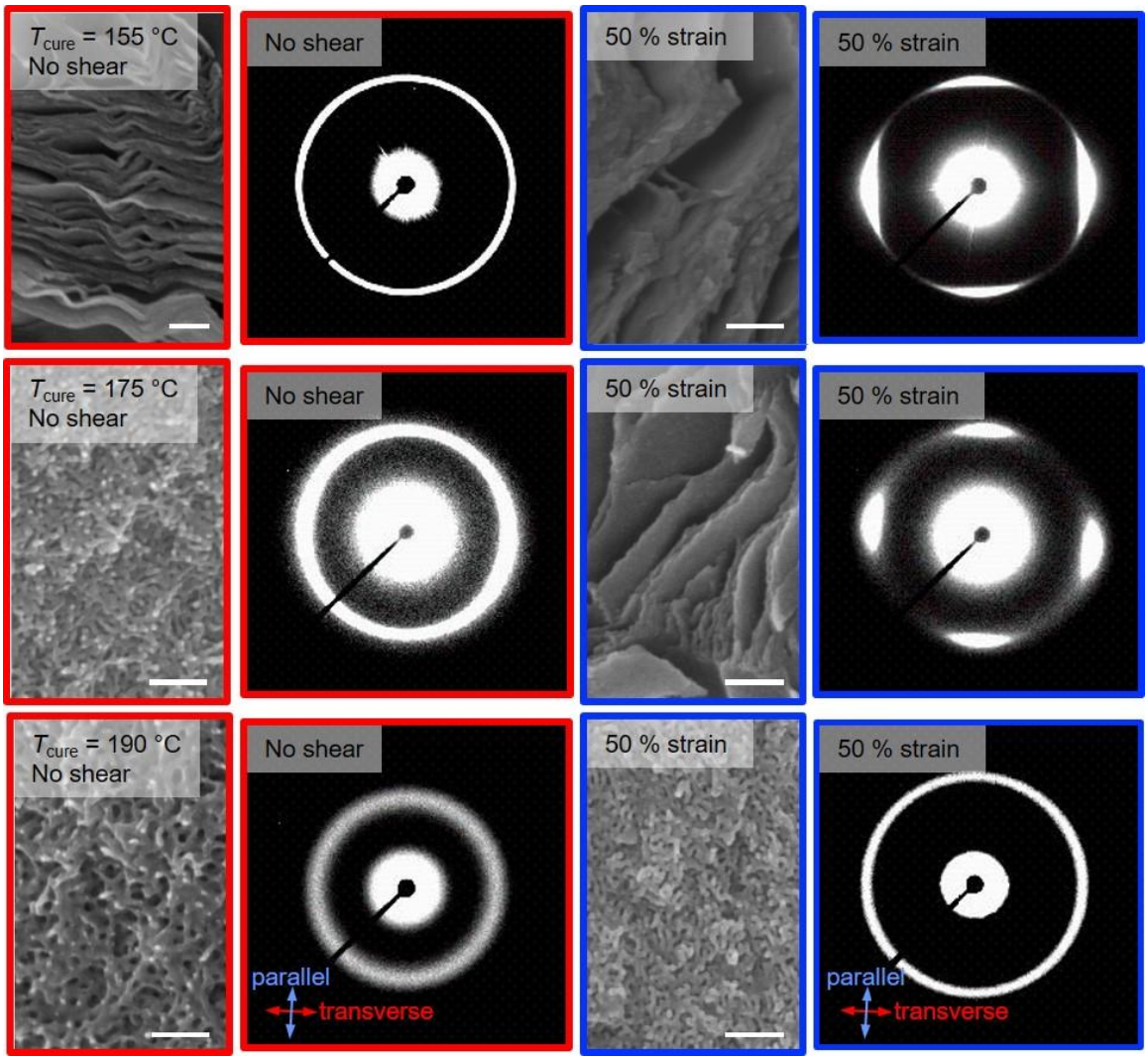

Figure 7.17. SEM images and 2D small angle X-ray scattering patterns of P(S-*s*-GMA)-17-PLA-23-XGMA-27 + 0.3 wt.% BTPH cured at 155 °C (T_{ODT} – 15 °C, top row), 175 °C (T_{ODT} + 5 °C, middle row), and 190 °C (T_{ODT} + 20 °C, bottom row). Samples were cured in the absence of shear (red borders, first and second columns) and under LAOS with a strain amplitude of 50 % (blue borders, third and fourth columns). SAXS patterns were obtained prior to PLA removal and SEM images were obtained following PLA removal. The scale bar corresponds to 200 nm for all SEM images. All SEM samples were coated with approximately 2 nm of Ir and imaged at 3.0 kV. The directions parallel and transverse to the shearing direction are indicated for each set of SAXS patterns.

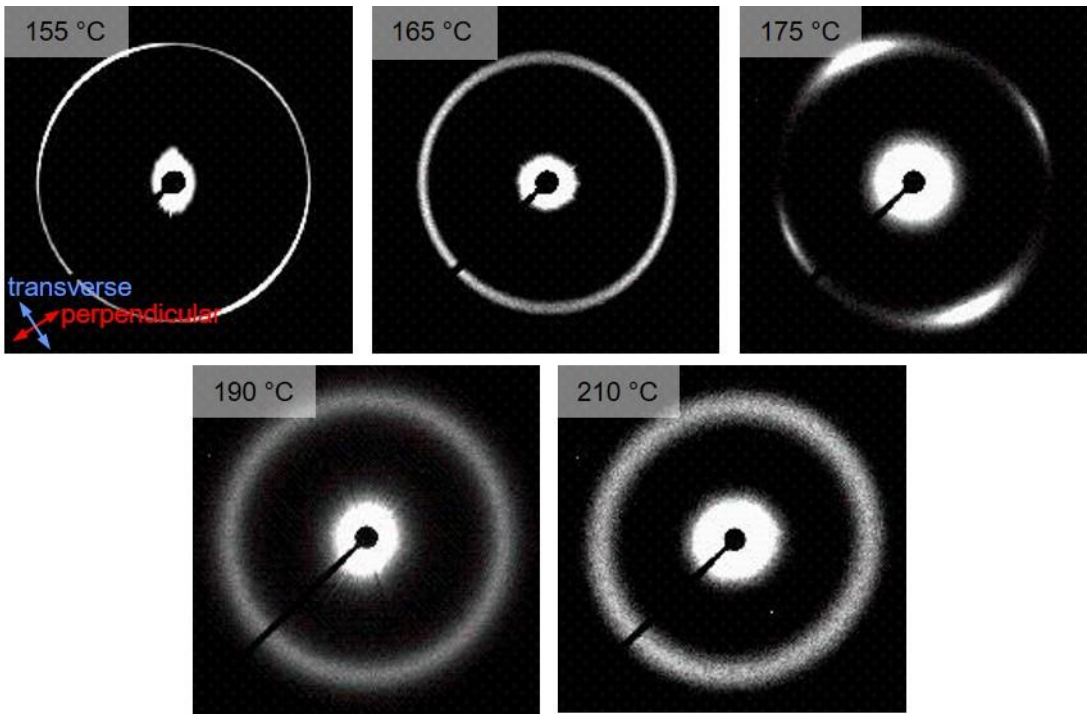

Figure 7.18. 2D small angle X-ray scattering patterns of the perpendicular-transverse (normal) plane for P(S-*s*-GMA)-17-PLA-23-XGMA-27 + 0.3 wt.% BTPH cured at 155, 165, 175, 180, 190, and 210 °C under a strain amplitude of 50 % prior to PLA removal. The directions that correspond to features that are perpendicular and transverse to the shearing direction are indicated on the first pattern. Slight variations in the azimuthal angles were a result of sample loading into the SAXS geometry.

For the sample cured at 175 °C (T_{ODT} + 5 °C), the SAXS pattern for the unsheared sample displayed a diffuse and isotropic ring indicative of a disordered morphology and consistent with the fluctuating disordered morphology observed by SEM. Cross-linking the same polymer at the same temperature under LAOS resulted in a strikingly different morphology. The SAXS pattern revealed four spots suggesting domain anisotropy, and SEM showed a layered morphology that resembled the lamellar state despite being nominally cured above T_{ODT}. These results corresponded well with those discussed previously for varying strain amplitude at a constant curing temperature slightly above T_{ODT}, and they demonstrate the reproducibility of the shear-induced disorder-order transition for different block polymers. In contrast, the application of 1 % strain during the

in-situ cross-linking at 175 °C resulted in an isotropic SAXS pattern and a disordered morphology by SEM (Figure 7.19) demonstrating that large strain amplitudes are critical for generating the symmetry breaking field necessary for inducing the morphological transformation from a disordered and bicontinuous state to an aligned lamellar state.[16,21,28]

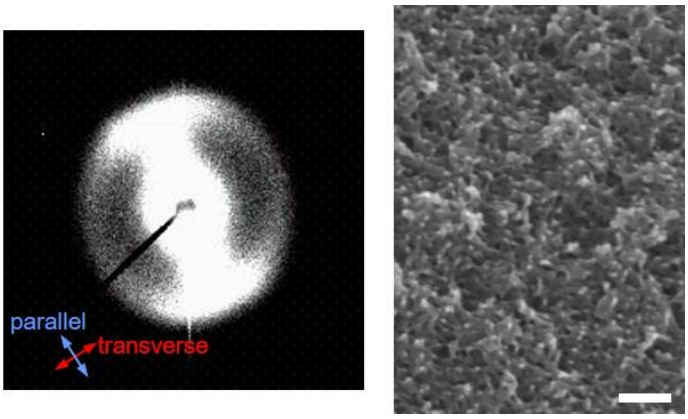

Figure 7.19. 2D small angle X-ray scattering pattern of the parallel-transverse (tangential plane) for P(S-*s*-GMA)-17-PLA-23-XGMA-27 + 0.3 wt.% BTPH cured at 168 °C under a strain amplitude of 1 % prior to PLA removal (left). The directions that correspond to features that are parallel and transverse to the shearing direction are indicated. SEM image of P(S-*s*-GMA)-17-PLA-23-XGMA-27 + 0.3 wt.% BTPH cured at 168 °C under a strain amplitude of 1 % (right). The scale bar corresponds to 200 nm.

Finally, the samples cured well above the T_{ODT} at 190 °C (T_{ODT} + 20 °C) exhibited negligible differences between the samples cured under 0 and 50 % strain by SAXS and SEM. Both samples had disordered and isotropic morphologies consistent with those that have previously been reported for block polymers cross-linked above T_{ODT}. These results may suggest that the existence of large amplitude composition fluctuations near the T_{ODT} played a key role in the morphological transition that occurred under LAOS. The observance of such a transition for cross-linking temperatures slightly above T_{ODT} (175 and 180 °C, T_{ODT} + 5 and 10 °C) and the absence of the transition for cross-linking temperatures *far* above T_{ODT} (190 and 210 °C, T_{ODT} + 20 and 40 °C) support this conclusion (Figure 7.20). Theory has predicted that LAOS anisotropically suppresses composition

fluctuations, thereby stabilizing the ordered state and effectively raising T_{ODT} toward the mean-field limit.[28] For cross-linking temperatures that were slightly higher than T_{ODT} (175 and 180 °C), the suppression of large amplitude fluctuations may have effectively increased the T_{ODT} above the curing temperature and induced ordering.[16] In contrast, for higher temperatures (190 and 210 °C), the elevated T_{ODT} under LAOS was possibly still below the curing temperature and the sample remained disordered.

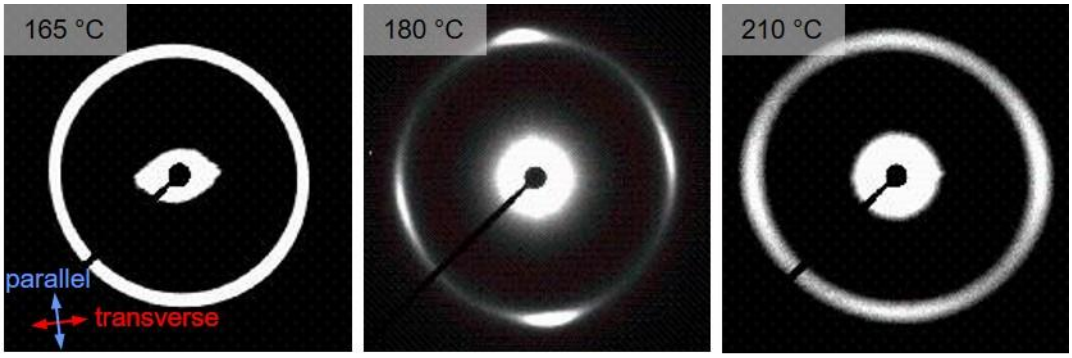

Figure 7.20. 2D small angle X-ray scattering patterns of the parallel-transverse (tangential) plane for P(S-*s*-GMA)-17-PLA-23-XGMA-27 + 0.3 wt.% BTPH cured at 165, 180, and 210 °C under a strain amplitude of 50 % prior to PLA removal. The directions that correspond to features that are parallel and transverse to the shearing direction are indicated on the first pattern. Slight variations in the azimuthal angles were a result of sample loading into the SAXS geometry.

After establishing that LAOS could induce domain orientation in these cross-linked samples, N_2 sorption analysis was performed on P(S-*s*-GMA)-17-PLA-23-XGMA-27 samples cured in both the absence of shear and under LAOS to establish correlations between morphology, domain orientation, and domain continuity (Figures 7.21 and 7.22). Samples cured below the nominal T_{ODT} exhibited negligible porosity for both the unsheared and sheared samples. This was consistent with previous work that reported a lack of measurable porosity for diblocks cross-linked in the ordered lamellar state due to the collapse of the mechanically unstable lamellae.[24,25,31,35]

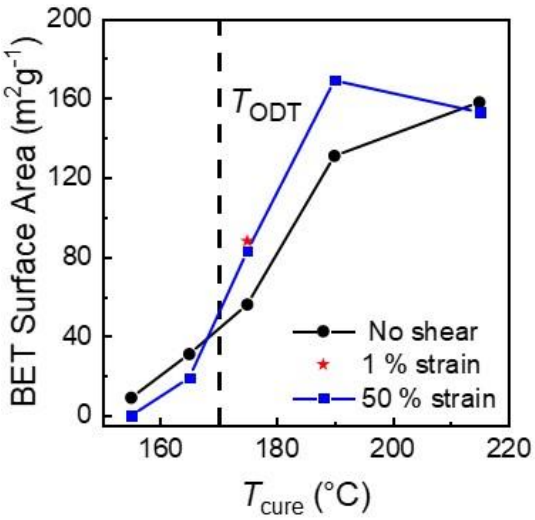

Figure 7.21. BET surface areas for P(S-*s*-GMA)-17-PLA-23-XGMA-27 + 0.3 wt.% BTPH samples cured under various strain amplitudes are presented as a function of curing temperature. Samples were cured with strain amplitudes of 0 % (●), 1 % (★), and 50 % (■). The T_{ODT} of the uncured block polymer precursor is denoted by a dashed line. The typical error in the calculation of the BET surface area is in the range of 5 to 10 m^2 g^{-1}.

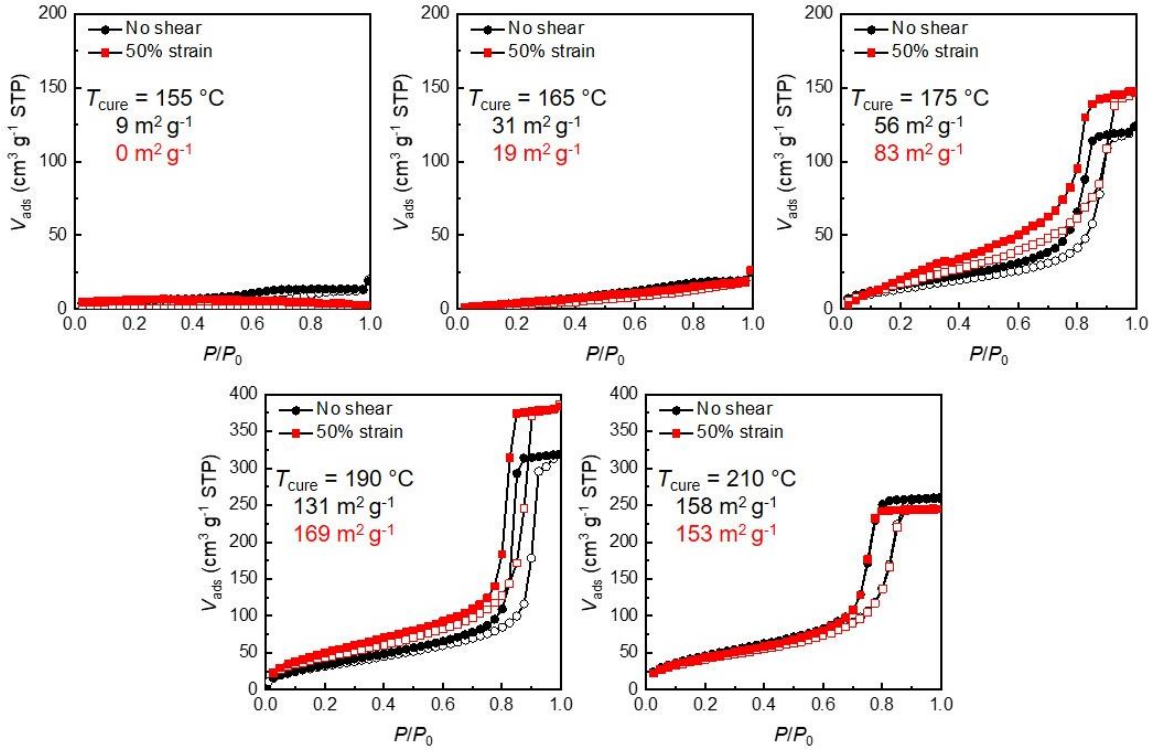

Figure 7.22. Nitrogen sorption isotherms for P(S-*s*-GMA)-17-PLA-23-XGMA-27 + 0.3 wt.% BTPH samples cured at 155, 165, 175, 180, 190, and 210 °C with a strain amplitude of 50 % (red) or in the absence of shear (black). BET surface areas for each sample are indicated on the corresponding plot.

A noticeable increase in the BET surface area was observed for the unsheared sample cross-linked at 175 °C (T_{ODT} + 5 °C), as the bicontinuous nature of the fluctuating disordered state enhanced the connectivity of the pore network, as we have established previously.[24,25,35] This conclusion was supported by the morphological picture obtained from SAXS and SEM. Interestingly, the sample cured under LAOS (50 % strain) at 175 °C displayed an even higher porosity than the unsheared sample despite exhibiting a lamellar morphology by SEM and SAXS. This result was inconsistent with previous reports that directly correlated the disordered morphology to the high degree of pore continuity.[24] Furthermore, the samples cured under LAOS at T_{ODT} - 5 °C displayed the expected lack of porosity despite exhibiting a morphology that was similar to the sample cured at T_{ODT} + 5 °C, suggesting that shear alignment alone did not enhance the porosity. This interesting discrepancy may be related to the shear-induced DOT observed for the sample subjected to LAOS at T_{ODT} + 5 °C. Theory has suggested that the ODT is a topological transition dictated by a change in interfacial curvature rather than domain composition.[8,36,37] Therefore, LAOS may have effectively reorganized the interfaces of the fluctuating disordered state into a kinked lamellar morphology with a degree of domain continuity and mechanical stability similar to the disordered state. This observation merits further investigation. Finally, similarly high BET surface areas were measured for both the unsheared and shear aligned samples cross-linked at temperatures well above T_{ODT}, consistent with their relatively similar morphologies observed by SAXS and SEM. As discussed previously, this behavior may be related to the lack of coupling between LAOS and the smaller amplitude of composition fluctuations at these higher temperatures.

However, the lack of domain orientation at high curing temperatures could instead be a consequence of the fast cross-linking kinetics at 190 and 210 °C. The gel times for P(S-*s*-GMA)-*b*-PLA + 0.3 wt.% BTPH are 6 min and 1 min at 190 and 210 °C respectively.[24] Gelation thus occurs on a similar timescale as the approximately 1 min required for the rheometer to establish thermal equilibrium at the curing temperature. Therefore, it is likely that the samples cured at the highest temperatures (and *far* above T_{ODT}) were already highly cross-linked prior to the onset of LAOS, although the observance of a crossover between G' and G'' suggests that complete gelation had yet to occur before shearing. If the degree of cross-linking is too high prior to the onset of LAOS, the domains could be kinetically trapped in an isotropic and disordered morphology and unable to readily reorganize into aligned domains under shear.

To test this hypothesis, a sample of P(S-*s*-GMA)-17-PLA-23-XGMA-27 + 0.3 wt.% was first cured at 180 °C under a low strain amplitude of 0.1 %, as monitored by an isothermal time sweep in DMA (Figure 7.23). After completion of the cross-linking reaction, a large strain amplitude of 50 % was immediately applied while maintaining the temperature. A large and instantaneous drop in G' was observed after increasing the strain amplitude to 50 % due to shear thinning (Figure 7.23). After this initial drop, G' remained relatively constant over the timescale of the experiment in contrast to the large decay previously observed for the sample that was cross-linked under LAOS at this same temperature (Figure 7.16). The sample was then removed from the rheometer and analyzed using SAXS (Figure 7.24).

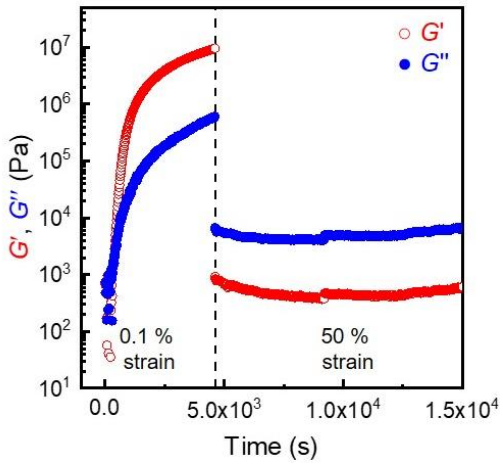

Figure 7.23. Isothermal time sweep for P(S-*s*-GMA)-17-PLA-23-XGMA-27 + 0.3 wt.% BTPH obtained at 180 °C. The sample was first cured at a low strain amplitude of 0.1 %. After the completion of the cross-linking reaction, the strain amplitude was immediately increased to 50 % while maintaining the temperature.

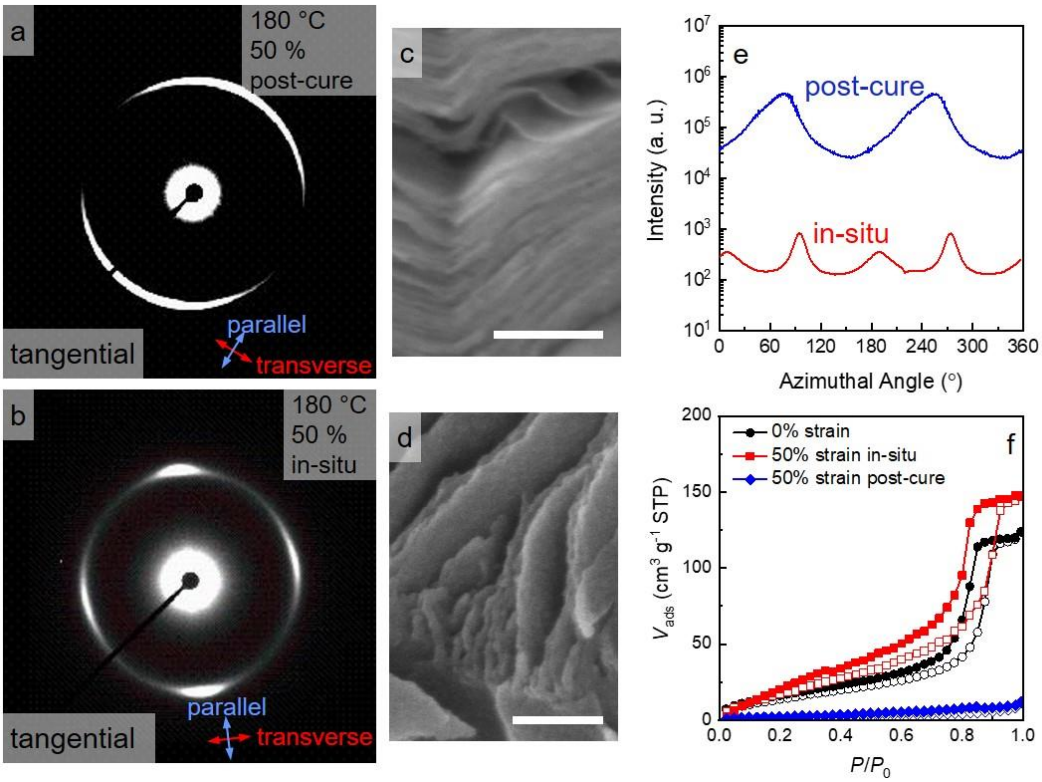

Figure 7.24. 2D small angle X-ray scattering patterns of the parallel-transverse (tangential) plane prior to PLA removal (a, b) and SEM after PLA removal (c, d) are presented for P(S-*s*-GMA)-17-PLA-23-XGMA-27 + 0.3 wt.% BTPH cured at 180 °C. One sample (post-cure) was first cured under 0.1 % strain and then sheared under 50 % strain post-gelation (a, c). The other sample (in-situ) was cured under 50 % strain (b, d). The directions that correspond to features parallel and transverse to the shearing direction are indicated. Integrated intensities of the 2D SAXS patterns as a functional of azimuthal angle along the principal scattering vector (e) are presented for patterns shown in (a) and (b). Nitrogen sorption isotherms are presented for the same samples after PLA removal in (f).

In contrast to the 4-spot scattering pattern observed for the sample cross-linked under LAOS, a 2-spot pattern consistent with domains oriented parallel to the shear direction was observed for the sample sheared post-curing (Figures 7.24a and 7.24b). SEM of this sample after PLA removal revealed a lamellar morphology that appeared to be qualitatively similar to the sample cured under LAOS, again suggesting a shear-induced disorder-order transition (Figures 7.24c and 7.24d). These results suggest that even samples that were cross-linked prior to the application of LAOS had sufficient chain mobility to reorganize into oriented domains upon shearing. However, the change from a SAXS pattern consistent with parallel-transverse kinked lamellae for the sample cured under LAOS to a SAXS pattern consistent with purely parallel lamellae for the sample subjected to LAOS post-curing is intriguing. These differences may suggest that the parallel-transverse kink bands may arise due to the complex interplay between stress relaxation and network formation during simultaneous shearing and curing. Such behavior may also be related to the previously discussed lamellar fracture observed for P(S-*s*-GMA)-14-PLA-18-XGMA-29 + 0.3 wt.% cured under 75 % strain, where the pre-cured domains lack the requisite mobility to relax these high shear stresses by forming kink bands. However, further investigation is required to make any definitive conclusions on either point. Additionally, the porosity of the sample subjected to LAOS post-curing was significantly lower than for the samples that were cured at the same temperature in the absence of shear and under LAOS. The high levels of parallel orientation of these lamellae was likely mechanically unstable after PLA removal and resulted in pore collapse, as has been previously observed for unoriented lamellae.[24,31] In contrast, the parallel-transverse kinked lamellae appear to

have a higher mechanical stability, and this resulted in a similar porosity to the unsheared and disordered sample.

Similar experiments were performed P(S-*s*-GMA)-14-PLA-18-XGMA-29 + 0.3 wt.% BTPH (Figure 7.25). A sample was first cured at 170 °C with a strain amplitude of 0.1 %. The strain amplitude was then immediately increased to 50 % following the completion of the cross-linking reaction. Curiously, only a very slight degree of domain orientation parallel to the shear direction was observed in SAXS in contrast to P(S-*s*-GMA)-17-PLA-23-XGMA-27, suggesting that the domains were mostly unoriented (Figure 7.26 and 6.27). However, SEM images of this sample after PLA removal displayed a lamellar morphology, indicating that a shear-induced disorder-order transition had occurred despite the lack of domain alignment (Figure 7.27). These results reflect that the symmetry breaking shear field was sufficient to suppress composition fluctuations and induce ordering, but it was insufficient to orient the domains. Due to its lower molar mass and higher XGMA, the cross-link density of P(S-*s*-GMA)-14-PLA-18-XGMA-29 was expected to be higher than of P(S-*s*-GMA)-17-PLA-23-XGMA-27. The chain mobility of this more heavily cross-linked polymer is expected to be restricted, hindering domain reorientation under LAOS.[22] This point merits further investigation, and a potential hypothesis for this proposed mechanism will be discussed in more detail in the following section.

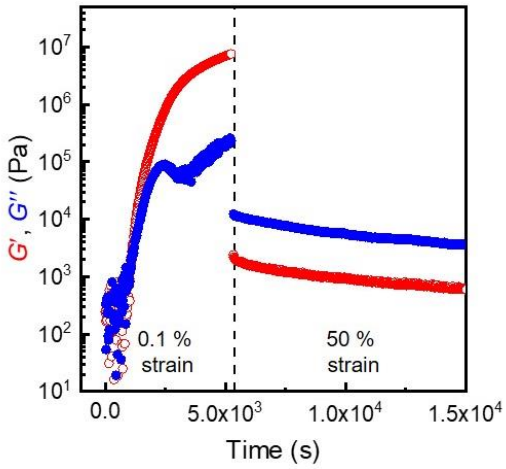

Figure 7.25. Isothermal time sweeps for P(S-*s*-GMA)-14-PLA-18-XGMA-29 + 0.3 wt.% BTPH obtained at 170 °C. The sample was loaded into the rheometer at 130 °C before rapidly heating to the experimental temperature. The sample was first cured at a low strain amplitude of 0.1 % (in the linear viscoelastic regime). After the completion of the cross-linking reaction, the strain amplitude was immediately increased to 50 % (outside the linear viscoelastic regime) while maintaining the temperature.

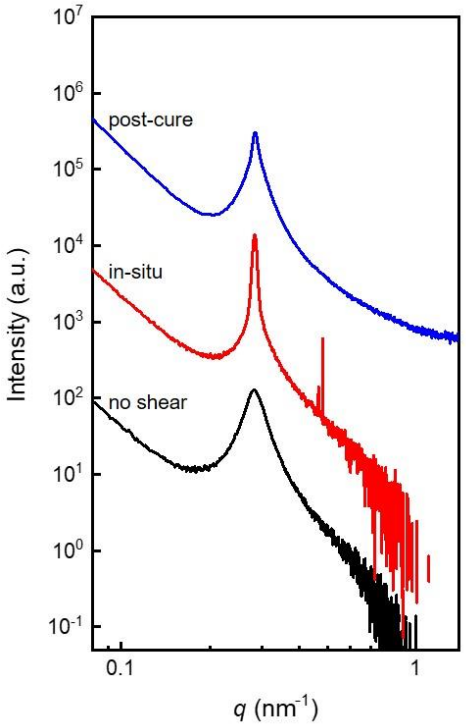

Figure 7.26. Room temperature integrated 1D SAXS patterns for P(S-*s*-GMA)-14-PLA-18-XGMA-29 + 0.3 w.% BTPH cross-linked at 168 °C under different strain conditions prior to etching. One sample was cross-linked in the absence of shear (no shear), one sample was cross-linked under a strain amplitude of 50 % (in-situ), and one sample was first cross-linked under a strain amplitude of 0.1 % and then sheared at a strain amplitude of 50 % following curing (post-cure).

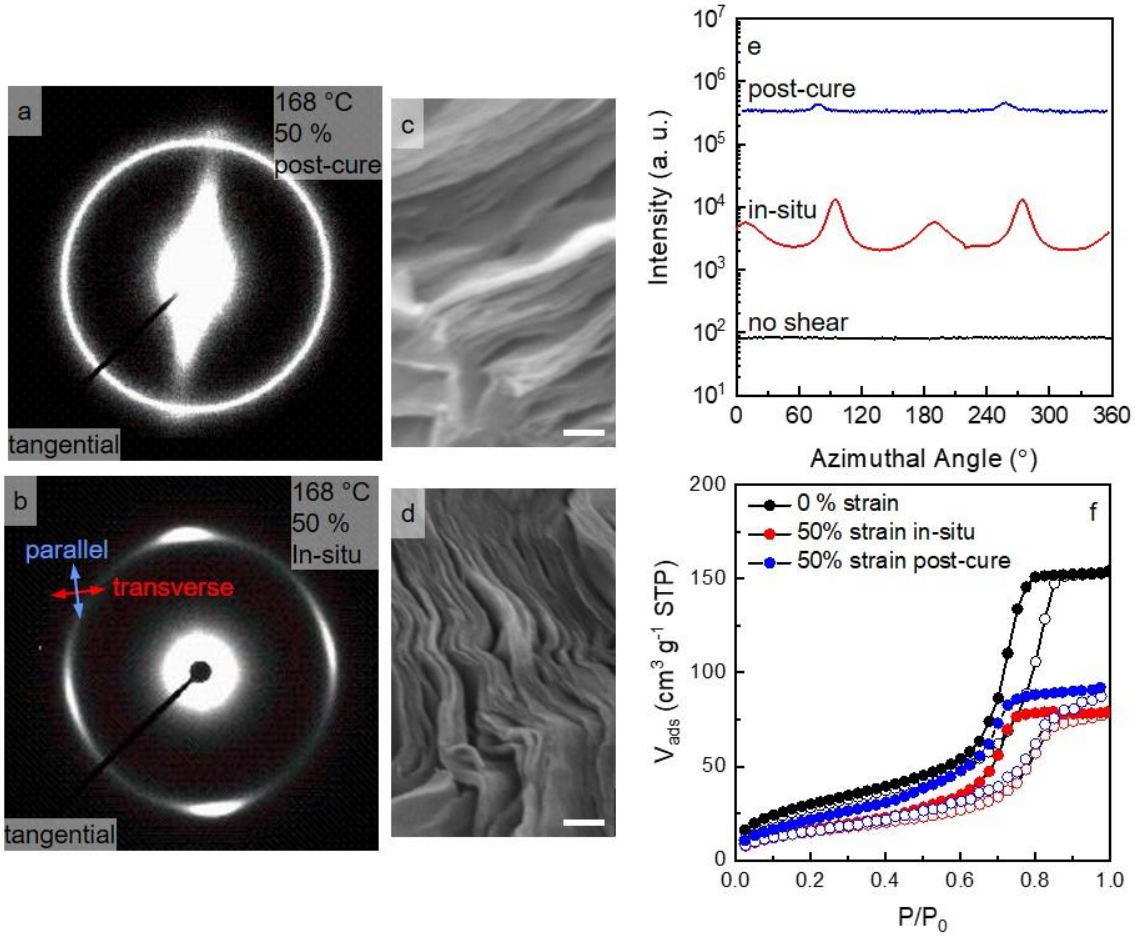

Figure 7.27. 2D small angle X-ray scattering patterns of the parallel-transverse (tangential) plane prior to PLA removal and SEM after PLA removal are presented for P(S-*s*-GMA)-14-PLA-18-XGMA-29 + 0.3 wt.% BTPH cured at 168 °C (a-d). One sample (post-cure) was first cured under a strain amplitude of 0.1 % and then sheared under a strain amplitude of 50 % post-curing (a, c). The other sample (in-situ) was cured under a strain amplitude of 50 % (b, d). The directions that correspond to features that are parallel and transverse to the shearing direction are indicated in (a and b). Integrated intensities of the 2D SAXS patterns as a functional of azimuthal angle along the principal scattering vector are presented for patterns shown in (a and b) and for an unsheared sample cross-linked at 168 °C (e). Nitrogen sorption isotherms are presented for the same samples after PLA removal in (f).

7.3.3 Effect of cross-linking on the ODT

To better understand the mechanisms behind domain reorganization in the cross-linked state under LAOS, P(S-*s*-GMA)-17-PLA-23-XGMA-27 + 0.3 wt.% BTPH was cross-linked and subsequently analyzed using variable temperature SAXS. Two different cross-linking temperatures were selected: 155 °C (T_{ODT} – 15 °C) and 190 °C (T_{ODT} + 20 °C). After cross-linking, the samples were ambiently cooled to room temperature and then annealed overnight at 100 °C under reduced pressure to prevent decomposition. The temperature dependence of the cross-linked morphology was then investigated using SAXS (Figure 7.28).

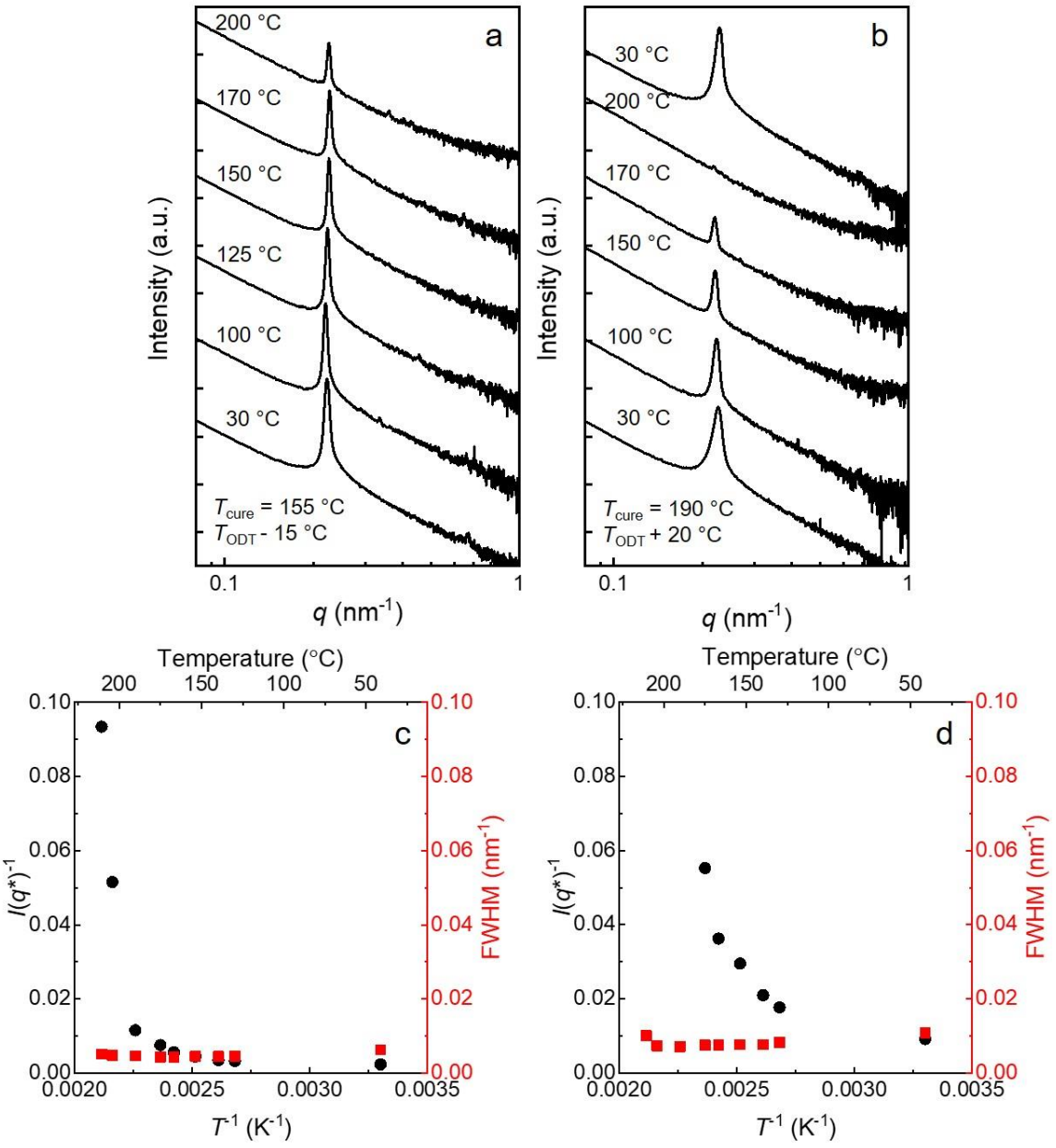

Figure 7.28. Variable temperature small angle X-ray scattering patterns for P(S-*s*-GMA)-17-PLA-23-XGMA-27 + 0.3 wt.% BTPH cured in the ordered state at 155 °C (T_{ODT} -15 °C, a) and in the disordered state at 190 °C (T_{ODT} + 20 °C, b). The samples were cured at the specified temperatures and then annealed overnight at 100 °C under reduced pressure prior to data acquisition. Samples were equilibrated for 2 minutes at each experimental temperature. The inverse intensity of the principal scattering peak, $I(q^*)^{-1}$, and the full width at half max, FWHM, of the principal scattering peak are plotted as a function of inverse temperature for T_{cure} = 155 °C (c) and 190 °C (d).

For the sample cured in the ordered state at 155 °C, a sharp principal scattering peak was observed at 30 °C, indicative of an ordered morphology and consistent with cross-linking below T_{ODT}. As the sample that was heated to 200 °C, a noticeable decrease in the intensity of the principal scattering peak was observed. Indeed, a rapid increase in the inverse intensity of the principal scattering peak, $I(q^*)^{-1}$, was observed beginning around 170 °C. Such behavior generally represents an ODT,[9] and the onset of this behavior was consistent with the T_{ODT} of the uncross-linked sample. This appears to suggest that the ODT is still accessible for this sample despite being cross-linked, which is consistent with previous observations for moderately cross-linked block polymers.[38,39] However, it is interesting to note that the full width at half max, FWHM, for the principal scattering peak remained nearly constant across the entire temperature range. This observation is inconsistent with the generally observed peak broadening (as indicated by a large increase in FWHM) as a sample is heated through the T_{ODT}.[38] The FWHM is inversely proportional to the correlation length (grain size) of the domains, so these results suggest that the local spatial correlations between the domains were fixed during cross-linking.[38,39] In effect, the cross-linked nature of the P(S-*s*-GMA) domains prevented phase mixing across the domain interface and effectively trapped the domain composition inherent to the cross-linking temperature. The combination of the temperature dependence of $I(q^*)^{-1}$ and FWHM suggest that as the temperature was increased thermal fluctuations and chain dynamics became increasingly important and the domains began to "fluctuate", resulting in the observed increase in $I(q^*)^{-1}$. However, the cross-linked nature of the P(S-*s*-GMA) domain hindered mass exchange across the PLA and P(S-*s*-GMA) domain interface and fixed the correlation length, resulting in the observed temperature invariance of FWHM (Figure 7.29).

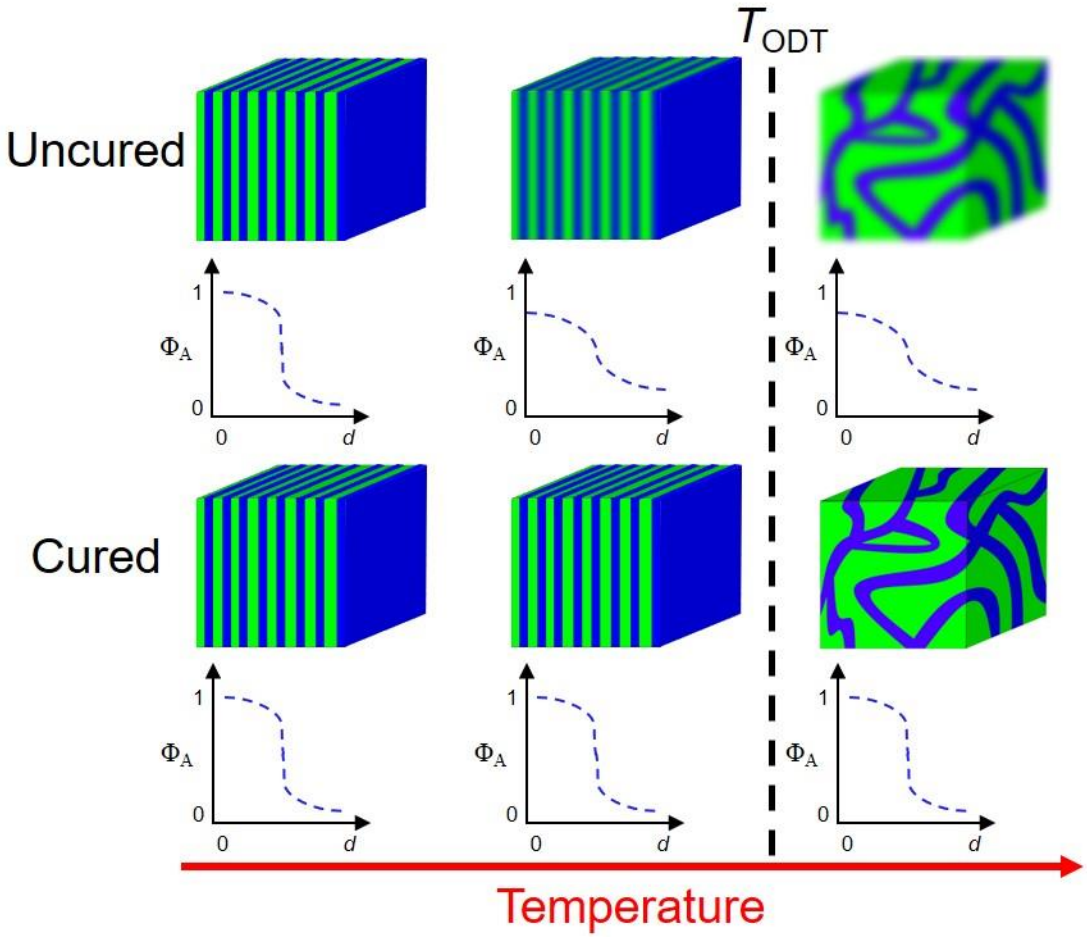

Figure 7.29. A cartoon representation of the hypothesized domain structures across T_{ODT} is provided for both an uncured lamellar diblock and a lamellar diblock cured in the ordered state. Sketches of the anticipated composition profile of the volume fraction of the A block (Φ_A) across one lamellar period (d) are provided below their corresponding illustrations. Cross-linking prevents chain exchange across the lamellar interface, likely resulting in a nearly constant domain composition across the entire temperature range. However, we believe that the cross-linked domains remained sufficiently mobile to rearrange above T_{ODT} for some systems.

The sample that was cross-linked in the disordered state at 190 °C displayed a broad scattering peak at room temperature, characteristic of a disordered morphology. The temperature dependence of $I(q^*)^{-1}$ and FWHM for this sample was qualitatively similar to the sample cross-linked at 155 °C. The intensity of the principal scattering peak decreased with increasing temperature with a large upturn in $I(q^*)^{-1}$ observed above approximately 170 °C. Furthermore, the FWHM remained relatively constant across all of the measured

temperatures. The initial disordered morphology was recoverable upon cooling the sample to 30 °C, suggesting that these observations represented a morphological change rather than sample degradation. As discussed for the sample cured at 155 °C, we believe that these results reflected domains whose relative spatial correlations were fixed by cross-linking, yet still had sufficient mobility to rearrange with increasing temperature. Similar experiments were performed and qualitatively similar results were obtained for P(S-*s*-GMA)-14-PLA-18-XGMA-29 + 0.3 w.% BTPH cured in the ordered state at 150 °C (T_{ODT} - 10 °C) and in the disordered state at 180 °C (T_{ODT} + 20 °C), Figure 7.30.

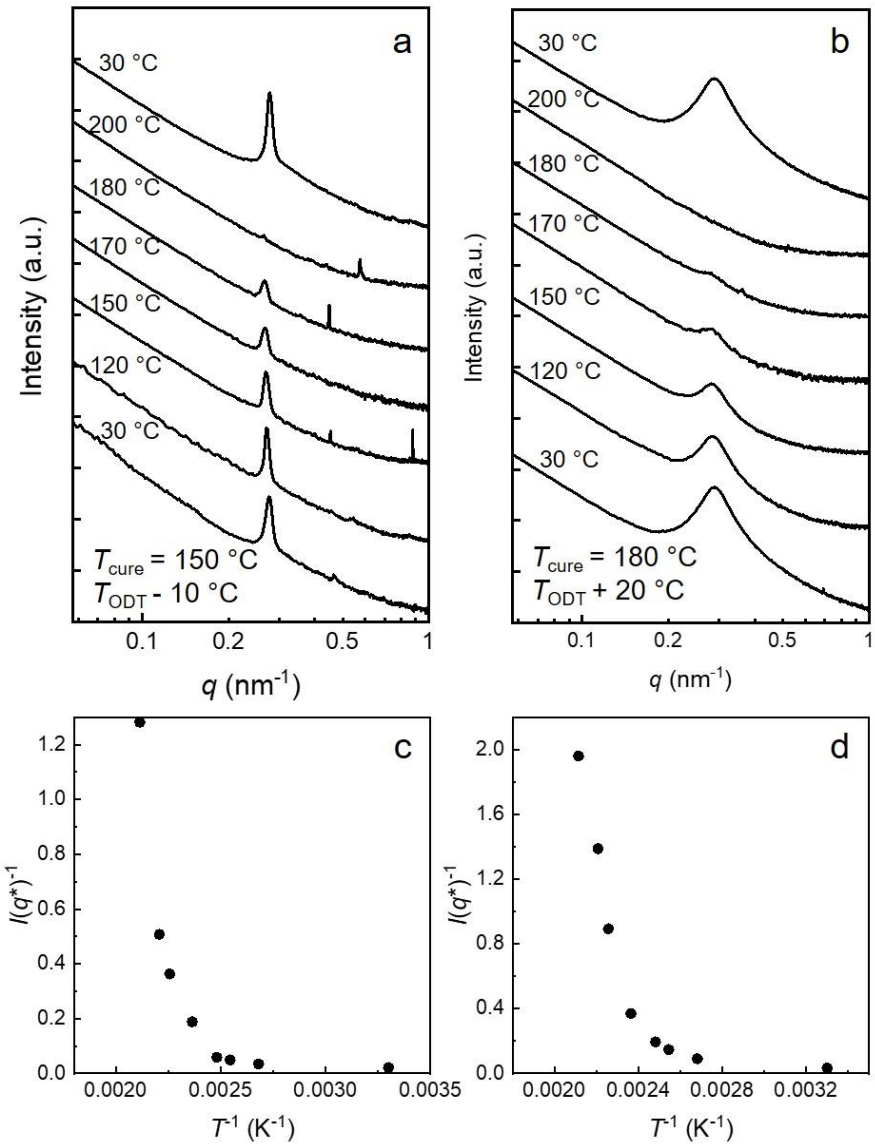

Figure 7.30. Variable temperature small angle X-ray scattering patterns for P(S-*s*-GMA)-14-PLA-18-XGMA-29 + 0.3 w.% BTPH cured in the ordered state at 150 °C (T_{ODT} - 10 °C, a) and in the disordered state at 180 °C (T_{ODT} + 20 °C, b). The samples were cured at the specified temperatures and then annealed overnight at 100 °C under reduced pressure prior to data acquisition. Samples were equilibrated for 2 minutes at each experimental temperature. The inverse intensity of the principal scattering peak, $I(q^*)$, is plotted as a function of inverse temperature for T_{cure} = 150 °C (c) and 180 °C (d).

The ability of these cross-linked domains to rearrange with temperature was further investigated by heating cross-linked samples above their initial T_{ODT} and rapidly quenching them in liquid nitrogen to kinetically trap the morphology by vitrification.[35,40] A sample of

P(S-*s*-GMA)-17-PLA-23-XGMA-27 + 0.3 wt.% BTPH was first cured in the ordered state at 155 °C (T_{ODT} - 15 °C) and then heated above the T_{ODT} to 190 °C. After annealing the sample at this temperature for 1 h, it was removed from the oven and immediately quenched below T_g to kinetically trap the morphology present at 190 °C. The PLA domains were then selectively removed to facilitate SEM and N_2 sorption characterization of the domain structure and continuity (Figure 7.31).

The sample that was cured at 155 °C without subsequently heating above T_{ODT} displayed the expected lamellar morphology by SEM and low porosity by N_2 sorption analysis, consistent with an ordered morphology and minimal domain interconnectivity. In contrast, the sample that was cured at 155 °C and then quenched from 190 °C displayed a disordered morphology and a high porosity, suggesting that an ODT had occurred upon heating. The observed morphological changes support the conclusion that the cross-linked domains of P(S-*s*-GMA)-17-PLA-23-XGMA-27 retained a sufficiently high mobility to reorganize upon heating above T_{ODT}, which was consistent with the variable temperature SAXS results. These results generally support the prevailing theoretical understanding that the ODT is primarily characterized by a change in interfacial curvature rather than by a significant change in domain composition[8,36,41], as the cross-linked nature of these domains is expected to significantly hinder mass exchange and domain mixing. Samples that were cured in the disordered state at 190 °C displayed similarly disordered morphologies and high porosities regardless of whether they were examined in the as-cured state or were reheated and quenched from above T_{ODT}.

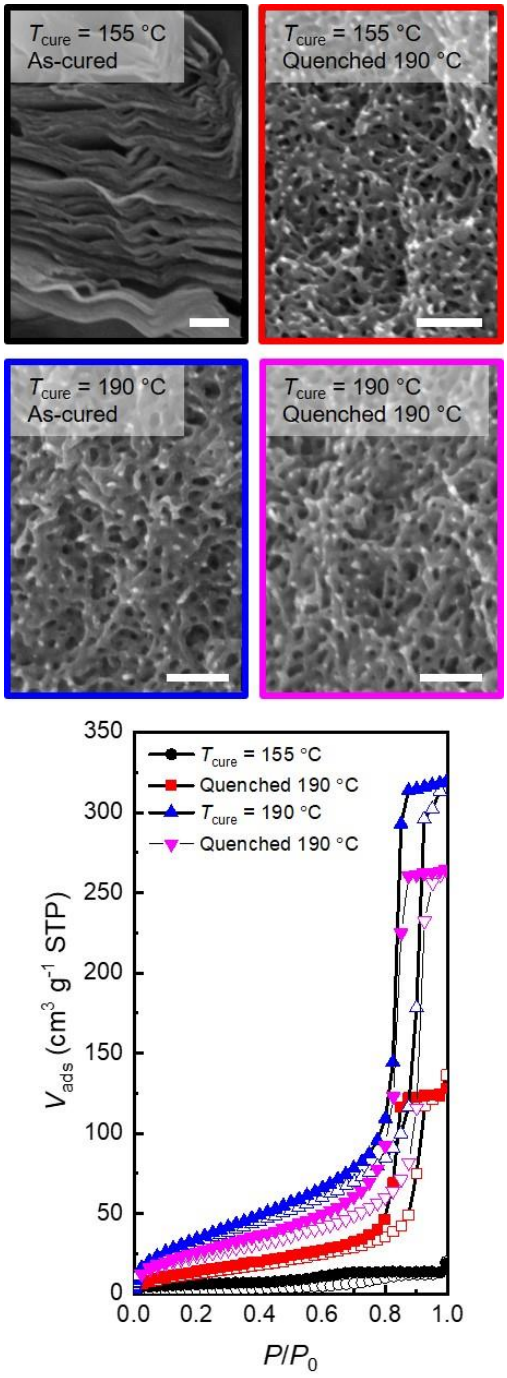

Figure 7.31. SEM images for P(S-*s*-GMA)-17-PLA-23-XGMA-27 + 0.3 wt.% BTPH cured in the ordered state at 155 (T_{ODT} – 15 °C, top images) and the disordered state at 190 °C (T_{ODT} + 20 °C, bottom images). Following the initial curing, a section of each thermoset was then annealed above the T_{ODT} at 190 °C before rapidly quenching in liquid nitrogen. The SEM images of the as-cured monoliths (left images) and the quenched monoliths (right images) were obtained following PLA removal. All SEM samples were coated with approximately 2 nm of Ir and imaged at 3.0 kV. Nitrogen sorption isotherms for all etched monoliths (T_{cure} = 155 and 190 °C, as-cured and quenched) are presented in the bottom panel.

Interestingly, samples of P(S-*s*-GMA)-14-PLA-18-XGMA-29 + 0.3 w.% BTPH cured in the ordered state at 150 °C (T_{ODT} - 10 °C) did not display any morphological transition upon reheating and quenching from above T_{ODT} at 185 °C (Figure 7.32). Lamellar-like morphologies were observed for both the as-cured and the quenched samples after PLA removal. Furthermore, both samples displayed significantly lower porosities than a sample cured in the disordered state at 185 °C. One possible explanation for this lack of an observable morphological change may be related to the higher cross-link density for P(S-*s*-GMA)-14-PLA-18-XGMA-29 as compared to P(S-*s*-GMA)-17-PLA-23-XGMA-27. This is expected to reduce the chain mobility in the cross-linked domains and prevent their reorganization upon heating. Indeed, such a transition from a thermally accessible T_{ODT} to a permanently fixed and temperature invariant morphology has previously been reported for cross-linked block polymers with increasing cross-link density.[38,39] These observations are also consistent with the inability to orient the domains of P(S-*s*-GMA)-14-PLA-28-XGMA-29 post-curing in contrast to P(S-*s*-GMA)-17-PLA-23-XGMA-27, as their higher cross-link density may preclude them from aligning along the shear direction. A more systematic investigation of these details may inform the design of novel adaptable materials from cross-linked block polymers.

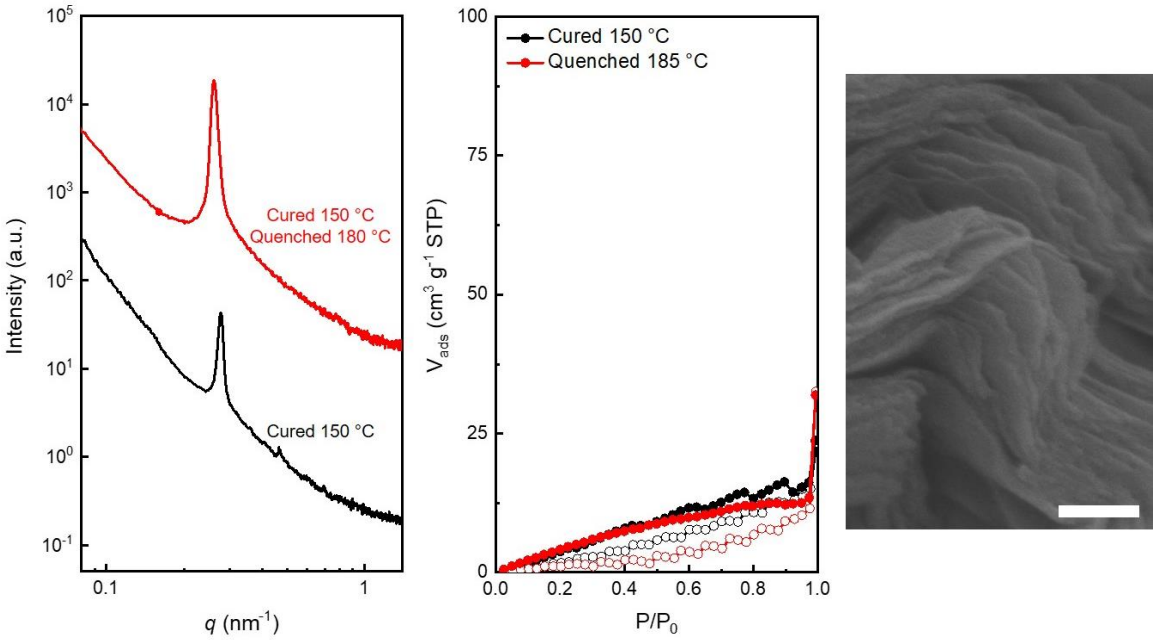

Figure 7.32. Room temperature SAXS patterns for P(S-*s*-GMA)-14-PLA-18-XGMA-29 + 0.3 w.% BTPH cross-linked at 150 °C in the absence of shear prior to etching (left). One sample analyzed as-cured (cured 150 °C) and one sample was heated to 180 °C after cross-linking before quenching in liquid nitrogen (cured 150 °C, quenched 180 °C). Nitrogen sorption isotherms for the same samples after PLA removal (middle). Low porosities were obtained for bot samples, as evidenced by a lack of H2 hysteresis. SEM image for P(S-*s*-GMA)-14-PLA-18-XGMA-29 + 0.3 w.% BTPH cross-linked at 150 °C and subsequently heated to 180 °C and quenched in liquid nitrogen (right).

7.4 Conclusions

Large amplitude oscillatory shear was used to control the domain orientation for P(S-*s*-GMA)-*b*-PLA block polymers cross-linked in the disordered state. By varying the strain amplitude, the nanostructure of the disordered domains was precisely tuned during the simultaneous cross-linking reaction. For a given curing temperature slightly above T_{ODT}, a shear-induced disorder-order transition was observed with increasing strain amplitude due to the suppression of composition fluctuations. Rather than uniaxially aligned domains along the shear direction, parallel-transverse kinked lamellae were observed due to the large mechanical contrast between the domains. The effect of cross-linking temperature on this shear-induced disorder-order transition was then investigated by selecting several

cross-linking temperatures both above and below T_{ODT} at a constant strain amplitude. For cross-linking temperatures near the T_{ODT} (both below and above), domain orientation and the formation of parallel-transverse kinked lamellae was observed under LAOS. However, there was no observable shear-induced disorder-order transition or domain alignment for cross-linking temperatures *far* above T_{ODT}. These results suggest that large amplitude composition fluctuations and/or slow curing kinetics relative to sample heating are required to obtain this transition. This point was further examined by first cross-linking samples under low strain amplitude and then applying LAOS post-gelation. For low cross-link densities, shear-induced domain orientation was observed parallel to the direction of shear, but the parallel-transverse orientation of samples cross-linked under LAOS was not observed. For a block polymer with a higher cross-link density, no alignment was observed post-gelation, presumably due to hindered chain mobility. These conclusions were supported by SAXS and SEM experiments for samples cross-linked in the ordered state and subsequently vitrified from above T_{ODT}. An ODT was observed for a diblock polymer with a low cross-link density, while no such transition was observed for a diblock with a higher cross-link density. These findings demonstrate that the application of LAOS during the in-situ cross-linking of a lamellar diblock polymer in the vicinity of the T_{ODT} can be a powerful tool to precisely control the alignment of microphase separated domains. Through the judicious selection of the cross-linking temperature and the strain amplitude, we have shown that it is possible to induce morphological transitions and to engineer the continuity and anisotropy of both the ordered and disordered states through mechanical processing.

7.5 References

1) Wang, D.; Kou, R.; Choi, D.; Yang, Z.; Nie, Z.; Li, J.; Saraf, L. V.; Hu, D.; Zhang, J.; Graff, G. L.; Liu, J.; Pope, M. A.; Aksay, I. A. Ternary Self-Assembly of Ordered Metal Oxide−Graphene Nanocomposites for Electrochemical Energy Storage. *ACS Nano* **2010**, *4*, 1587–1595.

2) Werber, J. R.; Osuji, C. O.; Elimelech, M. Materials for next-Generation Desalination and Water Purification Membranes. *Nature Reviews Materials* **2016**, *1*, 16018.

3) Peer, D.; Karp, J. M.; Hong, S.; Farokhzad, O. C.; Margalit, R.; Langer, R. Nanocarriers as an Emerging Platform for Cancer Therapy. *Nature Nanotechnology* **2007**, *2*, 751–760.

4) Bates, F. S.; Frederickson, G. Block Copolymers - Designer Soft Materials. *Phys. Today* **1999**, *52*, 32–38.

5) Bates, F.; Frederickson, G. Block Copolymer Thermodynamics: Theory and Experiments. *Annu. Rev. Phys. Chem.* **1990**, *41*, 525–557.

6) Bates, C. M.; Bates, F. S. 50th Anniversary Perspective: Block Polymers—Pure Potential. *Macromolecules* **2017**, *50*, 3–22.

7) Rosedale, J. H.; Bates, F. S.; Almdal, K.; Mortensen, K.; Wignall, G. D. Order and Disorder in Symmetric Diblock Copolymer Melts. *Macromolecules* **1995**, *28*, 1429–1443.

8) Lee, S.; Gillard, T. M.; Bates, F. S. Fluctuations, Order, and Disorder in Short Diblock Copolymers. *AIChE J.* **2013**, *59*, 3502–3513.

9) Bates, F. S.; Rosedale, J. H.; Fredrickson, G. H. Fluctuation Effects in a Symmetric Diblock Copolymer near the Order–disorder Transition. *The Journal of Chemical Physics* **1990**, *92*, 6255–6270.

10) Bates, F. S.; Rosedale, J. H.; Fredrickson, G. H.; Glinka, C. J. Fluctuation-Induced First-Order Transition of an Isotropic System to a Periodic State. *Phys. Rev. Lett.* **1988**, *61*, 2229–2232.

11) Sinturel, C.; Vayer, M.; Morris, M.; Hillmyer, M. A. Solvent Vapor Annealing of Block Polymer Thin Films. *Macromolecules* **2013**, *46*, 5399–5415.

12) Feng, X.; Kawabata, K.; Cowan, M. G.; Dwulet, G. E.; Toth, K.; Sixdenier, L.; Haji-Akbari, A.; Noble, R. D.; Elimelech, M.; Gin, D. L.; Osuji, C. O. Single Crystal Texture by Directed Molecular Self-Assembly along Dual Axes. *Nature Materials* **2019**, *18*, 1235–1243.

13) Mansky, P.; DeRouchey, J.; Russell, T. P.; Mays, J.; Pitsikalis, M.; Morkved, T.; Jaeger, H. Large-Area Domain Alignment in Block Copolymer Thin Films Using Electric Fields. *Macromolecules* **1998**, *31*, 4399–4401.

14) Hadziioannou, G.; Mathis, A.; Skoulios, A. Obtention de ≪ Monocristaux ≫ de Copolymères Triséquencés Styrène/isoprène/styrène Par Cisaillement Plan. *Colloid and Polymer Science* **1979**, *257*, 136–139.

15) Cohen, Y.; Albalak, R. J.; Dair, B. J.; Capel, M. S.; Thomas, E. L. Deformation of Oriented Lamellar Block Copolymer Films. *Macromolecules* **2000**, *33*, 6502–6516.

16) Koppi, K. A.; Tirrell, M.; Bates, F. S. Shear-Induced Isotropic-to-Lamellar Transition. *Phys. Rev. Lett.* **1993**, *70*, 1449–1452.

17) Bates, F. S.; Koppi, K. A.; Tirrell, M.; Almdal, K.; Mortensen, K. Influence of Shear on the Hexagonal-to-Disorder Transition in a Diblock Copolymer Melt. *Macromolecules* **1994**, *27*, 5934–5936.

18) Okamoto, S.; Saijo, K.; Hashimoto, T. Real-Time SAXS Observations of Lamella-Forming Block Copolymers under Large Oscillatory Shear Deformation. *Macromolecules* **1994**, *27*, 5547–5555.

19) Pinheiro, B. S.; Hajduk, D. A.; Gruner, S. M.; Winey, K. I. Shear-Stabilized Bi-Axial Texture and Lamellar Contraction in Both Diblock Copolymer and Diblock Copolymer/Homopolymer Blends. *Macromolecules* **1996**, *29*, 1482–1489.

20) Zeng, D.; Ribbe, A.; Kim, H.; Hayward, R. C. Stress-Induced Orientation of Cocontinuous Nanostructures within Randomly End-Linked Copolymer Networks. *ACS Macro Lett.* **2018**, *7*, 828–833.

21) Panyukov, S.; Rubinstein, M. Stress-Induced Ordering in Microphase-Separated Multicomponent Networks. *Macromolecules* **1996**, *29*, 8220–8230.

22) Aida, S.; Sakurai, S.; Nomura, S. Strain-Induced Ordering of Microdomain Structures in Polystyrene-Block-Polybutadiene-Block-Polystyrene Triblock Copolymers Cross-Linked in the Disordered State. *Polymer* **2002**, *43*, 2881–2887.

23) Hampu, N.; Hillmyer, M. A. Temporally Controlled Curing of Block Polymers in the Disordered State Using Thermally Stable Photoacid Generators for the Preparation of Nanoporous Membranes. *ACS Appl. Polym. Mater.* **2019**, *1*, 1148–1154.

24) Vidil, T.; Hampu, N.; Hillmyer, M. A. Nanoporous Thermosets with Percolating Pores from Block Polymers Chemically Fixed above the Order–Disorder Transition. *ACS Cent. Sci.* **2017**, *3*, 1114-1120.

25) Hampu, N.; Bates, M. W.; Vidil, T.; Hillmyer, M. A. Bicontinuous Porous Nanomaterials from Block Polymers Radically Cured in the Disordered State for Size-Selective Membrane Applications. *ACS Appl. Nano Mater.* **2019**, *2*, 4567-4577

26) Hampu, N.; Hillmyer, M. A. Molecular Engineering of Nanostructures in Disordered Block Polymers. *ACS Macro Lett.* **2020**, *9*, 382–388.

27) Kim, O.; Kim, S. Y.; Lee, J.; Park, M. J. Building Less Tortuous Ion-Conduction Pathways Using Block Copolymer Electrolytes with a Well-Defined Cubic Symmetry. *Chem. Mater.* **2016**, *28*, 318–325.

28) Cates, M. E.; Milner, S. T. Role of Shear in the Isotropic-to-Lamellar Transition. *Phys. Rev. Lett.* **1989**, *62*, 1856–1859.

29) Hamley, I. W. Structure and Flow Behaviour of Block Copolymers. *Journal of Physics: Condensed Matter* **2001**, *13*, R643–R671.

30) Stangler, S.; Abetz, V. Orientation Behavior of AB and ABC Block Copolymers under Large Amplitude Oscillatory Shear Flow. *Rheologica Acta* **2003**, *42*, 569–577.

31) Bertrand, A.; Hillmyer, M. A. Nanoporous Poly(lactide) by Olefin Metathesis Degradation. *J. Am. Chem. Soc.* **2013**, *135*, 10918–10921.

32) Polis, D. L.; Winey, K. I. Kink Bands in a Lamellar Diblock Copolymer Induced by Large Amplitude Oscillatory Shear. *Macromolecules* **1996**, *29*, 8180–8187.

33) Polis, D. L.; Winey, K. I. Controlling Kink Band Morphology in Block Copolymers: Threshold Criteria and Stability. *Macromolecules* **1998**, *31*, 3617–3625.

34) Zeng, D.; Ribbe, A.; Hayward, R. C. Anisotropic and Interconnected Nanoporous Materials from Randomly End-Linked Copolymer Networks. *Macromolecules* **2017**, *50*, 4668–4676.

35) Hampu, N.; Hillmyer, M. A. Molecular Engineering of Nanostructures in Disordered Block Polymers. *ACS Macro Lett.* **2020**, *9*, 382–388.

36) Medapuram, P.; Glaser, J.; Morse, D. Universal Phenomenology of Symmetric Diblock Copolymers near the Order−Disorder Transition. *Macromolecules* **2015**, *48*, 819–839.

37) Gillard, T. M.; Phelan, D.; Leighton, C.; Bates, F. S. Determination of the Lamellae-to-Disorder Heat of Transition in a Short Diblock Copolymer by Relaxation Calorimetry. *Macromolecules* **2015**, *48* , 4733–4741.

38) Gomez, E. D.; Das, J.; Chakraborty, A. K.; Pople, J.; Balsara, N. Effect of Cross-Linking on the Thermodynamics of Lamellar Block Copolymers. *Macromolecules* **2006**, *39*, 4848–4859.

39) Hahn, H.; Chakraborty, A. K.; Das, J.; Pople, J.; Balsara, N. Order-Disorder Transitions in Cross-Linked Block Copolymer Solids. *Macromolecules* **2005**, *38*, 1277–1285.

40) Hickey, R. J.; Gillard, T. M.; Irwin, M. T.; Lodge, T. P.; Bates, F. S. Structure, Viscoelasticity, and Interfacial Dynamics of a Model Polymeric Bicontinuous Microemulsion. *Soft Matter* **2016**, *12*, 53–66.

41) Yadav, M.; Bates, F. S.; Morse, D. C. Network Model of the Disordered Phase in Symmetric Diblock Copolymer Melts. *Phys. Rev. Lett.* **2018**, *121*, 127802.

Chapter 8. Co-casting Highly Selective Dual Layer Membranes with Disordered Block Polymer Selective Layers[5]

8.1 Introduction

Each year, inadequate water sanitation is estimated to account for ~1 million deaths globally. Reliable access to clean water sources is expected to be further stressed by the effects of continued industrialization, population growth, and climate change.[1] To meet the growing demand for clean and safe drinking water, membrane technologies have emerged as an effective and energy-efficient platform for the treatment of wastewater.[1–4] In particular, ultrafiltration (UF) membranes comprising continuous pores with sizes ranging from approximately 1 to 100 nm have received extensive interest for the removal of critical water-borne species (such as bacteria, viruses and dissolved macromolecules) from drinking water and wastewater.[4–6] UF membranes operate by a size-exclusion mechanism, where particles larger than the membrane pores are excluded and smaller species are able to permeate.[1,2] Two principal metrics are typically used to assess UF membrane performance: permeability and selectivity. The ideal UF membrane would exhibit both high water permeability (defined as water flux normalized to applied pressure difference) and high size-selectivity (defined as quantitative rejection of all particles larger than the average pore size).[1,2,4,7]

Commercial UF membranes are typically prepared via Non-solvent Induced Phase Separation (NIPS), where a homopolymer solution is cast into a film and then immersed

[5] This work was done in collaboration with Dr. Jay Werber

into a non-solvent coagulation bath to induce phase separation and pore formation.[3,8] These membranes demonstrate excellent water permeability due to their plurality of continuous pores. However, the stochastic nature of NIPS results in a broad pore size distribution, limiting their size-selectivity.[1,7–9] To improve upon the selectivity of NIPS membranes, block polymers have emerged as an intriguing alternative due to their ability to self-assemble into regularly ordered domains of uniform size.[5,10–12]

The implementation of block polymers into membrane technologies has been hindered by the scalability of existing fabrication and processing methods. Block polymer selective layers can be supported on pre-formed porous NIPS membranes by either direct solution casting (spin or blade coating) or by floating off thin films from a sacrificial substrate and placing them atop a support layer.[5,10,11,13,14] While successful on the lab-scale, practical challenges associated with solution casting thin films onto porous supports or with floating off large, module-size films have proven to be limiting for scale-up. Additionally, continuous pores (i.e., pores that percolate from one side of the membrane to the other) are necessary to achieve high water permeability. However, typical ordered block polymer morphologies are either anisotropic cylinders that require post-processing alignment techniques to orient domains perpendicular to the substrate surface,[5,10,15] or are isotropic and bicontinuous (e.g. gyroid) yet require precise syntheses to reliably access.[16] Selectively swelling unaligned cylinder-forming block polymers has been shown to produce continuous pores without orienting the domains, but these systems still require coating onto porous substrates.[11,17–19] Alternatively, recent work has addressed these processing limitations by forming free-standing membranes of block polymers using evaporation

induced Self-assembly followed by Non-solvent Induce Phase Separation (SNIPS). These SNIPS membranes exhibit an integral and asymmetric structure comprising a thin selective layer with a narrow pore size distribution supported by a highly porous block polymer substructure.[12,20,21] While promising, SNIPS membranes can require larger quantities of block polymer as well as stringent formulations, resulting in high materials expenses.

Recently our group has reported that the fluctuating disordered state in block polymers can be kinetically trapped by either cross-linking above the order-disorder transition temperature (T_{ODT}) or by rapidly cooling from above T_{ODT} to below the glass transition temperature (T_g).[22–25] Upon the selective removal of one domain, a bicontinuous network of pores within a supporting glassy matrix was obtained. The resulting pores were shown to have a narrow size distribution, while their disordered and bicontinuous nature eliminated the need for domain alignment during UF membrane fabrication.[22] Inspired by hybrid approaches for co-casting dual layer membranes comprising a SNIPS-derived block polymer selective layer and a NIPS-derived homopolymer support layer (SNIPS/NIPS),[21,26,27] we now report the development of a membrane fabrication process that combines homopolymer NIPS and disordered block polymer self-assembly to produce membranes with both high water permeability and high size-selectivity. This proof-of-concept study could result in the scalable production of high performing membranes, pending translation to more industrially-relevant coating processes.

8.2 Experimental Methods

To achieve this goal, we first spin coated a concentrated solution of polysulfone (PSF) to form the nascent support layer. While the PSF layer remained swollen in solvent, a second layer of poly(methyl methacrylate-*stat*-styrene)-*block*-polylactide, SML, was spin coated from a dilute solution onto the PSF layer to form a dual layer liquid film, assuming limited interlayer mixing due to the high viscosity mismatch. Processing techniques were then employed to disorder the SML layer while the PSF layer remained swollen in solvent. The film was immersed in an ice water coagulation bath to kinetically trap the disordered state in the block polymer layer and precipitate the PSF layer by NIPS. The subsequent removal of the PLA domains in the block polymer generated a porous selective layer. A detailed description of fabrication is provided in Chapter 3. A schematic depiction of this process is provided in Figure 8.1.

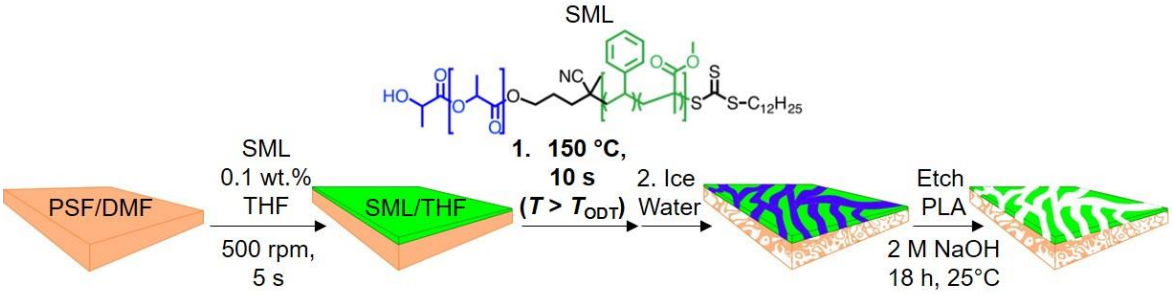

Figure 8.1. Schematic illustrating the fabrication procedure for the dual layer membranes. First a concentrated solution of PSF in DMF (typically 18-22 wt.% PSF) is spin coated onto a non-woven polyester backing at 500 rpm for 5 s. While the PSF layer is still swollen in DMF, a second layer of SML (chemical structure depicted) is spin coated from a 0.1 wt.% solution in THF on top of the PSF/DMF layer at 500 rpm for 5 s. The dual layer liquid film is then annealed above T_{ODT} at 150 °C for 10 s before immersing in an ice water coagulation bath to precipitate the PSF layer and trap the bicontinuous, fluctuating disordered state in the SML selective layer. The PLA domains are then selectively removed using aqueous base to generate a porous selective layer.

The SML block polymer used as the selective layer was synthesized by a reversible addition-fragmentation chain-transfer (RAFT) copolymerization of MMA and S from a

PLA macro chain transfer agent following a previously reported procedure.[25] Here we focus on a diblock with a number-average molar mass of the PLA block ($M_{n,\,PLA}$) of 19 kg mol^{-1}, a number-average molar mass of the P(MMA-*s*-S) block ($M_{n,\,P(MMA\text{-}s\text{-}S)}$) of 29 kg mol^{-1}, and a molar fraction of styrene in the P(MMA-*s*-S) block (XS) of 0.29, as determined by SEC and ^{1}H NMR end group analysis (Figures 8.2 – 8.4). This diblock will be referred to as SML-48. Dynamic mechanical analysis, DMA, (Figure 8.5) and variable temperature small angle X-ray scattering, SAXS, (Figure 8.6) for SML-48 demonstrated clear evidence of microphase segregation, yet the absence of higher order SAXS peaks and the lack of a clear rheological transition indicated a lack of long-range order.

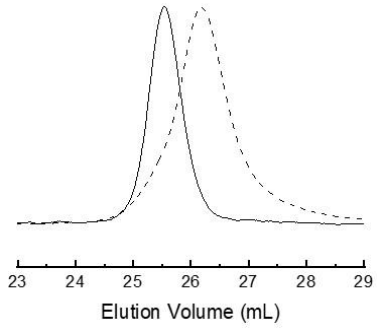

Figure 8.2. THF SEC elugrams for PLA-19 ($Đ$ = 1.07, dashed curve) and SML-48 ($Đ$ = 1.05, solid curve).

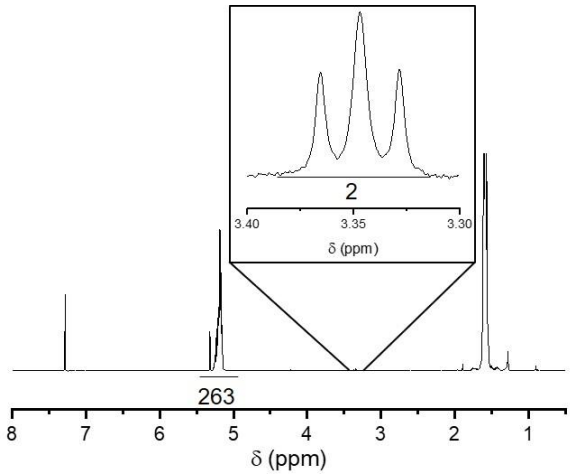

Figure 8.3. ^{1}H NMR spectrum for PLA-19. Regions of integration for the methine protons of the PLA backbone (5.00–5.40 ppm, 1*H*) and the methylene protons adjacent to the trithiocarbonate of the CTA (3.30-3.40 ppm, 2*H*) are indicated and the corresponding integral values are provided below the corresponding peak (M_n = 19 kg mol^{-1}).

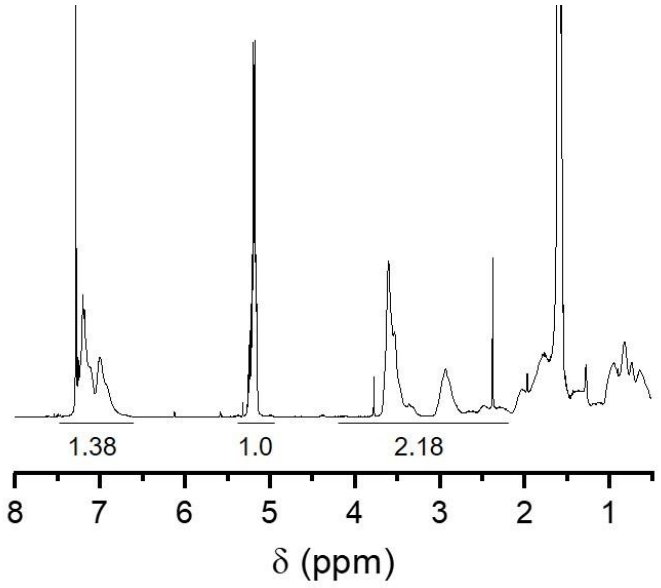

Figure 8.4. ^{1}H NMR spectrum for SML-48. Regions of integration for the PS aromatic protons (6.30–7.20 ppm, 5*H*), the methyl protons of PMMA (2.10–4.20 ppm, 3*H*), and the methine protons of the PLA backbone (5.00–5.40 ppm, 1*H*) are indicated along with their corresponding integral values ($M_{n,\,P(MMA\text{-}s\text{-}S)}$ = 29 kg mol^{-1}, XS = 29, f_{PLA} = 0.38).

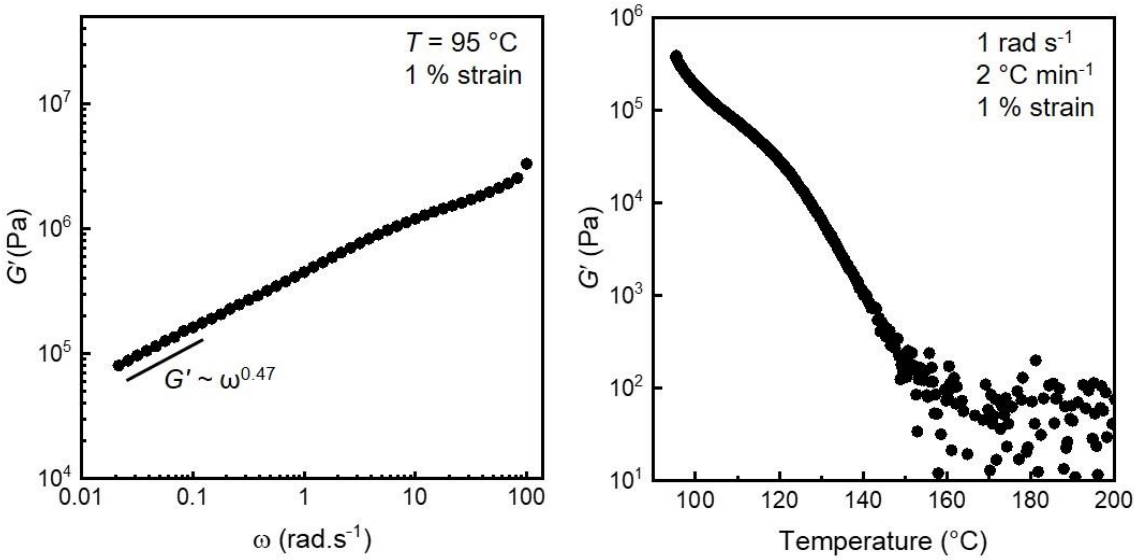

Figure 8.5 Frequency dependence of the storage modulus *G′* for SML-48 (left). The data were collected from approximately 100 to 0.01 rad s^{-1} at 95 ˚C and 1% strain. Temperature dependence of the storage modulus for SML-48 (right). Data were obtained using a frequency of 1 rad s^{-1}, 1 % strain, and a heating rate of 2 °C min^{-1}.

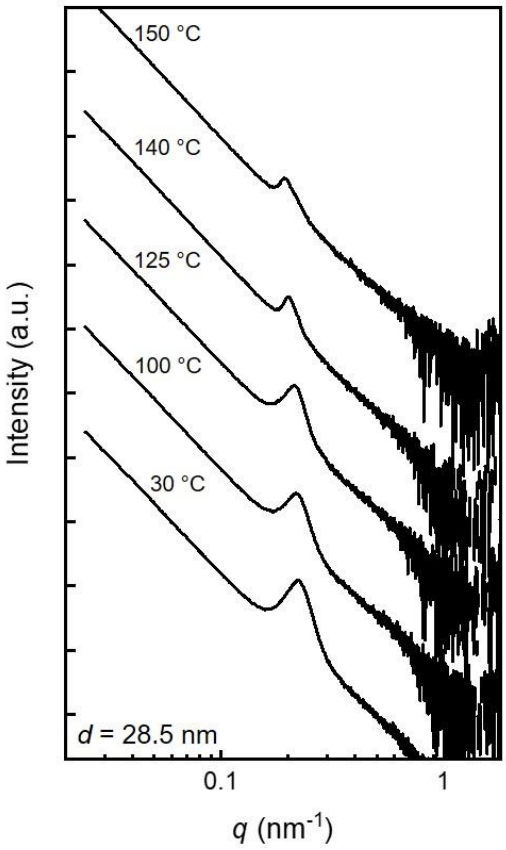

Figure 8.6. Variable temperature SAXS data for SML-48. The sample was annealed overnight at 100 °C under reduced pressure prior to measurement. The sample was equilibrated for at least 2 min at each temperature prior to data acquisition.

8.3 Results and Discussion

8.3.1 Co-casting dual layer membranes followed by thermal processing

To demonstrate that porous materials could be produced from SML-48, a monolithic sample was annealed in the disordered state at 150 °C and rapidly quenched in liquid nitrogen to kinetically trap disordered state composition fluctuations.[25] Following quenching, the PLA domains were selectively removed by immersing the monolith in a 2 M solution of NaOH in H_2O/MeOH (40/60 v/v) overnight at room temperature. Room temperature SAXS of the etched monolith displayed an increase in the scattered intensity as compared to the unetched precursor, while the scattering vector of the principal

scattering peak, q^*, remained unchanged (Figure 8.7). Additionally, a reticulated disordered morphology similar to other disordered and co-continuous polymers was observed by SEM after etching (Figure 8.7). These results indicated that a porous material templated by the block polymer structure was obtained with minimal pore collapse.[22,28] The three-dimensional continuity of these pores was confirmed by N_2 sorption analysis, which revealed a BET surface area of 83 m^2 g^{-1} and a monomodal pore size distribution with a mode of ~14 nm by QSDFT[29] (Figures 8.8 and 8.9). These results demonstrated that continuous pores with a narrow size distribution could be obtained from bulk samples, confirming the potential utility of SML-48 for membrane applications.

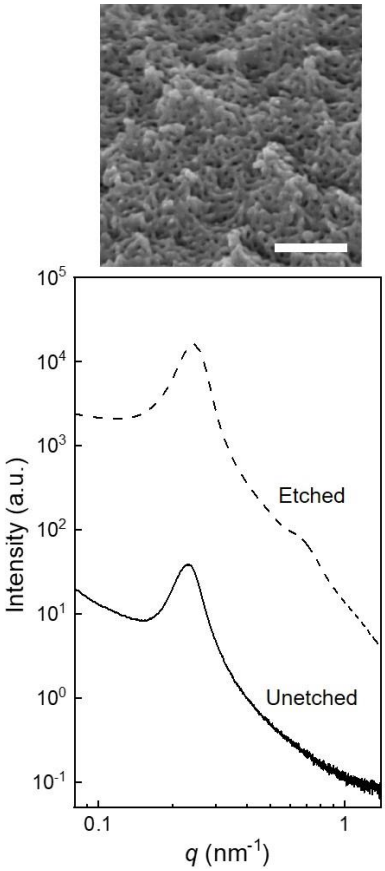

Figure 8.7. SEM of an etched monolith of SML-48 that was quenched from 150 °C (top). The scale bar corresponds to 200 nm, and the sample was coated with ~ 2 nm of Ir prior to imaging. Room temperature SAXS patterns of monolithic samples of SML-48 that were quenched from 150 °C (bottom). Patterns were obtained both before (solid curve) and after (dashed curve) PLA etching.

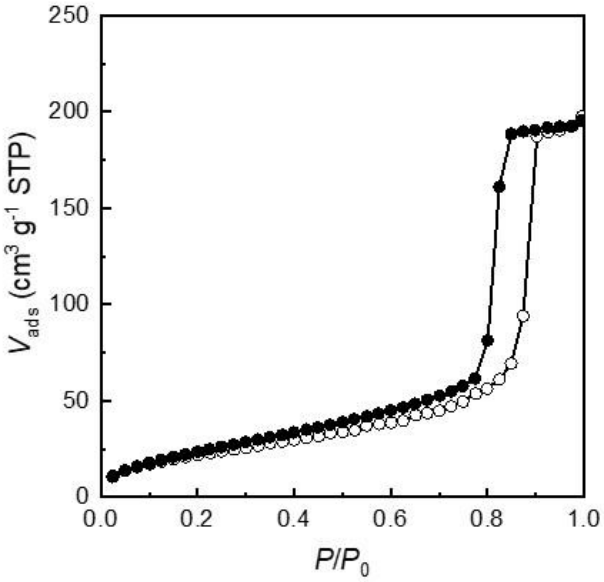

Figure 8.8. N_2 sorption isotherm for an etched SML-48 that was annealed for 1 h at 150 °C and quenched in liquid nitrogen. Open circles correspond to data taken upon adsorption and closed circles correspond to data taken upon desorption. The BET surface area is inset in the upper left corner.

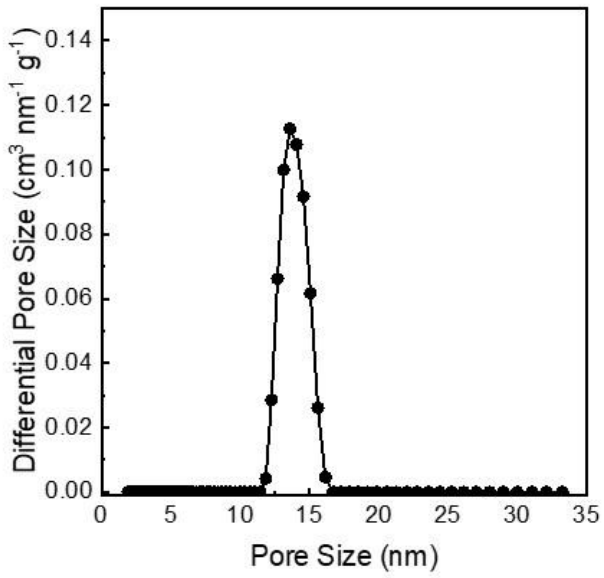

Figure 8.9. Pore size distribution calculated from QSDFT from the adsorption branch of an etched SML-48 that was annealed for 1 h at 150 °C and quenched in liquid nitrogen. The pore mode is inset in the upper left corner.

Polysulfone (PSF) was identified as an ideal homopolymer for the support layer. The high thermal and hydrolytic stability of PSF was compatible with the necessary thermal

annealing, solvents, and etching conditions used for the SML selective layer. In contrast, other polymers commonly used in NIPS membranes, such as polyacrylonitrile, were observed to undergo hydrolysis and a subsequent loss of dimensional stability upon exposure to the alkaline PLA-etching solution. Dual layer membrane fabrication began with spin coating a concentrated PSF solution in dimethyl formamide (DMF) onto a 6 cm by 6 cm non-woven polyester backing that was pre-wet with DMF and taped to a 7.5 cm by 7.5 cm glass plate to ensure uniform spreading of the casting solution.[30] Liquid discharge was observed along the walls of the spin coater, indicating that film spreading occurred by viscous flow (i.e. "spin off") despite the relatively high solution viscosity and slow spin speed. Next, a dilute solution of SML-48 in THF was filtered and deposited dropwise onto the center of the static PSF/DMF layer before spin coating. The dual layer liquid film was then annealed for a predetermined time at 150 °C to disorder the SML-48 layer and evaporate residual THF (normal boiling point of 66 °C), while the PSF layer remained swollen in the much less volatile DMF (normal boiling point of 150 °C). After annealing, the film was immersed in ice water to trap the disordered state in the SML selective layer and precipitate the PSF layer by NIPS.

To identify the effect that the support layer microstructure had on the dual layer membrane permeability and selectivity, the concentration of the PSF solution was varied while the coating parameters and annealing conditions for the selective layer were fixed. The concentration of the SML-48 solution was maintained at 0.1 wt.% in THF. The annealing temperature and time for all membranes was 150 °C and 10 s, as higher temperatures and longer annealing times led to the formation of defective or dense membranes. A spin

coating speed of 500 rpm for 5 s with a ramp rate of 500 rpm s^{-1} was selected for casting both layers, as much faster rates or much longer times resulted in an undesirably high degree of "spin off" from the support layer, leading to the formation of thin films with insufficient mechanical robustness for pressure-driven membrane operations. The concentration of the PSF solution was varied between 18 and 22 wt.% in DMF. Lower concentrations of PSF (≤ 16 wt.%) generally resulted in thin and highly defective membranes, while higher concentrations (≥ 25 wt.%) resulted in dense and water impermeable membranes. Visually, the dual layer membranes appeared white and macroscopically uniform following immersion in the ice water bath, generally resembling commercial membranes prepared by NIPS.

Following fabrication, the PLA domains in the selective layer were selectively removed to generate a porous structure. For comparison, analogous bare PSF membranes were prepared using an identical procedure, except that PLA homopolymer with a number-average molar mass of 19 kg mol^{-1} (referred to as PLA-19) was used as the second layer instead of SML-48. Subsequent etching of PLA-19 homopolymer produced a PSF membrane that was expected to approximate the morphology of the underlying support layer in the dual layer membranes containing block polymer. The surface morphologies of the porous membranes were then examined using SEM (Figure 8.10). The dual layer membranes exhibited a noticeably different surface morphology than their corresponding support layers, consistent with a selective layer being successfully deposited onto the PSF surface. The pore size of the PSF support layer was observed to significantly increase with decreasing PSF concentration, consistent with previously reported results.[7,8,30] In contrast,

the pore size of the block polymer selective layer was relatively unaffected by the concentration of the PSF casting solution.

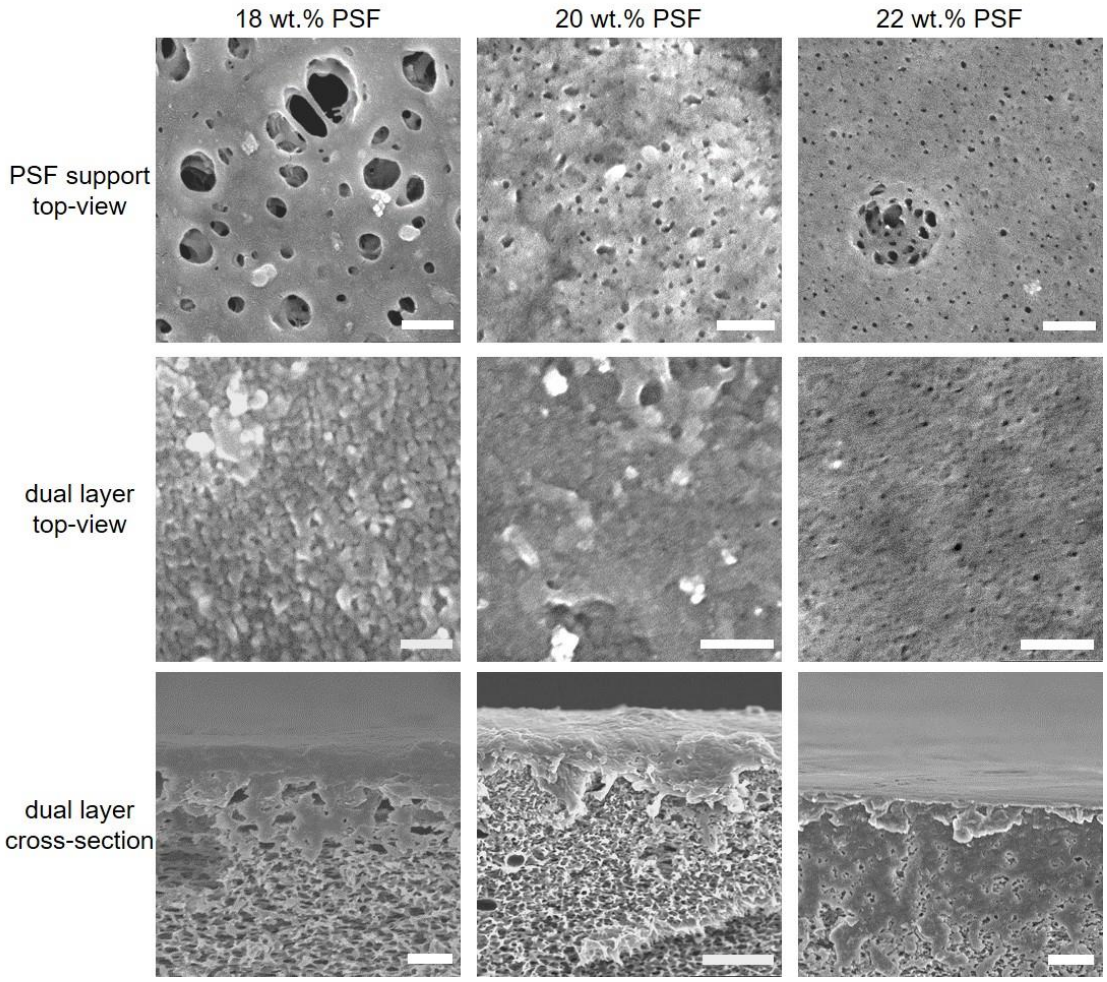

Figure 8.10. SEM of dual layer membranes fabricated on PSF supports cast from 18 (left column), 20 (middle column), and 22 (right column) wt.% solutions in DMF. Top view images of the bare PSF support (fabricated by selectively removing the PLA-19 homopolymer surface layer) are presented in the top row, and top view images of dual layer membranes with block polymer selective layers are presented in the middle row. Cross-sectional images of cryo-fractured dual layer membranes are presented in the bottom row. All membranes were selectively etched in 2 M NaOH prior to remove the PLA domains prior to imaging. The scale bars for the top view images correspond to 200 nm, and the scale bars for the cross-sectional images correspond to 2 μm.

Cross-sectional SEM images of cryo-fractured membranes confirmed the existence of a dual layer film, comprising a thin and dense SML selective layer on top of a thicker and

more porous PSF support layer (Figure 8.10). The thickness of the block polymer selective layer was approximately 800 – 1000 nm based on cross-sectional SEM, regardless of the PSF concentration. Based on the membrane area and the volume of the block polymer solution deposited during spin coating, a slightly thinner film (300 nm, neglecting any polymer mass lost during "spin off") was expected. The larger film thickness measured by SEM may reflect deformation of the thin block polymer selective layer during sample preparation or incomplete spreading of the SML/THF during spin coating, resulting in an overestimate of the experimentally measured thickness. Therefore, all calculations in this work will use the selective layer film thickness predicted by the volume of deposited block polymer solution, although this is also expected to overestimate the actual thickness due to mass loss during spin coating.

Clear evidence of two layers in the cross-sectional SEM images along with the observed differences in surface morphology between the dual layer and the bare PSF membranes suggests that the SML selective layer did not delaminate from the PSF support. In contrast, Nunes et al. reported that co-casting hybrid SNIPS/NIPS membranes resulted in poor adhesion and delamination of the block polymer selective layer when using industrially relevant support layers (e.g. PAN, polyethersulfone).[26] The dual layer membranes examined in the present work comprise a solid block polymer film on top of a DMF-swollen PSF support prior to immersion in the water bath, resulting in a large contact area between the layers that presumably promotes adhesion. Additionally, the thermal annealing process and the miscibility of PSF/DMF with the THF used to cast SML-48 may promote a small amount of interdiffusion of the SML-48 selective layer into the PSF support layer.

In comparison, the hybrid SNIPS/NIPS approach comprises highly porous surfaces on both sides of the selective layer-support layer interface, which minimizes the overall contact area and likely contributed to the previously reported poor adhesion.

Due to its uniformly sized pores, the self-assembled block polymer selective layer was expected to result in a superior size-selectivity as compared to the bare PSF support fabricated using NIPS. To demonstrate this feature, each membrane was subjected to a series of feed solutions containing fluorescently labeled dextran standards of varying hydrodynamic radii. Rejection was determined based on the ratio of the maximum absorbance for the permeate solution to the feed solution using UV-Vis spectroscopy.[23,24] The rejection profiles for the dual layer membranes and their corresponding bare PSF supports are presented in Figure 8.11a for membranes cast from 18, 20, and 22 wt.% solutions of PSF in DMF. The experimentally measured rejection values were corrected using the mass transfer coefficient to account for concentration polarization to give true rejection values.[31] The high stirring speed (300 rpm) and low applied pressure (0.5 bar) used during the filtration experiments minimized these concentration polarization effects.[10,31] For membranes cast from 18 and 20 wt.% PSF in DMF, the rejection of high dextran molar masses (large hydrodynamic radii, R_h) was significantly higher for the dual layer membranes than for the bare supports. These results were consistent with the conclusion that the block polymer selective layer had a smaller average pore size that could more completely reject larger molecules.[32] Furthermore, the rejection profile was significantly sharper for the dual layer membranes due to the narrow pore size distribution of the self-assembled block polymer in comparison to the NIPS support.[7,9] The R_h that

corresponds to the molecular weight cut-off (MWCO, defined as the molar mass where rejection is 90 %) of the dual layer membranes was ~ 5 nm, which was reasonably consistent with the mean pore radius of bulk monoliths of SML-48 subjected to an identical thermal processing history (~ 6.8 nm) as determined by QSDFT analysis (Figure 8.9). Indeed, the experimental data closely followed the theoretical prediction for the size-dependent rejection of solutes of radius, a, for an isoporous membrane with an average pore radius, r_p, of 6.8 nm

$$R = 1 - \left[2\left(1 - \frac{a}{r_p}\right)^2 - \left(1 - \frac{a}{r_p}\right)^4\right] \exp\left[-0.7146\left(\frac{a}{r_p}\right)^2\right] \quad \text{(eq. 1)}$$

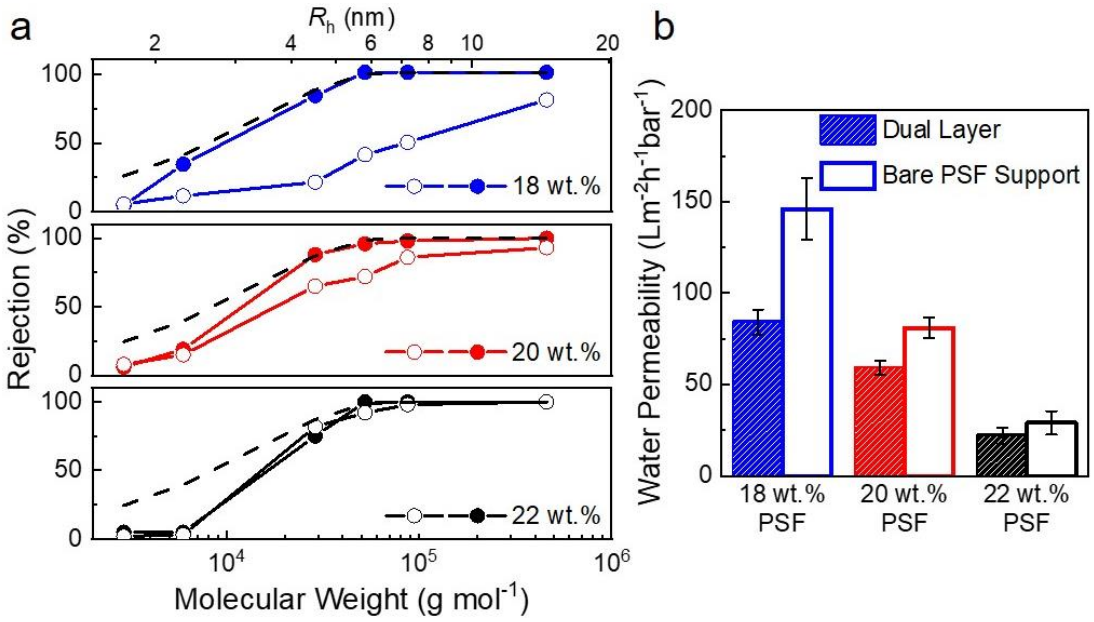

Figure 8.11. Rejection curves of fluorescently labeled dextran standards of dual layer and PSF support membranes cast from 18 (blue), 20 (red), and 22 wt.% (black) solutions of PSF in DMF (a). Closed circles correspond to dual layer membranes with an SML-48 selective layer, and open circles correspond to bare PSF support membranes. Rejection data was obtained in singlicate. The dashed black curve represents the theoretical rejection profile calculated using eq. 1 for an isoporous membrane with a pore radius of 6.8 nm. Experimental rejection was determined based on the ratio of the maximum UV-Vis absorbance for the permeate to the feed solution. The experimental data was then corrected using the mass transfer coefficient to account for concentration polarization, with the true rejection values shown in (a). Each data point was acquired for a feed solution comprised of a single molar mass dextran standard. Water permeability of dual layer (filled bars) and bare PSF support membranes (open bars) cast from 18 (blue), 20 (red), and 22 (black) wt.%

PSF (b). The permeability was determined based on the mean of three separate experiments, and the error bars correspond to the standard deviation.

Membranes cast from a 22 wt.% solution of PSF in DMF exhibited only slight differences in dextran rejection between the dual layer and bare PSF membranes (Figure 8.11a). A high rejection of dextran was observed in both cases. This high concentration of PSF likely resulted in a dense support layer with a comparable average pore size as SML-48, as evidenced by their similar MWCO. Overall, these results demonstrate that the uniform self-assembled block polymer domains significantly improve upon the size-selectivity of the bare support layer fabricated using a modified NIPS process.

One of the primary limitations of NIPS membranes is that they exhibit a significant trade-off between water permeability and size-selectivity due to their broad pore size distribution.[1,3,7] The presence of a small population of large pores in the active layer can enable the permeation of some solute particles that are larger than the average pore size. Therefore, the average pore size of a NIPS membrane needs to be significantly smaller than the hydrodynamic radius of the solute targeted for rejection to ensure complete removal. However, water permeability scales as r_p^4, for a fixed pore number density, so even modest decreases in the average pore size result in large decreases in the permeability.[10,33] Consequently, using NIPS membranes with smaller pore sizes enhances the solute rejection at the cost of significantly decreased water permeability. In contrast, the uniform pores of a block polymer selective layer should attenuate this trade-off, as a larger average pore size for an isoporous membrane can achieve an identical solute rejection as a NIPS membrane

with much smaller pores. For the dual layer membranes examined in this work, a sufficiently thin block polymer selective layer imparts a high size-selectivity without imposing a significant barrier to water transport. Conversely, the water permeability of the dual layer membrane is primarily dictated by the NIPS support without significantly altering the size-selectivity.

In particular, we observed that the water permeability of the dual layer membranes decreased from 84 ± 7 to 59 ± 4 to 22 ± 5 L m^{-2} h^{-1} bar^{-1} as the concentration of the PSF casting solution increased from 18 to 20 to 22 wt.% in DMF (Figures 8.11b and 8.12). The water permeability was noticeably lower prior to PLA removal, suggesting that pores primarily resulted from removal of the self-assembled PLA domains rather than by NIPS. Analogous measurements for the bare PSF supports displayed a qualitatively similar trend, decreasing from 146 ± 17 to 81 ± 6 to 29 ± 7 L m^{-2} h^{-1} bar^{-1} as the concentration of the PSF casting solution was increased from 18 to 20 to 22 wt.% in DMF (Figure 8.11b and 8.13). Furthermore, SEM images of the bare PSF membranes displayed larger surface pores (Figure 8.10) and more porous substructures (Figure 8.14) for lower concentrations of PSF. These results suggest that the water permeability of the dual layer membranes is dependent upon the microstructure and the permeability of the PSF support. The presence of a highly concentrated (and potentially solid) block polymer film may affect the diffusion of non-solvent into the support layer during NIPS, altering the precipitation pathway. This may result in selective layer pores that are not completely aligned with those in the support layer, unlike in conventional NIPS. However, since the disordered morphology of the selective layer is isotropic and co-continuous, misaligned pores are expected to increase

the effective path length (tortuosity) for water transport rather than completely block the porous channels.

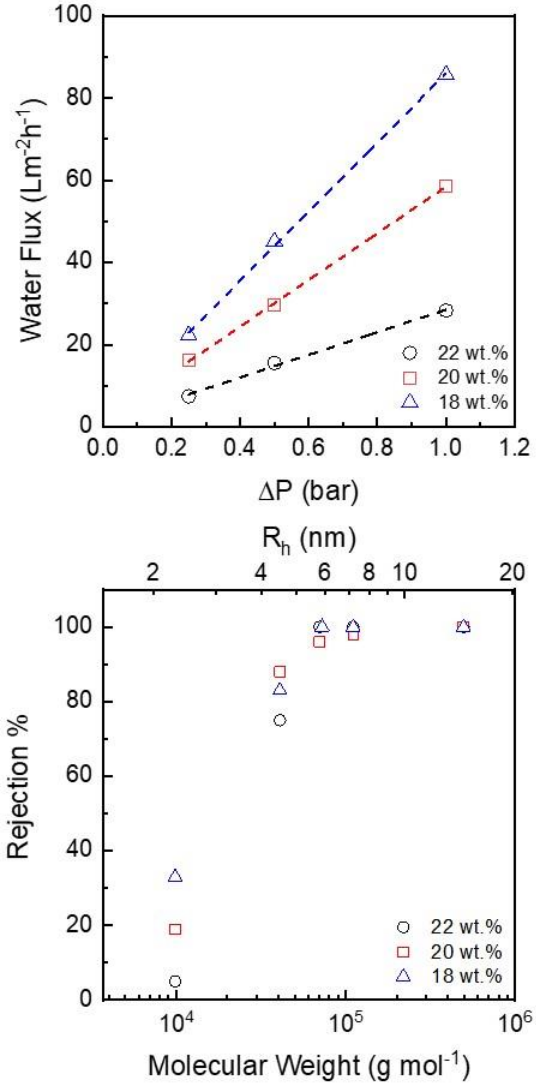

Figure 8.12. Water flux as a function of applied pressure difference (top) for dual layer membranes fabricated on PSF supports cast from 18 (blue triangles), 20 (red squares), and 22 (black circles) wt.% solutions in DMF. Permeability was determined by a linear fit to the collected data points as represented by the dashed lines. Rejection of fluorescently labeled dextran standards (bottom) for dual layer membranes fabricated on PSF supports cast from 18 (blue triangles), 20 (red squares), and 22 (black circles) wt.% solutions in DMF. Rejection was determined based on the ratio of UV-Vis absorbance for the permeate to the feed solution. Each data point was acquired for feed solution comprised of a single molar mass dextran standard.

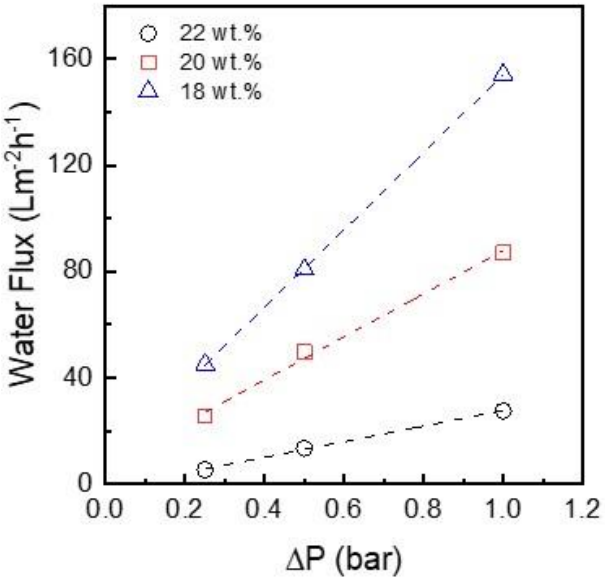

Figure 8.13. Water flux as a function of applied pressure difference for bare PSF support layers fabricated from 18 wt. % (black circles), 20 wt.% (red squares), and 22 wt.% (blue triangles) solutions in DMF. All membranes initially contained a non-porous PLA top layer that was subsequently removed by immersing the membrane in aqueous base to expose the underlying PSF layer.

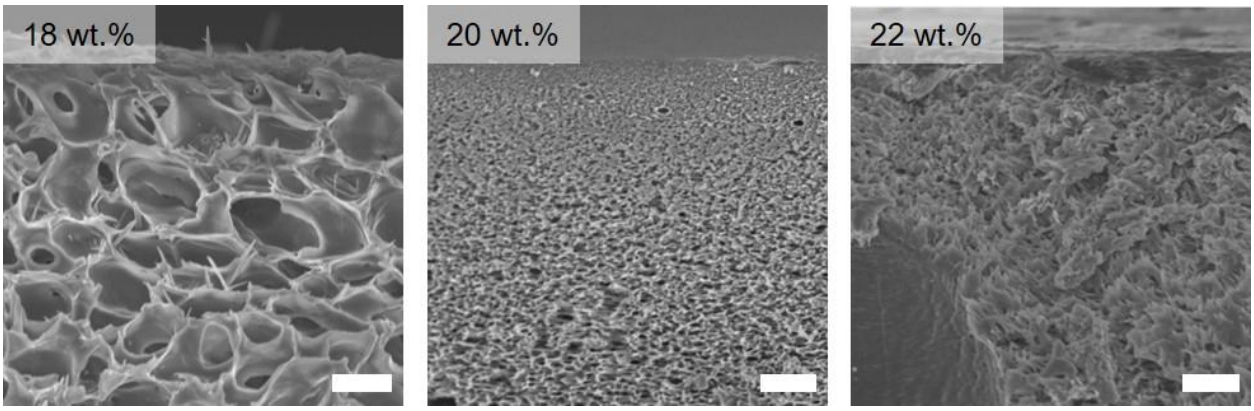

Figure 8.14. Cross-section SEM images from cryo-fractured PSF support layers fabricated from 18 wt. % (left), 20 wt.% (middle), and 22 wt.% (right) solutions in DMF. All membranes initially contained a non-porous PLA top layer that was subsequently removed by immersing the membrane in aqueous base to expose the underlying PSF layer. Samples were coated with approximately 2 nm of Ir prior to imaging. Scale bars correspond to 2 μm.

Despite the strong dependence of the water permeability on the PSF concentration, the size-selectivity and MWCO of the dual layer membranes remained essentially constant due

to the nearly uniform pore size in the self-assembled SML-48 selective layer (Figure 8.11). In contrast, variations in casting solution concentration for the bare PSF membranes resulted in a noticeable trade-off between the water permeability and the size-selectivity (Figures 8.11 and 8.13). These results confirmed that the rejection profile of the dual layer membranes was dictated by the uniform pores in the selective layer, while the water permeability was primarily governed by the support layer. This introduces the possibility of significantly increasing the water permeability without compromising the selectivity, helping to minimize the large permeability-selectivity trade-off inherent to NIPS membranes.[10,12,14]

8.3.2 Disordered selective layers by rapidly drying block polymer solutions

The preceding sections have primarily utilized temperature as the stimulus for accessing the disordered state in the block polymer selective layer, where the selection of quench temperatures above T_{ODT} resulted in segregation strengths, χN, that were lower than the critical value of approximately 10.5. However, χN can be significantly reduced under isothermal conditions by swelling a block polymer in a neutral solvent. This screens the unfavorable enthalpic interactions between the two blocks at the domain interface and effectively lowers the T_{ODT}.[34,35] We demonstrated this for bulk samples by hermetically sealing homogeneous mixtures of SML-48 in THF in DSC pans and analyzing the mixtures using SAXS to monitor the development of the structure factor, $S(q)$, as a function of polymer concentration.[35] For very low concentrations ($\phi_{polymer} < 0.4$), featureless scattering patterns were observed, indicative of an unstructured system at these low values of χN (Figure 8.15a). As the concentration increased ($\phi_{polymer} \geq 0.4$), a broad peak in the SAXS patterns was observed becoming increasingly sharp with increasing concentration,

characteristic of more strongly segregated domains (Figure 8.15a). These results are consistent with an increase in χN with increasing polymer concentration, and they suggest that solvent can serve a similar function as temperature in modulating the segregation strength of SML-48. Indeed, reasonably similar scattering patterns were observed for SML-48 heated to a temperature above T_{ODT} in the melt state (T = 150°C and $\phi_{polymer}$ = 1.0) and for SML-48 diluted below the ϕ_{ODT} in the solution state (T = 25 °C and $\phi_{polymer}$ = 0.7) (Figure 8.15b).

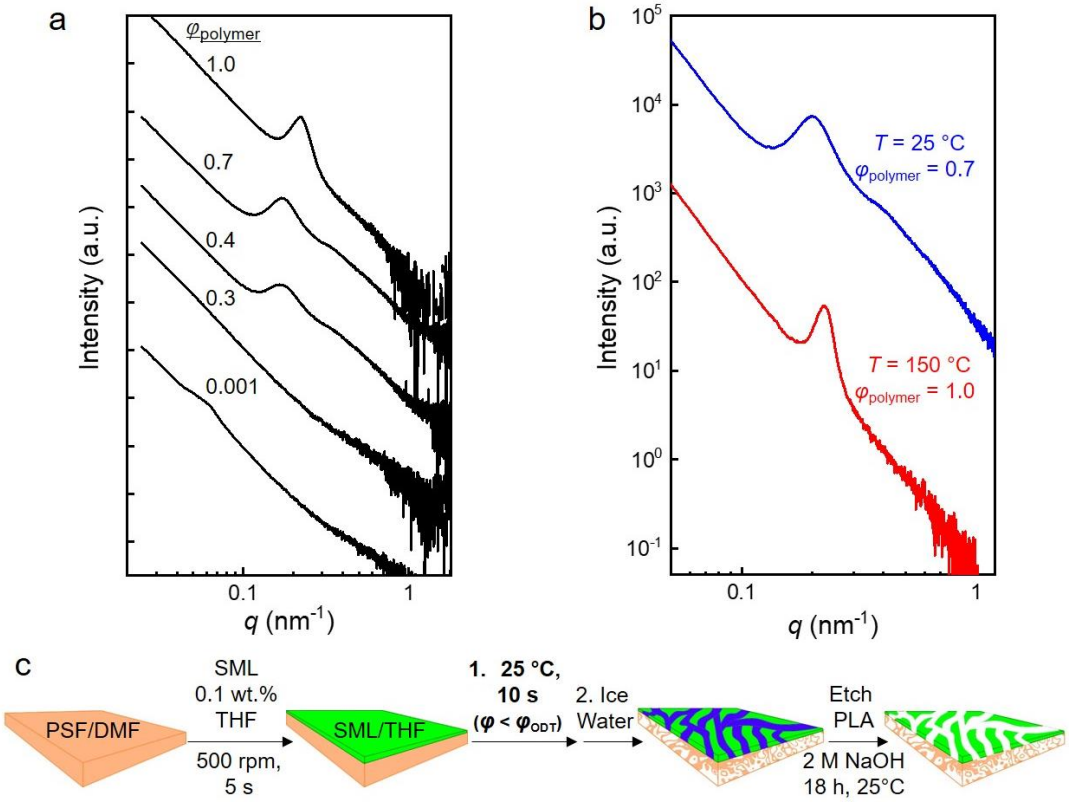

Figure 8.15. Room temperature SAXS of SML-48 diluted in THF to various concentrations (a). $\varphi_{polymer}$ corresponds to the weight fraction of SML-48 in the solution. Comparison between SAXS patterns obtained for SML-48 at 150 °C and $\varphi_{polymer}$ = 1.0 (red curve) and at 25 °C and $\varphi_{polymer}$ = 0.7 (blue curve) demonstrate that both temperature and solvent can be used to tune χN (b). Schematic illustrating the fabrication procedure for the as-cast dual layer membranes (c). The process is identical to the one depicted in Figure 8.1, except solvent rather than temperature is used to access the disordered state. After casting the SML-48 layer, the film rests for 10 s at 25 °C before immersing in an ice water coagulation bath. The PLA domains are then selectively removed using aqueous base to generate a porous selective layer.

Therefore, we anticipate that a disordered and bicontinuous morphology would be kinetically trapped in the selective layer at ambient temperature by rapidly drying a block polymer solution into a solid film during the spin coating process.[35-39] As the volatile THF solvent evaporates, the segregation strength of the block polymer selective layer will increase due to the increasing volume fraction of polymer. Eventually, at high block polymer concentrations, the system will solidify into a film, effectively vitrifying the morphology. If the drying process is sufficiently fast relative to the dynamics of the polymer chains, then the block polymer will be unable to order into its thermodynamically favored morphology prior to vitrification. Instead, it will be kinetically trapped in a disordered state that is expected to resemble the morphology that was observed after rapidly quenching from $T > T_{ODT}$. Indeed, disordered and worm-like morphologies have previously been observed in experiments and in simulations for block polymer thin films prepared after rapidly drying a dilute solution.[35–39]

To demonstrate this experimentally, we modified the membrane fabrication procedure described in Figure 8.1 by eliminating the thermal annealing step. Instead, the dual layer liquid film was equilibrated for approximately 10 s at room temperature following block polymer casting before it was immersed into an ice water coagulation bath and then selectively etched (Figure 8.15c). These membranes will be referred to as “as-cast” membranes, while the previously discussed thermally annealed membranes prepared using the process outlined in Figure 8.1 will now be referred to as “annealed” membranes.

As-cast membranes were prepared using a 0.1 wt.% solution of SML-48 in THF as the selective layer casting solution and an 18 wt.% solution of PSF in DMF as the support layer casting solution, as these concentrations resulted in the highest water permeability for the annealed membranes. Top view SEM images of the annealed and as-cast membranes (Figure 8.16a) revealed similar surface morphologies for the block polymer selective layers regardless of their processing history, while cross-sectional SEM images displayed reasonably similar selective layer thicknesses on the order of ~800–1000 nm (Figure 8.17). Again, these thicknesses likely overestimate the actual selective layer thickness, as the volume of deposited SML solution corresponds to a thickness of ~ 300 nm (assuming uniform spreading of the entire solution volume across the 6 cm by 6 cm substrate). The actual thickness is likely even lower than 300 nm due to mass loss expected during spin coating. These results suggested that the disordered morphology trapped in the as-cast membranes generally resembled the fluctuating disordered morphology obtained in the annealed membranes, supporting the conclusion that solvent can be used as an alternative to temperature for tuning the segregation strength.[37]

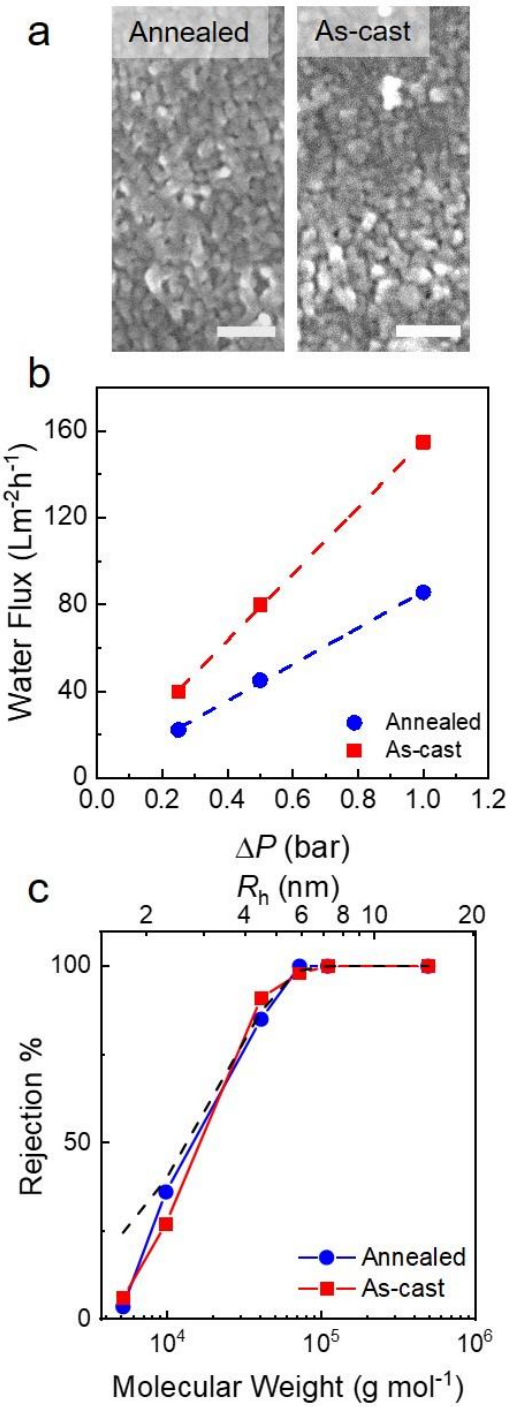

Figure 8.16. Top view SEM images (a), water flux as a function of applied pressure difference (b), and true rejection values of fluorescently labeled dextran standards (c) for thermally annealed and as-cast membranes dual layer membranes fabricated on PSF supports cast from an 18 wt.% solution in DMF. The experimental rejection data was corrected using the mass transfer coefficient to account for concentration polarization. The water flux and rejection data are for a representative data set. The scale bar corresponds to 200 nm.

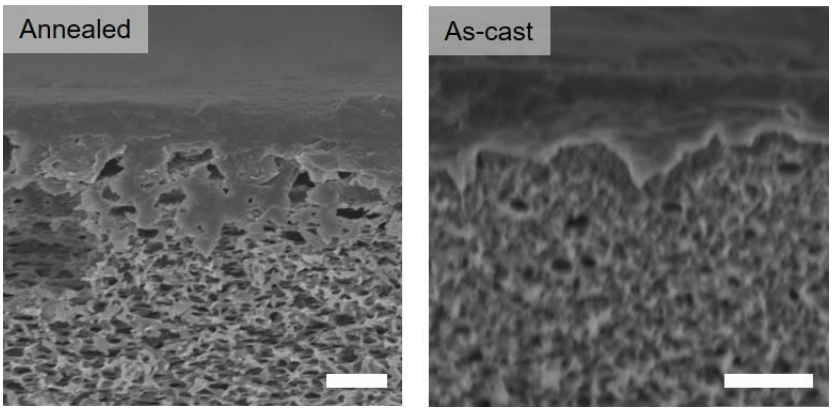

Figure 8.17. Cross-sectional SEM images for cryo-fractured dual layer membranes comprised of a support layer cast from an 18 wt.% solution of PSF in DMF and a selective layer cast from a 0.1 wt.% solution of SML-48 in THF. One membrane was thermally annealed for 10 s at 150 °C prior to immersion in an ice water coagulation bath (left). The other membrane rested for 10 s at room temperature prior to immersion in an ice water coagulation bath (right). The samples were coated with approximately 2 nm of Ir prior to imaging. Scale bars correspond to 2 μm.

Effectiveness of the solvent approach was confirmed by the sharp rejection curves with nearly identical MWCO observed for both the as-cast and annealed membranes, indicating that the block polymer selective layers had nearly uniform pores of similar size regardless of the thermal processing history (Figure 8.16). Despite their nearly identical rejection profiles, the water permeability of the as-cast membrane, 153 ± 8 L m^{-2} h^{-1} bar^{-1}, was nearly twice that of the annealed membrane, 84 ± 7 L m^{-2} h^{-1} bar^{-1} (Figure 8.16). Similar trends were observed for as-cast and annealed membranes with support layers cast from 20 and 22 wt.% PSF solutions in DMF (Figures 8.18 and 8.19). Overall, these results again confirmed that the dual layer membrane strategy outlined here allows for an increase in water permeability without compromising the size-selectivity.

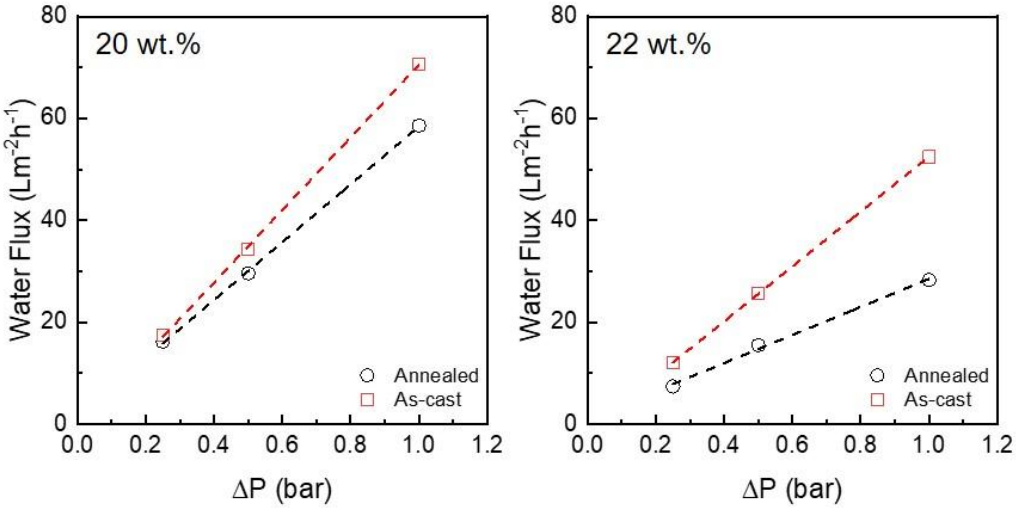

Figure 8.18. Water flux as a function of applied pressure difference for dual layer membranes fabricated on PSF supports cast from a 20 wt.% (left) and a 22 wt.% (right) solution in DMF. Thermally annealed membranes are represented by black circles and as-cast membranes are represented by red squares.

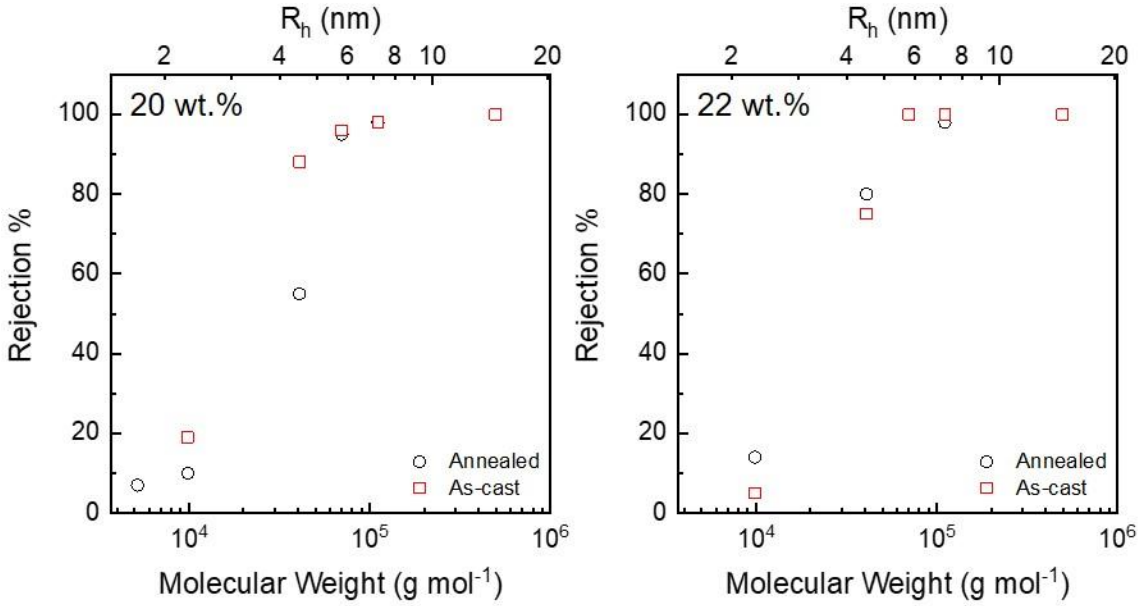

Figure 8.19. Rejection of fluorescently labelled dextran standards for dual layer membranes fabricated on PSF supports cast from a 20 wt.% (left) and a 22 wt.% (right) solution in DMF. Rejection was determined based on the ratio of UV-Vis absorbance for the permeate to the feed solution. Each data point was acquired for feed solution comprised of a single molar mass dextran standard. Thermally annealed membranes are represented by black circles and as-cast membranes are represented by red squares.

The significantly increased permeability for the as-cast membrane suggested that the thermal annealing process affected the phase behavior of the PSF layer, altering its precipitation pathway during NIPS and ultimately resulting in less porous and less permeable substructure without significantly increasing the pore continuity of the block polymer selective layer.[3,40] This was supported by a lower water permeability for the annealed bare PSF support (18 wt.% in DMF), 146 ± 17 L m^{-2} h^{-1} bar^{-1}, as compared to the analogous as-cast bare PSF support, 326 ± 12 L m^{-2} h^{-1} bar^{-1}. This decrease in permeability for the PSF support upon thermal annealing resulted in a subsequent decrease in the permeability of the dual layer membrane.[3,40]

8.3.3 Relative contributions of selective and support layer to water permeability

To better decouple the relative contributions of the support and selective layers to the dual layer membrane permeability, the dual layer membranes were modeled as resistors in series.[41,42] This model assumes that the resistance to water flow for each layer is inversely proportional to the water permeability (P) of each layer. Consequently, the water permeability of the dual layer membrane follows the relationship:

$$P_{\text{dual}}^{-1} = P_{\text{support}}^{-1} + P_{\text{selective}}^{-1} \quad \text{(eq. 2)}$$

While the intrinsic permeability of the selective layer, $P_{\text{selective}}$, is difficult to measure directly, it can be readily extracted using eq. 2, provided that P_{dual} and P_{support} are experimentally known, as is the case for this work. Using this approach, the effect that thermal annealing had on the water permeability for both the support and the selective layers was examined independently.

The experimentally measured values for P_{dual} and $P_{support}$ along with the values of $P_{selective}$ calculated using the model described in eq. 2 are provided in Figure 8.20 and Table 8.1 for both annealed and as-cast membranes. As discussed previously, both the concentration of the PSF casting solution and the thermal processing method had a strong effect on the water permeability of the dual layer membranes, ranging from 22 ± 5 L m^{-2} h^{-1} bar^{-1} for the annealed membrane prepared using an 22 wt.% PSF solution to 153 ± 8 L m^{-2} h^{-1} bar^{-1} for the as-cast membrane prepared using an 18 wt.% PSF solution. The calculated $P_{selective}$ ranged from 91 to 290 L m^{-2} h^{-1} bar^{-1} for all conditions examined here, exhibiting a weaker dependence on the selected processing parameters than $P_{support}$ (i.e., a factor of 3 difference as compared to a factor of 7 difference for the dual layer membranes). The calculated selective layer permeabilities were approximately a factor of 3 lower the theoretical value of 730 L m^{-2} h^{-1} bar^{-1} estimated using the Hagen-Poisseuille equation,

$$A = \frac{\varepsilon r_p^2}{8\tau^2 \mu \delta_m} \text{ (eq. 3)}$$

assuming a porosity (ε) of 0.4 (volume fraction of PLA in SML-48), a tortuosity (τ) of 1.5, a pore radius (r_p) of 6.8 nm, and a film thickness (l) of 300 nm (expected film thickness based on the volume of block polymer solution that was deposited during spin coating).[43] The lower experimental permeabilities may reflect that the block polymer selective layer contains some amount of discontinuous pores or a higher than expected pore tortuosity. Significant increases in the water permeability for dual layer membranes composed of an SML-48 selective layer will require engineering approaches to enhance the permeability of the PSF support. However, significantly higher permeabilities (i.e. greater than approximately 220 L m^{-2} h^{-1} bar^{-1}) will also require increasing the porosity and permeability of the SML selective layer. To demonstrate this point, an as-cast dual layer membrane was

fabricated from a 0.05 wt.% solution of SML-48 in THF and a 15 wt.% solution of PSF in DMF. This membrane displayed a very high water permeability of ~250 L m^{-2} h^{-1} bar^{-1} due to its thinner selective layer and more porous support layer (Figure 8.21). Additionally, a nearly identical rejection profile to the membranes cast from 0.1 wt.% solutions of SML-48 was obtained. However, these low PSF concentrations often resulted in the formation of defective membranes that lacked the required mechanical integrity for UF. For this reason, repeatable fabrication of these membranes was challenging. Consequently, other strategies are likely required to more reproducibly enhance the permeability of the dual layer membranes. Regardless, the results presented here offer a proof-of-concept for a promising membrane fabrication technique that can possibly be further improved upon optimization of the processing parameters.

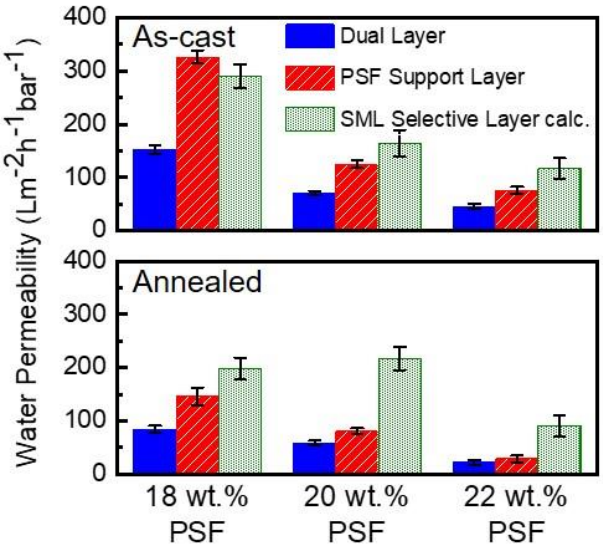

Figure 8.20. Bar graphs comparing the relative contributions of the PSF support layer (red bars) and the SML-48 selective layer (green bars) to the overall dual layer membrane permeability (blue bars) for different PSF concentrations. Data for thermally annealed membranes is presented in the lower panel and data for the as-cast membranes is presented in the upper panel. The dual layer and PSF support layer permeabilities were measured experimentally. The selective layer permeability was calculated using the resistors in series model described in eq. 2. The permeability was determined based on the mean of three separate experiments, and the error bars correspond to the standard deviation.

Table 8.1. Water permeability as a function of membrane fabrication parameters

PSF wt.%	Thermally Annealed			As-cast		
	P_{dual} ($Lm^{-2}h^{-1}bar^{-1}$)	$P_{support}$ ($Lm^{-2}h^{-1}bar^{-1}$)	$P_{selective}$ ($Lm^{-2}h^{-1}bar^{-1}$)	P_{dual} ($Lm^{-2}h^{-1}bar^{-1}$)	$P_{support}$ ($Lm^{-2}h^{-1}bar^{-1}$)	$P_{selective}$ ($Lm^{-2}h^{-1}bar^{-1}$)
18	84 ± 7	146 ± 17	198 ± 21	153 ± 8	326 ± 12	290 ± 22
20	59 ± 4	81 ± 6	217 ± 22	71 ± 4	125 ± 7	164 ± 25
22	22 ± 5	29 ± 7	91 ± 20	46 ± 5	76 ± 7	117 ± 20

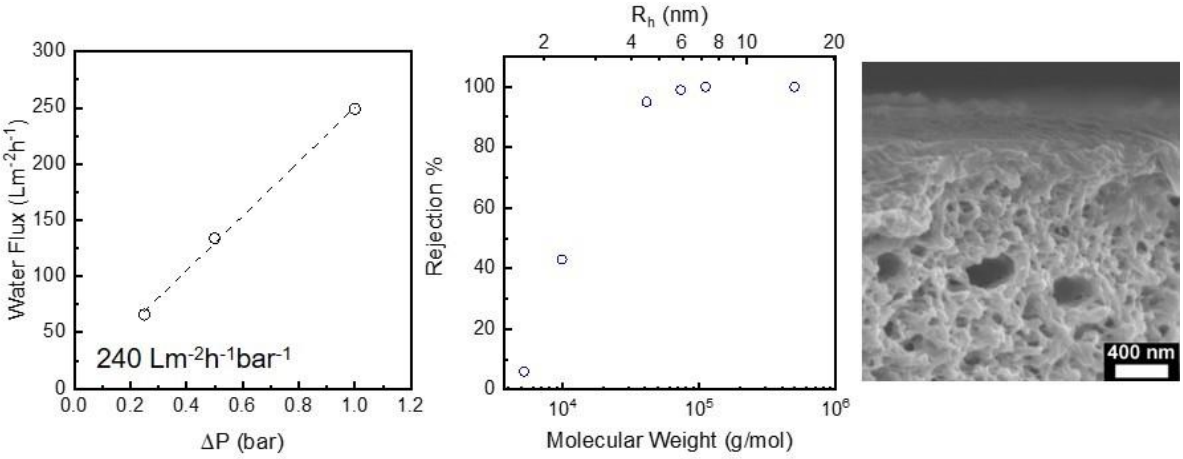

Figure 8.21. Pure water permeability, dextran rejection curve, and a cross-sectional SEM image of an as-cast dual layer membrane comprised of a 15 wt.% PSF in DMF support layer solution and a 0.05 wt.% SML-48 in THF selective layer solution.

8.4 Conclusion

In this work, we have reported a promising technique to make highly selective and highly permeable UF membranes comprising a disordered block polymer selective layer by co-casting PSF and block polymer solutions. A dilute P(MMA-*s*-S)-*b*-PLA solution in THF

was spin coated onto a DMF-swollen PSF film, rapidly heated to disorder the block polymer, and immersed in an ice water coagulation bath to kinetically trap the fluctuating disordered state in the block polymer layer and to precipitate the PSF support layer via NIPS. The subsequent removal of the PLA domains generated a dual layer UF membrane, as confirmed by SEM. We demonstrated that the permeability of the dual layer membranes could be tuned by adjusting the concentration of the PSF casting solution, while maintaining a nearly identical size-selectivity due to the narrow pore size distribution of the block polymer selective layer. Additionally, we investigated the effect of thermal processing on the permeability and selectivity of these membranes. Similar morphologies and size-selectivities, yet noticeably higher water permeabilities could be obtained for as-cast membranes as compared to thermally annealed membranes. Modeling the dual layer membranes as resistors in series revealed that the porosity of the PSF support layer was the primary influence on the water permeability of the dual layer membranes. The membrane fabrication procedure outlined in this work offers a promising approach towards simultaneously achieving high water permeability and high size-selectivity in UF membranes. This approach should also be compatible with draw coating and hollow fiber membrane fabrication protocols, potentially enabling its translation to more industrially scalable coating processes and relevant form factors. Further optimization of the PSF layer casting parameters should increase the permeability without compromising the size-selectivity and potentially offer a more commercially viable route towards block polymer UF membranes.

8.5 References

1) Werber, J. R.; Osuji, C. O.; Elimelech, M. Materials for next-Generation Desalination and Water Purification Membranes. *Nat. Rev. Mater.* **2016**, *1*, 16018.

2) Park, H. B.; Kamcev, J.; Robeson, L. M.; Elimelech, M.; Freeman, B. D. Maximizing the Right Stuff: The Trade-off between Membrane Permeability and Selectivity. *Science* **2017**, *356*, eaab0530.

3) Guillen, G. R.; Pan, Y.; Li, M.; Hoek, E. M. V. Preparation and Characterization of Membranes Formed by Nonsolvent Induced Phase Separation: A Review. *Ind. Eng. Chem. Res.* **2011**, *50*, 3798–3817.

4) Sadeghi, I.; Kaner, P.; Asatekin, A. Controlling and Expanding the Selectivity of Filtration Membranes. *Chem. Mater.* **2018**, *30*, 7328–7354.

5) Yang, S. Y.; Park, J.; Yoon, J.; Ree, M.; Jang, S. K.; Kim, J. K. Virus Filtration Membranes Prepared from Nanoporous Block Copolymers with Good Dimensional Stability under High Pressures and Excellent Solvent Resistance. *Adv. Funct. Mater.* **2008**, *18*, 1371–1377.

6) Yang, H.; Wang, Z.; Lan, Q.; Wang, Y. Antifouling Ultrafiltration Membranes by Selective Swelling of Polystyrene/poly(ethylene Oxide) Block Copolymers. *J. Membr. Sci.* **2017**, *542*, 226–232.

7) Mehta, A.; Zydney, A. L. Permeability and Selectivity Analysis for Ultrafiltration Membranes. *J. Membr. Sci.* **2005**, *249*, 245–249.

8) Smolders, C. A.; Reuvers, A. J.; Boom, R. M.; Wienk, I. M. Microstructures in Phase-Inversion Membranes. Part 1. Formation of Macrovoids. *J. Membr. Sci.* **1992**, *73*, 259–275.

9) Mochizuki, S.; Zydney, A. L. Theoretical Analysis of Pore Size Distribution Effects on Membrane Transport. *J. Membr. Sci.* **1993**, *82*, 211–227.

10) Phillip, W. A.; O'Neill, B.; Rodwogin, M.; Hillmyer, M. A.; Cussler, E. L. Self-Assembled Block Copolymer Thin Films as Water Filtration Membranes. *ACS Appl. Mater. Interfaces* **2010**, *2*, 847–853.

11) Yin, J.; Yao, X.; Liou, J.-Y.; Sun, W.; Sun, Y.-S.; Wang, Y. Membranes with Highly Ordered Straight Nanopores by Selective Swelling of Fast Perpendicularly Aligned Block Copolymers. *ACS Nano* **2013**, *7*, 9961–9974.

12) Peinemann, K.-V.; Abetz, V.; Simon, P. F. W. Asymmetric Superstructure Formed in a Block Copolymer via Phase Separation. *Nat. Mater.* **2007**, *6*, 992-996.

13) Jackson, E. A.; Lee, Y.; Hillmyer, M. A. ABAC Tetrablock Terpolymers for Tough Nanoporous Filtration Membranes. *Macromolecules* **2013**, *46*, 1484–1491.

14) Querelle, S. E.; Jackson, E. A.; Cussler, E. L.; Hillmyer, M. A. Ultrafiltration Membranes with a Thin Poly(styrene)-B-Poly(isoprene) Selective Layer. *ACS Appl. Mater. Interfaces* **2013**, *5*, 5044–5050.

15) Feng, X.; Tousley, M. E.; Cowan, M. G.; Wiesenauer, B. R.; Nejati, S.; Choo, Y.; Noble, R. D.; Elimelech, M.; Gin, D. L.; Osuji, C. O. Scalable Fabrication of Polymer Membranes with Vertically Aligned 1 Nm Pores by Magnetic Field Directed Self-Assembly. *ACS Nano* **2014**, *8*, 11977–11986.

16) Phillip, W. A.; Dorin, R. M.; Werner, J.; Hoek, E. M. V.; Wiesner, U.; Elimelech, M. Tuning Structure and Properties of Graded Triblock Terpolymer-Based Mesoporous and Hybrid Films. *Nano Lett.* **2011**, *11*, 2892–2900.

17) Shi, X.; Wang, Z.; Wang, Y. Highly Permeable Nanoporous Block Copolymer Membranes by Machine-Casting on Nonwoven Supports: An Upscalable Route. *J. Membr. Sci.* **2017**, *533*, 201–209.

18) Yan, N.; Wang, Z.; Wang, Y. Highly Permeable Membranes Enabled by Film Formation of Block Copolymers on Water Surface. *J. Membr. Sci.* **2018**, *568*, 40–46.

19) Wang, Y. Nondestructive Creation of Ordered Nanopores by Selective Swelling of Block Copolymers: Toward Homoporous Membranes. *Acc. Chem. Res.* **2016**, *49*, 1401–1408.

20) Dorin, R. M.; Marques, D. S.; Sai, H.; Vainio, U.; Phillip, W. A.; Peinemann, K.-V.; Nunes, S. P.; Wiesner, U. Solution Small-Angle X-Ray Scattering as a Screening and Predictive Tool in the Fabrication of Asymmetric Block Copolymer Membranes. *ACS Macro Lett.* **2012**, *1*, 614–617.

21) Abetz, V. Isoporous Block Copolymer Membranes. *Macromol. Rapid Commun.* **2015**, *36*, 10–22.

22) Vidil, T.; Hampu, N.; Hillmyer, M. A. Nanoporous Thermosets with Percolating Pores from Block Polymers Chemically Fixed above the Order–Disorder Transition. *ACS Cent. Sci.* **2017,** *3*, 1114-1120.

23) Hampu, N.; Hillmyer, M. A. Temporally Controlled Curing of Block Polymers in the Disordered State Using Thermally Stable Photoacid Generators for the Preparation of Nanoporous Membranes. *ACS Appl. Polym. Mater.* **2019**, *1*, 1148–1154.

24) Hampu, N.; Bates, M. W.; Vidil, T.; Hillmyer, M. A. Bicontinuous Porous Nanomaterials from Block Polymers Radically Cured in the Disordered State for Size-Selective Membrane Applications. *ACS Appl. Nano Mater.* **2019**, *2*, 4567-4577.

25) Hampu, N.; Hillmyer, M. A. Molecular Engineering of Nanostructures in Disordered Block Polymers. *ACS Macro Lett.* **2020**, *9*, 382–388.

26) Hilke, R.; Pradeep, N.; Behzad, A. R.; Nunes, S. P.; Peinemann, K.-V. Block Copolymer/homopolymer Dual-Layer Hollow Fiber Membranes. *J. Membr. Sci.* **2014**, *472*, 39–44.

27) Liu, Y.; Liu, T.; Su, Y.; Yuan, H.; Hayakawa, T.; Wang, X. Fabrication of a Novel PS4VP/PVDF Dual-Layer Hollow Fiber Ultrafiltration Membrane. *J. Membr. Sci.* **2016**, *506*, 1–10.

28) Seo, M.; Hillmyer, M. A. Reticulated Nanoporous Polymers by Controlled Polymerization-Induced Microphase Separation. *Science* **2012**, *336*, 1422.

29) Gor, G. Y.; Thommes, M.; Cychosz, K. A.; Neimark, A. V. Quenched Solid Density Functional Theory Method for Characterization of Mesoporous Carbons by Nitrogen Adsorption. *Carbon* **2012**, *50*, 1583–1590.

30) Tiraferri, A.; Yip, N. Y.; Phillip, W. A.; Schiffman, J. D.; Elimelech, M. Relating Performance of Thin-Film Composite Forward Osmosis Membranes to Support Layer Formation and Structure. *J. Membr. Sci.* **2011**, *367*, 340–352.

31) Oatley-Radcliffe, D. L.; Williams, S.; Lee, C.; Williams, P. Characterisation of Mass Transfer in Frontal Nanofiltration Equipment and Development of a Simple Correlation. *J. Memb. Separ. Tech.* **2015**, *4*, 149-160.

32) Zhang, Y.; Sargent, J. L.; Boudouris, B. W.; Phillip, W. A. Nanoporous Membranes Generated from Self-Assembled Block Polymer Precursors: Quo Vadis? *J. Appl. Polym. Sci.* **2015**, *132*, 41683.

33) Phillip, W. A.; Amendt, M.; O'Neill, B.; Chen, L.; Hillmyer, M. A.; Cussler, E. L. Diffusion and Flow Across Nanoporous Polydicyclopentadiene-Based Membranes. *ACS Appl. Mater. Interfaces* **2009**, *1*, 472–480.

34) Lodge, T. P.; Hanley, K. J.; Pudil, B.; Alahapperuma, V. Phase Behavior of Block Copolymers in a Neutral Solvent. *Macromolecules* **2003**, *36*, 816–822.

35) Baruth, A.; Seo, M.; Lin, C. H.; Walster, K.; Shankar, A.; Hillmyer, M. A.; Leighton, C. Optimization of Long-Range Order in Solvent Vapor Annealed Poly(styrene)-Block-Poly(lactide) Thin Films for Nanolithography. *ACS Appl. Mater. Interfaces* **2014**, *6*, 13770–13781.

36) Sinturel, C.; Vayer, M.; Morris, M.; Hillmyer, M. A. Solvent Vapor Annealing of Block Polymer Thin Films. *Macromolecules* **2013**, *46*, 5399–5415.

37) Hur, S.-M.; Khaira, G. S.; Ramírez-Hernández, A.; Müller, M.; Nealey, P. F.; de Pablo, J. J. Simulation of Defect Reduction in Block Copolymer Thin Films by Solvent Annealing. *ACS Macro Lett.* **2015**, *4*, 11–15.

38) Howard, M. P.; Lequieu, J.; Delaney, K. T.; Ganesan, V.; Fredrickson, G. H.; Truskett, T. M. Connecting Solute Diffusion to Morphology in Triblock Copolymer Membranes. *Macromolecules* **2020**. *In Press*.

39) Olayo-Valles, R.; Gu, S.; Lund, M. S.; Leighton, C.; Hillmyer, M. A. Perpendicular Domain Orientation in Thin Films of Polystyrene−Polylactide Diblock Copolymers. *Macromolecules* **2005**, *38*, 10101-10108.

40) Tsai, H.-A.; Huang, D.-H.; Ruaan, R.-C.; Lai, J.-Y. Mechanical Properties of Asymmetric Polysulfone Membranes Containing Surfactant as Additives. *Ind. Eng. Chem. Res.* **2001**, *40*, 5917-5922.

41) Werber, J. R.; Porter, C. J.; Elimelech, M. A Path to Ultraselectivity: Support Layer Properties To Maximize Performance of Biomimetic Desalination Membranes. *Environ. Sci. Technol.* **2018**, *52*, 10737–10747.

42) Henis, J. M. S.; Tripodi, M. K. Composite Hollow Fiber Membranes for Gas Separation: The Resistance Model Approach. *J. Membr. Sci.* **1981**, *8*, 233–246.

43) Epstein, N. On tortuosity and the tortuosity factor in flow and diffusion through porous media. *Chem. Eng. Sci.* **1989**, *44*, 777-779.

Bibliography

Abetz, V. Isoporous Block Copolymer Membranes. *Macromol. Rapid Commun.* **2015**, *36*, 10–22.

Ahn, H.; Park, S.; Kim, S.-W.; Yoo, P. J.; Ryu, D. Y.; Russell, T. P. Nanoporous Block Copolymer Membranes for Ultrafiltration: A Simple Approach to Size Tunability. *ACS Nano* **2014**, *8*, 11745–11752.

Aida, S.; Sakurai, S.; Nomura, S. Strain-Induced Ordering of Microdomain Structures in Polystyrene-Block-Polybutadiene-Block-Polystyrene Triblock Copolymers Cross-Linked in the Disordered State. *Polymer* **2002**, *43*, 2881–2887.

Akiba, M.; Hashim, A. S., Vulcanization and crosslinking in elastomers. *Progress in Polymer Science* **1997,** *22*, 475-521.

Akthakul, A.; Salinaro, R. F.; Mayes, A. M. Antifouling Polymer Membranes with Subnanometer Size Selectivity. *Macromolecules* **2004**, *37*, 7663–7668.

Allen, S. D.; Bobbala, S.; Karabin, N. B.; Scott, E. A., On the advancement of polymeric bicontinuous nanospheres toward biomedical applications. *Nanoscale Horizons* **2019**. *4*, 258-272.

Almdal, K.; Rosedale, J. H.; Bates, F. S.; Wignall, G. D.; Fredrickson, G. H. Gaussian- to Stretched-Coil Transition in Block Copolymer Melts. *Phys. Rev. Lett.* **1990**, *65*, 1112–1115.

Amendt, M. A.; Chen, L.; Hillmyer, M. A. Formation of Nanostructured Poly(dicyclopentadiene) Thermosets Using Reactive Block Polymers. *Macromolecules* **2010**, *43*, 3924-3934.

Antonietti, M.; Hentze, H.P. Synthesis of Sponge-like Polymer Dispersions via Polymerization of Bicontinuous Microemulsions. *Colloid and Polymer Science* **1996**, *274*, 696–702.

Asatekin, A.; Kang, S.; Elimelech, M.; Mayes, A. M. Anti-Fouling Ultrafiltration Membranes Containing Polyacrylonitrile-Graft-Poly(ethylene Oxide) Comb Copolymer Additives. *Journal of Membrane Science* **2007**, *298*, 136–146.

Ashraf, A. R.; Ryan, J. J.; Satkowski, M. M.; Lee, B.; Smith, S. D.; Spontak, R. J. Bicomponent Block Copolymers Derived from One or More Random Copolymers as an Alternative Route to Controllable Phase Behavior. *Macromol. Rapid Commun.* **2017**, *38*, 1700207.

Ashraf, A. R.; Ryan, J. J.; Satkowski, M. M.; Smith, S. D.; Spontak, R. J. Effect of Systematic Hydrogenation on the Phase Behavior and Nanostructural Dimensions of Block Copolymers. *ACS Appl. Mater. Interfaces* **2018**, *10*, 3186–3190.

Bailey, T. S.; Rzayev, J.; Hillmyer, M. A. Routes to Alkene and Epoxide Functionalized Nanoporous Materials from Poly(styrene-B-Isoprene-B-Lactide) Triblock Copolymers. *Macromolecules* **2006**, *39*, 8772–8781.

Baker, R. W. *Membrane Technology and Applications*, 2nd ed.; John Wiley & Sons, 2012.

Baruth, A.; Seo, M.; Lin, C. H.; Walster, K.; Shankar, A.; Hillmyer, M. A.; Leighton, C. Optimization of Long-Range Order in Solvent Vapor Annealed Poly(styrene)-Block-Poly(lactide) Thin Films for Nanolithography. *ACS Appl. Mater. Interfaces* **2014**, *6*, 13770–13781.

Basfar, A. A.; Abdel-Aziz, M. M.; Mofti, S., Influence of different curing systems on the physico-mechanical properties and stability of SBR and NR rubbers. *Radiation Physics and Chemistry* **2002,** *63*, 81-87.

Bates, C. M.; Bates, F. S. 50th Anniversary Perspective: Block Polymers—Pure Potential. *Macromolecules* **2017**, *50*, 3–22.

Bates, F. S., Block copolymers near the microphase separation transition. 2. Linear dynamic mechanical properties. *Macromolecules* **1984,** *17*, 2607-2613.

Bates, F. S.; Frederickson, G. Block Copolymers - Designer Soft Materials. *Phys. Today* **1999**, *52*, 32–38.

Bates, F. S.; Hillmyer, M. A.; Lodge, T. P.; Bates, C. M.; Delaney, K. T.; Fredrickson, G. H. Multiblock Polymers: Panacea or Pandora's Box? *Science* **2012**, *336*, 434.

Bates, F. S.; Koppi, K. A.; Tirrell, M.; Almdal, K.; Mortensen, K. Influence of Shear on the Hexagonal-to-Disorder Transition in a Diblock Copolymer Melt. *Macromolecules* **1994**, *27*, 5934–5936.

Bates, F. S.; Rosedale, J. H.; Fredrickson, G. H. Fluctuation Effects in a Symmetric Diblock Copolymer near the Order–disorder Transition. *The Journal of Chemical Physics* **1990**, *92*, 6255–6270.

Bates, F. S.; Rosedale, J. H.; Fredrickson, G. H.; Glinka, C. J. Fluctuation-Induced First-Order Transition of an Isotropic System to a Periodic State. *Phys. Rev. Lett.* **1988**, *61*, 2229–2232.

Bates, F.; Frederickson, G. Block Copolymer Thermodynamics: Theory and Experiments. *Annu. Rev. Phys. Chem.* **1990**, *41*, 525–557.

Bates, M. W.; Lequieu, J.; Barbon, S. M.; Lewis, R. M.; Delaney, K. T.; Anastasaki, A.; Hawker, C. J.; Fredrickson, G. H.; Bates, C. M. Stability of the A15 Phase in Diblock Copolymer Melts. *Proc. Natl. Acad. Sci.* **2019**, *116*, 13194.

Bertrand, A.; Hillmyer, M. A. Nanoporous Poly(lactide) by Olefin Metathesis Degradation. *J. Am. Chem. Soc.* **2013**, *135*, 10918–10921.

Bohbot-Raviv, Y.; Wang, Z.-G. Discovering New Ordered Phases of Block Copolymers. *Phys. Rev. Lett*. **2000**, *85*, 3428–3431.

Bohonak, D. M.; Zydney, A. L. Compaction and Permeability Effects with Virus Filtration Membranes. *Journal of Membrane Science* **2005**, *254*, 71–79.

Breulmann, M.; Davis, S. A.; Mann, S.; Hentze, H. P.; Antonietti, M. Polymer–Gel Templating of Porous Inorganic Macro-Structures Using Nanoparticle Building Blocks. *Adv. Mater.* **2000**, *12*, 502-507.

Bucher, T.; Filiz, V.; Abetz, C.; Abetz, V. Formation of Thin, Isoporous Block Copolymer Membranes by an Upscalable Profile Roller Coating Process—A Promising Way to Save Block Copolymer. *Membranes* **2018**, *8*.

Budd, W. E.; Oakey, R. W. Membrane Separation in Biological-Reactor Systems. 3472765A.

Capone, B.; Hansen, J.-P.; Coluzza, I. Competing Micellar and Cylindrical Phases in Semi-Dilute Diblock Copolymer Solutions. *Soft Matter* **2010**, *6*, 6075–6078.

Cates, M. E.; Milner, S. T. Role of Shear in the Isotropic-to-Lamellar Transition. *Phys. Rev. Lett.* **1989**, *62*, 1856–1859.

Cavicchi, K. A.; Zalusky, A. S.; Hillmyer, M. A.; Lodge, T. P. An Ordered Nanoporous Monolith from an Elastomeric Crosslinked Block Copolymer Precursor. *Macromol. Rapid Commun.* **2004**, *25*, 704–709.

Chen, L.; Hillmyer, M. A. Mechanically and Thermally Robust Ordered Nanoporous Monoliths Using Norbornene-Functional Block Polymers. *Macromolecules* **2009**, *42*, 4237–4243.

Chen, W.; Su, Y.; Peng, J.; Dong, Y.; Zhao, X.; Jiang, Z. Engineering a Robust, Versatile Amphiphilic Membrane Surface Through Forced Surface Segregation for Ultralow Flux-Decline. *Advanced Functional Materials* **2011**, *21*, 191–198.

Chen, W.; Su, Y.; Peng, J.; Zhao, X.; Jiang, Z.; Dong, Y.; Zhang, Y.; Liang, Y.; Liu, J. Efficient Wastewater Treatment by Membranes through Constructing Tunable Antifouling Membrane Surfaces. *Environ. Sci. Technol.* **2011**, *45*, 6545–6552.

Cheryan, M. *Ultrafiltration and Microfiltration Handbook*; CRC Press, 1998.

Choi, J.-G.; Bae, T.-H.; Kim, J.-H.; Tak, T.-M.; Randall, A. . The Behavior of Membrane Fouling Initiation on the Crossflow Membrane Bioreactor System. *Journal of Membrane Science* **2002**, *203*, 103–113.

Choo, Y.; Mahajan, L. H.; Gopinadhan, M.; Ndaya, D.; Deshmukh, P.; Kasi, R. M.; Osuji, C. O. Phase Behavior of Polylactide-Based Liquid Crystalline Brushlike Block Copolymers. *Macromolecules* **2015**, *48*, 8315–8322.

Chopade, S. A.; Au, J. G.; Li, Z.; Schmidt, P. W.; Hillmyer, M. A.; Lodge, T. P., Robust Polymer Electrolyte Membranes with High Ambient-Temperature Lithium-Ion

Conductivity via Polymerization-Induced Microphase Separation. *ACS Appl. Mater. Inter.* **2017,** *9*, 14561-14565.

Clodt, J. I.; Filiz, V.; Rangou, S.; Buhr, K.; Abetz, C.; Höche, D.; Hahn, J.; Jung, A.; Abetz, V. Double Stimuli-Responsive Isoporous Membranes via Post-Modification of pH-Sensitive Self-Assembled Diblock Copolymer Membranes. *Adv. Funct. Mater.* **2013**, *23*, 731–738.

Cochran, E. W.; Garcia-Cervera, C. J.; Fredrickson, G. H. Stability of the Gyroid Phase in Diblock Copolymers at Strong Segregation. *Macromolecules* **2006**, *39*, 2449–2451.

Cohen, Y.; Albalak, R. J.; Dair, B. J.; Capel, M. S.; Thomas, E. L. Deformation of Oriented Lamellar Block Copolymer Films. *Macromolecules* **2000**, *33*, 6502–6516.

Cote, P.; Alam, Z.; Penny, J. Hollow Fiber Membrane Life in Membrane Bioreactors (MBR). *Desalination* **2012**, *288*, 145–151.

Dalvi, M. C.; Lodge, T. P. Diffusion in Block Copolymer Melts: The Disordered Region and the Vicinity of the Order-Disorder Transition. *Macromolecules* **1994**, *27*, 3487–3492.

Dorin, R. M.; Marques, D. S.; Sai, H.; Vainio, U.; Phillip, W. A.; Peinemann, K.-V.; Nunes, S. P.; Wiesner, U. Solution Small-Angle X-Ray Scattering as a Screening and Predictive Tool in the Fabrication of Asymmetric Block Copolymer Membranes. *ACS Macro Lett.* **2012**, *1*, 614–617.

Dorin, R. M.; Phillip, W. A.; Sai, H.; Werner, J.; Elimelech, M.; Wiesner, U. Designing Block Copolymer Architectures for Targeted Membrane Performance. *Polymer* **2014**, *55*, 347–353.

Drews, A.; Kraume, M. Process Improvement by Application of Membrane Bioreactors. *Chemical Engineering Research and Design* **2005**, *83*, 276–284.

Dreyer, O.; Wu, M.-L.; Radjabian, M.; Abetz, C.; Abetz, V. Structure of Nonsolvent-Quenched Block Copolymer Solutions after Exposure to Electric Fields during Solvent Evaporation. *Advanced Materials Interfaces* **2019**, *6*, 1900646.

Ellison, C. J.; Mundra, M. K.; Torkelson, J. M., Impacts of Polystyrene Molecular Weight and Modification to the Repeat Unit Structure on the Glass Transition−Nanoconfinement Effect and the Cooperativity Length Scale. *Macromolecules* **2005,** *38*, 1767-1778.

Epstein, N. On tortuosity and the tortuosity factor in flow and diffusion through porous media. *Chem. Eng. Sci.* **1989**, *44*, 777-779.

Ercin, A. E.; Hoekstra, A. Y. Water Footprint Scenarios for 2050: A Global Analysis. *Environment International* **2014**, *64*, 71–82.

Fallahianbijan, F.; Giglia, S.; Carbrello, C.; Bell, D.; Zydney, A. L. Impact of Protein Fouling on Nanoparticle Capture within the Viresolve® Pro and Viresolve® NFP Virus Removal Membranes. *Biotechnology and Bioengineering* **2019**, *116*, 2285–2291.

Fasolka, M. J.; Mayes, A. M. Block Copolymer Thin Films: Physics and Applications. *Annual Review of Materials Science* **2001**, *31*, 323–355.

Feng, X.; Burke, C. J.; Zhuo, M.; Guo, H.; Yang, K.; Reddy, A.; Prasad, I.; Ho, R.-M.; Avgeropoulos, A.; Grason, G. M.; Thomas, E. L. Seeing Mesoatomic Distortions in Soft-Matter Crystals of a Double-Gyroid Block Copolymer. *Nature* **2019**, *575*, 175–179.

Feng, X.; Imran, Q.; Zhang, Y.; Sixdenier, L.; Lu, X.; Kaufman, G.; Gabinet, U.; Kawabata, K.; Elimelech, M.; Osuji, C. O. Precise Nanofiltration in a Fouling-Resistant Self-Assembled Membrane with Water-Continuous Transport Pathways. *Sci Adv* **2019**, *5*, eaav9308.

Feng, X.; Kawabata, K.; Cowan, M. G.; Dwulet, G. E.; Toth, K.; Sixdenier, L.; Haji-Akbari, A.; Noble, R. D.; Elimelech, M.; Gin, D. L.; Osuji, C. O. Single Crystal Texture by Directed Molecular Self-Assembly along Dual Axes. *Nat. Mater.* **2019**, *18*, 1235–1243.

Feng, X.; Tousley, M. E.; Cowan, M. G.; Wiesenauer, B. R.; Nejati, S.; Choo, Y.; Noble, R. D.; Elimelech, M.; Gin, D. L.; Osuji, C. O. Scalable Fabrication of Polymer Membranes with Vertically Aligned 1 Nm Pores by Magnetic Field Directed Self-Assembly. *ACS Nano* **2014**, *8*, 11977–11986.

Fox, T. G. Influence of Diluent and of Copolymer Composition on the Glass Temperature of a Polymer System. *Bull Am Phys Soc* **1956**, *1*, 123–125.

Frederickson, G.; Helfland, E. Fluctuation Effects in the Theory of Microphase Separation in Block Copolymers. *J Chem Phys* **1987**, *87*, 697–705.

Gillard, T. M.; Phelan, D.; Leighton, C.; Bates, F. S. Determination of the Lamellae-to-Disorder Heat of Transition in a Short Diblock Copolymer by Relaxation Calorimetry. *Macromolecules* **2015**, *48* , 4733–4741.

Gomez, E. D.; Das, J.; Chakraborty, A. K.; Pople, J.; Balsara, N. Effect of Cross-Linking on the Thermodynamics of Lamellar Block Copolymers. *Macromolecules* **2006**, *39*, 4848–4859.

Gopinadhan, M.; Deshmukh, P.; Choo, Y.; Majewski, P. W.; Bakajin, O.; Elimelech, M.; Kasi, R. M.; Osuji, C. O. Thermally Switchable Aligned Nanopores by Magnetic-Field Directed Self-Assembly of Block Copolymers. *Adv. Mater.* **2014**, *26*, 5148–5154.

Gor, G. Y.; Thommes, M.; Cychosz, K. A.; Neimark, A. V. Quenched Solid Density Functional Theory Method for Characterization of Mesoporous Carbons by Nitrogen Adsorption. *Carbon* **2012**, *50*, 1583–1590.

Grason, G. M.; Kamien, R. D. Interfaces in Diblocks: A Study of Miktoarm Star Copolymers. *Macromolecules* **2004**, *37*, 7371–7380.

Greenlee, L. F.; Lawler, D. F.; Freeman, B. D.; Marrot, B.; Moulin, P. Reverse Osmosis Desalination: Water Sources, Technology, and Today's Challenges. *Water Research* **2009**, *43*, 2317–2348.

Gröger, S.; Rittig, F.; Stallmach, F.; Almdal, K.; Štěpánek, P.; Papadakis, C. M. A Pulsed Field Gradient Nuclear Magnetic Resonance Study of a Ternary Homopolymer/diblock Copolymer Blend in the Bicontinuous Microemulsion Phase. *J. Chem. Phys.* **2002**, *117*, 396–406.

Gu, Y.; Wiesner, U. Tailoring Pore Size of Graded Mesoporous Block Copolymer Membranes: Moving from Ultrafiltration toward Nanofiltration. *Macromolecules* **2015**, *48*, 6153–6159.

Guillen, G. R.; Pan, Y.; Li, M.; Hoek, E. M. V. Preparation and Characterization of Membranes Formed by Nonsolvent Induced Phase Separation: A Review. *Ind. Eng. Chem. Res.* **2011**, *50*, 3798–3817..

Guo, L.; Wang, Y. Nanoslitting of Phase-Separated Block Copolymers by Solvent Swelling for Membranes with Ultrahigh Flux and Sharp Selectivity. *Chem. Commun.* **2014**, *50*, 12022–12025.

Guo, L.; Wang, Z.; Wang, Y. Perpendicular Alignment and Selective Swelling-Induced Generation of Homopores of Polystyrene-B-poly(2-Vinylpyridine)-B-Poly(ethylene Oxide) Triblock Terpolymer. *Macromolecules* **2018**, *51*, 6248–6256.

Hadziioannou, G.; Mathis, A.; Skoulios, A. Obtention de ≪ Monocristaux ≫ de Copolymères Triséquencés Styrène/isoprène/styrène Par Cisaillement Plan. *Colloid Polym. Sci.* **1979**, *257*, 136–139.

Hahn, H.; Chakraborty, A. K.; Das, J.; Pople, J.; Balsara, N. Order-Disorder Transitions in Cross-Linked Block Copolymer Solids. *Macromolecules* **2005**, *38*, 1277–1285.

Hahn, J.; Clodt, J. I.; Abetz, C.; Filiz, V.; Abetz, V. Thin Isoporous Block Copolymer Membranes: It Is All about the Process. *ACS Appl. Mater. Interfaces* **2015**, *7*, 21130–21137.

Hahn, J.; Clodt, J. I.; Filiz, V.; Abetz, V. Protein Separation Performance of Self-Assembled Block Copolymer Membranes. *RSC Adv.* **2014**, *4*, 10252–10260.

Hahn, J.; Filiz, V.; Rangou, S.; Clodt, J.; Jung, A.; Buhr, K.; Abetz, C.; Abetz, V. Structure Formation of Integral-Asymmetric Membranes of Polystyrene-Block-Poly(ethylene Oxide). *Journal of Polymer Science Part B: Polymer Physics* **2013**, *51*, 281–290.

Hamley, I. W. Ordering in Thin Films of Block Copolymers: Fundamentals to Potential Applications. *Progress in Polymer Science* **2009**, *34*, 1161–1210.

Hamley, I. W. Structure and Flow Behaviour of Block Copolymers. *Journal of Physics: Condensed Matter* **2001**, *13*, R643–R671.

Hampu, N.; Bates, M. W.; Vidil, T.; Hillmyer, M. A. Bicontinuous Porous Nanomaterials from Block Polymers Radically Cured in the Disordered State for Size-Selective Membrane Applications. *ACS Appl. Nano Mater.* **2019**, *2*, 4567-4577.

Hampu, N.; Hillmyer, M. A. Molecular Engineering of Nanostructures in Disordered Block Polymers. *ACS Macro Lett.* **2020**, *9*, 382–388.

Hampu, N.; Hillmyer, M. A. Temporally Controlled Curing of Block Polymers in the Disordered State Using Thermally Stable Photoacid Generators for the Preparation of Nanoporous Membranes. *ACS Appl. Polym. Mater.* **2019**, *1*, 1148–1154.

Hashimoto, T., Phase transition and self-assembly in block copolymers. *Macromolecular Symposia* **2001,** *174*, 69-84.

Hashimoto, T.; Shibayama, M.; Kawai, H., Ordered structure in block polymer solutions. 4. Scaling rules on size of fluctuations with block molecular weight, concentration, and temperature in segregation and homogeneous regimes. *Macromolecules* **1983**, *16*, 1093-1101.

Hashimoto, T.; Yamasaki, K.; Koizumi, S.; Hasegawa, H. Ordered Structure in Blends of Block Copolymers. 1. Miscibility Criterion for Lamellar Block Copolymers. *Macromolecules* **1993**, *26*, 2895–2904.

Haugan, I. N.; Lee, B.; Maher, M. J.; Zografos, A.; Schibur, H. J.; Jones, S. D.; Hillmyer, M. A.; Bates, F. S. Physical Aging of Polylactide-Based Graft Block Polymers. *Macromolecules* **2019**, *52*, 8878–8894.

Henis, J. M. S.; Tripodi, M. K. Composite Hollow Fiber Membranes for Gas Separation: The Resistance Model Approach. *J. Membr. Sci.* **1981**, *8*, 233–246.

Hester, J. F.; Banerjee, P.; Mayes, A. M. Preparation of Protein-Resistant Surfaces on Poly(vinylidene Fluoride) Membranes via Surface Segregation. *Macromolecules* **1999**, *32*, 1643–1650.

Hester, J. F.; Mayes, A. M. Design and Performance of Foul-Resistant Poly(vinylidene Fluoride) Membranes Prepared in a Single-Step by Surface Segregation. *J. Membr. Sci.* **2002**, *202*, 119–135.

Hester, J. F.; Olugebefola, S. C.; Mayes, A. M. Preparation of pH-Responsive Polymer Membranes by Self-Organization. *J. Membr. Sci.* **2002**, *208*, 375–388.

Hickey, R. J.; Gillard, T. M.; Irwin, M. T.; Lodge, T. P.; Bates, F. S. Structure, Viscoelasticity, and Interfacial Dynamics of a Model Polymeric Bicontinuous Microemulsion. *Soft Matter* **2016**, *12*, 53–66.

Hickey, R. J.; Gillard, T. M.; Irwin, M. T.; Morse, D. C.; Lodge, T. P.; Bates, F. S. Phase Behavior of Diblock Copolymer–Homopolymer Ternary Blends: Congruent First-Order Lamellar–Disorder Transition. *Macromolecules* **2016**, *49*, 7928–7944.

Hickey, R.; Gillard, T.; Lodge, T.; Bates, F. Influence of Composition Fluctuations on the Linear Viscoelastic Properties of Symmetric Diblock Copolymers near the Order− Disorder Transition. *ACS Macro Lett.* **2015**, *4*, 260–265.

Hiemenz, P. C.; Lodge, T. P., *Polymer Chemistry, Second Edition*. CRC Press: 2007.

Hilke, R.; Pradeep, N.; Behzad, A. R.; Nunes, S. P.; Peinemann, K.-V. Block Copolymer/homopolymer Dual-Layer Hollow Fiber Membranes. *J. Membr. Sci.* **2014**, *472*, 39–44.

Hilke, R.; Pradeep, N.; Madhavan, P.; Vainio, U.; Behzad, A. R.; Sougrat, R.; Nunes, S. P.; Peinemann, K.-V. Block Copolymer Hollow Fiber Membranes with Catalytic Activity and pH-Response. *ACS Appl. Mater. Interfaces* **2013**, *5*, 7001–7006.

Hillmyer, M. A.; Bates, F. S. Synthesis and Characterization of Model Polyalkane−Poly(ethylene Oxide) Block Copolymers. *Macromolecules* **1996**, *29*, 6994–7002.

Ho, J.; Sung, S. Anaerobic Membrane Bioreactor Treatment of Synthetic Municipal Wastewater at Ambient Temperature. *Water Environment Research* **2009**, *81*, 922–928.

Höhme, C.; Filiz, V.; Abetz, C.; Georgopanos, P.; Scharnagl, N.; Abetz, V. Postfunctionalization of Nanoporous Block Copolymer Membranes via Click Reaction on Polydopamine for Liquid Phase Separation. *ACS Appl. Nano Mater.* **2018**, *1*, 3124–3136.

Howard, M. P.; Lequieu, J.; Delaney, K. T.; Ganesan, V.; Fredrickson, G. H.; Truskett, T. M. Connecting Solute Diffusion to Morphology in Triblock Copolymer Membranes. *Macromolecules* **2020**. *In Press*.

Hsieh, I.-F.; Sun, H.-J.; Fu, Q.; Lotz, B.; Cavicchi, K. A.; Cheng, S. Z. D. Phase Structural Formation and Oscillation in Polystyrene-Block-Polydimethylsiloxane Thin Films. *Soft Matter* **2012**, *8*, 7937–7944.

Hur, S.-M.; Khaira, G. S.; Ramírez-Hernández, A.; Müller, M.; Nealey, P. F.; de Pablo, J. J. Simulation of Defect Reduction in Block Copolymer Thin Films by Solvent Annealing. *ACS Macro Lett.* **2015**, *4*, 11–15.

Ianiro, A.; Wu, H.; van Rijt, M. M. J.; Vena, M. P.; Keizer, A. D. A.; Esteves, A. C. C.; Tuinier, R.; Friedrich, H.; Sommerdijk, N. A. J. M.; Patterson, J. P. Liquid–liquid Phase Separation during Amphiphilic Self-Assembly. *Nature Chemistry* **2019**, *11*, 320–328.

Jackson, E. A.; Hillmyer, M. A. Nanoporous Membranes Derived from Block Copolymers: From Drug Delivery to Water Filtration. *ACS Nano* **2010**, *4*, 3548–3553.

Jackson, E. A.; Lee, Y.; Hillmyer, M. A. ABAC Tetrablock Terpolymers for Tough Nanoporous Filtration Membranes. *Macromolecules* **2013**, *46*, 1484–1491.

Jiang, Z.; Karan, S.; Livingston, A. G. Water Transport through Ultrathin Polyamide Nanofilms Used for Reverse Osmosis. *Adv. Mater.* **2018**, *30*, 1705973.

Jun, T.; Lee, Y.; Jo, S.; Ryu, C. Y.; Ryu, D. Y. Composition Fluctuation Inhomogeneity of Symmetric Diblock Copolymers: χN Effects at Order-to-Disorder Transition. *Macromolecules* **2018**, *51*, 282–288.

Jung, A.; Rangou, S.; Abetz, C.; Filiz, V.; Abetz, V. Structure Formation of Integral Asymmetric Composite Membranes of Polystyrene-Block-Poly(2-Vinylpyridine) on a Nonwoven. *Macromolecular Materials and Engineering* **2012**, *297*, 790–798.

Jung, J.; Park, H.-W.; Lee, S.; Lee, H.; Chang, T.; Matsunaga, K.; Jinnai, H. Effect of Film Thickness on the Phase Behaviors of Diblock Copolymer Thin Film. *ACS Nano* **2010**, *4*, 3109–3116.

Kaner, P.; Dudchenko, A. V.; Mauter, M. S.; Asatekin, A. Zwitterionic Copolymer Additive Architecture Affects Membrane Performance: Fouling Resistance and Surface Rearrangement in Saline Solutions. *J. Mater. Chem. A* **2019**, *7*, 4829–4846.

Kang, B.-G.; Kim, D.-G.; Register, R. A. Vinyl Addition Copolymers of Norbornylnorbornene and Hydroxyhexafluoroisopropylnorbornene for Efficient Recovery of N-Butanol from Dilute Aqueous Solution via Pervaporation. *Macromolecules* **2018**, *51*, 3702–3710.

Karunakaran, M.; Nunes, S. P.; Qiu, X.; Yu, H.; Peinemann, K.-V. Isoporous PS-B-PEO Ultrafiltration Membranes via Self-Assembly and Water-Induced Phase Separation. *J. Membr. Sci.* **2014**, *453*, 471–477.

Kennemur, J. G.; Hillmyer, M. A.; Bates, F. S. Rheological Evidence of Composition Fluctuations in an Unentangled Diblock Copolymer Melt near the Order–Disorder Transition. *ACS Macro Lett.* **2013**, *2*, 496–500.

Kennemur, J. G.; Hillmyer, M. A.; Bates, F. S., Rheological Evidence of Composition Fluctuations in an Unentangled Diblock Copolymer Melt near the Order–Disorder Transition. *ACS Macro Letters* **2013,** *2*, 496-500.

Kim, J.; Kim, K.; Ye, H.; Lee, E.; Shin, C.; McCarty, P. L.; Bae, J. Anaerobic Fluidized Bed Membrane Bioreactor for Wastewater Treatment. *Environ. Sci. Technol.* **2011**, *45*, 576–581.

Kim, K.; Arora, A.; Lewis, R. M.; Liu, M.; Li, W.; Shi, A.-C.; Dorfman, K. D.; Bates, F. S. Origins of Low-Symmetry Phases in Asymmetric Diblock Copolymer Melts. *Proc. Natl. Acad. Sci*. **2018**, *115*, 847.

Kim, K.; Schulze, M. W.; Arora, A.; Lewis, R. M.; Hillmyer, M. A.; Dorfman, K. D.; Bates, F. S. Thermal Processing of Diblock Copolymer Melts Mimics Metallurgy. Science 2017, 356, 520.

Kim, O.; Kim, S. Y.; Lee, J.; Park, M. J. Building Less Tortuous Ion-Conduction Pathways Using Block Copolymer Electrolytes with a Well-Defined Cubic Symmetry. *Chem. Mater.* **2016**, *28*, 318–325.

Kim, S.; Nealey, P. F.; Bates, F. S. Directed Assembly of Lamellae Forming Block Copolymer Thin Films near the Order–Disorder Transition. *Nano Lett.* **2014**, *14*, 148–152.

Kimura, K.; Hane, Y.; Watanabe, Y.; Amy, G.; Ohkuma, N. Irreversible Membrane Fouling during Ultrafiltration of Surface Water. *Water Research* **2004**, *38*, 3431–3441.

Koppi, K. A.; Tirrell, M.; Bates, F. S. Shear-Induced Isotropic-to-Lamellar Transition. *Phys. Rev. Lett.* **1993**, *70*, 1449–1452.

Kossuth, M. B.; Morse, D. C.; Bates, F. S. Viscoelastic Behavior of Cubic Phases in Block Copolymer Melts. *J. Rheol.* **1998**, *43*, 167–196.

Kruželák, J.; Sýkora, R.; Hudec, I., Peroxide vulcanization of natural rubber. Part I: effect of temperature and peroxide concentration. **2014,** *34*, 617-624.

Laîné, J.-M.; Vial, D.; Moulart, P. Status after 10 Years of Operation — Overview of UF Technology Today. *Desalination* **2000**, *131*, 17–25.

Lee, S.; Gillard, T. M.; Bates, F. S. Fluctuations, Order, and Disorder in Short Diblock Copolymers. *AIChE J.* **2013**, *59*, 3502–3513.

Lefèvre, N.; Daoulas, K. C.; Müller, M.; Gohy, J.-F.; Fustin, C.-A. Self-Assembly in Thin Films of Mixtures of Block Copolymers and Homopolymers Interacting by Hydrogen Bonds. *Macromolecules* **2010**, *43*, 7734–7743.

Leibler, L. Theory of Microphase Separation in Block Copolymers. *Macromolecules* **1980**, *13*, 1602–1617.

Lequieu, J.; Koeper, T.; Delaney, K. T.; Fredrickson, G. H. Extreme Deflection of Phase Boundaries and Chain Bridging in A(BA′)n Miktoarm Star Polymers. *Macromolecules* **2020**, *53*, 513–522.

Lesjean, B.; Huisjes, E. H. Survey of the European MBR Market: Trends and Perspectives. *Desalination* **2008**, *231*, 71–81.

Lewis, R. M.; Jackson, G. L.; Maher, M. J.; Kim, K.; Lodge, T. P.; Mahanthappa, M. K.; Narayanan, S.; Bates, F. S. A New Framework for X-Ray Photon Correlation Spectroscopy Analysis from Polycrystalline Materials. *Review of Scientific Instruments* **2018**, *89*, 123902.

Li, L.; Schulte, L.; Clausen, L. D.; Hansen, K. M.; Jonsson, G. E.; Ndoni, S. Gyroid Nanoporous Membranes with Tunable Permeability. *ACS Nano* **2011**, *5*, 7754–7766.

Li, L.; Szewczykowski, P.; Clausen, L. D.; Hansen, K. M.; Jonsson, G. E.; Ndoni, S. Ultrafiltration by Gyroid Nanoporous Polymer Membranes. *Journal of Membrane Science* **2011**, *384*, 126–135.

Li, T.; Zhou, C.; Jiang, M. UV Absorption Spectra of Polystyrene. *Polym. Bull.* **1991**, *25*, 211–216.

Lipic, P. M.; Bates, F. S.; Hillmyer, M. A. Nanostructured Thermosets from Self-Assembled Amphiphilic Block Copolymer/Epoxy Resin Mixtures. *J. Am. Chem. Soc.* **1998**, *120*, 8963–8970.

Liu, Y.; Liu, T.; Su, Y.; Yuan, H.; Hayakawa, T.; Wang, X. Fabrication of a Novel PS4VP/PVDF Dual-Layer Hollow Fiber Ultrafiltration Membrane. *J. Membr. Sci.* **2016**, *506*, 1–10.

Lodge, T. P.; Hanley, K. J.; Pudil, B.; Alahapperuma, V. Phase Behavior of Block Copolymers in a Neutral Solvent. *Macromolecules* **2003**, *36*, 816–822.

Lorain, O.; Espenan, J.-M.; Remigy, J.-F.; Rouch, J.-C.; Savart, T.; Gerard, P.; Magnet, S. Copolymer Having Amphiphilic Blocks, and Use Thereof for Manufacturing Polymer Filtration Membranes. US20160030896A1.

Lousada-Ferreira, M.; Geilvoet, S.; Moreau, A.; Atasoy, E.; Krzeminski, P.; van Nieuwenhuijzen, A.; van der Graaf, J. MLSS Concentration: Still a Poorly Understood Parameter in MBR Filterability. *Desalination* **2010**, *250*, 618–622.

Lowell, S.; Shields, J. E.; Thomas, M. A.; Thommes, M., *Characterization of porous solids and powders: surface area, pore size and density*. Springer Science & Business Media: 2012; Vol. 16.

Lu, G. Q.; Zhao, X. S., Nanoporous Materials - Science and Engineering. World Scientific.

Ma, D.; Zhou, J.; Wang, Z.; Wang, Y. Block Copolymer Ultrafiltration Membranes by Spray Coating Coupled with Selective Swelling. *Journal of Membrane Science* **2020**, *598*, 117656.

Majewski, P. W.; Gopinadhan, M.; Osuji, C. O. Magnetic Field Alignment of Block Copolymers and Polymer Nanocomposites: Scalable Microstructure Control in Functional Soft Materials. *Journal of Polymer Science Part B: Polymer Physics* **2012**, *50*, 2–8.

Mansky, P.; DeRouchey, J.; Russell, T. P.; Mays, J.; Pitsikalis, M.; Morkved, T.; Jaeger, H. Large-Area Domain Alignment in Block Copolymer Thin Films Using Electric Fields. *Macromolecules* **1998**, *31*, 4399–4401

Mao, H.; Hillmyer, M. A. Morphological Behavior of Polystyrene-Block-Polylactide/Polystyrene-Block-Poly(ethylene Oxide) Blends. *Macromol. Chem. Phys.* **2008**, *209*, 1647–1656.

Mao, H.; Hillmyer, M. A. Nanoporous Polystyrene by Chemical Etching of Poly(ethylene Oxide) from Ordered Block Copolymers. *Macromolecules* **2005**, *38*, 4038–4039.

Marques, D. S.; Dorin, R. M.; Wiesner, U.; Smilgies, D.-M.; Behzad, A. R.; Vainio, U.; Peinemann, K.-V.; Nunes, S. P. Time-Resolved GISAXS and Cryo-Microscopy Characterization of Block Copolymer Membrane Formation. *Polymer* **2014**, *55*, 1327–1332.

Marques, D. S.; Vainio, U.; Chaparro, N. M.; Calo, V. M.; Bezahd, A. R.; Pitera, J. W.; Peinemann, K.-V.; Nunes, S. P. Self-Assembly in Casting Solutions of Block Copolymer Membranes. *Soft Matter* **2013**, *9*, 5557–5564.

Maruf, S. H.; Wang, L.; Greenberg, A. R.; Pellegrino, J.; Ding, Y. Use of Nanoimprinted Surface Patterns to Mitigate Colloidal Deposition on Ultrafiltration Membranes. *Journal of Membrane Science* **2013**, *428*, 598–607.

Matsen, M. W.; Bates, F. S. Conformationally Asymmetric Block Copolymers. *J. Polym. Sci. B Polym. Phys.* **1997**, *35*, 945–952.

Matsen, M. W.; Bates, F. S. Origins of Complex Self-Assembly in Block Copolymers. *Macromolecules* **1996**, *29*, 7641–7644.

Matsen, M. W.; Bates, F. Unifying Weak- and Strong-Segregation Block Copolymer Theories. *Macromolecules* **1996**, *29*, 1091–1098.

Matsen, M. W.; Schick, M. Lamellar Phase of a Symmetric Triblock Copolymer. *Macromolecules* **1994**, *27*, 187–192.

Matsen, M. W.; Schick, M. Microphase Separation in Starblock Copolymer Melts. *Macromolecules* **1994**, *27*, 6761–6767.

Medapuram, P.; Glaser, J.; Morse, D. C., Universal Phenomenology of Symmetric Diblock Copolymers near the Order–Disorder Transition. *Macromolecules* **2015,** *48*, 819-840.

Mehta, A.; Zydney, A. L. Permeability and Selectivity Analysis for Ultrafiltration Membranes. *J. Membr. Sci.* **2005**, *249*, 245–249.

Mekonnen, M. M.; Hoekstra, A. Y. Four Billion People Facing Severe Water Scarcity. *Sci Adv* **2016**, *2*, e1500323.

Meuler, A. J.; Hillmyer, M. A.; Bates, F. S., Ordered Network Mesostructures in Block Polymer Materials. *Macromolecules* **2009,** *42*, 7221-7250.

Mickiewicz, R. A.; Ntoukas, E.; Avgeropoulos, A.; Thomas, E. L. Phase Behavior of Binary Blends of High Molecular Weight Diblock Copolymers with a Low Molecular Weight Triblock. *Macromolecules* **2008**, *41*, 5785–5792.

Microfiltration and Ultrafiltration Membranes for Drinking Water; AWWA, 2016.

Mochizuki, S.; Zydney, A. L. Theoretical Analysis of Pore Size Distribution Effects on Membrane Transport. *J. Membr. Sci.* **1993**, *82*, 211–227.

Morell, M.; Ramis, X.; Ferrando, F.; Serra, À. Effect of Polymer Topology on the Curing Process and Mechanical Characteristics of Epoxy Thermosets Modified with Linear or Multiarm Star Poly(ε-Caprolactone). *Polymer* **2011**, *52*, 4694–4702.

Mulvenna, R. A.; Weidman, J. L.; Jing, B.; Pople, J. A.; Zhu, Y.; Boudouris, B. W.; Phillip, W. A. Tunable Nanoporous Membranes with Chemically-Tailored Pore Walls from Triblock Polymer Templates. *Journal of Membrane Science* **2014**, *470*, 246–256.

Naughton, J.R.; Matsen, M.W., Limitations of the Dilution Approximation for Concentrated Block Copolymer/Solvent Mixtures. *Macromolecules* **2002**, *35*, 5688-5696.

Neimark, A. V.; Lin, Y.; Ravikovitch, P. I.; Thommes, M. Quenched Solid Density Functional Theory and Pore Size Analysis of Micro-Mesoporous Carbons. *Carbon* **2009**, *47*, 1617–1628.

Nobuyuki, A.; Izumi, K.; Takehisa, K., Dependence of the Crosslinking Efficiency on the Reaction Conditions in the Peroxide Crosslinking of Unsaturated Polyolefins. *Bulletin of the Chemical Society of Japan* **1967,** *40*, 2597-2603.

Nose, T. Pulsed-Field-Gradient NMR Studies of the Diffusion of Chain Molecules in Polymer Matrices. In *Annual Reports on NMR Spectroscopy*; Webb, G. A., Ed.; Academic Press, 1993; Vol. 27, pp 217–253.

Nunes, S. P. Block Copolymer Membranes for Aqueous Solution Applications. *Macromolecules* **2016**, *49*, 2905–2916.

Nunes, S. P.; Sougrat, R.; Hooghan, B.; Anjum, D. H.; Behzad, A. R.; Zhao, L.; Pradeep, N.; Pinnau, I.; Vainio, U.; Peinemann, K.-V. Ultraporous Films with Uniform Nanochannels by Block Copolymer Micelles Assembly. *Macromolecules* **2010**, *43*, 8079–8085.

Oatley-Radcliffe, D. L.; Williams, S.; Lee, C.; Williams, P. Characterisation of Mass Transfer in Frontal Nanofiltration Equipment and Development of a Simple Correlation. *J. Memb. Separ. Tech.* **2015**, *4*, 149-160.

Oh, J.; Seo, M. Photoinitiated Polymerization-Induced Microphase Separation for the Preparation of Nanoporous Polymer Films. *ACS Macro Lett.* **2015**, *4*, 1244–1248.

Okamoto, S.; Saijo, K.; Hashimoto, T. Real-Time SAXS Observations of Lamella-Forming Block Copolymers under Large Oscillatory Shear Deformation. *Macromolecules* **1994**, *27*, 5547–5555.

Oss-Ronen, L.; Schmidt, J.; Abetz, V.; Radulescu, A.; Cohen, Y.; Talmon, Y. Characterization of Block Copolymer Self-Assembly: From Solution to Nanoporous Membranes. *Macromolecules* **2012**, *4*, 9631–9642.

Panyukov, S.; Rubinstein, M. Stress-Induced Ordering in Microphase-Separated Multicomponent Networks. *Macromolecules* **1996**, *29*, 8220–8230.

Parent, L. R.; Bakalis, E.; Proetto, M.; Li, Y.; Park, C.; Zerbetto, F.; Gianneschi, N. C. Tackling the Challenges of Dynamic Experiments Using Liquid-Cell Transmission Electron Microscopy. *Acc. Chem. Res.* **2018**, *51*, 3–11.

Parent, L. R.; Bakalis, E.; Ramírez-Hernández, A.; Kammeyer, J. K.; Park, C.; de Pablo, J.; Zerbetto, F.; Patterson, J. P.; Gianneschi, N. C. Directly Observing Micelle Fusion and Growth in Solution by Liquid-Cell Transmission Electron Microscopy. *J. Am. Chem. Soc.* **2017**, *139*, 17140–17151.

Park, H. B.; Kamcev, J.; Robeson, L. M.; Elimelech, M.; Freeman, B. D. Maximizing the Right Stuff: The Trade-off between Membrane Permeability and Selectivity. *Science* **2017**, *356*, eaab0530.

Patel, A. J.; Mochrie, S.; Narayanan, S.; Sandy, A.; Watanabe, H.; Balsara, N. P. Dynamic Signatures of Microphase Separation in a Block Copolymer Melt Determined by X-Ray Photon Correlation Spectroscopy and Rheology. *Macromolecules* **2010**, *43*, 1515–1523.

Patel, A. J.; Narayanan, S.; Sandy, A.; Mochrie, S. G. J.; Garetz, B. A.; Watanabe, H.; Balsara, N. P. Relationship between Structural and Stress Relaxation in a Block-Copolymer Melt. *Phys. Rev. Lett.* **2006**, *96*, 257801.

Peer, D.; Karp, J. M.; Hong, S.; Farokhzad, O. C.; Margalit, R.; Langer, R. Nanocarriers as an Emerging Platform for Cancer Therapy. *Nat. Nanotech.* **2007**, *2*, 751–760.

Peinemann, K.-V.; Abetz, V.; Simon, P. F. W. Asymmetric Superstructure Formed in a Block Copolymer via Phase Separation. *Nat. Mater.* **2007**, *6*, 992-996.

Pendergast, M. M.; Mika Dorin, R.; Phillip, W. A.; Wiesner, U.; Hoek, E. M. V. Understanding the Structure and Performance of Self-Assembled Triblock Terpolymer Membranes. *J. Membr. Sci.* **2013**, *444*, 461–468.

Persson, K. M.; Gekas, V.; Trägårdh, G. Study of Membrane Compaction and Its Influence on Ultrafiltration Water Permeability. *Journal of Membrane Science* **1995**, *100*, 155–162.

Phillip, W. A.; Amendt, M.; O'Neill, B.; Chen, L.; Hillmyer, M. A.; Cussler, E. L. Diffusion and Flow Across Nanoporous Polydicyclopentadiene-Based Membranes. *ACS Appl. Mater. Interfaces* **2009**, *1*, 472–480.

Phillip, W. A.; Dorin, R. M.; Werner, J.; Hoek, E. M. V.; Wiesner, U.; Elimelech, M. Tuning Structure and Properties of Graded Triblock Terpolymer-Based Mesoporous and Hybrid Films. *Nano Lett.* **2011**, *11*, 2892–2900.

Phillip, W. A.; Dorin, R. M.; Werner, J.; Hoek, E. M. V.; Wiesner, U.; Elimelech, M. Tuning Structure and Properties of Graded Triblock Terpolymer-Based Mesoporous and Hybrid Films. *Nano Lett.* **2011**, *11*, 2892–2900.

Phillip, W. A.; Hillmyer, M. A.; Cussler, E. L. Cylinder Orientation Mechanism in Block Copolymer Thin Films Upon Solvent Evaporation. *Macromolecules* **2010**, *43*, 7763–7770.

Phillip, W. A.; O'Neill, B.; Rodwogin, M.; Hillmyer, M. A.; Cussler, E. L. Self-Assembled Block Copolymer Thin Films as Water Filtration Membranes. *ACS Appl. Mater. Interfaces* **2010**, *2*, 847–853.

Phillip, W. A.; Rzayev, J.; Hillmyer, M. A.; Cussler, E. L. Gas and Water Liquid Transport through Nanoporous Block Copolymer Membranes. *J. Membr. Sci.* **2006**, *286*, 144–152.

Ping Chu, H.; Li, X. Membrane Fouling in a Membrane Bioreactor (MBR): Sludge Cake Formation and Fouling Characteristics. *Biotechnology and Bioengineering* **2005**, *90*, 323–331.

Pinheiro, B. S.; Hajduk, D. A.; Gruner, S. M.; Winey, K. I. Shear-Stabilized Bi-Axial Texture and Lamellar Contraction in Both Diblock Copolymer and Diblock Copolymer/Homopolymer Blends. *Macromolecules* **1996**, *29*, 1482–1489.

Polis, D. L.; Winey, K. I. Controlling Kink Band Morphology in Block Copolymers: Threshold Criteria and Stability. *Macromolecules* **1998**, *31*, 3617–3625.

Polis, D. L.; Winey, K. I. Kink Bands in a Lamellar Diblock Copolymer Induced by Large Amplitude Oscillatory Shear. *Macromolecules* **1996**, *29*, 8180–8187.

Qin, J.; Grzywacz, P.; Morse, D. Renormalized One-Loop Theory of Correlations in Disordered Diblock Copolymers. The Journal of Chemical Physics 2011, 135 (8), 84902.

Querelle, S. E.; Jackson, E. A.; Cussler, E. L.; Hillmyer, M. A. Ultrafiltration Membranes with a Thin Poly(styrene)-B-Poly(isoprene) Selective Layer. *ACS Appl. Mater. Interfaces* **2013**, *5*, 5044–5050.

Radjabian, M.; Abetz, C.; Fischer, B.; Meyer, A.; Abetz, V. Influence of Solvent on the Structure of an Amphiphilic Block Copolymer in Solution and in Formation of an Integral Asymmetric Membrane. *ACS Appl. Mater. Interfaces* **2017**, *9*, 31224–31234.

Radjabian, M.; Abetz, V. Advanced Porous Polymer Membranes from Self-Assembling Block Copolymers. *Prog. Polym. Sci.* **2020**, *102*, 101219.

Radjabian, M.; Koll, J.; Buhr, K.; Handge, U. A.; Abetz, V. Hollow Fiber Spinning of Block Copolymers: Influence of Spinning Conditions on Morphological Properties. *Polym.* **2013**, *54*, 1803–1812.

Radjabian, M.; Koll, J.; Buhr, K.; Vainio, U.; Abetz, C.; Handge, U. A.; Abetz, V. Tailoring the Morphology of Self-Assembled Block Copolymer Hollow Fiber Membranes. *Polym.* **2014**, *55*, 2986–2997.

Rangou, S.; Buhr, K.; Filiz, V.; Clodt, J. I.; Lademann, B.; Hahn, J.; Jung, A.; Abetz, V. Self-Organized Isoporous Membranes with Tailored Pore Sizes. *J. Membr. Sci.* **2014**, *451*, 266–275.

Ren, Y.; Lodge, T. P.; Hillmyer, M.A., Synthesis, Characterization, and Interaction Strengths of Difluorocarbene-Modified Polystyrene−Polyisoprene Block Copolymers. *Macromolecules* **2000**, *33*, 866-876.

Rittig, F.; Kärger, J.; Papadakis, C. M.; Fleischer, G.; Almdal, K.; Štěpánek, P. Self-Diffusion in a Lamellar and Gyroid (Ordered) Diblock Copolymer Investigated Using Pulsed Field Gradient NMR. *Macromolecules* **2001**, *34*, 868–873.

Rodwogin, M. D.; Spanjers, C. S.; Leighton, C.; Hillmyer, M. A. Polylactide−Poly(dimethylsiloxane)−Polylactide Triblock Copolymers as Multifunctional Materials for Nanolithographic Applications. *ACS Nano* **2010**, *4*, 725–732.

Roe, R. J.; Nojima, S., Small-Angle X-Ray Scattering Study of Microand Macro-Phase Separations in Blends of Block Copolymer with Homopolymer. *MRS Online Proceedings Library Archive* **1986,** *79*, null-null.

Rokhlenko, Y.; Gopinadhan, M.; Osuji, C. O.; Zhang, K.; O'Hern, C. S.; Larson, S. R.; Gopalan, P.; Majewski, P. W.; Yager, K. G. Magnetic Alignment of Block Copolymer Microdomains by Intrinsic Chain Anisotropy. *Phys. Rev. Lett.* **2015**, *115*, 258302.

Rosedale, J. H.; Bates, F. S. Rheology of Ordered and Disordered Symmetric Poly(ethylenepropylene)-Poly(ethylethylene) Diblock Copolymers. *Macromolecules* **1990**, *23*, 2329–2338.

Rosedale, J. H.; Bates, F. S.; Almdal, K.; Mortensen, K.; Wignall, G. D. Order and Disorder in Symmetric Diblock Copolymer Melts. *Macromolecules* **1995**, *28*, 1429–1443.

Saba, S. A.; Lee, B.; Hillmyer, M. A., Tricontinuous Nanostructured Polymers via Polymerization-Induced Microphase Separation. *ACS Macro Letters* **2017,** *6*, 1232-1236.

Saba, S. A.; Mousavi, M. P. S.; Bühlmann, P.; Hillmyer, M. A. Hierarchically Porous Polymer Monoliths by Combining Controlled Macro- and Microphase Separation. *J. Am. Chem. Soc.* **2015**, *137*, 8896–8899.

Sadeghi, I.; Kaner, P.; Asatekin, A. Controlling and Expanding the Selectivity of Filtration Membranes. *Chem. Mater.* **2018**, *30*, 7328–7354.

Sakamoto, N.; Hashimoto, T. Ordering Dynamics of a Symmetric Polystyrene-Block-Polyisoprene. 2. Real-Space Analysis on the Formation of Lamellar Microdomain. *Macromolecules* **1998**, *31*, 3815–3823.

Sakamoto, N.; Hashimoto, T., Ordering Dynamics of a Symmetric Polystyrene-block-polyisoprene. 1. Ordering Mechanism from the Disordered State. *Macromolecules* **1998,** *31*, 3292-3302.

Sakurai, S.; Iwane, K.; Nomura, S. Morphology of Poly(styrene-Block-Butadiene-Block-Styrene) Triblock Copolymers Cross-Linked in the Disordered State. *Macromolecules* **1993**, *26*, 5479–5486.

Salazar-Peláez, M. L.; Morgan-Sagastume, J. M.; Noyola, A. Influence of Hydraulic Retention Time on Fouling in a UASB Coupled with an External Ultrafiltration Membrane Treating Synthetic Municipal Wastewater. *Desalination* **2011**, *277*, 164–170.

Sankhala, K.; Koll, J.; Radjabian, M.; Handge, U. A.; Abetz, V. A Pathway to Fabricate Hollow Fiber Membranes with Isoporous Inner Surface. *Adv. Mater. Interfaces* **2017**, *4*, 1600991.

Sardelis, K.; Michels, H. J.; Allen, G.; F.R.S, Graded block and randomized copolymers of butadiene-styrene. *Polym.* **1984,** *25*, 1011-1019.

Scalfani, V. F.; Bailey, T. S. Access to Nanostructured Hydrogel Networks through Photocured Body-Centered Cubic Block Copolymer Melts. *Macromolecules* **2011**, *44*, 6557–6567.

Scalfani, V. F.; Bailey, T. S. Thermally Stable Photocuring Chemistry for Selective Morphological Trapping in Block Copolymer Melt Systems. *Chem. Mater.* **2010**, *22*, 5992–6000.

Schmitt, A. K.; Mahanthappa, M. K. Characteristics of Lamellar Mesophases in Strongly Segregated Broad Dispersity ABA Triblock Copolymers. *Macromolecules* **2014**, *47*, 4346–4356.

Schneiderman, D. K.; Hillmyer, M. A. Aliphatic Polyester Block Polymer Design. *Macromolecules* **2016**, *49*, 2419–2428.

Schöttner, S.; Brodrecht, M.; Uhlein, E.; Dietz, C.; Breitzke, H.; Tietze, A. A.; Buntkowsky, G.; Gallei, M. Amine-Containing Block Copolymers for the Bottom-Up Preparation of Functional Porous Membranes. *Macromolecules* **2019**, *52*, 2631–2641.

Schöttner, S.; Schaffrath, H.-J.; Gallei, M. Poly(2-Hydroxyethyl Methacrylate)-Based Amphiphilic Block Copolymers for High Water Flux Membranes and Ceramic Templates. *Macromolecules* **2016**, *49*, 7286–7295.

Schubert, K. -V.; Strey, R.; Kline, S. R.; Kaler, E. W. Small Angle Neutron Scattering near Lifshitz Lines: Transition from Weakly Structured Mixtures to Microemulsions. *J. Chem. Phys.* **1994**, *101*, 5343–5355.

Schulte, L.; Grydgaard, A.; Jakobsen, M. R.; Szewczykowski, P. P.; Guo, F.; Vigild, M. E.; Berg, R. H.; Ndoni, S. Nanoporous Materials from Stable and Metastable Structures of 1,2-PB-B-PDMS Block Copolymers. *Polym.* **2011**, *52*, 422–429.

Schulze, M. W.; Hillmyer, M. A. Tuning Mesoporosity in Cross-Linked Nanostructured Thermosets via Polymerization-Induced Microphase Separation. *Macromolecules* **2017**, *50*, 997–1007.

Schulze, M. W.; McIntosh, L. D.; Hillmyer, M. A.; Lodge, T. P. High-Modulus, High-Conductivity Nanostructured Polymer Electrolyte Membranes via Polymerization-Induced Phase Separation. *Nano Lett.* **2014**, *14*, 122–126.

Segalman, R. A. Patterning with Block Copolymer Thin Films. *Materials Science and Engineering: R: Reports* **2005**, *48*, 191–226.

Semenov, A. Microphase Separation in Diblock-Copolymer Melts: Ordering of Micelles. *Macromolecules* **1989**, *22*, 2849–2851.

Semenov, A. N. Theory of Block Copolymer Interfaces in the Strong Segregation Limit. *Macromolecules* **1993**, *26*, 6617–6621.

Seo, M.; Hillmyer, M. A. Reticulated Nanoporous Polymers by Controlled Polymerization-Induced Microphase Separation. *Science* **2012**, *336*, 1422.

Seo, M.; Moll, D.; Silvis, C.; Roy, A.; Querelle, S.; Hillmyer, M. A. Interfacial Polymerization of Reactive Block Polymers for the Preparation of Composite Ultrafiltration Membranes. *Ind. Eng. Chem. Res.* **2014**, *53*, 18575–18579.

Serpico, J. M.; Ehrenberg, S. G.; Fontanella, J. J.; Jiao, X.; Perahia, D.; McGrady, K. A.; Sanders, E. H.; Kellogg, G. E.; Wnek, G. E. Transport and Structural Studies of Sulfonated Styrene−Ethylene Copolymer Membranes. *Macromolecules* **2002**, *35*, 5916-5921.

She, M.-S.; Lo, T.-Y.; Ho, R.-M. Controlled Ordering of Block Copolymer Gyroid Thin Films by Solvent Annealing. *Macromolecules* **2014**, *47*, 175–182.

Shevate, R.; Karunakaran, M.; Kumar, M.; Peinemann, K.-V. Polyanionic pH-Responsive Polystyrene-B-poly(4-Vinyl Pyridine-N-Oxide) Isoporous Membranes. *J. Membr. Sci.* **2016**, *501*, 161–168.

Shevate, R.; Kumar, M.; Cheng, H.; Hong, P.-Y.; Behzad, A. R.; Anjum, D.; Peinemann, K.-V. Rapid Size-Based Protein Discrimination inside Hybrid Isoporous Membranes. *ACS Appl. Mater. Interfaces* **2019**, *11*, 8507–8516.

Shevate, R.; Kumar, M.; Karunakaran, M.; Hedhili, M. N.; Peinemann, K.-V. Polydopamine/Cysteine Surface Modified Isoporous Membranes with Self-Cleaning Properties. *J. Membr. Sci.* **2017**, *529*, 185–194.

Shi, X.; Wang, X.; Wang, Y.; Wang, Y. Producing Nanoporosities in Block Copolymers within 30 S by Microwave-Boosted Selective Swelling. *Macromolecules* **2020**. *In Press*.

Shi, X.; Wang, Z.; Wang, Y. Highly Permeable Nanoporous Block Copolymer Membranes by Machine-Casting on Nonwoven Supports: An Upscalable Route. *J. Membr. Sci.* **2017**, *533*, 201–209.

Shi, X.; Xu, Z.; Huang, C.; Wang, Y.; Cui, Z. Selective Swelling of Electrospun Block Copolymers: From Perforated Nanofibers to High Flux and Responsive Ultrafiltration Membranes. *Macromolecules* **2018**, *51*, 2283–2292.

Silas, J. A.; Kaler, E. W. Effect of Multiple Scattering on SANS Spectra from Bicontinuous Microemulsions. *J. Colloid Interface Sci.* **2003**, *257*, 291–298.

Sing, K. S. W.; Everett, D. H.; Haul, R. A. W.; Moscou, L.; Pierotti, R. A.; Rouquerol, J.; Siemieniewska, T., Reporting Physisorption Data for Gas Solid Systems with Speical Reference to the Determination of Surface-area and Porosity (Recommendations 1984). *Pure Appl. Chem.* **1985,** *57*, 603-619.

Sinturel, C.; Bates, F. S.; Hillmyer, M. A. High χ–Low N Block Polymers: How Far Can We Go? *ACS Macro Lett.* **2015**, *4*, 1044–1050.

Sinturel, C.; Vayer, M.; Morris, M.; Hillmyer, M. A. Solvent Vapor Annealing of Block Polymer Thin Films. *Macromolecules* **2013**, *46*, 5399–5415.

Smolders, C. A.; Reuvers, A. J.; Boom, R. M.; Wienk, I. M. Microstructures in Phase-Inversion Membranes. Part 1. Formation of Macrovoids. *J. Membr. Sci.* **1992**, *73*, 259–275.

Stangler, S.; Abetz, V. Orientation Behavior of AB and ABC Block Copolymers under Large Amplitude Oscillatory Shear Flow. *Rheologica Acta* **2003**, *42*, 569–577.

Stegelmeier, C.; Filiz, V.; Abetz, V.; Perlich, J.; Fery, A.; Ruckdeschel, P.; Rosenfeldt, S.; Förster, S. Topological Paths and Transient Morphologies during Formation of Mesoporous Block Copolymer Membranes. *Macromolecules* **2014**, *47*, 5566–5577.

Steube, M.; Johann, T.; Galanos, E.; Appold, M.; Rüttiger, C.; Mezger, M.; Gallei, M.; Müller, A. H. E.; Floudas, G.; Frey, H. Isoprene/Styrene Tapered Multiblock Copolymers with up to Ten Blocks: Synthesis, Phase Behavior, Order, and Mechanical Properties. *Macromolecules* **2018**, *51*, 10246–10258.

Sundaramoorthi, G.; Hadwiger, M.; Ben-Romdhane, M.; Behzad, A. R.; Madhavan, P.; Nunes, S. P. 3D Membrane Imaging and Porosity Visualization. *Ind. Eng. Chem. Res.* **2016**, *55*, 3689–3695.

Sutisna, B.; Polymeropoulos, G.; Musteata, V.; Peinemann, K.-V.; Avgeropoulos, A.; Smilgies, D.-M.; Hadjichristidis, N.; Nunes, S. P. Design of Block Copolymer Membranes Using Segregation Strength Trend Lines. *Mol. Syst. Des. Eng.* **2016**, *1*, 278–289.

Sutisna, B.; Polymeropoulos, G.; Musteata, V.; Sougrat, R.; Smilgies, D.-M.; Peinemann, K.-V.; Hadjichristidis, N.; Nunes, S. P. Functionalized Nanochannels from Self-Assembled and Photomodified Poly(Styrene-B-Butadiene-B-Styrene). *Small* **2018**, *14*, 1701885.

Takuma, K.; Takata, T.; Endo, T. Cationic Polymerization of Epoxide with Benzyl Phosphonium Salts as the Latent Thermal Initiator. *Macromolecules* **1993**, *26*, 862–863.

Tang, P.; Qiu, F.; Zhang, H.; Yang, Y. Morphology and Phase Diagram of Complex Block Copolymers: ABC Star Triblock Copolymers. *J. Phys. Chem. B* **2004**, *108*, 8434–8438.

Tang, S.; Wang, Z.; Wu, Z.; Zhou, Q. Role of Dissolved Organic Matters (DOM) in Membrane Fouling of Membrane Bioreactors for Municipal Wastewater Treatment. *J. Hazardous Mater.* **2010**, *178*, 377–384.

Tchobanoglous, G.; Darby, J.; Bourgeous, K.; McArdle, J.; Genest, P.; Tylla, M. Ultrafiltration as an Advanced Tertiary Treatment Process for Municipal Wastewater. *Desalination* **1998**, *119*, 315–321.

Teran, A. A.; Mullin, S. A.; Hallinan, D. T.; Balsara, N. P. Discontinuous Changes in Ionic Conductivity of a Block Copolymer Electrolyte through an Order–Disorder Transition. *ACS Macro Lett.* **2012**, *1*, 305–309.

Teubner, M.; Strey, R. Origin of the Scattering Peak in Microemulsions. *J. Chem. Phys.* **1987**, *87*, 3195–3200.

Timachova, K.; Sethi, G. K.; Bhattacharya, R.; Villaluenga, I.; Balsara, N. P. Ion Diffusion across a Disorder-to-Order Phase Transition in a Poly(ethylene Oxide)-B-Poly(silsesquioxane) Block Copolymer Electrolyte. *Mol. Syst. Des. Eng.* **2019**, *4*, 357–364.

Ting, Y.-H.; Park, S.-M.; Liu, C.-C.; Liu, X.; Himpsel, F. J.; Nealey, P. F.; Wendt, A. E. Plasma Etch Removal of Poly(methyl Methacrylate) in Block Copolymer Lithography. *Journal of Vacuum Science & Technology B: Microelectronics and Nanometer Structures Processing, Measurement, and Phenomena* **2008**, *26*, 1684–1689.

Tiraferri, A.; Yip, N. Y.; Phillip, W. A.; Schiffman, J. D.; Elimelech, M. Relating Performance of Thin-Film Composite Forward Osmosis Membranes to Support Layer Formation and Structure. *J. Membr. Sci.* **2011**, *367*, 340–352.

Touris, A.; Chanpuriya, S.; Hillmyer, M. A.; Bates, F. S. Synthetic Strategies for the Generation of ABCA' Type Asymmetric Tetrablock Terpolymers. *Polym. Chem.* **2014**, *5*, 5551–5559.

Touve, M. A.; Figg, C. A.; Wright, D. B.; Park, C.; Cantlon, J.; Sumerlin, B. S.; Gianneschi, N. C. Polymerization-Induced Self-Assembly of Micelles Observed by Liquid Cell Transmission Electron Microscopy. *ACS Cent. Sci.* **2018**, *4*, 543–547.

Ulbricht, M., Advanced functional polymer membranes. *Polymer* **2006,** *47*, 2217-2262.

Urgun-Demirtas, M.; Stark, B. C.; Pagilla, K. R. Comparison of 2-Chlorobenzoic Acid Biodegradation in a Membrane Bioreactor by B. Cepacia and B. Cepacia Bearing the Bacterial Hemoglobin Gene. *Water Research* **2006**, *40*, 3123–3130.

Utroša, P.; Žagar, E.; Kovačič, S.; Pahovnik, D. Porous Polystyrene Monoliths Prepared from in Situ Simultaneous Interpenetrating Polymer Networks: Modulation of Morphology by Polymerization Kinetics. *Macromolecules* **2019**, *52*, 819-826.

van de Witte, P.; Dijkstra, P. J.; van den Berg, J. W. A.; Feijen, J. Phase Separation Processes in Polymer Solutions in Relation to Membrane Formation. *Journal of Membrane Science* **1996**, *117*, 1–31.

van Reis, R.; Zydney, A. Bioprocess Membrane Technology. *Journal of Membrane Science* **2007**, *297*, 16–50.

Vidil, T.; Hampu, N.; Hillmyer, M. A. Nanoporous Thermosets with Percolating Pores from Block Polymers Chemically Fixed above the Order–Disorder Transition. *ACS Cent. Sci.* **2017**, *3*, 1114-1120.

Vriezekolk, E. J.; Kudernac, T.; de Vos, W. M.; Nijmeijer, K. Composite Ultrafiltration Membranes with Tunable Properties Based on a Self-Assembling Block Copolymer/homopolymer System. *J. Polym. Sci. B: Polym. Phys.* **2015**, *53*, 1546–1558.

Vrijenhoek, E. M.; Hong, S.; Elimelech, M. Influence of Membrane Surface Properties on Initial Rate of Colloidal Fouling of Reverse Osmosis and Nanofiltration Membranes. *J. Membr. Sci.* **2001**, *188*, 115–128.

Walker, C. N.; Bryson, K. C.; Hayward, R. C.; Tew, G. N., Wide Bicontinuous Compositional Windows from Co-Networks Made with Telechelic Macromonomers. *ACS Nano* **2014,** *8*, 12376-12385.

Wanakule, N. S.; Panday, A.; Mullin, S. A.; Gann, E.; Hexemer, A.; Balsara, N. P. Ionic Conductivity of Block Copolymer Electrolytes in the Vicinity of Order−Disorder and Order−Order Transitions. *Macromolecules* **2009**, *42*, 5642–5651.

Wang, C.; Quan, X.; Liao, M.; Li, L.; Zhou, J. Computer Simulations on the Channel Membrane Formation by Nonsolvent Induced Phase Separation. *Macromol. Theory Simul.* **2017**, *26*, 1700027.

Wang, D.; Kou, R.; Choi, D.; Yang, Z.; Nie, Z.; Li, J.; Saraf, L. V.; Hu, D.; Zhang, J.; Graff, G. L.; Liu, J.; Pope, M. A.; Aksay, I. A. Ternary Self-Assembly of Ordered Metal Oxide−Graphene Nanocomposites for Electrochemical Energy Storage. *ACS Nano* **2010**, *4*, 1587–1595.

Wang, J.; Rahman, M. M.; Abetz, C.; Abetz, V. Bovine Serum Albumin Selective Integral Asymmetric Isoporous Membrane. *J. Membr. Sci.* **2020**, *604*, 118074.

Wang, Y. Nondestructive Creation of Ordered Nanopores by Selective Swelling of Block Copolymers: Toward Homoporous Membranes. *Acc. Chem. Res.* **2016**, *49*, 1401–1408.

Wang, Y.; Shi, X. S. Method to Enhance the Process of Selective Swelling-Induced Pores Generation for Separation Membrane. CN110124539 A.

Wang, Z.; Guo, L.; Wang, Y. Isoporous Membranes with Gradient Porosity by Selective Swelling of UV-Crosslinked Block Copolymers. *J. Membr. Sci.* **2015**, *476*, 449–456.

Wang, Z.; Liu, R.; Yang, H.; Wang, Y. Nanoporous Polysulfones with in Situ PEGylated Surfaces by a Simple Swelling Strategy Using Paired Solvents. *Chem. Commun.* **2017**, *53*, 9105–9108.

Wang, Z.; Yao, X.; Wang, Y. Swelling-Induced Mesoporous Block Copolymer Membranes with Intrinsically Active Surfaces for Size-Selective Separation. *J. Mater. Chem.* **2012**, *22*, 20542–20548.

Weidman, J. L.; Mulvenna, R. A.; Boudouris, B. W.; Phillip, W. A. Nanostructured Membranes from Triblock Polymer Precursors as High Capacity Copper Adsorbents. *Langmuir* **2015**, *31*, 11113–11123.

Weidman, J. L.; Mulvenna, R. A.; Boudouris, B. W.; Phillip, W. A. Unusually Stable Hysteresis in the pH-Response of Poly(Acrylic Acid) Brushes Confined within Nanoporous Block Polymer Thin Films. *J. Am. Chem. Soc.* **2016**, *138*, 7030–7039.

Wen, C.; Huang, X.; Qian, Y. Domestic Wastewater Treatment Using an Anaerobic Bioreactor Coupled with Membrane Filtration. *Process Biochemistry* **1999**, *35*, 335–340.

Werber, J. R.; Osuji, C. O.; Elimelech, M. Materials for next-Generation Desalination and Water Purification Membranes. *Nat. Rev. Mater.* **2016**, *1*, 16018.

Werber, J. R.; Porter, C. J.; Elimelech, M. A Path to Ultraselectivity: Support Layer Properties To Maximize Performance of Biomimetic Desalination Membranes. *Environ. Sci. Technol.* **2018**, *52*, 10737–10747.

Wickham, R. A.; Shi, A.-C.; Wang, Z.-G. Nucleation of Stable Cylinders from a Metastable Lamellar Phase in a Diblock Copolymer Melt. J. Chem. Phys. 2003, 118 (22), 10293–10305.

Widin, J. M.; Schmitt, A. K.; Im, K.; Schmitt, A. L.; Mahanthappa, M. K. Polydispersity-Induced Stabilization of a Disordered Bicontinuous Morphology in ABA Triblock Copolymers. *Macromolecules* **2010**, *43*, 7913–7915.

Wintgens, T.; Melin, T.; Schäfer, A.; Khan, S.; Muston, M.; Bixio, D.; Thoeye, C. The Role of Membrane Processes in Municipal Wastewater Reclamation and Reuse. *Desalination* **2005**, *178*, 1–11.

Wolf, J. H.; Hillmyer, M. A. Ordered Nanoporous Poly(cyclohexylethylene). *Langmuir* **2003**, *19*, 6553–6560.

Wu, D.; Howell, J. .; Field, R. . Critical Flux Measurement for Model Colloids. *Journal of Membrane Science* **1999**, *152*, 89–98.

Xiao, K.; Liang, S.; Wang, X.; Chen, C.; Huang, X. Current State and Challenges of Full-Scale Membrane Bioreactor Applications: A Critical Review. *Bioresource Technology* **2019**, *271*, 473–481.

Xu, J.; Mittal, V.; Bates, F. S. Toughened Isotactic Polypropylene: Phase Behavior and Mechanical Properties of Blends with Strategically Designed Random Copolymer Modifiers. *Macromolecules* **2016**, *49*, 6497–6506.

Yadav, M.; Bates, F. S.; Morse, D. C. Network Model of the Disordered Phase in Symmetric Diblock Copolymer Melts. *Phys. Rev. Lett.* **2018**, *121*, 127802.

Yamaguchi, D.; Hasegawa, H.; Hashimoto, T. A Phase Diagram for the Binary Blends of Nearly Symmetric Diblock Copolymers. 2. Parameter Space of Temperature and Blend Composition. *Macromolecules* **2001**, *34*, 6506–6518.

Yan, N.; Wang, Z.; Wang, Y. Highly Permeable Membranes Enabled by Film Formation of Block Copolymers on Water Surface. *J. Membr. Sci.* **2018**, *568*, 40–46.

Yang, H.; Guo, L.; Wang, Z.; Yan, N.; Wang, Y. Nanoporous Films with Superior Resistance to Protein Adsorption by Selective Swelling of Polystyrene-Block-Poly(ethylene Oxide). *Ind. Eng. Chem. Res.* **2016**, *55*, 8133–8140.

Yang, H.; Wang, Z.; Lan, Q.; Wang, Y. Antifouling Ultrafiltration Membranes by Selective Swelling of Polystyrene/poly(ethylene Oxide) Block Copolymers. *J. Membr. Sci.* **2017**, *542*, 226–232.

Yang, S. Y.; Park, J.; Yoon, J.; Ree, M.; Jang, S. K.; Kim, J. K. Virus Filtration Membranes Prepared from Nanoporous Block Copolymers with Good Dimensional Stability under High Pressures and Excellent Solvent Resistance. *Adv. Funct. Mater.* **2008**, *18*, 1371–1377.

Yang, S. Y.; Park, J.; Yoon, J.; Ree, M.; Jang, S. K.; Kim, J. K. Virus Filtration Membranes Prepared from Nanoporous Block Copolymers with Good Dimensional Stability under High Pressures and Excellent Solvent Resistance. *Advanced Functional Materials* **2008**, *18*, 1371–1377.

Yin, J.; Yao, X.; Liou, J.-Y.; Sun, W.; Sun, Y.-S.; Wang, Y. Membranes with Highly Ordered Straight Nanopores by Selective Swelling of Fast Perpendicularly Aligned Block Copolymers. *ACS Nano* **2013**, *7*, 9961–9974.

Yu, H.; Qiu, X.; Moreno, N.; Ma, Z.; Calo, V. M.; Nunes, S. P.; Peinemann, K.-V. Self-Assembled Asymmetric Block Copolymer Membranes: Bridging the Gap from Ultra- to Nanofiltration. *Angewandte Chemie International Edition* **2015**, *54*, 13937–13941.

Zalusky, A. S.; Olayo-Valles, R.; Wolf, J. H.; Hillmyer, M. A. Ordered Nanoporous Polymers from Polystyrene−Polylactide Block Copolymers. *J. Am. Chem. Soc.* **2002**, *124*, 12761–12773.

Zeng, D.; Ribbe, A.; Hayward, R. C. Anisotropic and Interconnected Nanoporous Materials from Randomly End-Linked Copolymer Networks. *Macromolecules* **2017**, *50*, 4668–4676.

Zeng, D.; Ribbe, A.; Kim, H.; Hayward, R. C. Stress-Induced Orientation of Cocontinuous Nanostructures within Randomly End-Linked Copolymer Networks. *ACS Macro Lett.* **2018**, *7*, 828–833.

Zhang, G.; Zhang, J.; Wang, S.; Shen, D. Miscibility and Phase Structure of Binary Blends of Polylactide and Poly(methyl Methacrylate). *J. Polym. Sci. Part B Polym. Phys.* **2003**, *41*, 23–30.

Zhang, Q.; Gu, Y.; Li, Y. M.; Beaucage, P. A.; Kao, T.; Wiesner, U. Dynamically Responsive Multifunctional Asymmetric Triblock Terpolymer Membranes with Intrinsic Binding Sites for Covalent Molecule Attachment. *Chem. Mater.* **2016**, *28*, 3870–3876.

Zhang, Q.; Huang, S.-Z.; Jin, J.; Liu, J.; Li, Y.; Wang, H.-E.; Chen, L.-H.; Wang, B.-J.; Su, B.-L., Engineering 3D bicontinuous hierarchically macro-mesoporous LiFePO4/C nanocomposite for lithium storage with high rate capability and long cycle stability. *Scientific Reports* **2016,** *6*, 25942.

Zhang, Q.; Li, Y. M.; Gu, Y.; Dorin, R. M.; Wiesner, U. Tuning Substructure and Properties of Supported Asymmetric Triblock Terpolymer Membranes. *Polymer* **2016**, *107*, 398–405.

Zhang, R.; Liu, Y.; He, M.; Su, Y.; Zhao, X.; Elimelech, M.; Jiang, Z. Antifouling Membranes for Sustainable Water Purification: Strategies and Mechanisms. *Chem. Soc. Rev.* **2016**, *45*, 5888–5924.

Zhang, Y.; Mulvenna, R. A.; Boudouris, B. W.; Phillip, W. A. Nanomanufacturing of High-Performance Hollow Fiber Nanofiltration Membranes by Coating Uniform Block Polymer Films from Solution. *J. Mater. Chem. A* **2017**, *5*, 3358–3370.

Zhang, Y.; Mulvenna, R. A.; Qu, S.; Boudouris, B. W.; Phillip, W. A. Block Polymer Membranes Functionalized with Nanoconfined Polyelectrolyte Brushes Achieve Sub-Nanometer Selectivity. *ACS Macro Lett.* **2017**, *6*, 726–732.

Zhang, Y.; Sargent, J. L.; Boudouris, B. W.; Phillip, W. A. Nanoporous Membranes Generated from Self-Assembled Block Polymer Precursors: Quo Vadis? *J. Appl. Polym. Sci.* **2015**, *132*, 41683.

Zhang, Y.; Vallin, J. R.; Sahoo, J. K.; Gao, F.; Boudouris, B. W.; Webber, M. J.; Phillip, W. A. High-Affinity Detection and Capture of Heavy Metal Contaminants Using Block Polymer Composite Membranes. *ACS Cent. Sci.* **2018**, *4*, 1697–1707.

Zhang, Z.; Rahman, M. M.; Abetz, C.; Höhme, A.-L.; Sperling, E.; Abetz, V. Chemically Tailored Multifunctional Asymmetric Isoporous Triblock Terpolymer Membranes for Selective Transport. *Adv. Mater.* **2020**, *32*, 1907014.

Zhao, W.; Su, Y.; Li, C.; Shi, Q.; Ning, X.; Jiang, Z. Fabrication of Antifouling Polyethersulfone Ultrafiltration Membranes Using Pluronic F127 as Both Surface Modifier and Pore-Forming Agent. *J. Membr. Sci.* **2008**, *318*, 405–412.

Zhao, X.; Su, Y.; Chen, W.; Peng, J.; Jiang, Z. pH-Responsive and Fouling-Release Properties of PES Ultrafiltration Membranes Modified by Multi-Functional Block-like Copolymers. *J. Membr. Sci.* **2011**, *382*, 222–230.

Zhao, X.; Su, Y.; Li, Y.; Zhang, R.; Zhao, J.; Jiang, Z. Engineering Amphiphilic Membrane Surfaces Based on PEO and PDMS Segments for Improved Antifouling Performances. *J. Membr. Sci.* **2014**, *450*, 111–123.

Zhao, Y.; Sivaniah, E.; Hashimoto, T., SAXS Analysis of the Order−Disorder Transition and the Interaction Parameter of Polystyrene-block-poly(methyl methacrylate). *Macromolecules* **2008,** *41*, 9948-9951.

Zhong, D.; Wang, Z.; Lan, Q.; Wang, Y. Selective Swelling of Block Copolymer Ultrafiltration Membranes for Enhanced Water Permeability and Fouling Resistance. *J. Membr. Sci.* **2018**, *558*, 106–112.

Zhou, H.-J.; Yang, G.-W.; Zhang, Y.-Y.; Xu, Z.-K.; Wu, G.-P. Bioinspired Block Copolymer for Mineralized Nanoporous Membrane. *ACS Nano* **2018**, *12*, 11471–11480.

Zhou, J.; Wang, Y. Selective Swelling of Block Copolymers: An Upscalable Greener Process to Ultrafiltration Membranes? *Macromolecules* **2020**, *53*, 5–17.

Zhou, N.; Bates, F. S.; Lodge, T. P. Mesoporous Membrane Templated by a Polymeric Bicontinuous Microemulsion. *Nano Lett.* **2006**, *6*, 2354–2357.

Zhu, G.; Ying, Y.; Li, X.; Liu, Y.; Yang, C.; Yi, Z.; Gao, C. Isoporous Membranes with Sub-10 Nm Pores Prepared from Supramolecular Interaction Facilitated Block Copolymer Assembly and Application for Protein Separation. *J. Membr. Sci.* **2018**, *566*, 25–34.

Zofchak, E. S.; LaNasa, J. A.; Mei, W.; Hickey, R. J. Polymerization-Induced Nanostructural Transitions Driven by In Situ Polymer Grafting. *ACS Macro Lett.* **2018**, *7*, 822–827.

Appendix A. Nanoporous Thermosets with Percolating Pores from Block Polymers Chemically Fixed Above the Order-Disorder Transition[6]

A.1 Introduction

Polymeric materials with nanoscopic interpenetrating and percolating domains that exhibit high surface to volume ratios are very useful for separation,[1] catalysis,[2] and energy technologies.[3] A rich variety of synthetic strategies to these materials have been developed with the aim of combining two discrete phases that form stable and interconnected domains.[4, 5] Block polymers have been extensively used for this purpose[6, 7] as they provide self-assembled nanostructures with well-defined geometries and domain size that can be readily controlled by tuning the molar mass and the chemical composition.[5, 8] However, commonly observed equilibrium morphologies typically either require additional post-synthetic processing to align the domains (cylinders and lamellae)[9-11] or exist over a narrow range of composition (double gyroid).[12] As a result, numerous reports have outlined strategies to kinetically trap non-equilibrium, bicontinuous morphologies.[13-15] In particular, microphase separation in crosslinkable systems involving polymeric precursors (e.g.,

[6] Reproduced with permission from Vidil T.; Hampu, N.; Hillmyer, M. A. Nanoporous Thermosets with Percolating Pores from Block Polymers Chemically Fixed Above the Order-Disorder Transition. *ACS Central Science*. **2017**, *3*, 1114-1120. Copyright 2019 American Chemical Society. Thomas Vidil was the primary researcher on this project. Nicholas Hampu contributed to the design of the experiments, data analysis and interpretation, and was the primary researcher on the membrane fabrication experiments.

Polymerization Induced Microphase Separation, PIMS[13] or randomly end-linked copolymer networks, RECNs[15]) has been successfully employed for the straightforward preparation of large-area samples with co-continuous nanodomains. A fine balance between the kinetics of the phase separation process and the crosslinking reaction ensures trapping of a non-equilibrium morphology comprised of interconnected domain. The bicontinuity of these morphologies has been correlated to their global disorder.[16]

We now report a new strategy for the preparation of robust bicontinuous nanostructured materials by exploiting the well-known order-disorder transition (ODT) of block polymers.[17] Theoretical studies indicate that this transition in block polymers is characterized by strong, thermally-induced local composition fluctuations that disrupt the long range order of the system.[18-22] As the order-disorder transition temperature (T_{ODT}) is approached from the disordered state, the fluctuations become large in amplitude and spatially correlated over short distances, resulting in the persistence of local microphase segregation despite the absence of global long-range order. Some view the ODT as a "pattern transition" resulting in only small changes in chain stretching and interfacial area, despite a loss in long-range order.[23, 24] Early works have also postulated that the resulting structure is bicontinuous, with a morphology that is topologically similar to other disordered, microphase separated systems.[17, 19, 24] In two important experimental studies, the persistence of microphase separation above T_{ODT} was demonstrated by the direct imaging of the morphology of reactive block polymers crosslinked in the disordered state.[25, 26] However, there have been very few attempts to characterize the three-dimensional connectivity of these domains or exploit this interesting state in

nanotechnology with the important exception of Balsara *et al.* who demonstrated that the conductivity of a lamellar diblock polymer loaded with a lithium salt increases in the vicinity of T_{ODT}, most likely as a consequence of the interconnectivity of the conductive domains induced by composition fluctuations.[27] Consequently, there is a strong motivation to further investigate the morphological development in the vicinity of the T_{ODT} so that the ODT could be leveraged for the design, discovery, and development of new materials.

Our aim is to utilize the order-disorder transition of reactive block polymers to prepare mesoporous materials with well-defined and continuous three-dimensional network structures (Figure A.1). This approach involves heating a reactive diblock polymer above its T_{ODT} in the presence of a thermally latent initiator that can trigger the crosslinking reaction for curing temperatures $T_{curing} \sim T_{ODT}$, thus kinetically trapping the disordered state. The concurrent use of a chemically etchable block allows for the subsequent removal of one of the nanodomains affording a nanoporous structure that can be easily characterized under ambient conditions. This method represents a new and versatile strategy for the design of mesoporous materials that retains all of the processability advantages of polymer-based systems. To demonstrate a potential application of this work we prepared novel membranes for the ultrafiltration of water.

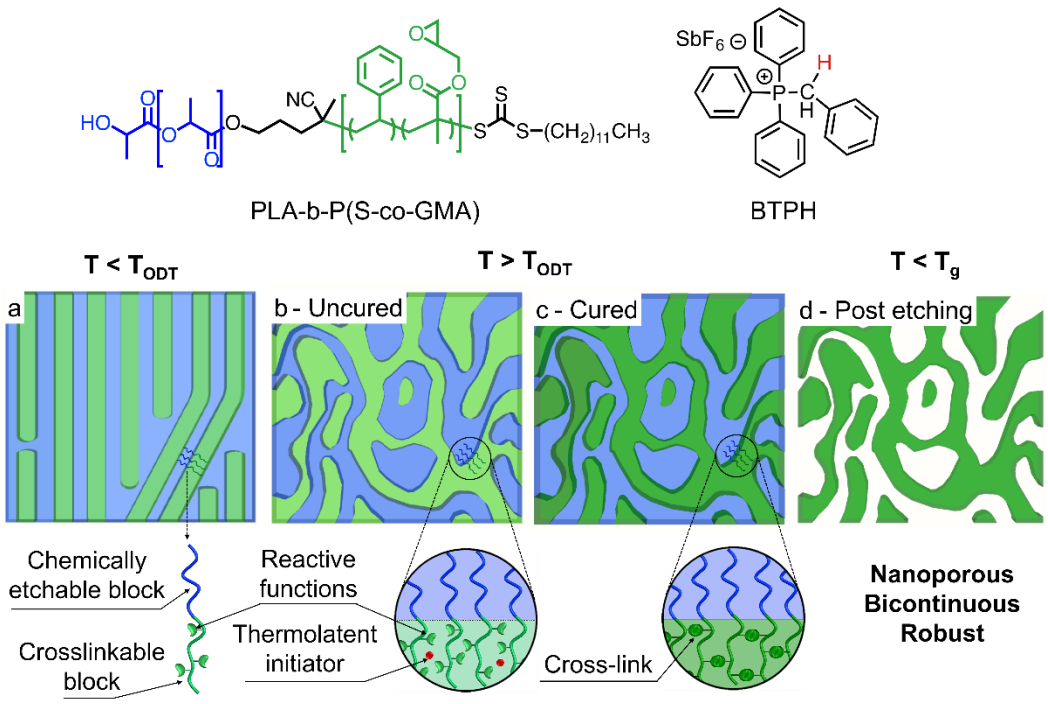

Figure A.1. The strategy employed to obtain a bicontinuous nanoporous structure by chemical crosslinking of a diblock polymer in the disordered state. The chemical structures of the components are represented at the top. (a) Lamellar diblock copolymer with an etchable block (blue) and a crosslinkable block (green) containing a thermally latent crosslinking initiator. (b) This mixture is heated above its order-disorder transition temperature (T_{ODT}) to adopt a disordered bicontinuous morphology. (c) The thermolatent initiator triggers the crosslinking reaction above T_{ODT}. (d) Once the crosslinkable phase is cured (darker green), the etchable block (blue) is removed to obtain well-defined percolating nanopores.

A.2 Experimental Design

We prepared a block polymer containing a chemically etchable polylactide (PLA) and a crosslinkable block consisting of a statistical copolymer of styrene (S) and glycidyl methacrylate (GMA) [PLA-*b*-P(S-*s*-GMA)] (Figure A.1, top). The synthetic route starts with a functionalized PLA precursor obtained by ring opening polymerization of ±-lactide initiated by an alcohol containing a chain transfer agent (CTA) for reversible addition−fragmentation chain transfer (RAFT). A series of PLA-*b*-P(S-*s*-GMA) samples with controlled molar masses and mole fractions of GMA in the crosslinkable block as well

as low values of dispersity ($Đ$ ~ 1.1) was obtained (Figures A.2 and A.3). The diblocks are labeled as PLA-α-P(S-*s*-GMA)-β-X_{GMA}-γ where α and β are the molar masses (in kg mol^{-1}) of the PLA and P(S-*s*-GMA) blocks, respectively, and γ is the molar percentage of GMA in the P(S-*s*-GMA) block (X_{GMA}). Two glass transition temperatures, T_g, were observed by differential scanning calorimetry (T_g(PLA) ~ 55 °C and T_g(P(S-*s*-GMA) ~ 70–80 °C, Figure A.4) implicating microphase separation.

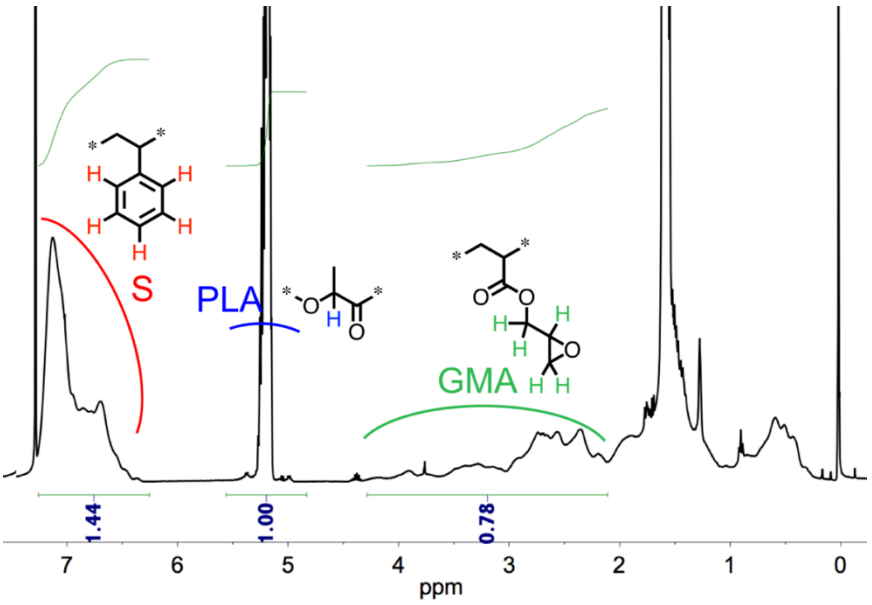

Figure A.2. ^{1}H-NMR spectrum of PLA-*b*-P(S-*s*-GMA) with indication of the signals of the aromatic protons of styrene, the glycidyl protons of GMA and the methine proton of PLA. These signals are used to estimate the molecular weight as well as the composition of the diblock.

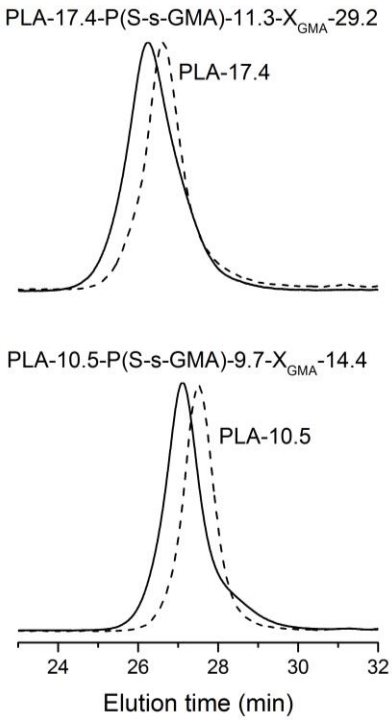

Figure A.3. SEC traces for PLA-17.4-P(S-*s*-GMA)-11.3-X_{GMA}-29.2 and PLA-10.5-P(S-*s*-GMA)-9.7-X_{GMA}-14.4 (solid lines). They are compared to the SEC traces of their PLA precursors (dashed lines).

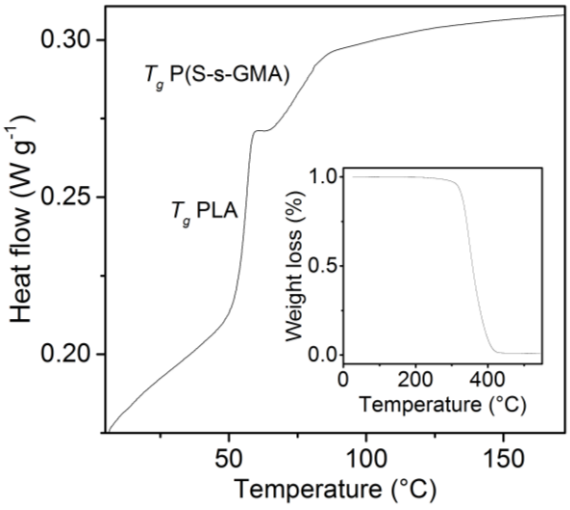

Figure A.4. Representative DSC thermogram obtained on the second heating at 10 °C min^{-1} for PLA-17.4-P(S-*s*-GMA)-11.9-X_{GMA}-32.1. The inset represents the TGA thermogram for the same polymer heated under nitrogen at a ramp rate of 10 °C min^{-1}. The decomposition temperature, T_d, is defined as 5% weight loss of the sample.

A.3. Results and Discussion

A.3.1 Characterization of T_{ODT}

Figure A.5a shows the temperature dependence of the low-frequency dynamic elastic shear modulus (G') for PLA-17-P(S-*s*-GMA)-11-X_{GMA}-29. The T_{ODT}, 174 ± 5 °C, was identified as the onset of the discontinuous drop in G' resulting in a liquid-like response. The linear viscoelastic responses of the melt at low frequency ($0.01 \leq \omega \leq 100$ rad s^{-1}) for two temperatures above and below T_{ODT} are also shown in Figure A.5a (insets). For T = 160 °C ($T < T_{ODT}$), the moduli obey a $G` \sim G`` \sim \omega^{1/2}$ power law typically observed for lamellar ordering.[18] Above T_{ODT} at 190 °C the moduli scale as $G' \sim \omega^{1.5}$ and $G'' \sim \omega^{1}$. The frequency dependence exponent of G' (1.5) is consistent with composition fluctuations in disordered phases close to the ordering transition[20, 28] where the longest relaxation time is shifted to lower frequencies due to the collective motion of the segregated domains.

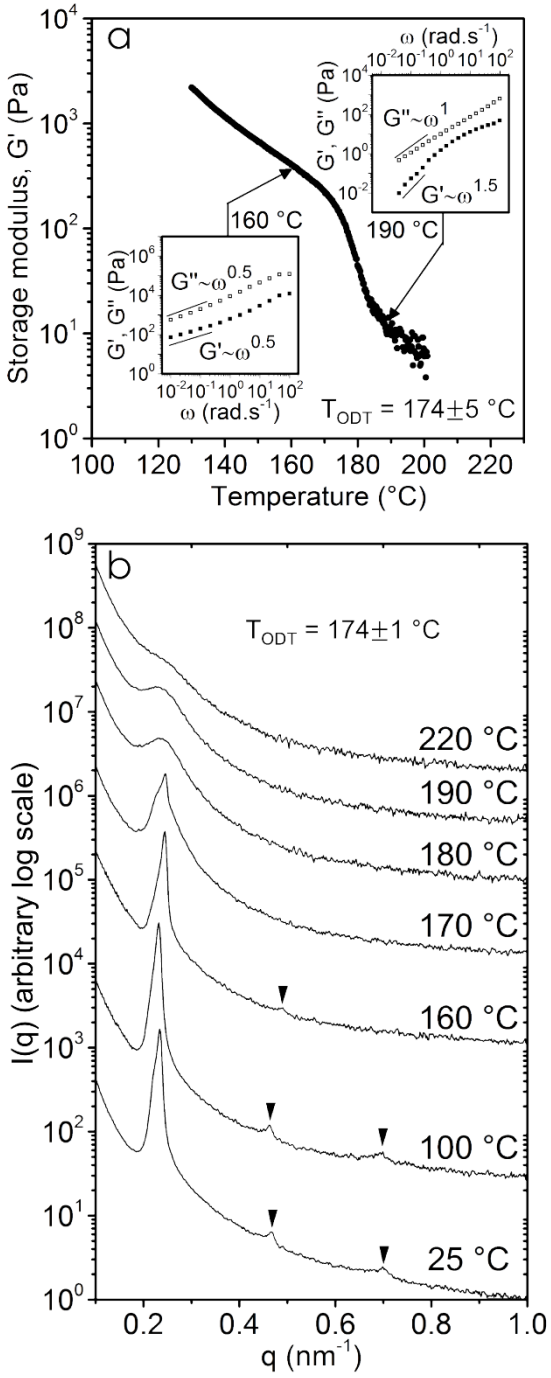

Figure A.5. (a) Temperature dependence of the low-frequency dynamic storage modulus (G') for PLA-17-P(S-*s*-GMA)-11-X_{GMA}-29. Ramp rate = 1 °C min^{-1} (strain, ε = 1%, frequency, ω = 1 rad s^{-1}). Insets: isothermal frequency sweeps (frequency, $0.01 \leq \omega \leq 100$ rad s^{-1}) acquired at 160 and 190 °C. (b) SAXS patterns obtained for PLA-17-P(S-*s*-GMA)-11-X_{GMA}-29. The sample was annealed 2 min at each temperature. For $T < T_{ODT}$, higher ordering peaks are marked by inverse triangles and are consistent with a lamellar morphology.

Figure A.5b illustrates representative small-angle scattering (SAXS) data for PLA-17-P(S-*s*-GMA)-11-X_{GMA}-29 upon heating from 25 to 220 °C. The SAXS pattern acquired at 25 °C exhibits a principal scattering peak $q^* = 0.23$ nm^{-1} and higher order peaks $2q^*$ and $3q^*$ that persist up to 160 °C and are consistent with a lamellar ordering with a domain spacing d = 27 nm. Above 160 °C, the principal scattering peak broadens and a single broad reflection is evident at 180 °C. In a series of related block polymers, we demonstrated that T_{ODT} is a decreasing function of the molar fraction of GMA in the crosslinkable block, X_{GMA}. This trend is consistent with the expectation that inclusion of GMA in the PS block increases its solubility parameter making it more compatible with PLA. We also showed that the tunable nature of T_{ODT} in this new block polymer system allows for independent tuning of the crosslinking temperature and nanodomain size (Figures A.6 and A.7).

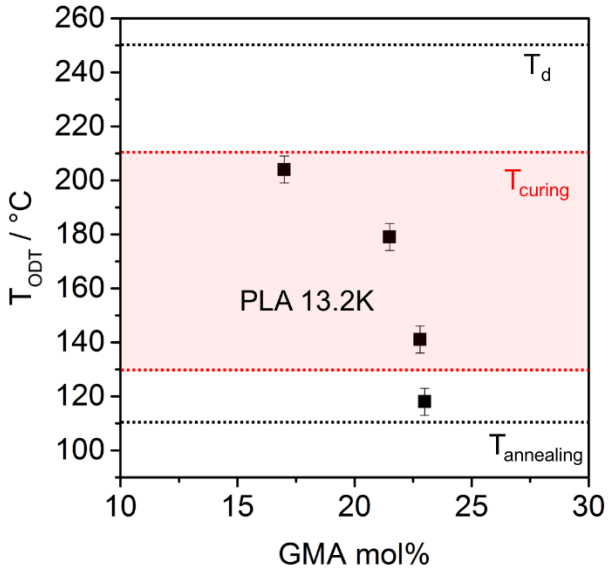

Figure A.6. Plot of the order-disorder transition temperature (T_{ODT}) as a function of the molar percentage of GMA in the crosslinkable block (X_{GMA}) for one representative series of PLA-*b*-P(S-*s*-GMA) obtained from PLA-13.2. The T_{ODT} values were measured by dynamic mechanical analysis. The bottom doted horizontal line indicates the position of the annealing temperature, $T_{annealing}$ = 110 °C. The top doted horizontal line indicates the position of the lowest degradation temperature observed for PLA-*b*-P(S-*s*-GMA), T_d (mass loss > 5% measured by thermogravimetric analysis). T_d ~ 250 °C. The red area indicates the temperature window with viable gel times, t_{gel}: 1 day ≥ t_{gel} ≥ 72 s for 130 °C ≤ T_{curing} ≤ 210 °C.

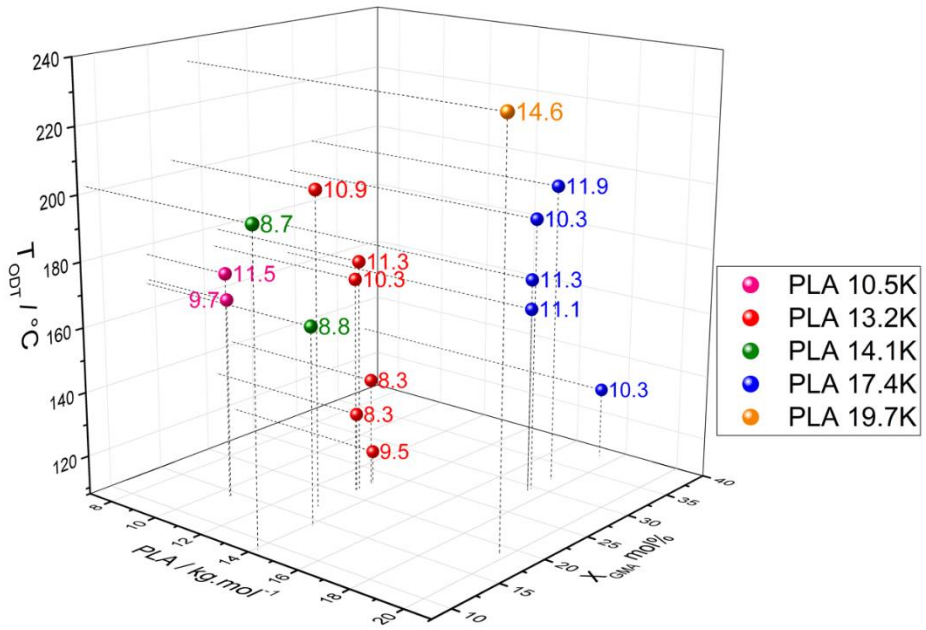

Figure A.7. 3D-plot of the order-disorder transition temperature (T_{ODT}) (*z* axis) as a function of the size of the PLA block (*x* axis) and the molar percentage of GMA in the crosslinkable block (X_{GMA}, *y* axis). The data points are labelled with the size of the P(S-*s*-GMA) block. The T_{ODT}'s were estimated by dynamic mechanical analysis.

A.3.2 Cross-linking in the Vicinity of T_{ODT}

Benzyl triphenylphosphonium hexafluoroantimonate (BTPH, Figure A.1 top)was used to initiate the cationic polymerization of the pendant epoxide moieties.[29] A film was prepared by casting a THF solution of PLA-17-P(S-*s*-GMA)-11-X_{GMA}-29 (24.7wt%) and BTPH (0.3wt%) (dried for 1 d at room temperature and 1 d at 60 °C). The film was annealed at 110 °C for 1 h, and complete removal of THF was confirmed gravimetrically. SEC and SAXS analysis of the initiator-loaded system indicate that the molar mass, dispersity, and morphology of the block polymer were not impacted by these low-temperature drying procedures, (Figure A.8 and A.9). Moreover, variable-temperature SAXS experiments show that the T_{ODT} of PLA-17.4-P(S-s-GMA)-11.3-X_{GMA}-29.2+BTPH0.3wt% (T_{ODT} = 178 °C) is only 4 °C higher than the T_{ODT} of the sample without initiator (T_{ODT} = 174 °C)

(Figure A.10). The T_{ODT} of the initiator-loaded polymer (178°C) is used as the reference T_{ODT} in the remainder of this paper.

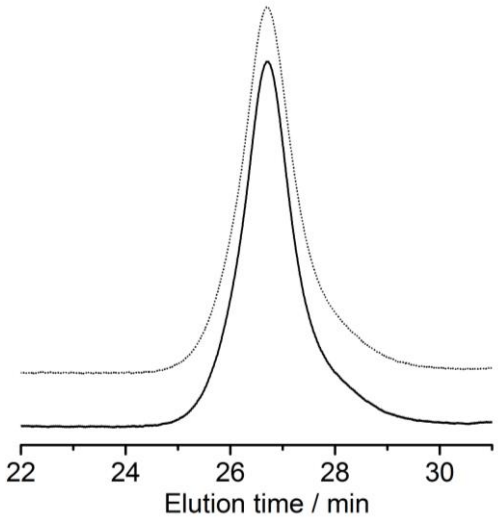

Figure A.8. SEC traces for the neat polymer PLA-17.4-P(S-*s*-GMA)-11.3-X_{GMA}-29.2 (solid line, M_n = 36.3 kg mol^{-1}, $Đ$=1.07) and PLA-17.4-P(S-*s*-GMA)-11.3-X_{GMA}-29.2+BTPH0.3wt% after annealing (dotted line, M_n = 38.1 kg mol^{-1}, $Đ$=1.07).

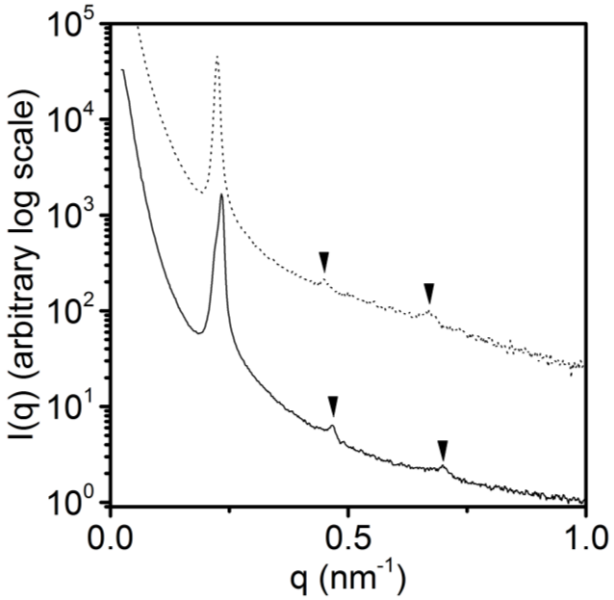

Figure A.9. SAXS patterns for the neat polymer PLA-17.4-P(S-*s*-GMA)-11.3-X_{GMA}-29.2 (solid line, q^* = 0.234 nm^{-1}, $d_{spacing}$= 26.8 nm) and PLA-17.4-P(S-*s*-GMA)-11.3-X_{GMA}-29.2+BTPH0.3wt% after annealing (dotted lines, q^* = 0.226 nm^{-1}, $d_{spacing}$= 27.8 nm).

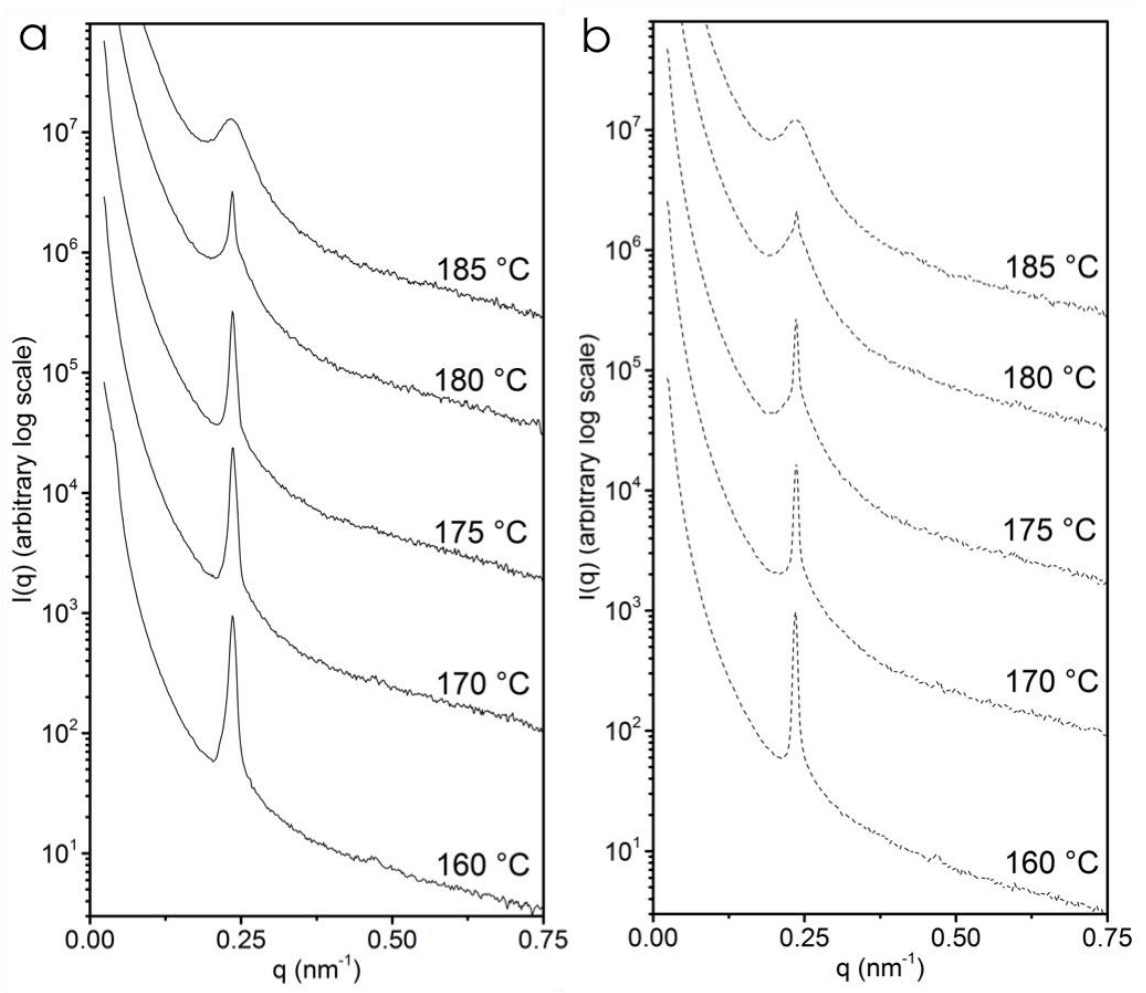

Figure A.10. SAXS patterns acquired at various temperature for PLA-17.4-P(S-*s*-GMA)-11.1-X_{GMA}-29.2 (neat, a) and PLA-17.4-P(S-*s*-GMA)-11.1-X_{GMA}-29.2+BTPH0.3wt% (b).

Initiator-loaded samples were then cured at various temperatures in the proximity of T_{ODT} of PLA-17-P(S-*s*-GMA)-11-X_{GMA}-29+BTPH(0.3wt%). Samples were cured below T_{ODT}, T_{curing} = 160 or 170 °C and above T_{ODT}, T_{curing} = 180, 190, 200, 210 or 220 °C. Curing times (t_{curing}) were chosen based on estimations of the gel times (t_{gel}) through independent rheological measurements (Figures A.11 and A.12, Table A.1, typically we utilized $t_{curing} > 3t_{gel}$). Thermogravimetric analysis was used to demonstrate that the polymer does not

lose significant mass during curing (Figure A.13), and in all cases the gel fraction of the cured samples was > 90% (Table A.2).

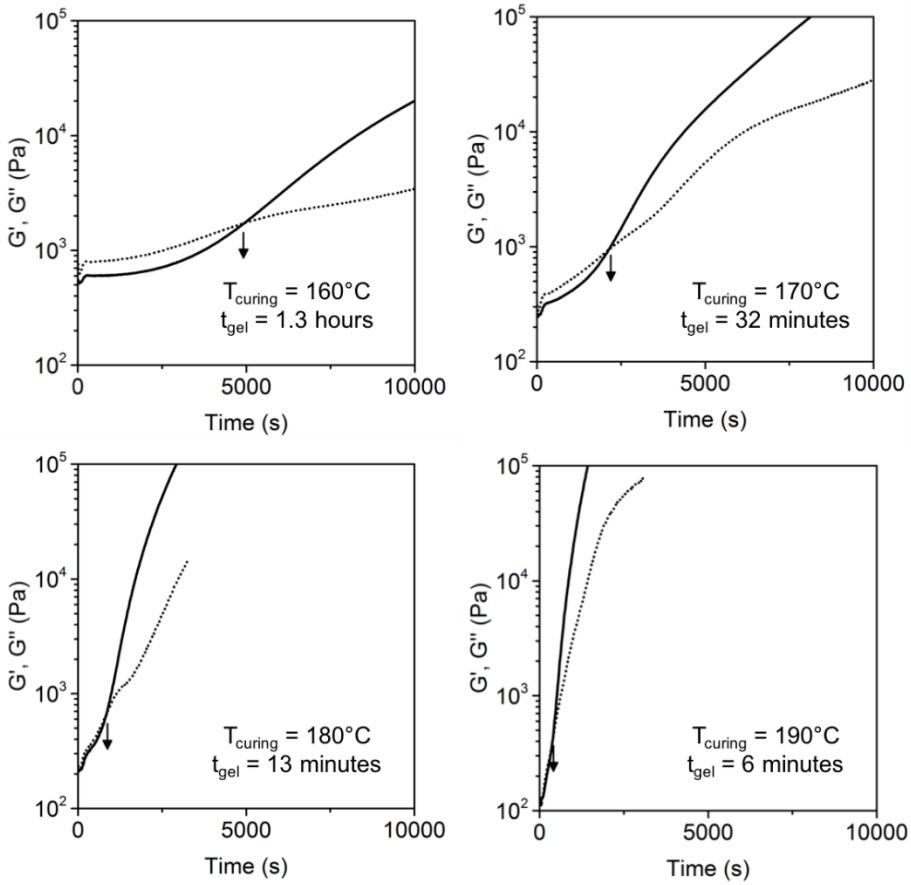

Figure A.11. Plots of the storage and loss moduli, *G*' (solid line) and *G*'' (dotted line), respectively, as a function of time for the curing of PLA-17.4-P(S-*s*-GMA)-11.9-X_{GMA}-32.1+BTPH0.3wt% at four different temperatures (ω = 1 rad s^{-1}, ε = 1%). The vertical arrows indicate the point of crossover of *G*′ and *G*″ used as an estimation of t_{gel}.

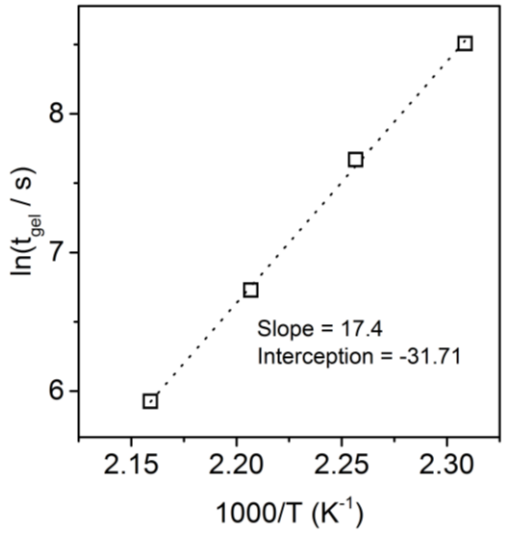

Figure A.12. Arrhenius plot of ln(t_{gel}) (t_{gel} in seconds) as a function of 1000/T (T in Kelvin) for the system PLA-17.4-P(S-*s*-GMA)-11.9-X_{GMA}-32.1+BTPH0.3wt%.

Table A.1. Gel times, t_{gel}, for PLA-17.4-P(S-*s*-GMA)-11.9-X_{GMA}-32.1+BTPH0.3wt% at various curing temperatures.

Curing temperature (°C)	t_{gel} determined by rheological measurements	t_{gel} extrapolated using Arrhenius parameters	t_{curing}
25	-	$12x10^3$ y	-
110	-	10.3 d	-
120	-	3.3 d	-
130	-	1.1 d	3 d
140	-	9.2 h	35 h
150	-	3.4 h	10 h
160	1.3 h	-	4 h
170	32 min	-	3 h
180	13 min	-	2 h
190	6 min	-	1.5h
200	-	2.6 min	1h
210	-	1.2 min	30 min
220	-	34 s	30 min

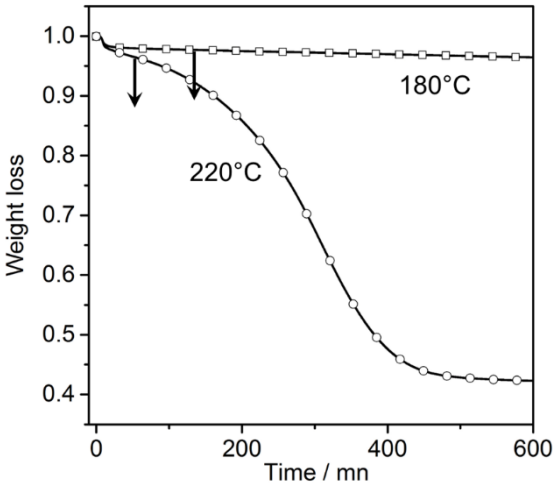

Figure A.13. Thermogravimetric analysis during heat and hold experiments for PLA-17.4-P(S-*s*-GMA)-11.3-X_{GMA}-29.2+BTPH0.3wt% at two different temperatures: 180 °C and 220 °C. The vertical arrows indicate the typical curing time, t_{curing}, corresponding to these curing temperatures.

Table A.2. Curing times (t_{curing}) and gel fractions for the crosslinking of PLA-17.4-P(S-*s*-GMA)-11.1-X_{GMA}-29.2+BTPH0.3wt% and PLA-17.4-P(S-*s*-GMA)-11.3-X_{GMA}-29.2+BTPH0.3wt% at different temperatures, T_{curing}.

T_{curing} (°C)	PLA-17.4-P(S-*s*-GMA)-11.1-X_{GMA}-29.2		PLA-17.4-P(S-*s*-GMA)-11.3-X_{GMA}-29.2	
	t_{curing} (h)	Gel fraction (%)	t_{curing} (h)	Gel fraction (%)
160	5.5	98	5	96
170	5.4	100	3.5	97
175	2	100	-	-
180	2	100	2	99
190	2.5	100	2.5	100
200	-	-	1	99
210	-	-	1.5	100
220	-	-	1.5	100

The cured samples were first characterized by SAXS experiments at room temperature. For T_{curing} = 160 °C or 18 °C below T_{ODT} ($\Delta T = T_{curing} - T_{ODT} = -18$ °C) the room temperature SAXS pattern exhibits a single sharp scattering peak (q^*) and two higher order peaks ($2q^*$

and 3q^*) indicating that a lamellar microstructure is kinetically trapped during the curing step (Figure A.14a, solid line). At T_{curing} = 190 °C or 12 °C above T_{ODT} (i.e., ΔT = +12 °C), a single broad reflection peak is consistent with a microphase-separated, but disorganized, structure (Figure A.14b, solid line). These room temperature SAXS data are consistent with the SAXS data for the initiator-free system acquired at temperatures corresponding to the curing conditions (see Figure A.5b).

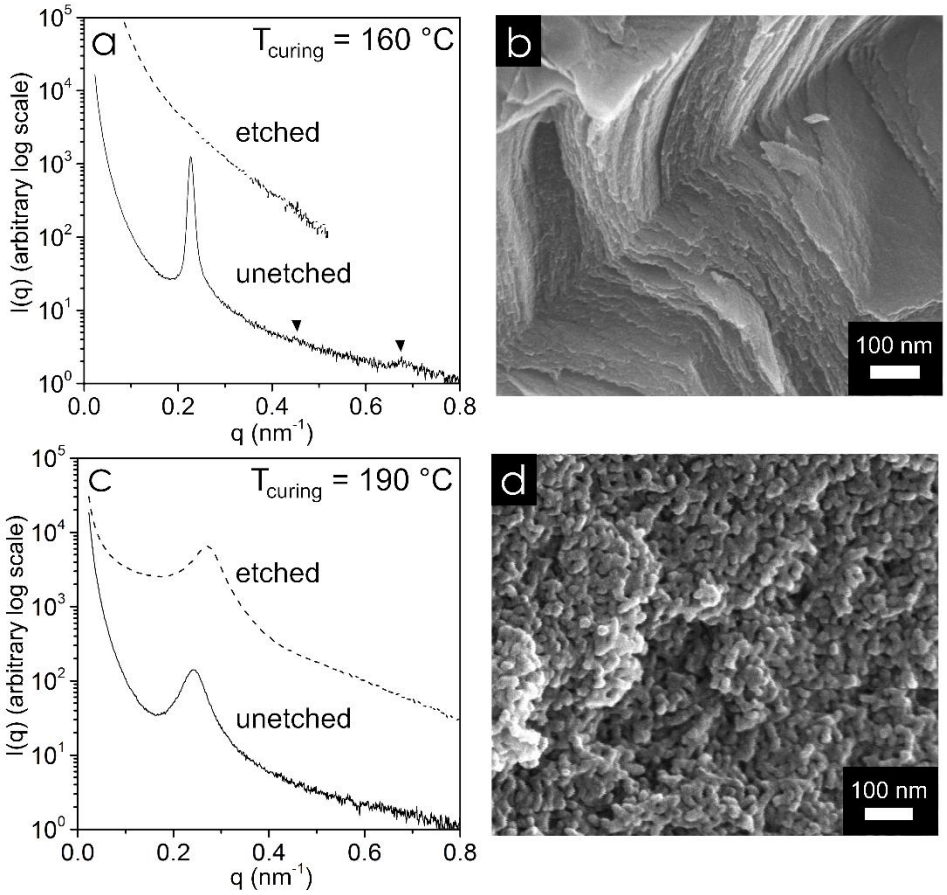

Figure A.14. Characterization of the structure of the materials obtained by curing PLA-17-P(S-*s*-GMA)-11-X_{GMA}-29+BTPH(0.3wt%) (T_{ODT} = 178 °C) at two different temperatures: T_{curing} = 160 °C (t_{curing} = 4 h) (a and b) and T_{curing} = 190 °C (t_{curing} = 1 h) (c and d) (a) SAXS pattern acquired at room temperature for the sample cured at 160 °C before (solid line) and after (dashed line) etching in a basic solution. (b) Representative SEM image of a cryo-fractured surface coated with Pt (~2nm) for the sample cured at 160 °C after etching in a basic solution. (c) and (d) represent the corresponding SAXS patterns and SEM image for the sample crosslinked at T_{curing} = 190 °C.

For the sample crosslinked in the ordered state at 160 °C, variable temperature SAXS experiments show that the microstructure remains ordered at temperatures as high as 250 °C, i.e., higher than the T_{ODT} of the original non-crosslinked system (Figure A.15). For $T < T_{ODT}$, the sample crosslinked in the disordered state is unable to recover lamellar ordering post-crosslinking even after thermal annealing at 120 °C (i.e., well below the original T_{ODT}) for 15 h (Figure A.16). Together, these observations confirm that the microstructure adopted at the curing temperature is kinetically and irreversibly trapped. In both cases the domain spacing is only slightly affected by the curing reaction (within 8% of spacing prior to curing, Figure A.5). For most other curing temperatures the SAXS results correlate well with the observations made for T_{curing} = 160 °C when $\Delta T < 0$ and for T_{curing} = 190 °C when $\Delta T > 0$ (see Figure A.17). A notable exception is the sample cured at 180 °C where the SAXS pattern exhibits a sharp principle scattering peak despite a curing temperature above the T_{ODT} of the uncrosslinked system. This unexpected behavior is attributed to its close proximity to the T_{ODT} (ΔT = +2 °C).

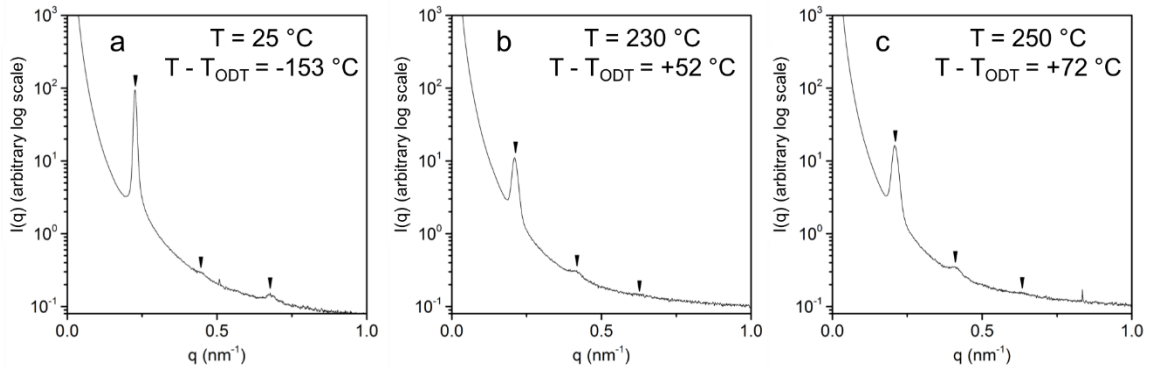

Figure A.15. Variable temperature SAXS patterns for a sample of PLA-17.4-P(S-*s*-GMA)-11.1-X_{GMA}-29.2+BTPH0.3wt% previously crosslinked at T_{curing} = 160 °C (5 h), i.e. below T_{ODT} (T_{curing}-T_{ODT} = -18 °C). (a) SAXS pattern acquired at T = 25 °C (T is the temperature used for the SAXS measurement), T- T_{ODT} = -153 °C, where T_{ODT} is the T_{ODT} of the pristine polymer (i.e., PLA-17.4-P(S-*s*-GMA)-11.1-X_{GMA}-29.2+BTPH0.3wt% prior to curing). (b) SAXS pattern acquired at T = 230 °C, T- T_{ODT} = +52 °C (c) SAXS pattern acquired at T = 250 °C, T- T_{ODT} = +72 °C. For (b) and (c), SAXS pattern are acquired at temperatures that are well above the T_{ODT} of the pristine polymer.

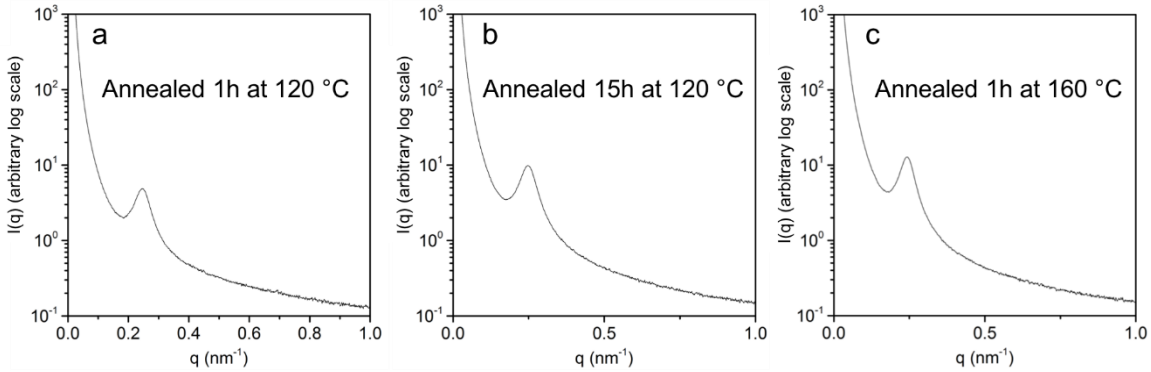

Figure A.16. SAXS patterns acquired at room temperature for three samples of PLA-17.4-P(S-*s*-GMA)-11.1-X_{GMA}-29.2+BTPH0.3wt% cured at T_{curing} = 190 °C for 2.5 h, i.e. for T_{curing} - T_{ODT} = +12 °C. (a) The crosslinked sample was annealed at 120 °C for 1 hour prior to the SAXS measurement, (b) The crosslinked sample was annealed at 120 °C for 15 hours prior to the SAXS measurement (c) The crosslinked sample was annealed at 160 °C for 1 hour prior to the SAXS measurement.

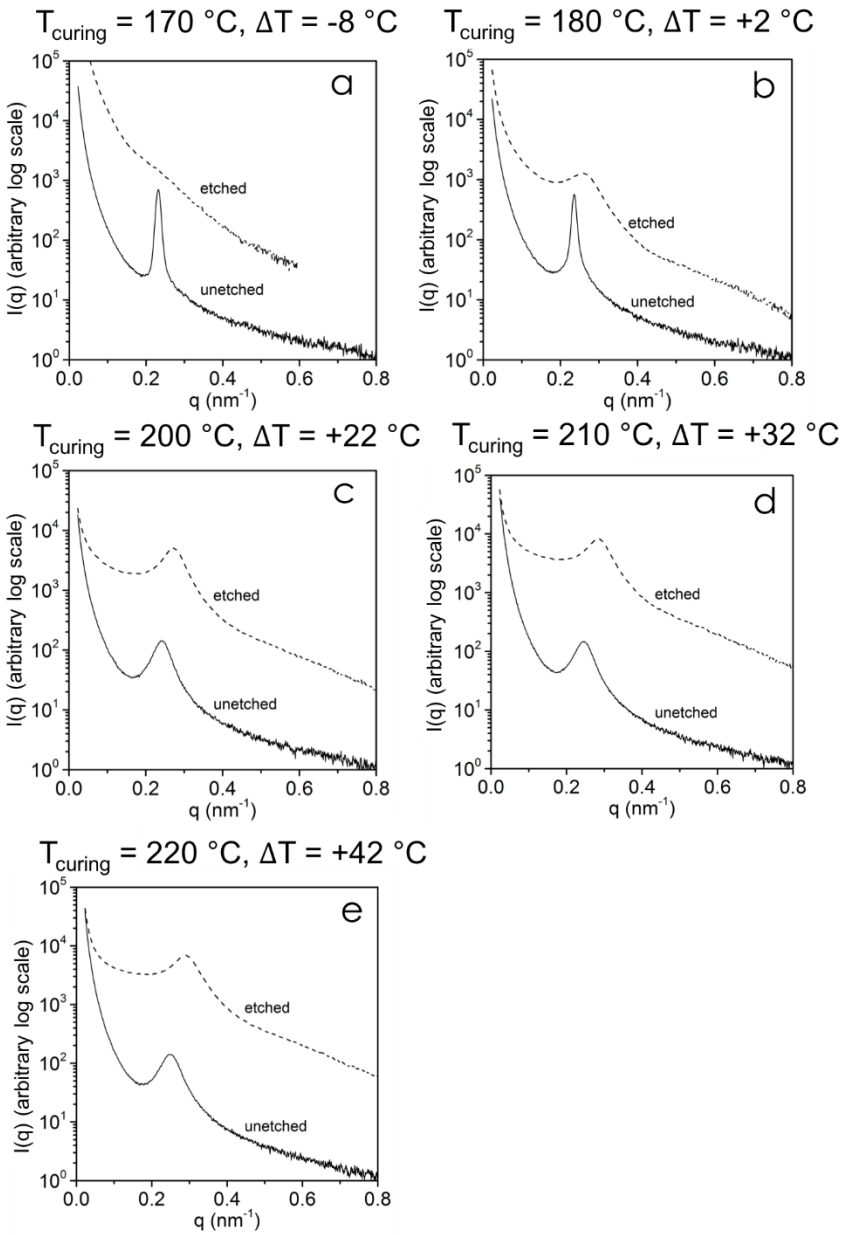

Figure A.17. SAXS pattern acquired at room temperature before (solid line) and after (dashed line) etching in a basic solution, for samples of PLA-17.4-P(S-*s*-GMA)-11.3-X_{GMA}-29.2+BTPH0.3wt% cured at various temperatures.

The PLA was subsequently removed in the cured samples by immersing the monoliths in a 0.5 M methanol (40% by volume)/water solution of NaOH. Complete removal of PLA was confirmed by gravimetric analysis with a mass loss in close agreement with the weight fraction of PLA in the block polymer, the absence of the PLA C=O vibration by IR

spectroscopy (Figure A.18). The removal of PLA was accompanied by a dramatic change of the SAXS pattern of the samples crosslinked below T_{ODT} ($\Delta T < 0$) with a total loss of the scattering characteristic of the lamellar ordering, likely due to the collapsing of the nanoporous structure (T_{curing} = 160 °C, ΔT = –18 °C, Figure A.14a, dashed line and T_{curing} = 170 °C, ΔT = –8 °C, Figure A.17a), consistent with previous reports of partial collapsing in nanoporous lamellar microstructure.[30, 31] Conversely, for all the samples crosslinked above 180 °C, the SAXS patterns retain a broad reflection post etching consistent with a disordered structure (T_{curing} = 190 °C, ΔT = +12 °C, Figure A.14c, dashed line and T_{curing} = 200 °C, 210 °C and 220 °C, ΔT = +22 °C, +32 °C, +42 °C, Figure A.17c–A.17e) and the domain spacing is within 9–14% of the spacing prior to etching. The dramatic difference in stability for the porous microstructures obtained from samples crosslinked above and below T_{ODT} is likely due to a difference in terms of continuity of their porous network. Indeed, while the etched lamellar structures result in large 2-dimensional sheets that are only separated by voided domains and eventually collapse,[30] bicontinuous network structures (e.g., gyroid[32] or samples from PIMS,[13] RCENs,[16] and bicontinuous microemulsions[33]) are known for providing three-dimensional structures that percolate the entire sample and are stable provided that their thermal and mechanical properties are appropriate. Thus, the SAXS results for the etched material shown in Figure A.5c are consistent with a cured sample with bicontinuous domains: one consisting of mesopores and one of the crosslinked P(S-*s*-GMA) polymer.

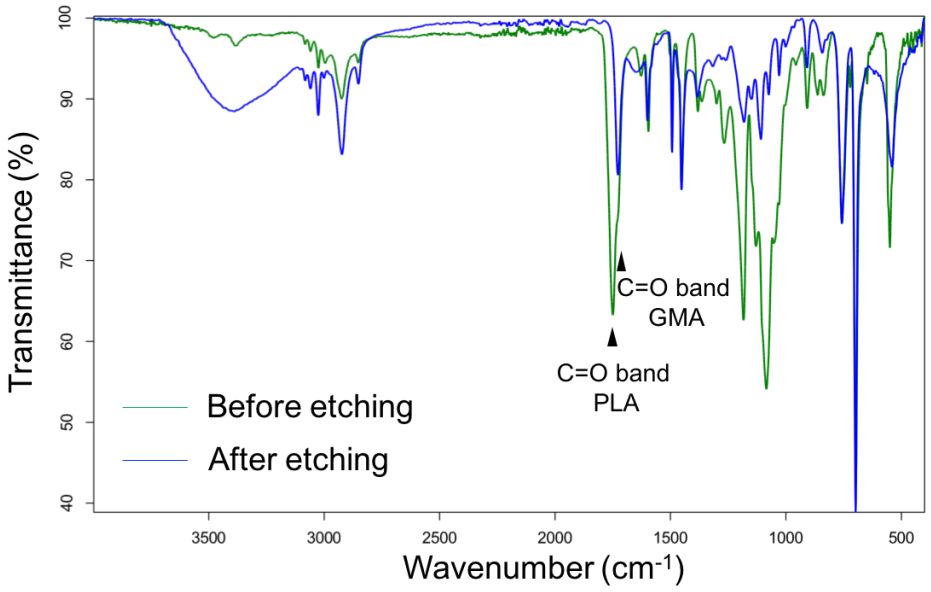

Figure A.18. IR spectra for a PLA-17.4-P(S-*s*-GMA)-11.3-X_{GMA}-29.2+BTPH0.3wt% monolith cured at 190 °C, before and after etching.

Scanning electron microscopy (SEM) observations of cryo-fractured and coated (Pt, ~ 2nm) surfaces of the samples are consistent with the results obtained from SAXS experiments. In agreement with the lamellar ordering indicated by the SAXS patterns in Figure A.14a, sheet-like and evidently collapsed layered objects are observed in Figure A.14b for the sample cured at T_{curing} = 160 °C (ΔT = –18 °C). The SEM image is also consistent with the lack of strong scattering in Figure A.14a for the etched sample. Similar images were obtained at T_{curing} = 170 °C (See Figure A.19a). For the sample cured at T_{curing}= 190 °C (ΔT = +15 °C) the SEM micrograph clearly reveals a nanoporous structures with interconnected pores homogeneously distributed throughout the material. Similar images were obtained for other curing temperatures above the ODT (see Figures A.19c–A.19e for T_{curing} = 200, 210 and 220 °C). This structure closely resembles the morphologies of other polymeric materials with percolating nanoporous network obtained from PIMS[13] and

RECNs[16] or using polymeric bicontinuous microemulsion.[33] This supports well the idea that the morphology of the disordered state of a symmetric diblock polymer is truly bicontinuous.

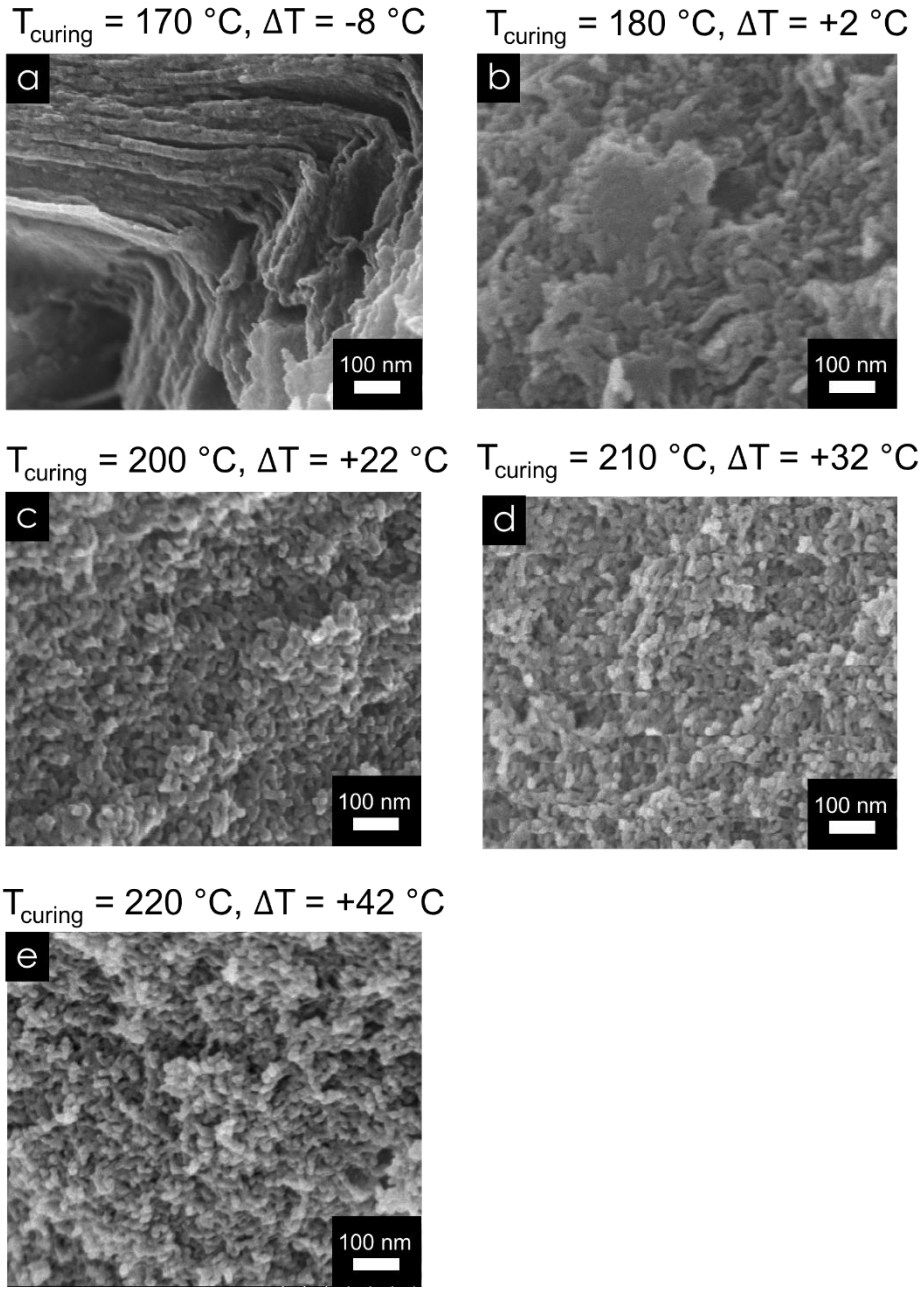

Figure A.19. Representative SEM image of cryo-fractured surfaces coated with Pt (~2nm) for samples of PLA-17.4-P(S-*s*-GMA)-11.3-X_{GMA}-29.2+BTPH0.3wt% cured at various temperatures in the vicinity of T_{ODT} and etched in a basic solution.

Transmission electron microscopy (TEM) of a microsection of porous sample cured at 190 °C is also consistent with a homogeneous disordered network of pores (Figure A.20). The bicontinuity of the nanostructure was further assessed using TEM tomography.[34] A tilt series of TEM micrographs of the same sample was collected for a layer-by-layer reconstruction of the 3D structure (Figure A.21). The tomogram reveals a network of highly branched channels that traverse the thickness of the sample and supports the idea of a bicontinuous network of pores. A computational reconstruction of the volume also confirms that the porous domains are highly interconnected (Figure A.22).

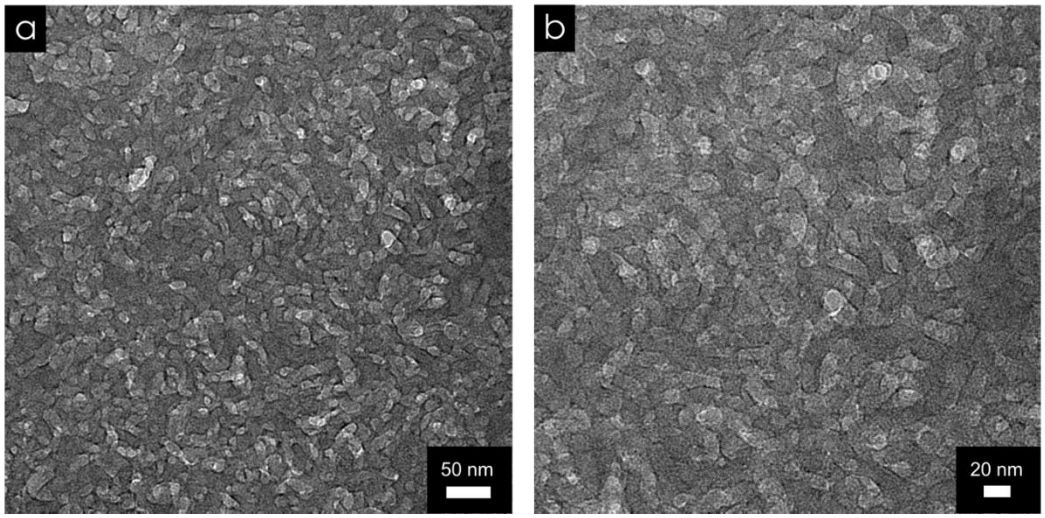

Figure A.20. Transmission electron microscopy (TEM) images of PLA-17.4-P(S-*s*-GMA)-11.3-XGMA-29.2+BTPH0.3wt% crosslinked at 190 °C and etched with a basic solution. The P(S-*s*-GMA) phase is dark, the porous phase is bright. Samples were cryo microtomed at −120 °C. The specimen was examined using a Tecnai TF30 300 kV FEG (FEI-Company, Hillsboro, OR, and Eindhoven, The Netherlands) at (a) 78,000x and (b) 93,000x nominal magnifications.

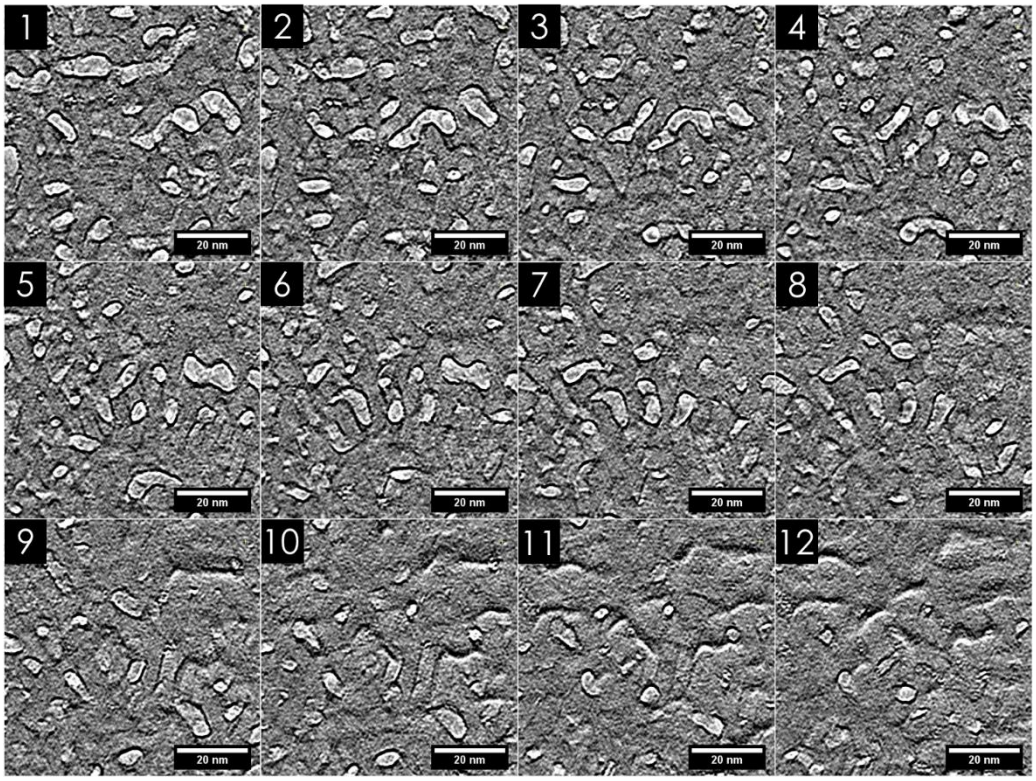

Figure A.21. Snapshots of slices of the reconstructed tomogram of PLA-17.4-P(S-*s*-GMA)-11.3-XGMA-29.2+BTPH0.3wt% crosslinked at 190 °C and etched with a basic solution. The montage comprises every 5th slice from the 60 slice reconstruction. The images are numbered in order of appearance as we go through the thickness of the sample. Note: As the edges of the sample are approached in the 3D reconstruction, there is a noticeable decrease in the clarity of the images (in particular, images 9 to 12) likely as a result of inhomogeneities in the thickness of the sample microsection as well as missing information due to the "missing wedge" phenomenon. Scale bars are 20 nm.

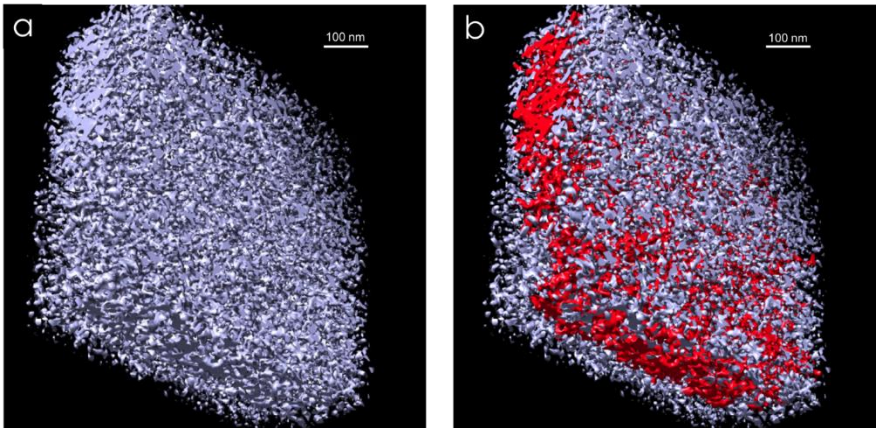

Figure A.22. Volume rendering performed in UCSF Chimera by applying a 3D Gaussian filter to the tomogram of PLA-17.4-P(S-*s*-GMA)-11.3-XGMA-29.2+BTPH0.3wt% crosslinked at 190 °C and etched with a basic solution. Pores are colored blue while the cross-linked P(S-*s*-GMA) matrix is transparent. In (b), we used the "color blob tool" to highlight a channel of pores. This channel spans the samples and is consistent with a percolating morphology.

A.3.3 Determination of Pore Continuity

Nitrogen sorption was further used to quantitatively analyze the porosity. As expected from their collapsed lamellar structures, the samples crosslinked below T_{ODT} ($\Delta T < 0$ °C) exhibit essentially featureless nitrogen adsorption isotherms (Figure A.23a–A.23b) indicating that the materials are not porous. For all the curing temperatures above T_{ODT} ($\Delta T > 0$ °C), the materials produced type IV isotherms with H2 hysteresis (Figure A.23c–A.23g). This again supports the idea that the porous structures associated with composition fluctuations in the disordered state are bicontinuous. For T_{curing} ranging from 190 to 220 °C (12 °C $\leq \Delta T \leq$ 42 °C), the pore size distributions, modeled using the adsorption branch of the isotherms and a quenched solid density functional theory kernel (QSDFT),[35] are monomodal with a sharp peak centered on 10 nm (Figure A.24). This correlates well with the values of the domain spacing determined by SAXS $d \sim 22$ nm and the overall volume fraction of the sacrificial PLA domains of 54%.

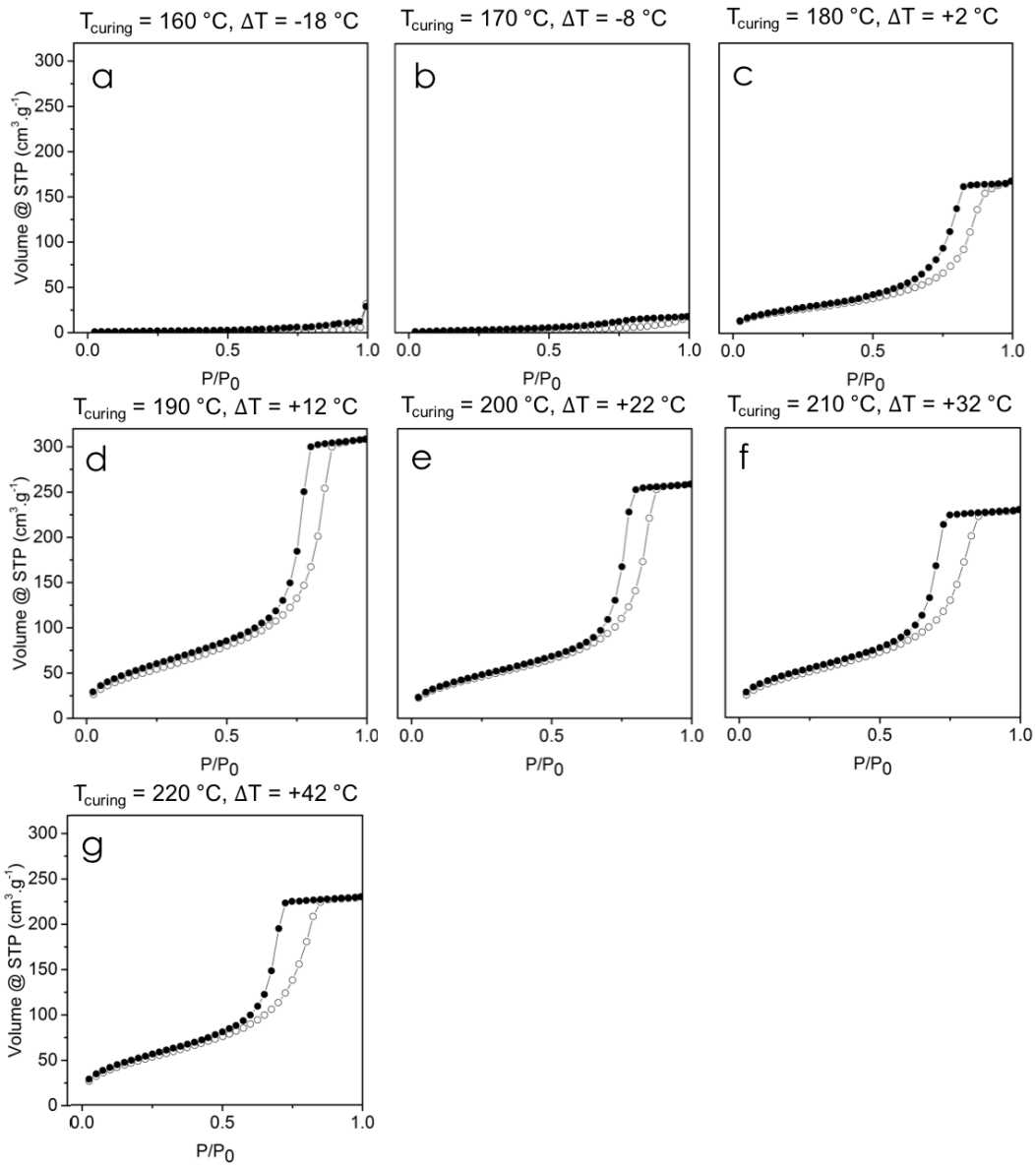

Figure A.23. Nitrogen sorption isotherm for samples of PLA-17.4-P(S-*s*-GMA)-11.3-X_{GMA}-29.2+BTPH0.3wt% cured at various temperatures and etched in a basic solution. Open circles (○) correspond to the adsorption branch and filled circles (●) to the desorption branch.

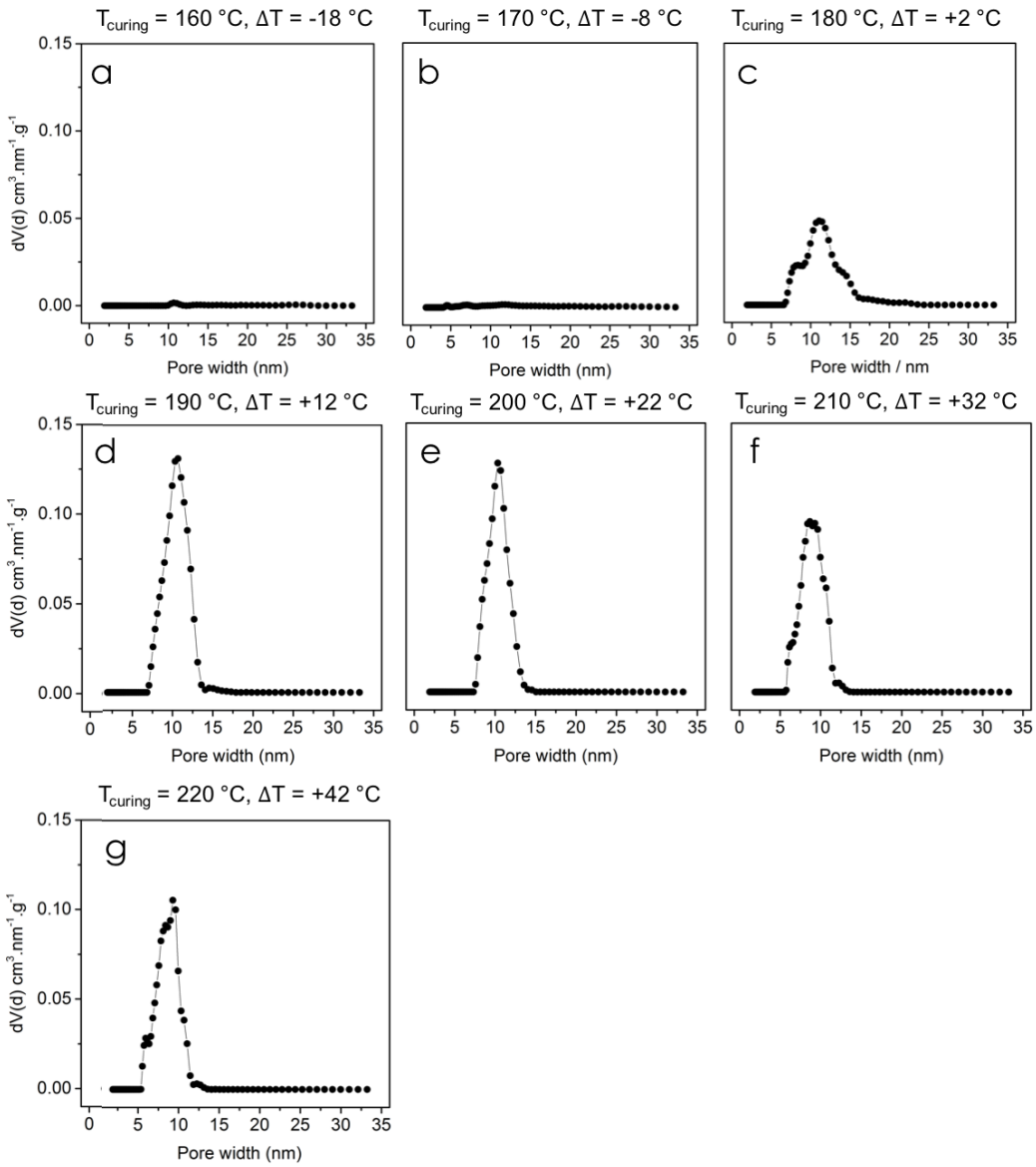

Figure A.24. Mesopore size distributions based on QSDFT analysis of the adsorption branch for samples of PLA-17.4-P(S-*s*-GMA)-11.3-X_{GMA}-29.2+BTPH0.3wt% cured at various temperatures and etched in a basic solution.

Figure A.25 represents the pore volume determined at P/P_o = 0.95 as well as the surface area estimated by a Brunauer-Emmett-Teller (BET) analysis as a function of $\Delta T = T_{curing} - T_{ODT}$, i.e. the relative distance between the curing conditions and the ODT in °C.[36] Maxima in both sets of data are reached for T_{curing} = 190 °C with a total pore volume of 0.47 $cm^3\ g^{-1}$ and an estimated surface area of 190 $m^2\ g^{-1}$. These values are essentially the same at

higher curing temperature. The material cured at 180 °C exhibits a low total pore volume of 0.22 cm^3 g^{-1} and a surface area of 90 m^2 g^{-1}. Again, this is attributed to the close proximity to the T_{ODT} (ΔT = +2 °C, see Figure A.23c and A.24c).

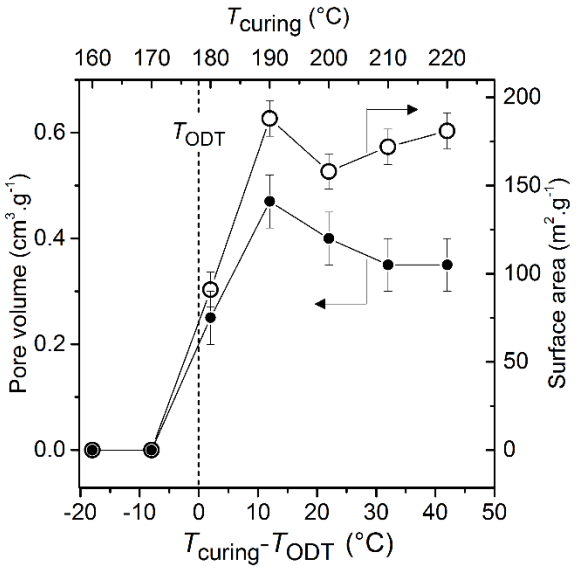

Figure A.25. Plot of the pore volume (filled squares) and the surface area (empty squares) as a function of $\Delta T = T_{curing} - T_{ODT}$, for PLA-17-P(S-*s*-GMA)-11-X_{GMA}-29+BTPH(0.3wt%) crosslinked at seven different temperatures (T_{curing} = 160, 170, 190, 200, 210 and 220 °C). The cured samples are subsequently etched in a basic solution and characterized by nitrogen sorption experiments. The pore volumes are determined at P/P_o = 0.95 and the surface areas are estimated based on a Brunauer-Emmett-Teller (BET) analysis.

A.3.4 Fabrication of Ultrafiltration Membranes

The system described in this report provides nanoporous material with narrow pore size distribution while retaining all of the processability advantages associated with polymeric materials. In particular, it can be solution processed to fabricate nanoporous thin film membranes that have the potential to combine both high flux and high size selectivity, two appealing attributes for ultrafiltration applications.[37] To demonstrate this, a 8 wt.% solution of PLA-17-P(S-*s*-GMA)-11-X_{GMA}-29+BTPH(0.3wt%) in chlorobenzene was coated onto a water-filled polyethersulfone (PES) membrane (pore diameter ~ 100 nm) using a wire-wound rod.[38] The resulting film was dried and cured above T_{ODT} (T_{curing} = 190 °C, Figure

A.26 top, see the supporting information for experimental details). After selective etching of PLA, SEM imaging of the composite membrane demonstrates that the crosslinked polymer form a ~500 nm homogeneous layer (Figure A.27) that efficiently covers the pores of the PES support (Figure A.26a and A.26b).

Pure water permeability of the composite membrane was determined to be 7 L m^{-2} h^{-1} bar^{-1} based on a linear fit of flux vs. ΔP (Figure A.28). The possibility to use the membrane for water ultrafiltration was first investigated by measuring the rejection of a solute with a hydrodynamic radius, R_h, greater than the dimensions expected for the pores of the selective layer. Based on the average pore radius measured by N_2 sorption for porous monoliths obtained from the corresponding polymer (~ 5 nm), we used a 0.5 mg mL^{-1} solution of TRITC-Dextran (M_w = 155 kDa, R_h ~ 7 nm), a polysaccharide labeled with a fluorescent dye.[39] UV-Vis analysis of the filtrate passed through the membrane demonstrates that 98% of the solute was rejected (Figure A.26c). The same polymer was also spin coated onto the PES membrane to provide a thinner selective layer (150 nm, Figure A.29) resulting in a significantly higher flux (196 L m^{-2} h^{-1} bar^{-1}, Figure A.30) and only a slight decrease of the TRITC-Dextran rejection (96%, Figure A.31).

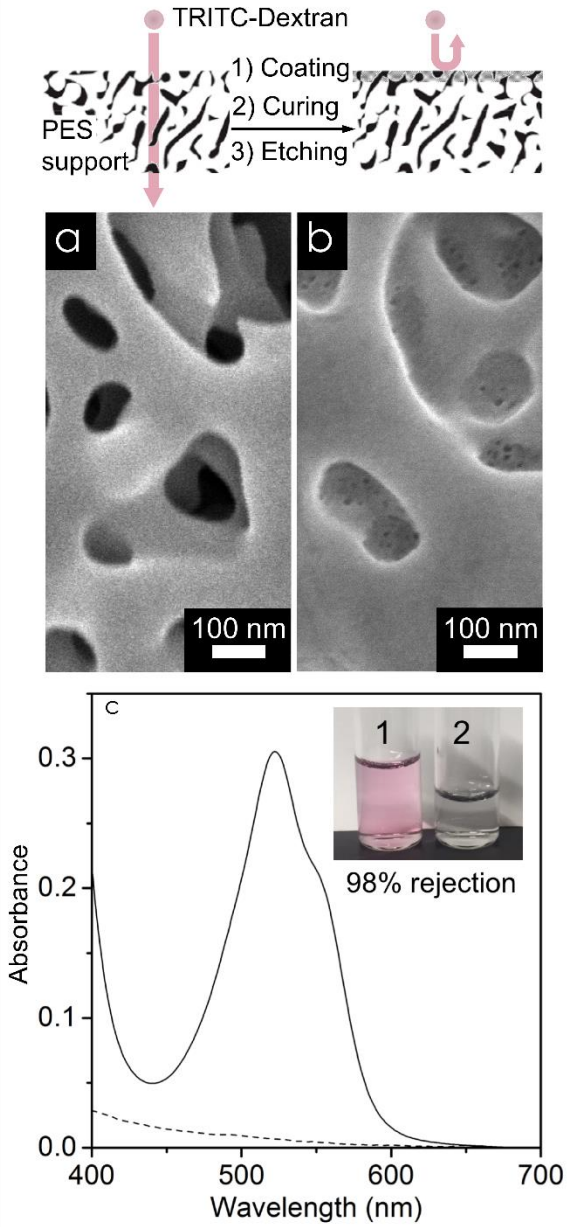

Figure A.26. Characterization of the composite membrane obtained by coating a 8 wt.% solution of PLA-17-P(S-*s*-GMA)-11-XGMA-29+BTPH(0.3wt%) (T_{ODT} = 178 °C) in chlorobenzene onto a PES support membrane followed by curing at T_{curing} = 190 °C and etching with a basic solution. The strategy employed for the design of the membrane and the rejection experiments is represented at the top. (a) SEM micrograph of the bare PES support membrane, (b) SEM micrograph of the nanoporous selective layer obtained after coating the PES support with PLA-17-P(S-*s*-GMA)-11-XGMA-29+BTPH(0.3wt%) followed by curing at T_{curing} = 190 °C and PLA etching (c) UV-vis absorbance results for the feed solution (solid line) of fluorescent TRITC-Dextran (0.5 mg mL^{-1}, M = 150 kg mol^{-1}, R_h ~ 7 nm) and the filtrate (dashed line) obtained after passing the feed solution through the composite membrane. Rejection was calculated as 98% based on the ratio of the absorbance of the feed solution to the absorption of the filtrate at 521 nm. Photographs of the feed solution (1) and the filtrate (2) are included in the inset.

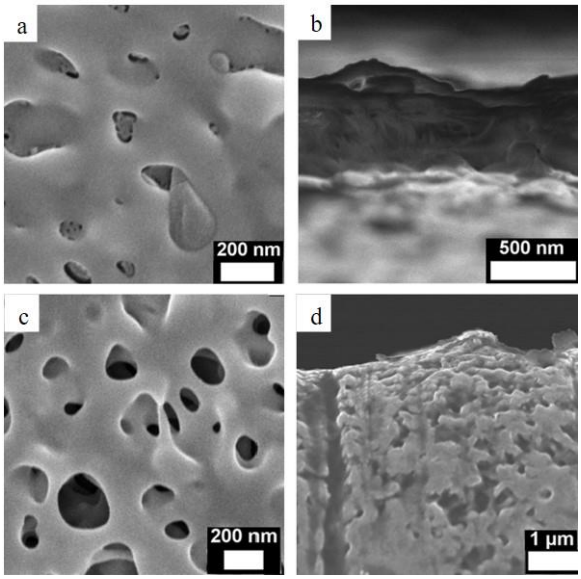

Figure A.27. Top (a) and cross-sectional (b) views of the PLA-17.4-P(S-*s*-GMA)-11.3-X_{GMA}-29.2+BTPH0.3wt% selective layer coated from an 8 wt.% solution in chlorobenzene using a wire-wound rod. Top (c) and cross-sectional (d) images of a bare PES support subjected to the same thermal processing parameters (1 h heating at 190 °C) are included for comparison.

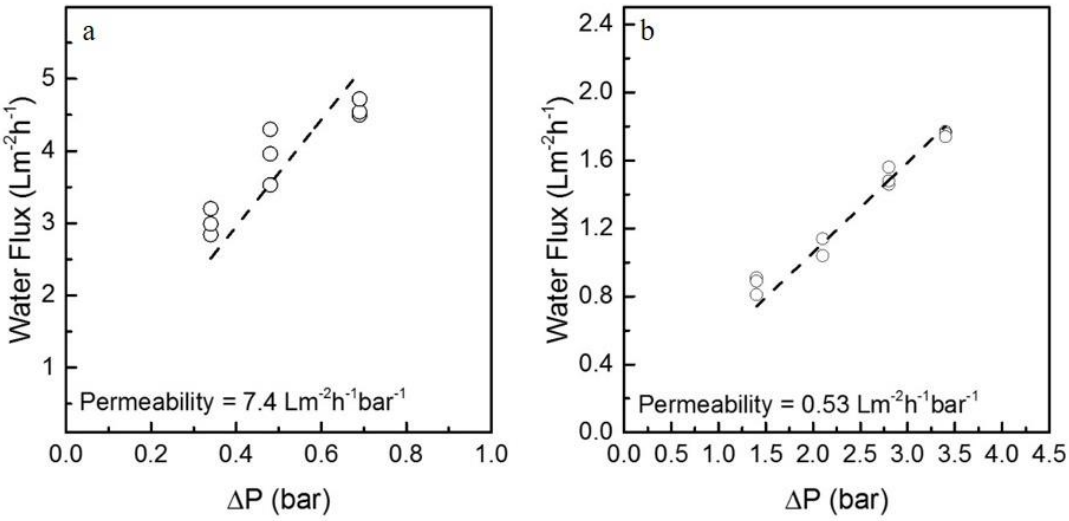

Figure A.28. Water flux for 500 nm P(S-*s*-GMA)-*b*-PLA selective layer on a PES was measured at three different pressure drops in triplicate before (a) and after (b) challenging with Dextran solutions. Pure water permeability was calculated via a linear fit of water flux vs. pressure difference. A significant reduction in permeability was observed after passing a Dextran solution through the membrane likely due to fouling. Additionally, the selective layer was shown to be mechanically stable at the highest pressure difference permitted by the UF cell, 3.4 bar. The specifications for the UF cell prevented the investigation of higher pressures.

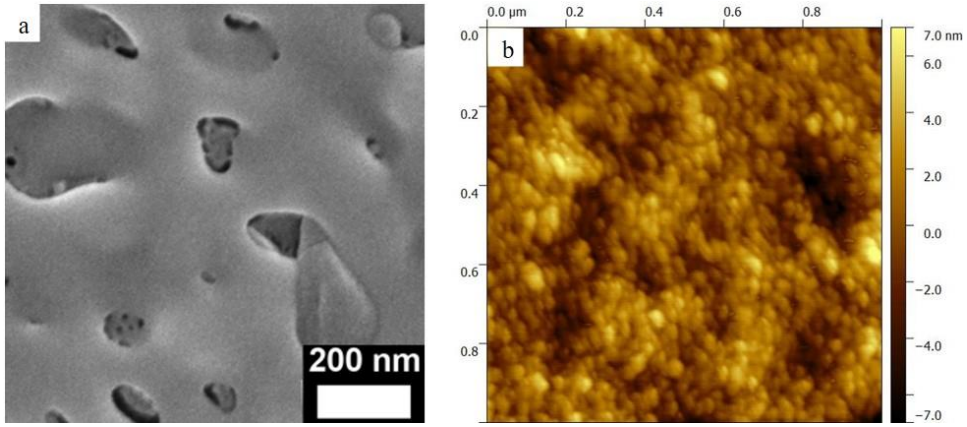

Figure A.29. SEM image of the top surface (a) for a PLA-17.4-P(S-*s*-GMA)-11.3-X_{GMA}-29.2+BTPH0.3wt% membrane spin coated at 1500 rpm from a 2 wt.% solution in chlorobenzene onto a PES support. An AFM phase image (b) for an analogous film spin coated onto an HMDS-modified Si wafer.

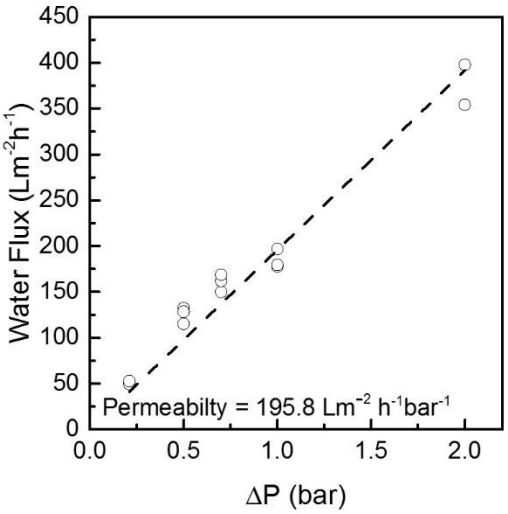

Figure A.30. Pure water permeability for a PLA-17.4-P(S-*s*-GMA)-11.3-X_{GMA}-29.2+BTPH0.3wt% membrane spin coated at 1500 rpm from a 2 wt.% solution in chlorobenzene was calculated as 195.8 L m^{-2} h^{-1} bar^{-1} based on a linear fit of water flux vs. pressure difference.

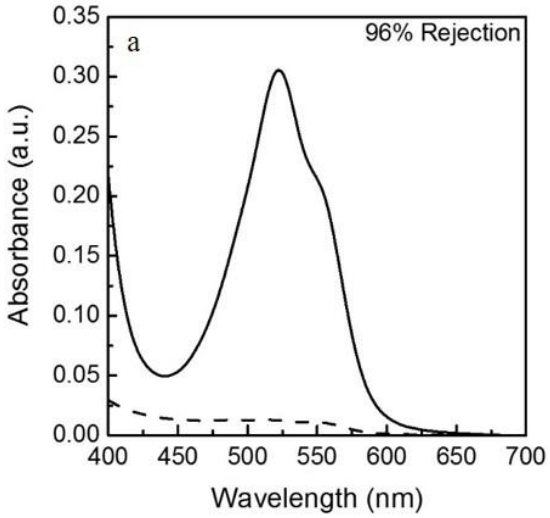

Figure A.31. Rejection experiments for a PLA-17.4-P(S-*s*-GMA)-11.3-X_{GMA}-29.2+BTPH0.3wt% membrane spin coated at 1500 rpm from a 2 wt.% solution in chlorobenzene. Rejection of a TRITC-Dextran standard (M = 150 kg mol^{-1}, R_h ~ 7 nm) was calculated as 96% using UV-Vis.

A.4 Conclusions

In this work we demonstrate that the ODT of a diblock polymer comprised of a crosslinkable block and an etchable block can be used to design new mesoporous materials with narrow pore size distributions and high surface to volume ratios. The characterization of the porous structure provides an unprecedented set of data confirming that the morphology of the disordered state is microphase separated and bicontinuous over a large sample area. The solution processability of the proposed system was demonstrated by directly coating the crosslinkable diblock on top of a commercial PES membrane. After curing and etching, the resulting composite membrane exhibits high permeability and sharp molecular weight cut-off that are suited for the ultrafiltration of water. Together with the chemical tunability of block polymers and the variety of crosslinking reactions available in thermoset technology, this new strategy may have utility for a large spectrum of advanced applications.

A.5. References

1) Akthakul, A.; Salinaro, R. F.; Mayes, A. M., Antifouling polymer membranes with subnanometer size selectivity. *Macromolecules* **2004,** *37*, 7663-7668.

2) Rolison, D. R., Catalytic nanoarchitectures - The importance of nothing and the unimportance of periodicity. *Science* **2003,** *299*, 1698-1701.

3) Schulze, M. W.; McIntosh, L. D.; Hillmyer, M. A.; Lodge, T. P., High-Modulus, High-Conductivity Nanostructured Polymer Electrolyte Membranes via Polymerization-Induced Phase Separation. *Nano Letters* **2014,** *14*, 122-126.

4) Pernot, H.; Baumert, M.; Court, F.; Leibler, L., Design and properties of co-continuous nanostructured polymers by reactive blending. *Nature Materials* **2002,** *1*, 54-58.

5) Mai, Y. Y.; Eisenberg, A., Self-assembly of block copolymers. *Chemical Society Reviews* **2012,** *41*, 5969-5985.

6) Seo, M., Robust Mesoporous Polymers Derived from Cross-Linked Block Polymer Precursors. In *Submicron Porous Materials*, 1st ed.; Bettotti, P., Ed. Springer International Publishing: Cham, Switzerland, 2017; pp 53-79.

7) Jackson, E. A.; Hillmyer, M. A., Nanoporous Membranes Derived from Block Copolymers: From Drug Delivery to Water Filtration. *Acs Nano* **2010,** *4*, 3548-3553.

8) Matsen, M. W.; Bates, F. S., Unifying weak- and strong-segregation block copolymer theories. *Macromolecules* **1996,** *29*, 1091-1098.

9) Hadziioannou, G.; Mathis, A.; Skoulios, A., Synthesis of 3-block styrene-isoprene-styrene copolymer single-crystals via plane shear-flow. *Colloid and Polymer Science* **1979,** *257*, 136-139.

10) Sinturel, C.; Vayer, M.; Morris, M.; Hillmyer, M. A., Solvent Vapor Annealing of Block Polymer Thin Films. *Macromolecules* **2013,** *46*, 5399-5415.

11) Gopinadhan, M.; Deshmukh, P.; Choo, Y.; Majewski, P. W.; Bakajin, O.; Elimelech, M.; Kasi, R. M.; Osuji, C. O., Thermally Switchable Aligned Nanopores by Magnetic-Field Directed Self-Assembly of Block Copolymers. *Advanced Materials* **2014,** *26*, 5148-5154.

12) Cochran, E. W.; Garcia-Cervera, C. J.; Fredrickson, G. H., Stability of the gyroid phase in diblock copolymers at strong segregation. *Macromolecules* **2006,** *39*, 2449-2451.

13) Seo, M.; Hillmyer, M. A., Reticulated Nanoporous Polymers by Controlled Polymerization-Induced Microphase Separation. *Science* **2012,** *336*, 1422-1425.

14) Pitet, L. M.; Amendt, M. A.; Hillmyer, M. A., Nanoporous Linear Polyethylene from a Block Polymer Precursor. *Journal of the American Chemical Society* **2010,** *132*, 8230.

15) Walker, C. N.; Bryson, K. C.; Hayward, R. C.; Tew, G. N., Wide Bicontinuous Compositional Windows from Co-Networks Made with Telechelic Macromonomers. *Acs Nano* **2014,** *8*, 12376-12385.

16) Zeng, D.; Ribbe, A.; Hayward, R. C., Anisotropic and Interconnected Nanoporous Materials from Randomly End-Linked Copolymer Networks. *Macromolecules* **2017,** *50*, 4668-4676.

17) Bates, F. S.; Fredrickson, G. H., Block copolymer thermodynamics - theory and experiment. *Annual Review of Physical Chemistry* **1990,** *41*, 525-557.

18) Rosedale, J. H.; Bates, F. S., Rheology of ordered and disordered symmetric poly(ethylenepropylene) poly(ethylethylene) diblock copolymers. *Macromolecules* **1990,** *23*, 2329-2338.

19) Bates, F. S.; Rosedale, J. H.; Fredrickson, G. H., Fluctuation effects in a symmetric diblock copolymer near the order-disorder transition. *Journal of Chemical Physics* **1990,** *92*, 6255-6270.

20) Kennemur, J. G.; Hillmyer, M. A.; Bates, F. S., Rheological Evidence of Composition Fluctuations in an Unentangled Diblock Copolymer Melt near the Order-Disorder Transition. *Acs Macro Letters* **2013,** *2*, 496-500.

21) Hickey, R. J.; Gillard, T. M.; Lodge, T. P.; Bates, F. S., Influence of Composition Fluctuations on the Linear Viscoelastic Properties of Symmetric Diblock Copolymers near the Order-Disorder Transition. *Acs Macro Letters* **2015,** *4*, 260-265.

22) Fredrickson, G. H.; Helfand, E., Fluctuation effects in the theory of microphase separation in block copolymers. *Journal of Chemical Physics* **1987,** *87*, 697-705.

23) Gillard, T. M.; Phelan, D.; Leighton, C.; Bates, F. S., Determination of the Lamellae-to-Disorder Heat of Transition in a Short Diblock Copolymer by Relaxation Calorimetry. *Macromolecules* **2015,** *48*, 4733-4741.

24) Lee, S.; Gillard, T. M.; Bates, F. S., Fluctuations, Order, and Disorder in Short Diblock Copolymers. *Aiche Journal* **2013,** *59*, 3502-3513.

25) Sakurai, S.; Iwane, K.; Nomura, S., Morphology of poly(styrene-block-butadiene-block-styrene) triblock copolymers cross-linked in the disordered state. *Macromolecules* **1993,** *26*, 5479-5486.

26) Gomez, E. D.; Das, J.; Chakraborty, A. K.; Pople, J. A.; Balsara, N. P., Effect of cross-linking on the structure and thermodynamics of lamellar block copolymers. *Macromolecules* **2006,** *39*, 4848-4859.

27) Teran, A. A.; Mullin, S. A.; Hallinan, D. T.; Balsara, N. P., Discontinuous Changes in Ionic Conductivity of a Block Copolymer Electrolyte through an Order-Disorder Transition. *Acs Macro Letters* **2012,** *1*, 305-309.

28) Jin, X. L.; Lodge, T. P., Fluctuation regime in the viscoelastic properties of block copolymer solutions. *Rheologica Acta* **1997,** *36*, 229-238.

29) Takuma, K.; Takata, T.; Endo, T., Cationic polymerization of epoxide with benzyl phosphonium salts as the latent thermal initiator. *Macromolecules* **1993,** *26*, 862–863.

30) Bertrand, A.; Hillmyer, M. A., Nanoporous Poly(lactide) by Olefin Metathesis Degradation. *Journal of the American Chemical Society* **2013,** *135*, 10918-10921.

31) Schulze, M.; Hillmyer, M. A., Tuning mesoporosity in crosslinked nanostructured thermosets via polymerization-induced microphase separation. *Macromolecules* **2017,** *50*, 997-1007.

32) Li, L.; Schulte, L.; Clausen, L. D.; Hansen, K. M.; Jonsson, G. E.; Ndoni, S., Gyroid Nanoporous Membranes with Tunable Permeability. *Acs Nano* **2011,** *5*, 7754-7766.

33) Zhou, N.; Bates, F. S.; Lodge, T. P., Mesoporous membrane templated by a polymeric bicontinuous microemulsion. *Nano Letters* **2006,** *6*, 2354-2357.

34) Jinnai, H.; Spontal, R. J., Transmission electron microtomography in polymer research. *Polymer* **2009,** *50*, 1067-1087.

35) Gor, G. Y.; Thommes, M.; Cychosz, K. A.; Neimark, A. V., Quenched solid density functional theory method for characterization of mesoporous carbons by nitrogen adsorption. *Carbon* **2012,** *50*, 1583-1590.

36) Brunauer , S.; Emmett , P. H.; Teller, E., Adsorption of Gases in Multimolecular Layers. *Journal of the american chemical society* **1938,** *60*, 309-319.

37) Werber, J. R.; Osuji, C. O.; Elimelech, M., Materials for next-generation desalination and water purification membranes. *Nature Reviews Materials* **2016,** *1*.

38) Phillip, W. A.; O'Neill, B.; Rodwogin, M.; Hillmyer, M. A.; Cussler, E. L., Self-Assembled Block Copolymer Thin Films as Water Filtration Membranes. *Acs Applied Materials & Interfaces* **2010,** *2*, 847-853.

39) Jackson, E. A.; Lee, Y.; Hillmyer, M. A., ABAC Tetrablock Terpolymers for Tough Nanoporous Filtration Membranes. *Macromolecules* **2013,** *46*, 1484-1491.

40) Phillip, W. A.; Amendt, M.; O'Neill, B.; Chen, L.; Hillmyer, M. A.; Cussler, E. L., Diffusion and Flow Across Nanoporous Polydicyclopentadiene-Based Membranes. *Acs Applied Materials & Interfaces* **2009,** *1*, 472-480.

Appendix B. Porous Materials Produced from Disordered Cylinder-forming Block Polymers

B.1 Introduction

A fundamental understanding of the order-disorder transition (ODT) in self-assembled soft materials is crucial for tailoring the design of targeted nanostructures. The complex interplay between the kinetics and thermodynamics of domain nucleation and growth has been shown to template the emergence of different metastable ordered states.[1–6] Mean-field theories predict a homogeneous and unstructured disordered state, with uncorrelated domains at the size scale of the macromolecular radius of gyration, R_g.[7] However, real systems exhibit large amplitude composition fluctuations near the ODT, resulting in the persistence of microphase segregated and nanostructured domains with short-range spatial correlations, even in the disordered state.[1,8–10] The domain structure of this fluctuating disordered state is well-documented for lamellar-forming systems, where theoretical predictions and experimental observations suggest the existence of tortuous and bicontinuous domains that topologically resemble transient patterns observed in spinodal decomposition.[1,9,11–14] There is a negligible change in the domain composition across the T_{ODT}, demonstrating that the ODT is primarily characterized by a change in interfacial curvature rather than mass transfer.[13–15] Indeed, the bicontinuous domains result from a change from zero mean and Gaussian curvature in the ordered lamellar state to zero mean curvature and negative Gaussian curvature in the disordered state.[1,16]

Recently, the disordered state for sphere-forming morphologies has also received significant attention in the literature.[2,17] Scattering, microscopy, and calorimetry techniques have revealed that spherical micelles persist in the disordered state for these systems, despite the loss in long-range translational order.[1,2,18,19] Interestingly, the size and spatial arrangement of these disordered micellar packings are believed to template the symmetry observed in the ordered state.[2] In contrast to the lamellar and spherical phases, the disordered state of cylinder-forming block polymers has been under-explored and is less well-understood. Small angle scattering experiments performed on hexagonally packed cylinder-forming diblock polymers have suggested that composition fluctuations result in a transition to undulating cylinders and ultimately to spherical micelles above T_{ODT}, although no there are no known reports that have directly imaged these systems in the disordered state.[3] Additionally, there have been few theoretical predictions focused on understanding the precise connectivity of these disordered cylindrical domains. This information could be particularly intriguing, as previous research has speculated that undulating and disordered cylindrical domains have a key role in the nucleation of the complex and often metastable network phases that are often observed near the cylinder-to-disorder transition.

B.2 Experimental Design

To directly investigate the nanostructure and domain continuity of cylinder-forming block polymers in the disordered state, we have designed a poly(styrene-*stat*-glycidyl methacrylate)-*block*-polylactide (P(S-*s*-GMA)-*b*-PLA) diblock terpolymer with a hexagonally packed cylindrical morphology, as revealed by small angle X-ray scattering,

SAXS (Figure B.1).[12] This diblock has a number average molar mass of the PLA block ($M_{n,\,PLA}$) of 11 kg mol^{-1}, a number average molar mass of the P(S-*s*-GMA) block ($M_{n,\,P(S\text{-}s\text{-}GMA)}$) of 15 kg mol^{-1}, and a molar fraction of styrene in the P(S-*s*-GMA) block (XGMA) of 0.14, and it will be subsequently referred to as P(S-*s*-GMA)-15-PLA-11-XGMA-14. The T_{ODT} was found to be ~180–185 °C by SAXS and dynamic mechanical analysis, DMA (Figures B.1 and B.2). The epoxide moieties of GMA and the thermally accessible T_{ODT} of this diblock allow it to be readily heated into the disordered state and subsequently cross-linked to kinetically trap the morphology associated with composition fluctuations.[12,20] The thermally latent cationic initiator, benzyl triphenylphosphonium hexafluoroantimonate (BTPH), was selected to controllably cure the diblock polymer, as its catalytic efficiency ensures favorable cross-linking kinetics for temperatures near T_{ODT}.[12]

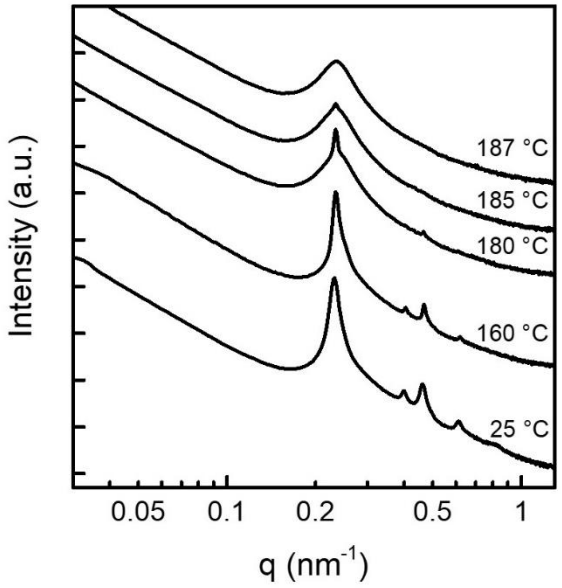

Figure B.1. Variable temperature small angle X-ray scattering patterns for P(S-*s*-GMA)-15-PLA-11-XGMA-14 after thermal equilibration at each temperature for 2 min. The sample was annealed for overnight at 100 °C prior to measurement.

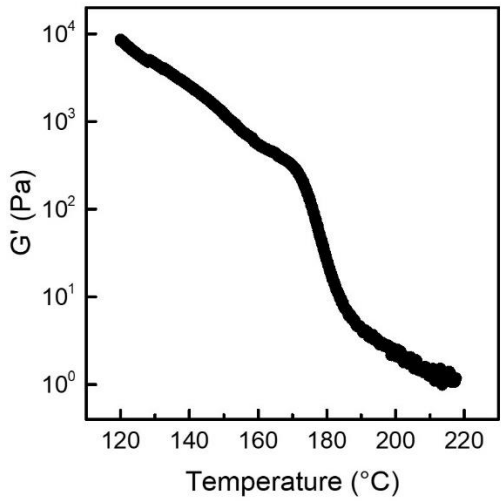

Figure B.2. Temperature dependence of the storage modulus *G′* for P(S-*s*-GMA)-15-PLA-11-XGMA-14 on heating obtained at 1 rad s^{-1}, 1% strain, and with a ramp rate of 2 °C min^{-1}. A precipitous drop in *G′* around 180 °C indicates the onset of the order-disorder transition.

B.3 Morphological Examination of Samples Cured Below and Above T_{ODT}

Monolithic samples of P(S-*s*-GMA)-15-PLA-11-XGMA-14 containing 0.3 wt.% BTPH were heated to the desired curing temperature near T_{ODT} and thermally cured. For a sample cured in the ordered state at 165 °C (T_{ODT} – 15 °C), SAXS revealed a sharp principal scattering peak and higher order peaks consistent with a hexagonally packed cylindrical morphology (Figure B.3). Following PLA removal, a high density of pores with a hexagonal symmetry was observed by SEM, consistent with the expected ordered morphology (Figure B.4).

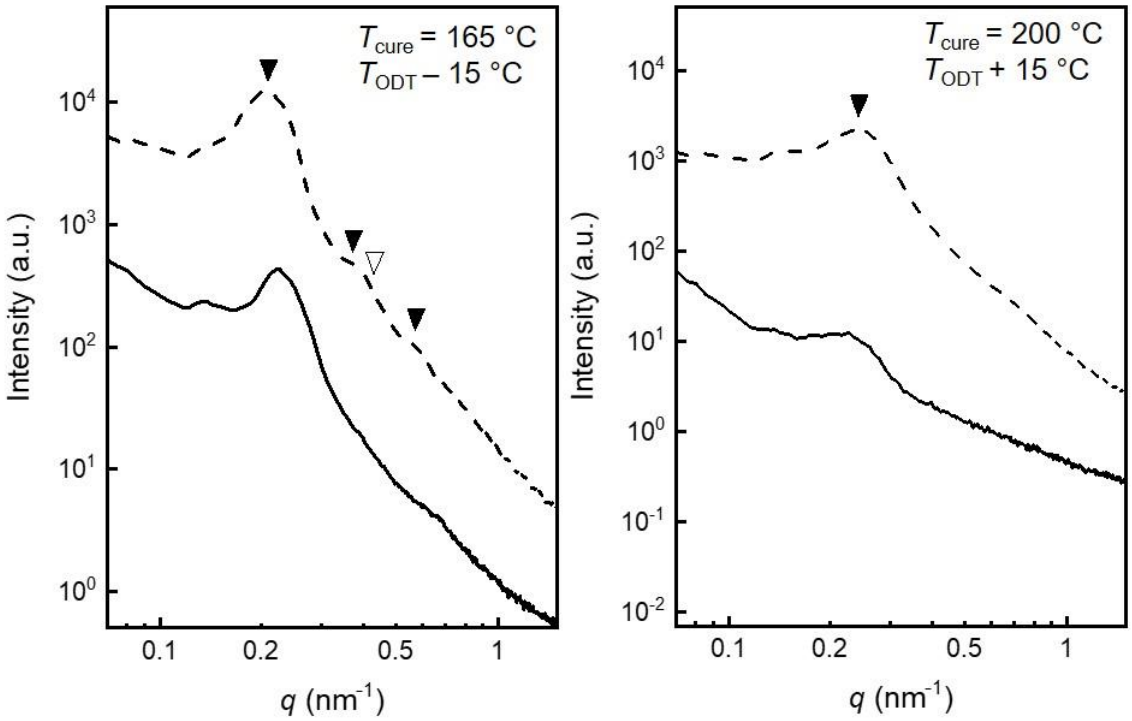

Figure B.3. Room temperature SAXS patterns obtained for P(S-*s*-GMA)-15-PLA-11-XGMA-14 + 0.3 wt.% BTPH cross-linked in the ordered state at 165 °C and in the disordered state at 200 °C. Solid curves correspond to patterns obtained prior to etching, and dashed curves correspond to patterns obtained after PLA etching.

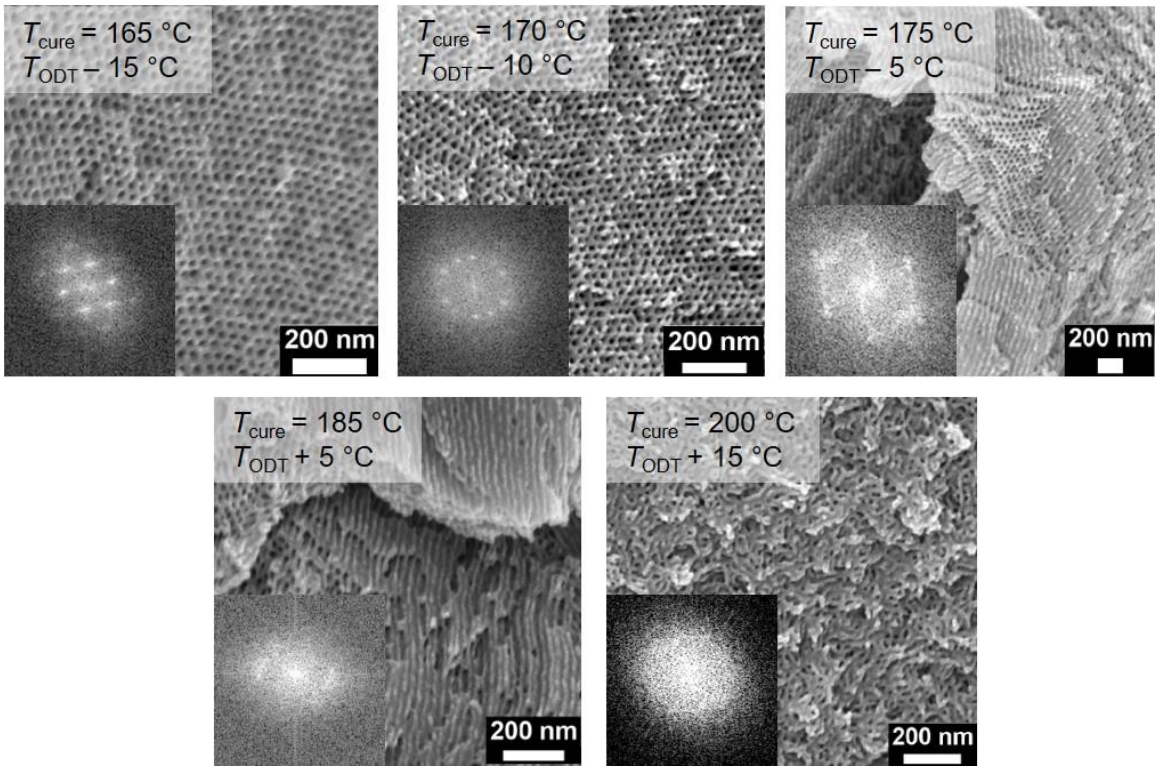

Figure B.4. SEM images obtained for P(S-*s*-GMA)-15-PLA-11-XGMA-14 + 0.3 wt.% BTPH cross-linked at 165, 175, 180, 190, and 200 °C after PLA etching. Curing temperatures, T_{cure}, for each sample are indicated on each micrograph. All samples were coated with ~2 nm of Ir prior to imaging. FFT are presented in the inset.

In contrast, a sample cured in the disordered state at 200 °C exhibited a much broader reflection by SAXS, indicating that the disordered state was kinetically trapped (Figure B.3). Removal of the PLA domains generated a porous material by SEM, consistent with the persistence of microphase segregated domains above T_{ODT} due to composition fluctuations (Figure B.4). These pores lacked the ordered symmetry observed for the sample cured below T_{ODT}, confirming that the kinetically trapped morphology was indeed disordered. The precise structure of this disordered state appears to be subtly different than the previously reported fluctuating disordered state of lamellar-forming diblock polymers, displaying a more elongated pore topology.[12,20,21] This observation is reasonably consistent

with the hypothesized undulating cylinder morphology for cylinder-forming diblocks above T_{ODT}.[3]

B.4 Domain Continuity of Disordered Cylindrical Domains

The ability to generate porous materials following PLA removal facilitates the utilization of N_2 sorption analysis as a method to more directly quantify the domain continuity in both the ordered and disordered states.[11,12] Samples cross-linked in the ordered state below T_{ODT} displayed reasonably high pore volumes and BET surface areas, consistent with continuous pores (Figure B.5). This observation is notably different from the lack of porosity that was previously observed for ordered lamellar diblocks, which was attributed to pore collapse stemming from the mechanically unstable free-standing lamellar sheets.[12,22] In contrast, the cross-linked matrix is well connected and able to support the pores for this ordered cylindrical system.

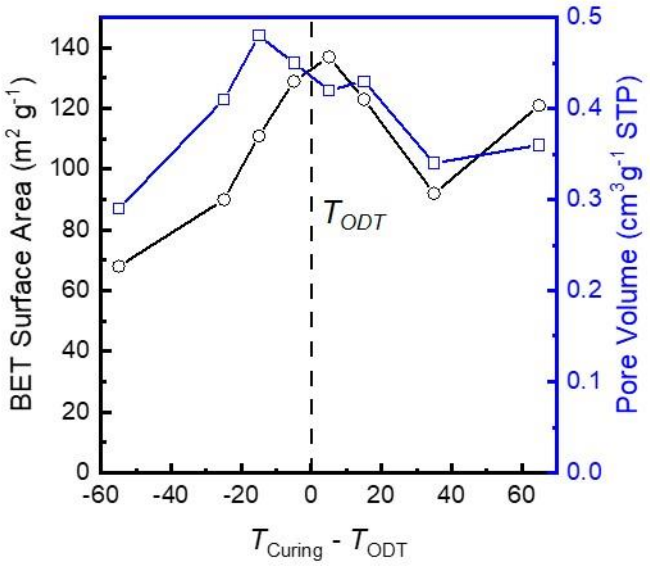

Figure B.5. BET surface area (black curve) and pore volume (blue curve) for P(S-*s*-GMA)-15-PLA-11-XGMA-14 + 0.3 wt.% BTPH cross-linked at various temperatures relative to T_{ODT} following PLA etching. The relative curing temperatures ($\Delta T = T_{curing} - T_{ODT}$) is indicated on the x-axis.

The porosity remained high for all samples cross-linked in the disordered state, with reasonably similar BET surface areas obtained across the ODT. These results indicate that the microphase segregated minority domains remain continuous in the disordered state due to composition fluctuations. Therefore, we expect that these domains are more likely to resemble undulating and distorted cylinders rather than randomly packed spherical micelles, at least for this range of temperatures above the T_{ODT}.[3]

The reasonably constant porosity observed for all samples, regardless of whether they were cured in the ordered or the disordered state, suggests that the ordered and the fluctuating disordered states have similar degrees of domain continuity for cylinder-forming block polymers. This is consistent with previous observations that the ionic conductivity remained constant across the ODT for a salt-doped PS-*b*-PEO block polymer with a hexagonally packed cylinder morphology.[23] Calorimetry experiments have also revealed that there is a much smaller enthalpy associated with a cylinder-to-disorder transition than with a lamellar-to-disorder transition.[1] The enthalpy of the lamellar-to-disorder transition has been speculated to reflect differences in interfacial curvature between the lamellar and fluctuating disordered states.[1] Extension of this hypothesis suggests that the cylinder-to-disorder transition results in a smaller change in the domain topology as compared to a lamellar-forming system. This hypothesis is generally consistent with the observations reported here, which clearly demonstrate that the porosity and thus the degree of domain continuity generally remains constant across the ODT. In effect, these results reflect an ODT that may be described as a transition from ordered and well-defined cylindrical domains to distorted and undulating cylindrical domains. The investigation of curing

temperatures even farther above T_{ODT} as well as further developments in tomographic imaging methods may provide additional insights into this point.

B.5 References

1) Lee, S.; Gillard, T.; Bates, F. Fluctuations, Order, and Disorder in Short Diblock Copolymers. *AIChE* **2013**, *59* (9), 3502–3513.

2) Kim, K.; Arora, A.; Lewis, R. M.; Liu, M.; Li, W.; Shi, A.-C.; Dorfman, K. D.; Bates, F. S. Origins of Low-Symmetry Phases in Asymmetric Diblock Copolymer Melts. *Proc Natl Acad Sci USA* **2018**, *115* (5), 847.

3) Bates, F. S.; Koppi, K. A.; Tirrell, M.; Almdal, K.; Mortensen, K. Influence of Shear on the Hexagonal-to-Disorder Transition in a Diblock Copolymer Melt. *Macromolecules* **1994**, *27* (20), 5934–5936.

4) Matsen, M. W.; Bates, F. S. Origins of Complex Self-Assembly in Block Copolymers. *Macromolecules* **1996**, *29* (23), 7641–7644.

5) Wickham, R. A.; Shi, A.-C.; Wang, Z.-G. Nucleation of Stable Cylinders from a Metastable Lamellar Phase in a Diblock Copolymer Melt. *J. Chem. Phys.* **2003**, *118* (22), 10293–10305.

6) Bohbot-Raviv, Y.; Wang, Z.-G. Discovering New Ordered Phases of Block Copolymers. *Phys. Rev. Lett.* **2000**, *85* (16), 3428–3431.

7) Leibler, L. Theory of Microphase Separation in Block Copolymers. *Macromolecules* **1980**, *13* (6), 1602–1617. \

8) Bates, F. S.; Rosedale, J. H.; Fredrickson, G. H.; Glinka, C. J. Fluctuation-Induced First-Order Transition of an Isotropic System to a Periodic State. *Phys. Rev. Lett.* **1988**, *61* (19), 2229–2232.

9) Bates, F. S.; Rosedale, J. H.; Fredrickson, G. H. Fluctuation Effects in a Symmetric Diblock Copolymer near the Order–disorder Transition. *The Journal of Chemical Physics* **1990**, *92* (10), 6255–6270.

10) Frederickson, G.; Helfland, E. Fluctuation Effects in the Theory of Microphase Separation in Block Copolymers. *J. Chem. Phys* **1987**, *87* (1), 697–705. \

11) Hampu, N.; Hillmyer, M. A. Molecular Engineering of Nanostructures in Disordered Block Polymers. *ACS Macro Lett.* **2020**, 382–388.

12) Vidil, T.; Hampu, N.; Hillmyer, M. A. Nanoporous Thermosets with Percolating Pores from Block Polymers Chemically Fixed above the Order–Disorder Transition. *ACS Cent. Sci.* **2017**.

13) Yadav, M.; Bates, F. S.; Morse, D. C. Network Model of the Disordered Phase in Symmetric Diblock Copolymer Melts. *Phys. Rev. Lett.* **2018**, *121* (12), 127802.

14) Medapuram, P.; Glaser, J.; Morse, D. Universal Phenomenology of Symmetric Diblock Copolymers near the Order−Disorder Transition. *Macromolecules* **2015**, *48*, 819–839.

15) Qin, J.; Grzywacz, P.; Morse, D. Renormalized One-Loop Theory of Correlations in Disordered Diblock Copolymers. *The Journal of Chemical Physics* **2011**, *135* (8), 84902.

16) Hickey, R. J.; Gillard, T. M.; Irwin, M. T.; Lodge, T. P.; Bates, F. S. Structure, Viscoelasticity, and Interfacial Dynamics of a Model Polymeric Bicontinuous Microemulsion. *Soft Matter* **2016**, *12* (1), 53–66. https://doi.org/10.1039/C5SM02009C.

17) Kim, K.; Schulze, M. W.; Arora, A.; Lewis, R. M.; Hillmyer, M. A.; Dorfman, K. D.; Bates, F. S. Thermal Processing of Diblock Copolymer Melts Mimics Metallurgy. *Science* **2017**, *356* (6337), 520.

18) Gillard, T. M.; Phelan, D.; Leighton, C.; Bates, F. S. Determination of the Lamellae-to-Disorder Heat of Transition in a Short Diblock Copolymer by Relaxation Calorimetry. *Macromolecules* **2015**, *48* (13), 4733–4741.

19) Rosedale, J. H.; Bates, F. S. Rheology of Ordered and Disordered Symmetric Poly(ethylenepropylene)-Poly(ethylethylene) Diblock Copolymers. *Macromolecules* **1990**, *23* (8), 2329–2338.

20) Hampu, N.; Hillmyer, M. A. Temporally Controlled Curing of Block Polymers in the Disordered State Using Thermally Stable Photoacid Generators for the Preparation of Nanoporous Membranes. *ACS Appl. Polym. Mater.* **2019**, *1* (5), 1148–1154.

21) Hampu, N.; Bates, M. W.; Vidil, T.; Hillmyer, M. A. Bicontinuous Porous Nanomaterials from Block Polymers Radically Cured in the Disordered State for Size-Selective Membrane Applications. *ACS Appl. Nano Mater.* **2019**.

22) Bertrand, A.; Hillmyer, M. A. Nanoporous Poly(lactide) by Olefin Metathesis Degradation. *J. Am. Chem. Soc.* **2013**, *135* (30), 10918–10921.

23) Wanakule, N. S.; Panday, A.; Mullin, S. A.; Gann, E.; Hexemer, A.; Balsara, N. P. Ionic Conductivity of Block Copolymer Electrolytes in the Vicinity of Order−Disorder and Order−Order Transitions. *Macromolecules* **2009**, *42* (15), 5642–5651.

Appendix C. Design of Low T_g Block Polymers for the In-Situ and Time-Resolved Visualization of Composition Fluctuations by TEM

[7]

C.1 Introduction

Disordered state composition fluctuations in block polymers represent transient patterns that oscillate in time.[1–4] At a given time point, these fluctuations have been postulated to result in a co-continuous nanostructure that resembles the late stages of spinodal decomposition.[1,3–5] These co-continuous domains present an interesting structural motif for a number of applications which require unimpeded mass and/or charge transport over macroscopic length scales.[6–8] Previous work has focused on kinetically trapping the disordered state by cross-linking or vitrifying block polymers above T_{ODT}.[8–11] Such approaches effectively freeze an otherwise transient pattern upon the initiation of the cross-linking reaction or vitrification process. This enables the use of a number of ex-situ characterization techniques, such as scanning electron microscopy (SEM), small angle X-ray scattering (SAXS), transmission electron microtomography (TEMT), and nitrogen sorption analysis, to probe the morphology of the fluctuating disordered state. These methods have confirmed the co-continuous nature of the fluctuating disordered state and have reveled subtle morphological variations as a function of segregation strength, χN.[8,10]

[7] This work was performed in collaboration with Dr. Subhajit Kundu, who performed the TEM experiments, and Prof. K. Andre Mkhoyan, who supervised the TEM experiments. Bongjoon Lee assisted with TEM sample preparation.

However, the transient nature of composition fluctuations implies that the nanostructure is constantly evolving with time, while the kinetically trapped nanostructures only represent a snapshot at a given time.[3] Additionally, these curing strategies are kinetic in nature with an associated time scale that reflects the elapsed time between the onset of the curing process and gelation.[9,10] The complex interplay between the kinetics of gelation and composition fluctuations likely results in a pattern that represents a time-averaged superposition of a number of different states. Consequently, the development of new characterization techniques will facilitate the analysis of the evolving nanostructure in real time.

Previous work has attempted to analyze the time scale of composition fluctuations using rheological measurements. Time-temperature superposition of rheological frequency sweeps revealed the collective dynamics of the fluctuating domains.[5,12,1] Nanoscale diffusion experiments, such as pulsed field gradient nuclear magnetic resonance spectroscopy (PFG-NMR), have also been used to correlate the diffusion of isotopically labelled polymer chains to the precise nanostructure of the disordered state.[13–16] These studies have demonstrated that tortuous and continuous domains exist at the nanoscale, consistent with the findings from kinetically trapped systems. Recently, X-ray photon correlation spectroscopy (XPCS) has been used to investigate the diffusion of composition fluctuations at the length scale of the self-assembled domains.[17–19] All of these previous studies have advanced the fundamental understanding of the dynamics of composition fluctuations. However, none of those techniques provide direct visualization of the

nanostructure. Therefore, the development of advanced microscopy methods that enable domain visualization at the nanoscale in real time with precise temperature and environmental control would be powerful. Recently, there has been significant progress in the development of protocols for imaging soft materials in their natural environment using liquid cell transmission electron microscopy (LC-TEM).[20–23] Previous studies involving the use of LC-TEM for polymeric systems have focused on the growth and transformation of micelles and vesicles in the solution state.[20,22,23] Here, we attempt to expand upon the principals developed for these solution state systems to directly monitor composition fluctuations in the melt state of block polymers using temperature controlled TEM.

C.2. Synthetic Design of Block Polymers Appropriate for In-situ TEM

To directly image a block polymer melt in-situ using TEM, a number of different criteria must be addressed in the synthetic design of the polymer. First, the T_{ODT} must be thermally accessible, meaning the block polymer must remain thermally stable above T_{ODT} *and* the TEM sample stage can be readily heated above T_{ODT}.[8,11] This generally requires χN to be sufficiently low, which can be achieved by using less strongly segregating polymers (lower χ) or lower polymer molar masses (lower N).[10] The latter is especially challenging from a practical perspective, as the size of the microphase segregated domains must be large enough to easily visualize by TEM. Consequently, identifying a polymer pair with a relatively low χ is crucial for accessing the T_{ODT} for systems with a sufficiently high N. Block architecture also significantly impacts the T_{ODT}, as a diblock polymer disorders below $\chi N \sim 10$ while a triblock disorders below $\chi N \sim 17$.[24,25] As a result, for a given molar mass and composition, a diblock polymer will have a higher T_{ODT} than an analogous

triblock. Additionally, the glass transition temperature, T_g, imposes a lower limit on the T_{ODT}. Therefore, a block polymer with a low T_g will enable lower T_{ODT}'s to be attained, mitigating the risk of thermal degradation. Finally, electron contrast is a major challenge in imaging soft materials at the nanoscale. Most polymers comprise similarly light elements (carbon, oxygen, hydrogen), which results in a low Z-contrast and difficulties in distinguishing between different domains. This challenge is often addressed by selectively staining one of the domains with a heavy metal, such as osmium tetroxide, to improve Z-number contrast,[26,27] but the effect that these heavy metals will have on the thermodynamics and kinetics of the block polymer domains is unknown. Therefore, this approach is undesirable for the present study. To address this challenge, we aim to design a block polymer where one domain comprises a heavier element, such as silicon, to provide inherent Z-number contrast without the need to selectively stain with metals.[28]

With these design considerations in mind, we focused our synthesis on block polymers derived from polydimethylsiloxane (PDMS). The siloxane backbone of PDMS contains Si atoms to provide inherent TEM contrast and long Si-O bonds that result in a low T_g.[28] Additionally, PDMS derivatives with mono or difunctional end groups are commercially available, enabling the rapid synthesis of a library of block polymer molecules with varying molar masses, chemistries, and block architectures. Of particular interest are PDMS polymers with mono and dihydroxyl end-functionalities, as these polymers can be used as macroinitiators for the ring-opening polymerization of lactone monomers to generate a variety of diblock and triblock polymers.[29] We have chosen to focus on derivatives of δ-

valerolactone due to their low *T*g's and the ability to precisely tune χ through the selection of the side chain length.[30]

Two different PDMS molar masses (5 and 10 kg mol^{-1}) along with two different end-functionalities (mono and dihydroxyl) were selected for initial screening. Additionally, three different derivatives of δ-valerolactone (δ-hexalactone, δ-octalactone, and δ-decalactone) were selected for the other block, ensuring that χ can be precisely tuned through the judicious selection of the side chain length (methyl, ethyl, and pentyl side chains, respectively). All of these δ-valerolactone derivatives have T_g's around ~-55 °C, so a broad range of T_{ODT}'s are possible.[30] All lactone polymerizations were performed in a N_2 filled glovebox using a PDMS-OH macroinitiatior and 1,5,7-triazabicyclo[4.4.0]dec-5-ene (TBD) as a catalyst (Figure C.1).[30] Polymer molar mass and composition was determined using ^{1}H NMR, and dispersity was determined using MALS-SEC (Table C.1). The polymers ranged from liquid oils to soft, waxy solids, depending upon the molar mass and morphology.

Table C.1. Summary of PDMS-based diblock and triblock polymers

Polyester	**Polymer**	**Molar Mass (kg mol^{-1})**	f_{PDMS}	**Morphology**	T_{ODT} **(°C)**
PδHL	HSH(4-10-4)	18	0.54	HEX	140
	HSH(6-10-6)	22	0.49	Unknown	>200
PδOL	OS(5-5)	10	0.49	LAM	>200
	OSO(4-5-4)	14	0.46	DIS	<25
	OSO(5-10-5)	20	0.49	LAM	150
PδDL	DS(6-5)	11	0.53	LAM	150
	DS(10-10)	20	0.51	LAM	>200
	DSD(2.5-5-2.5)	10	0.52	DIS	<-50
	DSD(5-10-5)	20	0.52	LAM	80
	DSD(6-10-6)	22	0.49	LAM	140
	DSD(7-10-7)	24	0.45	LAM	160

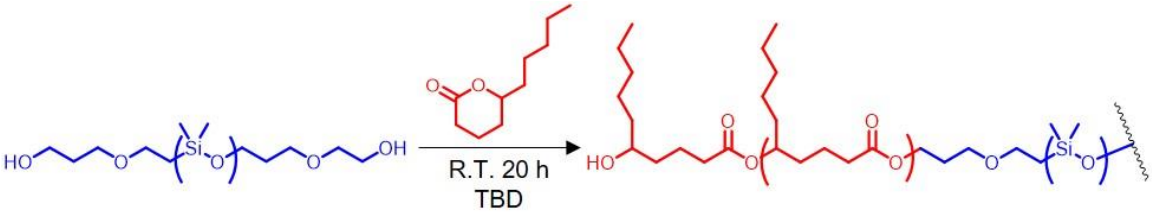

Figure C.1. Representative synthesis of a PδDL-*b*-PDMS-*b*-PδDL triblock polymer from a hydroxy-telechelic PDMS macroinitiator. By varying the PDMS end-functionality and the lactone side chain length, a series of block polymers were synthesized.

C.3 Determination of Morphology and T_{ODT}

The morphology and T_{ODT} of the block polymers were determined using a combination of dynamic mechanical analysis (DMA) and variable temperature SAXS. For a given block polymer molar mass and lactone chemistry, the T_{ODT} of the diblock architecture was observed to be higher than the corresponding triblock, consistent with the higher $(\chi N)_{ODT}$ for triblock polymers. For example, a 10 kg mol^{-1} PδDL-*b*-PDMS-*b*-PδDL triblock, DSD(2.5-5-2.5), was disordered at all temperatures, while the T_{ODT} of a 10 kg mol^{-1} PDMS-*b*-PδDL diblock, DS(5-5), was 160 °C (Figure C.2). The T_{ODT} of DS(5-5) was even higher than a triblock with double the overall molar mass, DSD(5-10-5), which had a T_{ODT} of 70 °C (Figure C.3). Additionally, for a given molar mass and block architecture, block polymers synthesized from δ-valerolactone derivatives with longer side chains resulted in lower T_{ODT}'s, reflecting a decrease in χ with an increase in side chain length. For example, the T_{ODT} of a 10 kg mol^{-1} PDMS-*b*-PδOL diblock, OS(5-5), was > 200 °C, while the T_{ODT} of a 10 kg mol^{-1} PDMS-*b*-PδDL diblock, DS(5-5), was 160 °C (Figure C.2). These results indicate that the T_{ODT} can be precisely tuned across a wide range of temperatures through subtle variations in lactone chemistry, block architecture, and molar mass. Therefore, the entire range of segregation strengths ranging from mean-field disordered to fluctuating

disordered to strongly ordered can be readily obtained and characterized by TEM within an appropriate temperature range.

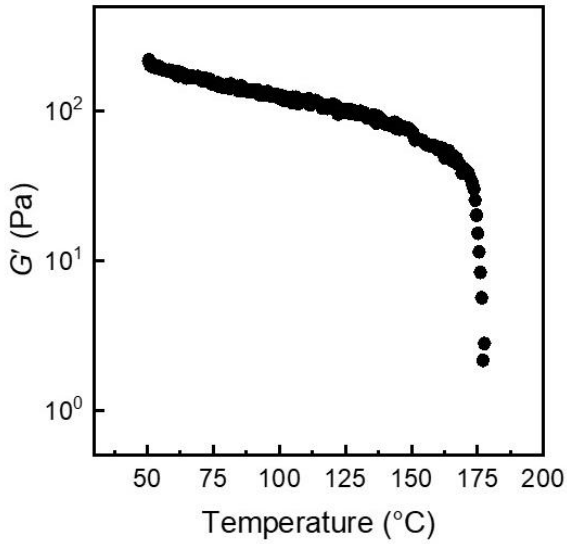

Figure C.2. Temperature dependence of the storage modulus G' for DS(5-5) on heating obtained at 1 rad s^{-1}, 1% strain, and with a ramp rate of 2 °C min^{-1}. A precipitous drop in G' around 160 °C indicates an order-disorder transition.

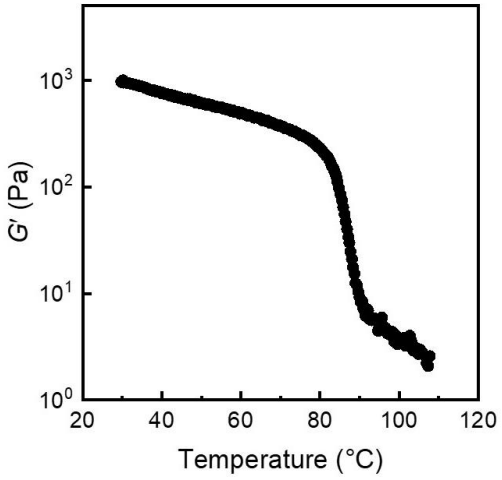

Figure C.3. Temperature dependence of the storage modulus G' for DSD(5-10-5) on heating obtained at 1 rad s^{-1}, 1% strain, and with a ramp rate of 2 °C min^{-1}. A precipitous drop in G' around 80 °C indicates an order-disorder transition.

The morphology and domain size of these block polymers were then analyzed using SAXS. Block polymer morphology was first identified from scattering patterns obtained at room temperature. DS(5-5) exhibited a strong principal scattering peak along with subsequent

higher order scattering peaks at integer multiples of q^*, consistent with the lamellar morphology expected for $f_{PDMS} \sim 0.5$ (Figure C.4). In contrast, DSD(2.5-5-2.5) displayed a single broad scattering peak, consistent with a disordered morphology and reflecting the low χN of this system. Interestingly, DSD(5-10-5) exhibited a doubling of the expected lamellar scattering peaks, suggesting the co-existence of lamellar domains of slightly different size (Figure C.5). This observation was unexpected and suggests that DSD(5-10-5) likely contains a non-negligible amount of diblock polymer impurity. Indeed, the commercial HO-PDMS-OH macroinitatiors used in this work likely also contain PDMS-OH. This diblock polymer impurity unexpectedly appears to immiscible with the corresponding triblock at the domain scale, as indicated by the twin sets of lamellar scattering peaks.[31–33]

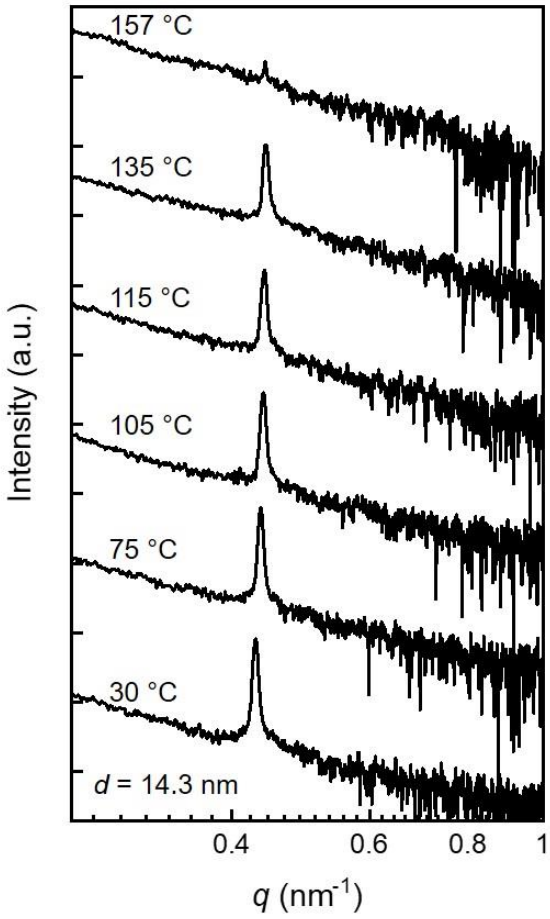

Figure C.4. Variable temperature small angle X-ray scattering patterns for DS(5-5) after thermal equilibration at each temperature for 2 min.

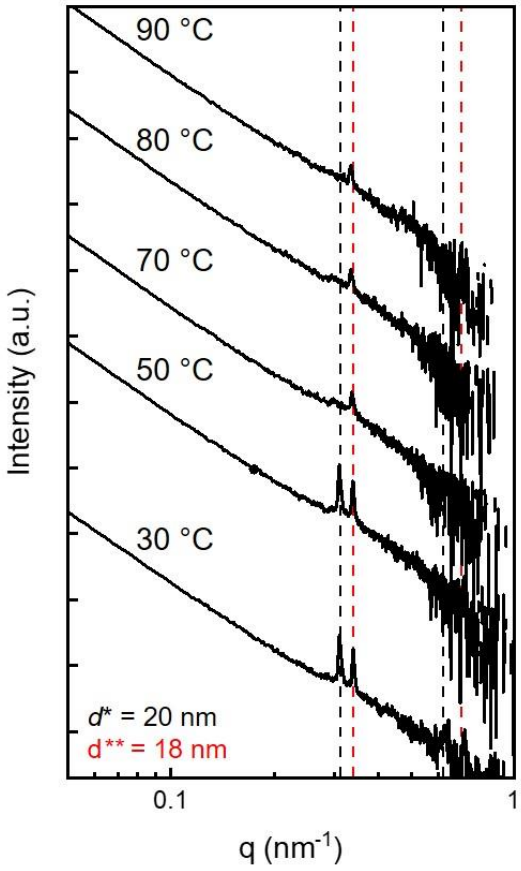

Figure C.5. Variable temperature small angle X-ray scattering patterns for DSD(5-10-5) after thermal equilibration at each temperature for 2 min.

After establishing the morphology of each block polymer, the temperature dependence of the morphology was examined using variable temperature SAXS. The T_{ODT} of each ordered block polymer was determined based upon the broadening of the principal scattering peaks.[1] The T_{ODT} of the lamellar-forming diblock polymers determined by SAXS was reasonably similar to the T_{ODT} determined by DMA, consistent with expectations.

The triblock polymers that exhibited co-existing lamellae at room temperature displayed similar behavior to the diblock polymers, albeit with some notable differences. As was observed for the diblocks, the T_{ODT} by SAXS was consistent with the results obtained from

DMA. However, as the temperature was increased in the ordered state, the initially twinned sets of lamellar reflections merged into a single set of peaks (Figure C.5). This behavior suggests that the initially co-existing lamellae mix at elevated temperatures to form lamellae with a single periodicity. The twinned sets of lamellar peaks reappeared upon cooling from above T_{ODT}, indicating that this morphology likely reflects a thermodynamic phenomenon rather than a kinetically trapped metastable state.

C.4. In-situ TEM Characterization

TEM micrographs represent a two-dimensional projection of three-dimensional space. This introduces a number of challenges in sample preparation and imaging. For example, a block polymer film that is thicker than the domain periodicity and contains unoriented lamellae will result in a micrograph that reflects a superimposition of several misoriented domain periods.[34] Therefore, the thickness of the block polymer film must be on the order of the domain spacing to ensure that the lamellae are oriented perpendicular to the interface through the entire film. This is often achieved by microtoming a bulk sample to produce film thicknesses on the order of several nanometers. The low T_g block polymers investigated in this study present an additional challenge, as they must be microtomed at cryogenic temperatures and immediately transferred to the TEM grid. If the sample remains at room temperature for too long, the viscoelastic nature of the polymer and the unfavorable polymer-surface interactions will result in the polymer dewetting from the grid, eventually forming a thick droplet rather than the desired thin film. Consequently, the TEM grids must be stored in a freezer between sample preparation and sample imaging to ensure that the sample remains sufficiently thin to image through the entire thickness.

This method was used to prepare a sample of the triblock polymer DSD(5-10-5) for TEM imaging. As a proof-of-concept, the sample was first imaged at room temperature (Figure C.6). Sheet-like features consistent with the expected lamellar morphology were observed. Two different domain periodicities were obtained from FFT analysis, 14 and 15 nm (Figure C.7), which were reasonably consistent with the co-existing domain periodicities of 18 and 20 nm observed in SAXS. The slightly smaller periodicity observed by TEM may reflect that several misoriented lamellae are projected in the micrograph.[34] Additionally, a closer inspection of the TEM micrograph revealed features that resemble perforations in the lamellar sheets, which could reflect the superimposition of multiple layers of misoriented lamellae. Alternatively, it could reflect that the co-existing lamellar domains observed in SAXS are mutually orthogonal.

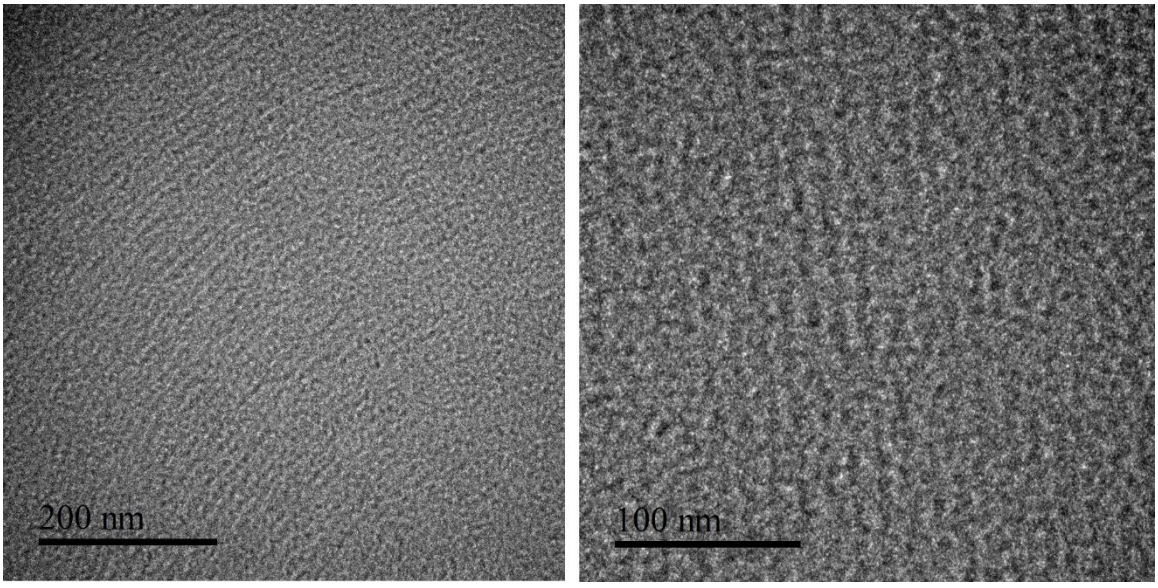

Figure C.6. TEM micrographs of DSD(5-10-5) obtained at ambient temperature. The samples were cryomicrotomed and mounted onto a carbon coated Cu grid for imaging.

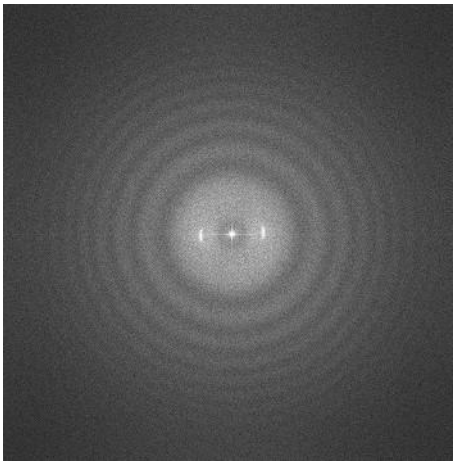

Figure C.7. FFT of the TEM micrographs of DSD(5-10-5) presented in Figure C.6. Domain periodicities of 14 and 15 nm were observed, as indicated by the arced white spots.

Similar room temperature experiments were performed for DS(5-5). High magnification micrographs displayed a disordered morphology with a periodicity of ~3 nm, inconsistent with the ordered lamellae with a periodicity of 14 nm observed in SAXS (Figure C.8). Lower magnification micrographs revealed significant terracing in the block polymer film, indicating that the presence of multiple lamellar periods in the TEM micrograph (Figure C.9). Since the lamellae in this diblock are expected to be isotropically arranged, the micrographs obtained at high magnification likely represent a superimposition of misoriented lamellae across several periods. The resulting projection thus contains features from each of these lamellar periods and thus the morphology appears disordered due to experimental artifacts. Challenges in obtaining uniformly thin and flat films from phase pure block polymers ultimately limited the progress of this project, particularly considering that the variable temperature TEM sample holder requires a high degree of precision in sample mounting. However, the PDMS and aliphatic polyester blocks displayed sufficient electron contrast to image in TEM without staining, and the tunability of the synthesis enables the targeted design of the desired nanostructure. Continued progress in developing

and refining the sample preparation and TEM protocols may enable composition fluctuations to be imaged in-situ.

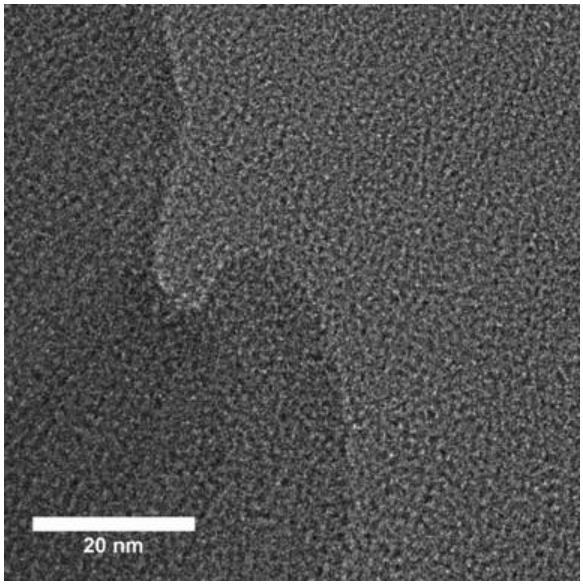

Figure C.8. TEM micrographs of DS(5-5) obtained at ambient temperature. The samples were cryomicrotomed and mounted onto a carbon coated Cu grid for imaging.

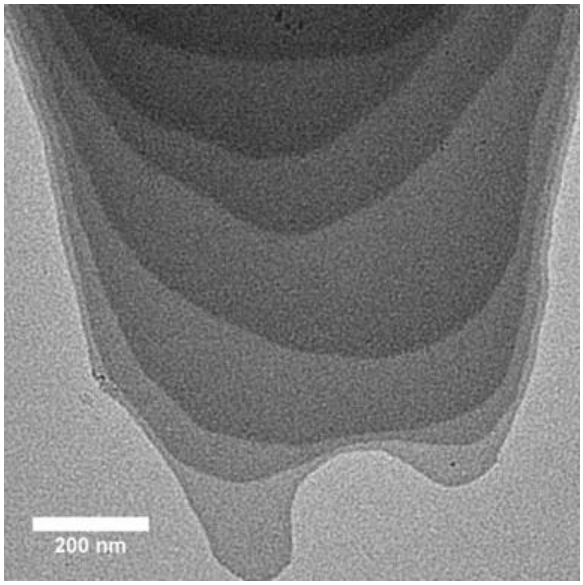

Figure C.9. TEM micrographs of DS(5-5) obtained at ambient temperature. The samples were cryomicrotomed and mounted onto a carbon coated Cu grid for imaging. The micrograph was obtained at a lower magnification than Figure C.8.

C.5 References

1) Bates, F. S.; Rosedale, J. H.; Fredrickson, G. H. Fluctuation Effects in a Symmetric Diblock Copolymer near the Order–disorder Transition. *The Journal of Chemical Physics* **1990**, *92*, 6255–6270.

2) Bates, F. S.; Rosedale, J. H.; Fredrickson, G. H.; Glinka, C. J. Fluctuation-Induced First-Order Transition of an Isotropic System to a Periodic State. *Phys. Rev. Lett.* **1988**, *61*, 2229–2232.

3) Yadav, M.; Bates, F. S.; Morse, D. C. Network Model of the Disordered Phase in Symmetric Diblock Copolymer Melts. *Phys. Rev. Lett.* **2018**, *121*, 127802.

4) Lee, S.; Gillard, T.; Bates, F. Fluctuations, Order, and Disorder in Short Diblock Copolymers. *AIChE* **2013**, *59*, 3502–3513.

5) Hickey, R. J.; Gillard, T. M.; Irwin, M. T.; Lodge, T. P.; Bates, F. S. Structure, Viscoelasticity, and Interfacial Dynamics of a Model Polymeric Bicontinuous Microemulsion. *Soft Matter* **2016**, *12*, 53–66.

6) Seo, M.; Hillmyer, M. A. Reticulated Nanoporous Polymers by Controlled Polymerization-Induced Microphase Separation. *Science* **2012**, *336*, 1422.

7) Schulze, M. W.; McIntosh, L. D.; Hillmyer, M. A.; Lodge, T. P. High-Modulus, High-Conductivity Nanostructured Polymer Electrolyte Membranes via Polymerization-Induced Phase Separation. *Nano Lett.* **2014**, *14*, 122–126.

8) Vidil, T.; Hampu, N.; Hillmyer, M. A. Nanoporous Thermosets with Percolating Pores from Block Polymers Chemically Fixed above the Order–Disorder Transition. *ACS Cent. Sci.* **2017**, *3*, 1114-1120.

9) Hampu, N.; Hillmyer, M. A. Temporally Controlled Curing of Block Polymers in the Disordered State Using Thermally Stable Photoacid Generators for the Preparation of Nanoporous Membranes. *ACS Appl. Polym. Mater.* **2019**, *1*, 1148–1154.

10) Hampu, N.; Hillmyer, M. A. Molecular Engineering of Nanostructures in Disordered Block Polymers. *ACS Macro Lett.* **2020**, *9*, 382–388.

11) Hampu, N.; Bates, M. W.; Vidil, T.; Hillmyer, M. A. Bicontinuous Porous Nanomaterials from Block Polymers Radically Cured in the Disordered State for Size-Selective Membrane Applications. *ACS Appl. Nano Mater.* **2019**, *2*, 4567-4577.

12) Rosedale, J. H.; Bates, F. S. Rheology of Ordered and Disordered Symmetric Poly(ethylenepropylene)-Poly(ethylethylene) Diblock Copolymers. *Macromolecules* **1990**, *23*, 2329–2338.

13) Dalvi, M. C.; Lodge, T. P. Diffusion in Block Copolymer Melts: The Disordered Region and the Vicinity of the Order-Disorder Transition. *Macromolecules* **1994**, *27*, 3487–3492.

14) Gröger, S.; Rittig, F.; Stallmach, F.; Almdal, K.; Štěpánek, P.; Papadakis, C. M. A Pulsed Field Gradient Nuclear Magnetic Resonance Study of a Ternary Homopolymer/diblock Copolymer Blend in the Bicontinuous Microemulsion Phase. *J. Chem. Phys.* **2002**, *117*, 396–406.

15) Rittig, F.; Kärger, J.; Papadakis, C. M.; Fleischer, G.; Almdal, K.; Štěpánek, P. Self-Diffusion in a Lamellar and Gyroid (Ordered) Diblock Copolymer Investigated Using Pulsed Field Gradient NMR. *Macromolecules* **2001**, *34*, 868–873.

16) Nose, T. Pulsed-Field-Gradient NMR Studies of the Diffusion of Chain Molecules in Polymer Matrices. In *Annual Reports on NMR Spectroscopy*; Webb, G. A., Ed.; Academic Press, 1993; Vol. 27, pp 217–253.

17) Lewis, R. M.; Jackson, G. L.; Maher, M. J.; Kim, K.; Lodge, T. P.; Mahanthappa, M. K.; Narayanan, S.; Bates, F. S. A New Framework for X-Ray Photon Correlation Spectroscopy Analysis from Polycrystalline Materials. *Review of Scientific Instruments* **2018**, *89*, 123902.

18) Patel, A. J.; Narayanan, S.; Sandy, A.; Mochrie, S. G. J.; Garetz, B. A.; Watanabe, H.; Balsara, N. P. Relationship between Structural and Stress Relaxation in a Block-Copolymer Melt. *Phys. Rev. Lett.* **2006**, *96*, 257801.

19) Patel, A. J.; Mochrie, S.; Narayanan, S.; Sandy, A.; Watanabe, H.; Balsara, N. P. Dynamic Signatures of Microphase Separation in a Block Copolymer Melt Determined by X-Ray Photon Correlation Spectroscopy and Rheology. *Macromolecules* **2010**, *43*, 1515–1523.

20) Parent, L. R.; Bakalis, E.; Ramírez-Hernández, A.; Kammeyer, J. K.; Park, C.; de Pablo, J.; Zerbetto, F.; Patterson, J. P.; Gianneschi, N. C. Directly Observing Micelle Fusion and Growth in Solution by Liquid-Cell Transmission Electron Microscopy. *J. Am. Chem. Soc.* **2017**, *139*, 17140–17151.

21) Parent, L. R.; Bakalis, E.; Proetto, M.; Li, Y.; Park, C.; Zerbetto, F.; Gianneschi, N. C. Tackling the Challenges of Dynamic Experiments Using Liquid-Cell Transmission Electron Microscopy. *Acc. Chem. Res.* **2018**, *51*, 3–11.

22) Touve, M. A.; Figg, C. A.; Wright, D. B.; Park, C.; Cantlon, J.; Sumerlin, B. S.; Gianneschi, N. C. Polymerization-Induced Self-Assembly of Micelles Observed by Liquid Cell Transmission Electron Microscopy. *ACS Cent. Sci.* **2018**, *4*, 543–547.

23) Ianiro, A.; Wu, H.; van Rijt, M. M. J.; Vena, M. P.; Keizer, A. D. A.; Esteves, A. C. C.; Tuinier, R.; Friedrich, H.; Sommerdijk, N. A. J. M.; Patterson, J. P. Liquid–liquid Phase Separation during Amphiphilic Self-Assembly. *Nature Chemistry* **2019**, *11*, 320–328.

24) Matsen, M. W.; Schick, M. Lamellar Phase of a Symmetric Triblock Copolymer. *Macromolecules* **1994**, *27*, 187–192.

25) Leibler, L. Theory of Microphase Separation in Block Copolymers. *Macromolecules* **1980**, *13*, 1602–1617.

26) Sakamoto, N.; Hashimoto, T. Ordering Dynamics of a Symmetric Polystyrene-Block-Polyisoprene. 2. Real-Space Analysis on the Formation of Lamellar Microdomain. *Macromolecules* **1998**, *31*, 3815–3823.

27) Sakurai, S.; Iwane, K.; Nomura, S. Morphology of Poly(styrene-Block-Butadiene-Block-Styrene) Triblock Copolymers Cross-Linked in the Disordered State. *Macromolecules* **1993**, *26*, 5479–5486.

28) Hsieh, I.-F.; Sun, H.-J.; Fu, Q.; Lotz, B.; Cavicchi, K. A.; Cheng, S. Z. D. Phase Structural Formation and Oscillation in Polystyrene-Block-Polydimethylsiloxane Thin Films. *Soft Matter* **2012**, *8*, 7937–7944.

29) Rodwogin, M. D.; Spanjers, C. S.; Leighton, C.; Hillmyer, M. A. Polylactide−Poly(dimethylsiloxane)−Polylactide Triblock Copolymers as Multifunctional Materials for Nanolithographic Applications. *ACS Nano* **2010**, *4*, 725–732.

30) Schneiderman, D. K.; Hillmyer, M. A. Aliphatic Polyester Block Polymer Design. *Macromolecules* **2016**, *49*, 2419–2428.

31) Mickiewicz, R. A.; Ntoukas, E.; Avgeropoulos, A.; Thomas, E. L. Phase Behavior of Binary Blends of High Molecular Weight Diblock Copolymers with a Low Molecular Weight Triblock. *Macromolecules* **2008**, *41*, 5785–5792.

32) Hashimoto, T.; Yamasaki, K.; Koizumi, S.; Hasegawa, H. Ordered Structure in Blends of Block Copolymers. 1. Miscibility Criterion for Lamellar Block Copolymers. *Macromolecules* **1993**, *26*, 2895–2904.

33) Yamaguchi, D.; Hasegawa, H.; Hashimoto, T. A Phase Diagram for the Binary Blends of Nearly Symmetric Diblock Copolymers. 2. Parameter Space of Temperature and Blend Composition. *Macromolecules* **2001**, *34*, 6506–6518.

34) Haugan, I. N.; Lee, B.; Maher, M. J.; Zografos, A.; Schibur, H. J.; Jones, S. D.; Hillmyer, M. A.; Bates, F. S. Physical Aging of Polylactide-Based Graft Block Polymers. *Macromolecules* **2019**, *52*, 8878–8894.